



## NEW PERSPECTIVES IN NANOCATALYSIS USING DESIGN OF EXPERIMENTS

Olivia Benkirane

**ADVERTIMENT.** L'accés als continguts d'aquesta tesi doctoral i la seva utilització ha de respectar els drets de la persona autora. Pot ser utilitzada per a consulta o estudi personal, així com en activitats o materials d'investigació i docència en els termes establerts a l'art. 32 del Text Refós de la Llei de Propietat Intel·lectual (RDL 1/1996). Per altres utilitzacions es requereix l'autorització prèvia i expressa de la persona autora. En qualsevol cas, en la utilització dels seus continguts caldrà indicar de forma clara el nom i cognoms de la persona autora i el títol de la tesi doctoral. No s'autoritza la seva reproducció o altres formes d'explotació efectuades amb finalitats de lucre ni la seva comunicació pública des d'un lloc aliè al servei TDX. Tampoc s'autoritza la presentació del seu contingut en una finestra o marc aliè a TDX (framing). Aquesta reserva de drets afecta tant als continguts de la tesi com als seus resums i índexs.

**ADVERTENCIA.** El acceso a los contenidos de esta tesis doctoral y su utilización debe respetar los derechos de la persona autora. Puede ser utilizada para consulta o estudio personal, así como en actividades o materiales de investigación y docencia en los términos establecidos en el art. 32 del Texto Refundido de la Ley de Propiedad Intelectual (RDL 1/1996). Para otros usos se requiere la autorización previa y expresa de la persona autora. En cualquier caso, en la utilización de sus contenidos se deberá indicar de forma clara el nombre y apellidos de la persona autora y el título de la tesis doctoral. No se autoriza su reproducción u otras formas de explotación efectuadas con fines lucrativos ni su comunicación pública desde un sitio ajeno al servicio TDR. Tampoco se autoriza la presentación de su contenido en una ventana o marco ajeno a TDR (framing). Esta reserva de derechos afecta tanto al contenido de la tesis como a sus resúmenes e índices.

**WARNING.** Access to the contents of this doctoral thesis and its use must respect the rights of the author. It can be used for reference or private study, as well as research and learning activities or materials in the terms established by the 32nd article of the Spanish Consolidated Copyright Act (RDL 1/1996). Express and previous authorization of the author is required for any other uses. In any case, when using its content, full name of the author and title of the thesis must be clearly indicated. Reproduction or other forms of for profit use or public communication from outside TDX service is not allowed. Presentation of its content in a window or frame external to TDX (framing) is not authorized either. These rights affect both the content of the thesis and its abstracts and indexes.

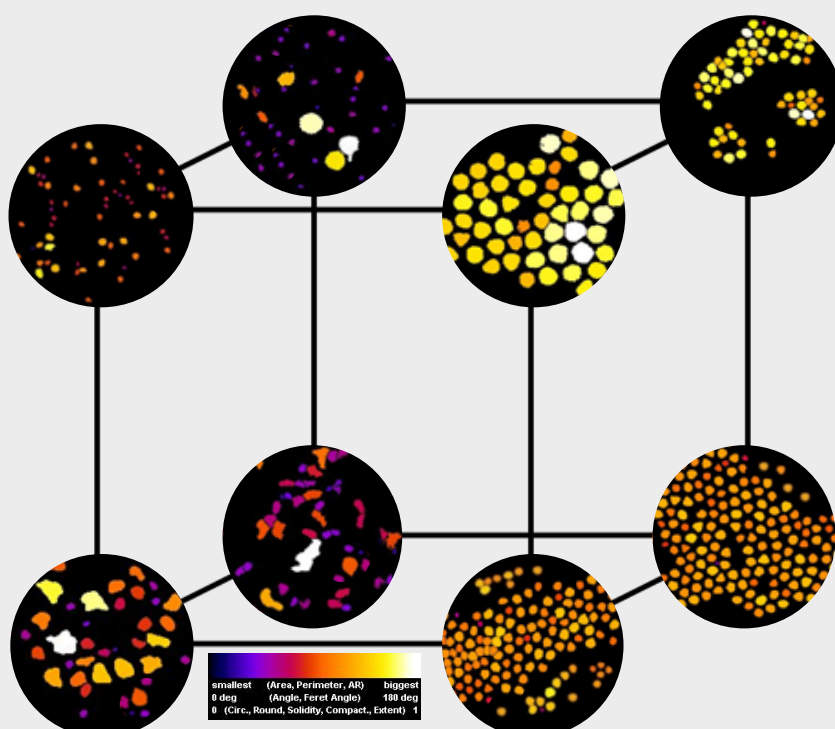


UNIVERSITAT  
ROVIRA I VIRGILI

# New perspectives in nanocatalysis using design of experiments

---

OLIVIA MAJDOULINE BENKIRANE



DOCTORAL THESIS  
2018









Olivia Majdouline Benkirane

# New perspectives in nanocatalysis using design of experiments

Doctoral Thesis

Supervised by:  
Prof. Carmen Claver  
Dr. Cyril Godard



UNIVERSITAT  
ROVIRA i VIRGILI

DEPARTMENT OF PHYSICAL AND INORGANIC  
CHEMISTRY



CENTRE TECNOLÒGIC DE LA QUÍMICA



TOTAL RESEARCH & TECHNOLOGY FELUY

TARRAGONA  
2018





UNIVERSITAT  
ROVIRA I VIRGILI

FACULTY OF CHEMISTRY  
DEPARTMENT OF PHYSICAL AND INORGANIC  
CHEMISTRY  
C/ Marcel·lí Domingo, s/n  
Edifici N4  
43007 Tarragona (Spain)  
[http://www.fq.urv.cat/en\\_index/](http://www.fq.urv.cat/en_index/)

I STATE that the present study, entitled “New perspectives in nanocatalysis using design of experiments” presented by Olivia Majdouline Benkirane for the award of the degree of Doctor, has been carried out under my supervision at the Departement of Physical and Inorganic Chemistry of this university.

Tarragona, 30<sup>th</sup> September 2018

Doctoral Thesis Supervisor/s

Prof. Carmen Claver

Dr. Cyril Godard

The presented work has been developed with a Martí Franquès scholarship (2015PMF-PIPF-69). It has been possible thanks to the funding of:

- Total Raffinage Chimie through the projects TQC13035S and TQC15043S.
- El Ministerio de Educación y Ciencia (MEDU) through the project CTQ2016-75016-R.
- La Agència de Gestió d'Ajuts Universitaris i de Recerca (AGAUR) through the project 2014 SGR 670.



*À ma famille*

*A David,*



## Acknowledgments

Primero quisiera dar las gracias a mis supervisores de tesis: Carmen Claver y Cyril Godard por haberme dado la oportunidad de desarrollar este trabajo de doctorado en su grupo de investigación. Carmen gracias por tus consejos, tu positividad ante cualquier situación y por valorar mi trabajo. Cyril gracias por haberme guiado, aconsejado y transmitido tus conocimientos a lo largo de esta etapa.

Luego, quería agradecer a Daniel Curulla-Ferré por ofrecerme la posibilidad de realizar mi estancia de tesis en Total. Una etapa en la que crecí mucho profesionalmente. Gracias por haberme transmitido tus conocimientos, métodos de trabajo y por introducirme al mundo del diseño de experimentos. Gracias por todos los consejos, el apoyo, los ánimos en esta recta final. Gracias por valorar mi trabajo y ayudarme a confiar en mis capacidades.

No puc parlar de disseny d'experiments sense fer un agraïment a Joan Ferré. Gràcies per ensenyar-me l'art d'aquesta metodologia, per la teva disponibilitat davant de qualsevol dubte o reunió d'última hora i per tots els consells i gran ajuda.

Gracias también al profesorado del departamento que me ha transmitido sus conocimientos y consejos a lo largo de esta tesis: Anna Masdeu, Aurora Ruiz, Pilar Salagre y Sergio Castellón. Por los mismos motivos gracias al profesorado de la etSEQ: Carlos Pozo, Daniel Montané, Frank Stüber, Josep María Mateo, Laureano Jiménez, Manuel Martínez y Sylvana Varela.

También quería dar enormes gracias a Elena Fernández. Gracias por haberme ayudado a llegar hasta aquí y por acogerme en tus clases de organometálicos durante mis primeros meses de tesis. Gracias por todos tus preciosos consejos, tu apoyo, por la ilusión y la positividad que transmites siempre.



Gracias a los miembros del equipo de gestión del CTQ por la disponibilidad y hacer que mi estancia haya sido agradable en el centro: Claude García, Josep María Montornés, Fernando Torres, Pablo Ramos y Víctor Márquez.

Gracias a los miembros del Servei que me han enseñado, ayudado y aconsejado acerca de distintas técnicas de caracterización durante el desarrollo de este proyecto: Antonio, Deborah, Francesc, Lukas, Mariana, Mercè y Rita.

Quería agradecer también al equipo de trabajo con el que he compartido la vida en el CTQ y la URV durante estos tres años: Aitor, Benedetta, Bernat, Bianca, Dolores, Fran, Isabel, Itziar, Jordi, Jorge, Miriam, Myriam, Mercè, Mimmo, Mónica, Montse, Nanette, Raquel, Rita, Sara G., Sara P. y Toni.

En particular gracias Jorge haberme transmitido tus conocimientos sobre el mundo de las nanos y por enseñarme lo que tenía que saber para poder desarrollar mi trabajo de la mejor forma. Gracias por ayudarme con los rompecabezas de los reactores y por tu disponibilidad.

También gracias Montse y Raquel por vuestra eficiencia en resolver cualquier problema relacionado con el laboratorio y hacer que el trabajo en ello sea más fácil. Gracias por vuestro apoyo tanto a nivel profesional que personal.

Benedetta, thank you for sharing with me all the good and the bad moments of the PhD life, the nice coffee break downstairs and our discussions on our way back. Thanks for teaching me chemistry (sometimes), Instagram and useful italian words!!!! Hope in a few I will introduce you to the dark side of the experimentation (DOE). I wish you the best for the end of your thesis!

Sara, que año hemos compartido, mi mañana favorita! Ha sido un placer poder compartir estos momentos contigo! Gracias por la ayuda de última hora, por animarte más que yo a la hora de depositar la tesis y por transmitir siempre positividad! Espero poder compartir pronto un finde en tus tierras!

Dolores, a pesar de haber compartido pocos meses juntas, has sido una de las primeras personas con quien hablé al llegar aquí. Me ayudaste muchísimo compartiendo conmigo tu experiencia y dándome consejos acerca de esta etapa que es el doctorado. Gracias también por la ayuda en el ICIQ con las caracterizaciones! Me alegro mucho haberte conocido y haber podido disfrutar de muchos momentos juntas fuera del CTQ.

Merci Myriam pour le soutien, pour les bons moments passés ensemble et nos discussions interminables ! Ce sera bientôt ton tour, je te souhaite plein de courage pour la fin et n'hésite pas si tu as besoin d'aide sur les nanos maintenant que tu as mit la main à la pâte !

Mimmo, gracias por alegrarnos el día siempre con tu sonrisa y tu cariño. Gracias por la ayuda, el apoyo y todos estos buenos momentos que hemos pasado juntos.

Pour finir je souhaiterais transmettre mes remerciements à trois étudiants de Toulouse qui ont partagé la vie du CTQ pendant quelques mois le temps d'un stage: Marion Duval, Clément Molinet et Suzanne Lachaux. Merci pour votre aide au sein du laboratoire. Merci pour toutes les nanoparticules mesurées, pour toutes les synthèses effectuées et pour tous les réacteurs montés. Sans vous le travail n'aurait pas avancé aussi vite.

Merci aux équipes du CRBC et SCC de Total pour votre accueil chaleureux, vos précieux conseils et votre aide durant mon séjour à Feluy : Alessandro Chieragato, Anne Massinon, Bart Vandegehuchte, Chantal Diverchy, Cindy Aquino, Daniel Feront, Delphine Minoux, Elena Borodina, Eric Killens, Filippo Fragale, Jacques Lachambre, Joseph Stewart, Luc Delattre, Moritz Schreiber, Nikolai Nesterenko, Olivier Miserque, Philippe Mathieux, Philippe Schouppe, Roxanne Noteboom, Virginie Olivanti et Yong Ly Tea.

A special thanks to Bart, Elena, Joseph and Moritz for the interesting talks about chemistry, the afterwork good moments and the daily carpooling to Feluy.

Egalement un grand merci à Virginie pour ton aide au sein du laboratoire et pour toutes les synthèses que tu as effectué.

Merci également aux membres du département analyses de TRTF: Christophe Cucuzzella, Cindy Saliez, Isabella Perotti, Michael Laplanche et Sylvie Ligot. En particulier, Christophe merci de m'avoir transmis tes connaissances sur le traitement d'images et analyses de TEM. Tout ce que j'ai appris avec toi m'a été très utile pour la fin de ma thèse.

To finish, thank you to Angela, Florian, Ivan and Ravi for all the good moments spent together during this stay in Total.

Quería dar las gracias a otro equipo en el que he formado parte durante esta etapa. A pesar de que no tenga que ver con la química, me ayudó mucho a desconectar de largos días de laboratorio y a volver con las pilas cargadas al día siguiente. Este equipo es el del Taller. Gracias a mis profes: Maribel, Gemma, Diana, Katia, Raquel, Jan, Álvaro por transmitirme vuestra pasión por el arte, confiar en mí y haberme dado la oportunidad de bailar en grandes escenarios. Un particular gracias a Gemma por la paciencia, por darme la oportunidad de acompañarte en la barra del balcón, por haber podido disfrutar de clases particulares de puntas contigo y por las horas extras de Gyrotonic. Aprendí muchísimo en tus clases y espero poder seguir haciéndolo pronto! También Diana gracias por haberme introducido al mundo del contempo, por transmitirme este respeto al arte, por haberme ayudado a confiar en mi calidades de bailarina y por haberme enseñado tanto en tan poco tiempo!

Gracias a mis queridas compañeras de batalla: Nuría, Alba, Marta, Elena y Carmen. Gracias por todos estos momentos compartidos dentro y fuera de un escenario. Un particular gracias a Marta que aparte del baile, me salvaste la vida con los TGA de última hora!! Gracias Nuría por estar siempre a mi lado, animarme y apoyarme en todo. Mi vida en Tarragona cambió cuando empezamos a formar este dúo, te quería dar las gracias por ello! Pronto le

volveremos a dar caña, ya tengo proyectos en mente... y inspiración...! Alba, el bebe del equipo y la otra ingeniera!! Gracias por tu alegría, tu cariño, tu risa comunicativa y por ser como eres! Gracias por todo el apoyo y los ánimos!!

Merci à mes perles de l'ENSIC d'avoir été là malgré la distance: Shasha, Mimi, Matmat et Cyril. Les filles merci de m'avoir soutenu dans cette étape, pour ces skypes nocturnes entre Paris, Montréal et Tarragone qui redonnent la patate ! Merci pour ces fous rires aigus qui font mal aux abdos et que je ne peux avoir avec personne d'autre que vous. Vous êtes irremplaçables et sans vous je ne serai pas arrivé jusqu'ici. On m'avait dit que les meilleures amitiés se font durant une thèse, mais mon avis c'est que rien ne surpassera l'ENSIC <3 ! Je vous aime fort !!! Matmat et Cyril, merci pour ces week-end de déconnexion aux quatre coins de l'Europe à faire des selfies bougie, faire la sardine sur la plage, manger de la glace comme des enfants, chouffer le soleil, goûter au salmojero, savourer un bon jamón et un rabo de toro sans savoir ce que s'est!

Quería dar mil gracias a la familia Fernández-Linares: Rosario, Enrique y Daniel por acogerme con los brazos abiertos y por hacer que la vida lejos de los míos sea mucho más agradable. Gracias por todo vuestro amor, apoyo, ánimos y por transmitirme vuestra positividad siempre.

J'aimerais dédier cette thèse à ma famille: Papa, Maman, Romain, Alexandre, Mamie, Guillain, Antoine, Tata, Eric, Charlotte et Raphaël. Je vous aime tous énormément et j'aimerais vous remercier pour votre soutien malgré les quelques kilomètres qui nous séparent. Vous m'avez tous beaucoup manqué pendant cette étape.

أبي،

كنت أول من عرف أنني شرعت في. تحضير الدكتوراة. كنت أول من هتأني بهذا الخبر  
كنت دائما فخور ومعتز بي، أنا ابنتك شكرا على دعمك لي المتواصل في هذه المرحلة ،  
و كذلك في باقي المحطات كنت دائما تؤمن بقدراتي و تشجعني، تحبني وتعزني جدا  
شكرا، شكرا، احبك أبي

Ma petite Maman, merci m'avoir toujours soutenu, de m'avoir (trop) bien éduquée, de m'avoir appris les valeurs de l'effort et du respect, de m'avoir transmis ton courage et ton goût pour l'art. Merci d'être un exemple de persévérance et pour ta patience avec nous tous ! C'est dur d'être loin de toi, merci pour nos heures passées au téléphone et merci d'avoir fait plusieurs fois le voyage pour partager des bons moments ensemble et de prendre soin de moi. Merci aussi de m'envoyer les dernières bêtises de ma grosse folle, elle redonne toujours la pêche !!

Merci Mamie et Guillaïn de m'avoir toujours soutenu, d'être fiers de votre petite fille et de m'avoir rendu visite partout où je suis partie travailler ! Vous êtes l'exemple que la deuxième jeunesse existe et qu'elle se croque à pleine dents. Merci de nous montrer que la vie est faite pour en profiter avec des voyages, de la bonne bouffe et surtout des bons moment en famille !

Romain et Alexandre, que vous dire ?! Mes piliers, mes références, mes exemples. Je réclamais une sœur à maman étant petite mais je n'avais pas compris que je n'en avais pas besoin car j'avais déjà les deux meilleurs grands frères que je n'avais jamais pu imaginer ! Je vous aime énormément. Merci pour tout. Merci d'avoir toujours prit soin de moi, de me soutenir, de m'aider pour tout et rien à la fois, simplement merci d'être là pour votre petite sœur chiante ! Merci aussi à Chacha de supporter Romain au quotidien ☺ et d'avoir apporté une vague de tranquillité dans la famille !

Raphaël, tu ne seras pas encore capable de lire ces mots mais je voulais te dire que je suis fière de t'avoir comme neveu. Tu as apporté de la joie dans la

famille et tes sourires me font oublier tout le reste, ils m'ont beaucoup aidé à tenir bon pendant l'écriture de cette thèse. Ici, on t'a rebaptisé «smiley baby»

Tata, tu es comme notre troisième grand-mère. Merci pour tous ces étés passés à Fressin à nous apprendre avec tonton à faire mille et une choses : la cuisine, le bricolage, le jardinage, à jouer aux acteurs pendant une nuit et aussi les devoirs !!! Merci pour nous avoir inculqué les valeurs du travail et du respect qui nous ont aidés à arriver jusqu'ici. Eric, merci de nous avoir appris que dans la vie, si on n'est pas content, faut râler !!! Sans rire, merci d'avoir pris soin de nous depuis petits, de nous faire rire et de récupérer nos chocolats à la liqueur !!! J'espère que tu seras fier de ta poussinette.

Merci à Moue, malgré la distance et les difficultés de communications, tu sais toujours nous transmettre ton amour et, au fond, je sais que tu es fière de tes petits enfants français.

Para terminar esta tesis va dedicada a David. Siempre te digo que sin ti probablemente no hubiera empezado esta aventura, pero lo que me olvido decirte es que sin ti tampoco la hubiese acabado. Gracias por haberme ayudado tanto, apoyado, animado, por hacerme reír, por tener paciencia conmigo y por haberme aguantado estos últimos meses que han sido difíciles. Gracias por compartir la vida conmigo y por estar aquí siempre tanto en los buenos que en los malos momentos. Pronto disfrutaremos juntos y bien orgullosos de haber llegado ambos a la cima de esta montaña. Te quiero.



## Summary

In the last decades, the modern society has been confronted to new challenges: preserve the planet resources while facing the current increase of energy demand. In this sense, the sustainable use of resources became an important ecological issue and, to reduce the impact of human beings on the environment, it is important to rethink our lifestyle. From an industrial point of view, it is traduced by the improvement of the manufacturing processes. For instance, the use of active and selective heterogeneous catalysts appears as an essential tool to minimize the formation of non-recyclable waste. Among the most commonly applied catalytic processes, the semi-hydrogenation of alkynes into alkenes has been the object of particular attention for its relevance in the petrochemicals, polymer and fine chemical industries. Indeed the selection of appropriate heterogeneous catalysts derives in productivity improvements preventing over-hydrogenation and/or oligomerization issues.

This PhD thesis deals with the synthesis and characterization of novel catalysts prepared by colloidal approach for their application in selective hydrogenation reactions. Design of experiments methodology was used to improve the experimentation efficiency and to provide robustness in the conclusions.

There are several contributions derived from this thesis. The first one is the synthesis of novel colloidal Pd nanoparticles (NPs). This study proposes an efficient planning of experiments, the use of a statistical test to demonstrate the reproducibility of different syntheses as well as an improvement of the analytical treatment of the data obtained by Transmission Electron Microscopy (TEM).



In a first phase, a screening of different polymer and surfactant stabilizers was performed to attempt the well-formation of Pd NPs under one set of reaction conditions. Then, after the selection of polyacrylamide as the most promising stabilizing agent, a “One-Factor-At-a-Time” (OFAT) study was detailed to assess the effects of several parameters on the Pd NPs formation. The synthesis temperature, time and polymer-to-Pd ratio were identified as key factors to control the NPs distribution, however no significant variation of size was observed. A well-defined scalable recipe of Pd-polyacrylamide NPs of *ca.* 3.7 nm was delivered. At this point, the reproducibility of this recipe was demonstrated by means of statistical Kolmogorov Smirnov test.

After that, a deeper analysis of the effect of each parameter and their interactions on the studied Pd-polyacrylamide NPs was provided applying a DOE approach. In this second phase, it has been possible to improve the NPs shape and distribution as well as to increase the synthesis efficiency with a combination of short synthesis time, low temperature, low polymer-to-Pd ratio, low Pd concentration and high stirring rate.

Finally, to ensure sustainability of industrial catalytic processes, the use of supported catalysts is usually preferred. That is why, in a last phase of the study, these Pd NPs were impregnated on different supports: activated carbon, aluminum oxide and titanium oxide. One pot and two-step syntheses were tested. The effect of the immobilization process, parameter of synthesis, the nature of the support, Pd content and scale of the synthesis on the Pd NPs size and dispersion were studied. Pd NPs size was affected by the reaction temperature and the support using the one pot methodology while it remained constant in the two-step syntheses. In addition, NPs agglomeration on the supports decreased drastically when the two-step syntheses were scaled up.

The second contribution of this thesis constitutes one of the first applications of Design Of Experiments (DOE) in the field of nanoparticles synthesis. This study shows that an appropriate design of experiments can considerably reduce the number of syntheses to be carried out and consequently the material, human and financial resources while generating a large amount of information. This methodology was applied to the complex synthesis of Pd NPs stabilized by hexadecyl(2-hydroxyethyl)dimethylammonium dihydrogenphosphate (HHDMA), that is used to prepare the commercial Pd Nanoselect catalyst patented by BASF. A structure-synthesis relationship study was performed and analyses of variance (ANOVA) were used to identify the significant factor contributions. Empirical models that describe the experimental data were provided. High amount of parameters and interactions were highlighted.

Afterwards, the third contribution consists in a kinetic study of the 1-octyne hydrogenation in stirred tank reactor. The objective was to compare the performances of polyacrylamide catalysts (prepared in two steps) with a commercial reference (Pd Nanoselect LF 200). These catalysts were studied with 24 catalytic tests that follow experimental designs (DOE). The 1-octyne concentration, hydrogen pressure and reaction temperature were varied according to factorial designs. The effects of these parameters on the 1-octyne conversion and reaction rate were studied and the kinetic parameters of each of the studied catalysts were obtained. The newly synthesized Pd-polyacrylamide catalysts were less active than the commercial reference (Pd Nanoselect LF 200). Different performances were also observed for the Pd-polyacrylamide catalysts depending on the pressure and temperature conditions.

The performances of two other Pd-polyacrylamide catalysts prepared by one pot synthesis were then compared to the three Pd-polyacrylamide catalysts

prepared by two steps and the reference under one set of reaction conditions (as the traditional OFAT study). The one pot catalyst supported on activated carbon revealed higher activity than all the other polyacrylamide catalysts but still lower than the reference. The differences in activity were attributed to the immobilization methodology and the nature of the support.

Summarizing, this thesis offers a analysis on the design of new Pd-based nanocatalysts for application in alkyne semi-hydrogenation reactions. It proposes the use of, not recent but not widely used, practical and efficient methodologies to provide robustness and confidence to the experimental conclusions.

## Résumé

Depuis plusieurs décennies, notre société est confrontée à un nouveau défi : faire face à la croissance des besoins énergétiques tout en sauvegardant les ressources de la planète. La préservation des ressources est devenue un enjeu écologique majeur et, afin de réduire l'impact de l'homme sur l'environnement, il est important de repenser notre mode de vie. D'un point de vue industriel, ceci se traduit par une amélioration de nos procédés de fabrication. Par exemple, l'utilisation de catalyseurs hétérogènes actifs et sélectifs est devenue un outil essentiel pour réduire la formation de déchets non recyclables. Parmi les procédés catalytiques les plus courants, l'hydrogénation sélective des alcynes en alcènes a fait l'objet d'une attention particulière pour sa pertinence dans les industries pétrochimiques, de polymères et de chimie fine. En effet, le choix de catalyseurs appropriés dans cette réaction permet d'améliorer son rendement en évitant la formation de sous-produits par hydrogénation et / ou oligomérisation.

L'objectif de cette thèse de doctorat est de mener à bien la synthèse et caractérisation de nouveaux catalyseurs préparés par approche colloïdale pour leur application dans des réactions d'hydrogénation sélective. Aussi, pour améliorer l'efficacité de l'expérimentation et aboutir à des conclusions robustes, l'étude a été menée suivant des plans d'expériences («Design Of Experiments», DOE).

Plusieurs contributions découlent de cette thèse. La première consiste en la synthèse de nouvelles nanoparticules colloïdales de Pd. Cette étude propose un planning efficace des expériences, l'utilisation d'un test statistique pour démontrer la reproductibilité de différentes synthèses ainsi qu'une amélioration du traitement analytique des données obtenues par microscopie («Transmission Electron Microscopy», TEM).

Dans une première phase, différents stabilisants (polymères et tensioactifs) ont été testés pour la synthèse de nanoparticules de Pd en utilisant un même ensemble de conditions de réaction : le polyacrylamide s'est révélé être le plus prometteur. La suite de l'étude a consisté à évaluer les effets de plusieurs paramètres de synthèse sur la formation des nanoparticules par la méthode OFAT «One-Factor-At-a-Time» («une variable à la fois»). La température, le temps et le rapport molaire entre le polyacrylamide et le Pd ont été identifiés comme des paramètres clés pour le contrôle de la distribution des nanoparticules. Aucune variation significative de leur taille n'a cependant été observée. Une recette de nanoparticules d'environ 3.7 nm avec une fine distribution a été obtenue. Sa reproductibilité a été validée par un test de Kolmogorov-Smirnov.

Une analyse plus approfondie de l'effet de chaque paramètre et de leurs interactions a été réalisée en utilisant un plan d'expérience (DOE). Dans cette deuxième phase, il a été possible d'améliorer la forme et la distribution des nanoparticules ainsi que d'augmenter l'efficacité de la synthèse grâce à une combinaison de temps de synthèse court, basse température, faible rapport molaire de polymère et de Pd, faible concentration de Pd et vitesse d'agitation élevée.

Pour assurer une durabilité des procédés catalytiques industriels, l'utilisation de catalyseurs supportés est souvent préférée. C'est pourquoi, dans une dernière phase, ces nanoparticules de Pd ont été imprégnées sur différents support : charbon actif, oxyde d'aluminium et oxyde de titane. Les méthodes «One pot» (une étape) et «Two steps» (deux étapes) ont été testées. Les effets du procédé d'immobilisation, des paramètres de synthèse, de la nature du support, de la teneur en Pd et de l'échelle de la synthèse sur la taille et la dispersion des nanoparticules ont été étudiés. La taille s'est avérée être affectée par la température de réaction et la nature du support lorsque l'imprégnation s'est réalisée en une étape («One pot»). Au contraire,

l'immobilisation en deux étapes («Two steps») n'a pas montré d'influence significative sur la taille des nanoparticules. Par ailleurs, l'agglomération des nanoparticules sur les supports a considérablement diminué dans les synthèses de deux étapes effectuées à grande échelle.

La seconde contribution de cette thèse consiste en l'utilisation des plans d'expériences (DOE) de manière plus approfondie pour la synthèse de nanoparticules. Cette étude montre qu'un plan d'expériences approprié permet de réduire considérablement le nombre de synthèses à réaliser, et par conséquent les ressources matériels, humaines et financières, tout en générant une grande quantité d'informations. Cette méthodologie a été appliquée à la synthèse de nanoparticules de Pd stabilisées par le hexadecyl(2-hydroxyethyl)dimethylammonium dihydrogenphosphate (HHDMA) utilisées pour la préparation du catalyseur commercial Pd Nanoselect breveté par BASF. Une étude de la relation structure-synthèse a été réalisée et des analyses de variance (ANOVA) ont été utilisées afin d'identifier les contributions significatives des paramètres étudiés. Une grande quantité de paramètres et d'interactions ont été identifiés comme importants pour le contrôle de la forme, taille et distribution des nanoparticules ainsi que l'efficacité de la synthèse démontrant la complexité du système étudié. Cette étude a permis de postuler des modèles empiriques permettant de décrire le comportement du système dans la zone d'étude.

La troisième contribution est une étude cinétique de l'hydrogénation du 1-octyne menée à bien dans un réacteur à cuve agitée. L'objectif était la comparaison des performances des catalyseurs de polyacrylamide (préparés en deux étapes) avec une référence commerciale (Pd Nanoselect LF 200). Pour cela, quatre catalyseurs ont été étudiés par le biais de vingt-quatre tests catalytiques suivant des plans d'expériences (DOE). La concentration en 1-

octyne, la pression d'hydrogène et la température ont été variés selon des plans factoriels. De cette manière, les effets de ces paramètres sur la conversion de 1-octyne et la vitesse de réaction ont été étudiés et les paramètres cinétiques de chacun des catalyseurs ont été obtenus. Les catalyseurs de polyacrylamide se sont avérés moins actifs que la référence commerciale (Pd Nanoselect LF 200). Ces catalyseurs ont également montrés des performances différentes en fonction des conditions de pression et de température.

Par ailleurs, deux autres catalyseurs de polyacrylamide obtenus par synthèse en une étape («One pot») ont été comparés aux trois catalyseurs obtenus en deux étapes («Two steps») en utilisant un même ensemble de conditions de réaction. Le catalyseur supporté sur charbon actif en une étape a révélé une activité bien supérieure à celle de tous les autres catalyseurs de polyacrylamide mais toujours légèrement inférieure à la référence commerciale. Les différences d'activité des catalyseurs de polyacrylamide ont été associées aux différences dans le procédé d'immobilisation et au support utilisé.

Cette thèse propose donc une analyse sur le design de nouveaux catalyseurs de Pd destinés à des réactions de semi-hydrogénation d'alcyne. L'utilisation de méthodologies non récentes mais peu fréquemment utilisés dans ce domaine malgré leur efficacité est proposé pour assurer robustesse et confiance dans les conclusions des résultats expérimentaux.

## Resumen

Durante las últimas décadas, nuestra sociedad ha tenido que enfrentarse a un nuevo desafío: satisfacer las crecientes necesidades energéticas protegiendo los recursos del planeta. La preservación de los recursos se ha convertido en un factor estructural, por lo que será necesario replantear nuestros comportamientos y acciones para poder reducir el impacto de los seres humanos sobre el medio ambiente. Desde un punto de vista industrial, esto implica una mejora de los procesos de fabricación. Por ejemplo, el uso de catalizadores heterogéneos activos y selectivos se ha convertido en una herramienta esencial para reducir la formación de residuos no reciclables. Además, entre los procesos catalíticos más comunes, la hidrogenación selectiva de alquinos a alquenos ha sido el centro de atención por su relevancia en las industrias petroquímica, de polímeros y de química fina. La elección de catalizadores adecuados en esta reacción permite mejorar su rendimiento, evitando la formación de subproductos por hidrogenación y/u oligomerización.

El objetivo de esta tesis doctoral es sintetizar y caracterizar nuevos catalizadores preparados mediante un enfoque coloidal para su aplicación en reacciones de hidrogenación selectiva. Además, para mejorar la eficiencia de la experimentación y obtener conclusiones más robustas, se ha aplicado la metodología del diseño de experimentos ("Design Of Experiments", DOE).

De esta tesis se extraen varias contribuciones. La primera consiste en la síntesis de nuevas nanopartículas coloidales de Pd. En este apartado, se propone un plan de experimentos eficiente, el uso de un test estadístico que permite demostrar la reproducibilidad de diferentes síntesis, así como una mejora del tratamiento analítico de los datos obtenidos por microscopía ("Transmission Electron Microscopy", TEM).



En una primera fase, se probaron diferentes estabilizantes (polímeros y surfactantes) para sintetizar nanopartículas de Pd bajo las mismas condiciones de reacción. La poliacrilamida resultó ser el estabilizante más prometedor. El resto del estudio consistió en evaluar los efectos de varios parámetros de síntesis en la formación de nanopartículas mediante el método OFAT "One-Factor-At-a-Time" ("una variable a la vez"). Se demostró que la temperatura, el tiempo y el ratio molar entre la poliacrilamida y el Pd fueron los parámetros más importantes para el control de la distribución de las nanopartículas. Sin embargo, no se observó variación significativa del tamaño de las mismas. Con esta experimentación se obtuvo una receta de nanopartículas de Pd de aproximadamente 3.7 nm con una distribución fina, y su reproducibilidad fue verificada con un test estadístico de Kolmogorov-Smirnov.

También se realizó un análisis más detallado del efecto de cada parámetro y sus interacciones en la formación de nanopartículas mediante la aplicación de un diseño factorial fraccionado. En esta segunda fase, se mejoró la forma y distribución de las nanopartículas y se aumentó la eficiencia de la síntesis mediante la combinación de varios parámetros: un tiempo de síntesis corto, una baja temperatura, una baja relación molar de polímero y Pd, una baja concentración de Pd y una alta velocidad de agitación.

Por otro lado, para garantizar la durabilidad de los procesos catalíticos industriales, a menudo se usan catalizadores soportados. Por esta razón, en una última fase del estudio, las nanopartículas de Pd se impregnaron en diferentes soportes (carbón activado, óxido de aluminio y óxido de titanio) aplicando los métodos de una etapa ("One pot") y dos etapas ("Two steps"). Se estudiaron los efectos del método de inmovilización, los parámetros de síntesis, la naturaleza del soporte, el contenido de Pd y la escala de la síntesis sobre el tamaño y la dispersión de las nanopartículas. El tamaño se vio afectado por la temperatura de reacción y la naturaleza del soporte cuando

la impregnación se llevó a cabo en una etapa (“One pot”). Al contrario, la inmovilización en dos etapas (“Two steps”) no mostró efectos significativos en el tamaño de las nanopartículas. Además, la aglomeración de las nanopartículas sobre los soportes disminuyó considerablemente en la síntesis de dos etapas llevadas a cabo a grande escala.

La segunda contribución de esta tesis consiste en el uso del diseño de experimentos (DOE) para la síntesis de nanopartículas. Este estudio demuestra que un plan de experimentos adecuado puede reducir considerablemente el número de síntesis a realizar y, en consecuencia, los recursos materiales, humanos y financieros y, a su vez, generar una gran cantidad de información. Esta metodología se ha aplicado a la síntesis de nanopartículas de Pd utilizadas para la preparación del catalizador comercial Pd Nanoselect patentado por BASF. Se realizó un estudio de la relación estructura-síntesis de las nanopartículas y se utilizó el análisis de varianza (ANOVA) para identificar las contribuciones significativas de los parámetros estudiados. Se identificaron una gran cantidad de parámetros e interacciones para el control de la forma, el tamaño y la distribución de las nanopartículas así como la eficiencia de la síntesis, lo que demuestra la complejidad del sistema. Este estudio permitió postular modelos empíricos para describir el comportamiento del sistema en el rango de estudio.

La tercera contribución consiste en un estudio cinético sobre la hidrogenación de 1-octino en un reactor de tanque agitado. El objetivo era comparar el rendimiento de los catalizadores de poliacrilamida (preparados en dos etapas) con una referencia comercial (Pd Nanoselect LF 200). Se estudiaron cuatro catalizadores a través de 24 catálisis siguiendo un diseño de experimentos (DOE). La concentración de 1-octino, la presión de hidrógeno y la temperatura se modificaron de acuerdo con diseños factoriales. De esta manera, se pudo estudiar el efecto de estos parámetros

sobre la conversión de 1-octino y la velocidad de reacción y se obtuvieron los parámetros cinéticos de cada uno de los catalizadores. Los catalizadores de poliacrilamida resultaron menos activos que la referencia comercial (Pd Nanoselect LF 200). Estos catalizadores también mostraron diferentes rendimientos en función de las condiciones de presión y temperatura. Luego, se compararon otros dos catalizadores de poliacrilamida (preparados con una síntesis de una etapa) con los tres catalizadores obtenidos con la síntesis de dos etapas, utilizando el mismo conjunto de condiciones de reacción. El catalizador soportado en carbón activado preparado en una etapa, mostró una actividad mucho más alta que todos los otros catalizadores de poliacrilamida, pero ligeramente más baja que la referencia comercial. Las diferencias en términos de actividad de los catalizadores de poliacrilamida se asociaron con las diferencias en el proceso de inmovilización y con el soporte utilizado.

En resumen, esta tesis ofrece un análisis del diseño de nuevos catalizadores de Pd para reacciones de semi-hidrogenación de alquinos. Se propone el uso de metodologías que no son recientes, pero que están poco utilizadas en este campo a pesar de su efectividad, para garantizar solidez y confianza en las conclusiones de los resultados experimentales.

## Content

<b>1. Chapter 1: Introduction .....</b>	<b>1</b>
1.1. Context and motivations .....	3
1.2. Metallic colloidal nanoparticles .....	5
1.2.1. Synthesis of metal nanoparticles .....	5
1.2.2. Stabilization of colloidal suspension of nanoparticles .....	9
1.3. Methods for the preparation of supported catalysts .....	12
1.4. Selective hydrogenation of alkynes .....	14
1.4.1. Mechanistic and thermodynamic selectivity .....	14
1.4.2. Reaction mechanism .....	15
1.4.3. Descriptors affecting selectivity .....	17
1.5. Strategies for the enhancement of alkene selectivity through colloidal approaches .....	20
1.5.1. Stabilizers .....	21
1.5.2. Metal nanoparticles structure.....	31
1.5.3. Role of the support .....	35
1.5.4. Dilution of the active phase: introduction of modifiers .....	38
1.5.5. Additives .....	39
1.6. Three-phase catalytic reactor .....	41
1.6.1. Stirred tank reactor .....	42
1.6.2. Fixed bed reactor .....	50
1.7. Design of experiments .....	51
1.7.1. Definition of the methodology .....	52
1.7.2. Application of the design of experiments .....	54
1.7.3. Description of the two types of design used in this thesis ...	56
1.7.4. Brief mathematical formulation .....	59
1.7.5. Uses of DOE for NPs synthesis and catalytic tests .....	60
1.8. References .....	62
<b>2. Chapter 2: Objectives .....</b>	<b>67</b>
<b>3. Chapter 3: Study of synthetic parameters effects on the formation of colloidal Pd-polyacrylamide NPs .....</b>	<b>71</b>
3.1. Introduction .....	73
3.2. Experimental Section .....	76
3.2.1. Material for colloidal NPs synthesis .....	76
3.2.2. Characterization .....	76

3.2.3. General recipe of Pd NPs stabilized by polyacrylamide (PAM) .....	79
3.3. Plan of Experiments for the structure-synthesis relationship study of colloidal Pd-PAM NPs .....	79
3.3.1. OFAT experiments for the study of the effects of the synthetic parameters on colloidal Pd NPs .....	80
3.3.2. DOE experiments for the study of the effects of the synthetic parameters on colloidal Pd NPs .....	80
3.4. Results and Discussion .....	86
3.4.1. Screening of stabilizing agents for colloidal NPs synthesis ...	86
3.4.2. Study of the effect of synthetic parameters on the formation of Pd-PAM NPs using OFAT experiments .....	89
3.4.3. Reproducibility of Pd-PAM 6 reference recipe .....	101
3.4.4. Characterization of the reference recipe Pd-PAM 6.....	108
3.4.5. Study of the effect of synthetic parameters on the formation of Pd-PAM NPs using DOE .....	111
3.5. Conclusions .....	139
3.6. Appendix .....	141
3.7. References .....	155
 <b>4. Chapter 4: Synthesis and characterization of supported Pd-polyacrylamide NPs .....</b>	 <b>157</b>
4.1. Introduction .....	159
4.2. Experimental Section .....	161
4.2.1. Material for supported NPs synthesis .....	161
4.2.2. Characterization .....	162
4.2.3. Immobilization of Pd-PAM NPs on various supports.....	164
4.3. Results and Discussion .....	168
4.3.1. Supported Pd-PAM NPs synthesized via one pot approach	168
4.3.2. Supported Pd-PAM NPs via two-step synthesis .....	183
4.3.3. Nanoparticles dispersion on the supports .....	191
4.3.4. Reproduction of the well-defined catalysts at larger scale ..	196
4.3.5. Characterization of the well-defined catalysts .....	202
4.4. Conclusions .....	214
4.5. Appendix .....	217
4.6. References .....	218

<b>5. Chapter 5: Structure-synthesis relationship study of Pd-HHDMA NPs using DOE and impregnation onto supports .....</b>	<b>219</b>
5.1. Introduction .....	221
5.2. Experimental Section .....	223
5.2.1. Set-ups used for the synthesis of colloidal NPs .....	223
5.2.2. Set-ups used for the synthesis of supported NPs .....	225
5.2.3. Characterization by Transmission Electron Microscopy .....	225
5.2.4. Recipe of the BASF patent for the synthesis of colloidal Pd-HHDMA NPs .....	226
5.2.5. Recipes of the supported Pd-HHDMA NPs onto different supports .....	227
5.3. Plan of Experiments for the structure-synthesis relationship study of colloidal Pd-HHDMA NPs .....	228
5.3.1. Factors included in the DOE .....	229
5.3.2. Design aspects .....	231
5.3.3. Experimental design .....	232
5.4. Results and Discussion .....	237
5.4.1. Colloidal NPs stabilized by HHDMA .....	237
5.4.2. Supported Pd-HHDMA NPs onto supports .....	282
5.5. Conclusions .....	289
5.6. Appendix .....	292
5.7. References .....	302
 <b>Chapter 6: Kinetic study of Pd-based catalysts in the selective hydrogenation of 1-octyne in stirred tank reactor using designed experiments .....</b>	 <b>303</b>
6.1. Introduction .....	305
6.2. Experimental Section .....	310
6.2.1. Set-up for catalytic semi-hydrogenation of 1-octyne .....	310
6.2.2. Starting procedure .....	313
6.2.3. Shut down procedure .....	315
6.2.4. Washing procedure .....	315
6.2.5. Characterization by GC-MS .....	316
6.3. Plan of experiments .....	319
6.3.1. Conditions for the kinetic regime .....	319
6.3.2. Study of the effect of the reaction conditions on the 1-octyne conversion and reaction rate .....	326
6.3.3. Intrinsic kinetics studied with DOE .....	329

---

6.4. Results and Discussion .....	333
6.4.1. Verification of mass transfer .....	333
6.4.2. Study of the effect of the reaction conditions on the 1-octyne conversion and reaction rate .....	337
6.4.3. Intrinsic kinetics studied with DOE .....	348
6.4.4. Comparison of the performances of the different tested catalysts .....	363
6.5. Conclusions .....	370
6.6. Perspectives .....	371
6.7. Appendix .....	374
6.8. References .....	378
 <b>Chapter 7: This chapter is subject to a confidentiality agreement (property of Total Research &amp; Technology Feluy).....</b>	 <b>379-400</b>
 <b>Chapter 8: General conclusions</b>	 <b>401</b>
 <b>Appendix</b>	 <b>405</b>

## Abbreviations and acronyms

### A

<i>ac.</i>	Approximately
AC	Activated Carbon
ANOVA	Analysis Of Variance

### C

CCD	Central Composite Design
CRA	Complex Reducing Agents
CTAB	Hexadecyltrimethylammonium bromide

### D

DOE	Design Of Experiments
-----	-----------------------

### E

<i>e.g.</i>	For example
eq.	Equivalent(s)
ESEM	Environmental Scanning Electron Microscopy

### F

FIC	Flow Indicating Controller
FWHH	Full Width at Half-Height

### G

GC-MS	Gas Chromatography-Mass Spectroscopy
-------	--------------------------------------

### H

h	Hour(s)
HHDMA	hexadecyl(2-hydroxyethyl)dimethylammonium dihydrogenphosphate
HRTEM	High Resolution Transmission Electron Microscopy



## I

ICP Inductively Coupled Plasma

*i.e.* That is

ILs Ionic Liquids

## L

LOF Lack of fit

## M

M Metal

MBE 2-methyl-3-buten-2-ol

MBY 2-methyl-3-butyn-2-ol

mL Millilitre(s)

## N

nm Nanometer(s)

NmL Normo milliliter(s)

NP(s) Nanoparticle(s)

## O

OFAT One-Factor-At-a-Time

## P

P Pressure

PAM Polyacrylamide

PIC Pressure Indicating Controller

PVA Poly(vinyl alcohol)

PVP Polyvinylpyrrolidone

PZC Point of Zero Charge

## R

RSD      Relative Standard Deviation

r.t.      Room temperature

## S

SDS      Sodium dodecyl sulfate

SEM      Scanning Electron Microscopy

SMSI      Strong Metal-Support Interactions

STEM      Scanning Transmission Electron Microscopy

STR      Stirred Tank Reactor

## T

T      Temperature

TEM      Transmission Electron Microscopy

TGA      ThermoGravimetric Analysis

TIC      Temperature Indicating Controller

TOF      TurnOver frequency

## V

VHH      Van Hardevel Hartog

vs.      Versus

## X

XPS      X-ray Photoelectron Spectroscopy

XRD      X-Ray Diffraction



# Chapter 1

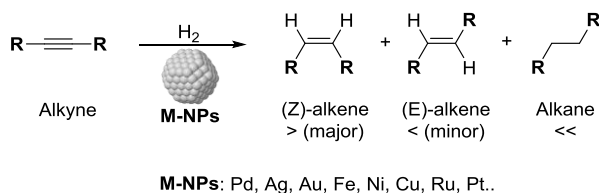
## Introduction



## 1.1. Context and motivations

One of the greatest challenges of the modern society is to face to the current increase of lifestyle needs and at the same time preserve the Earth resources. Global environmental issues such as energy resources, water access and use, land use and ecological damage need urgent and relevant solutions. Thus, the industries and scientific community have to adapt to this new society scheme and develop new economic and environmentally sustainable processes.<sup>1</sup>

In this context, the use of heterogeneous catalysts appeared as a key tool to achieve suitable utilization of energy and chemicals.<sup>2</sup> Among the most commonly applied catalytic processes, the selective hydrogenation of alkynes (Scheme 1.1) has been the object of particular attention for its relevance in the polymeric and fine chemical industries.<sup>3-5</sup> Indeed the alkene product is a feedstock of a wide variety of industrial reactions such as polymerization and alkylation. Thus, the development of chemo and stereoselective heterogeneous catalysts is highly desirable to improve the productivity of the corresponding processes and prevent the over-hydrogenation and/or oligomerisation of the substrate.<sup>6,7</sup>



Scheme 1.1. Selective alkyne hydrogenation catalyzed by metal nanoparticles<sup>8</sup>

Several transition metals catalysts were reported for the selective semi-hydrogenation of alkynes (*e.g.* Pd, Ni, Pt, Ag, Rh, Fe).<sup>9</sup> Among them, those with high hydrogen activation capacity such as Ni or Pt frequently present severe selectivity issues due to their strong over-hydrogenation activity. In contrast, high selectivity to the alkene useful product was reported for metals with low reactivity towards hydrogen such as Ag or Au, however they are hardly competitive in terms of activity.<sup>10</sup> Palladium was identified as the most efficient metal in terms of activity and selectivity for this reaction which has been attributed to the stronger adsorption of the C≡C group

(relative to C=C) on the Pd surface, thus preventing the over-reduction of the alkene product.<sup>11</sup>

Pd-based catalysts are generally dispersed on solid carriers such as oxides (Al<sub>2</sub>O<sub>3</sub>, TiO<sub>2</sub>, SiO<sub>2</sub>), CaCO<sub>3</sub> (Lindlar®) and carbon based materials (activated carbon, graphite, carbon nanofibers or nanotubes).<sup>12</sup> Classically, the preparation of such supported catalysts is performed by impregnation techniques, although these approaches often face difficulties in the fine control of the particle size and their distribution over the support.<sup>12</sup> In this context, the colloidal methods offer the possibility to prepare well-defined metallic nanoparticles through a precise control of their size, shape and structure at the nanometric scale.<sup>13</sup> The ability to adjust the properties of the nanoparticles and compare series of materials prepared in a similar way provides valuable information on how catalytic systems operate at molecular and atomic levels.<sup>14</sup> Moreover, such a control allows the maximization of the available metal surface area and thus improves the catalyst productivity.

An example of successful application of colloidal chemistry for the preparation of molecularly designed nanocatalysts is the BASF registered trademark, NanoSelect Pd catalysts.<sup>15,16</sup> This catalyst was reported as highly selective in the hydrogenation of alkynes. Using DFT calculations, Pérez-Ramírez and co-workers correlated the performance of this catalyst with accessibility constraints of reagents and products to the metal surface.<sup>16,17</sup> These findings demonstrated that the nanostructure defined at the colloidal preparation stage leads to the production of ultrasensitive catalysts.

In the following sections, an introduction on metal nanoparticles is given, explaining how they are synthesized and stabilized, which parameters influence their structure and how their immobilization on supports can be carried out. Furthermore, an analysis of the literature on the selective hydrogenation of alkynes catalyzed by metal nanoparticles prepared via colloidal approaches is presented. Afterwards, mixing and mass transfer steps that take place in a three-phase catalytic reactor are detailed. Finally, basic concepts of design of experiments are provided.

## 1.2. Metallic colloidal nanoparticles

Metal nanoparticles have been known for two millenniums and their optical properties were exploited for coloration of glasses, ceramics and pottery.<sup>18</sup> The decoration of the Lycurgus cup from the 4<sup>th</sup> century available in the British museum is a great example of the use of Au NPs for aesthetic purposes. They also have been exploited for their curative properties in the Middle Age. During the mid-19<sup>th</sup> century, Michael Faraday observed that the optical properties of colloidal Au NPs were different from those of the bulk metal.<sup>19</sup> He reported the synthesis of colloidal solution of Au NPs with colors ranging from ruby red to amethyst. He evidenced that the color variations were related to the size of the particles.

Besides their optical properties, noble metal nanoparticles revealed to have promising applications in many fields like biochemistry, sensing science and catalysis.<sup>18</sup> In this latter area, their small size provides a high ratio of surface-to-volume of atoms and leads to a high number of potential active sites at their surface.<sup>20,21</sup> Thus, the use of metal nanoparticles as catalysts allows efficient reactions under mild conditions which appear as a promising solution in the context of green chemistry.

### 1.2.1. Synthesis of metal nanoparticles

The synthesis of metal nanoparticles can be performed through two different methodologies: the “top-down” and the “bottom-up”.<sup>20</sup> The first one is a physical approach that consists in reducing macroscopic structure to the nanoscale. A common “top-down” example involves the mechanical grinding of bulk metals and the subsequent stabilization of the resulting nanosized metal particles by addition of protecting agents.<sup>22</sup> However, this physical route use to yield large NPs with broad distribution (>10 nm) and is subject to reproducibility issues. The second method is a chemical approach that relies on the fabrication of nanostructures from smaller units. This latter approach is more convenient for the control of the NPs size.

Several methodologies were developed to synthesize metal NPs via the “bottom-up” approach: the chemical reduction of metal salts, the electrochemical method, the



metal vapor synthesis, the organometallic approach, the thermal, photochemical and sonochemical decomposition is a non-exhaustive list.<sup>20</sup>

It is well-established that the size, shape, composition and structure of metal nanocrystals determine their properties. As an example in catalysis, the activity of a metal nanocrystal increases by reducing its size. The selectivity, however, is sensitive to nanocrystal structure (packing of atoms on the surface of exposed facets).<sup>23</sup> Hence, to tune the properties of a metal nanocrystal, it is important to understand its formation mechanism and how the different synthetic parameters can affect it.

The chemical reactions involved in metal nanocrystals synthesis are usually well-known, however the nucleation and growth mechanism that exist behind this chemistry are much more complex and, until today, the scientists have just begun to understand the complex physics that lead to the formation of nanocrystals with specific shape. In a rough approach, the typical synthesis of a metal nanocrystal occurs through 3 steps: the nucleation, the evolution of nuclei into seeds and the growth of seeds into nanocrystals. For Ag, Au and Pd it was established that the final shape of a nanocrystal was determined by the internal structure of the corresponding seed and the binding affinity with the stabilizer.<sup>23</sup>

In a typical synthesis, a metallic precursor is either decomposed or reduced to generate zero-valent metal atoms. It is still unclear how nuclei and nanocrystals evolve from a precursor.<sup>24</sup> Depending on the reaction conditions, the nucleation process can follow different pathways. However, this step is critical for obtaining well-defined metal NPs.

For the decomposition route, nucleation is expected to follow the LaMer mechanism as presented in Figure 1.1.

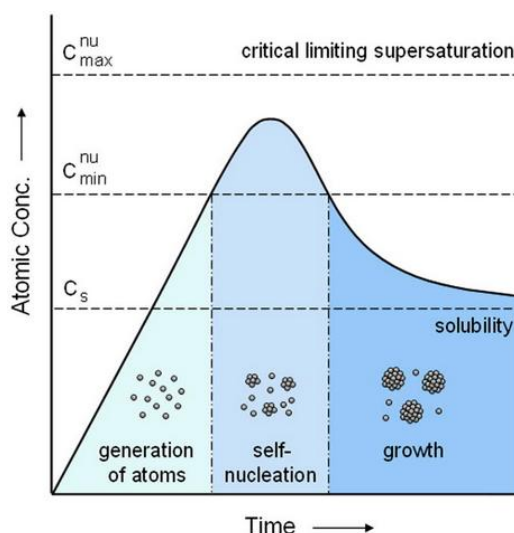


Figure 1.1 Plot of atomic concentration against time illustrating the generation of atoms, nucleation and subsequent growth<sup>23</sup>

The metal atoms concentration increases as the precursor is decomposed, once the atoms concentration reaches the supersaturation, the atoms start to aggregate into small clusters (nuclei) via homogeneous nucleation.<sup>23</sup>

In homogeneous nucleation, the seed particles are formed in situ and nucleation and growth mechanism follow the same chemical process.<sup>24</sup> This phenomenon occurs due to the driving force of the thermodynamics since the supersaturated solution is not stable in energy. The overall free energy change  $\Delta G$  corresponds to the sum of the free energy due to the formation of a new volume and the free energy due to the new surface created. For spherical particles, this energy depends on the molecular volume of the precipitated species ( $V$ ), the radius of the nuclei ( $r$ ), the Boltzmann constant ( $k_B$ ), the saturation ratio ( $S$ ) and the surface free energy per unit surface area ( $\gamma$ ) according to the following equation:

$$\Delta G = -\frac{4}{V}\pi r^3 k_B T \ln(S) + 4\pi r^2 \gamma \quad (1.1)$$

When the saturation ratio  $S$  is higher than 1, then  $\Delta G$  reaches a positive maximum at a critical size ( $r^*$ ). This maximum energy is the activation energy for nucleation. The critical nuclei size  $r^*$  is obtained by setting  $\frac{d\Delta G}{dr} = 0$ :

$$r^* = \frac{2V\gamma}{3k_B T \ln(S)} \quad (1.2)$$

For a given value of saturation ratio, all particles with a radius larger than the critical radius will grow and all particles with a radius lower than critical radius will dissolve. According to the equation (1.2), the higher is the saturation ratio, the smaller will be the critical nuclei size.<sup>25</sup>

Once the nuclei are formed, they grow via atomic addition in an accelerated way and the concentration of metal atoms in solution decreases. If the atoms concentration drops below the supersaturation point, the nucleation stops and particles continue to grow until the equilibrium concentration of the precipitated species is reached. In contrast if continuous supply of metal atoms is possible via ongoing precursor decomposition, the nuclei will grow into nanocrystals of increasingly larger size until reaching the equilibrium. Furthermore, the nuclei and nanocrystals can directly merge into larger nanocrystals by agglomeration (secondary growth).

Uniformity of the size distribution is achieved thanks to a short nucleation period that able the fast generation of all the nuclei. At this stage, the smaller particles grow faster than the larger ones because the free energy, which is the driving force, is larger for smaller particles than for larger ones. Nearly mono-dispersed size distribution can be obtained by stopping the reaction quickly or by supplying reactant source to maintain saturated conditions during the reaction. Otherwise, when the reactants are consumed by particle growth, the larger NPs will be able to keep growing and the smaller ones will get smaller and finally dissolve. Indeed, the saturation ratio will decrease when the corresponding critical nuclei size will increase and any particle smaller than this new critical size will thus dissolve. If the reaction reaches this stage, it is difficult to obtain mono-dispersed particles unless the reaction is extended to long enough times to completely deplete the supersaturation and the smaller nuclei. However in this case, the size of the particles will be relatively large and can extend into the micrometer size regime.<sup>25</sup>

Concerning the reduction route, the precursor compound is in a higher oxidation state than the atomic species. It is unclear if the precursor is reduced into zero-valent atoms

first which then aggregate into nuclei and grow into nanocrystals or if the unreduced metal species begin forming nuclei prior to reduction.<sup>23</sup>

Although homogeneous nucleation is the more common synthetic strategy due to the practical ease of performing a one-pot reaction, the heterogeneous nucleation was also reported.<sup>23</sup> This strategy consists in adding preformed seeds to a reactant mixture in order to separate nanocrystal nucleation and growth steps (seeded growth method). This methodology is used to obtain particles of distinct sizes.

As mentioned above, a wide variety of methodologies exists for the preparation of NPs via the “bottom-up” approach. During the development of this project, the chemical reduction of metal salts was used. This method was first published by Faraday in 1857 and became one of the most common and powerful synthetic method.<sup>22</sup> It consists in the reduction of a metallic salt in an aqueous or organic media in the presence of a stabilizer. As detailed above, the mechanisms of nucleation and growth of the NPs in solution are quite complex and each material can follow a distinct pathway depending on the reaction conditions. The chemical reduction methodology is widely used because of its easy implementation and its compatibility with a huge variety of metal salts, solvents, stabilizing agents and reducing agents. Moreover, one of the main advantages of the wet chemical reduction procedures is that the syntheses are highly reproducible and allow the preparation of colloidal NPs with a narrow size distribution at the multigram scale.<sup>22</sup> However, a disadvantage is that the introduction of “spectator compounds” such as counter ions contained in the precursor could coordinate the metal surface and thus affect the catalytic properties of the NPs.<sup>20</sup>

### **1.2.2. Stabilization of colloidal suspension of nanoparticles**

One of the main limitations of the nanoparticles is that they are unstable with respect to agglomeration to the bulk. Moreover their stability is decreasing at high temperature via sintering.<sup>20,26</sup> In most cases, agglomeration issues leads to a negative effect on the catalyst activity. Thus, the stabilization of the colloidal NPs is a critical

aspect to take into account during their synthesis and a way to preserve the particles in a finely dispersed state.

The explanation of the agglomeration phenomenon is that at short interparticle distances, the Van der Waals forces attract the metallic particles between each other.<sup>20</sup> These forces are inversely proportional to the distance between their surfaces. Thus, the colloidal NPs aggregate in the absence of repulsive forces opposed to the Van der Waals ones. The use of capping agents able to induce these repulsive forces is thus necessary to obtain stable NPs. Different stabilization procedures exist and those used during the development of this thesis are described below.

#### 1.2.2.1. Electrostatic stabilization

The electrostatic stabilization is created by ionic compounds such as halides, carboxylates or polyoxoanions.<sup>20</sup> The adsorption of these compounds and their related counter-ions on the metallic surface enables the formation of an electrical double-layer around the particles which results in a Coulombic repulsion between the metal NPs. If the electric potential associated with the double layer is high enough the electrostatic repulsion will prevent particle aggregation. A schematic representation of this stabilization strategy is given in Figure 1.2.

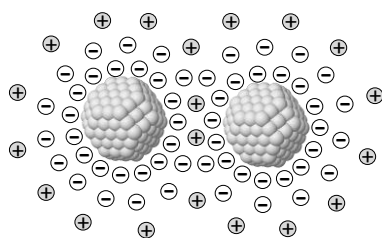


Figure 1.2. Schematic representation of electrostatic stabilization of metal NPs<sup>27</sup>

#### 1.2.2.2. Steric stabilization

The steric stabilization consists in the use of macromolecules such as polymers or oligomers to provide a protective layer at the surface of the metallic particles and prevent their aggregation.<sup>28</sup> In contrast to the electrostatic stabilization that is mainly

used in aqueous media, the steric stabilization can be used in organic and aqueous phases. A schematic representation of this stabilization strategy is given in Figure 1.3.

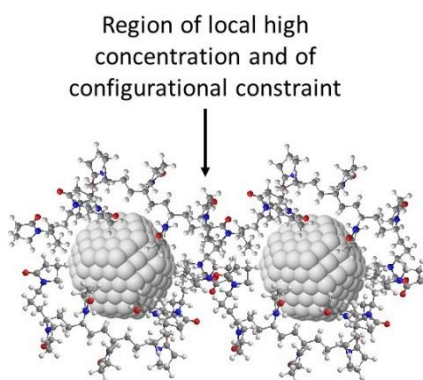


Figure 1.3. Schematic representation of steric stabilization of metal NPs<sup>29</sup>

Polymers such as poly(N-vinyl-2-pyrrolidone (PVP) and polyvinyl alcohol (PVA) are widely used to protect Pd NPs because of their commercial availability at relatively low cost and their solubility in a wide range of solvents including water.<sup>28</sup> It has been demonstrated that the length and/or the nature of the macromolecules adsorbed, influence the thickness of the protective layer and can thus modify the stability of the colloidal NPs.

#### 1.2.2.3. Electrosteric stabilization

The electrostatic and steric stabilizations can be combined. This strategy is usually provided by ionic surfactants.<sup>28</sup> Frequently, tetra-N-alkylammonium halide salts are used although other analogous materials such as imidazolium-based ionic liquids can act as stabilizers with the same mechanism. It was reported that the NPs strongly adsorb a layer of anions to the surface of the metal, which are surrounded then by a layer of countercations in order to preserve electroneutrality as shown in Figure 1.4.

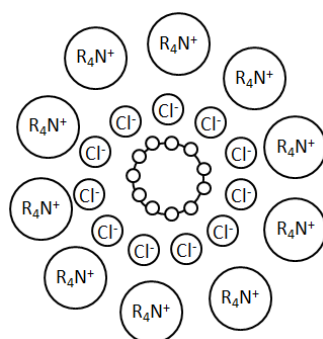


Figure 1.4. Schematic representation of electrosteric stabilization of NPs by a surfactant <sup>28</sup>

One of the major advantages of using surfactants as protecting agents is that their interactions with the metal surface is relatively weak and poorly defined, which gives to the reagents a high degree of accessibility to the surface of the NPs. For instance, tetra-*n*-alkylammonium halide stabilized Pd NPs demonstrated good catalytic activity in liquid phase hydrogenation reactions.<sup>28</sup>

### 1.3. Methods for the preparation of supported catalysts

The NPs can be immobilized over solid supports in order to overcome challenges related with product separation and catalyst recyclability.<sup>30</sup> The activity and selectivity of supported metallic nanocatalysts are related to their morphology, the active phase dispersion and the electrostatic interactions metal-support.<sup>31</sup> Various methodologies were reported to perform the deposition of an active metal onto solid carriers, among them the deposition-precipitation, deposition-reduction, impregnation and ion-exchange are the most common one.<sup>30</sup>

The deposition-precipitation consists in mixing the support and metal precursor in water and, by a pH increase, induce the metal precipitation onto the support. After precipitation the solid is reduced by addition of a reducing agent. An example of the use of this methodology is the commercially available Lindlar catalyst (5wt% Pd/CaCO<sub>3</sub> poisoned with lead) which is prepared via dissolution of PdCl<sub>2</sub> in previously acidified water.<sup>30</sup> Then the pH of this solution is increased before addition of CaCO<sub>3</sub>. Afterwards, the mixture is heated to 75-85°C and kept at this temperature until Pd precipitation. Finally the reduction is performed by addition of sodium formate. The

catalyst is filtered and slurried in water for addition of lead acetate. Another filtration is then performed and the catalyst is dried in an oven at 60-70°C. A limitation of this methodology is that the metal can precipitate in the solution instead of onto the catalytic carrier.

The deposition-reduction methodology consists in the metal precipitation onto the support upon reduction.<sup>30</sup>

Impregnation techniques are based on support pore filling with a solution of catalyst precursor. This solution should be prepared with sufficient metal salt concentration to reach the desired active metal loading since the entire precursor solution is expected to be retained on the support.<sup>29</sup> Two kinds of impregnation are available: the wet and the incipient wetness impregnation. In the first one, the volume of the metal precursor solution is higher than the total pore volume present in the support material. In the second one, the impregnation volume matches the pore volume.<sup>30</sup>

Finally, the ion-exchange technique consists in replacing an ion in interaction with the surface of the support by another species. The support containing this ion is mixed with an excess volume of a solution containing the active metal in ionic form. The active metal ion penetrates gradually into the pore of the support and replaces the ion initially present which passes to the solution until the equilibrium is reached.<sup>27</sup>

During the deposition steps, the point of zero (PZC) charge of the supports is an important property to take into account. It corresponds to the pH at which the surface charge of the material is zero in an aqueous media. To determine the PZC, various methods were reported: potentiometric titration, electrokinetic and electroacoustic mobility techniques including mass titration, ion adsorption and scanning force microscopy.<sup>32</sup> The acid-base potentiometric and mass titration methods were reported as suitable methods. Miyittah *et al.* studied both methodology and concluded that the techniques were similar and valid for oxides and activated carbon materials.<sup>32</sup>

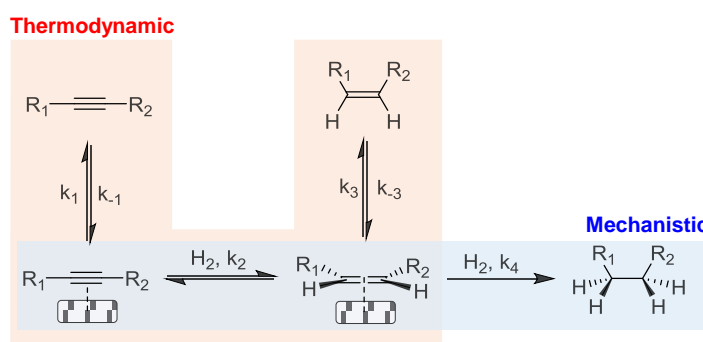


After these deposition steps, the catalysts are transformed into the required active compound by reduction, washing, separation (filtration or centrifugation), drying and calcination steps.

## 1.4. Selective hydrogenation of alkynes

### 1.4.1. Mechanistic and thermodynamic selectivity

In the semi-hydrogenation of alkynes, two types of selectivity to the alkene product were defined: the mechanistic and the thermodynamic selectivity that are presented in Scheme 1.2.<sup>33</sup>



Scheme 1.2. Simplified scheme of the mechanistic selectivity and the thermodynamic selectivity in the semi-hydrogenation of alkynes<sup>8</sup>

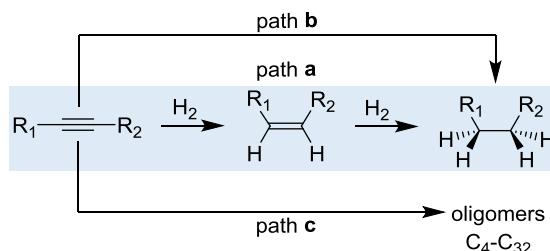
The mechanistic selectivity operates when the hydrogenation rate of the adsorbed alkyne is higher than the adsorbed alkene ( $k_2 \gg k_4$ ).<sup>34</sup> In contrast, the thermodynamic selectivity consists in the ability of a metal to adsorb preferentially the alkyne in the presence of the alkene ( $k_1/k_{-1} \gg k_3/k_{-3}$ ), thus suppressing the consecutive hydrogen addition which results in the alkane production. For the major part of the metals studied in the literature, the alkene hydrogenation rate resulted to be faster than that of alkyne hydrogenation, because selectivity is usually attributed to the stronger adsorption of the alkyne compared to that of the alkene (thermodynamic selectivity).<sup>35</sup> Under industrial conditions, the thermodynamic selectivity is of prime importance due to the high alkene content in the feedstock which favors the competitive adsorption with the alkyne at the metal surface. In addition, studies on

Pd, Au, Cu and Ni catalysts identified the thermodynamic selectivity as the most important selectivity indicator.<sup>36-38</sup>

This model offers a basis for the interpretation of the intrinsic selectivity of Pd. However, the selectivity favoring the alkene formation cannot be interpreted without the detailed knowledge of the reaction mechanism and the actual surface state of the active Pd sites.

### 1.4.2. Reaction mechanism

A simplified reaction mechanism for the hydrogenation of alkynes is displayed in Scheme 1.3. The path **a** corresponds to the sequential hydrogenation of the alkyne, first into the alkene that desorbs and re-adsorbs to be further hydrogenation into alkane. Path **b**, in turn, is the direct hydrogenation of the alkyne substrate to the alkane without any intermediate desorption/re-adsorption of the alkene. The relevance of these two paths depends on the morphological properties of the catalysts and the reaction conditions. For small and reactive alkynes such as acetylene, an additional route, corresponding to path **c**, can occur under certain conditions and consists in the oligomerization/polymerization of the substrate to form hydrocarbons from C<sub>4</sub> to C<sub>32</sub> called “green oil”. In acetylene hydrogenation reaction, the selectivity of the formation of these C<sub>4+</sub> was reported in the range between (20-40%), thus evidencing the relevance of this reaction path.<sup>39-42</sup>



Scheme 1.3. Reaction paths taking place during the alkyne hydrogenation<sup>8</sup>

For the hydrogenation of acetylene, several intermediates have been postulated based on surface characterization techniques combined, in some cases, with kinetic

studies.<sup>34,43,44</sup> The reaction starts by  $H_2$  dissociation and the adsorption of acetylene on the surface, both steps are exothermic. Then, the sequential addition of H takes place following a Horiuti-Polanyi mechanism.<sup>45</sup> For this substrate, despite its high adsorption enthalpy over Pd surfaces (thermodynamic selectivity), the hydrogenation of ethylene product has been observed even at high acetylene partial pressures.<sup>46</sup> This observation suggests the existence of a mixture of sites where acetylene is selectively hydrogenated to ethylene and others where ethylene is hydrogenated even in the presence of acetylene.<sup>47</sup>

The different adsorbed species that can participate in the mechanism of acetylene selective hydrogenation are displayed in Figure 1.5.

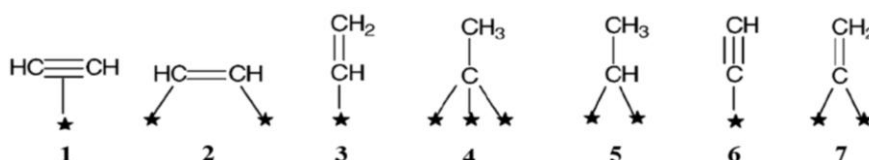


Figure 1.5. Species that can be formed at the catalyst surface during the selective acetylene hydrogenation reaction<sup>48</sup>

First, the  $\pi$ -adsorbed acetylene (1) can be transformed into a di- $\sigma$ -adsorbed acetylene (2) to give vinyl species (3) that are precursor to the ethylene formation. Then, the species that have multiple bonds with the catalyst surface, like (4) or (5) species are hydrogenated into ethane. Finally, the acetylene species (6) and vinylidene species adsorbed in a dissociative way (7) will be able to give rise to oligomers and benzene.<sup>48</sup>

The knowledge of the adsorbed species has enhanced the understanding of the models about acetylene selective hydrogenation mechanisms. Some studies reported that the apparent reactant orders and activation energies could vary with the temperature which supports a multiple mechanism rate expression. Vincent *et al.* reported the existence of two mechanisms: a competitive low-temperature mechanism and a non-competitive high temperature mechanism.<sup>49</sup>

### 1.4.3. Descriptors affecting selectivity

#### 1.4.3.1. External parameters

The performance of a catalyst in the partial hydrogenation of alkynes greatly depends on the reaction conditions. Parameters such as the temperature and pressure affect the kinetics of the reaction and therefore the alkene selectivity. For Pd-based catalyst, the hydrogen pressure is a parameter particularly relevant since the over-hydrogenation of alkyne is boosted by the extensive formation of sub-surface hydrides, which are favored under relatively high hydrogen partial pressures.<sup>50</sup>

Other parameters such as the reaction mixing (important for batch or semi-batch systems) need to be considered in order to prevent possible mass-transfer limitations which could affect the activity and/or the selectivity. Kiwi-Minsker and co-workers studied the interactions between mass and reaction kinetics for the three-phase catalytic hydrogenation of 2-methyl-3-butyne-2-ol (MBY) to 2-methyl-3-buten-2-ol (MBE) over a modified Pd/CaCO<sub>3</sub> catalyst under solvent free conditions.<sup>51</sup> No influence of gas-liquid mass transfer was observed for stirring speeds higher than 1500 rpm. Interestingly, the MBE selectivity increased at high stirring rates. Hydrogen liquid-solid mass transfer was found to be negligible, whereas the MBY liquid-solid mass transfer became important at high MBY conversions and high hydrogen concentration. These observations thus showed that mass transfer can affect both the activity and the selectivity of a catalyst in alkyne hydrogenation reactions.

The heating method used for the hydrogenation reaction can also impact the catalyst performances. Cravotto and co-workers, studied the partial hydrogenation of 2-butyne-1,4-diol in water under microwave irradiation catalyzed by a Pd/Bohemite catalyst.<sup>52</sup> Despite the low activity usually observed when water is the reaction solvent, the use of microwave irradiation enhanced the conversion while maintaining the alkene selectivity at *ca.* 97-100%. More recently, the same authors studied the effect of ultrasound in the semi-hydrogenation of phenylacetylene and diphenylacetylene catalyzed by Pd/Bohemite.<sup>53</sup> They observed that sonication increased the alkene selectivity in both cases and this positive effect of ultrasound was

explained by the increased desorption rate of the alkene product from the catalyst surface before over-reduction could occur.

#### **1.4.3.2. Sub-surface H and C and other C deposits**

It is well-reported that when a Pd catalyst is used in acetylene or acetylene-ethylene hydrogenation, it undergoes changes that modify its properties.

The formation of carbide and hydride phases in the sub-surface of the catalyst and their relationships with the catalyst selectivity have been discussed in various reports since Pd catalysts are extremely sensitive to the presence of sub-surface species.<sup>34</sup>

It was reported that during the reaction, the phase transition from  $\alpha$ -PdH to  $\beta$ -PdH could occur rapidly at sufficiently high hydrogen partial pressures and low acetylene to hydrogen ratios. Some studies of acetylene hydrogenation performed with in situ measurements of the  $\beta$ -PdH phase formation indicates that this phase is more active and less selective towards the ethylene product than the  $\alpha$ -PdH phase.<sup>50</sup>

Also, it was found that during the acetylene hydrogenation at moderate temperature, the carbon atoms produced by acetylene decomposition on the Pd surface, were able to gradually penetrate into the Pd lattice and form a solid solution of carbon in Pd.

In the presence of carbon, weaker adsorption energy was observed for ethylene in comparison with that on clean Pd surface inducing selectivity.<sup>54</sup>

Furthermore, during the hydrogenation of acetylene, heavy hydrocarbons ( $C_{8+}$ ) are formed and remain on the catalyst, and are frequently regarded as coke or carbonaceous deposits. The contribution of such deposits to the acetylene hydrogenation was reported by various authors.<sup>49,55,56</sup> They postulated the existence of different kinds of active sites produced by carbonaceous deposits. The first ones correspond to small spaces on the Pd surface between carbonaceous deposits that enable small molecules to be adsorbed. These spaces are so small that only acetylene and hydrogen are adsorbed leading to the selective hydrogenation to ethylene. Then, the second types of sites are large and enable the competitive absorption of ethylene, acetylene and hydrogen. These sites are generally responsible for undesired over-hydrogenation reactions.

Finally, the accumulation of oligomers on the support may increase hydrogen spillover and acetylene internal diffusion limitations. As a consequence, undesired ethane selectivity is increased. The importance of these phenomena depends on the catalyst support and the reaction conditions. Furthermore, the accumulation of coke and green oil in the support can cause deactivation of the catalyst.<sup>50</sup>

The catalyst deactivation is a technical, economic and ecological issue for industrial chemical processes. Investigations on the stability of a catalyst are as important as controlling its activity and selectivity performances. Usually, the deactivation rate depends on the applied process (reactor, reaction conditions, reactant composition, etc.).<sup>29</sup> It is of high importance to understand the causes and mechanism of catalyst deactivation in order to improve their stability.

#### **1.4.3.3. Substrate structure**

The structure of the substrate also influences the hydrogenation selectivity. For instance, the hydrogenation of terminal olefins was found to be much faster than that of internal olefins due to steric and accessibility constraints.<sup>57</sup> High alkene selectivity can therefore be obtained in the semi-hydrogenation of internal alkynes due to the slower over-reduction rate.<sup>58</sup> In contrast, in the hydrogenation of terminal alkynes, the first hydrogenation is generally slower than that of the corresponding alkene product for Ni, Pd, Pt, Rh catalysts.<sup>59,60</sup>

Moreover, the presence of hydroxyl groups in the alkyne structure was observed to retard the hydrogenation reaction, thus favoring the selectivity control to the alkene.<sup>61</sup> Regarding the stereoselectivity of the alkyne hydrogenation, the preferential formation of the Z product is usually observed, in agreement with the Horiuti–Polanyi mechanism.<sup>45</sup> However, some degree of Z/E isomerisation is sometimes observed depending on the catalytic system and reaction conditions.

## 1.5. Strategies for the enhancement of alkene selectivity through colloidal approaches

During the last decades, the preparation of metal nanocatalysts by colloidal methods attracted the interest of the scientific community, since they provide a precise control of the size, shape and structure of the resulting nanoparticles.<sup>20,62-64</sup> Moreover, the use of unsupported nanoparticles is also of high interest as they mimic metal surface activation and catalysis at the nanoscale, and can sometimes shed some light on the role of the support during catalysis.<sup>65</sup>

The main parameters that were reported to enhance the alkene selectivity in the semi-hydrogenation of alkynes using colloidal approaches are displayed in Figure 1.6:

1. The properties of the stabilizer used for the nanoparticles synthesis
2. The structural properties of the catalyst (size, shape and composition)
3. The properties of the support
4. The catalytic parameters such as additives or the use of reducing agents alternative to hydrogen.

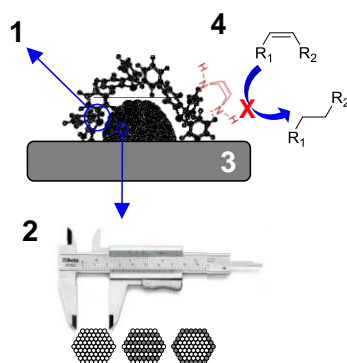


Figure 1.6. Schematic representation of the main parameters reported to enhance the alkene selectivity using colloidal approaches<sup>8</sup>

In the following sections, selected examples reported on the alkyne semi-hydrogenation catalyzed by metal nanoparticles are described according to each of these parameters.

### 1.5.1. Stabilizers

As mentioned above, organic compounds are typically employed during the synthesis of metal nanoparticles to prevent agglomeration of the metallic colloid.<sup>62</sup> Compounds such as polymers, dendrimers, surfactants, ionic liquids and ligands have been employed for the stabilization of metal nanoparticles. Traces of such compounds can induce electronic and steric modifications to the metal NPs that result in important variations in the catalyst activity/selectivity in hydrogenation reactions.<sup>66-68</sup>

Depending on the phase in which the catalytic reaction takes place (liquid or gas phase), the effect of the stabilizer can be more or less marked. In liquid phase, it is usually considered that stabilizers are quite flexible, thus most of the active sites remain accessible to the substrates. In contrast, when the catalytic reactions are performed in gas phase, the catalysts are previously dried, resulting in the collapse of the stabilizer over the NPs surface and consequently in the blockage of the active sites. For instance, after isolation of Pd NPs stabilized by hexadecyl(2-hydroxyethyl)dimethyl ammonium dihydrogenphosphate (HHDMA), no CO uptake could be observed in chemisorption measurements due to the presence of the stabilizer.<sup>15</sup>

#### 1.5.1.1. Catalysis in liquid substrates

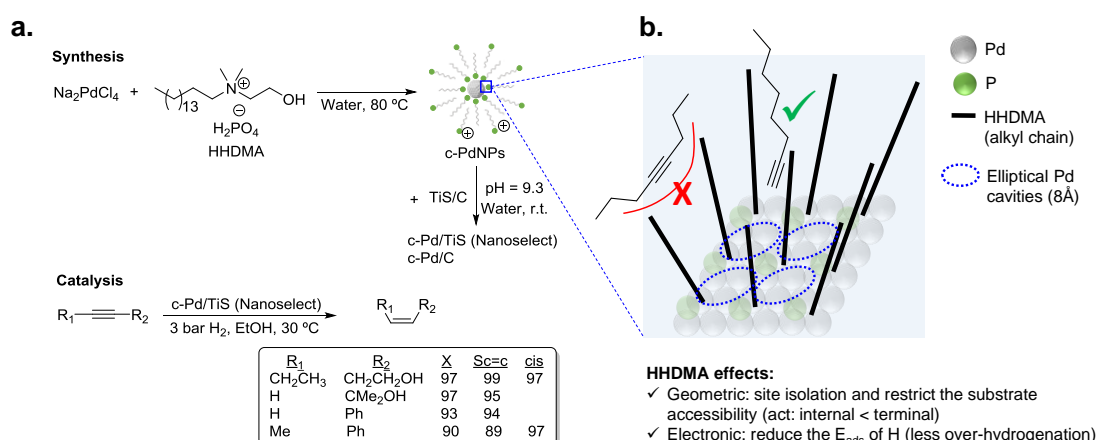
##### Surfactants

Surfactants are frequently used for the stabilization of metal nanoparticles in aqueous media since they are generally constituted by a polar group able to generate an electronic double layer and a lipophilic side chain that also provides steric repulsion between particles.<sup>20</sup>

An example that evidences the effect of the stabilizer on the catalyst performances in liquid phase hydrogenation reactions is the Pd Nanoselect catalyst.<sup>15,16</sup> It consists in Pd NPs of about 5-8 nm supported on activated carbon or titanium silicate. This catalyst exhibits alkene selectivity comparable to those provided by the Lindlar's catalyst in the semi-hydrogenation of a broad range of alkynes and alkynols, some results are



displayed in Scheme 1.4a.<sup>16</sup> The Pd NPs are prepared by chemical reduction using HDDMA as both stabilizer and reducing agent (together with the temperature). Based on deposition experiments onto functionalized surfaces (positive or negative), the authors proposed that the Pd NPs are surrounded by a double layer of HDDMA.<sup>15</sup> SEM analysis revealed a perfect egg-shell distribution of the Pd NPs onto the support. It was proposed that such a distribution was the reason of the high selectivity of the Nanoselect catalysts in the semi-hydrogenation of alkynes.



Scheme 1.4. a. Synthesis of Pd Nanoselect catalysts and hydrogenation of alkynes and alkynols.

b. Geometric and electronic effects of HDDMA stabilizer over the Pd NPs surface<sup>8</sup>

Pérez-Ramírez and co-workers investigated the selectivity patterns and accessibility constrains of this catalyst using experimental and theoretical approaches.<sup>17</sup> According to DFT calculations, HDDMA is adsorbed rigidly over the Pd surface and such an adsorption reduces both the number of active sites (geometric effect) and the hydride coverage at the Pd surface (electronic effect) (Scheme 1.4b). This explains its intrinsic alkene selectivity. However, under high H<sub>2</sub> pressures, the adsorption of H in the sub-surface is relatively easy and over-hydrogenation cannot be avoided. In addition, the authors correlated the hydrogenation performance of a series of Pd-based catalysts with structural descriptors. They concluded that the rigidly adsorbed ligands restrict the accessibility of the substrate to the catalyst active sites (forming cavities with elliptical shape), providing exceptional performance for the hydrogenation of terminal alkynes but low activity for disubstituted and bulky alkynes (Scheme 1.4b). These

findings demonstrated that the surface structure determined during the colloidal preparation step lead to the production of very selective catalysts.<sup>17</sup>

In a subsequent report, the same authors addressed the impact of the stabilizer content on the catalytic behavior of HHDMA stabilized Pd NPs supported on titanium silicate.<sup>69</sup> For this purpose, a series of Pd-HHDMA/TiSi<sub>2</sub>O<sub>6</sub> catalysts with distinct HHDMA contents (0.3–16.8wt%), was prepared while maintaining the average particle size to 5 nm and Pd content to 0.3wt%. Interestingly, an increase in the catalytic activity at higher ligand content was observed in the semi-hydrogenation of 1-hexyne. DFT calculations indicated that the ligand changed its adsorption configuration as a function of the HHDMA concentration. At low coverage, the organic layer is almost flat on the surface of the Pd NPs blocking a large number of metal sites while a high HHDMA coverage favors an extended three-dimensional configuration of the alkyl chain. Consequently, a lower fraction of Pd sites are blocked by the organic layer at high HHDMA coverage. Witte and co-workers also reported the semi-hydrogenation of 3-hexyn-1-ol catalyzed by Pd NPs using chiral phosphate stabilizers.<sup>70</sup> Small differences were observed in terms of activity and alkene selectivity using these chiral stabilizers in comparison with HHDMA.

## Polymers

Polymeric compounds are frequently applied in the preparation of metal nanoparticles since they can provide steric stabilization to the metal colloid.

In an early study, Hirai and Yakura prepared a series of Pd NPs stabilized by polyvinylpyrrolidone (PVP) of *ca.* 2 nm.<sup>67</sup> They used polymers of distinct molecular weights and they investigated the effect of the thickness of the adsorbed layer of polymer. The layer of polymer at the surface of the NPs resulted to increase from 3.8 to 15.6 nm when increasing the molecular weights from 6000 to 574000 g.mol<sup>-1</sup>. For NPs stabilized by PVP with a molecular weight of 175000 g.mol<sup>-1</sup>, the authors proposed that the protecting PVP molecules take a conformation constituted by a sequence of many short loops (segments in the solution and the NPs surface) and trains (segments

only in contact with the NPs surface) in alternating order with a long tail at both ends as shown in Figure 1.7. The catalytic performances of these Pd NPs stabilized by PVP were examined in the hydrogenation of 1,3-cyclooctadiene under mild conditions (30°C, atmospheric hydrogen pressure and in methanol). The results of the catalytic tests indicated that the specific surface area of these NPs was affecting more significantly to their activity than the adsorbed layer thickness.

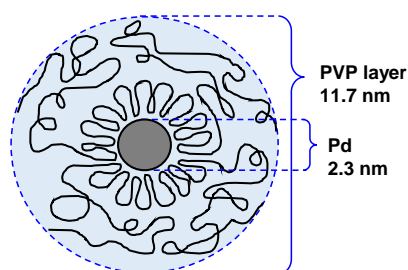


Figure 1.7. Conformation model of protecting PVP layer in suspension of Pd NPs. Preparation conditions: PVP Pw = 175000g.mol<sup>-1</sup> and PVP7Pd = 4<sup>8</sup>

In 2010, Evangelisti *et al.* reported the synthesis of Pd NPs stabilized by PVP by metal vapour synthesis technique.<sup>66</sup> The NPs were formed with different Pd-to-PVP ratio and with mean diameters in the range of 1.5 to 2.5 nm. They were tested in the hydrogenation of a series of aliphatic alkynes. Excellent alkene selectivities were obtained in the hydrogenation of 1-hexyne, 2-hexyne and 3-hexyne (from 96 to 99% at 95% conversion). For the case of internal alkynes, the authors ascribed the observed high stereoselectivity towards the Z isomer to the steric constriction of PVP surrounding the Pd NPs. Interestingly, when 3-hexyne-1-ol was tested; similar performances were observed independently to the Pd-to-PVP ratio.

Similarly, Kiwi-Minsker and co-workers reported the formation of Pd-PVP NPs of by colloidal techniques and their application in the selective hydrogenation of alkynols.<sup>9</sup> They compared the catalytic performances of NPs that was synthesized with a low PVP-to-Pd surface ratio with the performances of NPs that was formed with an extra amount of PVP. Both NPs had the same size of *ca.* 2.6 nm. No difference in terms of

activity or selectivity was observed suggesting that the surface of the NPs was already saturated by the polymer.

Jones and co-workers reported the application of Pd NPs supported on an aminopolymer–silica composite for the selective hydrogenation of alkynes in liquid media.<sup>71</sup> The NPs were synthesized by chemical reduction of Pd(II) precursors loaded into a mesoporous silica material functionalized with branched poly(ethyleneimine) polymers (PEI). The reducing agents used were either hydrogen (H<sub>2</sub>) or sodium borohydride (NaBH<sub>4</sub>) and the PEI served as both stabilizer and linker to the solid support. The rate of over-hydrogenation of phenylacetylene resulted to reduce significantly when support porosity and polymer molecular weight were increased. The beneficial effect of the aminopolymer on the alkene selectivity was attributed to the efficient competition of the amine groups with the alkenes for the surface palladium sites. The authors explained the fact that the branched PEI of large molecular weight had a stronger effect on the selectivity than the PEI of lower molecular weight by the possibility for the branched polymer to cover and passivate the Pd NPs more efficiently. The analysis of the tested catalysts by TEM and ICP indicated an excellent stability, recoverability, and recyclability of this catalytic system.

### **Micelles**

The use of amphiphilic compounds permit the formation of micelles which serve as host for metallic NPs. Depending on the structural characteristics of the amphiphilic compound (generally co-polymers), the metallic precursor and the polarity of the solvent, the core of the micelle can offer a hydrophilic or hydrophobic environment to the embedded metallic NPs.

Kiwi-Minsker and co-workers reported the selective partial hydrogenation of 2-butyne-1,4-diol catalyzed by Pd NPs stabilized in the micelle core of poly(ethylene-oxide)-block-poly-2-vinylpyridine (PEO-b-P2VP).<sup>72</sup> The amphiphilic character of the block co-polymer allowed the formation of micelles constituted by pyridine units in

the core stabilizing the Pd NPs and PEO chains in the shell responsible of its dispersion in water. Colloidal and supported NPs were prepared. The colloidal NPs were formed by reduction with  $\text{NaBH}_4$  and with a size of *ca.* 2 nm. The supported catalyst was prepared by incipient wetness impregnation on  $\gamma\text{-Al}_2\text{O}_3$  (powder form). Both catalysts revealed selectivity towards the alkenol close to 100% up to 94% conversion. Beyond this conversion limit, the over-reduced product was formed. The catalytic tests were performed at pH of 13.4 (by addition of KOH) to avoid the acid-catalyzed isomerization of the products. The authors reported that both pyridine units of micellar core and KOH added to the reaction media enable obtaining these high selectivities without the need to add hazardous additives. This system, presented exhibited stable activity and selectivity and could be recycled and reused several times with a simple ultra-filtration procedure.

Employing a similar supramolecular-micelle approach, Kaneda and co-workers described the stabilization of Pd NPs using poly(amidoamine) (PAMAM) dendrons which have a pyridine core and alkyl end groups assembled into spherical micelle-like structures.<sup>73</sup> Fine tuning of the Pd nanoparticle with a mean diameter ranging from 3 to 10 nm was achieved by adjusting the alkyl chain length and the structure of the dendrons. The resulting NPs could catalyze the highly selective semi-hydrogenation of dienes and acetylenes. In the hydrogenation of 1-phenyl-1-propyne, 98% selectivity to the Z-alkene product was obtained, at 96% conversion. The authors attributed the high alkene selectivity to the ligand effect of the pyridine core of the dendrons.

### **Ionic Liquids**

Ionic liquids (ILs) have been used as solvent and/or stabilizer for the preparation of metallic NPs applied in the semi-hydrogenation of alkynes. Their amphiphilic nature makes them excellent solvents for a wide variety of metallic precursors and organic compounds and since they usually contain polar groups, they can interact with the metal surface and stabilize metallic NPs. Depending on the miscibility properties of the

ILs, they can also permit the recycling of catalytic systems by simple solvent extraction processes.<sup>74</sup>

Dupont and co-workers reported the partial hydrogenation of terminal alkynes using Pd NPs stabilized by ILs.<sup>75</sup> The thermal treatment of palladium(II) acetate ( $\text{Pd}(\text{OAc})_2$ ) in 1-butyronitrile-3-methylimidazoliumN-bis(trifluoromethanesulfonyl)imide  $[(\text{BCN})\text{MI}.\text{NTf}_2]$  resulted in the formation of stable and monodispersed Pd NPs with a mean diameter of *ca.* 7.3 nm. Using these nanocatalysts, phenylacetylene was hydrogenated with 95% selectivity towards styrene at 97% conversion. Also, the possibility to recycle the catalyst was studied and, up to four times, no loss in activity nor selectivity was observed. In these experiments, the hydrogen pressure revealed to be critical to achieve high alkene selectivity. The authors attributed the high selectivity of these NPs to the electronic modification induced by the coordination of functionalized nitrile ILs to the metal surface.

Prechtl and co-workers developed a novel multiphase system with Ni NPs as catalyst embedded in a nitrile-functionalised imidazolium based ionic liquid.<sup>76</sup> This catalyst shows high selectivity in the hydrogenation of diphenylacetylene to (Z)-alkene using very mild conditions. They concluded that the nitrile group was crucial for obtaining high selectivity performances.

More recently, Peng *et al.* reported the preparation of a highly selective Pd/IL/MOF catalyst for the semi-hydrogenation of alkynes.<sup>77</sup> Initially the metal-organic framework template based on Cu was formed in the presence of a ionic liquid (1,1,3,3-tetramethylguanidinium trifluoroacetate, TMGT) and a palladium precursor ( $\text{K}_2\text{PdCl}_4$ ). The later, was subsequently reduced with L-ascorbic acid to form Pd NPs of *ca.* 2 nm. The IL was used to stabilize the NPs and to link both NPs and MOF support as presented in Figure 1.8.

This composite catalyst was tested in the semi-hydrogenation of a series of alkynes displaying excellent selectivities (>99% at >99% conversions). The authors proposed

that interactions between the N atoms of the IL and the Pd NPs surface were responsible for this high selectivity. Moreover, this catalytic system could be recycled up to 4 times without loss of activity nor selectivity. However, after the 5<sup>th</sup> run, some Pd leaching was detected.

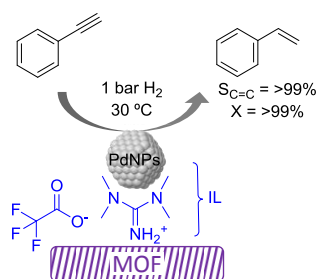


Figure 1.8. Semi-hydrogenation of alkynes catalyzed by Pd NPs supported by a MOF embedded in a IL<sup>8</sup>

## Ligands

Some ligands, frequently used in coordination chemistry, have also been employed as stabilizers for metal nanoparticles.<sup>63,78</sup>

Much before the popularization of the concept of nanoparticles, Caubère and co-workers introduced the preparation of new versatile reducing agents called complex reducing agents (CRA).<sup>79</sup> These reducing agents were prepared by reaction of transition metal salts with reducing systems such as LiAlH<sub>4</sub>, NaBH<sub>4</sub>, NaH. They consisted in non-pyrophobic black suspensions which, in presence of hydrogen, could catalyze selective hydrogenation reactions. These authors reported the preparation of the very active and highly specific nickel catalyst for alkene and alkyne hydrogenations.<sup>80</sup> This catalyst was prepared by chemical reduction of Ni(OAc)<sub>2</sub> using NaH in t-AmOH under nitrogen atmosphere. Then, they extended their studies on complex reducing agents using Pd catalysts. Following the same method, a colloidal Pd catalyst was prepared. The synthesis consisted in the reduction of Pd(OAc)<sub>2</sub> by sodium hydride (NaH) in the presence of 2-methylbutan-2-ol (t-AmOH).<sup>81</sup> This catalyst was active in the semi-hydrogenation of 1-heptyne and 1-octyne with olefin selectivity of 98% for both substrates at complete conversion. However, the presence of N-donor

compounds as catalyst modifiers during catalysis was required to avoid over-hydrogenation of the substrates, among them, quinoline provided the highest selectivities.

Recently, Godard and co-workers reported a versatile method for the preparation of efficient and reusable Pd nanocatalysts immobilized on paper for the selective hydrogenation of alkynes.<sup>82</sup> The Pd nanoparticles were synthesized by a one-pot methodology involving the decomposition of  $\text{Pd}_2(\text{dba})_3$  (dba = dibenzylideneacetone) under hydrogen in the presence of tricyclohexylphosphine ( $\text{PCy}_3$ ) and multi-walled carbon nanotubes (MWCNTs). Subsequently, a suspension of the Pd/MWCNTs was impregnated in the paper carrier by a simple painting process. The resulting paper-based catalyst was active and highly selective in the hydrogenation of a series of alkynes in the presence of quinoline and could be reused up to 5 times without loss of activity or selectivity.

#### 1.5.1.2. Acetylene hydrogenation

To the best of our knowledge, there is only one example of hydrogenation of acetylene using a purely colloidal catalyst. Zhang *et al.* reported the selective hydrogenation of acetylene in water using different monodisperse water soluble Pd NPs.<sup>83</sup> These NPs were synthesized by hydrogen reduction and stabilized by three water soluble stabilizers: hydroxyethyl cellulose (HEC, Mw: 90000), polyquaternium-10 or sodium carboxymethyl cellulose (CMC, Mw: 90000). The NPs mean diameter was respectively 3.2, 3.9 and 2.1 nm.

The Pd-CMC NPs resulted to be the most efficient: 50% of alkene selectivity at total conversion which is a higher performance than that reported for conventional Pd supported catalyst.

In this study, the selectivity was highly influenced by the  $\text{H}_2$ -to- $\text{C}_2\text{H}_2$  ratio and the reaction temperature. The highest ethylene selectivities were obtained with acetylene-rich streams ( $\text{H}_2$ -to- $\text{C}_2\text{H}_2 = 1.5$ ) and at low temperatures.



To date, there are few reports about the acetylene hydrogenation on supported catalysts prepared via colloidal chemistry.

Kiwi-Minsker and co-workers investigated the influence of the stabilizer and the reducing agent on the performance of supported Pd NPs supported on carbon nanofibers in the hydrogenation of acetylene.<sup>84</sup> These NPs were prepared using sodium di-2-ethylhexylsulfosuccinate (AOT), polyvinylalcohol (PVA), and polyvinyl pyrrolidone (PVP) as stabilizers. Also, various reducing agents were used: hydrazine hydrate, ascorbic acid, n-butanol, ethanol and methanol. The semi-hydrogenation of acetylene resulted to be insensitive to the nature of the reducing agent. Also, the authors reported a strong effect on the hydrogenation rate with electrostatic stabilizer as compared to the steric one. Indeed a decrease of the hydrogenation rate was observed when the Pd-AOT NPs were tested in comparison Pd-PVA and Pd-PVP NPs. In contrast, in terms of olefin selectivity, similar responses were obtained over Pd NPs with similar size, independently of the stabilizer used. Interestingly, when the polymeric stabilizer was removed by a combined ozone/H<sub>2</sub> treatment, the ethylene selectivity was negatively affected thus demonstrating the positive effect of the stabilizer in catalysis.

Other studies have addressed the importance of removing the stabilizer after the NPs immobilization on the support. The objective of this step prior to the catalysis is to maximize the number of accessible active sites.

The preparation of Pd-PVP nanocubes, their deposition on a carbon-based support and their subsequent treatment with UV–ozone (UVO) was reported by Kiwi-Minsler and co-workers.<sup>85</sup> This process allowed complete cleaning of the catalyst surface without affecting the morphology of particles. The removal of the PVP displayed a positive effect on the selective hydrogenation of acetylene; the activity was increased by four after the catalyst treatment.

In summary, the selection of the appropriate stabilizer for the preparation of colloidal nanoparticles is crucial to obtain selective catalysts for the hydrogenation of alkynes. It should be selected based on the substrate that is planned to be transformed. For instance, gas-solid reactions are highly sensitive to the presence of residues (even in trace amounts) at the catalyst surface, and therefore require the use of cleaning procedures. In this sense, stabilizers containing only C, H, O, and N (*e.g.* PVP, PVA) are ideal for gas-solid reactions since their decomposition products are generally volatile compounds which do not block the active sites. In contrast, liquid phase reactions permit the modulation of the reactivity of the metallic NPs through the electronic or steric properties of the stabilizers. A frequent strategy to improve the selectivity in the semi-hydrogenation of alkynes is the use of stabilizer containing nitrogen functionalities such as amines, pyridines or nitrile groups.

## 1.5.2. Metal nanoparticles structure

### 1.5.2.1. Control of the nanoparticles size

To study the structure-sensitivity of a metal NPs in a specific reaction, it is necessary to develop well-defined NPs with different size or shape in either supported or colloidal form. The NPs structure widely depends on the nucleation and growth kinetics. A large variety of parameters are able to affect these steps. Among them, the metal precursor nature and concentration, the type of stabilizing agent, the metal-to-stabilizer ratio, the solvent and the reduction temperature. Usually, an increase in the concentration of the reducing agent increases the reduction rate of metal ions leading to smaller metal nanoparticles. Moreover, it was extensively reported that the stabilizer and its relative ratio to the active metal highly influence the particle size and shape. Indeed the stabilizer plays an important role in directing particle size growth and restricting particle size interacting with metal surfaces during the reaction.<sup>86</sup>

Teranishi *et al.* reported a method to control the size of monodisperse Pd NPs from 1.7 to 3 nm by changing the amount of capping agent and the kind and/or concentration of alcohol in the solvent.<sup>87</sup> An increase of the amount of stabilizer led to

the formation of smaller NPs. On the other hand, monodispersed Pd NPs of smaller diameter were obtained in the order methanol/ethanol/1-propanol, indicating that a faster reduction rate of metal ions is an important factor to produce the smaller particles.

Then, the dependence of nanoparticle sizes on the initial concentration of metal ions was reported. Solovov *et al.* presented a method for the synthesis of Pd NPs by reduction of Pd(II) ions with hydrogen.<sup>88</sup> They indicated that the NPs sizes were determined by the initial concentration of palladium ions: the higher the concentration, the larger the nanoparticles.

The concentration of nuclei in the nucleation stage can also be regulated by the combination of two different precursors with different oxidation states. Tsung *et al.* synthesized Pt nanocubes with controlled sizes by introducing two Pt salts with Pt<sup>2+</sup> and Pt<sup>4+</sup>.<sup>89</sup> When higher was the quantity of Pt<sup>4+</sup> in the mixture precursor, the final size of nanocubes was increased by forming the fewer nuclei. Rh, Pd, Ru and their metallic nanoparticles as well as Pt have been prepared with controlled sizes in the 1-10 nm regimes sharing the same ideas.

Finally, the pH also influences the NPs size. Tangeysh *et al.* reported that decreasing the pH from 6.3 to 3.3, the synthesized Pd nanoparticles increased from 1.4 to 5 nm.<sup>90</sup> In the same way Peter T. Witte *et al.* investigated the effect of the metal crystallite size on the catalytic properties and prepared three sizes of colloidal Pd nanoparticles using the nanoselect method and varying the pH of the preparation: higher pH yields smaller Pd crystallites.<sup>16</sup>

#### **1.5.2.2. Metal NPs structure sensitivity – Effect of the NPs size and shape in selective alkyne hydrogenation**

The effects of the metallic particle size and shape is of high importance in heterogeneous catalysis since they can modify the catalytic properties.<sup>91</sup> Indeed, a variation in particle size leads to a modification of the surface-to-volume ratio and the

coordination numbers of the surface atoms affecting thus its reactivity. Large particles possess mainly large crystal planes, whereas small particles display mainly edge and corner atoms.<sup>92</sup> In general, low coordinated sites, located at edges and corners, would strengthen the adsorption of the reagents in comparison to crystal planes (*i.e.*, faces). Similarly the shape of the metal nanoparticles also conditions the fraction of the different types of surface atoms.<sup>92</sup>

Kiwi-Minsker and co-workers studied the structure-sensitivity of colloidal Pd NPs in the selective hydrogenation of 1-hexyne.<sup>93</sup> These NPs were prepared via reverse microemulsion water/AOT/isooctane. The NPS size was increased from 6 to 14 nm by increasing the water-to-surfactant ratio. An increase of TOF was observed when the NPs diameter increased from 11 to 14 nm while similar TOF were obtained in the range of 6 to 11 nm. However, the selectivity towards 1-hexene (96% at 85% conversion) was not affected by the particle size. Similar behavior in TOF and selectivity were observed in the semi-hydrogenation of MBY to MBE using the same catalysts.<sup>94</sup> In a complementary study on the semi-hydrogenation of MBY, the evaluation of Pd-PVP NPs in the range of 2 to 9 nm evidenced similar trends as a function of the particle size: higher specific activity (TOF) over larger Pd NPs and constant selectivity independently of the particle size.<sup>9</sup> The authors correlated the observed size effect on activity by the fact that the fraction of Pd<sub>plane</sub> active sites is more abundant in the large NPs.

Witte *et al.* studied the effect of the metal crystallite size in the hydrogenation of 3-hexyn-1-ol using Pd NPs between 5 and 25 nm prepared by the Nanoselect method.<sup>15</sup> Interestingly, when the smallest Pd NPs were used, the TOF decreased and the alkene selectivity was improved.

Zhou and co-workers studied the size effect on the selective hydrogenation of phenylacetylene catalyzed by Pd NPs between 4 and 12 nm supported on  $\alpha$ -Al<sub>2</sub>O<sub>3</sub>.<sup>95</sup> The catalysts were prepared by a two-step protocol. The first step consisted in the

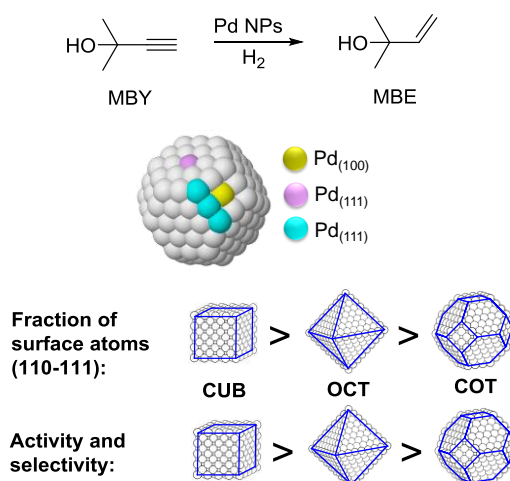
chemical reduction of  $\text{Pd}^{2+}$  by  $\text{NaBH}_4$  in the presence of PVP, followed by the deposition of the metal colloid onto  $\alpha\text{-Al}_2\text{O}_3$ . In catalysis, an increase in specific activity and styrene selectivity was observed when increasing the particle size from *ca.* 4 to 6 nm. Further increase of the particle size from *ca.* 6 to 12 nm resulted in a slight increase in specific activity while the styrene selectivity decreased gradually. The antipathetic size-sensitivity observed in this report is in the same line than studies performed using other substrates such as 1-hexyne and 2-methyl-3-butyn-2-ol. This behavior can be associated to the increase of the fraction of low index planes (faces) in larger nanoparticles considering that such a sites ( $\text{Pd}_{100}$ ) are more active in the hydrogenation of alkynes.

Concerning the acetylene reagent, Kiwi-Minsker and co-workers studied the particle size effects of Pd NPs in the range of 8 to 13 nm for supported Pd/CNF/SMF nanocatalysts (Carbon nanofibers/sintered metal fibers).<sup>96</sup> Similarly to what was observed for liquid substrates, the TOF was found to increase with the particle size up to a critical diameter of 11 nm. Above this value, the specific activity was size-independent. The initial selectivity was also found to be size independent. This size effect below 11 nm was suggested to be “geometric” in nature due to the size-sensitive formation of a  $\text{Pd-C}_x$  phase.<sup>97</sup> Therefore, for smaller particles, the C/Pd ratio is higher and carbonaceous deposits block most of the active Pd surface.

The particle shape can also have important impacts on the performance of metallic NPs in catalysis.

The effect of the nanocatalysts shape in the selective hydrogenation of MBY was studied using PVP stabilized Pd nanocubes (6 and 18 nm), octahedrons (31 nm), and cuboctahedrons (5.5 nm).<sup>98</sup> Based on the observed activity and selectivity two types of active sites were proposed for this reaction as displayed in Scheme 1.5: those on the planes where the semi-hydrogenation of MBY to MBE takes place and those at the edges that are responsible for the over-hydrogenation. By considering the surface

statistics for nanocrystals with different shapes and sizes, the optimal catalyst in terms of productivity and MBE selectivity was concluded to be cubes of *ca.* 3.5 nm.



Scheme 1.5. Effect of the Pd nanocrystals shape on the selective hydrogenation of MBY<sup>8</sup>

Nevertheless, an analogous study on the effect of the particle size and shape in the acetylene semi-hydrogenation pointed out that the NPs shape does not influence the catalyst selectivity, while the activity decreases in the order Pd<sub>octahedrons</sub> > Pd<sub>cuboctahedrons</sub> > Pd<sub>cubes</sub>.<sup>41</sup> The authors concluded that for acetylene, octahedron represents the optimal shape. Concerning the optimal particle size for this substrate, calculations predicted that Pd octahedrons of 3 nm would display the maximum catalyst activity.

In view of the distinct conclusions reported on the effect of the particle size/shape of Pd nanocrystals on catalyst performances, it can be assumed that these effects are sensitive to the studied substrate and therefore, cannot be generalized. Moreover, since the size and shape are closely related parameters, studies in this area need to consider the intrinsic correlation between them.

### 1.5.3. Role of the support

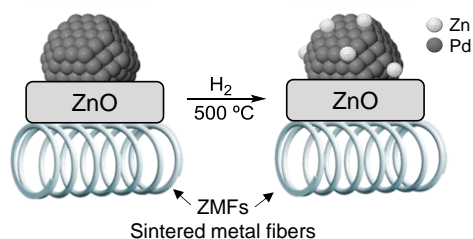
In 2012, a comprehensive discussion on the role of the support the selective hydrogenation of alkynes was reported by Kiwi-Minsker and co-workers.<sup>12</sup> The immediate role of the support is to dilute the active phase and to facilitate the catalyst

handling. However, the selection of the appropriate support can be a powerful tool to tune the catalyst properties. Indeed, the support allow some control of the NPs size, the metal dispersion and the stability of the NPs.<sup>99</sup> Furthermore, the performance of a catalyst can be modified by the chemical and electronic properties of the carrier via metal–support interactions while its structural properties affect the diffusion and adsorption of the reactants and products. The impact of the support will also depend on the thermal treatments, including activation steps, to which the catalytic material will be submitted. For instance, when reducible oxides are used as supports, their partial reduction during the thermal treatment may result in strong metal-support interactions (SMSI) which can cause site blocking via migration of partially reduced oxide species from the support or via the formation of new bimetallic phases.<sup>100,101</sup>

The surface characteristics and adsorption properties of a carrier can also be modified by the incorporation of functionalities in pre-treatment steps. For instance, the treatment of carbon materials with reagents such as O<sub>3</sub>, CO<sub>2</sub>, HNO<sub>3</sub>, HCl, H<sub>2</sub>O<sub>2</sub> and NaOH can modify their surface by introducing oxygen-containing groups.<sup>102</sup>

In the following paragraphs, the impact of the support on the performance of nanocatalysts in the selective hydrogenation of alkynes is discussed with a particular focus on the recent results involving the use of colloidal techniques for the preparation of the active phase.

High alkenol selectivity (95% at full conversion) was reported in the hydrogenation of 2-methyl-3-buten-2-ol (MBE) over a structured catalyst of Pd/ZnO on sintered metal fibers (SMFs).<sup>103</sup> This catalyst was prepared by deposition of a colloidal suspension of Pd NPs of 7 nm over ZnO/SMF followed by reduction by hydrogen at 500°C. Based on the comparison with a Pd/Al<sub>2</sub>O<sub>3</sub> catalyst, the high alkenol selectivity observed for the ZnO supported material was attributed to the alloyed structure of the active phase, Pd/PdZn, formed during the high-temperature treatment under hydrogen as shown in Scheme 1.6.



Scheme 1.6. Strong metal-support interactions (SMSI) in Pd/ZnO/SMF catalyst formed during the high temperature activation treatment<sup>8</sup>

Over the last years, several studies were dedicated to the preparation of colloidal NPs which incorporates materials frequently used as supports (*e.g.* iron oxides). In those cases, the purpose of such incorporation is the transmission of magnetic properties to the active phase as a strategy for recycling the colloidal catalyst. For instance, the preparation of magnetically recoverable Pd catalysts by thermal decomposition of palladium acetylacetonate ( $\text{Pd}(\text{acac})_2$ ) in the presence of iron oxide nanoparticles was reported.<sup>104</sup> In the semi-hydrogenation of 2-methyl-3-butyn-2-ol, these catalysts resulted to be more efficient than similar Pd NPs prepared in the absence of iron oxide NPs (96% selectivity at 95% conversion vs. 100% sel. at 6% conversion). The composition of the iron oxide NPs also revealed to influence the catalytic performance of the Pd NPs since those prepared from iron species in a lower oxidation state resulted to be the most active. According to the authors, electron transfer from the iron oxide NPs to the Pd surface could accelerate the reduction of the alkyne.

Another example of a very selective catalyst for the semi-hydrogenation of alkynes is the multi-walled carbon nanotubes (MWCNT) supported  $\text{Fe}_3\text{O}_4\text{-Cu}_2\text{O-Pd}$  nanocomposite.<sup>105</sup> This catalyst was prepared by initial deposition  $\text{Fe}_3\text{O}_4$  and CuNPs onto the MWCNTs followed by in situ galvanic replacement between Cu and  $\text{PdCl}_4^{2-}$ . Interestingly, this nanocomposite was only active in the hydrogenation of terminal alkynes leading to the formation of the corresponding alkenes without any over-hydrogenation. The authors demonstrated that  $\text{Cu}_2\text{O}$  played a crucial role in the selectivity since the absence of this material resulted in the loss of selectivity. However no explanation for such behavior was provided.



The encapsulation of the active phase into the solid support is also a rational strategy to enhance the selectivity of catalysts in the semi-hydrogenation of alkynes. In a very interesting contribution, Bal'zhinimaev and co-workers reported the preparation of Pd nanoclusters of 1-2 nm confined in fiberglass bulk.<sup>106</sup> These catalysts allow the selective hydrogenation of acetylene in the presence of large excess of ethylene. This fact was explained by the ability of glass to absorb predominantly readily polarizable molecules such as acetylene but not ethylene. In addition, this catalyst resulted to be highly resistant towards deactivation under the reaction conditions. This type of approaches could be very promising for the selective hydrogenation processes of gas substrates.

#### **1.5.4. Dilution of the active phase: introduction of modifiers**

The introduction of modifiers is a widely applied strategy to enhance the catalyst performances in the selective hydrogenation of alkynes. A modifier is a component of a catalyst that is able to improve the active substance performances without having necessarily a significant activity on its own. Common modifiers are metals with a lower affinity for hydrogen than the active Pd phase (*e.g.* Ag, Au, Cu, etc.) The introduction of a second metal results in the dilution of the active phase. The impact of such a dilution can be classified according to geometric and electronic effects. The geometric effect is attributed to the blockage of unselective active sites in order to enhance the alkene selectivity. The electronic effect concerns the ability of a modifier to affect the electronic properties of the active metal in order to enhance the thermodynamic selectivity and/or to suppress the formation of sub-surface species.

One of the classical examples of modified catalysts in alkyne hydrogenation is the Lindlar catalyst which consists of 5wt% Pd supported on porous calcium carbonate treated with lead and quinoline as modifiers. These two modifiers influence specific parameters which control the selectivity to the alkene: Pb enhances the thermodynamic factor and hinders the formation of hydrides, while quinoline

prevents the over-hydrogenation reaction by competition with the alkene for the Pd sites.<sup>107</sup>

### 1.5.5. Additives

#### 1.5.5.1. Liquid substrates

An additive can be considered as a process modifier since it is not properly included in the catalyst formulation but is added to the catalytic reaction at the desired dosage to enhance the activity or the selectivity of a catalyst. In terms of selectivity, the general purpose of an additive in the hydrogenation of alkynes is to prevent or retard the over-hydrogenation of the alkene through competition for the metal active sites. In general, the efficiency of an additive is a direct function of its concentration in the feed and its particular adsorption properties at the metal surface.

Recently, the role of surface modification of Pt and CoPt<sub>3</sub> nanoparticles was studied in the selective hydrogenation of 4-octyne.<sup>108,109</sup> This work was performed using experimental and computational approaches. They showed that the balance between the adsorption energetics of the additives and those of alkynes and alkenes at the NPs surface define the activity and selectivity of the nanocatalyst (Figure 1.9). To improve the selectivity toward the alkene product, the adequate additive should have an adsorption energy at the NP surface higher than that of the alkenes. For instance, the addition of primary alkylamines to Pt and CoPt<sub>3</sub>NPs resulted in a drastic increase of selectivity for alkene from 0 to over 90% at 99.9% conversion, indicating that the coverage of the catalyst surface with the alkylamine prevents the hydrogenation of alkenes into alkanes. This study provided new insights on how surface modification affects the activity and/or selectivity of nanocatalysts and constitutes one of the few examples reported on the selective alkyne hydrogenation catalyzed by highly active colloidal Pt NPs.<sup>108,109</sup>

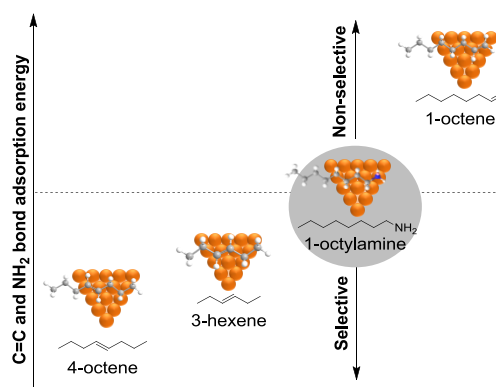


Figure 1.9. Correlation between C=C and NH<sub>2</sub> adsorption energy at the surface of a Pt cluster and the selectivity to the corresponding alkenes<sup>8</sup>

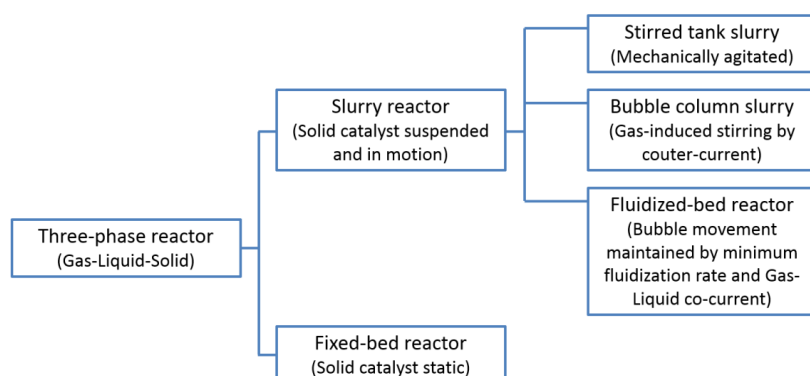
### 1.5.5.2. Acetylene

For the selective hydrogenation of acetylene CO, is the most common process modifier applied over Pd-based catalysts.<sup>100</sup> Based on DFT calculations and experimental results, Bridier *et al.* reported that CO forms a dense blanket that covers the Pd surface, improves the thermodynamic factor, reduces the amount of available H at the surface and the formation of sub-surface H species, and shrinks the size of active ensembles.<sup>58,110</sup> However, CO can also acts as a poison and reduce the number of active sites on the surface, depending on both temperature and pressure.<sup>11</sup> For the case of bimetallic preparations (*e.g.* PdM), an additional effect to be considered when using CO as process modifier is the possibility to induce segregation of the promoting metal. According to DFT calculations, none of the investigated PdM alloys (M = Cu, Ag, Au, Zn, Ga, Sn, Pb and Bi) exhibited sufficient resistance towards segregation under high CO pressures.<sup>11</sup>

Other types of compounds such as amines, alkali and sulfur compounds, have also been employed as molecular modifiers.<sup>100</sup> Recently, the grafting of nitrogen-containing modifiers (polyvinylpyridine or polyethylenimine) on the palladium based catalysts supported on CNF/SMF was shown to provide a significant increase in ethylene selectivity (up to 93%) where the catalyst shows remarkable stability during 120 h on-stream.<sup>84</sup>

## 1.6. Three-Phase Catalytic Reactor

The three-phase catalytic reactors are commonly used in heterogeneous hydrogenation reactions since they provide good heat transfer, temperature control and catalyst utilization.<sup>29</sup> A classification of various types of three-phase catalytic reactors used in industry is presented in Scheme 1.7.



Scheme 1.7. Industrial catalytic three-phase reactors<sup>29</sup>

It is important to select the adequate reactor to obtain the required information. The selection criteria for a reactor used for catalyst testing differ from those for an industrial reactor. Indeed, laboratory reactors are usually small-scale reactors in order to lower equipment costs, materials consumption, utility requirements, to form less waste, to reduce demands in laboratory infrastructure and finally to increase safety by reducing hazards of toxic emissions, explosions and fires. Small-scale laboratory reactors also require accurate experimentation and the use of representative samples. Depending on the application, the reactor type should be adapted.

During the work described in this thesis, two types of reactors were used: stirred tank and fixed bed. These types of reactors will be described in more details in the following sections.

### 1.6.1. Stirred Tank Reactor

This reactor, presented in Figure 1.10, is suitable for the determination of kinetics of a three-phase reaction system at laboratory scale if precise investigations about the potential mass transfer limitations are first performed.<sup>111</sup> Some advantages of this type of reactor are that highly active catalysts can be used, the control of the temperature is usually good, low pressure drop occurs, high liquid-solid mass transfer rates are usually obtained and the design and scale-up are usually easier than for other kind of reactors. However in a stirred tank reactor, poor gas-liquid mass transfer rate are often observed, catalyst attrition occurs, the separation between catalyst and product at the end of the reaction can be difficult and it is hard to detect catalyst deactivation.

To perform surface reactions in three-phase catalysis, the gaseous reactant has to be dissolved first in the liquid phase and later be adsorbed together with the liquid reagents at the catalyst surface. This pathway involves a number of mass transfer steps. Both mass transfer and kinetics are sometimes modeled simultaneously; however this approach complicates the correct estimation of the kinetic parameters.<sup>51,112</sup> Using this methodology, the velocity expressions obtained depend strictly on the studied system and cannot be transposed to another reactor (the kinetics are not intrinsic). Therefore, it is recommended to check whether the selected reaction operates under kinetic regime before comparing different catalysts of considering kinetic expressions.<sup>112</sup> Moreover, performing catalytic tests under conditions that ensure the intrinsic kinetic regime enable a maximization of the process efficiency and a better understanding of the reaction mechanism.<sup>51</sup>

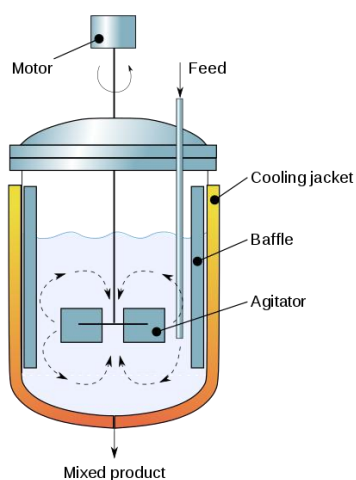


Figure 1.10. Typical stirred tank reactor that can be operated in continuous or batch mode

#### 1.6.1.1. Mixing and Mass Transfer

The activity and selectivity of a catalytic reaction depends on the intrinsic characteristics of the catalysts but also on the effective contact between reactants and catalysts and on the existence of mass and heat transport limitations between phases. These phenomena can slow down the global reaction rate. Therefore, to obtain intrinsic catalyst properties from experimental data, it is necessary to find out the reaction conditions ensuring the kinetic regime.<sup>113</sup>

#### Particle suspension

The choice of the agitation type and velocity is of high importance to provide a good contact between the different phases.<sup>29</sup> For a maximization of the catalyst utilization, the particles should be uniformly suspended in the reaction media during the entire catalytic test. To avoid the catalyst precipitation, a minimum agitation rate is required during the tests. This value depends on the reactor geometry, the agitator type, the properties of the catalyst, the properties of the liquid substrate and the operation conditions. Zwietering *et al.*<sup>114</sup> proposed a correlation that enables the estimation of the minimum agitation required to ensure complete suspension of the catalyst in a stirred vessel:

$$N_m = \frac{\beta d_p^{0.2} \mu_L^{0.1} g^{0.45} (\rho_p - \rho_L)^{0.45} \omega^{0.13}}{\rho_L^{0.55} d_I^{0.85}} \quad (1.3)$$

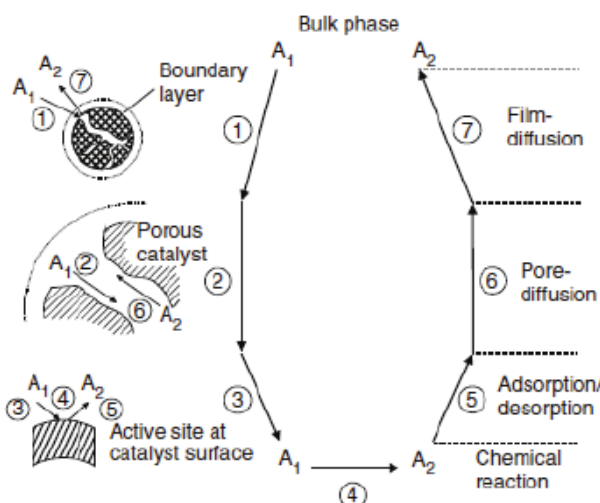
Where  $d_p$  is the reactor inside diameter,  $\mu_L$  is the liquid viscosity at the operating conditions,  $g$  is the gravitational acceleration,  $\rho_p$  is the catalyst density,  $\rho_L$  is the liquid density at the operating conditions,  $\omega$  is the catalyst loading and  $d_I$  the stirrer diameter.  $\beta$  corresponds to a dimensionless number for a given system geometry. Nienow<sup>115</sup> showed that an approximate value of this number is given by:

$$\beta = 2 \left( \frac{d_T}{d_I} \right)^{1.33} \quad (1.4)$$

### Transport Limitation

The efficiency of a reaction highly depends not only on the catalyst intrinsic activity and selectivity but also on the interaction of mass and heat transfer with chemical kinetics. External gas-liquid (G-L) and liquid-solid (L-S), as well as internal mass transfer usually control the reaction rates and selectivity.<sup>51</sup> Therefore before considering kinetic expressions or comparing catalysts performances, it is necessary to check if the selected reaction system proceeds in kinetic regime. The classical seven steps for a catalytic reaction are presented in Scheme 1.8:

- ① Diffusion of the reactants from the bulk phase to the external surface of the catalyst pellet.
- ② Diffusion of the reactant from the pore mouth through the catalyst pores to the immediate proximity of the internal catalytic surface (the point where the chemical transformation occurs).
- ③ Adsorption of the reactants on the inner catalytic surface.
- ④ Reaction at specific active sites on the catalyst surface.
- ⑤ Desorption of the products from the inner surface.
- ⑥ Diffusion of the products from the interior of the pellet to the pore mouth at the external surface.
- ⑦ Diffusion of the products from the external pellet surface to the bulk fluid.



Scheme 1.8. Individual steps of a simple heterogeneous catalytic fluid-solid reaction  $A \rightarrow B$  carried out on a porous catalyst<sup>113</sup>

The transport of reagents and products between phases can limit the reaction rate. In this case, the experimental parameters should be adjusted to either lower the reaction rate (*i.e.*, lower reaction temperature, pressure, different reaction concentrations) and/or increase the rate of mass (or heat) transfer (*i.e.*, increase agitation rate, increase flow rate, decrease catalyst particle size). If diffusion or mass transfer steps (1, 2, 6 and 7) take place very quickly, the resistances of the mass transfer from the bulk to the particle surface and from the particle surface to the active site in the pore can be neglected. Thus, the concentration around the catalytic site is supposed to be the same as that of the bulk phase and the reaction rate is not affected by the mass transfer steps.

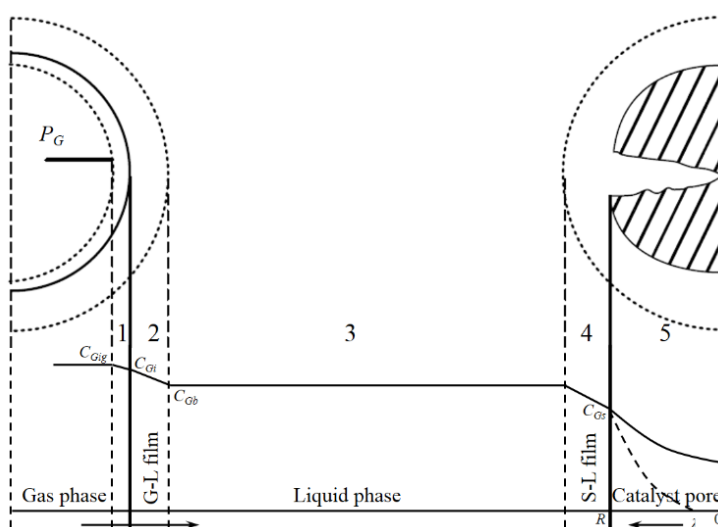
In the three-phase catalytic systems, the transport rate of gas from the gaseous phase to the liquid phase is usually significant. Thus, the apparent reaction rate is affected by the mass transfer and diffusion between phases more specifically when the intrinsic surface reaction is quite fast such as alkynes hydrogenation over a Pd-based catalyst.



## External Transport Limitations

The diffusion of the reactant from the bulk phase to the external surface of the catalyst (step 1 on Scheme 1.8) occurs through four major mass transfer resistances displayed in Scheme 1.9:

- Diffusion in the bulk gas phase (1)
- Mass transfer in the gas-liquid interface (2)
- Diffusion in the bulk liquid phase (3)
- Mass transfer in the liquid-solid film (4)



Scheme 1.9. Mass transport resistances of gaseous reactant in three-phase catalytic reaction system<sup>29</sup>

- *Diffusion in the bulk gas phase (1)*

The gaseous reactant G is initially present in the reactor as gas bubbles, its concentration in the interior of these bubbles is  $C_{Gg}$  and on the gas-side of the gas-liquid interface is  $C_{Gl}$ . The diffusion rate of the gaseous reactant in the gas bubble is defined as:  $r_G = k_g a (C_{Gg} - C_{Gl})$ , where  $k_g$  represents the gas film mass transfer coefficient and  $a$  is the gas-liquid interfacial area per unit volume of liquid. This part of the diffusion resistance used to be neglected since the diffusivity in gases is much greater than in liquids.<sup>116</sup>

- *Mass transfer in the gas-liquid interface (2)*

The rate of mass transfer between gas and liquid is defined as:  $r_G = k_L a (C_{Gi} - C_{Gb})$ , where  $k_L a$  is the volumetric liquid-side mass transfer coefficient and  $(C_{Gi} - C_{Gb})$  the concentration difference of gaseous reactant between the liquid-side of the gas-liquid interface and the liquid-bulk.

The volumetric liquid-side mass transfer coefficient may be affected by the geometry of the reactor, the stirrer type and its diameter, the stirring speed and the operating conditions. A common approach to check experimentally if the mass transport resistance at the gas-liquid interface is negligible in the studied system is to perform catalytic tests at different stirring rates.

- *Diffusion in the bulk liquid phase (3)*

The resistance to the diffusion of the gas reactant in the liquid substrate can be neglected if the applied agitation rate is superior to the minimum agitation  $N_m$ .<sup>29</sup>

- *Mass transfer in the liquid-solid film (4)*

The rate of the gas transport from the liquid to the solid film is defined as  $r_G = k_s a_s (C_{Gb} - C_{Gs})$ , where  $k_s$  is the liquid-solid mass transfer coefficient,  $a_s$  the external specific surface area of the catalyst and  $(C_{Gb} - C_{Gs})$  the concentration difference between the liquid bulk and the catalyst surface.

The stirring speed tests are useful to check the presence of resistance by mass transfer at the gas-liquid and liquid-solid interphases. However, it was reported that the agitation affects mostly the gas-liquid transport and thus these tests might not be sufficient to evidence liquid-solid transport limitations.<sup>29</sup> Indeed, when small catalyst particles are used, they tend to move together with the liquid and the slip velocity will not just increase by increasing the stirring rate. Consequently, to identify possible mass transfer into the liquid-solid film, mass transfer, additional tests varying the amount of catalyst can be performed.

## Internal Transport Limitations

The rate of internal diffusion can be expressed as:  $r_G = \omega k_{int} C_s \eta_c$ , where  $k_{int}$  is the intrinsic reaction rate,  $\omega$  the catalyst loading,  $C_s$  the reactant concentration on the catalyst surface and volumetric liquid-side mass transfer coefficient and  $\eta_c$  the internal effectiveness factor.

The catalytic effectiveness factor  $\eta$  is defined as the ratio between the actual overall rate of reaction and the rate of reaction that would result if entire interior surface were exposed to the external pellet surface conditions.<sup>111</sup> When this factor tends to 1, it means that the reactor operates at maximum efficiency. If  $\eta$  is less than 1, the system presents intraparticle transport resistance.

To determine if the reaction presents internal transport limitations, a dimensionless criterion can be estimated, the Weisz-Prater modulus:  $\Phi = \frac{-r_G \rho_p d_p^2}{D_{\varepsilon,G} [D^I]}$ .

Where  $r_G$  is the observed reaction rate of gas per unit gram of catalyst particles,  $\rho_p$  is the catalyst density,  $d_p$  is the mean diameter of catalyst particles,  $[D^I]$  is the initial concentration of gas reactant in the bulk liquid and  $D_{\varepsilon,G}$  is the effective diffusivity of the gas in the liquid.

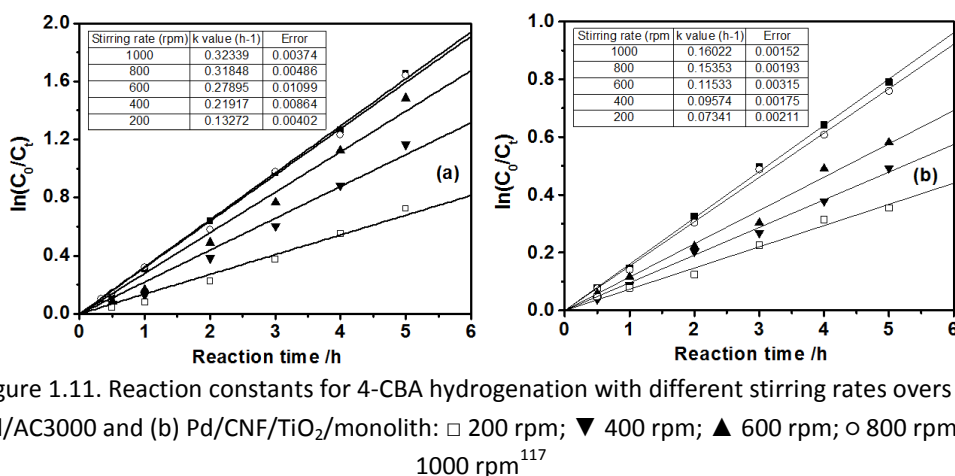
It was reported that the use of very small catalyst particles (mainly smaller than 200  $\mu\text{m}$ ) can minimize the intraparticle concentration gradients.<sup>29</sup>

## Verification of the kinetic regime in hydrogenation reactions

To verify the absence of external mass transfer limitations, a common approach is to carry out catalytic tests under different stirring rates and compare the reaction rates obtained.

In a kinetic study of the partial hydrogenation of 1-hetpyne, Maccarrone *et al.* reported the absence of external gas-liquid limitations at agitation speed higher than 500 rpm.<sup>112</sup> Similarly, Zhu *et al.* studied the influence of the external diffusion on the selective hydrogenation of 4-CBA over Pd-based catalysts.<sup>117</sup> The apparent reaction rate of 4-CBA hydrogenation was estimated for agitation speeds between 200 and 1000 rpm over Pd/AC3000 and Pd/CNF/TiO<sub>2</sub>/monolith catalysts. The results are

displayed in Figure 1.11. The reaction rate remained constant from 800 rpm indicating the absence of external diffusion limitations with stirring speeds higher than this value.



Finally, Kiwi-Minsker and coworkers studied the mass transfer interactions with intrinsic reaction kinetics for the three-phase selective hydrogenation of MBY to MBE over a modified Pd/CaCO<sub>3</sub> catalyst.<sup>51</sup> They probed the existence of external and internal mass transfer limitations through the estimation of volumetric Gas-Liquid (G-L) and Liquid-Solid (L-S) mass transfer coefficients. The volumetric G-L mass transfer coefficient ( $k_L a$ ) of hydrogen in MBY was estimated in the absence of catalyst particles by gas adsorption experiments at different stirring speeds. It was concluded that G-L mass transfer was not influencing the global hydrogenation rate at agitation speed higher than 1500 rpm for the given reactor set-up and under the reaction conditions used. Then, to estimate the influence of L-S mass transfer on the catalytic reaction, the Carberry numbers (ratio of the observed reaction rate to the maximum mass transfer rate) at various stirring speed and for two concentrations of dissolved hydrogen were calculated. The alkyne mass transfer became important at high alkyne conversions, high hydrogen concentrations and low stirring speed. Thus, reaction conditions providing the kinetic regime were established at low hydrogen concentration and high stirring rate.

Concerning the verification of the internal mass transfer limitations, a first approach is to carry out catalytic tests using catalyst support of different sizes and compare the different reaction rate obtained.

For instance, Maccarrone *et al.* studied the kinetics of the partial hydrogenation of 1-heptyne over Ni/Al<sub>2</sub>O<sub>3</sub> and Pd/Al<sub>2</sub>O<sub>3</sub> catalysts.<sup>112</sup> They milled catalyst pellets to samples of different particle size. A fraction bigger than 100 mesh (<150 µm), a fraction of 60-100 mesh (250-150 µm) and pellets of 1500 µm (not milled) were tested. The values of 1-heptyne conversion obtained were the same for the two milled fractions indicating the absence of internal diffusion limitations for catalyst particles lower than 250 µm.

Zhu *et al.* also performed an experimental study about the effect of mass transfer on the catalyst performances in the selective hydrogenation of 4-carboxybenzaldehyde (4-CBA).<sup>117</sup> They compared the catalytic results of a Pd catalyst supported on carbon nanofiber coating on cordierite monolith (Pd/CNF/TiO<sub>2</sub>/monolith) to Pd catalysts supported on different size activated carbon (Pd/AC3000 pellets, Pd/AC160 µm and Pd/AC50 µm) and on carbon nanofibers aggregates (Pd/CNF160 µm). The initial reaction rates per mole of surface-Pd were calculated. The Weisz-Prater numbers, Thiele modulus and internal diffusion effectiveness factor were also calculated. The results indicated insignificant internal diffusion limitations for Pd/AC50, Pd/CNF160 and Pd/CNF/TiO<sub>2</sub>/monolith. The data showed a minor influence of diffusion on the performances of the Pd/AC160, whereas the performances of Pd/AC3000 were strongly affected by diffusion limitations. The catalytic performances of the Pd/CNF/TiO<sub>2</sub>/monolith were comparable to Pd/CNF and the Pd/AC with the particles of 50 µm, while Pd/AC with larger support particles resulted in a lower activity per Pd active surface site, due to internal mass transfer limitations.

### 1.6.2. Fixed bed reactor

A wide variety of catalytic reactions are performed in fixed bed reactors (Figure 1.12), since they are easy to operate, use relatively simple technology and are inexpensive to build.<sup>111</sup>

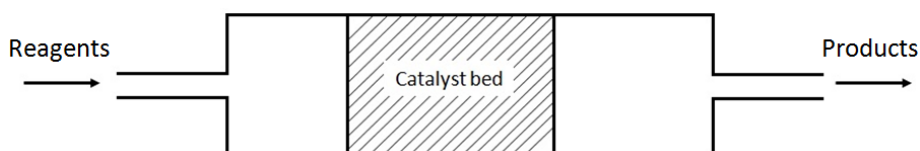


Figure 1.12. Scheme of a typical fixed bed reactor

Nevertheless, a current problem in catalysis is the catalyst deactivation over time. In this type of reactors, if the tested catalyst activity decays significantly during an experiment, the initial reaction rates will be significantly different from the final reaction rates, adding thus a level of complexity to the studied system. The reaction may follow different paths as the catalyst activity decays, leading to variation in the selectivity to the desired product during the course of the experiment. Therefore, sorting out kinetic parameters and reaction pathways are not straightforward tasks. A wide variety of mechanisms have been proposed by Butt and Petersen to explain and model catalyst deactivation.<sup>118</sup>

As detailed above, mass transfer limitations are present in a large number of industrial reactions. In mass transfer-dominated reactions, the overall rate of a reaction is limited by the rate of transfer of reactants from the bulk gas or liquid phase to the active site. In consequence, mass transfer-limited reactions respond in different ways to variation of temperature and flow conditions. To ensure the direct measurement of intrinsic reaction kinetics, transport limitations can be assessed. To do so, several correlations can be used such as the Carberry number for external mass transfer limitation or the Weisz modulus for internal diffusion limitation, however they depend on a wide variety of parameters (reactor geometry, reaction conditions or catalyst).<sup>111</sup>

## 1.7. Design Of Experiments

As detailed in this introduction, the development of novel metallic nanocatalysts and the catalytic evaluation of their performances are complex processes that depend on a large amount of variables. Therefore, in this thesis, the planning and analysis of the major part of the experiments were carried out using Design Of Experiments (DOE).

This methodology is not recent and, despite presenting advantages, has not been widely used in the nanocatalysis field. A presentation of the main concepts of this methodology is provided in this section.

### 1.7.1. Definition of the methodology

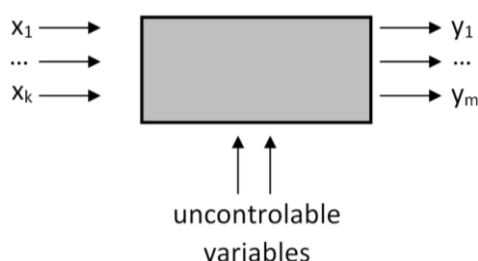
Experimentation plays a fundamental role in research and development. Its aim is to collect significant data from a system of interest. However, data are meaningful within the frame of a conceptual model. Sometimes, the phenomenon under study is well-understood and it is possible to postulate a model based on an appreciation of physical or mechanistic theory: these models are called theoretical models. For instance, an equation rate gives the relation between the concentration of a component as the function of the time and follow the chemical kinetic theory. However, sometimes the mechanism of the studied system is not understood sufficiently or is too complicated to allow an exact model to be postulated from theory. For instance, the mechanism of formation of metallic NPs is still not well-understood and there is no theoretical model that allows the prediction of the effects of synthetic parameters on their size and shape. In such circumstances, empirical models are useful.<sup>119</sup>

The Design Of Experiments is used to decide the pattern of experiments that will provide the most meaningful data and that will be useful to construct a descriptive model of the system of interest. Then, these models are used to understand better a system and are useful to make decisions to optimize or improve its quality.<sup>120</sup>

Usually, the ability to experiment is limited by time and resources. Moreover, the observed result of an experiment includes error. This result ( $y$ ) is defined as:  $y = \eta + \varepsilon$ , where  $\eta$  is the true (but unknown) result of the experiment in absence of experimental noise and  $\varepsilon$  a random contribution that varies each time the experiment is repeated. The joint analysis of the factor settings and the observed responses will allow drawing conclusions on the system under study and guide the choice of future

actions. Analysis will necessarily involve the use of statistics, since this discipline provides the tools to work in uncertain environments.

The DOE is usually applied to systems as shown in Scheme 1.10. In these systems, the variables that are measured as the result of an experiment are called response ( $y$ ). They depend on the value of one or more controllable independent variables called factors ( $x$ ). The observed responses may also be influenced by other variables that are not controlled by the experimenter.



Scheme 1.10. Representation of a system studied using experimental design (DOE): factors ( $x$ ) and responses ( $y$ )<sup>120</sup>

When the experiments are run following DOE, it is possible to know how many experiments will be needed to obtain the desired information. The individual effects of each parameter and their interactions can be studied independently from each other from a single set of designed experiments. There is interaction between two factors A and B when the effect of the factor A is different depending on which value the factor B takes.<sup>120</sup>

Finally, the DOE approach enables the evaluation of the significance of the effect of the parameters and it is possible to distinguish true effect from random variation.<sup>121</sup>

The traditional experimentation method is the variation of “One-Factor-At-a-Time” while keeping the rest constant (OFAT).<sup>121</sup> This approach consists in making one experiment and, depending on the result, decides the next experiment. Although the desired results may be obtained fast, this methodology is usually time-consuming.<sup>121</sup> Moreover, it presents the risk that the obtained solution does not correspond to the optimum position. Indeed, the experimenter perceives that the optimum is reached



because the response does not improve when the factor is changed, but he could be working far away from the real optimum position as shown in Figure 1.13. Other drawbacks of the OFAT are that it does not reveal the existence of interactions between factors, the differentiation of random variation from true effect of factor is not straightforward and, with this approach, it is not easy to foresee how many experiments will be needed to achieve the desired objectives.<sup>121</sup>

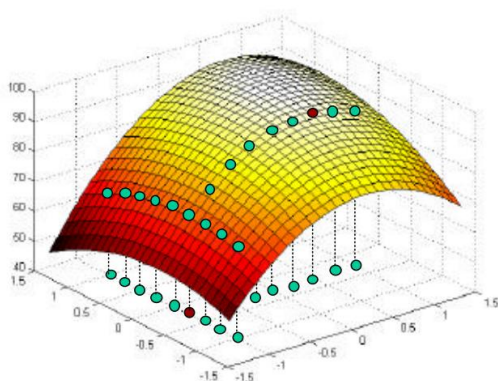


Figure 1.13. Limitations of the OFAT methodology when determining the optimum of a system<sup>120</sup>

Hence, the use of mathematical and statistical methodology to guide the optimal planning of experiments, namely the Design Of Experiments (DOE), is recommended. In this way, experimentation cost and influence of experimental error can be minimized. Unlike the OFAT approach, the statistical DOE provides the mathematical framework to vary all factors simultaneously and the effects are obtained by combining the results of the entire set of experiments. This methodology helps the experimenter to select the optimal strategy in order to obtain the desired information with a small number of experiments, *i.e.* with the maximum efficiency. It also enables the evaluation of the experimental results with a maximum reliability.

### 1.7.2. Application of the design of experiments

The DOE usually follows the procedure detailed below.

1. To understand well the problem and define clearly the objectives. It is necessary to collect all available and relevant information about the studied

system. The experimenter will have to define how much information he wants to gain. The possibilities are:

- a. To find out which single factor affects the most the system (out of many): linear model with the study of the main effects.
  - b. To study the single effects and the interactions of a rather small number of factors: linear model with the study of interaction effects.
  - c. To find out the optimum values of a small number of factors: quadratic model that includes the main, interaction and square effects.
2. To define the output variables (responses) that will be relevant to answer to the problem raised. These variables will be the result measured of each experiment.
  3. To identify which input variables (factors) can potentially influence the responses. For each factor, the experimenter must decide whether it will remain constant or will vary controllably during the set of experiments. In addition, the non-controllable but measurable and non-controllable and non-measurable factors must be identified. The experimenter should be aware of the potential that each factor could have on the response. Uncontrolled factors can introduce random variations in the response that hinder the analysis of experimental results.

For each controlled factor, the values to be studied must be specified. These are called the levels of the factors. Generally, two levels are studied for each factor (the high level, coded +1, and the low level, coded -1, but it is also possible to perform multi-level experiments (more than two levels for each factors or a mixed between two-levels and higher levels for some factors).

4. To establish the experimental strategy (experimental design) to gain the desired information in the most economical way and create the experimental plan.

5. To perform the planned experiments. They have to be performed in a random order to ensure that the non-controllable factors do not introduce confusion and bias in the results.
6. Finally, to analyze and interpret the collected data. Once the experimental results are available, it is possible to calculate the effects of the studied factors and their interactions. The statistical tests allow to check whether the calculated effects are significant compared with the experimental error.

In this thesis, the objectives of the designs implemented were the study of the effect of single factors and interactions on a defined response, thus full factorial and fractional factorial designs were used. These types of design are detailed in the next section.

### **1.7.3. Description of the two types of design used in this thesis**

#### **1.7.3.1. Full factorial design**

When the objective of a study is to determine how the factors influence a response and find out whether they interact with each other, the full factorial design  $2^k$ , where  $k$  is the number of studied factors, is the most adequate strategy. This design enables the exploration of a chosen area of the experimental domain.<sup>122</sup> It is intentionally constructed so that each factor is independent from the others and from any combination of them (interaction). A fixed number of values (levels), two in the case of a  $2^k$  factorial design, are chosen for each studied factor and the experiments are planned for all possible combinations of them. A design of  $k$  factors involves  $2^k$  experiments. For  $n$  levels, the design is denoted  $n^k$  and consists of  $n^k$  experiments.<sup>123</sup> Example of experimental matrix for the study of 2, 3 and 4 factors at two levels are given in Figure 1.14.

RUN	$x_1$	$x_2$	RUN	$x_1$	$x_2$	$x_3$	RUN	$x_1$	$x_2$	$x_3$	$x_4$
1	-	-	1	-	-	-	1	-	-	-	-
2	+	-	2	+	-	-	2	+	-	-	-
3	-	+	3	-	+	-	3	-	+	-	-
4	+	+	4	+	+	-	4	+	+	-	-
			5	-	-	+	5	-	-	+	-
			6	+	-	+	6	+	-	+	-
			7	-	+	+	7	-	+	+	-
			8	+	+	+	8	+	+	+	-
							9	-	-	-	+
							10	+	-	-	+
							11	-	+	-	+
							12	+	+	-	+
							13	-	-	+	+
							14	+	-	+	+
							15	-	+	+	+
							16	+	+	+	+

Figure 1.14. Example of experimental matrix corresponding to full factorial design  $2^2$ ,  $2^3$  and  $2^4$  for the study of 2, 3 and 4 factors, respectively, at two levels

Full factorial designs are attractive when the number of studied factors is not greater than four; otherwise the number of experiments highly increases and this strategy become too long and costly to implement.<sup>124</sup> In these cases, the uses of fractional factorial designs are more appropriate.

### 1.7.3.2. Fractional factorial design

These designs are based on the fact that the main effects and the low-order interactions are usually more important than higher-order interactions. Thus the number of experiments can be reduced without losing relevant information by confounding the single factor effects with negligible higher-order interactions resulting in less experiments than the corresponding full factorial design.<sup>123,124</sup> A fractional factorial design of  $k$  factors studied at two levels will lead to  $2^{k-p}$  experiments with  $p < k$  defined by the experimenter. The choice of the  $p$  number is usually made keeping in mind the number of studied factors, the limitation of the number of experiments and how clearly the effects of the factors need to be separated (resolution of the design). The higher the resolution, the lower the degree of

confounding (confusion between single factor effects and interactions). Indicated in roman letter, the most commonly used resolutions are the III, IV and V and are detailed as follow.

- Resolution III: the main effects (or single factor effect) are not confounded with each other but aliased with two-factor interactions (or two-order interactions).
- Resolution IV: the main effects are not confounded with each other and not aliased with two-factor interactions either but they are aliased with three-factor interactions. Also the two-factor interactions are aliased between each other.
- Resolution V: the main effects are not confounded with each other and not aliased with two-factor interactions either. The two-factor interactions are not aliased with each other but with three-factor interactions.

The confusions of the design are decided by the experimenter and are called the relation of definition. For instance, the full factorial design  $2^4$  given in Figure 1.14 involves sixteen experiments. If the experimenter want to reduce the number of experiments to eight, it is possible to confound one single factor with a third-order interaction:  $x_4$  with  $x_1x_2x_3$  or, as written in this thesis, 4 confounded with 123 (read one two three). The resulting matrix of experiment is given in Figure 1.15. In this case the resulting relation of definition is 1234 (the factor 4 was confounded with the triple interaction 123).

RUN	$x_1$	$x_2$	$x_3$	$x_4 = x_1x_2x_3$
1	-	-	-	-
2	+	-	-	+
3	-	+	-	+
4	+	+	-	-
5	-	-	+	+
6	+	-	+	-
7	-	+	+	-
8	+	+	+	+

Figure 1.15. Example of experimental matrix corresponding to a fractional factorial design  $2^{4-1}$

## 1.7.4. Brief mathematical formulation

### 1.7.4.1. Estimation of the effect

The effects  $b$  are calculated by  $b_i = 2a_i$  where  $a_i$  correspond to the coefficients of the model that are estimated using the least squares formula:  $a_i = (X^T X)^{-1} X^T y_i$  where  $X$  is the designed matrix and  $y_i$  the responses of each experiment.

### 1.7.4.2. Estimation of the standard error of the effects

In this thesis, the variability of the studied systems was estimated from replicas of the central point of the design and assuming that the standard error calculated at this point was similar to the standard error at all the studied experimental points.

The central point of a design correspond to the experimental run performed at level 0 (in coded value) of the studied factors as the RUN 5 given in the example of Figure 1.16.

RUN	Coded value		Real variables	
	$T (^{\circ}C)$	$P (bar)$	$T (^{\circ}C)$	$P (bar)$
1	-	-	30	5
2	+	-	50	5
3	-	+	30	15
4	+	+	50	15
5	0	0	40	10

Figure 1.16. Example of experimental matrix  $2^2$  with central point

Note that to transform a coded value to a real variable or vice versa, the equation is the following:  $\text{coded value} = \frac{(\text{real variable}) - (\text{center variable})}{\frac{1}{2}(\text{range})}$

To estimate the standard error of replicas, the following formula is used:  $\text{std}(b) = \sqrt{\text{var}(b)}$  where  $\text{var}(b) = \frac{4}{N} \sigma^2$  with  $N$  the number of observations and  $\sigma^2$  the variance of the population. It is estimated from replicas by  $s^2 = \frac{\sum_{i=1}^n (y - \bar{y})^2}{n-1}$  where  $n$  is the number of replicas,  $y$  an observation and  $\bar{y}$  the sample average.<sup>119</sup>

### 1.7.5. Uses of DOE for NPs preparation and catalytic tests

Although the DOE methodology brought a revolutionary change in pharmaceutical industry for the development of nanotechnology, it was not widely used in nanocatalysis field.<sup>125</sup>

Few examples of application of the DOE methodology for nanocatalysts preparation or testing were reported. They are described in this section.

Ag NPs synthesis for p-nitrophenol reduction was performed using a multivariate optimization by O. Santos *et al.*<sup>126</sup> Three factors were studied (concentrations of reducing agent, stabilizer and salt precursor) with a two-level Central Composite Design (CCD). The studied responses were evaluated by an equation that considered the maximum absorbance, which is related to the yield of Ag NPs formed; the wavelength at the maximum absorbance, which is relevant to the size of the Ag NPs; and the full width at half-height (FWHH), which is associated with the size distribution. It was reported that the reducing agent concentration did not reveal major influence on the Ag NPs formation for the studied range. In contrast the concentrations of stabilizer and salt precursors did have an effect. Increasing both factors, the response increased reaching a saddle point indicating an interaction between both factors. Optimum conditions were determined leading to very stable NPs.

Then, an example of the use of a full factorial design for the determination of the key parameters in the selective hydrogenation of acetylene over GaPd<sub>2</sub> catalyst was given by Zimmermann *et al.*<sup>127</sup> A 2<sup>4</sup> design was implemented to study the effect of the temperature, pressure, gas flow and H<sub>2</sub>-to-C<sub>2</sub>H<sub>2</sub> ratio. The studied responses were the acetylene conversion, the specific activity and the ethylene selectivity. Temperature and pressure changes were affected all responses strongly. The H<sub>2</sub>-to-C<sub>2</sub>H<sub>2</sub> ratio was of limited impact and the gas flow resulted not to affect significantly in the studied range. With sixteen experiments the authors concluded about “optimal” operating conditions. However, further CCD considering the identified key factors could reveal more precisely the region of optimal conditions thanks to the drawing of a response surface.

Finally, an interesting example of the application of the DOE for obtaining kinetic parameters was reported by Kiwi-Minsker and co-workers.<sup>128</sup> They studied the solvent-free selective hydrogenation of MBY to MBE over Pd/ZnO catalyst. The reaction kinetics was modeled using a Langmuir-Hinshelwood mechanism considering competitive adsorption for the organic species and dissociative adsorption for hydrogen. After determination of the apparent kinetic constants and adsorption constants, the apparent activation energy and reaction order toward hydrogen for the main reaction (MBY to MBE) was estimated following a central composite design (CCD). The choice of this design enabled the verification of quadratic and interaction effects that could modify the final rate expression. In contrast the traditional determination of kinetic data via OFAT experiments assumes a linear influence of the factors which is not always true.

The work described in this thesis deals with the synthesis of novel catalytic system using colloidal approaches and design of experiments for their application in the selective hydrogenation of alkynes. The effects of synthetic parameters on the formation of Pd nanocatalysts were studied and catalytic tests were performed under batch and continuous conditions.



## 1.8. References

- (1) Marteel-Parrish, A. E.; Abraham, M. A. In *Green Chemistry and Engineering*; John Wiley & Sons, Inc: 2013, p 1.
- (2) Descorme, C.; Gallezot, P.; Geantet, C.; George, C. *ChemCatChem* **2012**, *4*, 1897.
- (3) Ross, J. R. H. *Heterogeneous Catalysis*; Elsevier: Amsterdam, 2012.
- (4) Carenco, S.; Leyva-Pérez, A.; Concepción, P.; Boissière, C.; Mézailles, N.; Sanchez, C.; Corma, A. *Nano Today* **2012**, *7*, 21.
- (5) Carenco, S.; Le Goff, X. F.; Shi, J.; Roiban, L.; Ersen, O.; Boissière, C.; Sanchez, C.; Mézailles, N. *Chem. Mater.* **2011**, *23*, 2270.
- (6) Planken, K. L.; Kuipers, B. W. M.; Philipse, A. P. *Anal. Chem.* **2008**, *80*, 8871.
- (7) Hori, J.; Murata, K.; Sugai, T.; Shinohara, H.; Noyori, R.; Arai, N.; Kurono, N.; Ohkuma, T. *Adv. Synth. Catal.* **2009**, *351*, 3143.
- (8) Delgado, J. A.; Benkirane, O.; Claver, C.; Curulla-Ferre, D.; Godard, C. *Dalton Trans.* **2017**, *46*, 12381.
- (9) Yarulin, A.; Yuranov, I.; Cárdenas-Lizana, F.; Abdulkin, P.; Kiwi-Minsker, L. *J. Phys. Chem. C* **2013**, *117*, 13424.
- (10) Vilé, G.; Baudouin, D.; Remediakis, I. N.; Copéret, C.; López, N.; Pérez-Ramírez, J. *ChemCatChem* **2013**, *5*, 3750.
- (11) Lopez, N.; Vargas-Fuentes, C. *Chem. Commun.* **2012**, *48*, 1379.
- (12) Crespo-Quesada, M.; Cárdenas-Lizana, F.; Dessimoz, A.-L.; Kiwi-Minsker, L. *ACS Catal.* **2012**, *2*, 1773.
- (13) Odom, T. W.; Pileni, M.-P. *Acc. Chem. Res.* **2008**, *41*, 1565.
- (14) Beaumont, S. K. *PCCP* **2014**, *16*, 5034.
- (15) Witte, P. T.; Boland, S.; Kirby, F.; van Maanen, R.; Bleeker, B. F.; de Winter, D. A. M.; Post, J. A.; Geus, J. W.; Berben, P. H. *ChemCatChem* **2013**, *5*, 582.
- (16) Witte, P.; Berben, P.; Boland, S.; Boymans, E.; Vogt, D.; Geus, J.; Donkervoort, J. *Top. Catal.* **2012**, *55*, 505.
- (17) Vilé, G.; Almora-Barrios, N.; Mitchell, S.; López, N.; Pérez-Ramírez, J. *Chem. Eur. J* **2014**, *20*, 5926.
- (18) Astruc, D. *Inorg. Chem.* **2007**, *46*, 1884.
- (19) Moores, A.; Goettmann, F. *New J. Chem.* **2006**, *30*, 1121.
- (20) Roucoux, A.; Schulz, J.; Patin, H. *Chem. Rev.* **2002**, *102*, 3757.
- (21) Amiens, C.; Chaudret, B.; Ciuculescu-Pradines, D.; Colliere, V.; Fajerweg, K.; Fau, P.; Kahn, M.; Maisonnat, A.; Soulantica, K.; Philippot, K. *New J. Chem.* **2013**, *37*, 3374.
- (22) Helmut, B.; Ryan M., R. *Eur. J. Inorg. Chem.* **2001**, *2001*, 2455.
- (23) Xia, Y.; Xiong, Y.; Lim, B.; Skrabalak, S. E. *Angew. Chem. Int. Ed.* **2009**, *48*, 60.
- (24) Tao, A. R.; Habas, S.; Peidong, Y. *Small* **2008**, *4*, 310.
- (25) Burda, C.; Chen, X.; Narayanan, R.; El-Sayed, M. A. *Chem. Rev.* **2005**, *105*, 1025.
- (26) Mäki-Arvela, P.; Murzin, D. Y. *App. Catal. A Gen.* **2013**, *451*, 251.
- (27) Delgado, J. A., (2014) Cobalt NPs for Fischer-Tropsch Synthesis: from colloidal to well-defined supported nanocatalysts (PhD thesis). Universidad Rovira i Virgili, Tarragona.
- (28) Cookson, J. *Platinum Metals Rev.* **2012**, *56*.

- (29) Zhu, J., (2014) Synthesis of precious metal NPs supported on bacterial biomass for catalytic applications in chemical transformations (PhD thesis). University of Birmingham.
- (30) Boymans, E. H., (2015) Pd and Pt NPs as selective hydrogenation catalysts (PhD thesis). Technische Universiteit Eindhoven.
- (31) Agostini, G.; Groppo, E.; Piovano, A.; Pellegrini, R.; Leofanti, G.; Lamberti, C. *Langmuir* **2010**, *26*, 11204.
- (32) Miyittah, M. K.; Tsaywo, F. W.; Kumah, K. K.; Stanley, C. D.; Rechcigl, J. E. *Commun. soil sci. plan.* **2015**, *47*, 101.
- (33) Börger, L.; Cölfen, H.; Springer Berlin Heidelberg: Berlin, Heidelberg, 1999, p 23.
- (34) Molnár, Á.; Sárkány, A.; Varga, M. *J. Mol. Catal. A: Chem.* **2001**, *173*, 185.
- (35) Bond, G. C.; Webb, G.; Wells, P. B.; Winterbottom, J. M. *J. Catal.* **1962**, *1*, 74.
- (36) Cölfen, H.; Völkel, A. *Eur. Biophys. J.* **2003**, *32*, 432.
- (37) Vossmeier, T.; Katsikas, L.; Giersig, M.; Popovic, I. G.; Diesner, K.; Chemseddine, A.; Eychmueller, A.; Weller, H. *J. Phys. Chem.* **1994**, *98*, 7665.
- (38) Jamison, J. A.; Krueger, K. M.; Yavuz, C. T.; Mayo, J. T.; LeCrone, D.; Redden, J. J.; Colvin, V. L. *ACS Nano* **2008**, *2*, 311.
- (39) Duca, D.; Arena, F.; Parmaliana, A.; Deganello, G. *App. Catal. A Gen.* **1998**, *172*, 207.
- (40) Osswald, J.; Kovnir, K.; Armbrüster, M.; Giedigkeit, R.; Jentoft, R. E.; Wild, U.; Grin, Y.; Schlögl, R. *J. Catal.* **2008**, *258*, 219.
- (41) Yarulin, A. E.; Crespo-Quesada, R. M.; Egorova, E. V.; Kiwi-Minsker, L. L. *Kinet. Catal.* **2012**, *53*, 253.
- (42) Zhang, Y.; Diao, W.; Monnier, J. R.; Williams, C. T. *Catal. Sci. Technol.* **2015**, *5*, 4123.
- (43) Molero, H.; Bartlett, B. F.; Tysoe, W. T. *J. Catal.* **1999**, *181*, 49.
- (44) Sandell, A.; Beutler, A.; Jaworowski, A.; Wiklund, M.; Heister, K.; Nyholm, R.; Andersen, J. N. *Surf. Sci.* **1998**, *415*, 411.
- (45) Horiuti, I.; Polanyi, M. *T. Faraday Soc.* **1934**, *30*, 1164.
- (46) McGown, W. T.; Kemball, C.; Whan, D. A. *J. Catal.* **1978**, *51*, 173.
- (47) Leviness, S.; Nair, V.; Weiss, A. H.; Schay, Z.; Gucci, L. *J. Mol. Catal.* **1984**, *25*, 131.
- (48) Peng, G., (2010) Etude de l'hydrogénation sélective de l'acétylène sur des nanoparticules de palladium à forme contrôlée: cinétique et sensibilité à la structure. Ecole Polytechnique Fédérale de Lausanne.
- (49) Vincent, M. J.; Gonzalez, R. D. *App. Catal. A Gen.* **2001**, *217*, 143.
- (50) Borodziński, A.; Bond, G. C. *Catal. Rev.* **2006**, *48*, 91.
- (51) Bruehwiler, A.; Semagina, N.; Grasmann, M.; Renken, A.; Kiwi-Minsker, L.; Saaler, A.; Lehmann, H.; Bonrath, W.; Roessler, F. *Industrial & Engineering Chemistry Research* **2008**, *47*, 6862.
- (52) Wu, Z.; Calcio Gaudino, E.; Rotolo, L.; Medlock, J.; Bonrath, W.; Cravotto, G. *Chem.Eng. Process.* **2016**, *110*, 220.
- (53) Wu, Z.; Cravotto, G.; Gaudino, E. C.; Giacomino, A.; Medlock, J.; Bonrath, W. *Ultrason. Sonochem.* **2017**, *35, Part B*, 664.
- (54) García-Mota, M.; Bridier, B.; Pérez-Ramírez, J.; López, N. *J. Catal.* **2010**, *273*, 92.
- (55) Borodziński, A.; Cybulski, A. *Appl. Catal., A* **2000**, *198*, 51.

- (56) Bos, A. N. R.; Botsma, E. S.; Foeth, F.; Sleyster, H. W. J.; Westerterp, K. R. *Chem. Eng. Process.* **1993**, *32*, 53.
- (57) Brown, C. A. *J. Chem. Soc. D* **1970**, 139.
- (58) Brus, L. E. *J. Chem. Phys.* **1984**, *80*, 4403.
- (59) Anderson, J. A.; García, M. F. *Supported Metals in Catalysis*; 2nd ed.; Vol. 11.
- (60) Wu, L.; Lian, H.; Willis, J. J.; Goodman, E. D.; McKay, I. S.; Qin, J.; Tassone, C. J.; Cargnello, M. *Chem. Mater.* **2018**, *30*, 1127.
- (61) Phua, P.-H.; Lefort, L.; Boogers, J. A. F.; Tristany, M.; de Vries, J. G. *Chem. Commun.* **2009**, 3747.
- (62) Ott, L. S.; Finke, R. G. *Coord. Chem. Rev.* **2007**, *251*, 1075.
- (63) Chaudret, B. *C. R. Phys.* **2005**, *6*, 117.
- (64) Balanta, A.; Godard, C.; Claver, C. *Chem. Soc. Rev.* **2011**, *40*, 4973.
- (65) Astruc, D.; Lu, F.; Aranzaes, J. R. *Angew. Chem., Int. Ed.* **2005**, *44*, 7852.
- (66) Evangelisti, C.; Panziera, N.; D'Alessio, A.; Bertinetti, L.; Botavina, M.; Vitulli, G. *J. Catal.* **2010**, *272*, 246.
- (67) Hirai, H.; Yakura, N. *Polym. Adv. Technol.* **2001**, *12*, 724.
- (68) Telkar, M. M.; Rode, C. V.; Chaudhari, R. V.; Joshi, S. S.; Nalawade, A. M. *App. Catal. A Gen.* **2004**, *273*, 11.
- (69) Albani, D.; Vile, G.; Mitchell, S.; Witte, P. T.; Almora-Barrios, N.; Verel, R.; Lopez, N.; Perez-Ramirez, J. *Catal. Sci. Technol.* **2016**, *6*, 1621.
- (70) Kirby, F.; Moreno-Marrodan, C.; Baán, Z.; Bleeker, B. F.; Barbaro, P.; Berben, P. H.; Witte, P. T. *ChemCatChem* **2014**, *6*, 2904.
- (71) Long, W.; Brunelli, N. A.; Didas, S. A.; Ping, E. W.; Jones, C. W. *ACS Catal.* **2013**, *3*, 1700.
- (72) Semagina, N.; Joannet, E.; Parra, S.; Sulman, E.; Renken, A.; Kiwi-Minsker, L. *App. Catal. A Gen.* **2005**, *280*, 141.
- (73) Mizugaki, T.; Murata, M.; Fukubayashi, S.; Mitsudome, T.; Jitsukawa, K.; Kaneda, K. *Chem. Commun.* **2008**, 241.
- (74) Olivier-Bourbigou, H.; Magna, L.; Morvan, D. *App. Catal. A Gen.* **2010**, *373*, 1.
- (75) Venkatesan, R.; Precht, M. H. G.; Scholten, J. D.; Pezzi, R. P.; Machado, G.; Dupont, J. *J. Mater. Chem.* **2011**, *21*, 3030.
- (76) Konnerth, H.; Precht, M. H. G. *Chem. Commun.* **2016**, 52, 9129.
- (77) Peng, L.; Zhang, J.; Yang, S.; Han, B.; Sang, X.; Liu, C.; Yang, G. *Green Chem.* **2015**, *17*, 4178.
- (78) Philippot, K.; Chaudret, B. *C. R. Chim.* **2003**, *6*, 1019.
- (79) Caubère, P. *Angew. Chem. Int. Ed.* **1983**, *22*, 599.
- (80) Brunet, J. J.; Gallois, P.; Caubère, P. *Tetrahedron Lett.* **1977**, *18*, 3955.
- (81) Brunet, J. J.; Caubère, P. *J. Org. Chem.* **1984**, *49*, 4058.
- (82) Montiel, L.; Delgado, J. A.; Novell, M.; Andrade, F. J.; Claver, C.; Blondeau, P.; Godard, C. *ChemCatChem* **2016**, *8*, 3041.
- (83) Zhang, H.; Yang, Y.; Dai, W.; Yang, D.; Lu, S.; Ji, Y. *Catal. Sci. Technol.* **2012**, *2*, 1319.
- (84) Lamey, D.; Prokopyeva, I.; Cárdenas-Lizana, F.; Kiwi-Minsker, L. *Catal. Today* **2014**, *235*, 79.
- (85) Crespo-Quesada, M.; Andanson, J.-M.; Yarulin, A.; Lim, B.; Xia, Y.; Kiwi-Minsker, L. *Langmuir* **2011**, *27*, 7909.

- (86) An, K.; Somorjai, G. A. *ChemCatChem* **2012**, *4*, 1512.
- (87) Teranishi, T.; Miyake, M. *Chem. Mater.* **1998**, *10*, 594.
- (88) Solovov, R. D.; Ershov, B. G. *Colloid J.* **2014**, *76*, 595.
- (89) Tsung, C.-K.; Kuhn, J. N.; Huang, W.; Aliaga, C.; Hung, L.-I.; Somorjai, G. A.; Yang, P. *J. Am. Chem. Soc.* **2009**, *131*, 5816.
- (90) Tangeysh, B.; Fryd, M.; Ilies, M. A.; Wayland, B. B. *Chem. Commun.* **2012**, *48*, 8955.
- (91) Bond, G. C. *Chem. Soc. Rev.* **1991**, *20*, 441.
- (92) Van Hardeveld, R.; Hartog, F. *Surf. Sci.* **1969**, *15*, 189.
- (93) Semagina, N.; Renken, A.; Kiwi-Minsker, L. *J. Phys. Chem. C* **2007**, *111*, 13933.
- (94) Semagina, N.; Renken, A.; Laub, D.; Kiwi-Minsker, L. *J. Catal.* **2007**, *246*, 308.
- (95) Hu, J.; Zhou, Z.; Zhang, R.; Li, L.; Cheng, Z. *J. Mol. Catal. A: Chem.* **2014**, *381*, 61.
- (96) Ruta, M.; Semagina, N.; Kiwi-Minsker, L. *J. Phys. Chem. C* **2008**, *112*, 13635.
- (97) Teschner, D.; Vass, E.; Hävecker, M.; Zafeiratos, S.; Schnörch, P.; Sauer, H.; Knop-Gericke, A.; Schlögl, R.; Chamam, M.; Wootsch, A.; Canning, A. S.; Gamman, J. J.; Jackson, S. D.; McGregor, J.; Gladden, L. F. *J. Catal.* **2006**, *242*, 26.
- (98) Crespo-Quesada, M.; Yarulin, A.; Jin, M.; Xia, Y.; Kiwi-Minsker, L. *J. Am. Chem. Soc.* **2011**, *133*, 12787.
- (99) Uzio, D.; Berhault, G. *Catal. Rev.* **2010**, *52*, 106.
- (100) Borodziński, A.; Bond, G. C. *Catal. Rev.* **2008**, *50*, 379.
- (101) Corma, A.; Serna, P.; Concepción, P.; Calvino, J. J. *J. Am. Chem. Soc.* **2008**, *130*, 8748.
- (102) Moreno-Castilla, C.; Ferro-Garcia, M. A.; Joly, J. P.; Bautista-Toledo, I.; Carrasco-Marin, F.; Rivera-Utrilla, J. *Langmuir* **1995**, *11*, 4386.
- (103) Semagina, N.; Grasmann, M.; Xanthopoulos, N.; Renken, A.; Kiwi-Minsker, L. *J. Catal.* **2007**, *251*, 213.
- (104) Easterday, R.; Leonard, C.; Sanchez-Felix, O.; Losovyj, Y.; Pink, M.; Stein, B. D.; Morgan, D. G.; Lyubimova, N. A.; Nikoshvili, L. Z.; Sulman, E. M.; Mahmoud, W. E.; Al-Ghamdi, A. A.; Bronstein, L. M. *ACS Appl. Mater. Interfaces* **2014**, *6*, 21652.
- (105) Yang, S.; Cao, C.; Peng, L.; Zhang, J.; Han, B.; Song, W. *Chem. Commun.* **2016**, *52*, 3627.
- (106) Gulyaeva, Y. K.; Kaichev, V. V.; Zaikovskii, V. I.; Suknev, A. P.; Bal'zhinimaev, B. S. *App. Catal. A Gen.* **2015**, *506*, 197.
- (107) García-Mota, M.; Gómez-Díaz, J.; Novell-Leruth, G.; Vargas-Fuentes, C.; Bellarosa, L.; Bridier, B.; Pérez-Ramírez, J.; López, N. *Theor. Chem. Acc.* **2011**, *128*, 663.
- (108) Kwon, S. G.; Krylova, G.; Sumer, A.; Schwartz, M. M.; Bunel, E. E.; Marshall, C. L.; Chattopadhyay, S.; Lee, B.; Jellinek, J.; Shevchenko, E. V. *Nano Lett.* **2012**, *12*, 5382.
- (109) Shevchenko, E. V.; Talapin, D. V.; Rogach, A. L.; Kornowski, A.; Haase, M.; Weller, H. *J. Am. Chem. Soc.* **2002**, *124*, 11480.
- (110) Mitsudome, T.; Yamamoto, M.; Maeno, Z.; Mizugaki, T.; Jitsukawa, K.; Kaneda, K. *J. Am. Chem. Soc.* **2015**, *137*, 13452.
- (111) Fogler, H. S. *Elements of chemical reaction engineering*; Fourth ed., 1999.
- (112) Maccarrone, M.; Torres, G.; Lederhos, C.; Badano, J.; Vera, C.; Quiroga, M.; Yori, J. J. *Chem. Technol. Biotechnol.* **2012**, *87*, 1521.
- (113) Klaewkla, R.; Arend, M.; Hoelderich, W. F. *Intech* **2011**, 667.

- (114) Zwietering, T. N. *Chem. Eng. Sci.* **1958**, *8*, 244.
- (115) Nienow, A. W. *Chem. Eng. J.* **1975**, *9*, 153.
- (116) Fernández, M. B.; Tonetto, G. M.; Crapiste, G. H.; Damiani, D. E. *J. Food Eng.* **2007**, *82*, 199.
- (117) Zhu, J.; Wu, F.; Li, M.; Zhu, J.; van Ommen, J. G.; Lefferts, L. *App. Catal. A Gen.* **2015**, *498*, 222.
- (118) Butt, J. B.; Petersen, E. E. In *Activation, Deactivation, and Poisoning of Catalysts*; Elsevier: 1988.
- (119) Box, G. E. P.; Hunter, W. G.; Hunter, J. S. *Statistics for Experimenters: An Introduction to Design, Data Analysis, and Model Building*, 1978.
- (120) Ferré, J.; Rius, F. X. *Técnicas de laboratorio* **2003**, 24.
- (121) Esbensen, K. H.; Guyot, D.; Westad, F.; Houmoller, L. P. *Multivariate data analysis - In Practice. An introduction to multivariate data analysis and experimental design*; 5th ed.; CAMO ASA, 2001.
- (122) Ferré, J. *Técnicas de laboratorio* **2004**.
- (123) Goicoechea, A. B., Facultad de Química de la Universidad del País Vasco, 2010.
- (124) Dunn, K. *Process Improvement Using Data: <https://learnche.org/pid/>*, consulted in 2018.
- (125) Trivedi, D.; Karri, V. V. S. R.; M, A. S. K.; Kuppusamy, G. *Chem. Sci. Rev. Lett.* **2015**, *4*, 13.
- (126) Santos, K. d. O.; Elias, W. C.; Signori, A. M.; Giacomelli, F. C.; Yang, H.; Domingos, J. B. *J. Phys. Chem. C* **2012**, *116*, 4594.
- (127) R., Z. R.; Tobias, H.; Wladimir, R.; Marc, A. *ChemPhysChem* **2017**, *18*, 2517.
- (128) Crespo-Quesada, M.; Grasemann, M.; Semagina, N.; Renken, A.; Kiwi-Minsker, L. *Catal. Today* **2009**, *147*, 247.

# Chapter 2

## Objectives



The work described in this thesis deals with the synthesis and characterization of Pd-based catalysts prepared via colloidal approach using design of experiments for application in selective hydrogenation of alkynes. The main objectives of this PhD thesis are summarized as follow.

The objectives of the chapter 3 are:

- To carry out the synthesis of novel colloidal Pd NPs.
- To study the effects of various synthetic parameters on the NPs size and distribution.
- To deliver recipes of well-defined colloidal Pd NPs.

The objectives of the chapter 4 are:

- To synthesize and characterize well-defined Pd NPs supported on different materials (activated carbon, aluminum oxide and titanium oxide).
- To study the effects of the type of support, Pd content, immobilization process (one pot and two-step syntheses) and scale of the synthesis on the NPs size and dispersion.

The objectives of the chapter 5 are:

- To use of DOE methodology applied to the structure-synthesis relationship study based on a reported recipe of colloidal Pd-HHDMA NPs.
- To demonstrate the high potential of this methodology applied to the synthesis of nanocatalysis.
- To provide knowledge about the studied system highlighting the key parameters and interactions which affect the NPs formation.
- To understand the immobilization process of these Pd-HHDMA NPs on the selected supports using one pot and two-step syntheses.



The objectives of the chapter 6 are:

- To study the performances of a reference and newly synthesized Pd-based catalysts (obtained in chapter 4) in the selective hydrogenation of 1-octyne in a stirred tank reactor.
- To study the effect of the reaction conditions on the 1-octyne conversion and reaction rate.
- To perform the kinetic study of 1-octyne hydrogenation over Pd-based catalysts using DOE methodology.

The objectives of the chapter 7 are subject to a confidentiality agreement with Total Research & Technology Feluy.

## Chapter 3

Study of synthetic parameter effects on the  
formation of colloidal Pd-polyacrylamide NPs



### 3.1. Introduction

The ability to design well-defined nanocatalysts has attracted considerable attention during the last decades since tailoring a catalysts at atomic or molecular level usually improve its performances.<sup>1,2</sup>

Nowadays, colloidal chemistry appears as one of the most versatile method to modulate the NPs structures.<sup>3</sup> Using this methodology, a large variety of NPs sizes, shapes, compositions and even complex structures were reported.<sup>4-9</sup>

Most of these studies were developed using trial-and-error approaches since, unfortunately, the nucleation and growth mechanisms, that highly influence the final NPs structure, are still complex to interpret and to understand.<sup>1</sup> The conclusions of these investigations revealed the importance of adjusting the reaction conditions to prepare well-defined NPs.

In this chapter, a study on the effects of some synthetic parameters on the formation of Pd NPs is described. Some reported effects on the Pd NPs size and distribution are detailed below.

Kiwi-Minsker and co-workers reported the preparation of fcc Pd NPs of 6, 8, 11 and 13 nm by a simple reverse microemulsion method.<sup>10</sup> The increase of sizes was made possible by the increase of the water-to-surfactant molar ratio. The application of this microemulsion system based on water/AOT/isooctane for the synthesis of Pd NPs was also reported by other authors.<sup>11-16</sup> Among them, Perez-Coronado *et al.* studied the effect of the reaction time, water-to-surfactant ratio, reducing agent type and the reducing agent-to-metal ratio on the NPs size and distribution.<sup>16</sup> They concluded that short reaction time led to a slight improvement of the NPs size distribution. Smaller NPs sizes were obtained when the water-to-surfactant ratios were decreased as previously reported by Kiwi-Minsker and co-workers.<sup>10</sup> Then, the use of NaBH<sub>4</sub> instead of N<sub>2</sub>H<sub>4</sub> as reducing agent resulted in smaller size and narrower distribution (*ca.* 4 nm and 7 nm for NaBH<sub>4</sub> and N<sub>2</sub>H<sub>4</sub>, respectively). Finally, an increase in reducing agent-to-metal molar ratio resulted in an important decrease in the NPs size from *ca.* 14 nm to 7 nm.

The formation of near spherical shape Pd NPs with controlled sizes between 2 nm and 50 nm was reported by Solovov *et al.*<sup>17</sup> These NPs were synthesized by reduction of chemical ions using hydrogen in aqueous solutions. The dependence of the initial concentration of Pd(II) ions with the NPs sizes was established: larger NPs sizes were obtained with high Pd concentration.

The effect of the stabilizing agent type and concentration, reaction temperature and stirring rate on the formation of Pd NPs was reported by Jung *et al.*<sup>18</sup> They performed the reduction of Pd(II) chloride by reaction with sodium borohydride and in presence of a stabilizer. Polyvinylpyrrolidone (PVP), sodium dodecyl sulfate (SDS) and cetyltrimethylammonium bromide (CTAB) were tested. The NPs size resulted to decrease while increasing the amount of PVP and CTAB. In contrast, no significant effects on the size were observed when SDS concentration was varied. Then, an increase of Pd NPs size was obtained by increasing the reaction temperature. Finally, an increase in stirring rate caused a decrease in sizes.

Kim *et al.* studied the influence of the metal precursor concentration, polymeric stabilizer concentration, its molecular weight and the reducing agent type on the formation of Pd NPs.<sup>7</sup> They concluded that an increase in Pd concentration led to an increase in Pd NPs size. Moreover, they observed that the molecular weight of the PVP stabilizer, the smaller the Pd NPs and an increase of its concentration in the reaction media enabled the formation of smaller NPs. Finally, they reported that the morphology of Pd NPs were dependent on the reducing agents: hydrogen led to aggregation of NPs in contrast to NaBH<sub>4</sub>.

A more recent study emphasized the difficulty to predict the formation of well-defined NPs due to a lack of in-depth mechanistic understanding of reaction kinetics related to a lack of proper experimental set-ups.<sup>1</sup> They proposed the use of synchrotron-based small-angle X-ray scattering (SAXS) to follow the in situ formation of Pd NPs by thermal decomposition. The effects of different ligands on the synthesis of Pd NPs were

studied (*i.e.*, oleylamine, TOP and oleic acid). Analyses of the real-time SAXS data enable obtaining NPs size, distribution and Pd concentration during the syntheses. The authors reported that TOP and oleic acid were highly affecting the precursor reactivity which controlled the nucleation kinetics and determined the final NPs size. In contrast, they observed that oleylamine did not affect the precursor reactivity but promote the formation of nuclei due to strong ligand-NP binding leading to small sizes.

They proposed a theoretical model to demonstrate the dependence of the nucleation and growth kinetics with both precursor reactivity and ligand-NP binding affinity. This study provides a quantitative understanding of the impact of different ligands on the formation of Pd NPs. The NPs sizes were varied from 3 nm to 11 nm with a nanometer size control. The authors proposed the extension of these in situ SAXS measurements coupled with a reactor in order to increase the knowledge about a large variety of NPs formation mechanisms.

As it was shown in the presented examples, a wide variety of methodologies can be used to synthesize Pd NPs and the resulting NPs size, shape and distribution depend on several synthetic parameters.

The chemical reduction in aqueous solution provided an environmentally friendly route for the synthesis of Pd NPs without involving organic solvents.<sup>19</sup> Using this approach, it was proposed to study the effect of synthetic parameters on the formation of Pd NPs. The objective was to gain knowledge about the NPs tuning and to provide a novel recipe of Pd NPs for application in alkyne hydrogenation reactions.

This chapter first presents a screening of stabilizing agents for the formation of well-defined Pd NPs. After the selection of the most efficient stabilizer, a study of several synthetic parameter effects on Pd NPs formation is detailed using typical OFAT experiments. At that point, the question of synthesis reproducibility is discussed as well as the existence of some limitations related to analytical methods. Methodological improvements are proposed and applied in a second structure-synthesis relationship study using DOE approach. The goal of this smaller study is to

provide deeper knowledge about the effect of each parameter and interaction on Pd NPs synthesis. It also aims at demonstrating the potential of the DOE methodology to obtain higher amount of information with less experiments and resources.

## **3.2. Experimental Section**

### **3.2.1. Material for colloidal NPs synthesis**

In this chapter, all the Pd NPs were synthesized by chemical reduction method. The use of hydrogen as reducing agent, water as solvent and mild temperature and pressure conditions were preferred for future industrial economic and environmental scale up. The metal precursors used were commercially available:  $\text{Na}_2\text{PdCl}_4$  and  $\text{Pd}(\text{NO}_3)_2$ .

The NPs were synthesized in 200 mL Fischer Porter vessels previously cleaned with aqua regia, soap solution and rinsed with distilled water. Note that these vessels can hold a maximum pressure of 3 bar.

The heating set-up consisted in a stirrer-hot plate IKA RCT BASIC<sup>TM</sup> and a 1000 mL polyethylene glycol bath. The thermocouple measured the temperature from the bath.

The metal precursors were purchased from Alfa Aesar, the stabilizers from Sigma Aldrich, the polyethylene glycol from Merck and the hydrogen gas from Linde (Hydrogen 5.0 with a purity of 99.999%). The milli-Q water used for the syntheses came from a Millipore Ultrapure Water Purification system.

### **3.2.2. Characterization**

#### **3.2.2.1. Transmission Electron Microscopy (TEM)**

All the synthesized Pd NPs were routinely characterized by conventional TEM using bright field image modality.

The grids were prepared from the fresh suspension of Pd NPs without any pretreatment since it was noticed that the NPs were not easily observable after the isolation step. The TEM samples were prepared by adding 20 drops of the fresh

colloidal suspensions on a Cu-formvar grid. The grids were dried under air prior to analysis.

The measurements were performed at the “Servei de Recursos Científics i Tècnics” of the Rovira i Virgili University (Tarragona, Spain) with a JEOL 1011 Transmission Electron Microscope operating at 100 kV. The images obtained were monochromatic with a 0.2 nm of resolution. The increases oscillated between 200x and 1000000x. Images were systematically taken at a nominal magnification between 100000x and 400000x on three different points of the grid as minimum. To record images, iTEM® imaging platform from Olympus was used.

The NPs presented in sections 3.4.2. and 3.4.3. were manually measured with Image J software. A minimum of 400 measurements was systematically carried out. The data were processed with Origin Lab® software fitting a Gaussian function. The estimation of the average diameter and standard deviation of each sample was given from the arithmetic mean of the fitted curve.

Concerning the NPs presented in section 3.4.5. , the images obtained after the TEM characterization were treated automatically with Fiji Is Just ImageJ software. The precise procedure for this automatic treatment is given in appendix 3.6.1. Thanks to this treatment, information about size, area and shape descriptors could be obtained. The data were adjusted to a Gaussian function using a Matlab® routine.

### **3.2.2.2. X-Ray Diffraction (XRD)**

The measurements were performed at the “Servei de Recursos Científics i Tècnics” of the Rovira i Virgili University (Tarragona, Spain) with a Siemens D5000 diffractometer (Bragg-Brentano parafocusing geometry and vertical  $\theta$ - $\theta$  goniometer) fitted with a curved graphite diffracted-beam monochromator, incident and diffracted-beam Soller slits, a 0.06° receiving slit and scintillation counter as a detector. Unless stated, the angular  $2\theta$  diffraction range was between 25° and 95°. The data were collected with an angular step of 0.05° at 16 sec per step and sample rotation. A low background Si



(510) wafer was used as sample holder. Cuk $\alpha$  radiation was obtained from a copper X-ray tube operated at 40 kV and 30 mA.

#### **3.2.2.3. X-ray Photoelectron Spectroscopy (XPS)**

XPS was performed to evaluate the amount of Pd<sup>2+</sup> and Pd<sup>0</sup> at the surface of the synthesized catalysts. The analyses were performed at the “Instituto de Carboquímica” (Zaragoza, Spain) with an ESCAPlus Omicron equipped with a hemispherical electron energy analyzer. The spectrometer operated at 225 W (15 mA, 15 kV), using a non-monochromatized MgK $\alpha$  anode (1253.6 eV) and under vacuum ( $<5.10^{-9}$ ) over an area of sample of 1.75x2.75 mm. A survey scan was acquired between 0 and 1000 eV at 0.5 eV/step, 0.3 s/dwell and 50 eV of pass energy. Detailed scans for C 1s, O 1s, N 1s and Pd 3d were obtained at 0.1 eV/step, 0.5 s/dwell and 20 eV of pass energy. For calibration purposes, the C 1s binding energy was referred at 284.5 eV. The data were analyzed with CASAXPS® software.

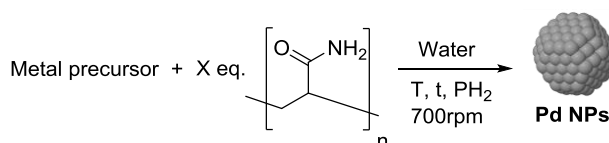
#### **3.2.2.4. Thermogravimetric analysis (TGA)**

TGA was used to estimate the percentage of water and remaining stabilizer on the synthesized catalysts. The analysis was performed at the “Chromatography, Thermal Analysis & Electrochemistry Unit” of the Research Support Area of the Institut Català d’Investigació Química (ICIQ, Tarragona, Spain) using a Mettler Toledo DSC822 with a 56-point Au-AuPd thermopile FRS5 sensor. This equipment enables the measuring range from room temperature up to 1100°C with an accuracy of  $\pm 0.25^\circ\text{C}$  and the balance enables a measuring range up to 1 g with a resolution of 1  $\mu\text{g}$ .

In a typical TGA analysis, 1-5 mg of sample was placed in an alumina crucible and heated under nitrogen flow from room temperature to 900°C with a heating ramp of 10°C/min. The sample mass was recorded continuously during the analysis.

### 3.2.3. General recipe of Pd NPs stabilized by polyacrylamide (PAM)

A typical synthesis of Pd-polyacrylamide NPs (Pd-PAM NPs) consisted in the chemical reduction of a metal precursor in water using hydrogen as reducing agent and in the presence of a stabilizer as presented in Scheme 3.1.



Scheme 3.1. General recipe used for the formation of Pd-PAM NPs via chemical reduction

The precise procedure consisted in mixing the corresponding amount of metal precursor, stabilizer and solvent (only water was used in this project) in a Fischer Porter reactor. The solution was then homogenized and preheated to the desired reaction temperature. Once this temperature was reached, the reactor was charged with hydrogen. The inlet valve of the reactor was opened for 15 seconds and then the system was closed (batch mode). The reaction was stirred at the reaction temperature during the desired synthesis time. At the end of the reaction, the reactor was first cooled down using an ice or cold water bath and then depressurized. The TEM sample was taken directly from this fresh solution to prepare the grid. For XRD characterization the colloidal NPs were isolated and washed by centrifugation.

### 3.3. Plan of Experiments for the structure-synthesis relationship study of colloidal Pd-PAM NPs

In this chapter, two approaches of study were used: the one-factor-at-a-time (OFAT) and the design of experiments (DOE). Both plans of experiments are detailed in this section.

### **3.3.1. OFAT experiments for the study of the effects of the synthetic parameters on colloidal Pd NPs**

In a first approach, OFAT experiments were performed in order to study the effect of the synthetic parameters on the formation of Pd NPs.

The following parameters were varied one-at-a-time following the general recipe provided in section 3.2.3.

- The molar ratio of PAM-to-Pd
- The temperature of synthesis
- The time of synthesis
- The nature of metal precursor
- The pressure of hydrogen
- The concentration of Pd in the reaction media
- The stirring rate

### **3.3.2. DOE experiments for the study of the effects of the synthetic parameters on colloidal Pd NPs**

In a second approach, the set of experiments was completed with DOE approach in order to understand better how each parameter was affecting on the NPs formation and to quantify these effects.

The general recipe used in this study was the same than that presented in section 3.2.3.

#### **3.3.2.1. Factors included in the DOE**

The first step of the study was the identification of the factors that could potentially influence the formation of the Pd NPs.

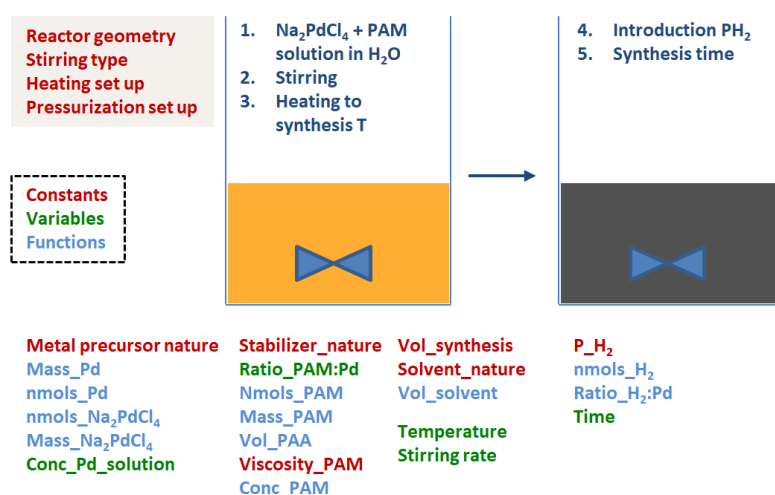
The complete set of experimental factors can be divided into 4 mains subsets.

- The variables that correspond to the experimental factors that can be varied independently one from each other. Each variables can remain constant or vary controllably (being a controlled factor of the design).

- The functions that correspond to the set of experimental factors that depend on one or multiple independent variables.
- Some potentially influencing experimental factors that cannot be controlled by the experimenter but measured. In this case it is of high importance to record their value.
- Other experimental factors which are not controllable nor measurable.

It is important to be aware of the potential effect that can have each factor on the response. Uncontrolled factors can introduce random variations in the response that hinder the analysis of experimental results.

The analysis of the general recipe and the experimental set-up led to the identification of the factors presented in Scheme 3.2.



Scheme 3.2. Steps of the Pd-PAM NPs synthesis and identification of the experimental factors that can influence the process and responses

The entire set of experimental factors were classified in constants (in red), controlled variables (in green), functions (in blue) and not controllable but measurable variables. The factors that might have an effect on the Pd particle size, distribution, shape and agglomeration and that were selected as controllable variables for the study are the following:

- The time of synthesis (SYNTIME)
- The molar ratio of PAM-to-Pd (RATIO)
- The temperature of synthesis (SYNTEMP)
- The concentration of the Pd in the reaction media (CONCPD)
- The stirring rate (STIRRING)

The DOE study was performed with the set-up described in section 3.2.1. Therefore, the reactor geometry, stirring type, heating set-up and pressurization set-up remained constant. The reagents used remained constant:  $\text{Na}_2\text{PdCl}_4$  as metal precursor, polyacrylamide (PAM) as stabilizer and milli-Q water as solvent. The viscosity of the polymer was assumed to be constant and close to 1 cP at 20°C since it was diluted in a huge amount of water.

The volume of the synthesis was fixed to 30 mL to avoid scale issues. The number of moles of Pd (introduced as  $\text{Na}_2\text{PdCl}_4$ ) was a function of this volume and the chosen values of Pd concentration (variable of the study). Then, the amount of stabilizer to introduce was function of the studied PAM-to-Pd molar ratio. Finally the volume of solvent was that necessary to complete until the fixed total volume.

The pressure of hydrogen remained at 3 bar since it was not expected to highly affect the formation of the NPs in the permitted range of work (from 1 to 3 bar). Indeed, in both cases, the hydrogen gas will be in large excess compared to Pd (*ca.* 20 eq and 60 eq., respectively).

Some non-controllable but measurable factors were identified and their values were recorded for each experiment: the pH of the solution before and after the synthesis at room temperature and the hydrogen consumption of a synthesis estimated by the pressure drop observed in the reactor.

The studied experimental factors were varied at two levels. Their values are given in Table 3.1.

Table 3.1. Levels of the studied factors with the DOE

Nº	Factor	Low level	High level
		-1	+1
1	SYNTIME, h	1	5.5
2	RATIO, mol/mol	40	60
3	SYNTEMP, °C	50	70
4	CONCPD, mmol/L	8.4	10.4
5	STIRRING, rpm	700	900

Possible block effects related to the reagents used for the synthesis were minimized by the use of the same lot of the reagent for all the experiments (metal precursor and stabilizer).

### 3.3.2.2. Design aspects

Due to time restrictions, it was decided to limit the number of experiments to eight. Thus, to study the five identified factors with this fixed number of experiments, a fractional factorial design  $2^{5-2}$  was implemented. This design with resolution III implies a screening of the primary effects excluding second order effects.

### 3.3.2.3. Experimental design

#### Matrix of experiments

The matrix of the DOE is displayed in Table 3.2. Three factors were varied according to the reduced  $2^3$  full factorial design:

- Factor 1 which was defined as the time of synthesis (SYNTIME)
- Factor 2 which was defined as the temperature of synthesis (SYNTEMP)
- Factor 3 which was defined as the PAM-to-Pd ratio (RATIO)

Two factors were confounded with second-order interactions:

- Factor 4 which was defined as the Pd concentration (CONCPD) and was confounded with the interaction 23 (interaction between SYNTEMP and RATIO)
- Factor 5 which was defined as the stirring rate (STIRRING) and was confounded with the interaction 13 (interaction between SYNTIME and RATIO)

Table 3.2. Fractional Factorial Design  $2^{5-2}$

RUN	SYNTIME h 1	SYNTEMP °C 2	RATIO mol/mol 3	CONCPD mmol/L 4=23	STIRRING rpm 5=13
<b>01</b>	-1	-1	-1	1	1
<b>02</b>	1	-1	-1	1	-1
<b>03</b>	-1	1	-1	-1	1
<b>04</b>	1	1	-1	-1	-1
<b>05</b>	-1	-1	1	-1	-1
<b>06</b>	1	-1	1	-1	1
<b>07</b>	-1	1	1	1	-1
<b>08</b>	1	1	1	1	1

In Table 3.3 the experimental plan resulting from the factorial design  $2^{5-2}$  is given. Experiments were run in random order to avoid bias.

Table 3.3. Experiments corresponding to the designed matrix  $2^{5-2}$

RUN	SYNTIME h 1	SYNTEMP °C 2	RATIO mol/mol 3	CONCPD mmol/L 4=23	STIRRING rpm 5=13
<b>01</b>	1.0	50	40	10.4	900
<b>02</b>	5.5	50	40	10.4	700
<b>03</b>	1.0	70	40	8.4	900
<b>04</b>	5.5	70	40	8.4	700
<b>05</b>	1.0	50	60	8.4	700
<b>06</b>	5.5	50	60	8.4	900
<b>07</b>	1.0	70	60	10.4	700
<b>08</b>	5.5	70	60	10.4	900

## Generators

The selected generating relations were 234 and 135. The relation 234 means that the contribution of the factor 4 (CONCPD) was chosen to be confused with the interaction between the factor 2 and 3 (SYNTEMP and RATIO, respectively). In the same way, the relation 135 means that the contribution of the factor 5 (STIRRING) was decided to be confounded with the interaction between the factor 1 and 3 (SYNTIME and RATIO, respectively). The complete defining relation of this design was an expansion of four words ( $2^2$ ):  $G = 0 + 135 + 234 + 1245$ . The terms 1245 came from the multiplication of the matrix 135 and 234. This defining relation is used to obtain the equations that

indicate the confusions introduced in this fractional factorial design. For the studied case, these equations are detailed below.

Second-order interactions

In this part, our knowledge and chemical intuition about the studied system were used in order to try to predict the importance of the second-order interactions. They were qualitatively classified in three categories:

- (H) high: interactions that were expected to be significant
- (M) moderate: interactions that were expected to play a moderate role
- (L) low: interactions that were not expected to be significant

From our current understanding, two high significant interactions were identified as shown in Table 3.4:

- (12): Synthesis time and synthesis temperature
- (14): Synthesis time and Pd concentration

Three moderate interactions were also identified:

- (15): Synthesis time and stirring rate
- (35): PAM-to-Pd ratio and stirring rate
- (45): Pd concentration and stirring rate

The remaining second-order interactions are expected to be of low significance. The metal concentration and PAM-to-Pd ratio were function since it was decided to fix the reaction volume.

Table 3.4. Previous qualitative evaluation of the importance of second-order interactions

		SYNTIME	SYNTEMP	RATIO	CONCPD	STIRRING
		1	2	3	4=23	5=13
SYNTIME	1					
SYNTEMP	2	H				
RATIO	3	L	L			
CONCPD	4=23	H	L	function		
STIRRING	5=13	M	L	M	M	



## Confounding of effects

The purpose of this design is to screen the significance of primary effects on the formation of Pd-PAM NPs, however second-order interactions might be relevant. The significance of certain second-order interactions can be anticipated and an a priori potential source of error of misinterpretation of the results of this DOE can be assessed.

The equations of the confounding of effects, obtained from the relation of definition, are given below. They present the confusion of factors and interactions hidden in the estimation of an effect.  $L_i$  represents the estimated effect associated to the factor  $i$  and  $b$  the real contribution of the factor or interaction. It is of high importance to keep in mind these confusions when interpreting the effects.

$$L_0 = b_0 + b_{135} + b_{234} + b_{1245}$$

$$L_1 = b_1 + b_{35} + b_{245} + b_{1234}$$

$$L_2 = b_2 + b_{34} + b_{145} + b_{1235}$$

$$L_3 = b_3 + b_{15} + b_{24} + b_{12345}$$

$$L_{12} = b_{12} + b_{45} + b_{235} + b_{134}$$

$$L_{13} = b_{13} + b_5 + b_{124} + b_{2345}$$

$$L_{23} = b_{23} + b_4 + b_{125} + b_{1345}$$

$$L_{123} = b_{123} + b_{14} + b_{25} + b_{345}$$

**Note:** The expected significant second-order interactions (H) are in dark orange; expected moderate second-order interactions (M) are in light orange.

## Responses of the DOE

The numerical responses of this design were defined in a way they could describe as well as possible the observed results by TEM. They are described in results and discussions section 3.4.5.

## 3.4. Results and Discussion

### 3.4.1. Screening of stabilizing agents for colloidal NPs synthesis

Five polymers and four surfactants were chosen for the screening, their structure are given in Figure 3.1. Among them, some nitrogen containing compounds were selected

since it has been reported that the selectivity in the semi-hydrogenation of alkynes could be improved by the use of stabilizer containing nitrogen functionalities.<sup>20</sup>

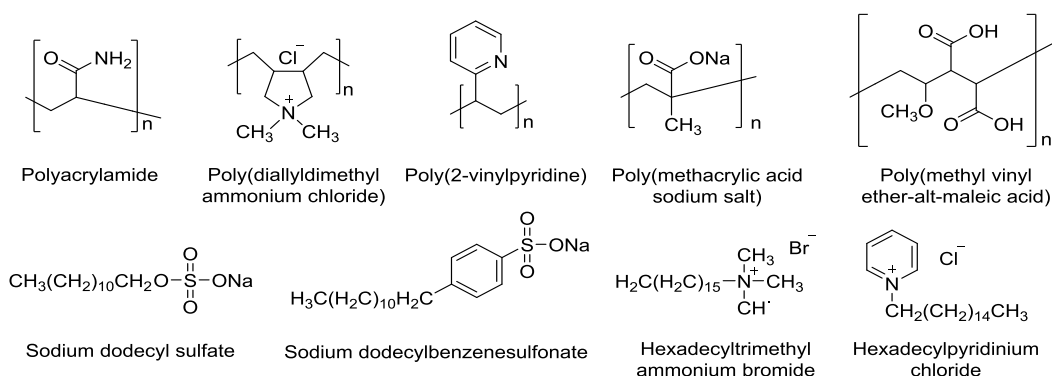
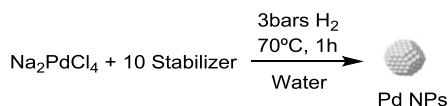


Figure 3.1. Stabilizing agents tested for the formation of new colloidal Pd NPs

The syntheses consisted in the reduction of  $Pd^{2+}$  to  $Pd^0$  as  $Na_2PdCl_4$  under 3 bar of hydrogen in presence of 10 molar equivalents of stabilizer during 1 hour at 70°C as shown in Scheme 3.3.

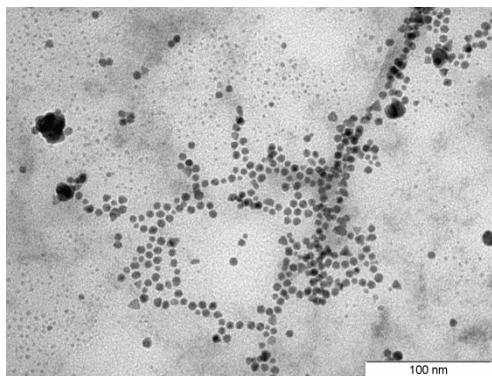


Scheme 3.3. Recipe used for the screening of stabilizers for the preparation of colloidal Pd NPs

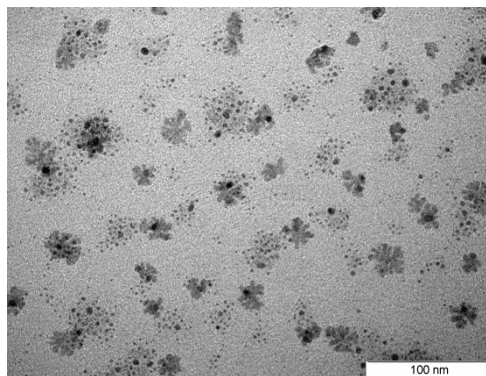
Using this methodology, stable suspensions of colloidal Pd NPs were observed when polyacrylamide, poly(diallyldimethylammonium chloride), poly(methyl vinyl ether-alt-maleic acid) and hexadecyltrimethylammonium bromide were used.

In the other cases, a precipitate of Pd agglomerates was obtained, which is synonym of a poor NPs stabilization under the tested reaction conditions. The stable suspensions of NPs were characterized by TEM and are presented in Figure 3.2.

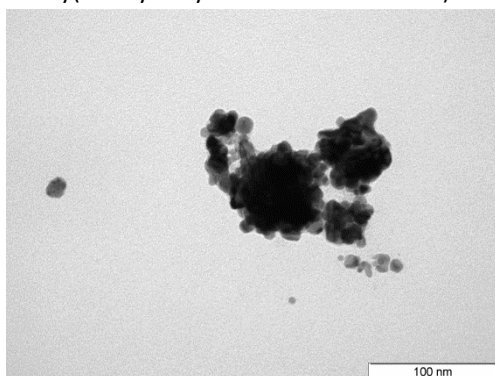
a. Polyacrylamide



b. Poly(diallyldimethylammonium chloride)



c. Poly(methyl vinyl ether-alt-maleic acid)



d. Hexadecyltrimethylammonium bromide

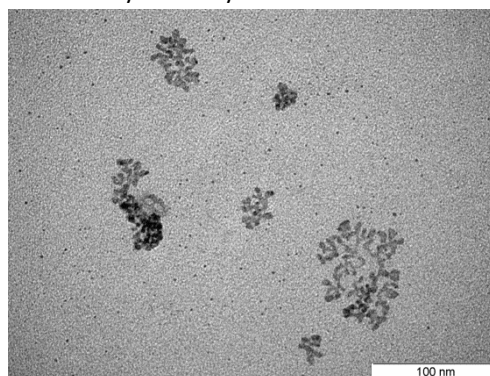


Figure 3.2. TEM micrograph of the Pd NPs stabilized by the newly tested stabilizer

When poly(diallyldimethylammonium chloride), poly(methyl vinyl ether-alt-maleic acid) and hexadecyltrimethylammonium bromide were used, the TEM images revealed really large agglomerates, non-spherical NPs and very wide distribution of sizes. When polyacrylamide was used, the NPs were spherical with a double distribution of sizes (around 2 and 5 nm). Agglomerates were also observed but in much smaller amounts. Therefore this stabilizer was selected for further optimization of the synthesis of colloidal Pd NPs.

### **3.4.2. Study of the effect of synthetic parameters on the formation of Pd-PAM NPs using OFAT experiments**

The objective of this study was to deliver a method for the synthesis of well-defined colloidal monometallic Pd NPs stabilized by polyacrylamide (PAM). To do so, it was important to understand how the synthetic parameters could affect their formation.

In a first approach, the effects of the synthetic parameters on the Pd-PAM NPs were studied by OFAT experiments. In this study, all the Pd-PAM NPs were synthesized in water by chemical reduction using hydrogen. Variation of the PAM-to-Pd molar ratio, temperature of synthesis, time of synthesis, metal precursor nature, pressure of hydrogen, Pd concentration and stirring rate was performed.

Table 3.5 summarizes the variations of the parameters and the resulting mean NPs size and size distribution obtained in each case. In the following subsections, each parameter is discussed in details.

Table 3.5. Variation of experimental parameters for the synthesis of Pd-PAM NPs

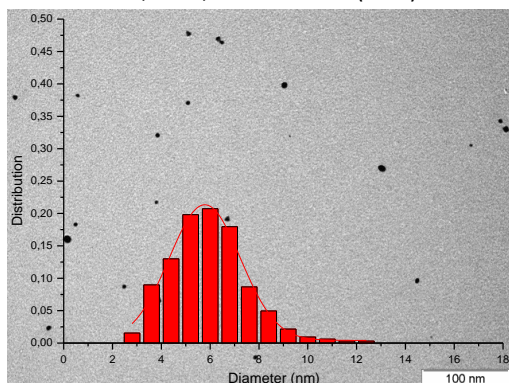
Metal precursor + X eq.  $\left[ \text{O}=\text{C}-\text{CH}_2-\text{CH}(\text{NH}_2) \right]_n$   $\xrightarrow[\text{700rpm}]{\text{Water, [Pd]=9.4mM, T, t, PH}_2}$  Pd NPs

Entry	NPs	Metal precursor	PAM:Pd ratio	T, °C	t, h	PH <sub>2</sub> , bar	TEM size, nm (%RSD)
1	<b>Pd-PAM 1</b>	Na <sub>2</sub> PdCl <sub>4</sub>	20:1	70	1.0	3	5.8 ± 1.8 (31%)
2	<b>Pd-PAM 2</b>	Na <sub>2</sub> PdCl <sub>4</sub>	40:1	70	1.0	3	4.6 ± 1.3 (28%)
3	<b>Pd-PAM 3</b>	Na <sub>2</sub> PdCl <sub>4</sub>	80:1	70	1.0	3	4.6 ± 1.0 (22%)
4	<b>Pd-PAM 4</b>	Na <sub>2</sub> PdCl <sub>4</sub>	40:1	90	1	3	1-20
5	<b>Pd-PAM 5</b>	Na <sub>2</sub> PdCl <sub>4</sub>	40:1	50	1	3	3.3 ± 1.0 (29%)
6	<b>Pd-PAM 6a</b>	Na <sub>2</sub> PdCl <sub>4</sub>	40:1	50	5.5	3	4.0 ± 0.8 (19%)
7	<b>Pd-PAM 6b</b>	Na <sub>2</sub> PdCl <sub>4</sub>	40:1	50	5.5	3	3.6 ± 0.8 (22%)
8	<b>Pd-PAM 7</b>	Na <sub>2</sub> PdCl <sub>4</sub>	40:1	35	5.5	3	3.9 ± 1.1 (27%)
9	<b>Pd-PAM 8</b>	Na <sub>2</sub> PdCl <sub>4</sub>	40:1	25	5.5	3	3.2 ± 1.0 (30%)
10	<b>Pd-PAM 9</b>	Na <sub>2</sub> PdCl <sub>4</sub>	40:1	50	15.5	3	3.8 ± 0.8 (21%)
11	<b>Pd-PAM 10</b>	Na <sub>2</sub> PdCl <sub>4</sub>	40:1	50	20.5	3	1.9 ± 0.6 (32%) 4.2 ± 1.1 (26%)
12	<b>Pd-PAM 11</b>	Na <sub>2</sub> PdCl <sub>4</sub>	40:1	50	72.0	3	/
13	<b>Pd-PAM 12</b>	Na <sub>2</sub> PdCl <sub>4</sub>	40:1	50	66.5	3	4.1 ± 0.8 (20%)
14	<b>Pd-PAM 13</b>	Na <sub>2</sub> PdCl <sub>4</sub>	40:1	r.t.	66.5	/	Non-spherical
15	<b>Pd-PAM 14</b>	Pd(NO <sub>3</sub> ) <sub>2</sub>	40:1	50	5.5	3	Worm shape
16	<b>Pd-PAM 15</b>	Na <sub>2</sub> PdCl <sub>4</sub>	40:1	50	5.5	1	3.6 ± 0.7 (19%)

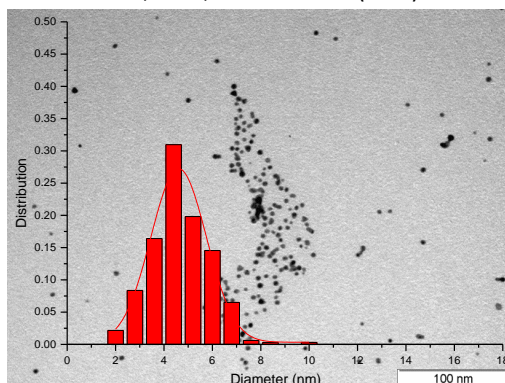
### 3.4.2.1. Molar ratio of PAM-to-Pd

The effect of the PAM-to-Pd molar ratio was studied by testing the following ratios: 20:1, 40:1 and 80:1. All the other parameters were fixed to the values given in Table 3.5 (from entry 1 to 3). The TEM micrographs and size distribution histograms obtained for these three syntheses are displayed in Figure 3.3.

a. **Pd-PAM 1**, 20:1,  $5.8 \pm 1.8$  nm (31%)



b. **Pd-PAM 2**, 40:1,  $4.6 \pm 1.3$  nm (28%)



c. **Pd-PAM 3**, 80:1,  $4.6 \pm 1.0$  nm (22%)

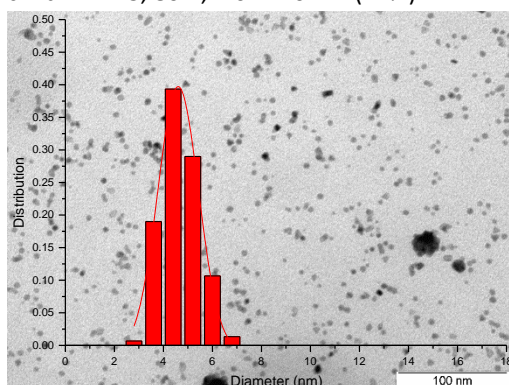


Figure 3.3. TEM micrographs and size distribution histograms of colloidal Pd-PAM NPs synthesized with a PAM-to-Pd molar ratio of a. 20:1, b. 40:1 and c. 80:1

The NPs obtained from these tests were spherical and measured  $5.8 \pm 1.8$  nm,  $4.6 \pm 1.3$  nm and  $4.6 \pm 1.0$  nm for 20:1, 40:1 and 80:1 PAM-to-Pd molar ratio respectively.

A slight increase of the mean NPs diameter was observed while decreasing to 20:1 eq the amount of stabilizer, however the variation was not highly significant.

Improvements in terms of size distribution were observed when a higher amount of stabilizer was used. Indeed the relative standard deviation (RSD) decrease from 31% to 22% when the amount of stabilizer was four times higher. This observation suggests that a higher concentration of protective layer in the reaction media leads to a more accurate control of NPs formation.

Jung *et al.* studied the effect of the amount of PVP, CTAB and SDS stabilizers on the formation of Pd NPs.<sup>18</sup> They observed a decrease in size when the concentrations PVP



and CTAB were increased as usually observed.<sup>7</sup> However in the case of SDS they also observed that the Pd NPs remained constant when the stabilizer concentration was increased.

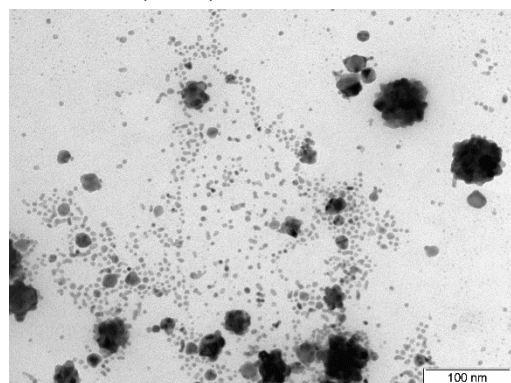
The results obtained using 80:1 PAM-to-Pd molar ratio seemed to be promising to obtain well-defined NPs. However, the use of such amount of polymer during the colloidal synthesis involved the implementation of an effective washing procedure to remove the large excess of polymer for future catalytic applications. Since difficulties in the isolation process of this suspension of NPs were already observed, it was preferred to continue the OFAT experiments with a PAM-to-Pd molar ratio of 40:1.

#### 3.4.2.2. Temperature of synthesis

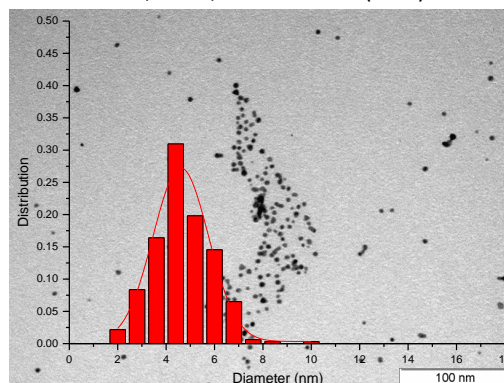
The effect of the synthesis temperature on the NPs size and size distribution was studied between 25°C and 90°C. All the other parameters were fixed to the value given in Table 3.5.

The TEM micrographs and size distribution histograms obtained at 90°C, 70°C and 50°C are displayed in Figure 3.4.

a. Pd-PAM 4, 90°C, 1-20 nm



b. Pd-PAM 2, 70°C, 4.6 ± 1.3 nm (28%)



c. **Pd-PAM 5**, 50°C,  $3.3 \pm 1.0$  nm (29%)

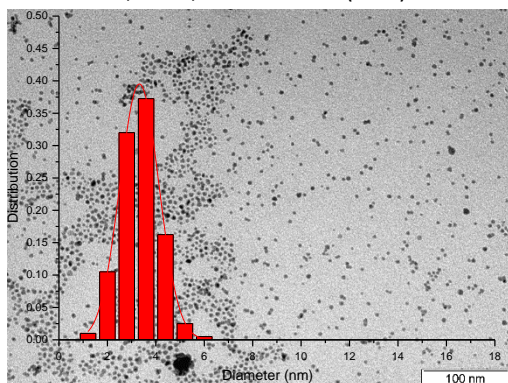


Figure 3.4. TEM micrographs and size distribution histograms of colloidal Pd-PAM NPs synthesized at a. 90°C, b. 70°C and c. 50°C

For the NPs synthesized at 90°C, wide size distribution and large amount of agglomerates were observed. This result suggests that an increase of temperature affects negatively the formation of well-defined Pd-PAM NPs. In contrast, the NPs synthesized at 70°C and 50°C revealed similar distributions. Slightly larger NPs were observed at 70°C in comparison to 50°C.

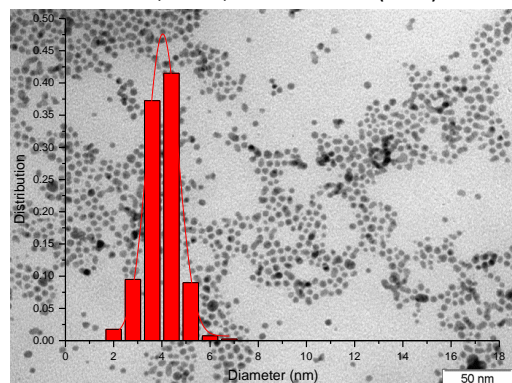
Jung *et al.* also studied the effect of the temperature on the formation of Pd NPs and observed an increase in NPs size when the temperature was increased.<sup>18</sup>

Additional tests at lower temperatures were performed (50°C, 35°C and 25°C). However, in these tests, the synthesis time was increased to five hours and a half since it was supposed that low temperatures could slow down the chemical reduction process. All the other experimental parameters remained fixed to the value given in Table 3.5 (entry 6, 8 and 9).

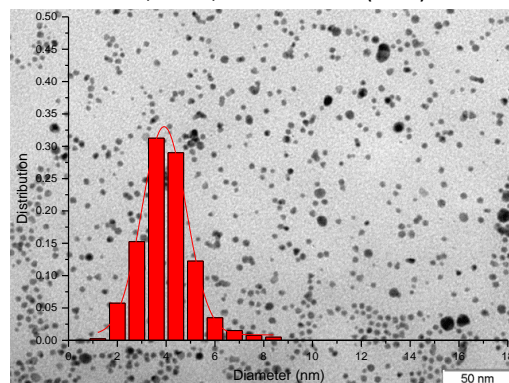
The TEM micrographs and size distribution histograms obtained with these lower temperatures are displayed in Figure 3.5.



a. **Pd-PAM 6a**, 50°C,  $4.0 \pm 0.8$  nm (19%)



b. **Pd-PAM 7**, 35°C,  $3.9 \pm 1.1$  nm (27%)



c. **Pd-PAM 8**, 25°C,  $3.2 \pm 1.0$  nm (30%)

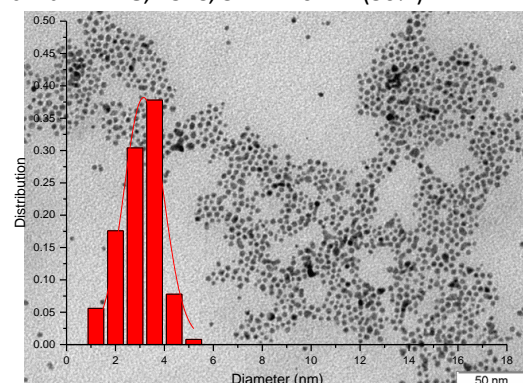


Figure 3.5. TEM micrographs and size distribution histograms of colloidal Pd-PAM NPs synthesized at a. 50°C, b. 35°C and c. 25°C

The relative standard deviation of the Pd-PAM NPs synthesized at 50°C, 35°C and 25°C were respectively 19%, 27% and 30%. These results indicate that when the temperature was decreased from 50°C to 25°C, the size distribution became wider.

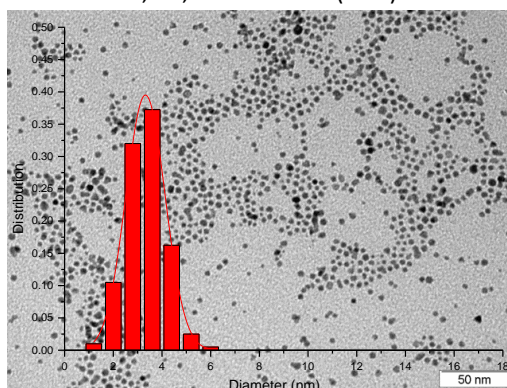
Interestingly, syntheses **Pd-PAM 5** and **Pd-PAM 6a** performed at 50°C during one hour and five hours and a half, respectively, showed different relative standard deviations. The NPs synthesized during five hours and a half resulted to have a narrower distribution than the NPs synthesized during one hour. These results indicate that the synthesis time affects the size distribution of colloidal Pd-PAM NPs. A detailed study of this parameter (*i.e.*, time of synthesis) is provided in the next section.

### 3.4.2.3. Time of synthesis

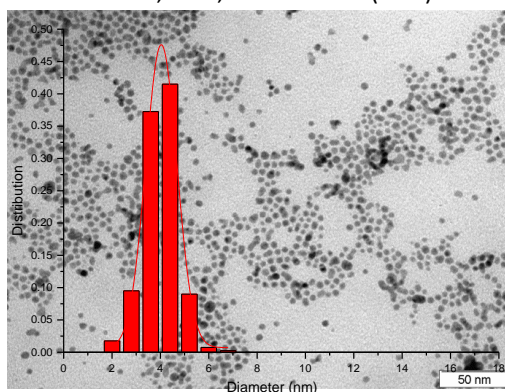
To evaluate the effect of the time of synthesis on the size distribution of colloidal Pd-PAM NPs, **Pd-PAM 5** and **Pd-PAM 6a** were compared with NPs synthesized during 15.5, 20.5 and 72 hours (from entry 10 to 12 in Table 3.5). The other experimental parameters remained unchanged.

The TEM micrographs and size distribution histograms obtained with these variations of time are displayed in Figure 3.6.

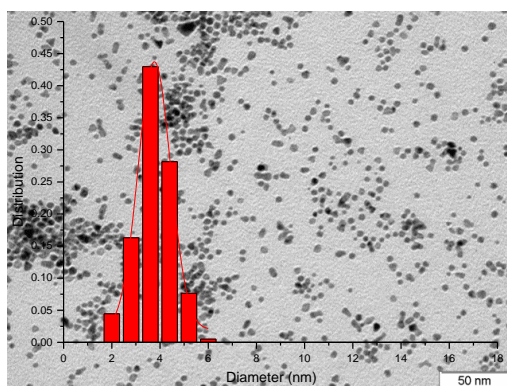
a. **Pd-PAM 5**, 1h,  $3.3 \pm 1.0$  nm (29%)



b. **Pd-PAM 6a**, 5.5h,  $4.0 \pm 0.8$  nm (19%)



c. **Pd-PAM 9**, 15.5h,  $3.8 \pm 0.8$  nm (21%)



d. **Pd-PAM 10**, 20.5h,  $1.9 \pm 0.6$  nm (32%)  
 $4.2 \pm 1.1$  nm (26%)

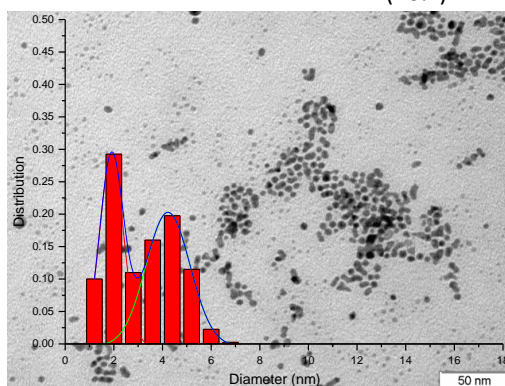


Figure 3.6. TEM micrographs and size distribution histograms of colloidal Pd-PAM NPs synthesized during a. 1h, b. 5.5h, c. 15.5h and d. 20.5h

The NPs synthesized during 1, 5.5 and 15.5 hours presented unimodal and narrow distributions while the NPs resulted from 20.5 hours of reaction showed a population of smaller NPs (*ca.* 2 nm) leading to double distribution.

After 72 hours of reaction, black bulk metal and translucent supernatant were observed indicating a non-stable suspension of NPs.

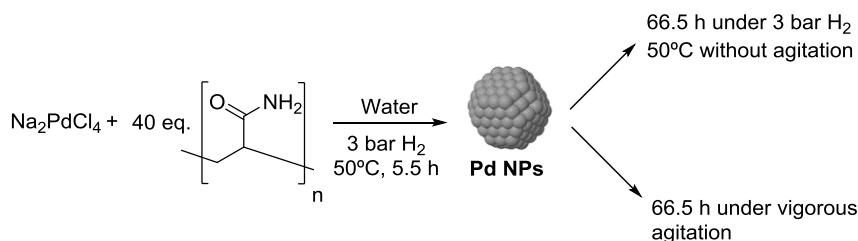
These results suggest that the synthesis time highly influence the formation of the NPs and very long reaction times lead to their decomposition.

Perez-Coronado and co-workers also reported the effect of the synthesis time on the formation of Pd NPs. They observed that NPs size distributions were improved at shorter reaction times.<sup>16</sup>

From this set of experiments, the narrower relative standard deviations were obtained for **Pd-PAM 6a** and **Pd-PAM 9**, respectively for 5.5 and 15.5 hours of reaction. Due to experimental reasons, it was preferred to keep working with shorter reaction times (5.5 hours).

An additional test was performed in order to understand why long reaction times affected negatively to the formed NPs. The hypothesis was that the NPs decomposition could be produced by the effect of mechanical strength due to vigorous stirring of the reaction media during a large period of time.

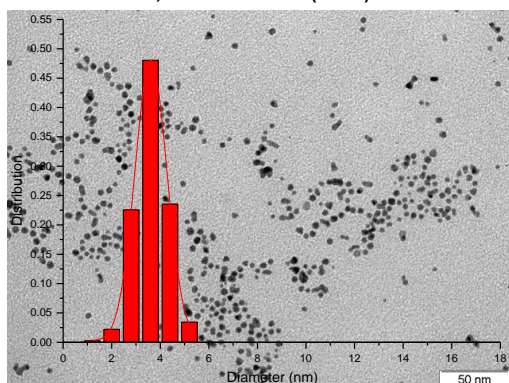
The NPs were synthesized during 5.5 hours using the synthesis conditions of the **Pd-PAM 6** NPs. After this time, a sample was taken to check the well-formation of the NPs by TEM. Then, a part of the solution of NPs was extracted from the Fischer Porter reactor and left under vigorous stirring and aerobic conditions during 66.5 hours while the other part of the solution was left in the Fischer Porter at 50°C, under 3 bar of hydrogen and without stirring during 66.5 hours as detailed in Scheme 3.4.



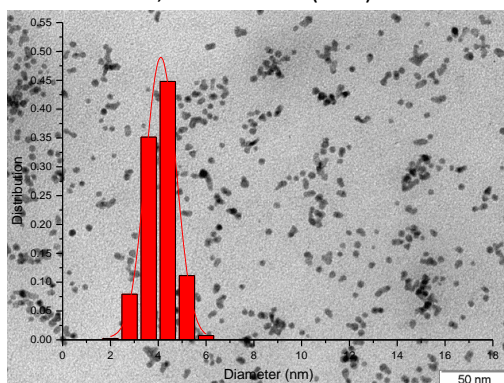
Scheme 3.4. Study of the effect of the synthesis time correlated with the stirring rate

The TEM micrographs and size distribution histograms of the three steps of the synthesis are displayed in Figure 3.7.

a. **Pd-PAM 6b**,  $3.6 \pm 0.8$  nm (22%)



b. **Pd-PAM 12**,  $4.1 \pm 0.8$  nm (20%)



c. **Pd-PAM 13**, non-spherical and multiple distribution of NPs

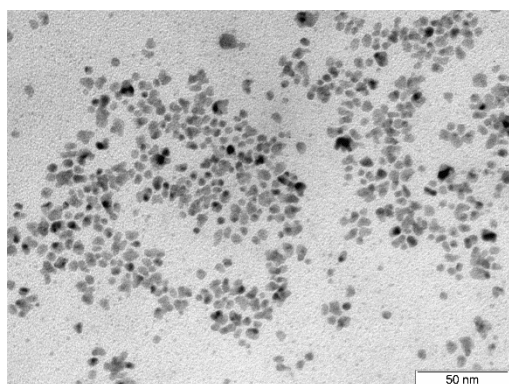


Figure 3.7. Effect of the synthesis time correlated with the stirring rate – TEM micrographs and size distribution histograms of a. **Pd-PAM 6b**, synthesized during 5.5h, b. **Pd-PAM 12** suspension of NPs left under temperature and hydrogen without agitation during 66.5h and c. **Pd-PAM 13** suspension of NPs left under stirring at r.t. during 66.5h

These results indicate that the NPs formed after 5.5 hours of reaction were not relevantly affected by the additional 66.5 hours in the Fischer Porter under pressure and temperature conditions and without agitation. In contrast, the NPs subjected to high stirring rate during long time showed non-spherical shapes and multiple distributions. This result indicates that a high stirring rate during a long period of time affects negatively the shape and distribution of the NPs.



#### 3.4.2.4. Nature of metal precursor

A test using  $\text{Pd}(\text{NO}_3)_2$  as metal precursor was performed (**Pd-PAM 14**). The synthesis was performed using the conditions that provided the lower relative standard deviation from the set of experiments performed, *i.e.*, 40:1 PAM-to-Pd molar ratio, 50°C, 5.5 hours, 700 rpm and 3 bar of  $\text{H}_2$ . The TEM micrograph is presented in Figure 3.8.

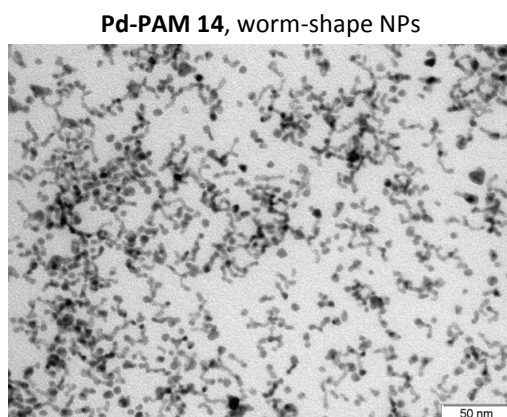


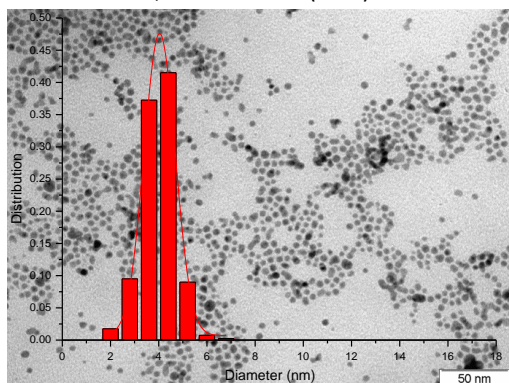
Figure 3.8. TEM micrograph of Pd-PAM NPs synthesized using  $\text{Pd}(\text{NO}_3)_2$  as metal precursor

In this synthesis, a majority of worm shape NPs were observed together with a very small amount of spherical NPs. This result indicates that the nature of the metal precursor clearly affected the shape of the NPs under the reaction conditions.

#### 3.4.2.5. Pressure of hydrogen

The effect of hydrogen pressure on Pd-PAM NPs formation was investigated. Since the NPs were prepared in a glass Fischer Porter reactor, the working pressure range was relatively narrow. It was proposed to decrease the pressure from 3 to 1 bar while the other synthesis conditions were fixed to 40:1 of PAM-to-Pd molar ratio, 50°C, 5.5 hours and 700 rpm.

a. **Pd-PAM 6a**,  $4.0 \pm 0.8$  nm (19%)



b. **Pd-PAM 15**,  $3.6 \pm 0.7$  nm (19%)

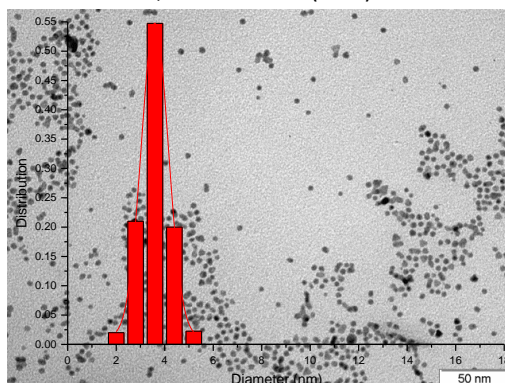


Figure 3.9. TEM micrographs and size distribution histograms of colloidal Pd-PAM NPs synthesized by hydrogen reduction at a. 3 bar and b. 1 bar

The size and size distribution of the NPs obtained in both cases were similar. This result suggests that hydrogen pressure does not affect to a large extent the formation of the Pd-PAM NPs under the tested conditions. It could be explained by the fact that in both cases, the hydrogen was introduced in a very large excess compared to the Pd, respectively 22.5 and 67.5 molar equivalents for 1 bar and 3 bar. To perform this reaction in stoichiometric proportions, the pressure of hydrogen should be lowered to 0.045 bar under the chosen reaction conditions. Such a low pressure cannot be adjusted in the used set-up due to technical limitations.

Perez-Coronado and co-workers observed an important decrease in NPs size when the reducing agent-to-metal molar ratio was increased.<sup>16</sup>

The choice of a lower hydrogen pressure makes sense from an economic and safety point of view. However, at laboratory scale, it was preferred to keep working with 3 bar of hydrogen due to easier handling. For instance, in case of slight gas leak, there will still have enough hydrogen in the Fischer Porter to reduce effectively the NPs.

#### 3.4.2.6. Conclusions of the study of the effect of synthetic parameters on the formation of Pd-PAM NPs using OFAT experiments

The results obtained by the OFAT experiments are summarized as follow.

- The PAM-to-Pd molar ratio, temperature of synthesis and time of synthesis resulted to be key factors for the control of the NPs size distribution.
- When high PAM-to-Pd ratios were used, narrow size distribution were obtained.
- An optimum seemed to appear at 50°C under the tested reaction conditions. Indeed, the size distribution was reduced when the synthesis temperature decreased from 90°C to 50°C in a 1 hour reaction however when it was decreased to 25°C in a 5 hours reaction, the size distribution became wider. A DOE experimentation plan could help to confirm this curvature trend.
- It was observed that until 15.5 hours of reaction, NPs could be well-formed but at longer reaction times they start to decompose (first in double distributed population and then in a non-stable suspension).
- In all the syntheses performed, the NPs remained spherical except when  $\text{Pd}(\text{NO}_3)_2$  was used, indicating that the nature of the metal precursor affected the NPs shape.
- No significant effect in terms of NPs size and distribution was observed while decreasing the hydrogen pressure from 3 to 1 bar.
- No significant variations of NPs size were observed during this set of experiments.

Finally, using polyacrylamide as stabilizer, a recipe of well-defined Pd NPs was obtained (**Pd-PAM 6a**:  $4.0 \pm 0.8$  nm, 19%). This recipe was chosen as reference recipe to perform further immobilization on different supports. After a verification of the robustness of this recipe, the characterization of these NPs was performed and is detailed in section 3.4.4.

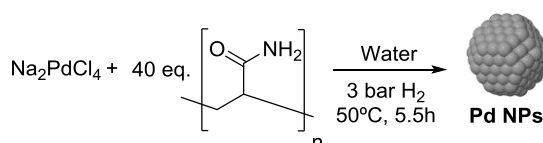
During this OFAT study, NPs agglomeration was observed in some samples, but in this first approach, it was not quantified.

### 3.4.3. Reproducibility of Pd-PAM 6 reference recipe

The recipe of well-defined Pd-PAM NPs obtained after the OFAT set of experiments (**Pd-PAM 6**) was the chosen reference recipe for further immobilization studies and catalytic tests. The robustness of this synthesis was checked by ten reproductions and by measuring manually a total of 5000 NPs in each batch of NPs.

The objectives of this study were to demonstrate the robustness of the selected reference recipe and to investigate whether the data processing method can affect the average NPs size and size distribution results. The effect of the chosen bin size and the number of measured NPs were also investigated.

The selected reference recipe for Pd-PAM NPs synthesis was the following:



Scheme 3.5. Reference recipe **Pd-PAM 6** NPs

The TEM micrographs and size distribution histograms of the ten batches (from **Pd-PAM 6c** to **Pd-PAM 6l**) are displayed in appendix 3.6.2. and NPs sizes and distributions obtained are summarized in Table 3.6.

Table 3.6. Sum up of the NPs size, distribution and relative standard deviation obtained from the ten reproduction of the Pd-PAM 6

Batch of Pd NPs	NPs size (nm)	Relative Standard Deviation (%)
<b>Pd-PAM 6c</b>	$3.7 \pm 1.0$	26
<b>Pd-PAM 6d</b>	$3.8 \pm 1.0$	27
<b>Pd-PAM 6e</b>	$3.7 \pm 0.9$	25
<b>Pd-PAM 6f</b>	$4.0 \pm 1.1$	28
<b>Pd-PAM 6g</b>	$3.5 \pm 0.8$	22
<b>Pd-PAM 6h</b>	$3.8 \pm 1.0$	25
<b>Pd-PAM 6i</b>	$4.5 \pm 1.2$	26
<b>Pd-PAM 6j</b>	$3.9 \pm 1.0$	26
<b>Pd-PAM 6k</b>	$4.0 \pm 1.0$	26
<b>Pd-PAM 6l</b>	$4.0 \pm 1.1$	27



In all the cases, the results show monodisperse, spherical and well-defined NPs with narrow size distribution. The average size obtained was between 3.5 nm and 4.5 nm with relative standard deviations between 22% and 28%. The graphical evaluation of the synthesis reproducibility was performed by means of the cumulative distributions of the ten NPs batches, as shown in Figure 3.10.

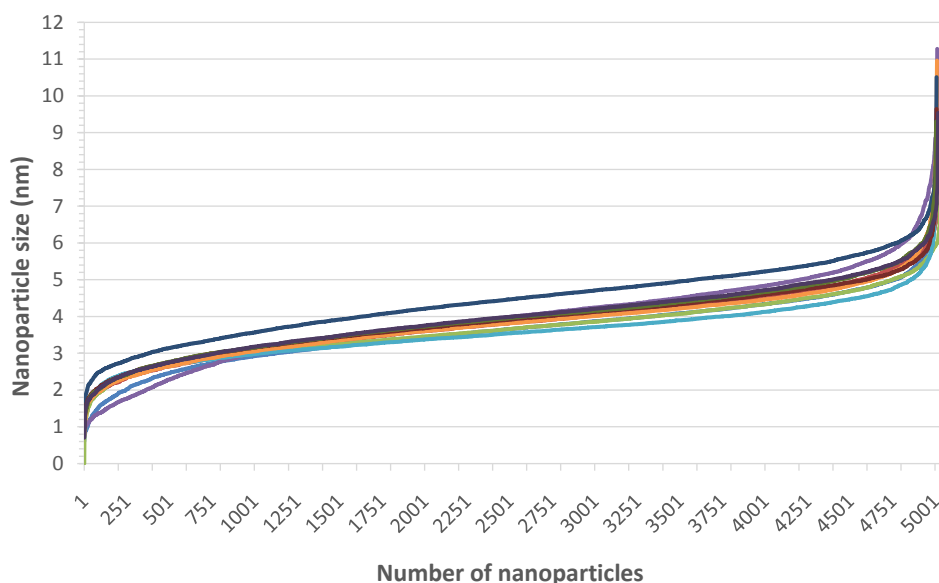


Figure 3.10. Cumulative distributions of the ten batches of Pd-PAM NPs

The representation of the cumulative distributions highlights that all the synthesized NPs show similar distribution centered on *c.a.* 3.9 nm. However one batch (**Pd-PAM 6i**) shows similar size distribution but slightly larger size (*c.a.* 4.5 nm).

These results suggest that from the ten batches of NPs, nine of them could be well-reproduced with similar average size and one of them formed 15% larger NPs.

To verify this observation, the statistical Kolmogorov-Smirnov test (K-S test) was used. This test is a nonparametric test that compares the cumulative distributions of two datasets. It does not require the data to follow a Gaussian distribution (or any other defined distribution). It computes a value that test the null hypothesis that both groups have the same distribution. This value is obtained from the maximum difference between the two cumulative distributions and the sample size. The null

hypothesis is rejected when this maximum difference exceeds a certain critical value that is obtained in a probability table (K-S tables), these tables are given in appendix 3.6.3.

This test was applied using the values of the 0.5 bins in the range of 0 to 10 nm, thus the degree of freedom was equal to 20.

It was decided to apply the K-S test to the two batches of nanoparticles that possess the most different diameter of the set of 10 batches: the **Pd-PAM 6g** and **Pd-PAM 6i** ( $3.5 \pm 0.8$  nm and  $4.5 \pm 1.2$  nm, respectively).

The cumulative distributions of both nanoparticles were plotted from the bin cumulative frequency and are depicted in Figure 3.11.

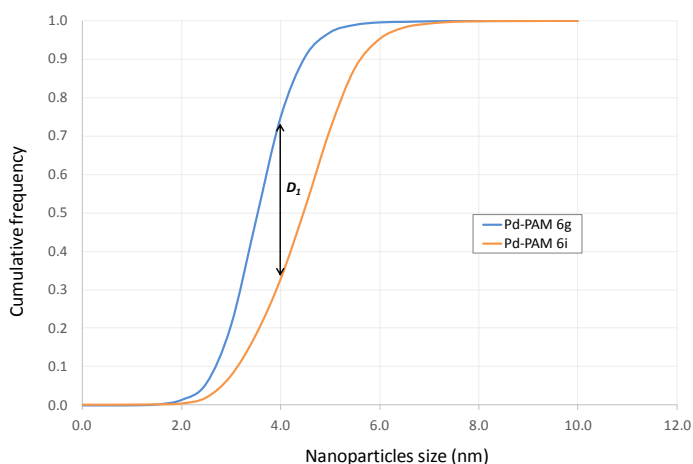


Figure 3.11. Cumulative distribution of the batches of Pd-PAM NPs – Kolmogorov Smirnov test between **Pd-PAM 6g** and **Pd-PAM 6i** ( $D_1$ )

The  $D$  value corresponds to the maximum difference between the two cumulative distributions. It is compared to the corresponding  $p$  value of the table of the K-S tests based on the established level of significance and sample size:

- If  $D < p(\text{table}, n, \alpha)$  where  $n$  is the degree of freedom and  $\alpha$  the level of significance, the null hypothesis is accepted indicating that samples have the same distribution.
- If  $D > p(\text{table}, n, \alpha)$ , the null hypothesis is rejected meaning that the distributions are different.

In the case of **Pd-PAM 6g** and **Pd-PAM 6i**: the  $D_1$  value was equal to 0.421 and was superior to the p value (0.294 for  $\alpha=0.05$ ). The null hypothesis was rejected and thus it was concluded that the sample distributions were different. This result is not surprising since it was noticed that the Pd-PAM 6i revealed slightly larger size than the other batches.

It was proposed to apply the K-S test between the two batches of NPs that possess the most different diameter of the set of 9 batches (excluding the **Pd-PAM 6i** batch): **Pd-PAM 6g** and **Pd-PAM 6l**. The cumulative distributions of both nanoparticles were plotted from the bin cumulative frequency and are depicted in Figure 3.12.

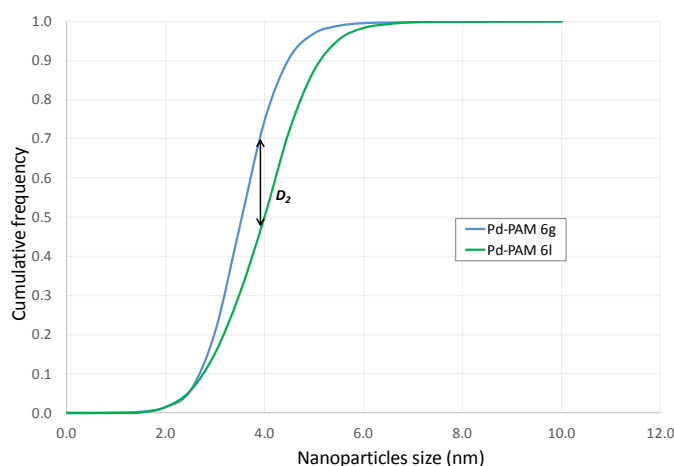


Figure 3.12. Cumulative distribution of the batches of Pd-PAM NPs – Kolmogorov Smirnov test between **Pd-PAM 6g** and **Pd-PAM 6l** ( $D_2$ )

In the case of **Pd-PAM 6g** and **Pd-PAM 6l**: the  $D_2$  value was equal to 0.246 and was inferior to the p value (0.294 for  $\alpha=0.05$ ). The null hypothesis was accepted and it was concluded that the sample distributions were similar.

Since the 10 batches of NPs revealed Gaussian narrow distributions, it was suggested that the batches of nanoparticles included in the range of sizes between **Pd-PAM 6g** and **Pd-PAM 6l** were also similar in terms of size and distribution. Consequently, it was concluded that 9 of the 10 batches of Pd-polyacrylamide NPs were reproducible and gave NPs sizes between 3.5 and 4 nm.

Afterwards, the effect of the chosen bin size on the mean NPs size and size distribution was checked. For this analysis, the NPs with the higher and lower relative standard deviations (RSD) from the set of experiments were chosen: **Pd-PAM 6f** and **Pd-PAM 6g**, respectively. The bin size was varied from 0.01 nm to 0.80 nm and the corresponding size and size distribution were calculated. The results are displayed in Table 3.7.

Table 3.7. Effect of the bin size on the average size and size distribution of the **Pd-PAM 6f** and **Pd-PAM 6g** NPs

Nº batch	Bin size (nm)	Average diameter $\pm \frac{FWHM}{2}$ (nm)	RSD (%)
<b>Pd-PAM 6f</b>	0.01	$4.03 \pm 1.10$	27.2
	0.10	$4.03 \pm 1.10$	27.3
	0.50	$4.03 \pm 1.12$	27.9
	0.80	$4.03 \pm 1.15$	28.5
<b>Pd-PAM 6g</b>	0.01	$3.53 \pm 0.78$	22.2
	0.10	$3.53 \pm 0.78$	22.2
	0.50	$3.52 \pm 0.79$	22.5
	0.80	$3.52 \pm 0.84$	23.8

It could be observed that the variation of the bin size did not affect the average size. However, for both batches, the size distributions were slightly higher with a bin size of 0.80 nm. In consequence the relative standard deviations were slightly higher. For bin sizes from 0.50 nm to 0.01 nm, the results were similar, which indicates that a bin size lower than 0.50 nm did not affect the NPs size and size distribution in the studied system. However it is important to note that the effect of the bin size could vary as a function of the range of sizes of the studied NPs. For the presented study, a bin size of 0.40 nm was chosen.

Once the bin size was determined, the effect of the number of measured NPs was studied. To do so, the cumulative moving NPs average as function of the number of measured NPs was plotted for the ten batches. This cumulative moving average (CMA) was calculated following the NPs measurement order and using this equation:

$$CMA_n = \frac{x_1 + \dots + x_n}{n}.$$

From the set of experiments, two different trends were observed and are summarized by the two plots of the batches **Pd-PAM 6c** and **Pd-PAM 6l** (Figure 3.13). The plots of the rest of batches are given in appendix 3.6.4.

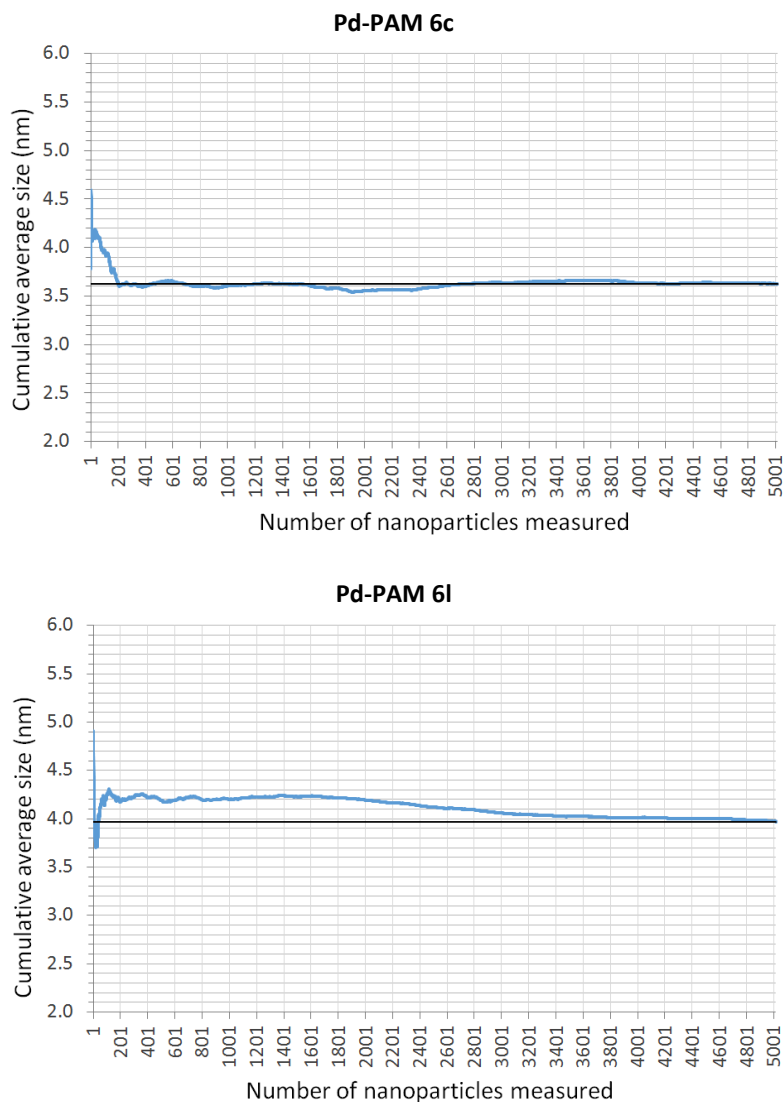


Figure 3.13. NPs cumulative moving average as a function of the number of NPs measured: a. Pd-PAM 6c and b. Pd-PAM 6l

The first trend observed was described by the batch **Pd-PAM 6c**. The NPs average size obtained from the manual measurements of 200 NPs was very close to the NPs average size obtained after 5000 NPs measurements. It indicates that the

measurement of only 200 NPs average size would have been enough to obtain a representative average size of the sample.

The second trend observed was represented by the batch **Pd-PAM 6l**. The NPs average size became constant after the measurement of a large number of NPs (*ca.* 3500). In this sample, if only 400 NPs would have been measured, the NPs average size obtained would have shown an error of 6% regarding to the NPs average size obtained after 5000 NPs manual measurements.

It was considered that 400 NPs is a manageable number of NPs to measure manually, therefore the percentage of error of the NPs average size obtained after 400 NPs measurements regarding to 5000 was calculated for the ten batches using the following equation:  $\%error = \frac{|\bar{y}_{5000} - \bar{y}_{400}|}{\bar{y}_{400}} \times 100$ , where  $\bar{y}$  is the mean NPs size for the measurement of 5000 or 400NPs. The results are displayed in Table 3.8.

Table 3.8. Percentage of error on the NPs average size between 400 NPs and 5000 NPs manual measurements

NPs	%error
<b>Pd-PAM 6c</b>	0.6
<b>Pd-PAM 6d</b>	2.5
<b>Pd-PAM 6e</b>	3.3
<b>Pd-PAM 6f</b>	8.3
<b>Pd-PAM 6g</b>	5.8
<b>Pd-PAM 6h</b>	0.2
<b>Pd-PAM 6i</b>	8.7
<b>Pd-PAM 6j</b>	2.1
<b>Pd-PAM 6k</b>	4.6
<b>Pd-PAM 6l</b>	6.4

The percentage of error on the NPs average size obtained by the measurement of 400 NPs regarding 5000 NPs, varied from 0.6% to 8.7%. We note that manual measurements are highly conditioned by the way in which the experimenter measures the NPs (*e.g.*, focusing on the small or large NPs instead of measuring in a more homogeneous way).

Anyway, the major error obtained after this test (*i.e.*, 8.7%) is acceptable considering that the manual measurement of more than 1000 NPs is a highly time-consuming activity.

However, in this thesis, tools to improve this analytical part by reducing the effect of the experimenter on the results were implemented. In this sense, the use of automatic measurements to obtain a precise description of the NPs from TEM images has been studied. In the next section and the next chapter, a deeper study about this automatic methodology is provided.

#### **3.4.4. Characterization of the colloidal reference recipe Pd-PAM 6**

The characterization of the Pd-PAM NPs synthesized by the reference recipe was performed using TEM, XRD, XPS and TGA.

The TEM was carried out and presented in section 3.4.2. Moreover, HRTEM was performed but high resolution images could not be obtained. As detailed above, the preparation of the grid was carried out by addition of the fresh suspension of NPs without any pretreatment (washing and isolation process). The presence of high amount of organic material on the grid caused its destruction when the electron beam was projected onto the sample. Various attempts of dispersion of the washed and isolated NPs on a grid were performed but the NPs resulted to agglomerate during the process and could not be well-observed either.

The X-Ray Diffraction (XRD) was performed and the obtained pattern is given in Figure 3.14.

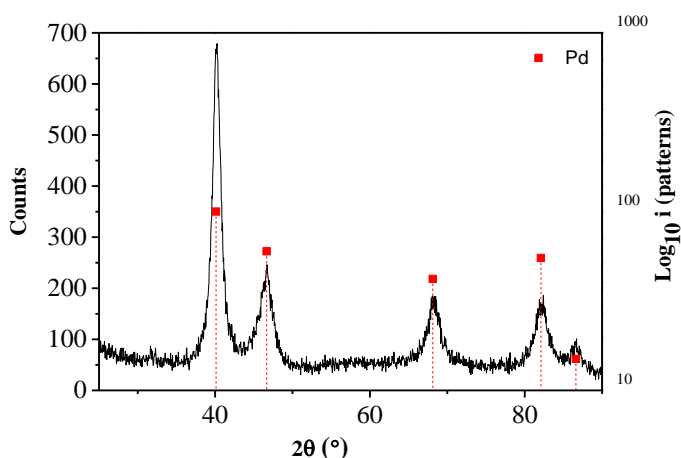


Figure 3.14. XRD pattern of Pd-PAM NPs

The crystalline structure of the colloidal Pd-PAM revealed the presence of five bands centered at 40°, 46°, 68° and 82° and 86° attributed to Pd-fcc packing. The average size obtained for the crystalline part of these NPs was 3.59 nm.

The NPs surface analysis was performed by X-Ray Photoelectron Spectroscopy (XPS). The full XPS spectra, displayed in Figure 3.15, revealed the presence of O, N, Pd, C and a small amount of Cl according to the peaks observed at their characteristic binding energies (respectively 532.0, 400.0, 335.5, 285.5 and 198.5 eV).

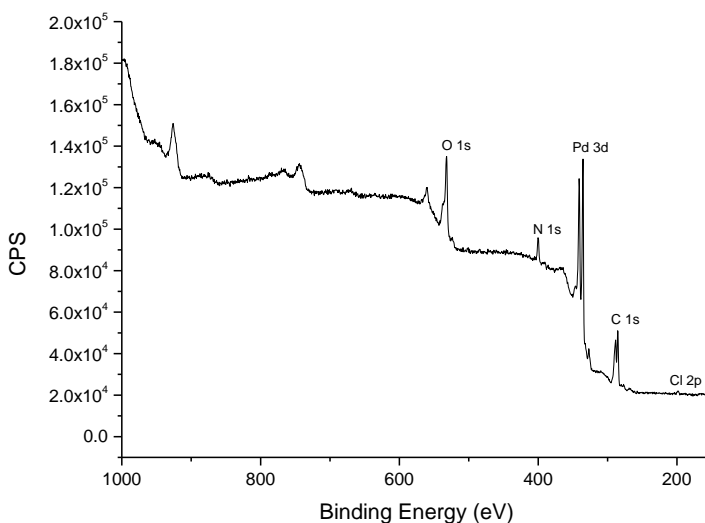


Figure 3.15. Full XPS spectra for Pd-PAM NPs



The deconvolution of Pd 3d<sub>5/2</sub> and Pd 3d<sub>3/2</sub> peaks was performed using Tressaud data for Pd species.<sup>21</sup> The XPS spectrum of colloidal Pd-PAM NPs is displayed in Figure 3.16. It exhibits two important peaks around 335 and 340 eV assigned to Pd 3d<sub>5/2</sub> and Pd 3d<sub>3/2</sub> of the Pd<sup>0</sup> species and two smaller peaks at 337 and 342 eV assigned to Pd 3d<sub>5/2</sub> and Pd 3d<sub>3/2</sub> of Pd<sup>2+</sup> species.

The fractions of Pd<sup>0</sup> and Pd<sup>2+</sup> were extracted from the decomposition of the spin orbit peak of low energy. The content of Pd<sup>0</sup> was 84.4% and the content of Pd<sup>2+</sup> was 15.6%.

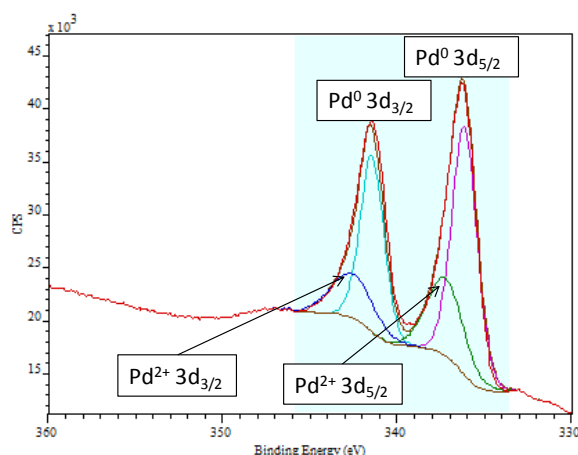


Figure 3.16. XPS spectra of Pd-PAM NPs - Deconvolution of Pd 3d<sub>5/2</sub> and Pd 3d<sub>3/2</sub> peaks

Finally, the NPs thermal stability was examined by TGA analysis. The thermogram corresponding to the Pd-PAM NPs is displayed in Figure 3.17.

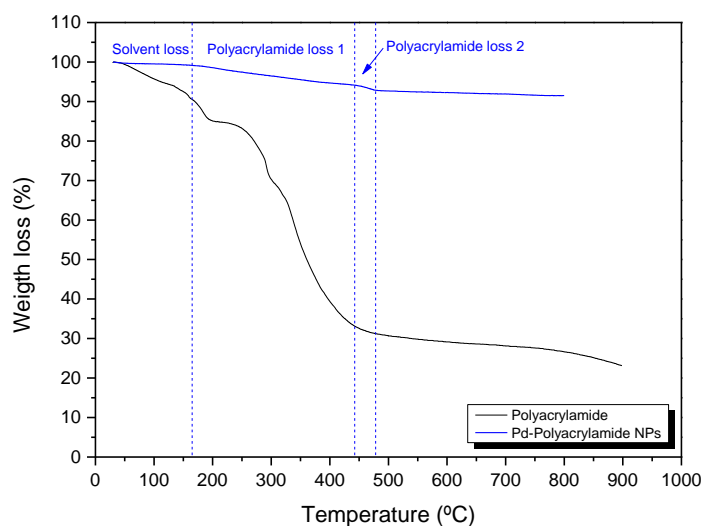


Figure 3.17. TGA thermogram of colloidal Pd-PAM NPs

The thermogram corresponding to polyacrylamide showed a 14.6% weight loss between 30 and 190°C attributed to the loss of absorbed solvent. The decomposition of the polymer occurred between 200 and 500°C.

The thermogram corresponding to Pd-PAM NPs showed less than 1% weight loss between 30 and 165°C. This loss being attributed to the absorbed solvent, this result suggests that the PdNPs sample was well-dried.

Then, in the polymer decomposition range (200-500°C), two slopes were observed. The first one could correspond to the loss of the outer layer of polymer (weak bonds): 5.15% and the second one to the polymer layer directly bonded to the metal (stronger bonding): 1.4%. The total weight loss attributed to PAM was 6.55%.

Finally, the total number of Pd atoms per NPs and the fraction of atoms present at the surface were estimated using the Van Hardeveld and Hartog (VvH) model and the average mean size obtained by TEM (*ca.* 3.9 nm).<sup>22</sup> A total number of 2137 atoms were obtained of which a fraction of 0.324 was located at the surface.

To conclude the characterization of the recipe of colloidal Pd-PAM NPs obtained after the OFAT study revealed small and well-defined NPs of *ca.* 3.7 nm confirmed by TEM and XRD. These NPs were mainly at the zero valent state (*ca.* 85% of Pd<sup>0</sup>) and a small amount of polymer remained on their surface after the washing and isolation step (*ca.* 6.5%).

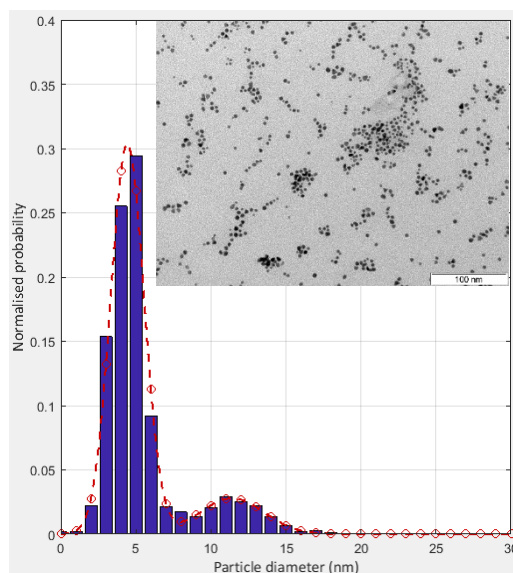
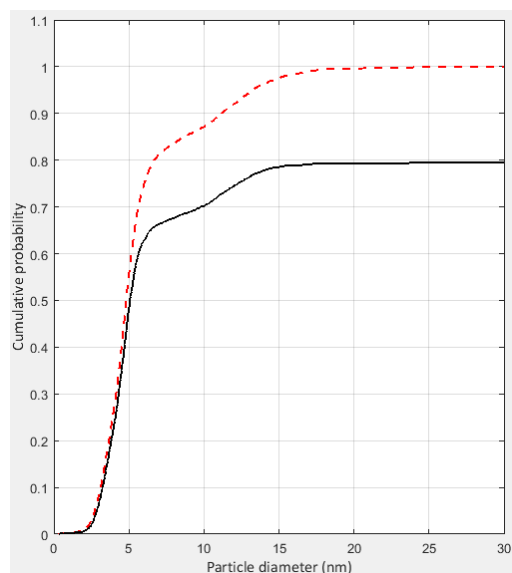
### **3.4.5. Study of the effect of synthetic parameters on the formation of Pd-PAM NPs using DOE**

In order to study the effect of the synthetic parameters over the Pd-PAM NPs formation, eight experiments were performed following the  $2^{5-2}$  designed matrix presented in section 3.3.2.3.

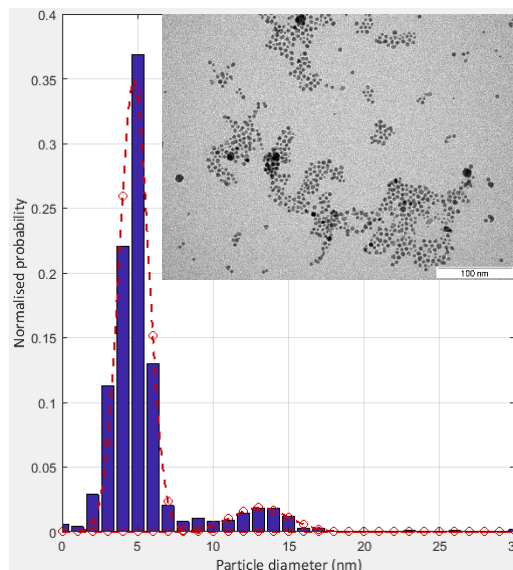
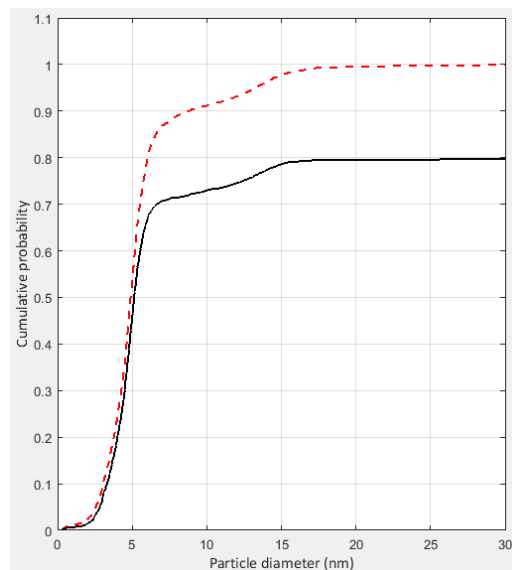
The TEM micrographs, size distribution histograms and cumulative probability plots of the eight experiments are displayed in Figure 3.18. The cumulative probability plots

are given for the equivalent diameter of the fraction of spherical NPs (black line) and the equivalent diameter of all the NPs (dashed red line).

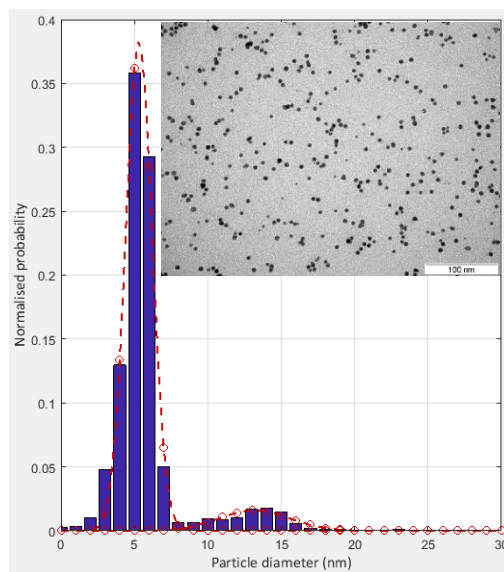
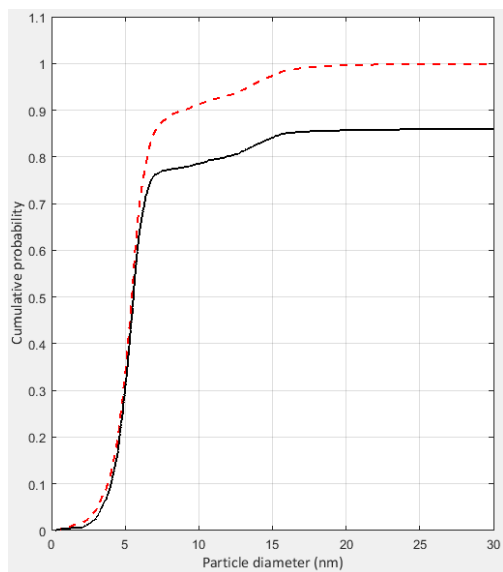
### RUN01



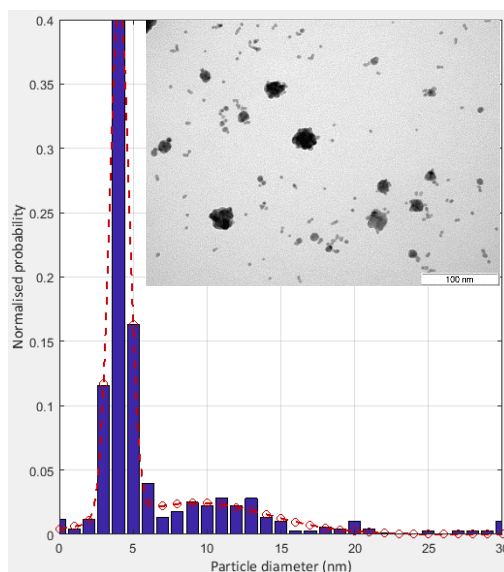
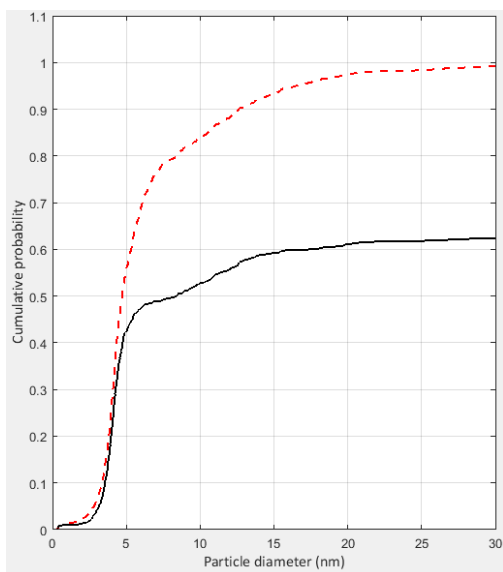
### RUN02



### RUN03

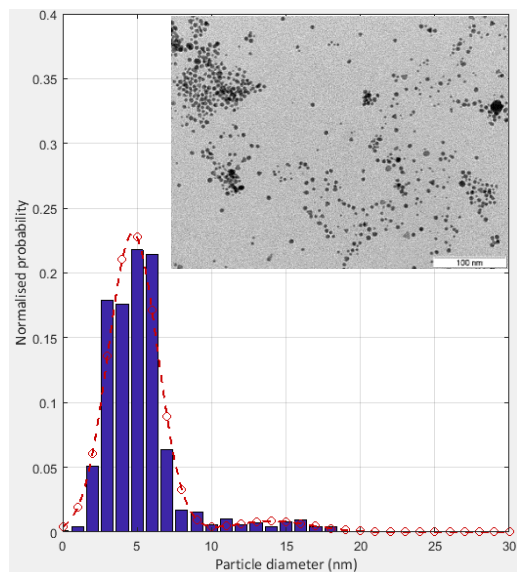
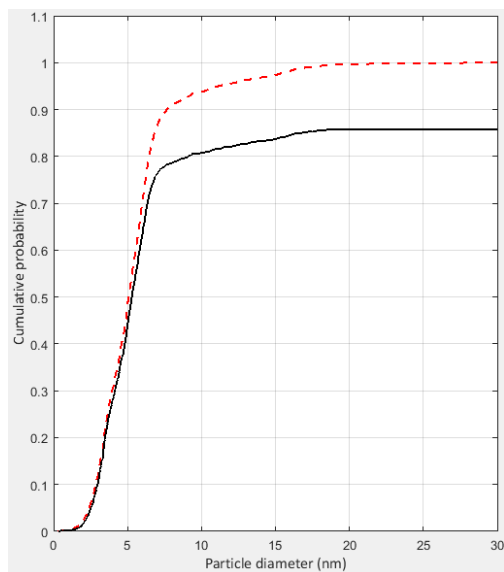


### RUN04

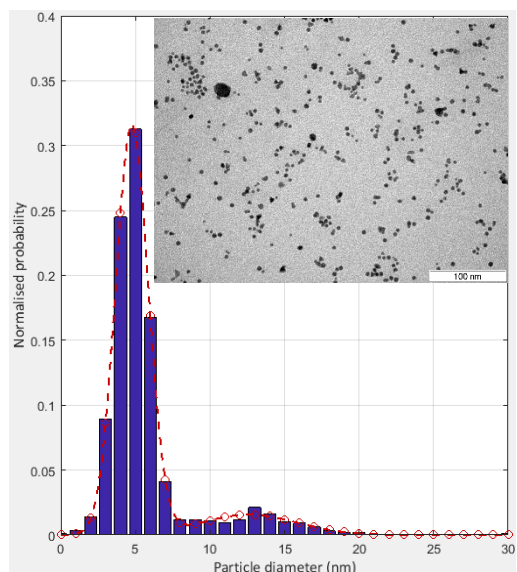
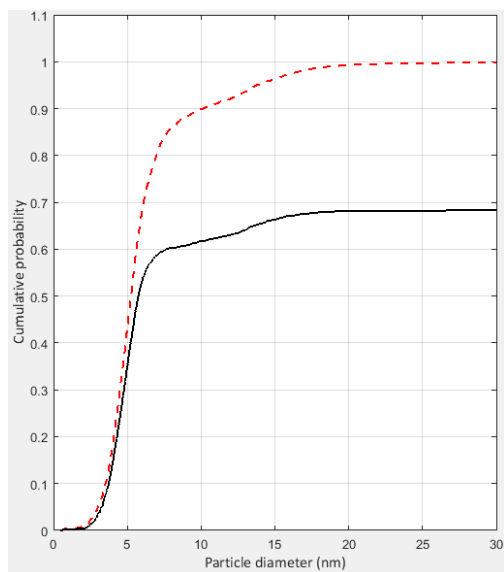


Study of synthetic parameter effects on the formation of colloidal Pd-polyacrylamide NPs

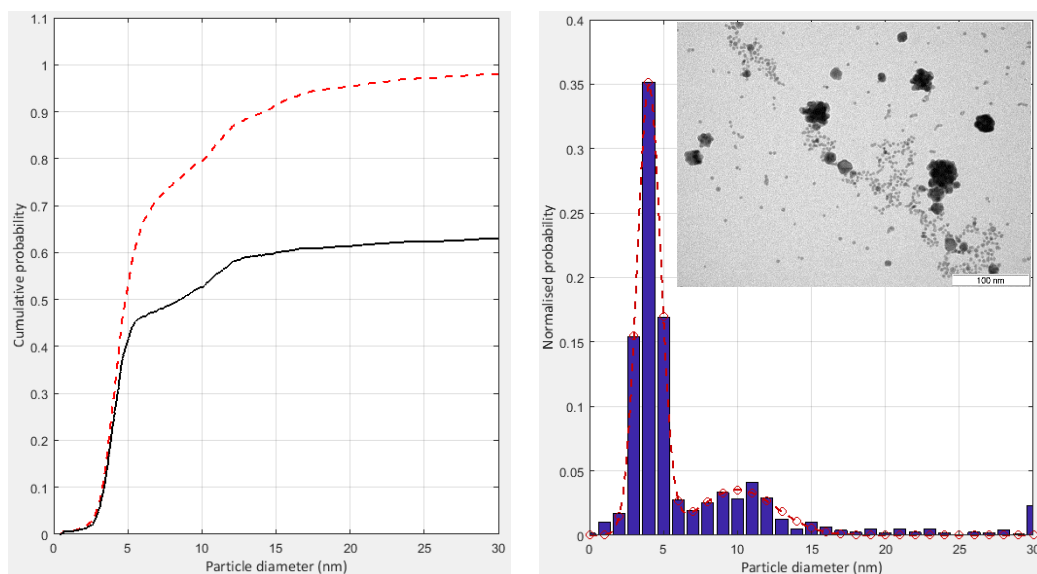
**RUN05**



**RUN06**



### RUN07



### RUN08

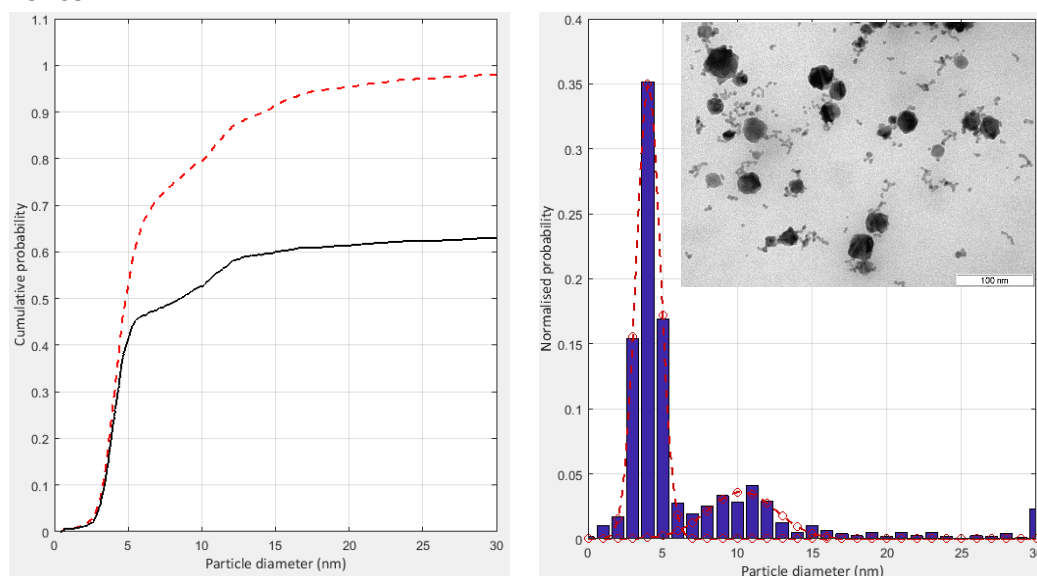


Figure 3.18. TEM micrographs, size distribution histograms and cumulative probability plot of the eight experiments of the fractional factorial design  $2^{5-2}$

#### 3.4.5.1. Definition of the responses of the design

The aim of this study was the identification of the experimental factors that affect the most on Pd-PAM morphology. Therefore to calculate the effects of these factors, it was of high importance to define numerical responses that characterize well what was

observed on the TEM images (shape of the NPs, size, distribution and presence of agglomeration). The details of the responses of this design are described as follow.

- *Y1: Percentage of spherical NPs in the sample*

One important aspect of the NPs is their size. Most of the NPs observed in the TEM samples seemed to be spherical; a criterion was defined in order to be able to estimate the percentage of these spherical NPs in the samples.

As presented in Figure 3.19, the projection of a 3D spherical particle can be approximated to a 2D circular shape, for this reason the percentage of spherical NPs was estimated from the percentage of circular NPs observed in the TEM images.

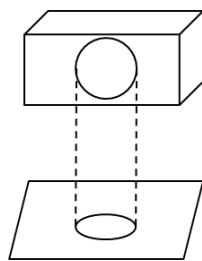


Figure 3.19. Projections of images on a plane<sup>23</sup>

To estimate the amount of spherical NPs in a sample, the aspect ratio shape descriptor was used (AR), considering as spherical those NPs with an AR lower than 1.3.

The aspect ratio corresponds to the ratio between the largest feret diameter of a particle and the smallest feret diameter orthogonal to it, as depicted in Figure 3.20. The feret diameter of a particle corresponds to its size along a specified direction. Usually, it is defined as the distance between two tangents to the contour of the object in a well-defined orientation.

Based on a visual estimation of a hypothetical sample of NPs, a criterion was used to define the sphericity of a particle: for an AR higher than 1.3, the NPs were no longer considered as spherical. To decide such criterion, hypothetical spherical particles were drawn as circles with fixed areas, then hypothetical non-spherical particles were approximated to ellipses and were drawn with the same areas as the corresponding circles as presented in Figure 3.21. The corresponding ARs of the ellipses were

calculated and it was decided that the visual difference between both geometries was acceptable for ARs between 1 and 1.3.

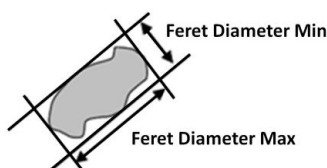


Figure 3.20. Graphical representation of the largest and smallest feret diameters of a particle

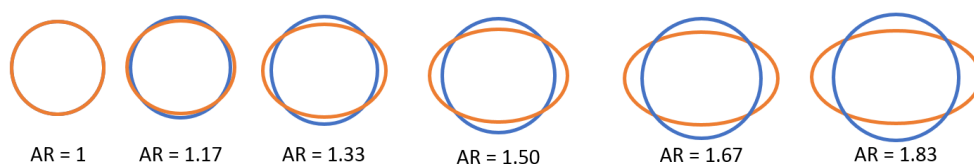


Figure 3.21. Circles and ellipses with the same area and the corresponding aspect ratio of the ellipses

Finally, the percentage of spherical NPs in the sample was estimated dividing the number of spherical NPs by the total number of NPs measured.

- *Y2: Nanoparticles size*

The NPs diameter considered in all the study was the equivalent spherical diameter (later called equivalent diameter). The equivalent spherical diameter of irregular shaped particles considered in this study corresponds to the diameter of a sphere of equivalent area.

The analysis of the effects of factors on the NPs size was carried out using the mean NPs size of the largest area peak obtained by fitting one or more Gaussian functions to the histogram. In some cases, double distributions of NPs were observed; however the area of these second peaks was not significant. Therefore, it was decided to perform the analysis of the effects of the studied factors on the NPs size corresponding to the largest area peak.

Note that the population belonging to the second distribution was taken into account in the study of the synthesis efficiency (cf. Y3 below).



- *Y3: Synthesis efficiency*

It was noticed that some NPs samples presented agglomeration. The quantification of agglomerated NPs was approximated to the fraction of non-spherical NPs and the fraction of large NPs. Indeed as shown in Figure 3.22, two types of agglomeration appeared in the TEM samples: large agglomeration of NPs in a spherical configuration (left side) or small agglomerates with a non-spherical shape (right side).

From one side, the fraction of non-spherical NPs was estimated thanks to the criteria defined above.

From the other side, the fraction of large agglomerates was defined as the fraction of NPs with an equivalent diameter larger than the  $y + 3s$  of the largest area peak of the fitted Gaussian function(s) (where 99.7% of the distribution is defined,  $y$  is the average mean diameter and  $s$  the estimated standard deviation). In this way, the population belonging to a second distribution larger in size was included in the percentage of NPs agglomerated.

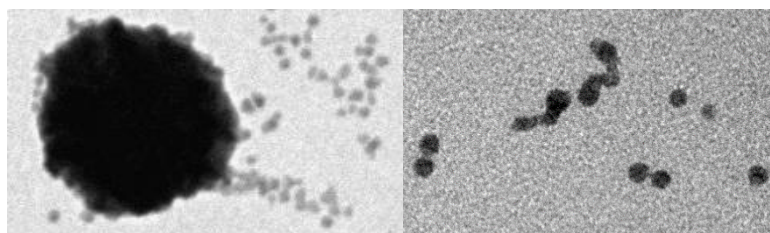


Figure 3.22. Types of agglomeration observed in TEM samples

It was decided to analyze the effects of the studied parameters on the efficiency of the syntheses. This efficiency was defined as the fraction of NPs with spherical shape and with a size included in a well-defined Gaussian distribution (*i.e.*, within the  $y \pm 3s$  of the largest area peak). In other words, the total number of non-agglomerated NPs.

- *Y4: Relative standard deviation*

To study the effects on the NPs size distribution, the relative standard deviations (RSD) of the samples were used. It corresponds to the average standard deviation obtained by fitting one or more Gaussian functions to the resulting histogram with bin size of 1 nm weighted by their corresponding area divided by the average mean NPs size as

given in the following equation:  $RSD = \frac{\bar{s}}{\bar{y}} = \frac{s_1 A_1 + s_2 A_2}{y_1 A_1 + y_2 A_2}$  where  $s_1$ ,  $s_2$  correspond to the standard deviations of both peak,  $y_1$ ,  $y_2$  are the estimated mean NPs size of both peak and  $A_1$ ,  $A_2$  the contribution percentages of each area of the corresponding peaks as shown in Figure 3.23.

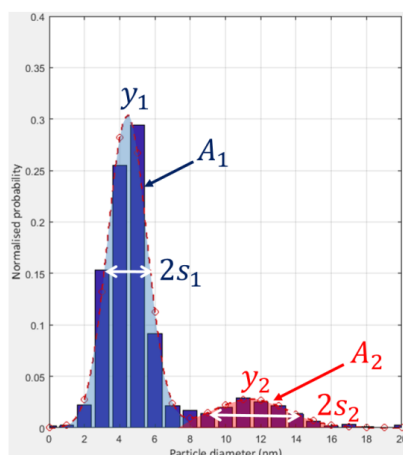


Figure 3.23. Example of TEM histogram obtained from Matlab®- Identification of  $y_1$  and  $y_2$  (the estimation of the mean size of the distributions) and  $A_1$  and  $A_2$  (the respective contribution percentage of the area of the peaks)

Using these defined responses, the numerical results obtained for the eight experiments performed are summarized in Table 3.9. The details of the analysis of these responses are given in the next sections.

Table 3.9. Sum up of the numerical results obtained for the eight experiment of the fractional factorial design  $2^{5-2}$

	Spherical NPs (%)	Main peak mean NPs size (nm)	RSD (%)	Efficiency (%)
<b>RUN01</b>	79.3	4.43	23.1	30.7
<b>RUN02</b>	79.1	4.75	19.2	36.1
<b>RUN03</b>	85.1	5.31	17.1	46.0
<b>RUN04</b>	62.1	4.07	34.7	11.6
<b>RUN05</b>	85.6	4.71	32.9	51.6
<b>RUN06</b>	68.1	4.76	23.9	28.6
<b>RUN07</b>	63.8	4.02	22.7	6.6
<b>RUN08</b>	39.4	4.38	42.1	3.1

### 3.4.5.2. Analysis of the effect of synthetic parameters on the formation of spherical Pd-PAM NPs

From the eight experiments performed, the percentage of spherical NPs was estimated using the criterion defined above (response  $Y1$ ).

The lowest percentage of spherical NPs obtained was 39.4% while the highest was 85.6%. The bar chart of the effects of the studied factors on this fraction of spherical NPs is displayed in Figure 3.24.

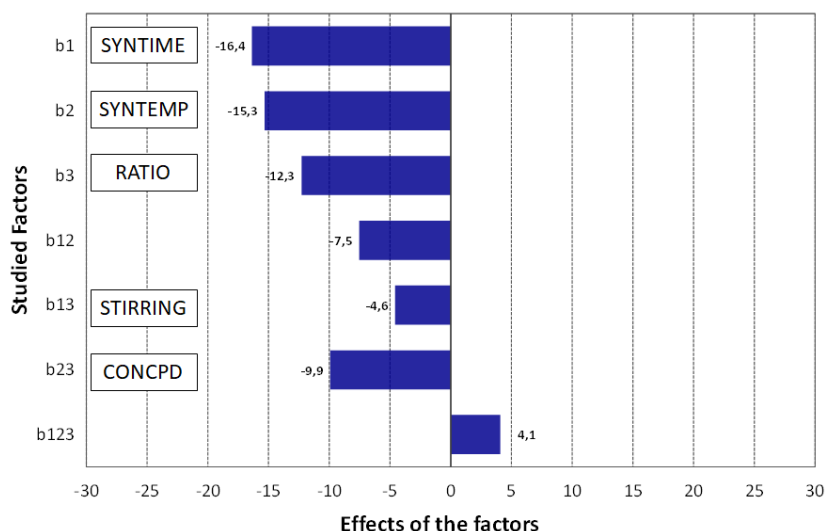


Figure 3.24. Effect of the studied factors and interactions on the fraction of spherical NPs (response  $Y1$ )

These results suggest that the factors 1 (SYNTIME) and 2 (SYNTEMP) are those that affect the most the formation of spherical NPs. Indeed the calculated effects  $b_1$  and  $b_2$  gave the higher absolute values:  $|-16.4|$  and  $|-15.3|$ , respectively. Their estimated effects were negative indicating that low levels of these factors promoted the formation of larger fractions of spherical NPs (which corresponds to syntheses of 1 hour and at 50°C).

The factor 3 (RATIO) and 4 (CONCPD, which contributes through the interaction 23) also revealed important contributions on the formation of spherical NPs. Their estimated effects were both negative values ( $b_3 = -12.3$  and  $b_{23} = b_4 = -9.9$ ),

meaning that low levels of these factors promoted the formation of large percentages of spherical NPs. It corresponds to syntheses performed with 40 eq. of PAM-to-Pd ratio and 8.4 mM of Pd concentration.

Consequently, according to these observations, NPs synthesized at low levels of the factors 1, 2, 3 and 4 (SYNTIME, SYNTEMP, RATIO and CONCPD, respectively) should result in large fraction of spherical NPs.

However, to reduce the number of experiments to eight while studying the effect of five factors, a fractional factorial design was chosen reducing thus the resolution to III. The effects of single factors were confounded with the effects of second-order interactions that might be important. Therefore the interpretation had to be made carefully. The detailed analysis taking into account these confusions is given below.

The confusions with interactions equal to or greater than three factors were neglected. The equations of the confounding of effects given in section 3.3.2.3. indicate the following confusions:

- $L_1 = b_1 + b_{35}(+b_{245} + b_{1234})$

The effect of the factor 1 (SYNTIME) was confounded with the interaction between the parameters 3 and 5 (RATIO and STIRRING, respectively).

- $L_2 = b_2 + b_{34}(+b_{145} + b_{1235})$

The effect of the factor 2 (SYNTEMP) was confounded with the interaction between the factors 3 and 4 (RATIO and CONCPD).

- $L_3 = b_3 + b_{15} + b_{24}(+b_{12345})$

The effect of the factor 3 (RATIO) was confounded with the interaction between the factors 1 and 5 (SYNTIME and STIRRING).

- $L_{23} = b_{23} + b_4(+b_{125} + b_{1345})$

The effect of the factor 4 (CONCPD) was confounded with the interaction between the factors 2 and 3 (SYNTEMP and RATIO).

From our current understanding, these second-order interactions were considered to play a moderate role or to be insignificant in comparison with the main effects. Therefore, taking into account this hypothesis, it could be concluded that experiments performed at short time, low temperature, PAM-to-Pd ratio and Pd concentration should give highly spherical NPs independently of the stirring rate. In other words, the experiments performed with the combination of (-1, -1, -1, -1,  $\pm 1$ ) for the factors (1, 2, 3, 4, 5), respectively.

In the studied design, the factor 4 (CONCPD) was confounded with the interaction between the factor 2 (SYNTEMP) and 3 (RATIO). Therefore, the experiment that corresponds to the combination (-1, -1, -1, -1,  $\pm 1$ ) for the parameters (1, 2, 3, 4, 5), respectively was not conducted during this set of experiments. Nevertheless, one opposite combination (+1, +1, +1, +1, +1) was carried out and the resulting NPs showed large agglomeration and worm-shape NPs, leading to the sample with the smallest fraction of spherical NPs from all the set of experiments (*ca.* 39.4%).

From the set of experiments, the combinations of factors that enabled the formation of the highest percentages of spherical NPs were (-1, +1, -1, -1, +1) and (-1, -1, +1, -1, -1) giving 85.5% (**RUN03**) and 85.6% (**RUN05**), respectively. In both combination the factors 1 (SYNTIME) and 4 (CONCPD) were fixed at their low levels (1 hour and 8.4 mM, respectively) while the factors 2 (SYNTEMP) and 3 (RATIO) did not remain at the same levels (+1,-1 for the **RUN03** and -1,+1 for the **RUN05** for the factors 2,3 respectively). This observation indicates that the control of the factors 1 and 4 combined with one of the factor 2 or 3 (at low levels) was enough to obtain highly spherical NPs.

Other two combinations of factors led to good percentages of spherical NPs: the **RUN01** (-1, -1, -1, +1, +1) and the **RUN02** (+1, -1, -1, +1, -1), giving 79.3% and 79.1% respectively. In both combinations, the factors 2 (SYNTEMP) and 3 (RATIO) were fixed to their low levels (50°C and 40 eq., respectively) and the factor 4 (CONCPD) to its high level (10.4 mM).

These results demonstrate that, with the restriction of the selected independent generator 234 that impede the factors 2, 3 and 4 to be at their low levels simultaneously, the control of the spherical NPs formation was more efficient when the levels of the factors 1 (SYNTIME) and 4 (CONCPD) were fixed to their low levels than the factors 2 (SYNTEMP) and 3 (RATIO). Nevertheless, as detailed above, the best option seemed to be the combination parameters 1, 2, 3 and 4 at their low levels, independently of parameter 5 (STIRRING).

To conclude, the synthesis time, temperature, PAM-to-Pd ratio and Pd concentration highly influence the fraction of spherical NPs. As summarize in Figure 3.25, low levels of these factors are preferred to obtain large percentages of spherical NPs. In contrast, the stirring rate was not influencing to this response.

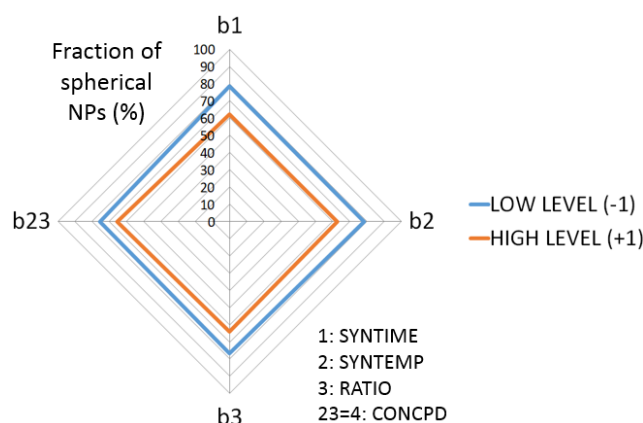


Figure 3.25. Radar diagram of the averaged effects at low and high levels of  $b_1$  (SYNTIME),  $b_2$  (SYNTEMP),  $b_3$  (RATIO) and  $b_{23}$  (CONCPD) on the percentage of spherical NPs obtained

### 3.4.5.3. Analysis of the effect of synthetic parameters on the mean NPs size

From the eight experiments performed, the mean NPs equivalent diameter varied between 4.0 nm and 5.3 nm, which shows that significant variation of NPs sizes were not obtained. The same remark was made in the OFAT study presented above. However, these slight variations were analysed in order to get insights about the way to modify even more the NPs size. Figure 3.26 displays the bar chart with the effect of

the studied factors and interactions on the mean NPs size of the largest area peak obtained by fitting one or more Gaussian functions to the TEM histograms (response Y2).

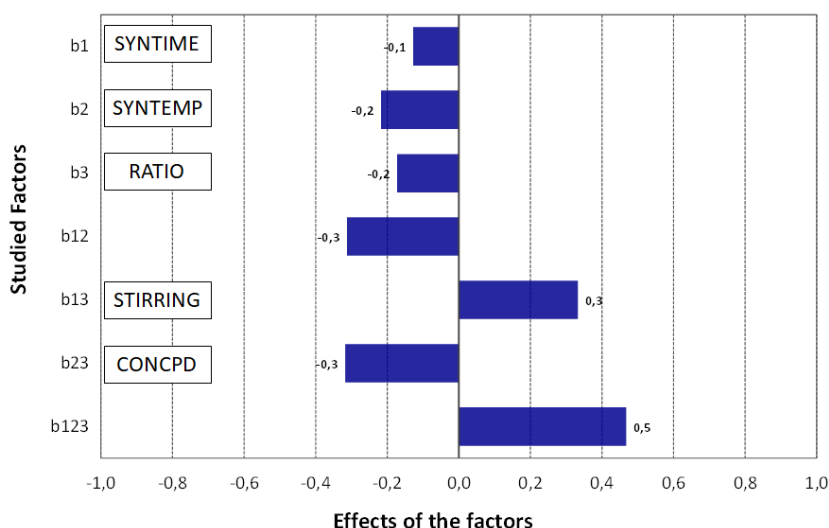


Figure 3.26. Effect of the studied factors and interactions on the mean particle size of the largest area peak obtained by fitting one or more Gaussian functions to the TEM size histograms (response Y2)

Interestingly, the third-order interaction between the factors 1, 2 and 3 (SYNTHIME, SYNTEMP and RATIO, respectively) showed the major effect on the NPs size. The double interactions 12, 13 and 23 also resulted to affect significantly the system. Since the interaction effects are much larger than the single effects, the interpretation of these terms must be considered before the main effects in order to avoid incorrect conclusions.

As in the previous section, the interpretation of the factor and interaction effects had to be made carefully since confounding were induced in this design. The equations of the confounding of effects given in section 3.3.2.3. indicate the following confusions:

- $L_{123} = b_{123} + b_{14} + b_{25} (+b_{345})$

The effect of the third-order interaction 123 which corresponds to the interaction between the factors 1, 2 and 3 (SYNTHIME, SYNTEMP and RATIO, respectively) was

confounded with the interaction between the factors 1 (SYNTH) and 4 (CONCPD) and with the interaction between the factors 2 (SYNTEMP) and 5 (STIRRING). From our understanding, it was supposed that the interaction 14 would affect the NPs size in a more significant way than the interactions 25 and 123. Thus it was assumed that the large effect observed for the interaction 123 in Figure 3.26 came from the influence of the second-order interaction 14 (SYNTH x CONCPD).

- $L_{12} = b_{12} + b_{45}(+b_{235} + b_{134})$

The effect of the double interaction 12 which corresponds to the interaction between the factor 1 (SYNTH) and 2 (SYNTEMP) was confounded with the second-order interaction 45 (CONCPD x STIRRING). In the initial qualitative classification of the interactions significance, displayed in Table 3.4, the interaction between the factor 1 (SYNTH) and 2 (SYNTEMP) was identified as potentially significant while 45 (CONCPD x STIRRING) as moderated interaction. However, from the eight experiments performed, the largest NPs were obtained by the combination of (-1, +1, -1, -1, +1) (**RUN03**) and the smallest NPs by the combination of (-1, +1, +1, +1, -1) (**RUN07**) for the factors (1, 2, 3, 4, 5) respectively. In both cases the interaction 12 was fixed to (-1, +1) suggesting that this interaction did not have significant influence on the NPs size.

- $L_{13} = b_{13} + b_5(+b_{124} + b_{2345})$

For the construction of the fractional design matrix, the factor 5 (STIRRING) was confounded with the interaction between the factors 1 (SYNTH) and 3 (RATIO), since it was not expected to be significant. Thus the effect observed for the interaction 13 in Figure 3.26 was assumed to come from the only influence of the factor 5 (STIRRING).

- $L_{23} = b_{23} + b_4(+b_{125} + b_{1345})$

In the same way, for the construction of the fractional design matrix, the factor 4 (CONCPD) was confounded with the interaction between the factor 2 (SYNTEMP) and 3 (RATIO), since it was not expected to be relevant. Therefore the effect observed for the interaction 23 in Figure 3.26 was assumed to come from the only influence of the factor 4 (CONCPD).



After having analysed the confusions, the analysis of the effects of each factor and interaction was performed and is detailed as follow.

First, it was assumed that the effect  $b_{123}$  presented in Figure 3.26 represents the only influence of the interaction between the factor 1 (SYNTIME) and 4 (CONCPD). This effect was positive (0.5) indicating that a high level of this interaction led to larger NPs sizes. A high level of this interaction is traduced by two possible combinations of factors: (-1, -1) or (+1, +1) for (1, 4) respectively. In order to figure out which of these combinations enabled the formation of larger NPs, the diagram of this interaction was plotted and is presented in Figure 3.27.

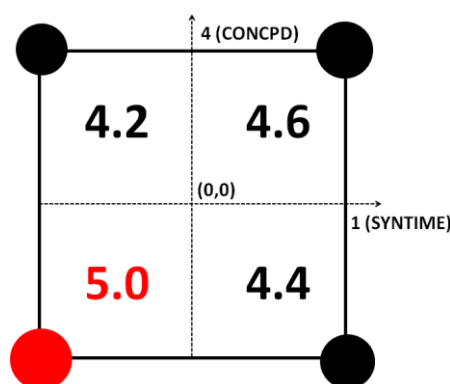


Figure 3.27. Diagram of interaction the 14 (SYNTIME x CONCPD) for the response Y2 (NPs size in nm)

This diagram represents the averaged NPs sizes obtained for the experiments performed at (1, 1), (1, -1), (-1, 1) and (-1, -1) of the factors (1, 4), respectively. It could be seen on this diagram that the combination (-1, -1) for the factors (1, 4), respectively, led to slightly larger NPs size. In other words, larger NPs were obtained with a combination of short synthesis time (1 hour) and low Pd concentrations (8.4 mM).

Then, the contribution of  $b_{12}$  showed in Figure 3.26 was attributed to the only influence of the interaction 45 (CONCPD x STIRRING). This effect was negative (-0.3), indicating that a low level of this interaction enabled the formation of larger NPs. Two

combinations of parameters were thus possible: (-1, +1) or (+1, -1) for (4, 5), respectively. The diagram of this interaction is given in Figure 3.28.

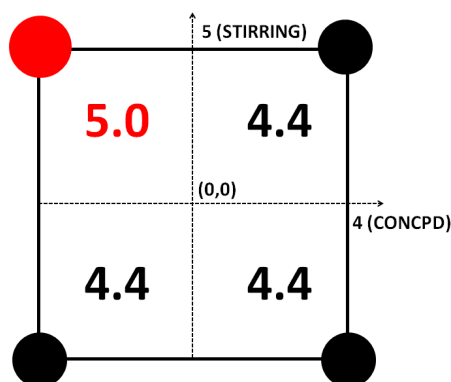


Figure 3.28. Diagram of interaction the 45 (CONCPD x STIRRING) for the response Y2 (NPs size in nm)

This plot indicates that the combination of (-1, 1) for the factors (4, 5), respectively favoured the formation of large Pd NPs. This combination corresponds to low Pd concentration (8.4 mM) and high stirring rate (900 rpm).

The contributions of  $b_{23}$  and  $b_{13}$  were attributed to the influence of the factors 4 (CONCPD) and 5 (STIRRING), respectively. A negative effect was found for the factor 4 (-0.3) indicating that large NPs were obtained at lower Pd concentration which is in agreement with the conclusion of the previous interaction (45). In contrast, a positive effect was found for the factor 5 (0.3) indicating that large NPs were obtained at higher stirring rates, which again agree with the conclusion of the previous interaction (45).

Finally, although their effects were less significant, the plot of effects displayed in Figure 3.26 indicates that larger NPs were obtained at low levels of the factors 1, 2 and 3. In other words, the formation of larger NPs were slightly promoted by short synthesis time, low temperature and low PAM-to-Pd ratio.

To conclude, the analysis of the effects of the studied factors revealed that the interactions 14 (SYNTIME x CONCPD) and 45 (CONCPD x STIRRING) as well as the

factors 4 (CONCPD) and 5 (STIRRING) were highly influencing the NPs size. These effects are summarized on the radar plot in Figure 3.29.

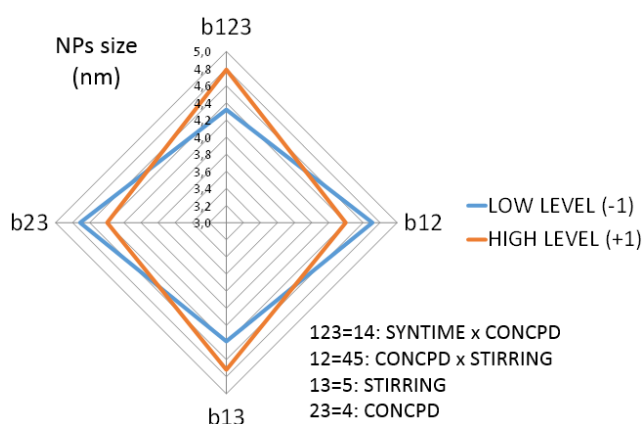


Figure 3.29. Radar diagram of the averaged effects at low and high levels of  $b_{123}$ ,  $b_{12}$ ,  $b_{13}$  and  $b_{23}$  on the mean particle size of the largest area peak obtained by fitting one or more Gaussian functions to the TEM histogram

The combination (-1, -1, -1, -1, +1) for the factors (1, 2, 3, 4, 5), respectively should provide large NPs. This combination corresponds to short reaction time combined with low temperature, PAM-to-Pd ratio, Pd concentration and high stirring rate.

Concerning the Pd concentration, Solovov *et al.* and Kim *et al.* reported the opposite trend.<sup>7,17</sup> They found that larger NPs sizes were obtained at high Pd concentrations. Concerning the stirring rate, Jung *et al.* also reported an opposite trend: they observed a decrease in size when increasing the agitation speed.<sup>18</sup>

#### 3.4.5.4. Analysis of the effect of synthetic parameters on the NPs synthesis efficiency

As described in the OFAT study, agglomeration of NPs was observed in some TEM samples. This fraction of agglomerated NPs was estimated during this DOE study thanks to automatic measurement of the TEM samples and using the definition given in section 3.4.5.1.

In this section, the effect of the studied factors on the ability to form well-defined NPs without large agglomeration was assessed and a synthesis efficiency score was provided.

The estimated efficiencies of the eight syntheses performed were between 3.1% and 51.6%. The bar chart of the effect of the synthetic parameters on this fraction is displayed in Figure 3.30.

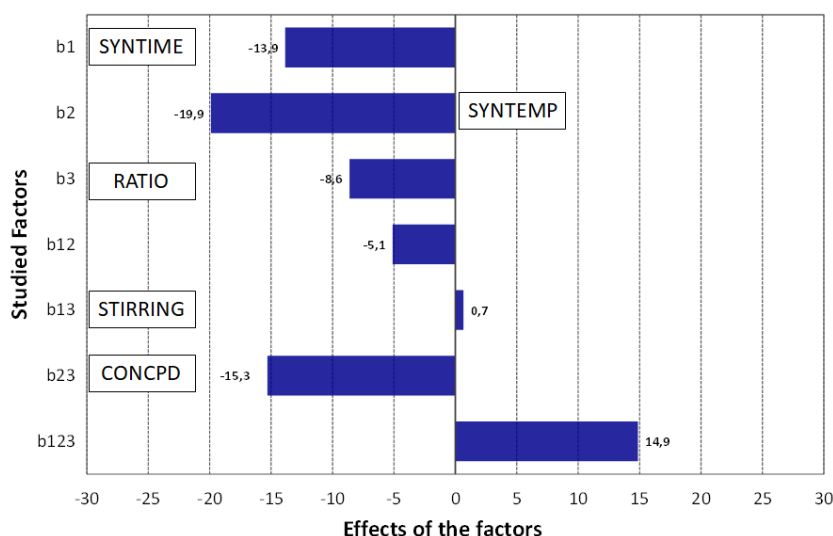


Figure 3.30. Effect of the studied factors and interactions on the efficiency of the NPs syntheses (response Y3)

This plot revealed significant effects (in descending order) of the factor 2 (SYNTEMP), factor 4 (CONCPD, through the interaction 23), interaction 123 and the factor 1 (SYNTIME).

First the effect attributed to the factor 2 (SYNTEMP) was negative ( $-19.9$ ) indicating that high efficiencies were obtained at low temperatures ( $50^{\circ}\text{C}$ ).

As detailed before, the contribution of the interaction 23 was approximated to the only contribution of the single factor 4 (CONCPD). Its estimated effect was negative ( $-15.3$ ), meaning that higher efficiencies were obtained at lower Pd concentrations ( $8.4\text{ mM}$ ).

As explained above, the third-order interaction 123 was confounded with the second-order interactions 14 and 25 and 14 was assumed to prevail over 25 and 123. The plot

of effects displayed in Figure 3.30 shows that higher efficiencies were obtained when the interaction 14 was fixed to its high level (positive value of effect: 14.9). The diagram of this interaction is given in Figure 3.31.

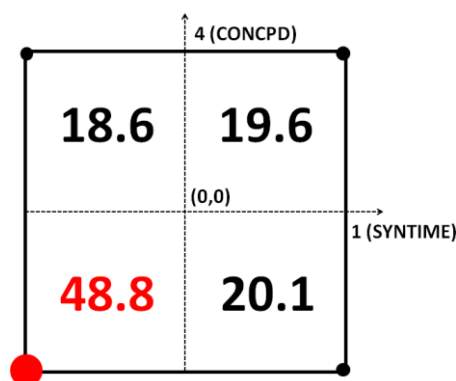


Figure 3.31. Diagram of interaction 14 (SYNTIME x CONCPD) for the response Y3 (NPs synthesis efficiency in %)

According to this diagram, it is clear that the best combination to obtain a high synthesis efficiency corresponds to (-1, -1) for the factors (1, 4) respectively. In other words, high efficiencies were obtained combining short synthesis time (1 hour) with low Pd concentration (8.4 mM).

The plot of effect Figure 3.30 also indicates that higher efficiencies were obtained when the single factor 1 (SYNTIME) was fixed to its low level. This observation is in agreement with the previous conclusion (shorter time is preferred to avoid agglomeration and increase the synthesis efficiency).

Finally, factor 3 (RATIO) did not reveal significant effect but low PAM-to-Pd ratio seemed to favour the efficiency of the syntheses (the effect of this factor was negative: -8.6)

To conclude the temperature of synthesis, Pd concentration, synthesis time and interaction between the Pd concentration and the synthesis time were of high importance to control the efficiency of the Pd NPs synthesis. As recalled in Figure 3.32,

high efficiencies were obtained at short reaction time, low temperature and low Pd concentration.

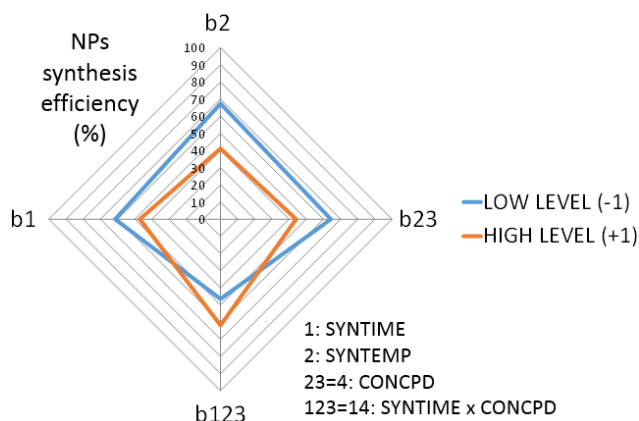


Figure 3.32. Radar diagram of the averaged effects at low and high levels of  $b_1$ ,  $b_2$ ,  $b_{23}$  and  $b_{123}$  on the NPs synthesis efficiency (%)

This interpretation leads to the combination of factors  $(-1, -1, -1, -1, \pm 1)$  for the parameters (1, 2, 3, 4, 5) respectively to obtain a high synthesis efficiency. In other words the use of short synthesis time, low temperature, PAM-to-Pd ratio and Pd concentration (independently of the stirring rate) avoid the formation of large agglomerates during the synthesis of Pd-PAM NPs.

#### 3.4.5.5. Analysis of the effect of synthetic parameters on the NPs relative standard deviation

From the eight experiments performed, the relative standard deviation (RSD) as defined in section 3.4.5.1. varied from 18% to 42%. The plot of effects is given in Figure 3.33.

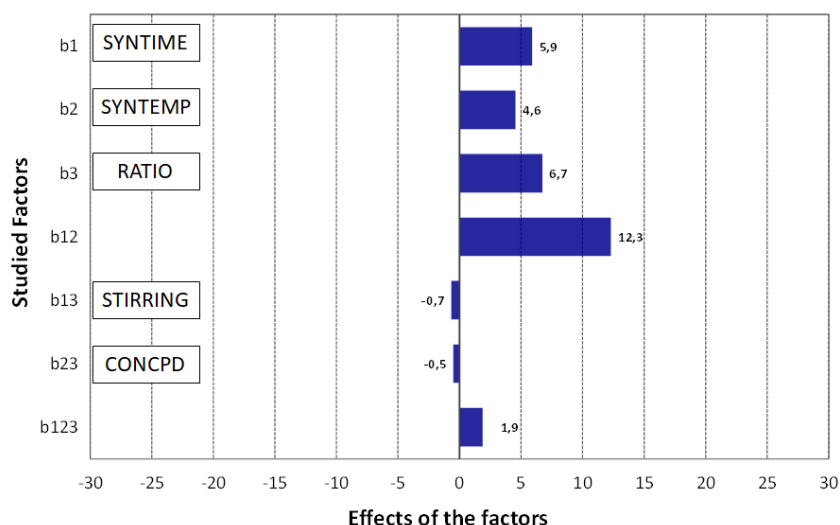


Figure 3.33. Effect of the studied factors and interactions on the relative standard deviation of the NPs (response Y4)

These results indicate that the interaction between the factor 1 (SYNTIME) and 2 (SYNTEMP) and the single factors 1, 2, 3 (SYNTIME, SYNTEMP and RATIO, respectively) were highly influencing the NPs distribution. In contrast, the interactions 13, 23 and 123 were not significant. Since the second-order interactions 23 and 13 were confounded with the factors 4 (CONCPD) and 5 (STIRRING) respectively, it means that the stirring rate and the Pd concentration were not affecting the NPs distribution.

The plot of effects of Figure 3.33 shows a positive value for the interaction 12 (12.3) indicating that high relative standard deviations were obtained with high level of this interaction. Since the objective is to form well-defined NPs, the relative standard deviation should be minimized. Therefore, a low level of this interaction should be fixed to improve the NPs size distribution. As it was seen above, this interaction was confounded with the interaction 45. No effects of the single factors 4 and 5 were observed, however it did not mean that a significant interaction between both parameters could not exist. In view of the results obtained, the discrimination between both interactions was not easy. Thus it was decided to analyse the results in two steps.

In the first analysis, the interaction between the factor 1 (SYNTIME) and 2 (SYNTEMP) was assume to prevail over the interaction 45. The diagram of this interaction is given in Figure 3.34.

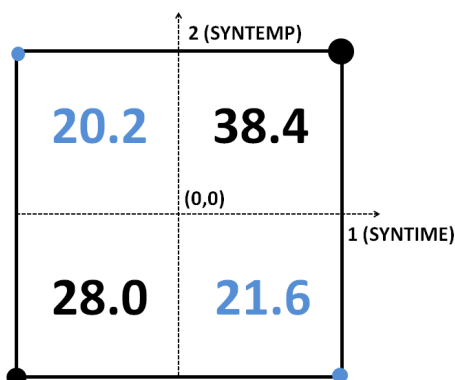


Figure 3.34. Diagram of interaction 12 (SYNTIME x SYNTEMP) for the response Y4 (RSD in %)

This diagram indicates that there was no major difference between the combination (+1, -1) and (-1, +1) for the value of (1, 2) respectively.

Then, the plot of effects presented in Figure 3.33 indicates that higher relative standard deviation were obtained when the factors 1 (SYNTIME), 2 (SYNTEMP) and 3 (RATIO) were at their high level. Therefore, narrower NPs size distributions were obtained when these factors were at their low level. However the combination of these 3 factors at a same level was not compatible with the fact that the interaction 12 had to be fixed to its low level too. Thus, the possible combinations of factors that, in this case, should provide narrow NPs size distribution were (-1, +1, -1,  $\pm 1$ ,  $\pm 1$ ) or (+1, -1, -1,  $\pm 1$ ,  $\pm 1$ ) for (1, 2, 3, 4, 5) respectively. From the set of eight experiments, two of these combinations were performed: the **RUN02** (+1, -1, -1, +1, -1) and the **RUN03** (-1, +1, -1, -1, +1) leading to 19% and 18% of relative standard deviation respectively (the lowest values obtained).

In the second analysis, the interaction between the factor 4 (CONCPD) and 5 (STIRRING) was assume to prevail over the interaction 12. The diagram of this interaction is given in Figure 3.35.



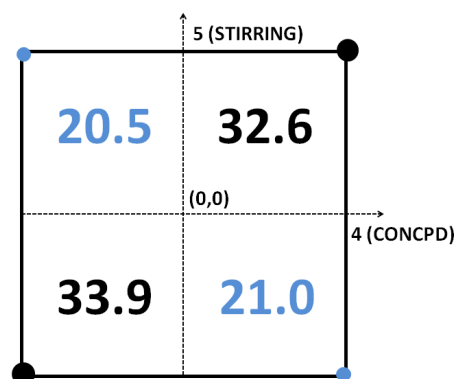


Figure 3.35. Diagram of interaction 45 (CONCPD x STIRRING) for the response  $Y_4$  (RSD in %)

As observed before, no major differences between the combination (+1, -1) and (-1, +1) for the value of (4, 5). Since the plot of effects presented in Figure 3.33 reveals that narrower size distribution were obtained at low levels of the factors (SYNTIME), 2 (SYNTEMP) and 3 (RATIO), two combinations of factors were expected to form narrow NPs size distribution: (-1, -1, -1, -1, +1) and (-1, -1, -1, +1, -1) for (1, 2, 3, 4, 5) respectively. Since the designed matrix was restricted by the independent generators 234 and 135, these experiments were not conducted.

To conclude, this analysis demonstrates that the distribution of the NPs were highly affected by the synthesis time, temperature, the PAM-to-Pd ratio and the interaction between the synthesis time and temperature and/or the interaction between the Pd concentration and the stirring rate. As recalled in Figure 3.36, lower relative standard deviations were obtained with:

- Short synthesis time (1 h) combined with high temperature (70°C) or long synthesis time (5.5 h) combined with low temperature (50°C).
- Low Pd concentration (8.4 mM) combined with high stirring rate (900 rpm) or high Pd concentration (10.4 mM) combined with low stirring rate (700 rpm).
- Short synthesis time (1 h).
- Low temperature (50°C).
- Low PAM-to-Pd ratio (40 eq.)

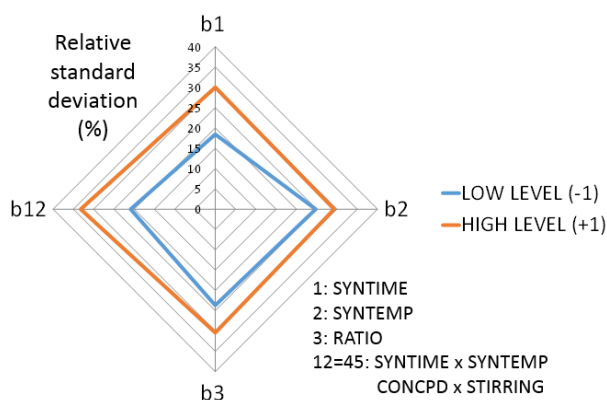


Figure 3.36. Radar diagram of the averaged effects at low and high levels of  $b_1$ ,  $b_2$ ,  $b_3$  and  $b_{12}$  on the relative standard deviation (%)

### 3.4.5.6. Conclusions of the study of the effect of synthetic parameters on the formation of Pd-PAM NPs using DOE

The analysis of the effects of synthesis time, synthesis temperature, PAM-to-Pd molar ratio, Pd concentration and stirring rate on the formation of colloidal Pd-PAM NPs was performed by means of design of experiments methodology. More precisely, the studied responses were focused on the ability to synthesize in an efficient way spherical NPs with large size and narrow distribution. To limit to eight the number of experiments and, at the same time, be able to study the effect of five parameters, the plan of experiments had to follow a fractional factorial design that involved confusions between single factors and second-order interactions. Therefore, the interpretation of the results was performed using assumptions based on our chemical knowledge and experimental observations. From these interpretations, different combinations of factors were found for each studied response (percentage of spherical NPs, NPs size, synthesis efficiency and relative standard deviation) and are summarized in Table 3.10.

Table 3.10. Combinations of factors highlighted for each studied responses

Higher percentage of spherical NPs (Y1)	(-1, -1, -1, -1, ±1)
Larger mean NPs size (Y2)	(-1, -1, -1, -1, +1)
Higher efficiency of the synthesis (Y3)	(-1, -1, -1, -1, ±1)
Lower relative standard deviation (Y4)	(-1, +1, -1, ±1, ±1)
	(+1, -1, -1, ±1, ±1)
	(-1, -1, -1, -1, +1)
	(-1, -1, -1, +1, -1)

Interestingly, one combination of factors was common to the four studied responses: (-1, -1, -1, -1, +1). This combination means that high percentage of spherical NPs, large NPs, high synthesis efficiency and low relative standard deviation were obtained at short reaction time, low temperature, low PAM-to-Pd ratio, low Pd concentration and high stirring rate.

To confirm these conclusions, one additional synthesis (called **RUN09**) was performed using the following combination: (-1, -1, -2, -2, +2). During the OFAT and DOE studies, it was observed that the size of the NPs was not significantly modified (in the range of 3 to 5 nm). Therefore, to attempt an increase of size, it was preferred to test the conditions (-1, -1, -2, -2, +2) instead of (-1, -1, -1, -1, +1) since the three last parameters (RATIO, CONCPD and STIRRING) were significantly affecting the NPs size, thus their levels (values) were increased in absolute value to a higher step (instead of a step of 1, a step of 2 was chosen). This combination of factors corresponds to a synthesis performed during 1 h, at 50°C with 30 eq. of PAM-to-Pd molar ratio, 7.4 mM of Pd concentration and 1100 rpm of stirring rate. The TEM micrograph and size distribution histogram obtained for the automatic measurement of more than 5000NPs are displayed in Figure 3.37 and Figure 3.38.

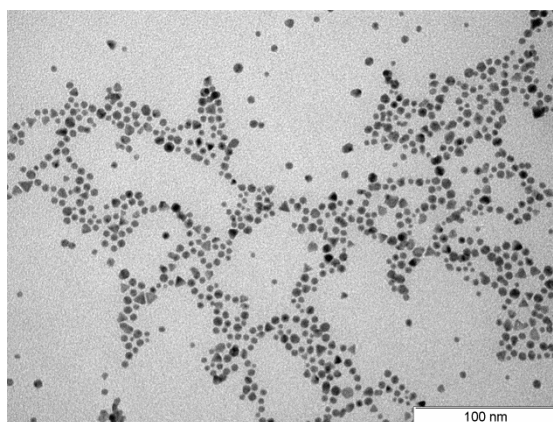


Figure 3.37. TEM micrographs of the **RUN09** performed during 1h, at 50°C with 30 eq. of PAM-to-Pd molar ratio, 7.4 mM of Pd concentration and 1100 rpm of stirring rate (combination -1, -1, -2, -2, +2 for respectively factors 1, 2, 3, 4, 5)

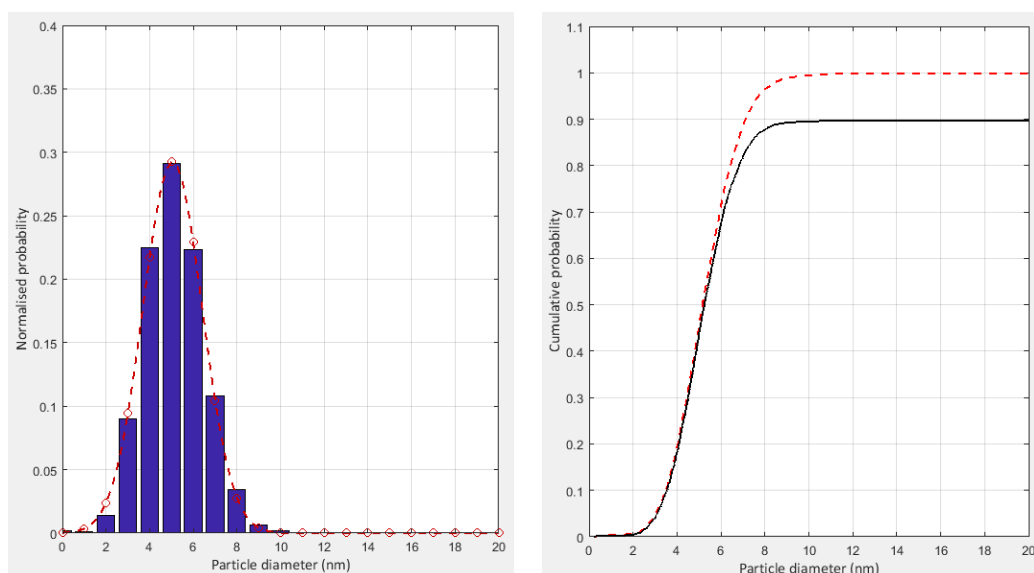


Figure 3.38. Results of **RUN09**. Left side: Size distribution histogram with bin size of 1 nm obtained by the fitting of one Gaussian function to the automatic measurement of 5190 NPs. Right side: Cumulative probability plot of the equivalent diameter of the spherical NPs (in black) and the equivalent diameter of all the NPs

The NPs obtained were 90% spherical which represent an increase of *ca.* 5% in comparison with the higher percentage of spherical NPs obtained in the experiments of the designed matrix. Moreover, the synthesis efficiency showed an increase of 25% in comparison with the best result obtained during the DOE study: *ca.* 77%. The NPs presented a mean size of  $5.05 \pm 1.36$  nm. The NPs size remained constant indicating that the studied parameters did not enable the formation of NPs larger than 5 nm in the studied range of values. Other parameters could be contemplated to attempt a variation of size such as the pH, the nature of the reducing agent, the nature of the solvent or the nature of the polymer.

For example, P. Witte *et al.* performed a variation of Pd NPs size from 5 to 15 nm by pH modification.<sup>24</sup> Then, Braun and co-workers reported the effect of the polymer molecular weight on NPs sizes.<sup>25</sup> In their study the mean diameter of the NPs decreased with increasing the polymer weight. Finally Cheng and co-workers reported the preparation of colloidal Pd NPs by a reduction-by-solvent method.<sup>26</sup> NaBH<sub>4</sub> was used as reducing agent to reduce Pd<sup>2+</sup> ion in a C<sub>2</sub>H<sub>5</sub>OH/H<sub>2</sub>O solvent system in presence

of polyvinylpyrrolidone (PVP) as stabilizer. They found that varying the amount of  $\text{NaBH}_4$ ,  $\text{C}_2\text{H}_5\text{OH}$  and PVP, different NPs sizes were obtained. In the same way, Perez-Cordonado and co-workers reported the effect of the reducing agent nature on the NPs size and an important decrease in NPs size when the reducing agent-to-metal ratio was increased.<sup>16</sup>

To conclude, this DOE study allowed finding in which direction the synthetic parameters had to be modified to increase the fraction of spherical Pd-PAM NPs and the synthesis efficiency. Moreover it was shown that the NPs size could not be varied more than in the range of 3 to 5 nm indicating that this characteristic was not determined by the studied reaction conditions.

The use of DOE methodology helped to understand better how each parameter affect a concrete response (sphericity, size, distribution or efficiency) and to highlight important interactions. This study demonstrates that this chemical system is complex and, in most of the cases, the major part of the studied parameters and interactions highly affected the responses. Thus, the DOE methodology is a powerful methodology to guide the identification of the combinations of factors that allow obtaining the desired well-defined NPs.

The common factors studied in the OFAT and DOE structure-synthesis relationship studies were the PAM-to-Pd ratio, the temperature and synthesis time. Concerning the PAM-to-Pd ratio, higher values led to narrower size distributions in the OFAT study. In the DOE study, the opposite trend was observed but the interaction between the synthesis time and temperature appeared more significant than this ratio for the control of the relative standard deviation.

Then, in both studies, shorter times and lower reaction temperature resulted in better defined NPs.

However, a direct comparison between both studies is not straightforward. Indeed, the data analysis procedure was different in both study (manual vs. automatic measurements of the NPs). Moreover these studies were performed with three years

of difference using the same batch of PAM stabilizer since the later was not anymore commercially available. Aging effects were detected on this reagent which was affecting slightly the NPs formation. This remark is of high importance for industrial considerations. Indeed, knowing the negative effects of a long-term storage, the production schedules could be adapted to avoid this issue as much as possible.

### 3.5. Conclusions

In this chapter, the study of the effects of several synthetic parameters on a novel Pd-polyacrylamide NPs (Pd-PAM NPs) formed by chemical reduction in aqueous solution was described. This study was first performed using a classical OFAT approach and was then completed with eight experiments that followed a DOE matrix.

The main conclusions of the OFAT study are reminded as follow.

- No significant variations of sizes were observed from the set of experiments. Significant improvements in terms of size distribution were highlighted.
- The key parameters were the stabilizer-to-metal ratio, synthesis temperature and synthesis time.
- In contrast to the typical reported trend, when the amount of stabilizer was increased from 20 eq. to 80 eq., the NPs size did not varied significantly but their distribution drastically improved.
- An optimum seemed to appear at 50°C leading to the narrowest NPs size distribution under the tested reaction conditions. Nevertheless, this non-linear comportment could be confirmed with DOE approach.
- Until 15.5 hours of reaction, the Pd-PAM NPs were well-formed but longer reaction times led to their decomposition in a non-stable suspension
- From this OFAT study, a recipe of well-defined NPs of *ca.* 3.9 nm was obtained and called **Pd-PAM 6**. They were synthesized at 50°C with 40 equivalents of polyacrylamide under 3 bar of hydrogen, 700 rpm of stirring rate and during 5.5 hours. The robustness of this recipe was checked and the NPs characterization was provided.

During this study, limitations of the manual measurements of the TEM micrographs were pointed out (accuracy and lack of information of NPs shape and agglomeration). Consequently, automatic measurements of NPs were proposed combined with the use of a Matlab® routine that enabled the estimation of the fraction of spherical NPs in a sample, the efficiency of a synthesis, the mean NPs size and distribution.

An additional structure-synthesis relationship study was proposed using the DOE approach. The main conclusions these eight experiments are given as follow.

- The direction that should follow each of the studied parameters in order to increase the fraction of spherical NPs and the synthesis efficiency was determined.
- The NPs size remained equal to *ca.* 5 nm under the studied reaction conditions as in the previous OFAT study.
- Short synthesis time, low temperature, low PAM-to-Pd ratio, low Pd concentration and high stirring rate led to the formation of highly spherical NPs with a low fraction of agglomerates and a narrow NPs distributions.

## 3.6. Appendix

### 3.6.1. Appendix 1: NPs automatic measurement procedure for colloidal suspensions

The pictures obtained after analysis with the TEM were treated with an image processing and image analysis software: Fiji Is Just ImageJ. The NPs were measured with an automatic treatment described as follow.

First, the image scale was defined. To do so, a straight line was drawn on the picture scale. Then in the menu “analyze” and “set scale”, the known distance and unit of length were filled as shown in Figure 3.39. The corresponding distance in pixels was then calculated by the software and was taken into account for the measurements.

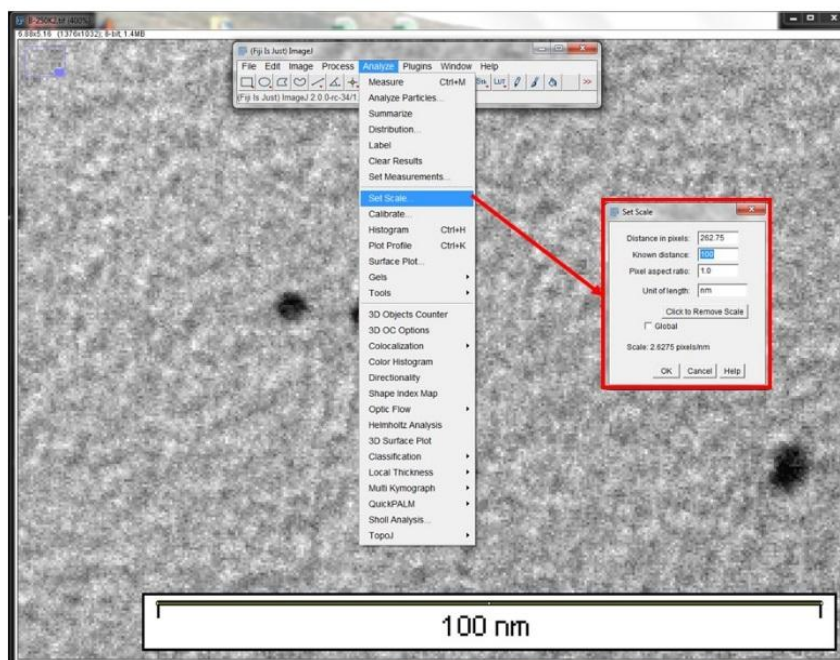


Figure 3.39. Fiji – Image J: Scale setting

The image was then transformed to a 8-bit image as shown in Figure 3.40.



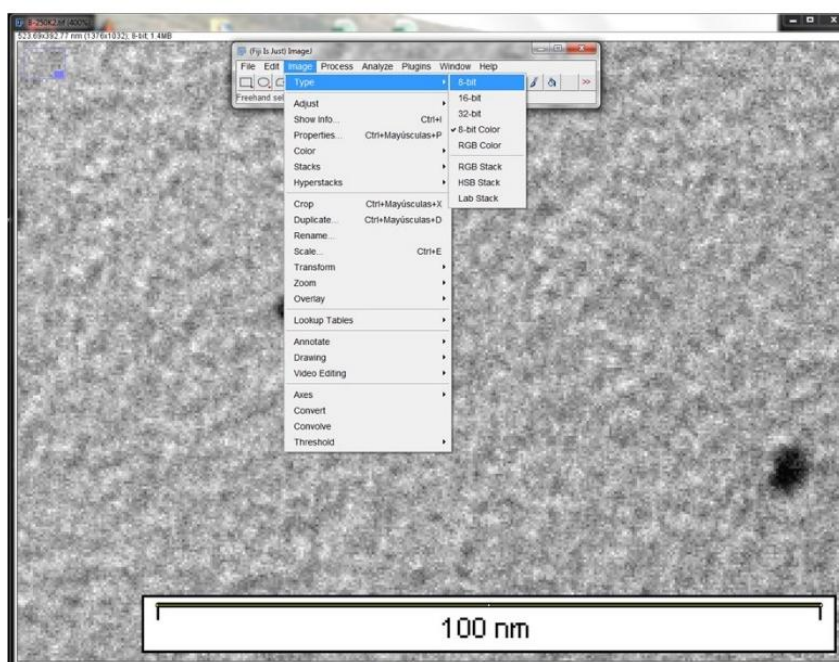


Figure 3.40. Fiji – Image J: Transformation to 8-bit image

The mean filter was applied to the image to smooth the background and make the treatment easier, as displayed in Figure 3.41.

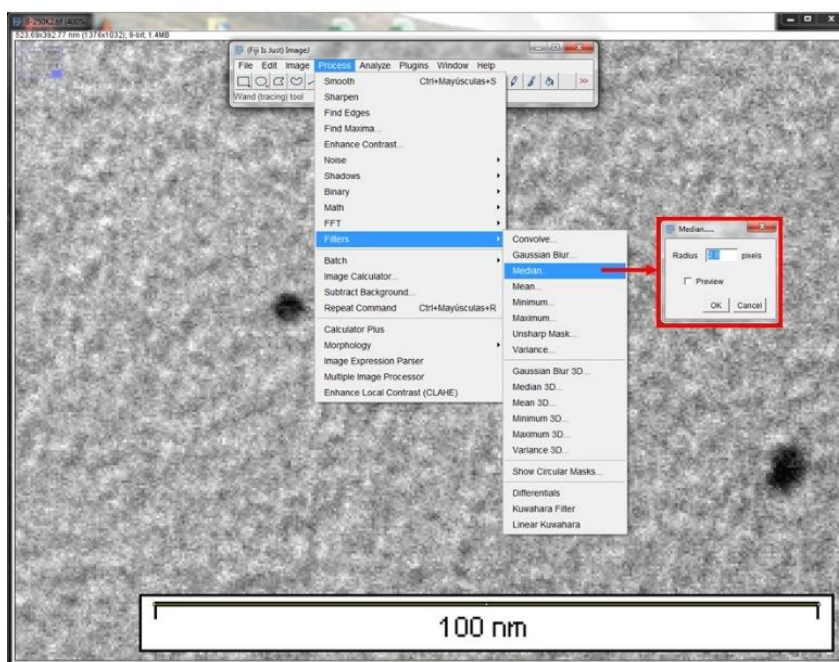
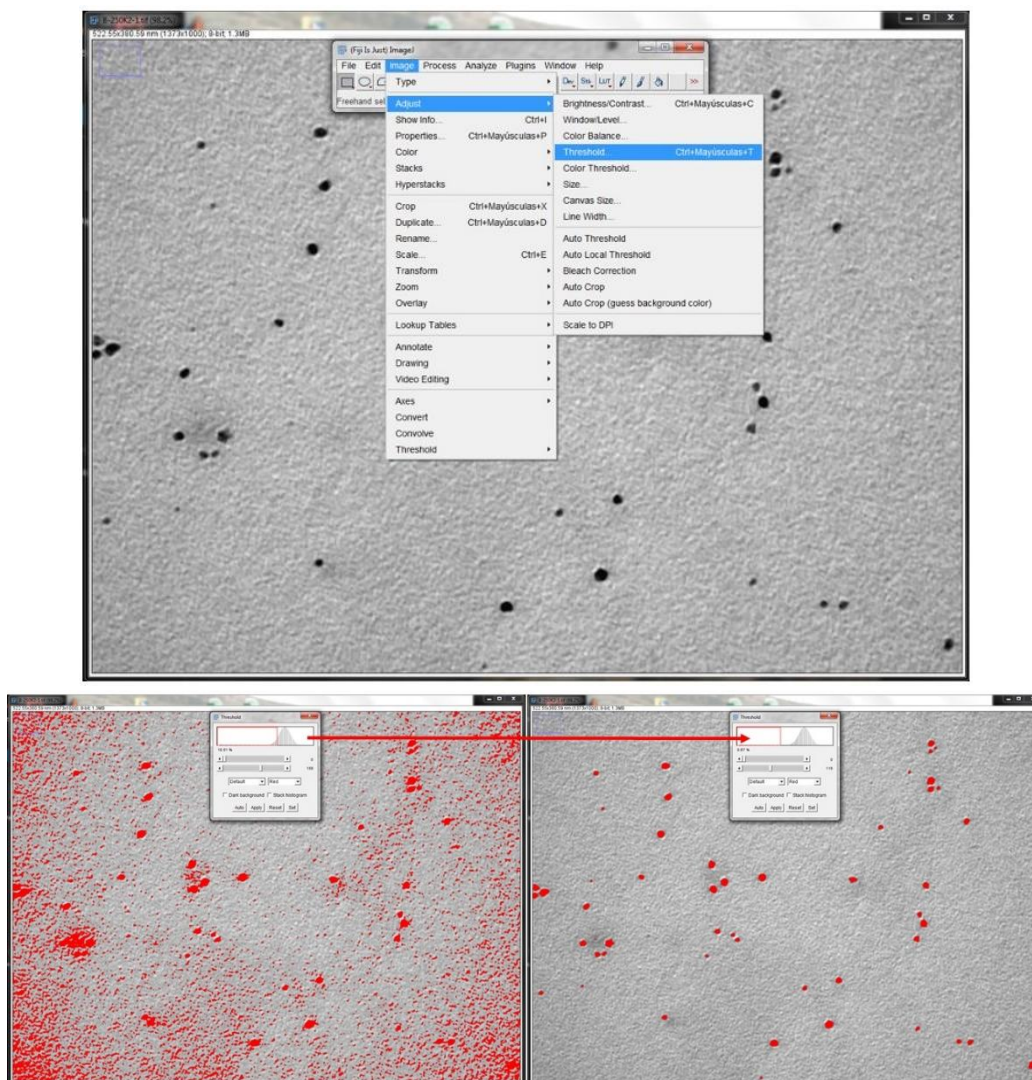


Figure 3.41. Fiji – Image J: Use of filters

Then the image was transformed to a binary image. To do so the threshold of the image was adjusted (cf. Figure 3.42). This step had to be made carefully in order to avoid bias in the analysis.



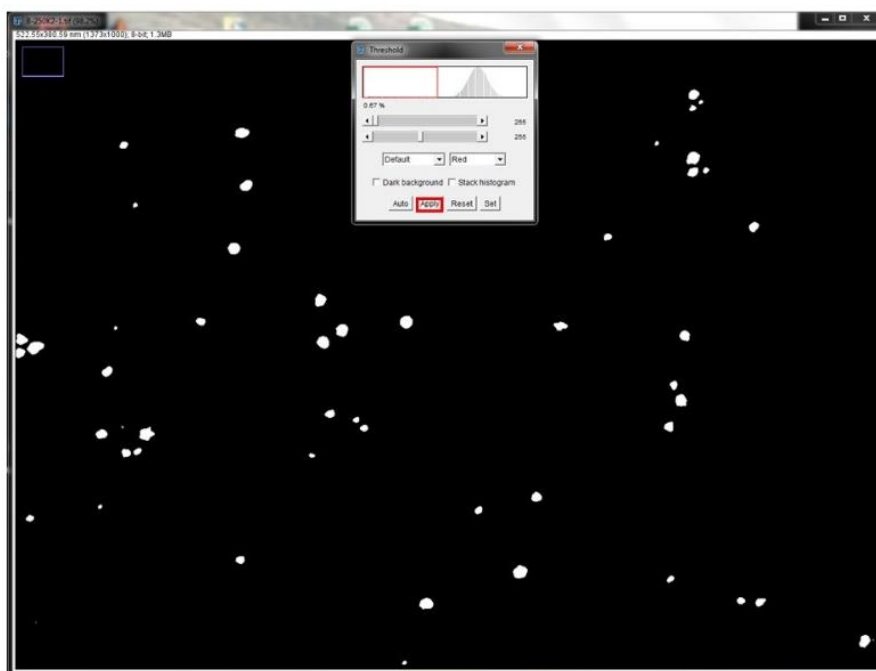


Figure 3.42. Fiji – Image J: Threshold adjustment

If linked particles were present on the image, the watershed function could be used to separate them (cf. Figure 3.43).

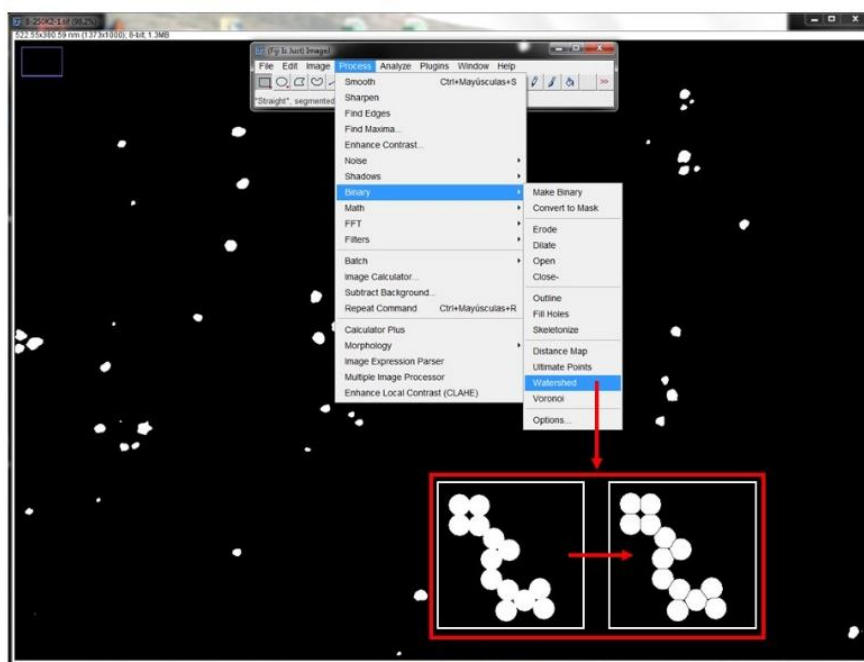
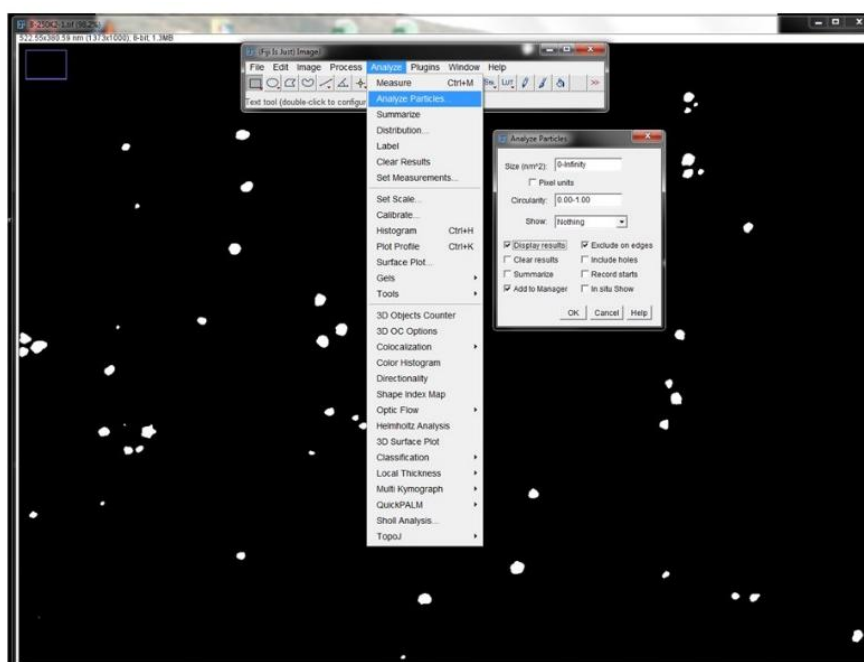
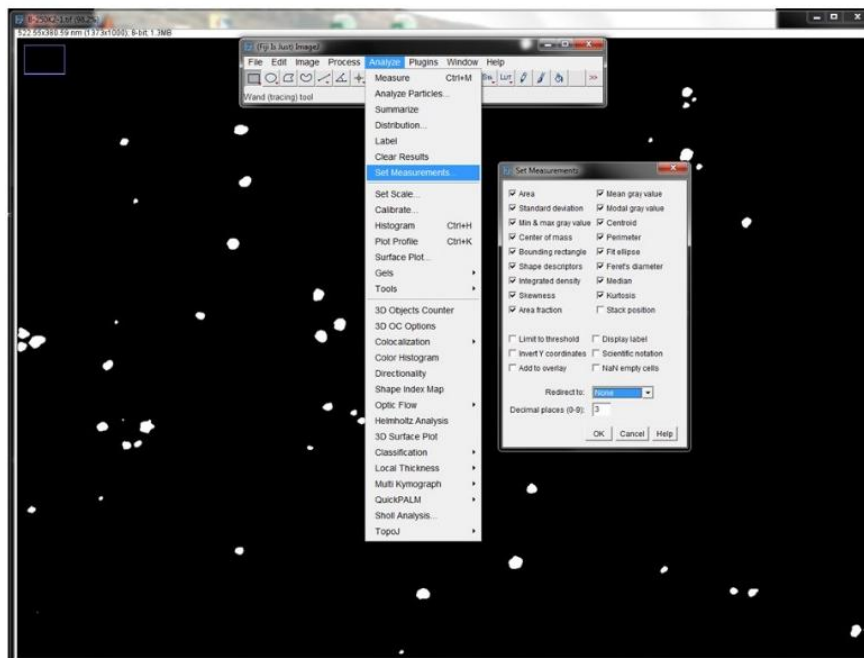


Figure 3.43. Fiji – Image J: Watershed tool

Finally the measurements setting were chosen and the particles were analyzed. Usually the option “exclude on edges” was selected to avoid the counting of cut particles.



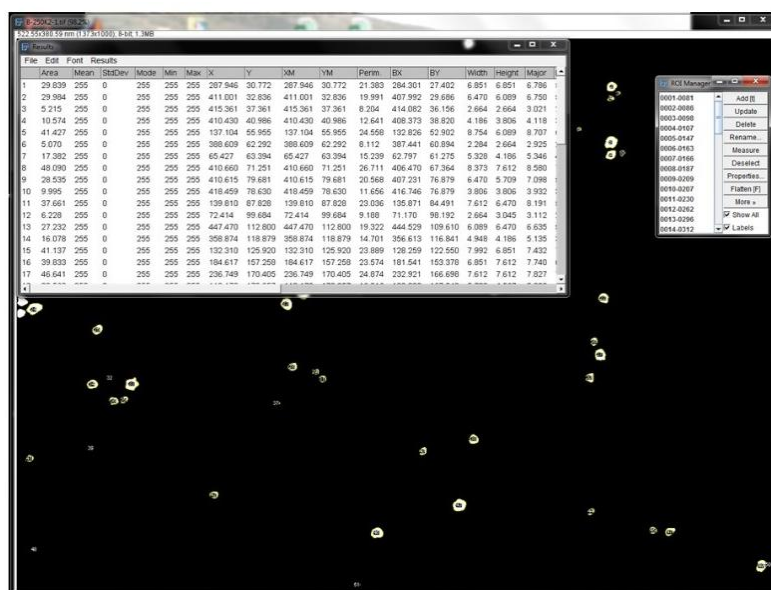


Figure 3.44. Fiji – Image J: Measurements setting and analysis of the particles

To facilitate and speed up the image processing, macros were used to perform automatically the steps 1, 2 and 3.

The results were processed with a Matlab® routine. This routine enabled the determination of the following parameters:

- The number of NPs measured in the sample
- The number of spherical NPs according to the defined criteria ( $AR < 1.3$ )
- The median and mean diameter of the spherical NPs
- The standard deviation calculated from the set of spherical NPs

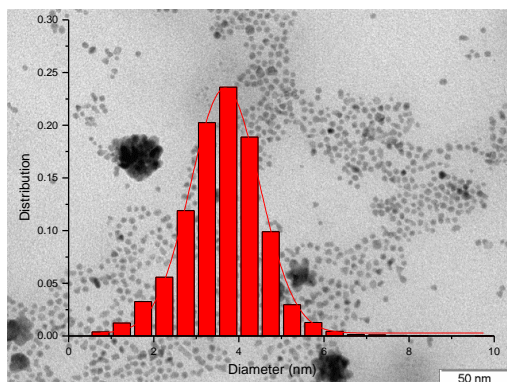
One or more Gaussian functions could be adjusted to the set of data and the following parameters were deduced:

- The mean particle size(s) of the fitted Gaussian function(s)  $y_i$
- The standard deviation(s) of the population(s)  $s_i$
- The determination coefficient  $R^2$  that provides a measure of the goodness of fit of a model to a set of observations.
- The fraction of agglomerated NPs according to the defined criteria. An agglomerates was assumed to be non-spherical and/or to have a very large equivalent diameter (above the  $y + 3s$  of the Gaussian distribution).

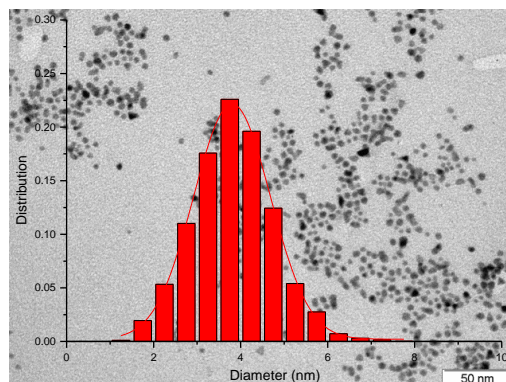


### 3.6.2. Appendix 2: TEM micrographs and size distribution histograms of the ten batches of the reference recipe Pd-PAM 6 NPs

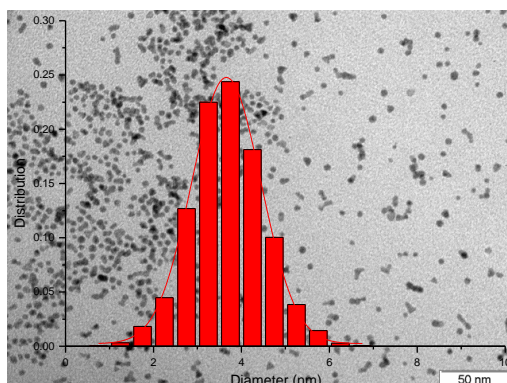
a. Pd-PAM 6c,  $3.7 \pm 1.0$  nm (26%)



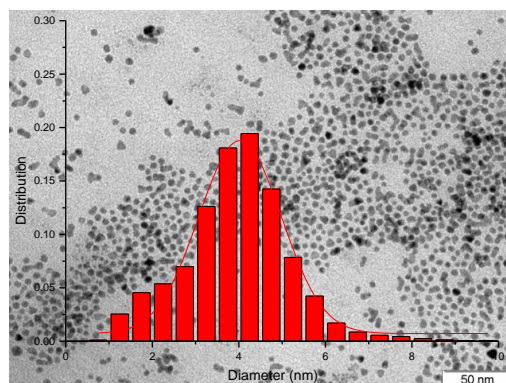
b. Pd-PAM 6d,  $3.8 \pm 1.0$  nm (27%)



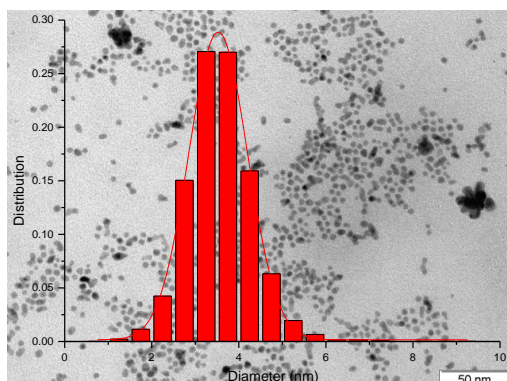
c. Pd-PAM 6e,  $3.7 \pm 0.9$  nm (25%)



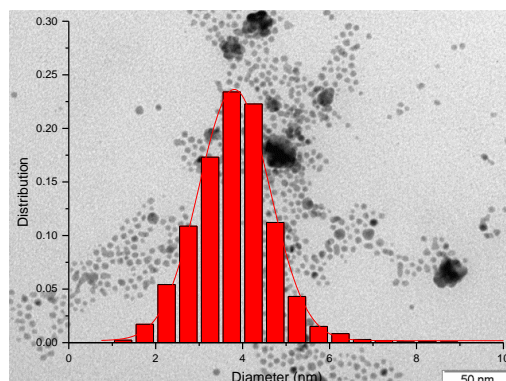
d. Pd-PAM 6f,  $4.0 \pm 1.1$  nm (28%)



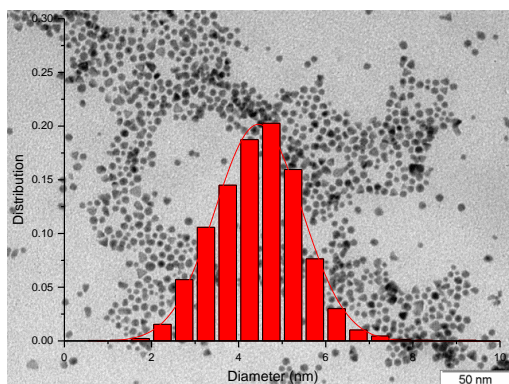
e. Pd-PAM 6g,  $3.5 \pm 0.8$  nm (22%)



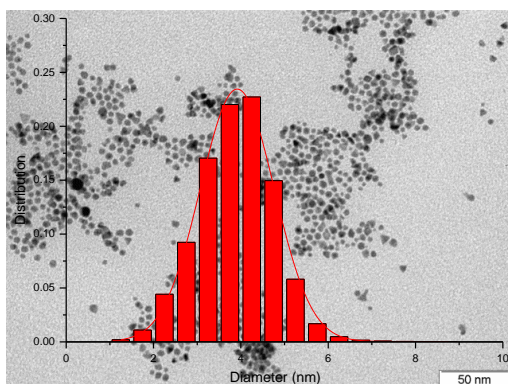
f. Pd-PAM 6h,  $3.8 \pm 1.0$  nm (25%)



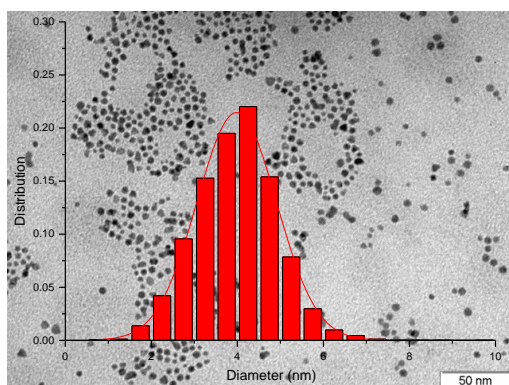
g. **Pd-PAM 6i**,  $4.5 \pm 1.2$  nm (26%)



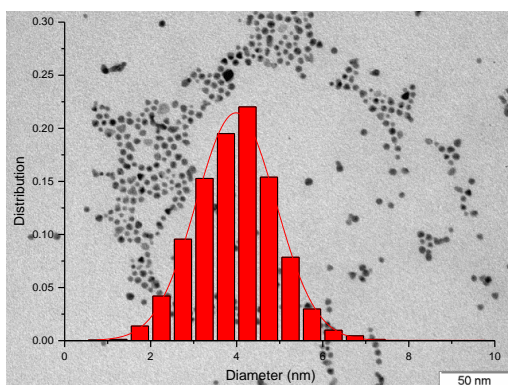
h. **Pd-PAM 6j**,  $3.9 \pm 1.0$  nm (26%)



i. **Pd-PAM 6k**,  $4.0 \pm 1.0$  nm (26%)



j. **Pd-PAM 6l**,  $4.0 \pm 1.1$  nm (27%)



### 3.6.3. Appendix 3: Kolmogorov Smirnov tables

Critical values,  $d_{\alpha;n}$ , of the maximum absolute difference between sample  $F_n(x)$  and population  $F(x)$  cumulative distribution.

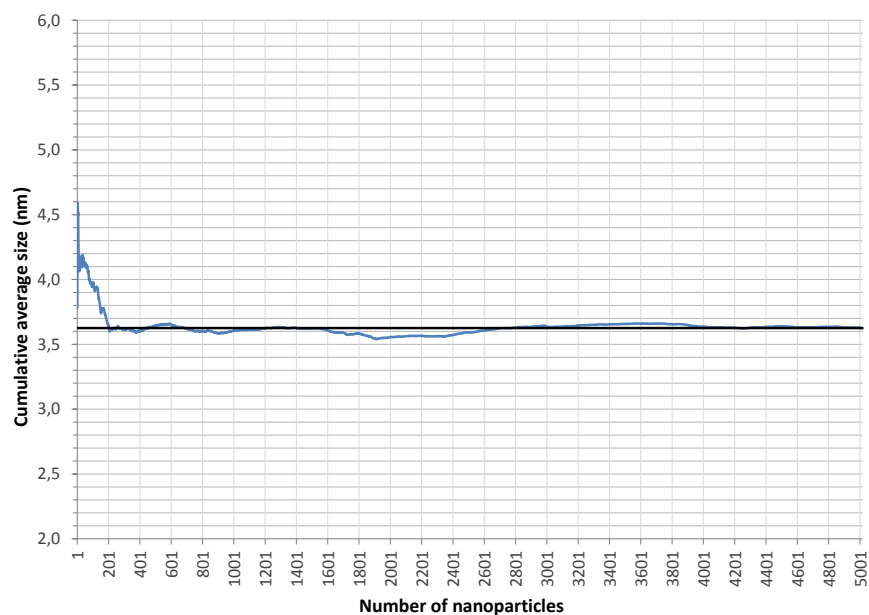
Number of trials, $n$	Level of significance, $\alpha$			
	0.10	0.05	0.02	0.01
1	0.95000	0.97500	0.99000	0.99500
2	0.77639	0.84189	0.90000	0.92929
3	0.63604	0.70760	0.78456	0.82900
4	0.56522	0.62394	0.68887	0.73424
5	0.50945	0.56328	0.62718	0.66853
6	0.46799	0.51926	0.57741	0.61661
7	0.43607	0.48342	0.53844	0.57581
8	0.40962	0.45427	0.50654	0.54179
9	0.38746	0.43001	0.47960	0.51332
10	0.36866	0.40925	0.45662	0.48893
11	0.35242	0.39122	0.43670	0.46770
12	0.33815	0.37543	0.41918	0.44905
13	0.32549	0.36143	0.40362	0.43247
14	0.31417	0.34890	0.38970	0.41762
15	0.30397	0.33760	0.37713	0.40420
16	0.29472	0.32733	0.36571	0.39201
17	0.28627	0.31796	0.35528	0.38086
18	0.27851	0.30936	0.34569	0.37062
19	0.27136	0.30143	0.33685	0.36117
20	0.26473	0.29408	0.32866	0.35241
21	0.25858	0.28724	0.32104	0.34427
22	0.25283	0.28087	0.31394	0.33666
23	0.24746	0.27490	0.30728	0.32954
24	0.24242	0.26931	0.30104	0.32286

*Practical Reliability Engineering*, Fifth Edition. Patrick D. T. O'Connor and Andre Kleyner.  
 © 2012 John Wiley & Sons, Ltd. Published 2012 by John Wiley & Sons, Ltd.

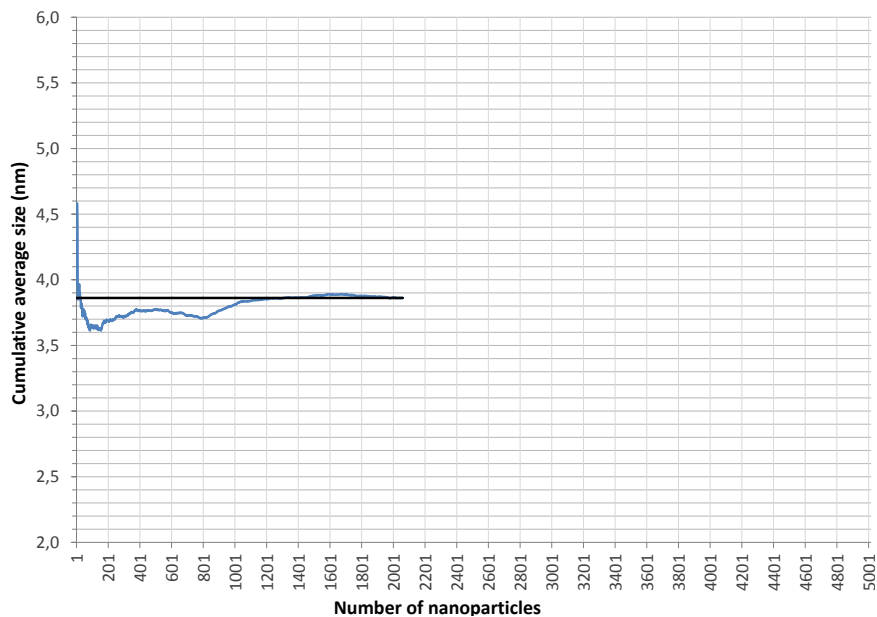


### 3.6.4. Appendix 4: Cumulative moving averages of the NPs: Pd-PAM 6c to Pd-PAM 6l

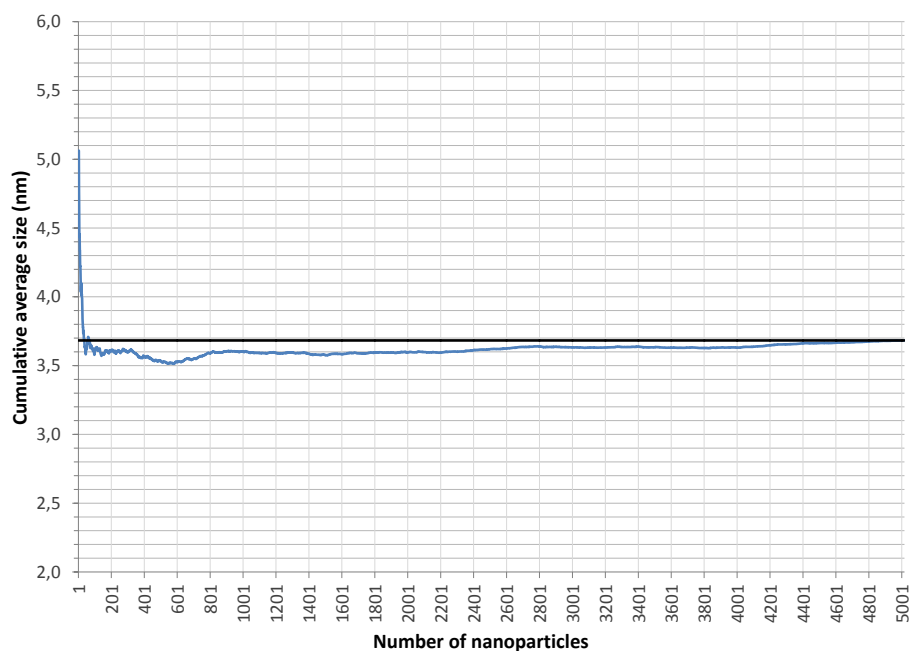
**Pd-PAM 6c**



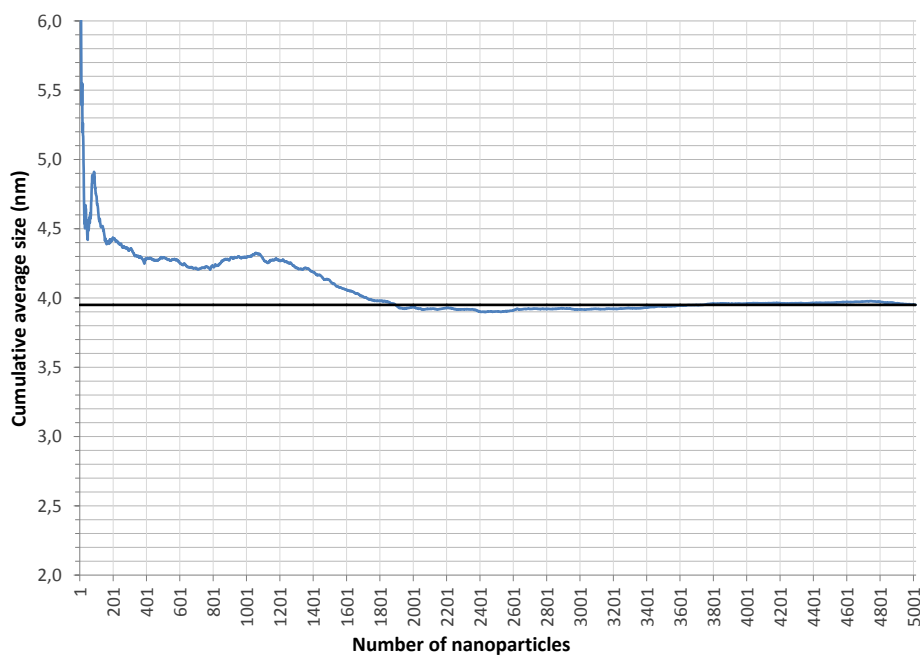
**Pd-PAM 6d**



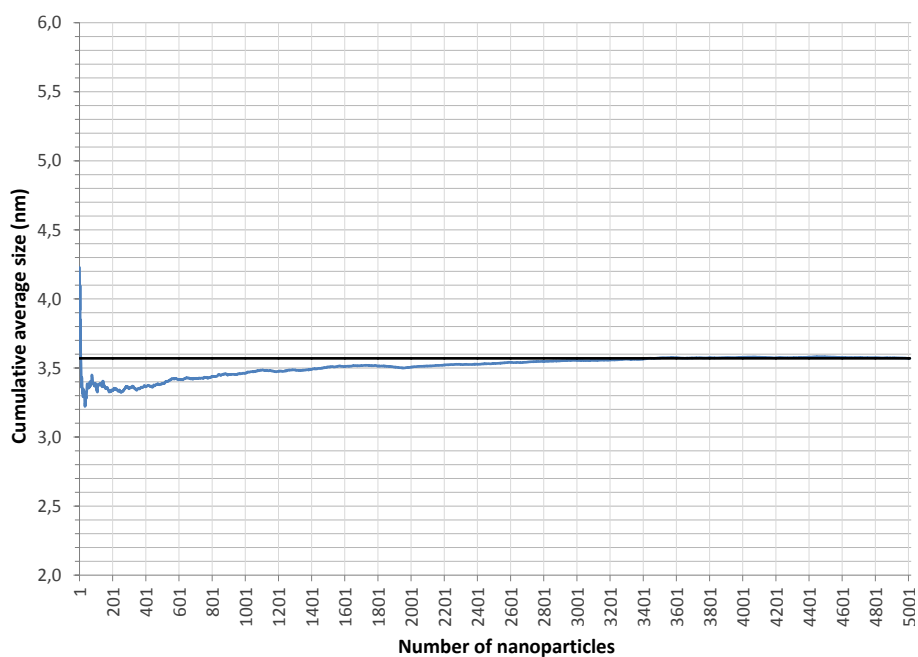
### Pd-PAM 6e



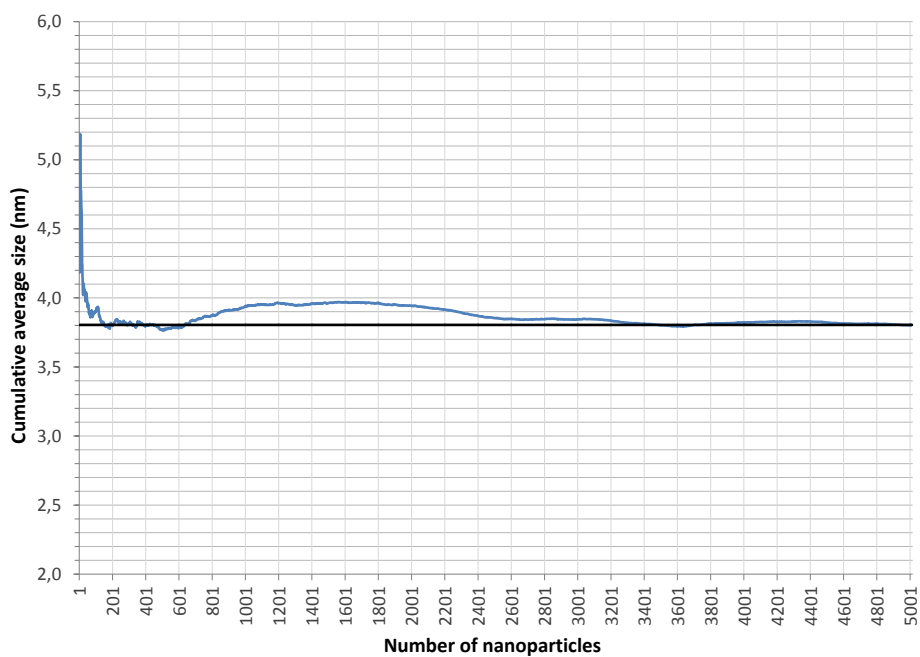
### Pd-PAM 6f



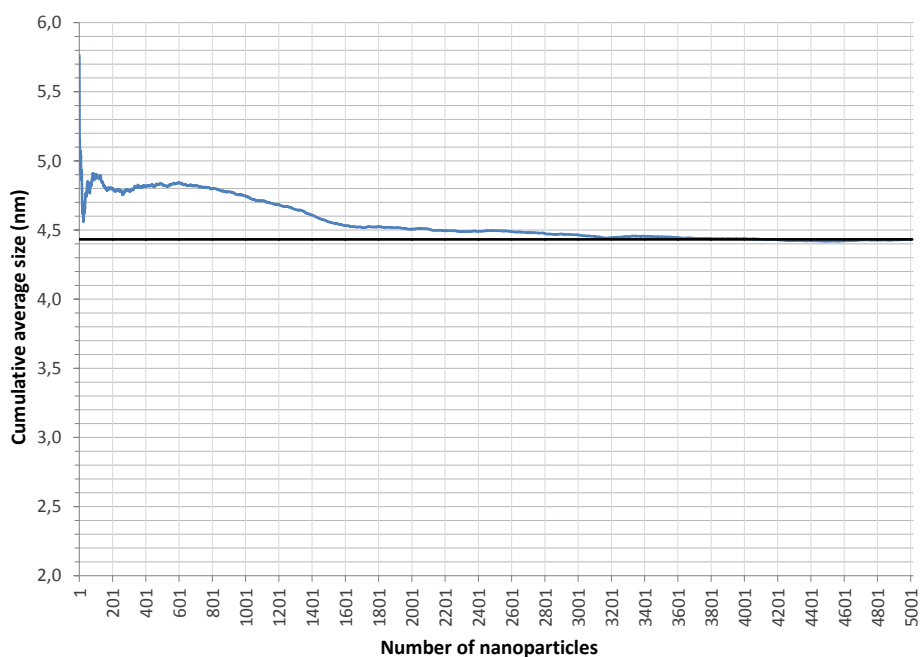
### Pd-PAM 6g



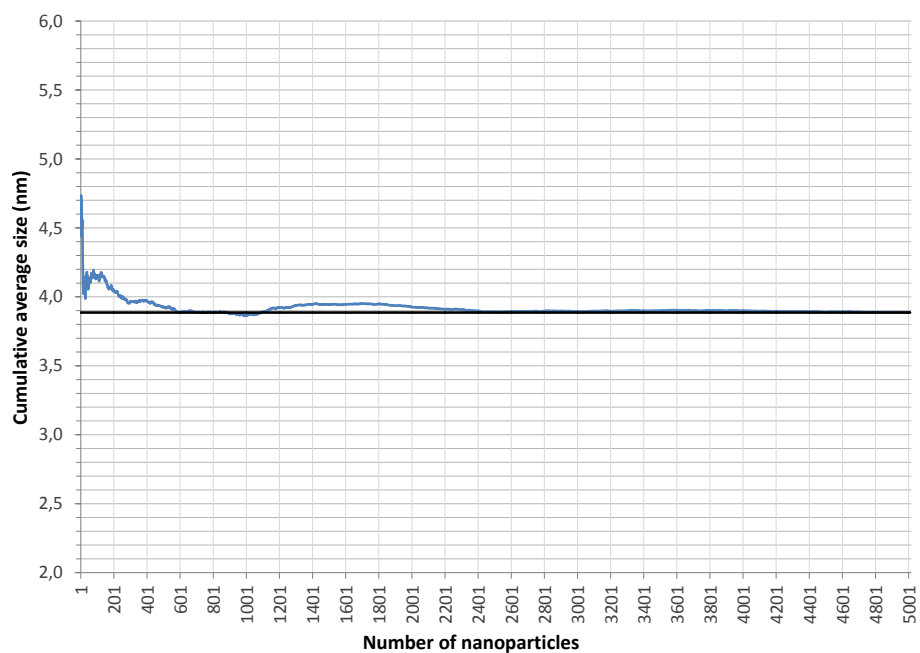
### Pd-PAM 6h



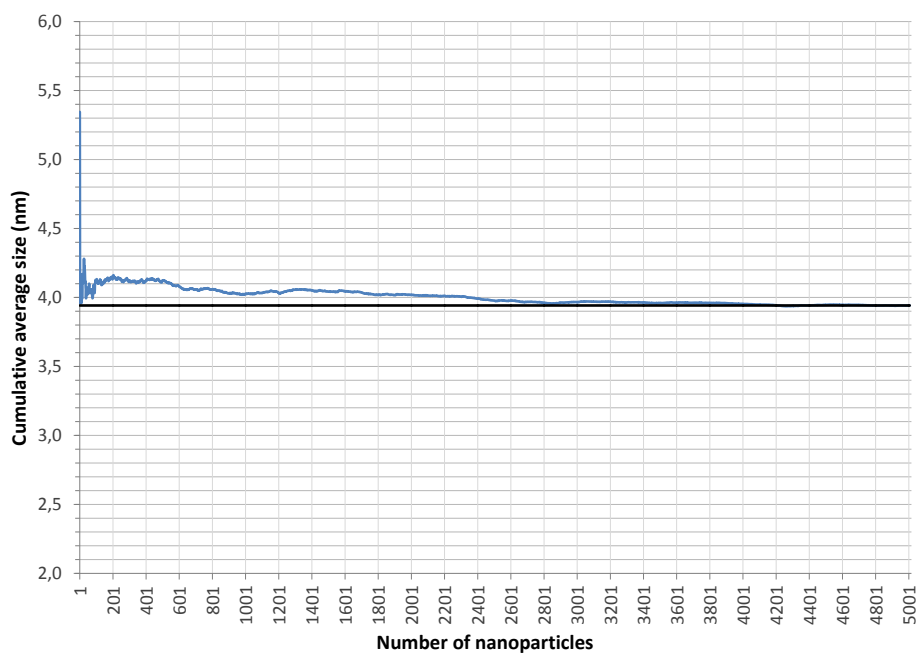
### Pd-PAM 6i



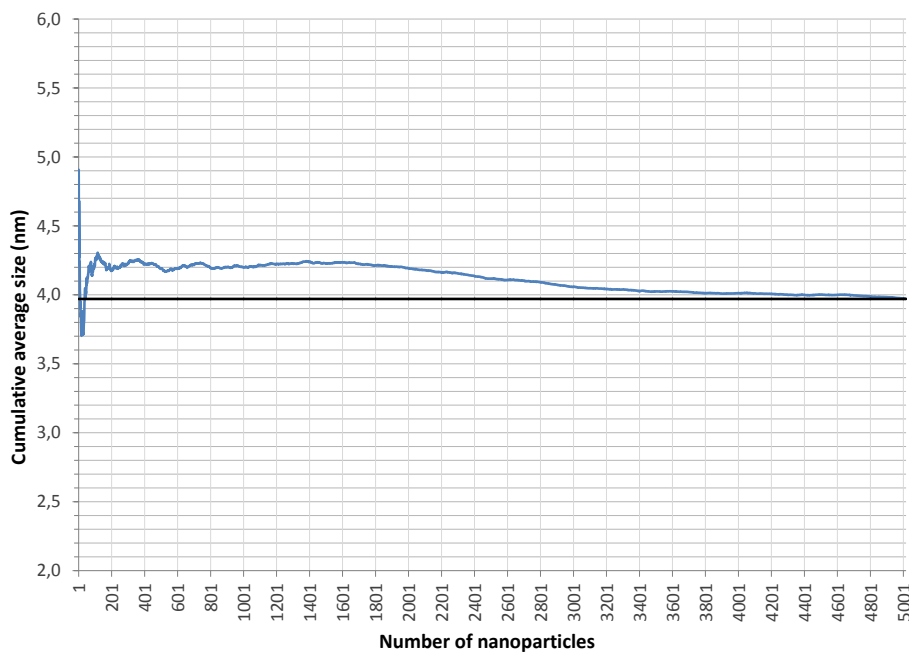
### Pd-PAM 6j



### Pd-PAM 6k



### Pd-PAM 6I



### 3.7. References

- (1) Wu, L.; Lian, H.; Willis, J. J.; Goodman, E. D.; McKay, I. S.; Qin, J.; Tassone, C. J.; Cargnello, M. *Chem. Mater.* **2018**, *30*, 1127.
- (2) Somorjai, G. A.; Park, J. Y. *Angew. Chem. Int. Ed.* **2008**, *47*, 9212.
- (3) Na, K.; Zhang, Q.; Somorjai, G. A. *J. Cluster Sci.* **2014**, *25*, 83.
- (4) Duff, D. G.; Edwards, P. P.; Johnson, B. F. G. *J. Phys. Chem.* **1995**, *99*, 15934.
- (5) Agostini, G.; Groppo, E.; Piovano, A.; Pellegrini, R.; Leofanti, G.; Lamberti, C. *Langmuir* **2010**, *26*, 11204.
- (6) Long, N. V.; Hayakawa, T.; Matsubara, T.; Chien, N. D.; Ohtaki, M.; Nogami, M. *J. Exp. Nanosci.* **2012**, *7*, 426.
- (7) Kim, S. C.; Jung, S. C.; Park, Y.-K.; Ahn, H. G.; Seo, S. G. *J. Nanosci. Nanotechnol.* **2013**, *13*, 1961.
- (8) Chen, A.; Ostrom, C. *Chem. Rev.* **2015**, *115*, 11999.
- (9) Papp, S.; Patakfalvi, R.; Dékany, I. *Nastajanje i stabilnost nanočestica plemenitih kovina.* **2007**, *80*, 493.
- (10) Semagina, N.; Renken, A.; Laub, D.; Kiwi-Minsker, L. *J. Catal.* **2007**, *246*, 308.
- (11) Heshmatpour, F.; Abazari, R.; Balalaie, S. *Tetrahedron* **2012**, *68*, 3001.
- (12) Kosydar, R.; Góral, M.; Gurgul, J.; Drelinkiewicz, A. *Catal. Commun.* **2012**, *22*, 58.
- (13) Hanaoka, T.; Arakawa, H.; Matsuzaki, T.; Sugi, Y.; Kanno, K.; Abe, Y. *Catal. Today* **2000**, *58*, 271.
- (14) Martínez, A.; Prieto, G. *J. Catal.* **2007**, *245*, 470.
- (15) Noh, J.-H.; Meijboom, R. *J. Colloid Interface Sci.* **2014**, *415*, 57.
- (16) Perez-Coronado, A. M.; Calvo, L.; Alonso-Morales, N.; Heras, F.; Rodriguez, J. J.; Gilarranz, M. A. *Colloids Surf A Physicochem Eng Asp* **2016**, *497*, 28.
- (17) Solovov, R. D.; Ershov, B. G. *Colloid J.* **2014**, *76*, 595.
- (18) Jung, S. C.; Park, Y.-K.; Jung, H.-Y.; Kim, S. C. *J. Nanosci. Nanotechnol.* **2017**, *17*, 2833.
- (19) Lim, B.; Xiong, Y.; Xia, Y. *Angew. Chem. Int. Ed.* **2007**, *46*, 9279.
- (20) Delgado, J. A.; Benkirane, O.; Claver, C.; Curulla-Ferre, D.; Godard, C. *Dalton Trans.* **2017**, *46*, 12381.
- (21) Tressaud, A.; Khairoun, S.; Touhara, H.; Watanabe, N. Z. *Anorg. Allg. Chem.* **1986**, *540*, 291.
- (22) Van Hardeveld, R.; Hartog, F. *Surf. Sci.* **1969**, *15*, 189.
- (23) Matyi, R. J.; Schwartz, L. H.; Butt, J. B. *Catalysis Reviews* **1987**, *29*, 41.
- (24) Witte, P. T.; Boland, S.; Kirby, F.; van Maanen, R.; Bleeker, B. F.; de Winter, D. A. M.; Post, J. A.; Geus, J. W.; Berben, P. H. *ChemCatChem* **2013**, *5*, 582.
- (25) Shimmin, R. G.; Schoch, A. B.; Braun, P. V. *Langmuir* **2004**, *20*, 5613.
- (26) Hu, J.; Zhou, Z.; Zhang, R.; Li, L.; Cheng, Z. *J. Mol. Catal. A: Chem.* **2014**, *381*, 61.



# Chapter 4

## Synthesis and characterization of supported Pd-polyacrylamide NPs





## 4.1. Introduction

Over the past decades, the interest in metallic NPs increased since they revealed high potential for a wide variety of applications in fields such as biomedicine, optical, electronics and catalysis among others.<sup>1,2</sup>

The use of colloidal NPs in catalysis showed some disadvantages such as the loss of activity due to agglomeration issues or difficulties to recycle and reuse the catalyst.<sup>3,4</sup>

Therefore, the use of supported catalysts was preferred to ensure sustainable processes. Moreover, the support has been widely used to tune the catalyst properties.<sup>5</sup> Indeed the performances of a supported catalyst are largely influenced by the properties of the support and the metal/support interactions. The preparation methods can also affect the resulting catalyst.<sup>6</sup>

Several approaches were reported for the immobilization of metal NPs.<sup>2,7</sup> Among them, the one pot procedure was attractive for an experimental point of view. However, it has been observed that the control over the NPs size and dispersion depend on a wide variety of synthetic parameters and can become a difficult task.

To overcome this issue, the immobilization in two steps was investigated. This second methodology has the advantage to allow the fine modulation of the NPs size and their detailed characterization before immobilization on solid support.<sup>8</sup>

The study of the effect of the synthetic parameters and the immobilization methodology (one pot or two steps) on the NPs size and dispersion on the support was contemplated in this chapter.

Some examples of application of these methodologies are described below.

Godard and co-workers reported a simple one pot procedure to prepare small and well-defined Ni NPs stabilized by N-heterocyclic carbenes (NHC) supported on carbon nanotubes.<sup>9</sup> An increase in NPs size was observed in comparison with the corresponding colloidal system for Ni NPs supported with 0.2 and 0.5 equivalents of NHC-stabilizer. In contrast, supported Ni NPs with 1 equivalent of NHC per Ni

remained similar in terms of size but revealed a wider distribution in comparison with the colloidal.

Furthermore, Claver and co-workers proposed a new approach for the preparation of Rh and Pt NPs supported on a phosphine-functionalized silica by one pot.<sup>4</sup> Using this strategy, smaller supported Rh/P-SiO<sub>2</sub> NPs were obtained in comparison to the non-supported analogues. In the case of Pt/P-SiO<sub>2</sub> NPs, the NPs size remained similar for supported and colloidal system. In this study, they demonstrated that the surface modification of the silica support with phosphine improved the stabilization of both Rh and Pt NPs.

Finally, Montiel *et al.* reported the one pot synthesis of Pd NPs involving the decomposition of Pd<sub>2</sub>(dba)<sub>3</sub> (dba=dibenzylideneacetone) under hydrogen in the presence of tricyclohexylphosphine and multiwalled carbon nanotubes.<sup>10</sup> The analysis of the resulting material evidenced the homogeneous deposition of small NPs with narrow size distribution of *ca.* 2.4 nm.

In contrast, Delgado *et al.* reported the two-step immobilization of cobalt NPs on TiO<sub>2</sub> support.<sup>8</sup> First the colloidal suspension was prepared by chemical reduction of cobalt chloride using sodium borohydride in presence of water soluble polymeric stabilizers. These NPs were then isolated by centrifugation and re-dispersed in hexane solvent before being added dropwise over a slurry of TiO<sub>2</sub> to induce the immobilization. The authors confirmed that the size remained unchanged after the immobilization process and a high dispersion of the NPs on the support. They concluded about the advantages of the two steps: fine modulation of the NPs possible as well as easy immobilization onto the solid support.

Marcia Rossi and co-workers proposed the use of ligand-modified supports to tune the activity and selectivity of Pd nanocatalysts.<sup>11</sup> They prepared the catalysts by addition of a ligand-modified silica support to an aqueous solution containing previously synthesized Pd NPs stabilized by poly(vinyl alcohol) (PVA). The size and size distribution of the PVA-stabilized Pd NPs were determined by TEM, before the

immobilization process and no significant change in size were reported after their immobilization.

Finally Cheng and co-workers reported a two-step procedure that consisted in the synthesis of colloidal Pd NPs by a reduction-by-solvent method followed by impregnation onto  $\alpha$ -Al<sub>2</sub>O<sub>3</sub>.<sup>12</sup> In the first step, Pd<sup>2+</sup> was reduced by NaBH<sub>4</sub> in a C<sub>2</sub>H<sub>5</sub>OH/H<sub>2</sub>O solvent system in presence of polyvinylpyrrolidone (PVP) as stabilizer. The amount of NaBH<sub>4</sub>, C<sub>2</sub>H<sub>5</sub>OH and PVP showed effects on the Pd NPs sizes. Then the impregnation on  $\alpha$ -Al<sub>2</sub>O<sub>3</sub> consisted in the mixture at room temperature between a slurry of support and the Pd NPs. The solid was then filtered, washed, dried and finally calcined at 450°C to enhance the interaction between the metal and the support. The supported NPs showed larger sizes than their corresponding colloidal suspensions. This grow was attributed to the calcination process.

In this chapter, the colloidal Pd-PAM NPs synthesized in chapter 3 were supported on different materials. The objective was to deliver recipe for the formation of well-defined supported Pd nanocatalysts via colloidal approach.

Both one pot and two-step methodologies were tested and the effect of the immobilization process, the parameter of synthesis and the nature of the support on the NPs size and dispersion were studied.

## 4.2. Experimental Section

### 4.2.1. Material for supported NPs synthesis

Immobilization of Pd NPs was performed by two different procedures: one pot or two-step syntheses.

The materials used for the one pot syntheses were the same than that used for colloidal NPs synthesis presented in the chapter 3.

The two-step immobilizations of Pd NPs were performed in beaker vessels. The magnetic stirring set-up consisted in a stirrer-hot plate IKA RCT BASIC<sup>TM</sup>. The controlled addition of colloidal NPs suspensions was performed manually with a 25 mL

burette and a chronometer. Ultrasounds treatments were applied using an Elmasonic S unit.

The NPs were supported on the following powder form supports: activated carbon ( $\leq 40$  nm from Sigma Aldrich), alpha-aluminium oxide (250-450 nm from Alfa Aesar) and titanium oxide (21 nm from Sigma Aldrich).

## 4.2.2. Characterization

### 4.2.2.1. Transmission Electron Microscopy (TEM)

In this chapter, all the synthesized Pd NPs supported on different supports were routinely characterized by conventional TEM using bright field image modality.

The grids were prepared from the fresh aqueous suspensions of Pd NPs without any pretreatment since it has been noticed that the NPs were not easily observable after the isolation step. The grids (Cu-formvar) were prepared by addition of three drops of a dilution of 0.1 mL of the fresh solution in 0.9 mL of milli-Q water and dried under air prior to analysis.

The measurements were performed at the “Servei de Recursos Científics i Tècnics” of the Rovira i Virgili University (Tarragona, Spain) with a JEOL 1011 Transmission Electron Microscope operating at 100 kV. The images obtained were monochromatic with a 0.2 nm of resolution. The increases oscillated between 200x and 1000000x. Images were systematically taken at a nominal magnification between 100000x and 400000x on three different points of the grid as minimum. To record images, iTEM® imaging platform from Olympus was used.

The NPs presented in this chapter were manually measured with Image J software. A minimum of 400 measurements was systematically carried out. The data were processed with Origin Lab® software. A LogNormal function was adjusted since it fitted better to the set of data than a Gaussian function. The estimation of the average diameter and standard deviation of each sample was given from the arithmetic mean of the fitted curve.

#### **4.2.2.2. X-Ray Diffraction (XRD)**

In this chapter, the well-defined supported NPs were characterized by XRD to obtain information on their crystalline structure. The measurements were performed in the same equipment and with the same procedure than that presented in chapter 3.

#### **4.2.2.3. X-ray Photoelectron Spectroscopy (XPS)**

The well-defined supported NPs with 2 wt% of Pd content presented in this chapter were characterized by XPS to obtain information about their surface properties. The measurements were performed in the same equipment and with the same procedure than that presented in chapter 3.

#### **4.2.2.4. Thermogravimetric analysis (TGA)**

The well-defined supported NPs obtained by the scale up syntheses were analyzed by TGA. The measurements were performed using the same equipment than that presented in chapter 3.

#### **4.2.2.5. Environmental Scanning Electron Microscopy (ESEM)**

In this chapter, ESEM characterization was performed on the supported nanocatalysts to observe the NPs dispersion on the support. The dried samples of catalyst powder were deposited on a microscope stub on which, previously, a ultrathin layer of electrically conductive material was deposited.

The samples were at the “Servei de Recursos Científics i Tècnics” of the Rovira i Virgili University (Tarragona, Spain) with a FEI Quanta 600 ESEM equipped with an EDX detector from Oxford Instruments operating at an accelerating voltage of 20kV and 10 mm of working distance.

The backscattering detector was used to allow the visualization of metallic NPs on the different catalytic carriers and elemental analysis of the metal was determined by EDX. using INCA® software.

#### **4.2.2.6. Inductively Coupled Plasma (ICP)**

In this chapter, synthesized catalysts were characterized by ICP to determine their Pd content. The analyses were performed at Total Research and Technology Feluy (Seneffe, Belgium) in the “Département d’Analyses Elementaires” with a Spectro Arcos ICP-AES. The samples were prepared using an Ultrawave digestion system which consisted in heating the samples in a pressurized PTFE reactor (40 bar of argon).

#### **4.2.2.7. N<sub>2</sub> Physisorption**

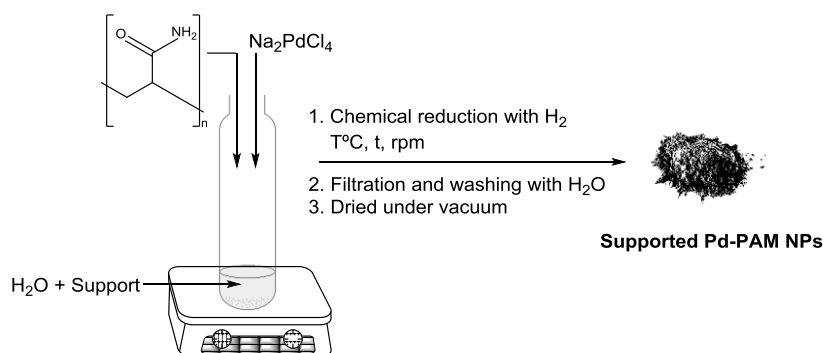
N<sub>2</sub> physisorption measurements were performed at Total Research and Technology Feluy (Seneffe, Belgium) in the Synthesis of Catalyst and Characterization (SCC) service with an ASAP 2460 from micromeritics. The total surface area was calculated using the BET model (Brunauer, Emmett and Teller).<sup>13</sup> The total pore volume was determined using the single point method at  $P/P_0 = 0.99$ , while pore size distribution were obtained from the analysis of the desorption branch of the N<sub>2</sub> isotherm using the BJH method (Barrett Joyner and Halenda).<sup>14</sup>

### **4.2.3. Immobilization of Pd-PAM NPs on various supports**

The immobilization of the Pd-PAM NPs was performed using different methodologies (one pot and two steps) and various supports (activated carbon, aluminium oxide and titanium oxide). The experimental procedures are described in this section.

#### **4.2.3.1. One pot synthesis**

The one pot synthesis consists in the formation and immobilization of the NPs at once. Therefore, the recipe used for the preparation of supported Pd NPs via one pot was the same than that of colloidal NPs presented in chapter 3 except that the corresponding amount of support was introduced at the beginning of the reaction as the same time that all the other reagents as shown in Scheme 4.1. The immobilized NPs were filtered off and washed with water. Acetone was passed through the filter to remove the excess of water and fasten the drying step. This last step was carried out under vacuum at room temperature.



Scheme 4.1. General recipe for the preparation of supported Pd-PAM NPs via one pot

#### 4.2.3.2. Two-step synthesis

For the immobilization of Pd-PAM NPs on solid supports, the Point of Zero Charge (PZC) of these supports and the  $\zeta$  potential of the colloidal NPs were determined.

The surface chemistry of a material is determined by the acidic or basic character of its surface; therefore the pH at which the surface charge of the material is zero in an aqueous media, *i.e.* the point of zero charge, constitutes an important information.

The  $\zeta$  potential corresponds to the electric potential in the interfacial double layer of the particle. Knowing the intrinsic charge of the colloidal NPs and the way to modify the surface charge of the supports, the interactions between both materials can be optimized. The experimental procedures that were used for their determination are given as follows.

#### Determination of the Point of Zero Charge of the supports

Different methodologies were reported for the determination of the PZC of a material such as potentiometric titration, electrokinetic and electroacoustic mobility, techniques including mass titration, ion adsorption and scanning force microscopy.<sup>15</sup>

The acid-base potentiometric (PT) and mass titration (MT) methods were reported as suitable methods. Stanley and co-workers studied these methodologies, they concluded that similar results were obtained for both techniques and that they were valid for oxides and activated carbon materials.

In the presented study, the mass titration technique was preferred since the procedure was simple and only required a pH meter. The studied materials were



mixed with a KCl background electrolyte (0.01 M) with different weight percentages. The solutions were bubbled with nitrogen for three minutes to expel the dissolved CO<sub>2</sub>. The solutions were stirred overnight at room temperature (*ca.* 16 hours, time for which pH equilibrium is reached in all the cases). The pH of each solution was measured and the value of the PZC was determined on a curve of pH vs. percentage mass-to-volume ratio of the materials.

### **Determination of the $\zeta$ potential of colloidal Pd-HHDMA NPs**

The  $\zeta$  potential corresponds to the potential difference between the dispersion medium and the stationary layer of fluid attached to the dispersed particle as shown in Figure 4.1. It was determined using a Malvern Nano ZS (Zeta Sizer). The charge or  $\zeta$  potential of particles is determined by measuring their velocity while they are moving due to electrophoresis. Particles that have a  $\zeta$  potential migrate towards an electrode if a field is applied. The speed they move is proportional to the field strength and their  $\zeta$  potential. Knowing the field applied, the speed of the movement is measured using a laser Doppler electrophoresis and then established theories are applied to calculate the  $\zeta$  potential. The whole measurement procedure is automated.<sup>16</sup>

The  $\zeta$  potential provides important information for the immobilization of the NPs on different supports and also gives insights about the stability of the suspension. Indeed, the  $\zeta$  potential arises from the surface charge and the concentration and types of ions in the solution. Since NPs of similar charge repel each other, those with high charges resist flocculation and aggregation for longer periods making such samples more stable. Thus, the stability could be modified by altering the pH or the ionic concentration for example.<sup>16</sup>

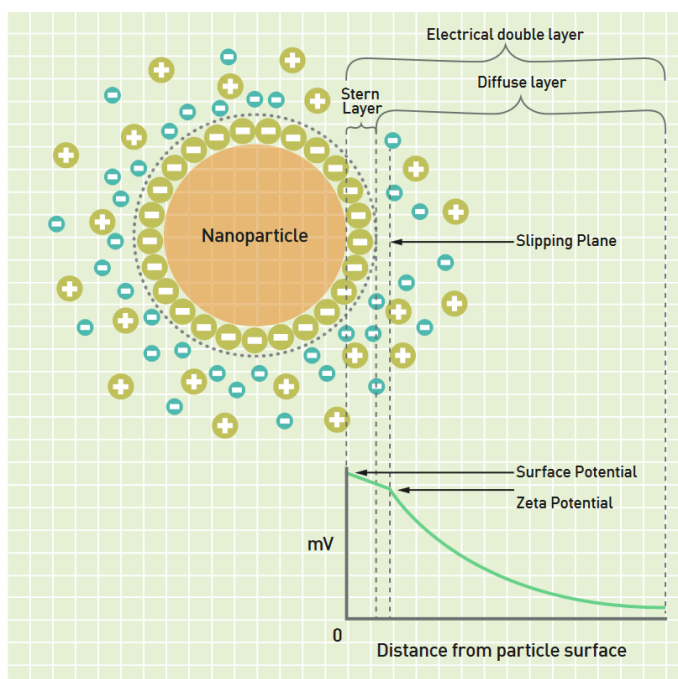


Figure 4.1.  $\zeta$  potential – Diagram showing the ionic concentration and potential difference as a function of distance from the charged surface of a particle suspended in a dispersion medium<sup>16</sup>

### Immobilization via pH modification

An attempt of immobilization of Pd-PAM NPs on AC via pH modification was performed following a similar methodology than that reported by P. Witte in a BASF patent.<sup>17</sup> The proportions were reduced by *ca.* 76 regarding the reported recipe and the volume of NPs suspension added to the support was calculated to obtain 2w% of Pd content.

A slurry of 0.98 g of AC in 9.8 mL of milli-Q water was stirred for an hour at room temperature. Then, 20 mL of a NPs colloidal suspension was added in 25 mL/min. The mixture was stirred for 45 minutes. Then, the pH of the mixture was adjusted from 2 to 9 by addition of 10% NaOH solution. The mixture was stirred during additional 30 minutes while the pH was maintained between 9.0 and 9.5. The solid supported catalyst was filtered and washed with water before their drying under vacuum.

### **Immobilization via simple mixing methodology**

Another two-step immobilization methodology was implemented consisting in a simple mixing between colloidal NPs and support.

After their synthesis, the colloidal NPs were treated with ultrasound during 30 minutes to remove small agglomerates. In parallel, a slurry of solid support in water was stirred for 30 minutes at room temperature. It consisted in respectively 661 mg of support in 8 mL of milli-Q water and 195 mg of support in 2.5 mL of milli-Q water for 0.6 wt% and 2 wt% of Pd content. Then, 4 mL of the colloidal suspension (containing 9.4 mM of Pd) was added to the support in 12 mL/min. The mixture was treated with ultrasound for 1 hour during which short stirring cycles were performed every 15 minutes.

The obtained supported catalyst was filtered and washed with a large quantity of water (*ca.* 400 mL) and acetone (*ca.* 100 mL) and dried under vacuum.

## **4.3. Results and Discussion**

In the previous chapter, a reference recipe for the formation of well-defined colloidal Pd-PAM NPs was delivered (called **Pd-PAM 6**). The next stage was the study of protocols for the immobilization of these NPs on different supports. Two methodologies were tested: the one pot and the two-step synthesis. The effects of some synthetic parameters on the formation of supported Pd-PAM NPs via one pot approach were studied. Then, two-step methodologies were tested and are presented in this chapter. Finally the effects of the immobilization process, the Pd content and the nature of the support on the NPs dispersion on the support are detailed.

### **4.3.1. Supported Pd-PAM NPs synthesized via one pot approach**

The one pot synthesis involves the formation and immobilization of NPs in the same step. Using this methodology, the effect of some parameters on the formation of supported Pd-PAM NPs was studied with one-factor-at-a-time (OFAT) experiments. The main objective was to deliver recipes of well-defined heterogeneous catalysts prepared via colloidal method. This study was also useful to understand how the

studied parameters affect the NPs size, size distribution and immobilization on the support. All the catalysts presented in this section were prepared following the general recipe detailed in 4.2.3.1.

#### 4.3.1.1. Pd-PAM NPs supported on activated carbon (AC)

The first attempt of immobilization of Pd-PAM NPs on activated carbon (AC) was performed following the conditions of the colloidal reference recipe (see **Pd-PAM 6** reference recipe from the OFAT study presented in chapter 3 section 3.4.3.).

From this point, variations of the synthesis temperature, PAM-to-Pd molar ratio, Pd concentration and Pd content were performed. Table 4.1 summarizes the variations of these parameters and the resulting NPs size and size distribution obtained in each case. In the following subsections, each parameter is discussed in detail.

Table 4.1. Variation of experimental parameters for the synthesis of supported Pd-PAM NPs on activated carbon via one pot

Entry	NPs	T, °C	PAM:Pd ratio, mol/mol	[Pd], mM	Pd content, wt%	TEM size, nm (%RSD)
1	<b>Pd-PAM/AC 1</b>	50	40:1	9.4	2.0	3.7 ± 1.0 (27%)
2	<b>Pd-PAM/AC 2</b>	25	40:1	9.4	2.0	2.5 ± 0.7 (28%)
3	<b>Pd-PAM/AC 3</b>	35	40:1	9.4	2.0	2.1 ± 0.5 (24%)
4	<b>Pd-PAM/AC 4</b>	65	40:1	9.4	2.0	2-10 + non-supported NPs
5	<b>Pd-PAM/AC 5</b>	50	20:1	9.4	2.0	3.1 ± 0.9 (29%)
6	<b>Pd-PAM/AC 6</b>	50	10:1	9.4	2.0	2.9 ± 1.5 (52%)
7	<b>Pd-PAM/AC 7</b>	50	40:1	6.3	2.0	1-10
8	<b>Pd-PAM/AC 8</b>	50	40:1	14.1	2.0	2.1 ± 0.9 (43%)
9	<b>Pd-PAM/AC 9</b>	50	40:1	9.4	0.6	3.6 ± 0.7 (19%)

The first supported Pd-PAM NPs on AC catalyst was the **Pd-PAM/AC 1** (entry 1 of Table 4.1) and it was prepared using the same synthesis conditions than the reference recipe of colloidal Pd-PAM NPs (*i.e.*, 50°C, 700 rpm, 3 bar of H<sub>2</sub>, 40:1 of PAM-to-Pd molar ratio and 5.5 hours) with 2 wt% of Pd on AC. The TEM micrograph and size distribution

histogram of this catalyst are displayed in Figure 4.2. The observed NPs were spherical, monodisperse and well-defined and exhibited similar size than the corresponding colloidal Pd-PAM NPs (*ca.* 3.7 nm). The crystallite size was confirmed by X-Ray Diffraction: 3.9 nm. Nevertheless, the distribution was slightly affected by the presence of the support in the reaction media which could be related with the homogeneity of the suspension. Indeed, the colloidal NPs synthesized under the same conditions showed a relative standard deviation close to 20%, whereas the supported NPs showed a relative standard deviation of 27%.

Some authors reported that supported NPs via one pot give usually smaller sizes than the corresponding unsupported system. For instance, Llop *et al.* synthesized Rh NPs on phosphine-functionalized silica via one pot approach and they obtained supported NPs of  $1.17 \pm 0.18$  nm slightly smaller than the equivalent colloidal (*ca.* 1.5 nm).<sup>4</sup>

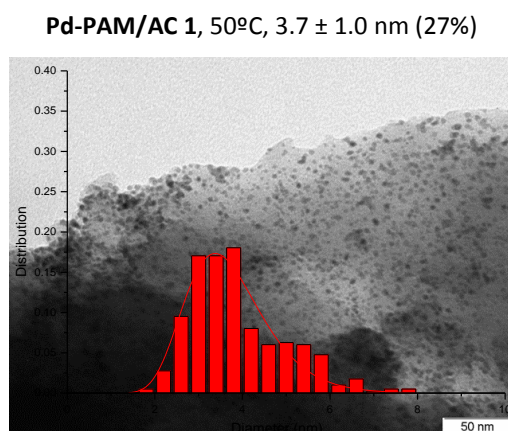


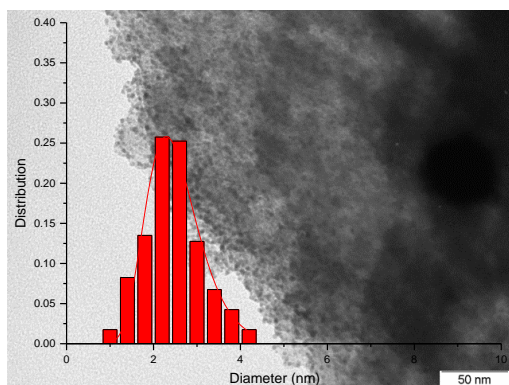
Figure 4.2. TEM micrographs and size distribution histograms of 2 wt% Pd-PAM/AC synthesized by one pot at 50°C

### Effect of the temperature of synthesis

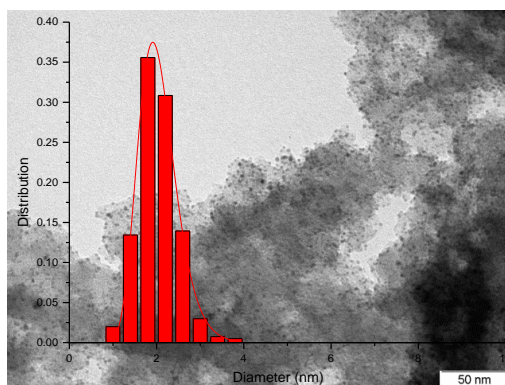
During the study of the synthesis parameter effect on the formation of colloidal Pd-PAM NPs, the temperature was identified as a key parameter to control the NPs size distribution. To study whether this parameter also affect the formation of the supported Pd-PAM NPs, the temperature was varied from 25°C to 65°C remaining all the other parameter unchanged (see from entry 2 to entry 4 in Table 4.1). The TEM

micrographs and size distribution histograms of the corresponding catalysts at these temperatures are depicted in Figure 4.3.

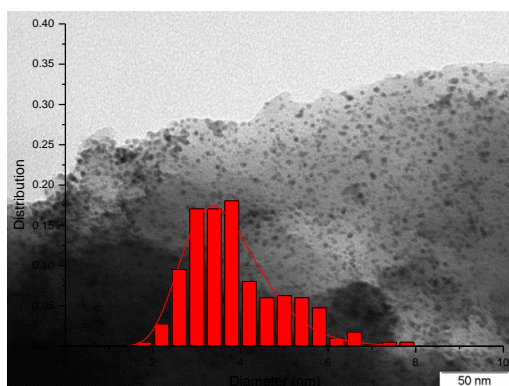
a. **Pd-PAM/AC 2**, 25°C,  $2.5 \pm 0.7$  nm (28%)



b. **Pd-PAM/AC 3**, 35°C,  $2.1 \pm 0.5$  nm (24%)



c. **Pd-PAM/AC 1**, 50°C,  $3.7 \pm 1.0$  nm (27%)



d. **Pd-PAM/AC 4**, 65°C, 2-10 nm

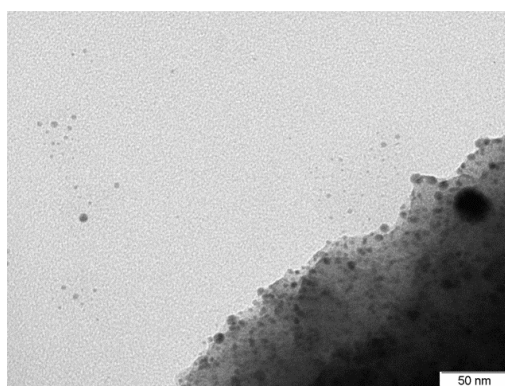


Figure 4.3. TEM micrographs and size distribution histograms of 2 wt% Pd-PAM/AC synthesized by one pot at a. 25°C, b. 35°C, c. 50°C and d. 65°C

The supported NPs obtained by the synthesis at 25°C and 35°C resulted to be smaller than those produced at 50°C (*ca.* 2.5 nm, 2.1 nm and 3.7 nm, respectively). Moreover, these NPs were spherical and monodisperse and the relative standard deviations were 28% and 24% respectively. However, when the reaction was performed at 65°C, a very broad size distribution was observed on the TEM sample (from 2 nm to 10 nm) as well as the presence of non-supported NPs. These results indicated that the temperature also affect the formation of supported Pd-PAM NPs, *i.e.*, low temperatures allow the production of NPs with small sizes whereas high temperatures affect negatively the size distribution and the immobilization of the NPs on the AC support.

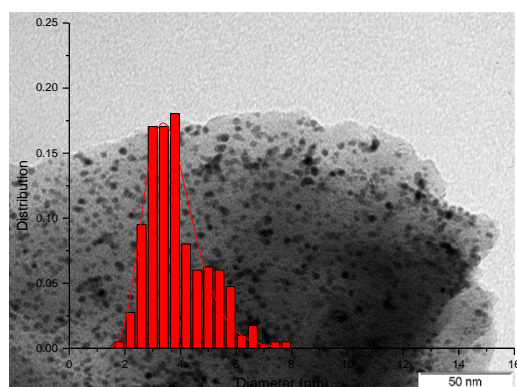


Finally, two well-defined Pd-PAM NPs supported on AC were obtained with two different sizes: *ca.* 2.1 nm and 3.7 nm at 35°C and 50°C, respectively.

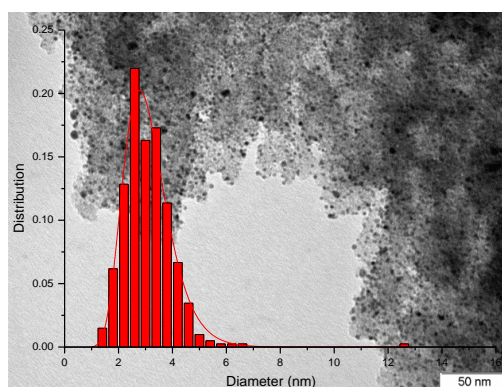
### Effect of the PAM-to-Pd molar ratio

The effect of the stabilizer-to-Pd ratio on the NPs size and size distribution was also studied. The NPs were synthesized by one pot methodology using 40:1, 20:1 and 10:1 PAM-to-Pd ratios (Entries 1, 5 and 6 from Table 4.1, respectively). The TEM micrographs and size distribution histograms at these different ratios are displayed in Figure 4.4.

a. **Pd-PAM/AC 1**, 40:1,  $3.7 \pm 1.0$  nm (27%)



b. **Pd-PAM/AC 5**, 20:1,  $3.1 \pm 0.9$  nm (28%)



c. **Pd-PAM/AC 6**, 10:1,  $2.9 \pm 1.5$  nm (51%)

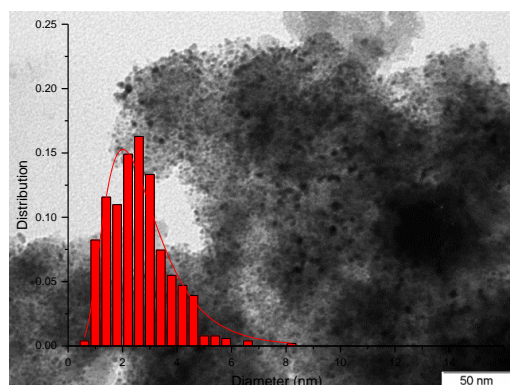


Figure 4.4. TEM micrographs and size distribution histograms of 2 wt% of Pd-PAM NPs supported on AC synthesized by one pot with PAM-to-Pd ratio of a. 40:1, b. 20:1 and c. 10:1

The NPs synthesized with 40:1 and 20:1 PAM-to-Pd ratio were spherical, monodisperse, well-defined and they measured *ca.* 3.7 nm and 3.1 nm, respectively. These results indicate that a decrease of the PAM-to-Pd ratio from 40 to 20 molar equivalents did not affect significantly the shape, size and distribution of the NPs.

However, the NPs size distribution became wider when the ratio was decreased to 10 molar equivalents, thus indicating the existence of a minimum amount of PAM to maintain a narrow distribution of the supported NPs.

The opposite trend was reported by Godard and co-workers in the study of NHC-stabilized Ni NPs. In this case, increasing the stabilizer-to-metal ratio from 0.5 to 1 equivalent per Ni, wider distribution was observed with a decrease in NPs size.<sup>9</sup>

### Effect of the metal concentration

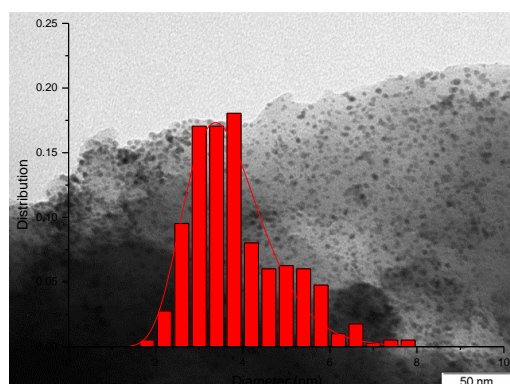
The effect of the metal precursor concentration on the formation of supported Pd-PAM NPs was also investigated. The concentration was increased and decreased by a factor of 1.5 in reference to the usual 9.4 mM (entry 7 and 8 of Table 4.1). However, the synthesized NPs showed multiple distributions in both cases making difficult an accurate conclusion about the effect of this parameter. The range of tested values was probably too wide. These results indicate that the metal concentration highly affects the NPs size distribution and small variations of this parameter can lead to negative effects in terms of size distribution.

### Effect of the Pd content on the support

Finally, the effect of the Pd content was also looked at. The reference recipe used to synthesize **Pd-PAM/AC 1** was reproduced but, in this case, using 0.6 wt% of Pd instead of 2 wt%. This value was selected since the commercial reference catalyst used in this project contains this amount of Pd. The TEM micrographs and size distribution histograms at different Pd contents are depicted in Figure 4.5.



a. **Pd-PAM/AC 1**, 2 wt%,  $3.7 \pm 1.0$  nm (27%)



b. **Pd-PAM/AC 9**, 0.6 wt%,  $3.6 \pm 0.7$  nm (19%)

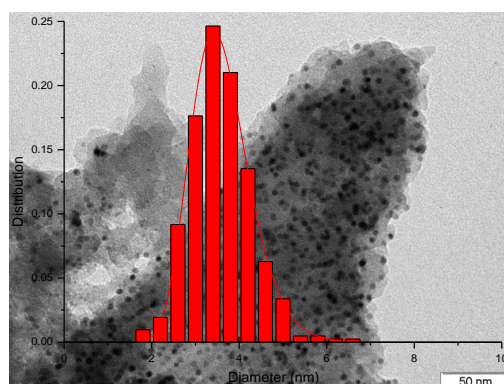


Figure 4.5. TEM micrographs and size distribution histograms of Pd-PAM NPs supported on AC synthesized by one pot with a. 2 wt% and b. 0.6 wt% of Pd content

No significant effect in terms of NPs size was observed when different Pd contents were used. However, the Pd-PAM NPs immobilized with a lowest Pd content show a narrower relative standard deviation. This result indicates that the NPs formation is better controlled when less Pd metal is used.

#### 4.3.1.2. Pd-PAM NPs supported on alpha-aluminium oxide

The first attempt of immobilization of Pd-PAM NPs on alpha-aluminium oxide ( $\alpha\text{-Al}_2\text{O}_3$ ) was performed following the conditions of the reference recipe. The temperature of synthesis, PAM-to-Pd ratio and Pd content were varied via OFAT experiments.

Table 4.2 summarizes the set of experiments performed as well as the NPs size and size distributions obtained from these experiments. In the following subsections, each parameter is discussed in detail.

Table 4.2. Variation of experimental parameters for the synthesis of supported Pd-PAM NPs on  $\alpha$ -Al<sub>2</sub>O<sub>3</sub> via one pot

$$\text{Na}_2\text{PdCl}_4 + \text{X eq. } \left[ \text{O} \begin{array}{c} \text{NH}_2 \\ \text{C} \\ \text{CH}_2 \end{array} \right]_n \xrightarrow[\text{3 bars H}_2, 700\text{rpm, 5.5h, 9.4mM of Pd}]{\text{H}_2\text{O, } \alpha\text{-Al}_2\text{O}_3} \text{Pd-PAM/}\alpha\text{-Al}_2\text{O}_3 \text{ NPs}$$

$T$  (°C), x wt% of Pd

Entry	NPs	T, °C	PAM: Pd ratio, mol/mol	Pd content, wt%	TEM size, nm (%RSD)
1	<b>Pd-PAM/<math>\alpha</math>-Al<sub>2</sub>O<sub>3</sub> 1</b>	50	40:1	2.0	4.5 ± 1.1 (23%)
2	<b>Pd-PAM/<math>\alpha</math>-Al<sub>2</sub>O<sub>3</sub> 2</b>	35	40:1	2.0	3.5 ± 1.1 (32%)
3	<b>Pd-PAM/<math>\alpha</math>-Al<sub>2</sub>O<sub>3</sub> 3</b>	25	40:1	2.0	2-3 + non-supported NPs
4	<b>Pd-PAM/<math>\alpha</math>-Al<sub>2</sub>O<sub>3</sub> 4</b>	35	80:1	2.0	2-6 + non-supported NPs
5	<b>Pd-PAM/<math>\alpha</math>-Al<sub>2</sub>O<sub>3</sub> 5</b>	50	40:1	0.6	4.8 ± 1.0 (21%)

The first supported Pd-PAM NPs on alpha aluminium oxide was the **Pd-PAM/ $\alpha$ -Al<sub>2</sub>O<sub>3</sub> 1** (entry 1 from Table 4.2) and was prepared using the same conditions than the reference recipe of colloidal Pd-PAM NPs (*i.e.*, 50°C, 700 rpm, 3 bar of H<sub>2</sub>, 40:1 of PAM-to-Pd molar ratio and 5.5 hours of synthesis) with 2 wt% of Pd on  $\alpha$ -Al<sub>2</sub>O<sub>3</sub>. The TEM micrograph and size distribution histogram of this catalyst are displayed in Figure 4.6a. The NPs observed showed spherical shape, narrow size distribution, and the size was slightly larger (*ca.* 4.5 nm) than the NPs synthesized by the same recipe but on AC (*ca.* 3.7 nm). This result indicates that the support also affects the NPs size.

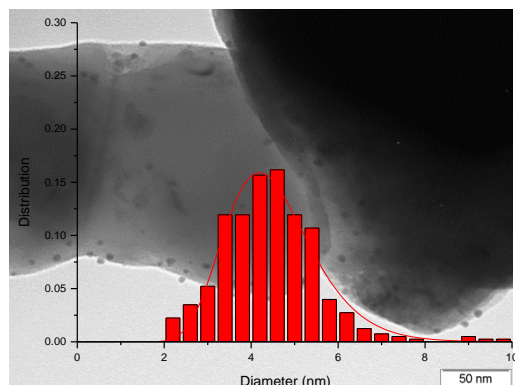
Llop *et al.* reported a new approach for the preparation of well-defined Rh and Pt NPs on silica.<sup>4</sup> In this study they demonstrated that the modification of SiO<sub>2</sub> support by an anchoring a phosphine improved the stabilization of both Rh and Pt NPs. Moreover a decrease of Rh NPs size was observed between the non-modified silica and the phosphine-functionalized silica (*ca.* 2.6 nm and 1.2 nm, respectively) indicating an effect of the support in the formation of well-defined NPs via one pot approach.

### Effect of the temperature of synthesis

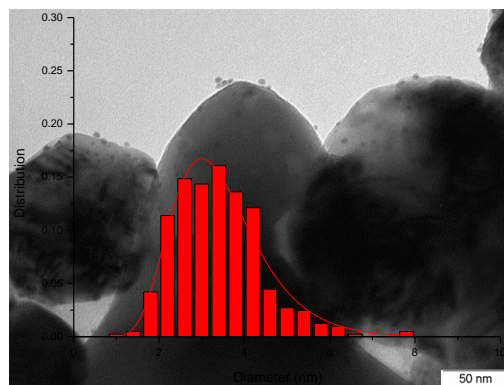
First, the effect of the temperature of synthesis was studied. The synthesis of **Pd-PAM/  $\alpha$ -Al<sub>2</sub>O<sub>3</sub> 1** was repeated but decreasing the temperature to 35°C and 25°C (entries 2 and 3 from Table 4.2). The TEM micrographs and size distribution

histograms of the corresponding catalysts at different temperatures are displayed in Figure 4.6.

a. **Pd-PAM/ $\alpha$ -Al<sub>2</sub>O<sub>3</sub> 1**, 50°C, 4.5 ± 1.1 nm (23%)



b. **Pd-PAM/ $\alpha$ -Al<sub>2</sub>O<sub>3</sub> 2**, 35°C, 3.5 ± 1.1 nm (32%)



c. **Pd-PAM/ $\alpha$ -Al<sub>2</sub>O<sub>3</sub> 3**, 25°C, 2-3 nm

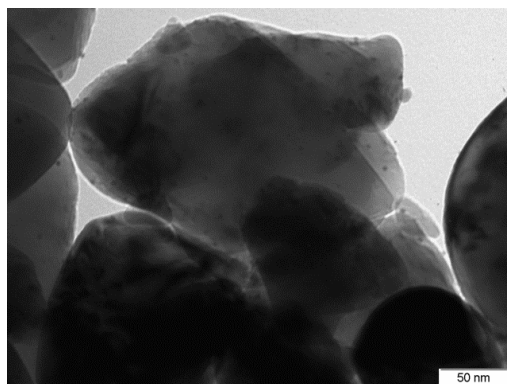


Figure 4.6. TEM micrographs and size distribution histograms of 2 wt% of Pd-PAM NPs supported on α-Al<sub>2</sub>O<sub>3</sub> synthesized by one pot at a. 50°C, b. 35°C and c. 25°C

The NPs formed at 35°C were smaller than those synthesized at 50°C (*ca.* 3.5 nm and 4.5 nm, respectively). When the temperature was decreased to 25°C, the NPs exhibited an even lower diameter (*ca.* 2-3 nm), but a large amount of non-supported NPs was observed in the TEM images. These results suggest that a temperature decrease from 50°C to 35°C favors the formation of smaller NPs (as observed previously in the AC case). However, when the temperature was further decreased to 25°C, the immobilization was not efficient anymore.

Finally, since the relative standard deviation of the NPs synthesized at 35°C was slightly wider than that of the NPs formed at 50°C (35% and 23%, respectively), an increase of PAM-to-Pd ratio was tested and presented in the next section.

### Effect of the PAM-to-Pd ratio

The amount of PAM was increased from 40 to 80 molar equivalents at 35°C. The NPs formed were widely distributed and a large amount of small non-supported NPs was also observed. This result suggests that a high quantity of stabilizer in the reaction media impede an efficient immobilization of the NPs on the  $\alpha$ -Al<sub>2</sub>O<sub>3</sub> support.

### Effect of the Pd content

Finally, the effect of the Pd content on the NPs size and size distribution was examined. The synthesis of the **Pd-PAM/  $\alpha$ -Al<sub>2</sub>O<sub>3</sub> 1** was reproduced using 0.6 wt% of Pd instead of 2 wt%. The TEM micrographs and size distribution histograms at different Pd contents are depicted in Figure 4.7.

a. **Pd-PAM/  $\alpha$ -Al<sub>2</sub>O<sub>3</sub> 1**, 2 wt%, 4.5 ± 1.1 nm (23%)      b. **Pd-PAM/  $\alpha$ -Al<sub>2</sub>O<sub>3</sub> 5**, 0.6 wt%, 4.8 ± 1.0 nm (21%)

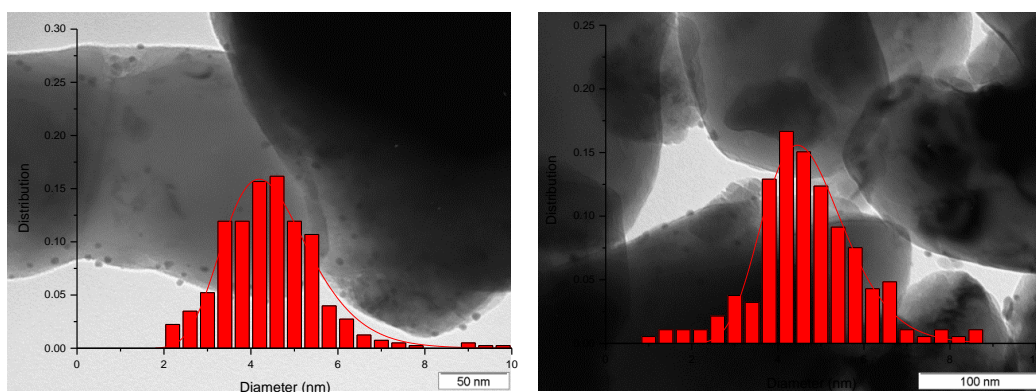


Figure 4.7. TEM micrographs and size distribution histograms of Pd-PAM NPs supported on  $\alpha$ -Al<sub>2</sub>O<sub>3</sub> synthesized by one pot with a. 2 wt% and b. 0.6 wt% of Pd content

The NPs formed with 0.6 wt% of Pd on  $\alpha$ -Al<sub>2</sub>O<sub>3</sub> showed similar NPs size and size distribution than those containing 2 wt% of Pd, suggesting that the formation of the NPs was not affected by a decrease in Pd content.

4.3.1.3. Pd-PAM NPs supported on titanium oxide


The first attempt of immobilization of Pd-PAM NPs on titanium oxide (TiO<sub>2</sub>) was performed following the conditions of the reference recipe. The Pd content and Pd concentration were varied.

Table 4.3 summarizes the set of experiments performed as well as the NPs size and size distributions obtained from these experiments. In the following subsections, each parameter is discussed in detail.

Table 4.3. Variation of experimental parameters for the synthesis of supported Pd-PAM NPs on TiO<sub>2</sub> via one pot

$$\text{Na}_2\text{PdCl}_4 + 40 \left[ \begin{array}{c} \text{O} \\ \parallel \\ \text{---C---} \\ | \\ \text{NH}_2 \end{array} \right]_n \xrightarrow[\text{T (}^\circ\text{C), x mM of Pd}]{\text{H}_2\text{O, TiO}_2, \text{ 3 bars H}_2, 700\text{rpm, 5.5h}} \text{Pd-PAM/TiO}_2 \text{ NPs}$$

x wt% Pd



Entry	NPs	T, °C	Pd content, wt%	[Pd], mM	TEM size, nm (%RSD)
1	Pd-PAM/TiO <sub>2</sub> 1	50	2.0	9.4	2.6 ± 0.7 (28%)
2	Pd-PAM/TiO <sub>2</sub> 2	35	2.0	9.4	3.8 ± 1.1 (29%)
3	Pd-PAM/TiO <sub>2</sub> 3	50	0.6	9.4	Multiple distribution
4	Pd-PAM/TiO <sub>2</sub> 4	50	0.6	3.1	2.5 ± 0.9 (36%)

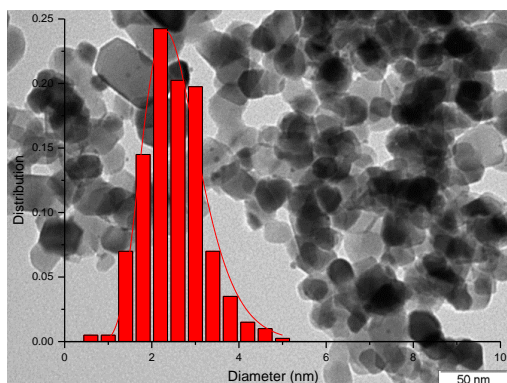
The first catalyst supported on TiO<sub>2</sub> was the **Pd-PAM/TiO<sub>2</sub> 1** (entry 1 from Table 4.3). The conditions were the same than those used for the reference recipe of colloidal Pd-PAM NPs (*i.e.*, 50°C, 700 rpm, 3 bar of H<sub>2</sub>, 40:1 of PAM-to-Pd molar ratio and 5.5 hours of synthesis) with a Pd content of 2 wt% on TiO<sub>2</sub>. The TEM micrograph and size distribution histogram of this catalyst are displayed Figure 4.8a. The NPs observed were spherical and measured *ca.* 2.6 nm. This result confirms that NPs size highly depends on the selected support. Indeed, using the same recipe different Pd-PAM NPs sizes were obtained: *ca.* 2.6 nm, 3.7 nm and 4.5 nm on TiO<sub>2</sub>, AC and α-Al<sub>2</sub>O<sub>3</sub>, respectively.

Effect of the temperature of synthesis

The synthesis of **Pd-PAM/TiO<sub>2</sub> 1** described above was repeated decreasing the temperature from 50°C to 35°C. The TEM micrographs and size distribution

histograms of the corresponding catalysts at different temperatures are depicted in Figure 4.8.

a. **Pd-PAM/TiO<sub>2</sub> 1**, 50°C,  $2.6 \pm 0.7$  nm (28%)



b. **Pd-PAM/TiO<sub>2</sub> 2**, 35°C,  $3.8 \pm 1.1$  nm (29%)

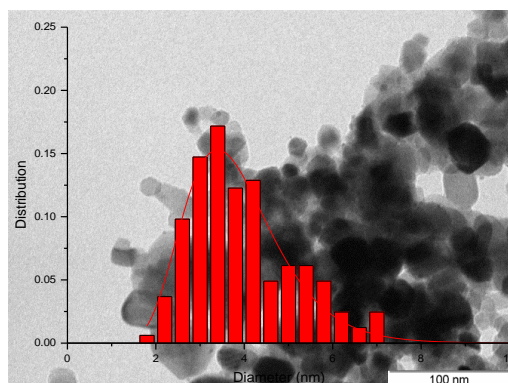


Figure 4.8. TEM micrographs and size distribution histograms of 2 wt% Pd-PAM NPs supported on TiO<sub>2</sub> by one pot synthesis at a. 50°C and b. 35°C

The NPs formed at 35°C were larger than those obtained at 50°C. This is the opposite trend than in the case of AC and  $\alpha$ -Al<sub>2</sub>O<sub>3</sub> supports. On the other hand, the NPs size distribution was negatively affected by the temperature decrease. Therefore, these results indicate that the effect of the temperature on the NPs size and size distribution varies depending on the support used. For this reason, general trends cannot be easily concluded.

### Effect of the Pd content

The effect of the Pd content was also investigated when using TiO<sub>2</sub>. The synthesis of **Pd-PAM/TiO<sub>2</sub> 1** was reproduced using 0.6 wt% of Pd instead of 2 wt%. The TEM micrographs and size distribution histograms at these different Pd contents are displayed in Figure 4.9.



a. **Pd-PAM/TiO<sub>2</sub> 1**, 2 wt%,  $2.6 \pm 0.7$  nm (28%)

b. **Pd-PAM/TiO<sub>2</sub> 3**, 0.6 wt%, 1-11 nm

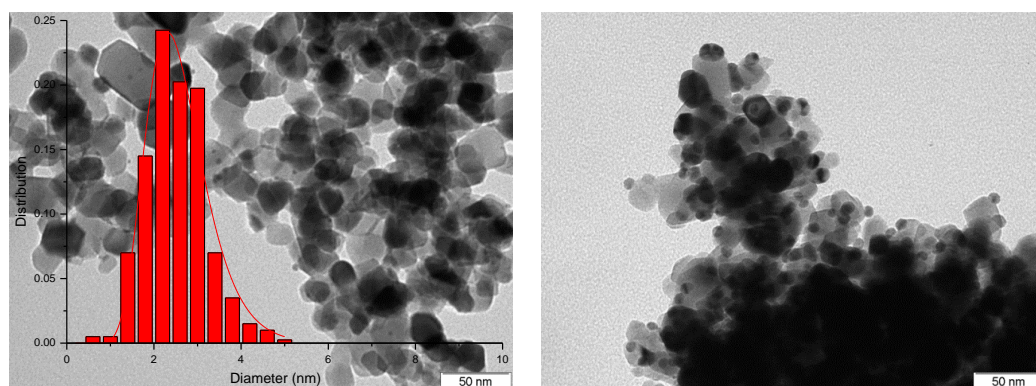


Figure 4.9. TEM micrographs and size distribution histograms of Pd-PAM NPs supported on TiO<sub>2</sub> by one pot with a. 2 wt% and b. 0.6 wt% of Pd content

The synthesized NPs presented a very wide distribution (from 1 to 11 nm). In contrast to the NPs immobilized on AC and  $\alpha$ -Al<sub>2</sub>O<sub>3</sub>, the NPs supported on TiO<sub>2</sub> were negatively affected by the decrease of Pd content. The decrease of Pd content was performed by increasing the amount of support in the Fischer Porter reactor and keeping the volume, the other reagents and the stirring rate to a constant value. However, the corresponding amount of TiO<sub>2</sub> occupied a large volume in the reactor (much larger than the corresponding amount of AC and  $\alpha$ -Al<sub>2</sub>O<sub>3</sub>). Therefore, the mixture was thicker and the homogenization of the suspension was not efficient which could potentially explain why the obtained NPs were not well-defined.

To attempt obtaining well-defined Pd-PAM NPs on TiO<sub>2</sub> with 0.6 wt% of Pd content, it was proposed to reduce the Pd concentration in the reaction media. The results of this test are presented in the next subsection.

### Effect of the Pd concentration

The recipe of the **Pd-PAM/TiO<sub>2</sub> 3** was repeated but, in this case, reducing by three the amount of metal, support and stabilizer while maintaining the same amount of solvent (30mL). Therefore the metal concentration was decreased to 3.1 mM. The TEM micrograph and size distribution histogram at this new Pd concentration is displayed in Figure 4.10.

a. **Pd-PAM/TiO<sub>2</sub> 4**, 0.6 wt%,  $2.5 \pm 0.9$  nm (36%)

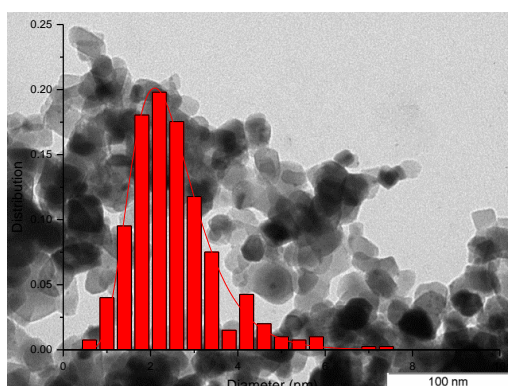


Figure 4.10. TEM micrograph and size distribution histogram of Pd-PAM NPs on TiO<sub>2</sub> synthesized by one pot with 3.1 mM of Pd concentration in the reaction media and 0.6 wt% of Pd content

The NPs synthesized under diluted conditions (3.1 mM) were better defined than those synthesized with the usual Pd concentration (9.4 mM) resulting in well-defined NPs.

These results show the importance of the preliminary analysis of the experimental set-up and syntheses procedures before beginning a series of experiments in order to anticipate these kinds of issues and adapt the plan of experiments.

#### 4.3.1.4. Conclusions of the structure-synthesis relationship study of the supported Pd-PAM NPs synthesized by one pot

During the study of the one pot immobilization of Pd-PAM NPs on AC,  $\alpha$ -Al<sub>2</sub>O<sub>3</sub> and TiO<sub>2</sub> supports, eight well-defined catalysts were prepared and characterized by TEM. Their NPs sizes and distributions are summarized in Table 4.4.

From this set of experiments, it was observed that reducing the synthesis temperature from 50°C to 35°C enables the formation of smaller NPs on AC and  $\alpha$ -Al<sub>2</sub>O<sub>3</sub> (*ca.* 2 nm and 3.5 nm, respectively). The opposite trend was obtained on TiO<sub>2</sub> (increase from *ca.* 2.6 nm to 3.8 nm at 50°C and 35°C, respectively). These results indicate that the effect of the synthesis parameters over the NPs size also highly depend on the support.



Then, the Pd content was reduced from 2 wt% to 0.6 wt% on all the supports tested. No effect was observed on AC and  $\alpha$ -Al<sub>2</sub>O<sub>3</sub> since well-defined NPs were obtained with the same size and distribution than those synthesized with 2 wt% of Pd. In contrast, on TiO<sub>2</sub>, the decrease in Pd content dramatically affects the formation of well-defined NPs. This could be explained by the intrinsic properties of this solid support. The corresponding mass of support took a large volume in the Fischer Porter reactor and impeded an efficient homogenization of the mixture with the set-up used. Therefore, a decrease of metal concentration was tested to immobilize 0.6 wt% of Pd on TiO<sub>2</sub>. It resulted in a strong improvement since the NPs obtained showed a similar size and size distribution than the corresponding 2 wt% NPs.

The effect of the PAM-to-Pd ratio was also studied using AC support. Well-defined NPs were obtained when this ratio was reduced from 40:1 to 20:1. However, when the ratio was further reduced, wide distributions were obtained.

Table 4.4. List of the well-defined supported Pd-PAM NPs obtained by one pot synthesis

Catalyst name	Pd content, wt%	TEM size, nm (RSD, %)
<b>Pd-PAM/AC 1</b>	2.0	3.7 ± 1.0 (27%)
<b>Pd-PAM/AC 3</b>	2.0	2.1 ± 0.5 (24%)
<b>Pd-PAM/AC 9</b>	0.6	3.6 ± 0.7 (19%)
<b>Pd-PAM/<math>\alpha</math>-Al<sub>2</sub>O<sub>3</sub> 1</b>	2.0	4.5 ± 1.1 (23%)
<b>Pd-PAM/<math>\alpha</math>-Al<sub>2</sub>O<sub>3</sub> 2</b>	2.0	3.5 ± 1.1 (32%)
<b>Pd-PAM/<math>\alpha</math>-Al<sub>2</sub>O<sub>3</sub> 5</b>	0.6	4.8 ± 1.0 (21%)
<b>Pd-PAM/TiO<sub>2</sub> 1</b>	2.0	2.6 ± 0.7 (28%)
<b>Pd-PAM/TiO<sub>2</sub> 4</b>	0.6	2.5 ± 0.9 (36%)

This study showed that the control of the NPs size and size distribution via one pot synthesis is not a straightforward task and depends on a high number of parameters. For this reason, another approach was probed: the two-step synthesis presented in the following section.

It is noteworthy that the one pot methodology was also tested for the immobilization of Pd-PAM NPs on SiO<sub>2</sub> and  $\gamma$ -Al<sub>2</sub>O<sub>3</sub> supports, but no suitable results were obtained. On SiO<sub>2</sub> the NPs were not well immobilized and irregular distribution of sizes were obtained in the tested conditions. When  $\gamma$ -Al<sub>2</sub>O<sub>3</sub> was used, the reduction with

hydrogen was not performed because the reactant mixture was not homogeneous. The solubility of the metal precursor ( $\text{Na}_2\text{PdCl}_4$ ) was negatively affected by the addition of this support in the reaction media. A possible explanation is that the addition of the support affected the pH of the solution and the dissolution of the metal precursor. To verify this hypothesis, the point of zero charge of this support could be measured. We also note that this support is a micron size support, and it is more difficult to obtain a homogeneous suspension in this case.

### 4.3.2. Supported Pd-PAM NPs via two-step synthesis

As detailed above, the use of two-step syntheses was proposed in order to improve the control over NPs size.

Several methodologies were tested to form Pd-PAM NPs on AC,  $\alpha\text{-Al}_2\text{O}_3$  and  $\text{TiO}_2$  supports.

#### 4.3.2.1. Immobilization via pH modification

The first attempt of immobilization of Pd-PAM NPs was performed on AC using a similar methodology than that reported by P. Witte for the immobilization of Pd NPs on AC via two-step colloidal approach.<sup>17</sup> The procedure consisted in the addition of colloidal Pd-PAM NPs on a slurry of AC support followed by an increase of pH from 2 to 9 to induce the immobilization. A TEM image is presented in Figure 4.11.

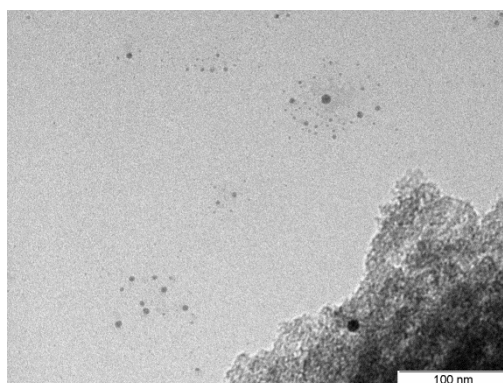


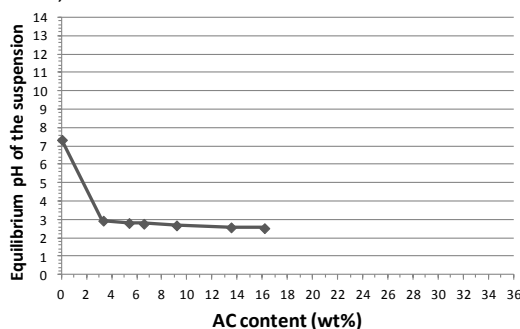
Figure 4.11. TEM micrograph and Pd-PAM NPs supported on AC immobilized via pH modification method

A large amount of non-supported NPs was observed indicating that this methodology was not efficient to immobilize properly the Pd-PAM NPs on AC. To understand why this methodology was not adapted to this system of NPs, the PZC of the supports and the  $\zeta$  potential of these NPs were determined following the procedure described in section 4.2.3.2.

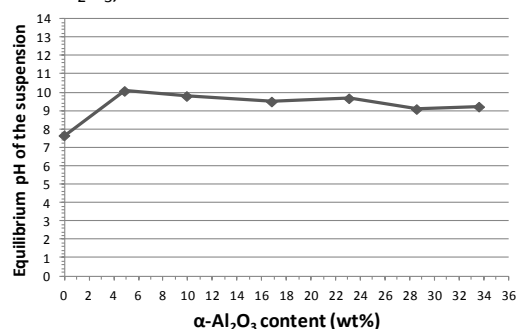
#### 4.3.2.2. Determination of the PZC of the supports and the $\zeta$ potential of the Pd NPs

The PZC of AC,  $\alpha\text{-Al}_2\text{O}_3$  and  $\text{TiO}_2$  supports were determined by mass titration. The curves of pH vs. percentage mass-to-volume ratio of each support are displayed in Figure 4.12.

a. AC,  $\text{PZC} = 2.6$



b.  $\alpha\text{-Al}_2\text{O}_3$ ,  $\text{PZC} = 9.2$



c.  $\text{TiO}_2$ ,  $\text{PZC} = 4.6$

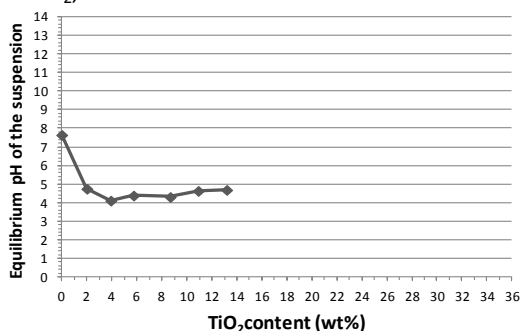


Figure 4.12. Point of Zero Charge of a. AC, b.  $\alpha\text{-Al}_2\text{O}_3$  and c.  $\text{TiO}_2$  determined by mass titration

The PZC of the AC,  $\alpha\text{-Al}_2\text{O}_3$  and  $\text{TiO}_2$  supports were equal to 2.6, 9.2 and 4.6, respectively. As example, for AC support the value of 2.6 means that if the pH of an aqueous solution is lower than 2.6, the AC will have a positive surface charge and will interact with negatively charged NPs. On the contrary, if the pH of the aqueous

solution is higher than 2.6, the AC will have negative surface charge and will interact with positively charged NPs. This example is schematized in Figure 4.13.

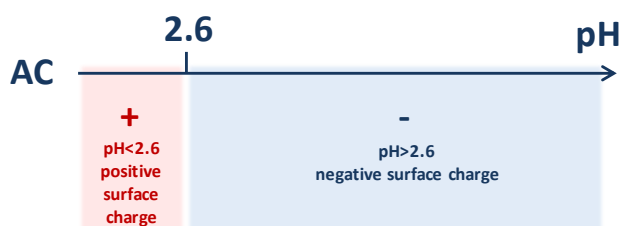


Figure 4.13. PZC of AC

Afterwards, the  $\zeta$  potential of the colloidal Pd-PAM NPs was measured and was equal to  $-14$  indicating that these NPs have a negative charge at the interfacial double layer.

Once the Pd-PAM NPs potential and the pH of the aqueous AC and Pd-PAM NPs mixture were determined, it was possible to understand why the immobilization via pH modification was not efficient. When the NPs were added to the slurry of solid support, the pH was equal to 2 (a value lower than the PZC of AC). Therefore, in these conditions, AC support had positive surface charge and could interact with the negatively charged Pd-PAM NPs since they revealed a surface charge of  $-14$ . However the recipe followed involved a pH increase to 9, so the AC support became negatively charged (as the NPs) and provoked repulsion between both materials.

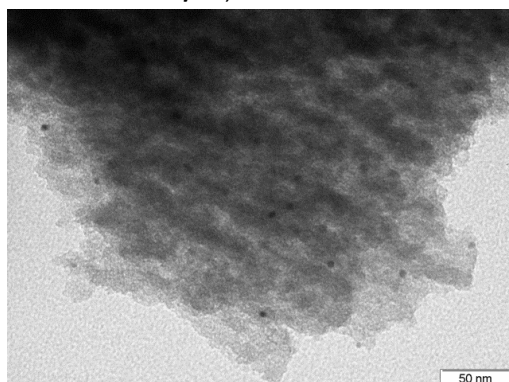
Looking at the respective charges of the Pd-PAM NPs and the selected supports, it seems that a simple mixing methodology could induce the immobilization process. Indeed the pH of the support mixed with the colloidal NPs is equal to 2, 7 and 3 for AC,  $\alpha\text{-Al}_2\text{O}_3$  and  $\text{TiO}_2$ , respectively. Therefore, in all the cases the support has a positive surface charge and can attract the NPs by electrostatic interactions. This simple mixing procedure for immobilization was tested and is presented in the next subsection.

#### 4.3.2.3. Immobilization by a simple mixing methodology

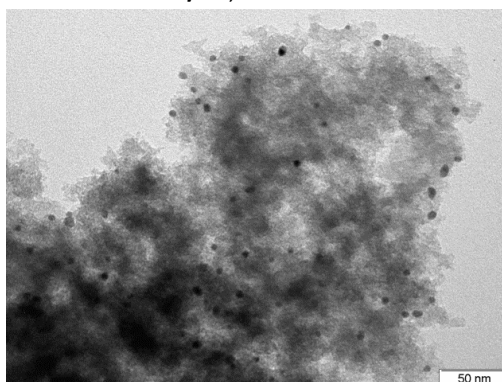
The second attempt of immobilization of Pd-PAM NPs was done using a simple mixing methodology combined with ultrasound treatments. The detailed procedure was described in section 4.2.3.2.

This procedure was tested to support Pd-PAM NPs on AC,  $\alpha$ -Al<sub>2</sub>O<sub>3</sub>, TiO<sub>2</sub> supports. Visually, the NPs seemed to be well anchored on the supports since translucent supernatants were obtained after filtration. The immobilization was performed on the three supports with 0.6 wt% and 2 wt% of Pd content, resulting in the following catalysts: **Pd-PAM 6c/AC**, **Pd-PAM 6c/ $\alpha$ -Al<sub>2</sub>O<sub>3</sub>**, **Pd-PAM 6c/TiO<sub>2</sub>**, **Pd-PAM 6d/AC**, **Pd-PAM 6d/ $\alpha$ -Al<sub>2</sub>O<sub>3</sub>** and **Pd-PAM 6d/TiO<sub>2</sub>**. The TEM of these six catalysts were performed and are given in Figure 4.14.

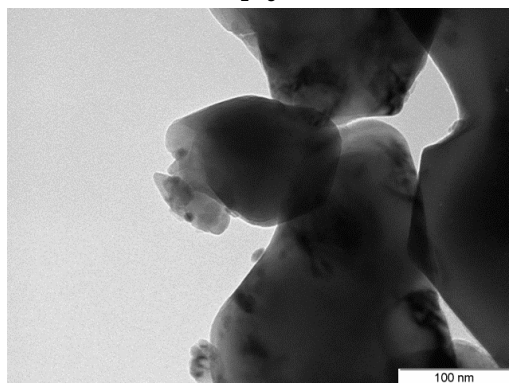
a. **Pd-PAM 6c Pd/AC**, 0.6 wt%



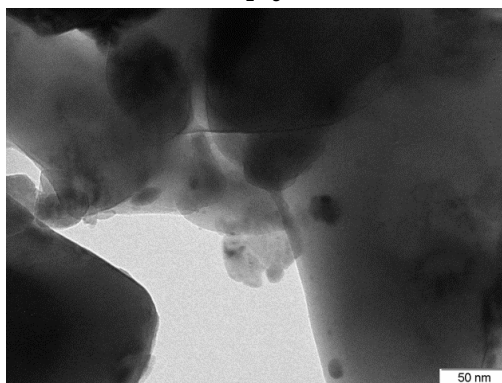
b. **Pd-PAM 6d Pd/AC**, 2 wt%



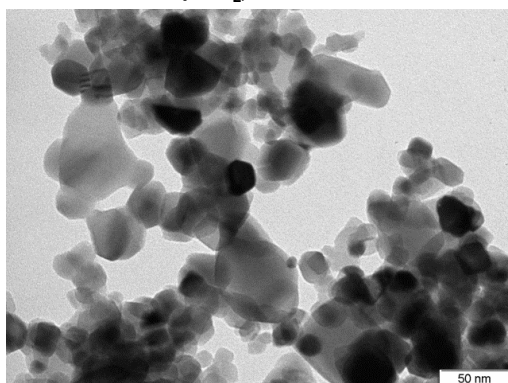
c. **Pd-PAM 6c Pd/ $\alpha$ -Al<sub>2</sub>O<sub>3</sub>**, 0.6 wt%



d. **Pd-PAM 6d Pd/ $\alpha$ -Al<sub>2</sub>O<sub>3</sub>**, 2 wt%



e. Pd-PAM 6c Pd/TiO<sub>2</sub>, 0.6 wt%



f. Pd-PAM 6c Pd/TiO<sub>2</sub>, 2 wt%

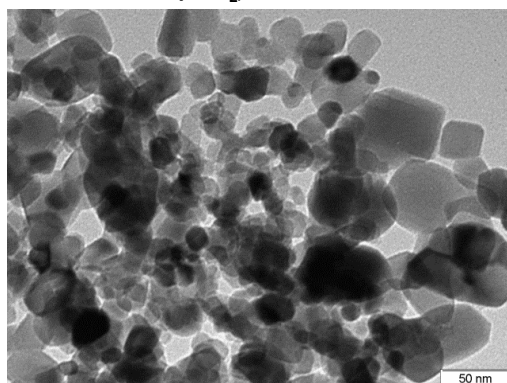


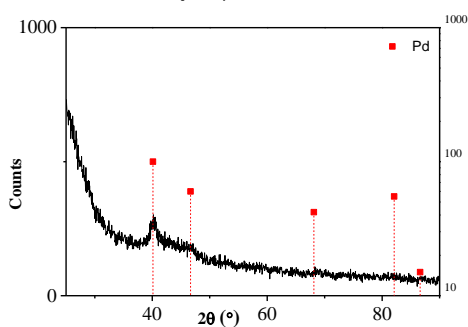
Figure 4.14. TEM micrographs of Pd-PAM NPs supported by simple mixing two-step synthesis

In the case of AC support, some single NPs could be observed for Pd content of 2 wt% and 0.6 wt%, but not enough to accurately measure their size and size distribution. In the rest of the samples, large agglomerates were observed.

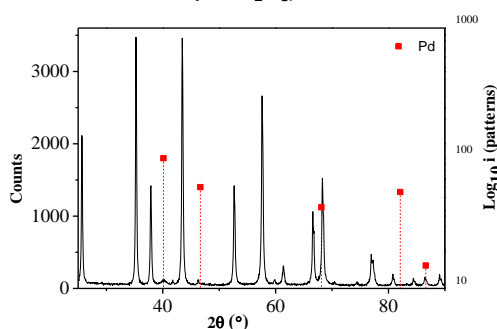
In the cases of  $\alpha$ -Al<sub>2</sub>O<sub>3</sub> and TiO<sub>2</sub> supports, single NPs were not observed and some contrasted zones suggested the presence of large agglomerates. Using TEM characterization it was not possible to confirm if the NPs sizes and size distributions were affected by the proposed immobilization procedure.

To obtain information about the crystallite sizes of Pd metal on the different supports, X-Ray diffraction analyses were carried out on the 2 wt% catalysts and are displayed in Figure 4.15.

a. Pd-PAM 6d Pd/AC, 2 wt%



b. Pd-PAM 6d Pd/ $\alpha$ -Al<sub>2</sub>O<sub>3</sub>, 2 wt%





c. **Pd-PAM 6d Pd/TiO<sub>2</sub>, 2 wt%**

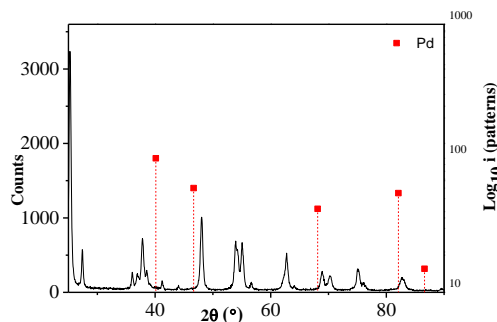
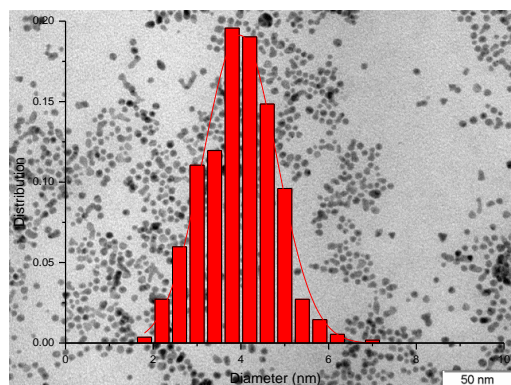


Figure 4.15. X-Ray Diffraction pattern of Pd-PAM NPs supported by two-step synthesis with 2 wt% of Pd content

The Pd peaks observed showed very low intensities. The presence of Pd was confirmed but estimation of the crystallite sizes was not possible.

Thereafter, it was proposed to carry out a similar two-step synthesis with a higher Pd content and perform X-Ray Diffraction analysis to obtain the Pd NPs crystallite size. Pd NPs were supported on AC with 10 wt% of Pd content under the conditions described above. AC was selected as support because it is less crystalline than  $\alpha$ -Al<sub>2</sub>O<sub>3</sub> or TiO<sub>2</sub>, thus the Pd peaks could be better distinguished. The TEM and XRD characterization results are displayed in Figure 4.16 and Figure 4.17.

a. **Pd-PAM 6e, 4.0 ± 1.0 nm (25%)**



b. **Pd-PAM 6e/AC**

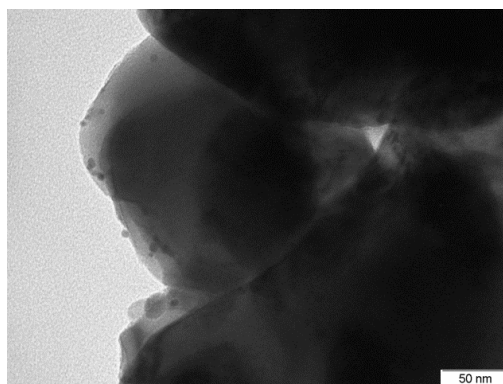


Figure 4.16. TEM micrographs of a. the reference recipe of **Pd-PAM 6e** NPs and b. the supported **Pd-PAM 6e/AC** by two-step synthesis with 10 wt% of Pd content

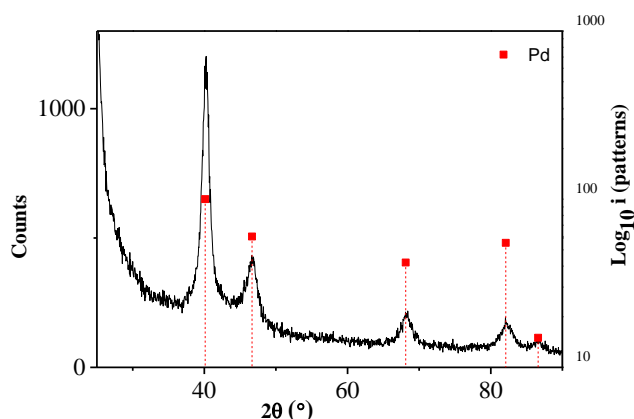


Figure 4.17. XRD patterns of **Pd-PAM 6e/AC** supported by two-step synthesis with 10 wt% of Pd content

The TEM images of the **Pd-PAM 6e/AC** showed few single NPs immobilized on the support as in the case of 0.6 wt% and 2 wt% of Pd content. Moreover, some non-supported NPs were observed which could indicate that the AC support surface was saturated by the large amount of colloidal suspension of Pd.

The XRD showed the five characteristic bands of the Pd-fcc packing (40°, 46°, 68°, 82° and 86°). The average NPs crystallite size obtained was 4.52 nm which was close to the 4.0 nm size measured by TEM. These results suggest that the immobilization of colloidal NPs on support by the simple mixing two-step methodology did not affect the average NPs size.

Delgado *et al.* reported the immobilization of Co NPs on  $\text{TiO}_2$  support by the direct addition of these NPs previously dispersed in hexane over a stirred suspension of  $\text{TiO}_2$  in the same solvent.<sup>8</sup> Similarly, they observed that the NPs size remained unchanged after the immobilization process.

Since the supported Pd NPs could not be well-observed by TEM, it was proposed to perform ESEM characterizations to observe their agglomeration of the support. In the next section, the effects of the immobilization process, Pd content, nature of the support and scale of the synthesis of the NPs dispersion were investigated.



#### **4.3.2.4. Conclusions of the study of the immobilization of Pd-PAM NPs by two steps**

In the previous part, the complexity of a precise NPs size control by one pot synthesis was demonstrated. Therefore the two-step immobilization process was tested.

In a first hand, an attempt of immobilization of the Pd-PAM NPs on AC was carried out following the recipe reported by P. Witte in the BASF patent.<sup>17</sup> This methodology consisted in the mixture of a slurry of support with the previously synthesized suspension of Pd NPs, followed by a pH modification to induce the NPs precipitation. However, this recipe resulted to be inefficient to induce the immobilization of Pd-PAM NPs on the AC support. Therefore, the PZC of the solid supports used and the  $\zeta$ -potential of the Pd-PAM NPs were determined. Without any pH variations, the studied supports and the Pd-PAM NPs resulted to have opposite surface charges suggesting that a simple mixture between both materials could be enough to induce the immobilization of the NPs.

This simple mixing methodology was thus applied to support Pd-PAM NPs on AC,  $\alpha$ - $\text{Al}_2\text{O}_3$  and  $\text{TiO}_2$  with 0.6 wt% and 2 wt% of Pd content. These catalysts were characterized by TEM, but the NPs could not be easily observed. The XRD analysis indicated that Pd was present on the three supports, however the low peak intensity did not enable the estimation of the crystallite sizes of the NPs.

Thus, Pd-PAM NPs were immobilized through this methodology with 10 wt% of Pd content. The XRD characterization confirmed a crystallite size close to the NPs size of the corresponding colloidal NPs indicating that this methodology did not affect the NPs size. Nevertheless, the NPs dispersion on the support is also an important property that could influence the catalysts activities and selectivities. So, the effects of the immobilization process, Pd content and support on the NPs dispersion were studied and are presented in the next section.

### 4.3.3. Nanoparticles dispersion on the supports

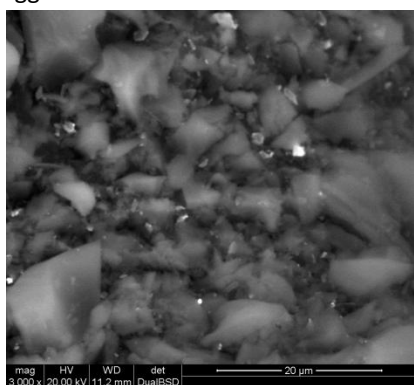
#### 4.3.3.1. Study of the effect of the immobilization process, the Pd content and the support via ESEM characterization

In this section, the supported catalysts Pd-PAM NPs on AC,  $\alpha$ -Al<sub>2</sub>O<sub>3</sub> and TiO<sub>2</sub> containing 0.6 wt% and 2 wt% of Pd synthesized by one pot are compared with the Pd-PAM NPs on AC,  $\alpha$ -Al<sub>2</sub>O<sub>3</sub> and TiO<sub>2</sub> containing 0.6 wt% and 2 wt% of Pd obtained by two steps.

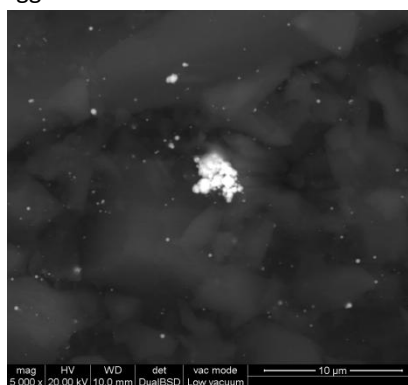
In this way, the effect of the immobilization process, the nature of the support and the Pd content were studied.

In Figure 4.18 the ESEM images of the catalysts supported with 0.6 wt% of Pd content are presented.

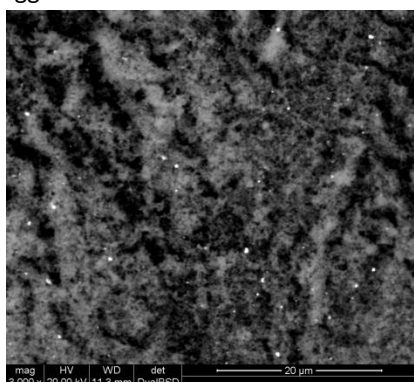
a. **Pd-PAM/AC 9**, one pot  
agglomerates <100-1500 nm



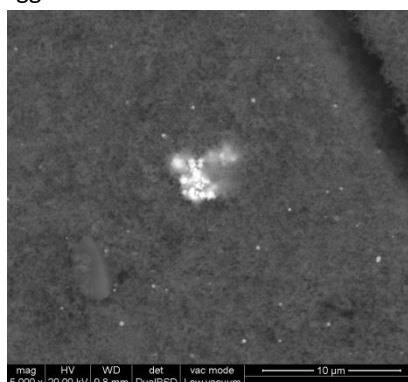
b. **Pd-PAM 6c/AC**, two steps  
agglomerates <100-2500 nm



c. **Pd-PAM/ $\alpha$ -Al<sub>2</sub>O<sub>3</sub> 5**, one pot  
agglomerates <100-1000 nm



d. **Pd-PAM 6c/ $\alpha$ -Al<sub>2</sub>O<sub>3</sub>**, two steps  
agglomerates <100-2000 nm



e. **Pd-PAM/TiO<sub>2</sub> 3**, one pot

Multiple distribution of NPs obtained  
 ESEM not performed

f. **Pd-PAM 6c/TiO<sub>2</sub>**, two steps  
 agglomerates <100-1000 nm

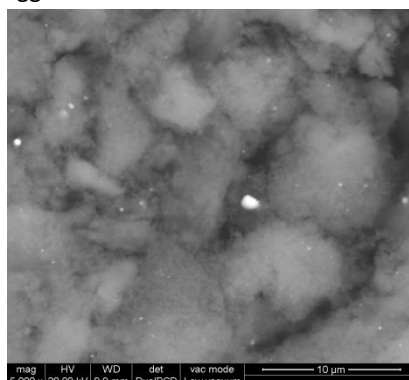


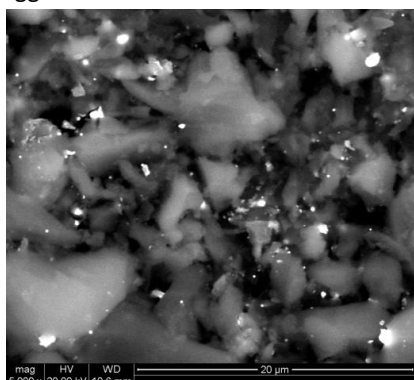
Figure 4.18. ESEM images of Pd-PAM NPs supported on AC,  $\alpha$ -Al<sub>2</sub>O<sub>3</sub> and TiO<sub>2</sub> with 0.6 wt% of Pd content via one pot (a, c and e) and two-step syntheses (b, d and f)

The bright spots observed on the ESEM images confirmed agglomeration in the samples. The ranges of agglomerates sizes were measured.

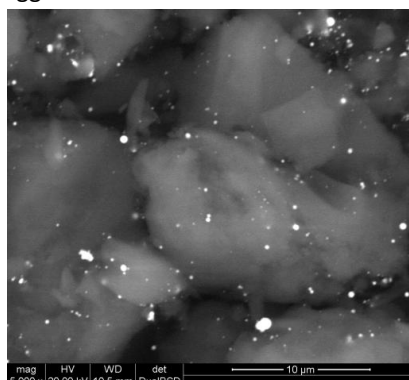
The agglomerates obtained via two-step syntheses were larger than those obtained by one pot, which could explain why the NPs synthesized by two steps could not be easily observed by TEM. These results suggest that the one pot synthesis enables a more homogeneous dispersion of the NPs on the support (in AC and  $\alpha$ -Al<sub>2</sub>O<sub>3</sub> supports) than the two-step synthesis. Furthermore, for both type of synthesis, the largest agglomerates were observed on AC support and the smallest agglomerates on TiO<sub>2</sub> support.

Figure 4.19 displays the ESEM characterizations of the catalysts supported with a Pd content of 2 wt%.

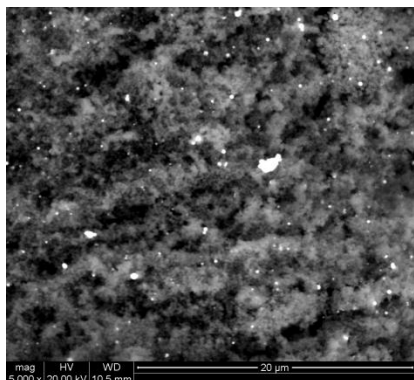
**a. Pd-PAM/AC 1, one pot**  
 agglomerates <100-2500 nm



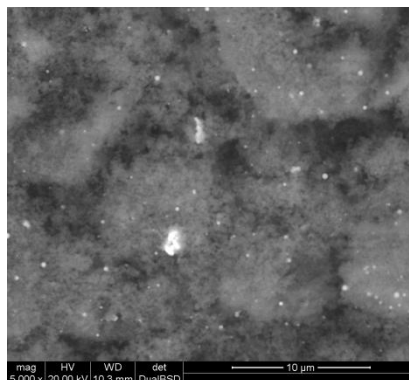
**b. Pd-PAM 6d/AC, two steps**  
 agglomerates <100-1200 nm



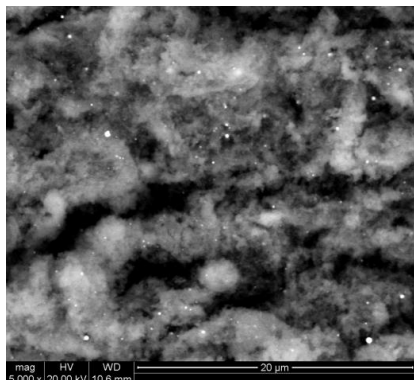
**c. Pd-PAM/ $\alpha$ -Al<sub>2</sub>O<sub>3</sub> 1, one pot**  
 agglomerates <100-1800 nm



**d. Pd-PAM 6d/ $\alpha$ -Al<sub>2</sub>O<sub>3</sub>, two steps**  
 agglomerates <100-1500 nm



**e. Pd-PAM/TiO<sub>2</sub> 1, one pot**  
 agglomerates <100-1500 nm



**f. Pd-PAM 6d/TiO<sub>2</sub>, two steps**  
 agglomerates <100-1100 nm

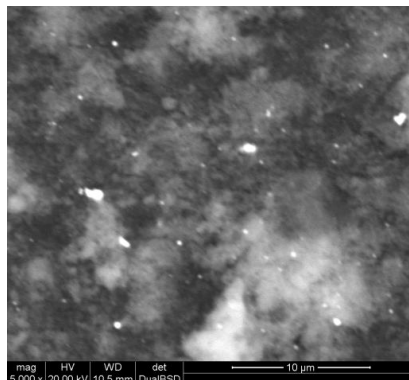


Figure 4.19. ESEM images of Pd-PAM NPs supported on AC,  $\alpha$ -Al<sub>2</sub>O<sub>3</sub> and TiO<sub>2</sub> with 2 wt% of Pd content via one pot (a, c and e) and two-step syntheses (b,d and f)

In the case of Pd-PAM NPs supported on AC, the agglomerates obtained using the two-step syntheses were smaller than those obtained using the one pot. In the case of  $\alpha$ - $\text{Al}_2\text{O}_3$  and  $\text{TiO}_2$ , the agglomeration was quite similar using both immobilization processes. Once again, the largest agglomerates were observed on AC and the smallest agglomerates on  $\text{TiO}_2$ .

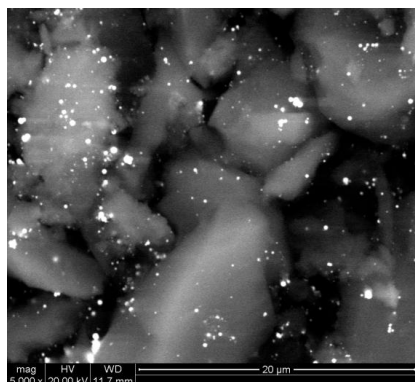
These results show that the NPs dispersion on the support is affected by the support and the immobilization process. Moreover, the trends observed between the 0.6 wt% and the 2 wt% catalysts were in opposition, indicating that the Pd content also affects the formation of well-defined supported Pd NPs. Further chemisorption characterizations would be useful to confirm these observed trends.

#### 4.3.3.2. Study of the effect of the metal concentration and its addition velocity in the two-step synthesis via ESEM characterization

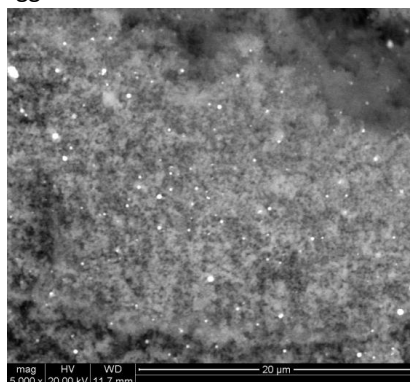
A modified recipe for two-step immobilization of Pd-PAM NPs on AC,  $\alpha$ - $\text{Al}_2\text{O}_3$  and  $\text{TiO}_2$  with 2 wt% of Pd content was tested. This recipe consisted in diluting the slurry of solid support and in decreasing the addition velocity of the colloidal NPs, in order to attempt a reduction of the agglomeration by means of a modification of mechanical parameters. The slurries of supports were diluted by 10 and the addition velocity of the suspension of colloidal NPs was also lowered by a factor of *ca.* 10.

The ESEM characterizations are presented in Figure 4.20.

a. Pd-PAM 6f/AC,  
agglomerates <100-1200 nm



b. Pd-PAM 6f/  $\alpha$ - $\text{Al}_2\text{O}_3$ ,  
agglomerates <100-600 nm



**c. Pd-PAM 6f /TiO<sub>2</sub>,**

agglomerates <100-800 nm

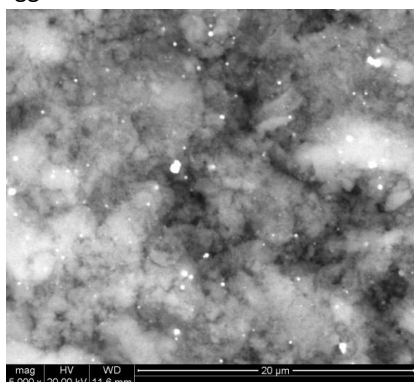


Figure 4.20. ESEM images of Pd-PAM NPs supported on AC,  $\alpha$ -Al<sub>2</sub>O<sub>3</sub> and TiO<sub>2</sub> with 2 wt% of Pd content by a modified two-step synthesis

In the case of Pd NPs supported on AC, the agglomerates observed by ESEM showed approximately the same size than those obtained using the previous two-step recipe. In contrast, the Pd NPs supported on  $\alpha$ -Al<sub>2</sub>O<sub>3</sub> and TiO<sub>2</sub> via the modified two-step recipe showed lower agglomeration. In the Pd NPs supported on  $\alpha$ -Al<sub>2</sub>O<sub>3</sub>, the ranges of agglomerates were [1500-100] nm and [600-100] nm for the initial and the modified recipe, respectively. In the supported Pd NPs supported on TiO<sub>2</sub>, the ranges of agglomerates were [1100-100] nm and [800-100] nm for the initial and the modified recipe, respectively.

**4.3.3.3. Conclusion of the study of the NPs dispersion on the supports**

ESEM characterization indicated that in all the cases, the agglomerates were the smallest on TiO<sub>2</sub> and the largest on AC. These results suggest that the NPs dispersion is influenced by the intrinsic properties of each support. Indeed, AC is a non-porous support while  $\alpha$ -Al<sub>2</sub>O<sub>3</sub> and TiO<sub>2</sub> are mesoporous. Therefore when the NPs are immobilized on AC, there is no geometrical limitations that can impede the agglomeration. In contrast, the presence of a large amount of pore can block the NPs agglomeration on  $\alpha$ -Al<sub>2</sub>O<sub>3</sub> and TiO<sub>2</sub>. Moreover, these supports possess functional groups like hydroxyl groups than can favor the NPs stabilization and avoid high agglomeration issues.

When the catalysts contained 0.6 wt% of Pd, the smaller agglomerates were obtained by one pot synthesis. In contrast, the agglomeration was similar for the 2 wt% catalysts synthesized by one pot and two steps on  $\alpha$ -Al<sub>2</sub>O<sub>3</sub> and TiO<sub>2</sub>. These results suggest that the effect of the immobilization process cannot be generalized and depends on the reaction conditions and specifically the Pd content.

Finally, a reduction of the metal concentration and its addition velocity in the two-step syntheses improved the NPs dispersion on  $\alpha$ -Al<sub>2</sub>O<sub>3</sub> and TiO<sub>2</sub>. This suggests that the modification of mechanical parameters in the recipe contribute to better NPs dispersions on mesoporous supports.

#### 4.3.4. Reproduction of the well-defined catalysts at larger scale

The well-defined catalysts were reproduced in larger amount to perform catalytic tests and to complete their characterization.

##### 4.3.4.1. Pd-PAM NPs supported by one pot synthesis

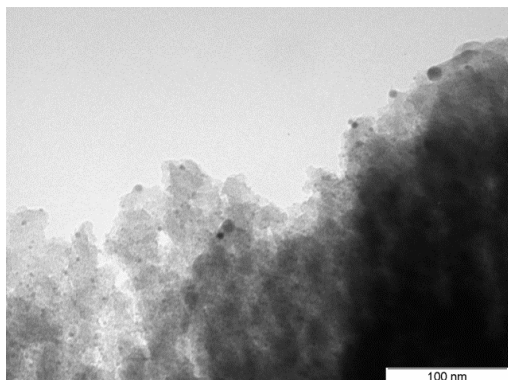
The catalysts **Pd-PAM/AC 9** and **Pd-PAM/ $\alpha$ -Al<sub>2</sub>O<sub>3</sub> 5** that contain 0.6 wt% of Pd were reproduced at usual scale since the recipes provide *ca.* 5 g of catalyst.

Then, the recipes of the catalysts **Pd-PAM/AC 1** and **Pd-PAM/ $\alpha$ -Al<sub>2</sub>O<sub>3</sub> 1** that contain 2 wt% of Pd provide *ca.* 1.4 g of catalyst, thus a scale up was attempted. The quantities of all the reagents were proportionally multiplied by 1.7 in the same Fischer Porter reactor and under the same stirring rate.

The TEM micrographs and size distribution histograms of the resulting NPs are displayed in Figure 4.21.



a. Scale up of **Pd-PAM/AC 1**  
2-20 nm



b. Scale up of **Pd-PAM/ $\alpha$ -Al<sub>2</sub>O<sub>3</sub> 1**  
Presence of non-supported NPs

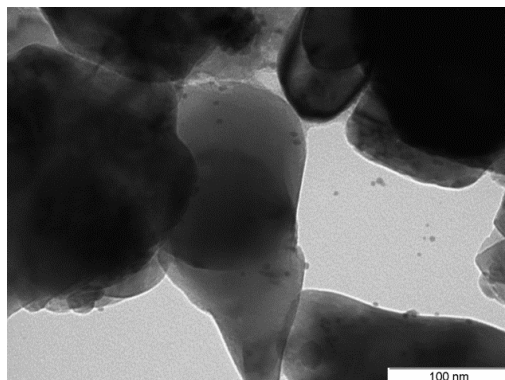


Figure 4.21. TEM micrographs of the scale up of **Pd-PAM/AC 1** and **Pd-PAM/ $\alpha$ -Al<sub>2</sub>O<sub>3</sub> 1**

In the case of the scale up of **Pd-PAM/AC 1**, the TEM results revealed a multiple distribution (NPs between 2 and 20 nm) indicating that the scale up of this synthesis affect negatively to the NPs distribution.

In the case of the scale up of **Pd-PAM/ $\alpha$ -Al<sub>2</sub>O<sub>3</sub> 1**, the TEM results showed the presence of non-supported NPs indicating that the scale of this synthesis affect negatively to the NPs immobilization.

The ESEM characterization was not performed since the results were not conclusive.

To obtain the necessary amount of these catalysts for tests in selective hydrogenation of alkynes, the syntheses were performed several times at the usual scale (30 mL) and the resulting catalysts were mixed together.

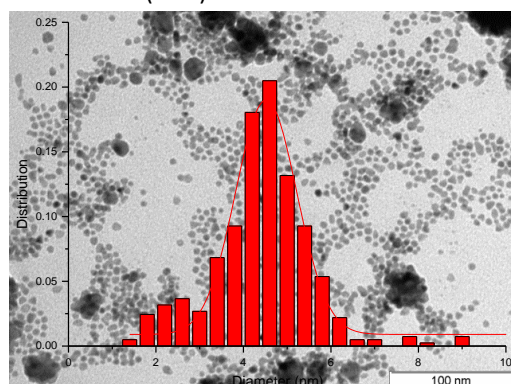
#### 4.3.4.2. Pd-PAM NPs supported by two-step synthesis

The catalysts supported on AC,  $\alpha$ -Al<sub>2</sub>O<sub>3</sub> and TiO<sub>2</sub> with 0.6 wt% of Pd content by two-step synthesis were reproduced. The colloidal step was performed at usual scale (30 mL of colloidal suspension) while the immobilization step was scaled up by doubling the reactant quantities. The TEM micrographs of the colloidal NPs and the supported catalysts are displayed in Figure 4.22.

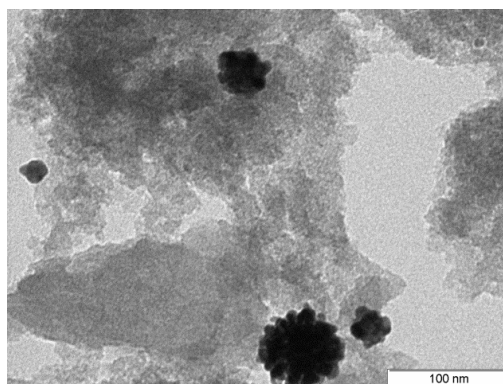


a. **Pd-PAM 6g** (normal scale)

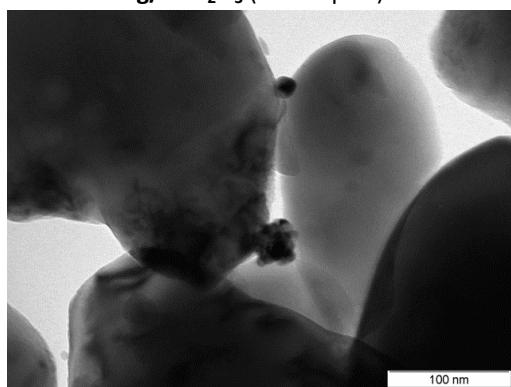
$4.5 \pm 1.5$  nm (33%)



b. **Pd-PAM 6g/AC** (scale up x2)



c. **Pd-PAM 6g/ $\alpha$ -Al<sub>2</sub>O<sub>3</sub>** (scale up x2)



d. **Pd-PAM 6g/TiO<sub>2</sub>** (scale up x2)

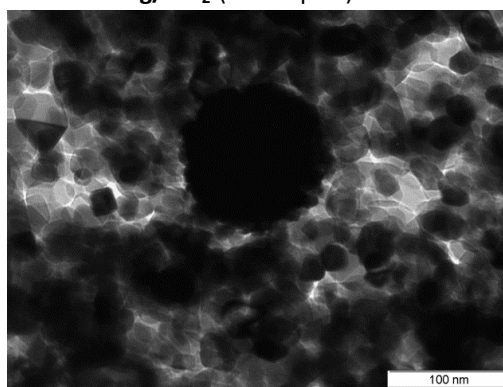


Figure 4.22. TEM micrographs of colloidal Pd-PAM 6g NPs and Pd-PAM 6g NPs supported by a scale up two-step synthesis on AC,  $\alpha$ -Al<sub>2</sub>O<sub>3</sub> and TiO<sub>2</sub> with 0.6 wt% of Pd

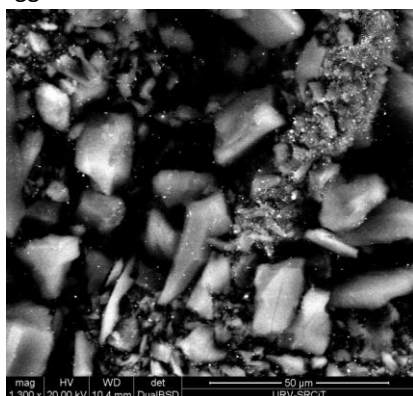
The colloidal **Pd-PAM 6g** NPs revealed a slightly larger size than usual (4.5 vs. *ca.* 3.9 nm). As in the previous two-step syntheses, single NPs could not be easily seen by TEM characterization of the supported catalysts.

X-Ray Diffraction was attempted with different analytical conditions in order to obtain more intensity of the Pd peaks and be able to estimate the NPs crystallite size despite the very low Pd content. The Pd crystallite size was obtained only for **Pd-PAM 6g/ $\alpha$ -Al<sub>2</sub>O<sub>3</sub>**: 4.77 nm. This value is close to the value of the NPs size measured by TEM of the corresponding colloidal suspension. Therefore, it was concluded that the presented two-step immobilization did not to affect the Pd NPs size.

The ESEM characterization was then performed to verify the presence of agglomeration in the samples. The results are displayed in Figure 4.23.

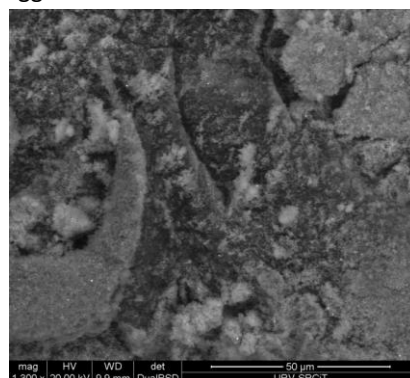
**a. Pd-PAM 6g/AC**

agglomerates <100-1500 nm



**b. Pd-PAM 6g/ $\alpha$ -Al<sub>2</sub>O<sub>3</sub>**

agglomerates <100-600 nm



**c. Pd-PAM 6g/TiO<sub>2</sub>**

agglomerates <100-400 nm

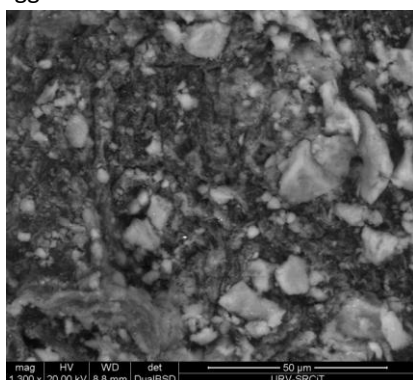


Figure 4.23. ESEM images of the scale up (2:1) of the two-step synthesis of Pd-PAM NPs on a. AC, b.  $\alpha$ -Al<sub>2</sub>O<sub>3</sub> and c. TiO<sub>2</sub> with 0.6 wt% of Pd content

The 0.6 wt% Pd catalysts supported on AC presented a higher concentration of agglomerates but with smaller sizes than that of the previously synthesized catalysts ([100-1500] nm vs. [100-2500] nm).

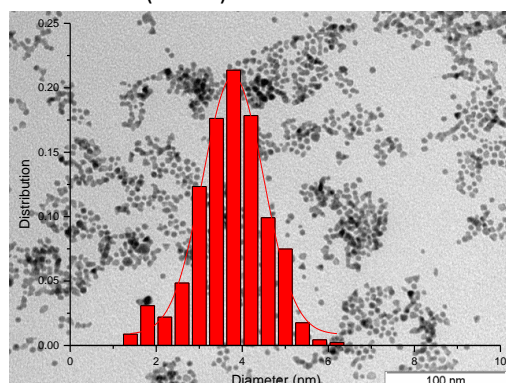
Then, on  $\alpha$ -Al<sub>2</sub>O<sub>3</sub> and TiO<sub>2</sub> supports, the agglomeration resulted to be much smaller than that obtained in the previously synthesized catalysts (without scale up): respectively [100-600] nm vs. [100-2000] nm and [100-400] nm vs. [100-1000] nm.

These results indicate that the scale up performed improved drastically the NPs dispersion on the supports.

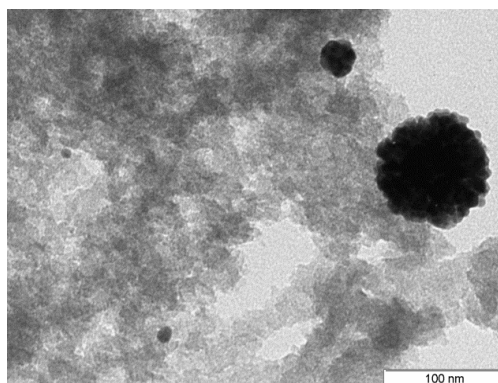
Then, the catalysts supported on AC,  $\alpha$ -Al<sub>2</sub>O<sub>3</sub> and TiO<sub>2</sub> with 2 wt% of Pd content by two-step synthesis were reproduced. The colloidal step was scaled up by a factor of 3 and the immobilization step was scaled up by a factor of 6.25. The TEM micrographs of the colloidal NPs and the supported catalysts are displayed in Figure 4.24.

a. **Pd-PAM 6h** (scale up x3)

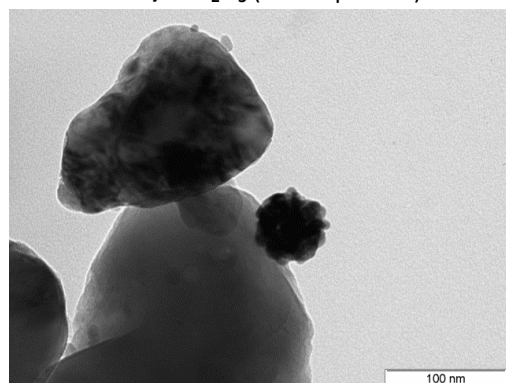
$3.8 \pm 0.8$  nm (22.0%)



b. **Pd-PAM 6h/AC** (scale up x6.25)



c. **Pd-PAM 6h/ $\alpha$ -Al<sub>2</sub>O<sub>3</sub>** (scale up x6.25)



d. **Pd-PAM 6h/TiO<sub>2</sub>** (scale up x6.25)

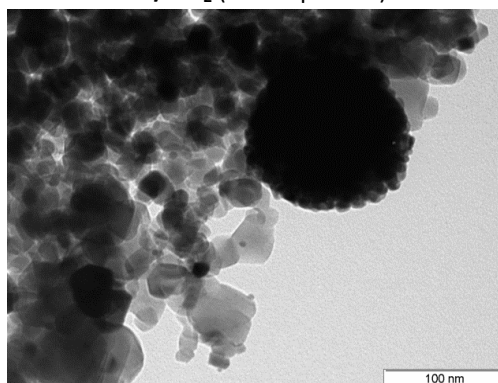


Figure 4.24. TEM micrographs of a scale up of colloidal Pd-PAM 6h NPs and supported Pd-PAM 6h on AC,  $\alpha$ -Al<sub>2</sub>O<sub>3</sub> and TiO<sub>2</sub> via two-step synthesis with 2 wt% of Pd

The colloidal **Pd-PAM 6h** revealed a size of  $3.8 \pm 0.8$  nm (22%) which is very similar to the usual size and size distribution values for these Pd-PAM NPs. This result demonstrates that this reference recipe is quite robust and could be scaled up with a factor of 3 without affecting the formation of the well-defined colloidal NPs.

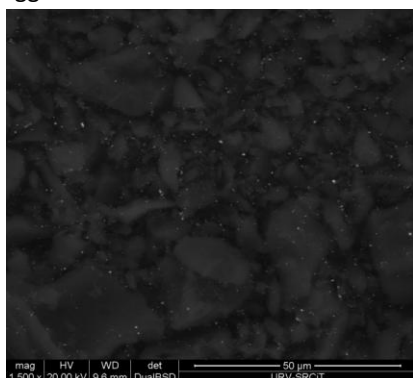
As in the previous two-step syntheses, single NPs could not be easily seen by TEM. The Pd crystallite sizes could be obtained and were equal to 6.02 nm, 5.95 nm and 5.93 nm

for, respectively, **Pd-PAM 6h/AC**, **Pd-PAM 6h/ $\alpha$ -Al<sub>2</sub>O<sub>3</sub>** and **Pd-PAM 6h/TiO<sub>2</sub>**. These sizes were slightly larger than that estimated by TEM.

The ESEM characterization was then performed to verify the presence of agglomeration in the samples. The results are displayed in Figure 4.25.

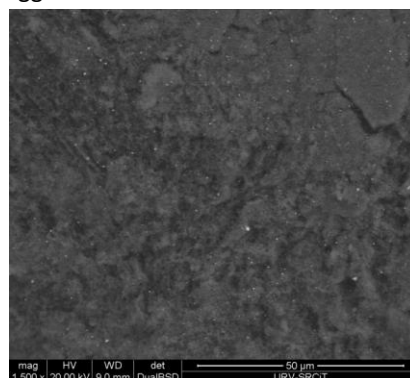
**a. Pd-PAM 6h/AC**

agglomerates <100-700 nm



**b. Pd-PAM 6h/ $\alpha$ -Al<sub>2</sub>O<sub>3</sub>**

agglomerates <100-900 nm



**c. Pd-PAM 6h/TiO<sub>2</sub>**

agglomerates <100-500 nm

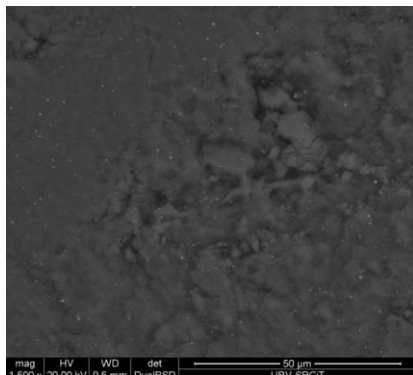


Figure 4.25. ESEM images of the scale up (6.25:1) of the two-step synthesis of Pd-PAM NPs on  
 a. AC, b.  $\alpha$ -Al<sub>2</sub>O<sub>3</sub> and c. TiO<sub>2</sub> with 2 wt% of Pd content

The 2 wt% Pd catalysts supported on AC,  $\alpha$ -Al<sub>2</sub>O<sub>3</sub> and TiO<sub>2</sub> presented more or less the same concentration of agglomerates but with much smaller sizes than that observed in the previously synthesized catalysts (without scale up) respectively [100-700] nm vs. [100-12000] nm, [100-900] nm vs. [100-1500] nm and [100-500] nm vs [100-1100] nm.

#### 4.3.4.3. Conclusions of the scale up experiments

An attempt of scale up synthesis of the well-defined supported Pd-PAM NPs on AC and  $\alpha$ -Al<sub>2</sub>O<sub>3</sub> via one pot with 2 wt% of Pd content was performed. However the scale up negatively affects the resulting NPs (wide distributions and NPs not well-immobilized on the support). These results suggest that these catalysts are highly sensitive to a geometry or stirring modification. Indeed the reactor used and the stirring rate applied were the same than in the usual scale but the liquid volume inside the reactor was multiplied by almost two leading to differences in the suspension homogenization and in the hydrogen gas diffusion. To obtain similar catalysts, deeper scale up study should be carried out. However to respect the schedule of the project the option of reproducing several small scale batches of catalysts was preferred.

After that, the scale up of the two-step syntheses was performed and revealed positive effect in terms of NPs dispersion. In both cases 0.6 wt% and 2 wt% of Pd content, the ESEM characterization showed a drastic reduction of the agglomerates sizes.

Finally, it is noteworthy that a scale up of the reference recipe of colloidal Pd-PAM NPs was performed (for the two-step syntheses of 2 wt% Pd content catalysts). The robustness of this recipe was confirmed since the resulting NPs were similar to the NPs usually synthesized at small scale.

#### 4.3.5. Characterization of the well-defined catalysts

The TEM and ESEM characterization of these catalysts were presented in the previous sections. The XRD, TGA, XPS, ICP and N<sub>2</sub> physisorption of these catalysts are given in this section.

CO chemisorptions were attempted but the remaining amount of polyacrylamide on the catalyst involved analysis issues. Therefore, calcinations or pyrolysis treatment should be applied to these catalysts in order to remove completely this stabilizer. However, this kind of thermal treatment can affect the NPs size and dispersion on the support, thus study of the effect of the thermal treatment on the resulting NPs should



be previously performed. Due to time limitations, no data were obtained from this characterization.

#### 4.3.5.1. XRD

The X-Ray Diffraction was performed and the obtained crystallite sizes are summarized in Table 4.5.

Table 4.5. X-Ray Diffraction of the well-defined supported Pd-PAM catalysts - Sum up of the crystallite sizes obtained for each of these catalysts

Catalyst	Synthesis type	Theoretical Pd content (wt%)	Crystallite size (nm)	NPs size measured by TEM (nm)	ESEM aggl. range (nm)
<b>Pd-PAM/AC 1</b>	One pot	2.00	5.86	3.7	100-2500
<b>Pd-PAM/AC 9</b>	One pot	0.60	<sup>a</sup>	3.6	100-1500
<b>Pd-PAM 6h/AC</b>	Two steps	2.00	6.02	3.9 <sup>b</sup>	100-700
<b>Pd-PAM 6g/AC</b>	Two steps	0.60	<sup>a</sup>	3.9 <sup>b</sup>	100-1500
<b>Pd-PAM/<math>\alpha</math>-Al<sub>2</sub>O<sub>3</sub> 1</b>	One pot	2.00	4.10	4.5	100-1800
<b>Pd-PAM/<math>\alpha</math>-Al<sub>2</sub>O<sub>3</sub> 5</b>	One pot	0.60	3.60	4.8	100-1000
<b>Pd-PAM 6h/<math>\alpha</math>-Al<sub>2</sub>O<sub>3</sub></b>	Two steps	2.00	5.95	3.9 <sup>b</sup>	100-900
<b>Pd-PAM 6g/<math>\alpha</math>-Al<sub>2</sub>O<sub>3</sub></b>	Two steps	0.60	4.77	3.9 <sup>b</sup>	100-600
<b>Pd-PAM 6h/TiO<sub>2</sub></b>	Two steps	2.00	5.93	3.9 <sup>b</sup>	100-500
<b>Pd-PAM 6g/TiO<sub>2</sub></b>	Two steps	0.60	<sup>a</sup>	3.9 <sup>b</sup>	100-400

<sup>a</sup>: The XRD characterization was performed but a too low intensity of the Pd peaks did not enable the estimation of the crystallite size

<sup>b</sup>: The value corresponds to the mean NPs size of the reference colloidal suspension.

The crystalline structure of the supported Pd-PAM catalysts was attributed to fcc packing. For three of the ten analysed catalysts, the crystallite size could not be estimated due to a too low intensity of the Pd peaks (these catalysts corresponds to a theoretical amount of Pd of 0.6 wt%).

For the other catalysts the average size obtained for the crystalline part was obtained and resulted to be slightly larger than the NPs size measured by TEM except for two catalysts: **Pd-PAM/ $\alpha$ -Al<sub>2</sub>O<sub>3</sub> 1** and **Pd-PAM/ $\alpha$ -Al<sub>2</sub>O<sub>3</sub> 5**. Nevertheless the range of value was similar.

It is necessary to keep in mind that the nature of the measurement of both techniques is different and thus a direct comparison of the obtained sizes is not straightforward. Indeed, transmission electron microscopy is a tool to have an overview of the homogeneity of a sample. The average size and size distribution of a series of NPs depends on the consideration of several hundreds of particles and to the adjustment of a representative function (usually, Gaussian or LogNormal functions are used). Lack of contrast or overlap of particles frequently complicates the TEM analysis because the particle boundaries cannot always be seen precisely.<sup>18,19</sup>

X-Ray Diffraction is an indirect method but provide more reliable information from a statistical point of view. However, the size obtained by diffraction cannot be easily compared to the sizes determined by other techniques. Sizes obtained from XRD measurements do not represent the particle size but the size of the crystalline domain within the particle. Since we do not necessarily have perfect single crystal, the particles may consist of more than one domain and the size would be potentially underestimated.<sup>18</sup> XRD is sensitive to the size of coherent scattering domains which can significantly differ from the particle size in the case of eventually present lattice defects or amorphous surface layers.<sup>19</sup>

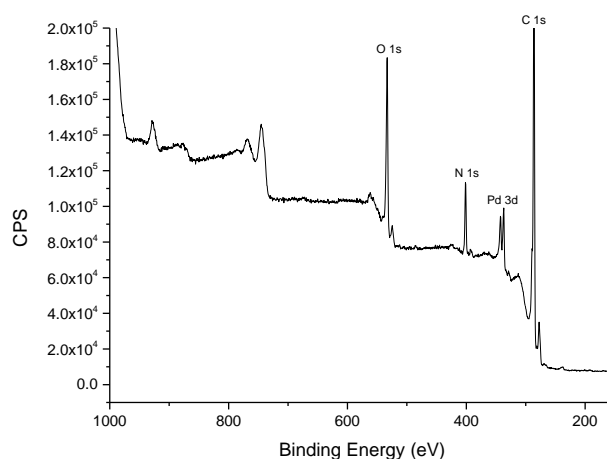
It must be kept in mind that TEM allows a measure of the particle size while the XRD provide the crystallite size. These two parameters do not have the same meaning. For instance, negative deviations of the XRD size compared to the TEM size could occur when the particles are composed from several small crystallites or when a fraction of the particles are not fully crystalline.

In contrast, positive deviation of the XRD size compared to the TEM size could be related to deficiencies in the TEM sampling which are intrinsic to the analysis.

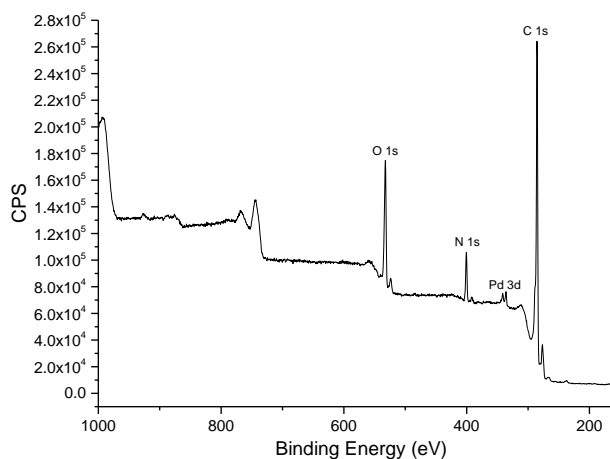
#### **4.3.5.2. XPS of the 2 wt% Pd content catalysts**

The NPs surface analysis was performed by X-Ray Photoelectron Spectroscopy (XPS). The full XPS spectra of the 2 wt% supported Pd-PAM NPs are displayed in Figure 4.26.

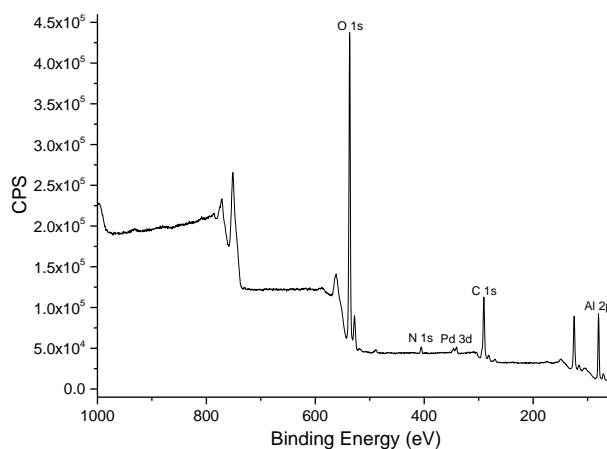
**a. Pd-PAM/AC 1**



**b. Pd-PAM 6h/AC**

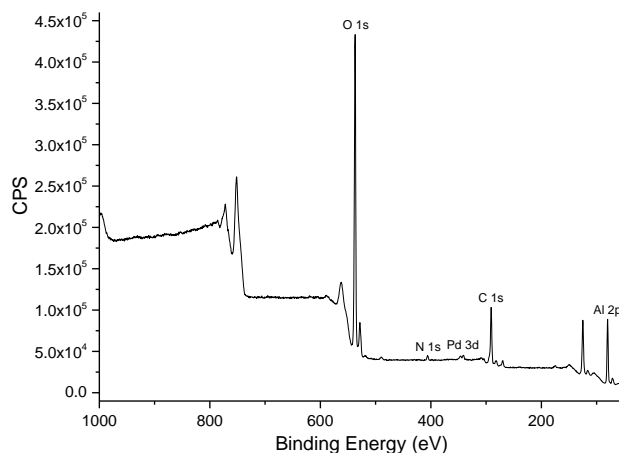


**c. Pd-PAM/ $\alpha$ -Al<sub>2</sub>O<sub>3</sub> 1**





**d. Pd-PAM 6h/ $\alpha$ -Al<sub>2</sub>O<sub>3</sub>**



**e. Pd-PAM 6h/TiO<sub>2</sub>**

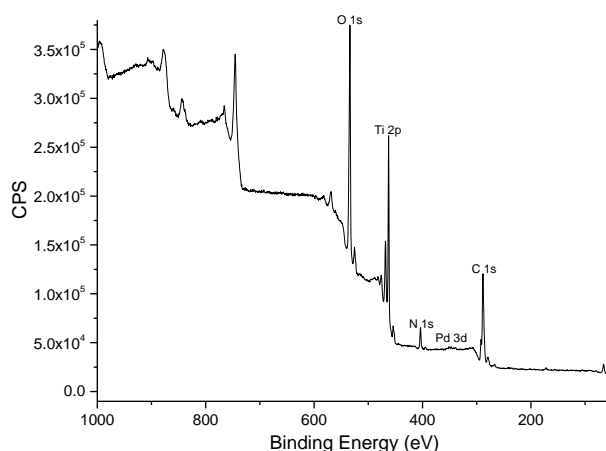
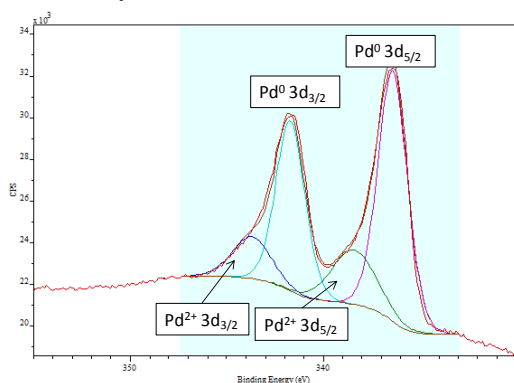


Figure 4.26. Full XPS spectra of the 2 wt% Pd-PAM NPs catalysts

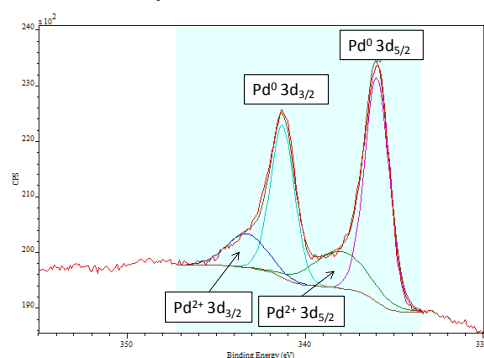
In all the cases, the full XPS spectra revealed the presence of O, N, Pd and C according to the peaks observed at their characteristic binding energies (respectively 532.0, 400.0, 335.5 and 285.5 eV). Al and Ti were also detected in the catalyst supported on  $\alpha$ -Al<sub>2</sub>O<sub>3</sub> and TiO<sub>2</sub>, respectively.

The deconvolution of Pd 3d<sub>5/2</sub> and Pd 3d<sub>3/2</sub> peaks was performed using Tressaud data from Pd species and are presented in the XPS spectra of Pd in Figure 4.27.<sup>20</sup>

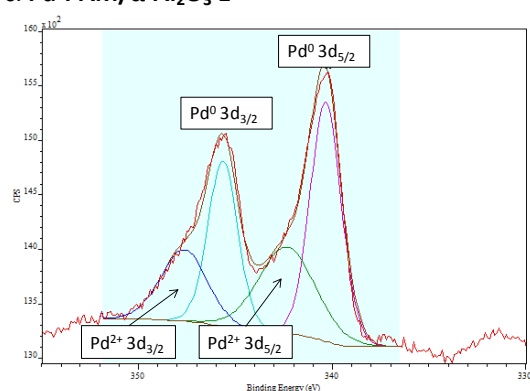
a. Pd-PAM/AC 1



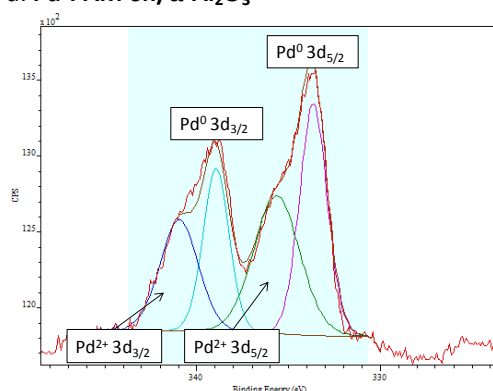
b. Pd-PAM 6h/AC



c. Pd-PAM/ $\alpha$ -Al<sub>2</sub>O<sub>3</sub> 1



d. Pd-PAM 6h/ $\alpha$ -Al<sub>2</sub>O<sub>3</sub>



e. Pd-PAM 6h/TiO<sub>2</sub>

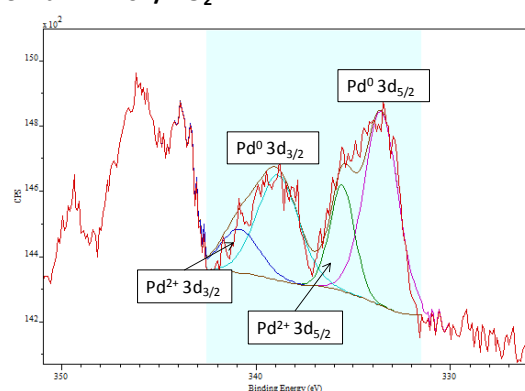


Figure 4.27. XPS spectra of Pd for the 2 wt% Pd-PAM catalysts - Deconvolution of Pd 3d<sub>5/2</sub> and Pd 3d<sub>3/2</sub> peaks

The spectra exhibited two important peaks around 335 and 340 eV assigned to Pd 3d<sub>5/2</sub> and Pd 3d<sub>3/2</sub> of the Pd<sup>0</sup> species and two smaller peaks at 337 and 342 eV assigned to Pd 3d<sub>5/2</sub> and Pd 3d<sub>3/2</sub> of Pd<sup>2+</sup> species.

The fraction of  $\text{Pd}^0$  and  $\text{Pd}^{2+}$  were extracted from the decomposition of the spin orbit peak of low energy. The contents of  $\text{Pd}^0$  and  $\text{Pd}^{2+}$  for each of the analyzed catalysts are summarized in Table 4.6.

Table 4.6. XPS analysis of the 2 wt% Pd-PAM supported catalysts - Sum up of the estimated percentage of  $\text{Pd}^0$  and  $\text{Pd}^{2+}$  at the surface of the catalysts

Catalyst	Synthesis type	$\text{Pd}^0$ (%)	$\text{Pd}^{2+}$ (%)
<b>Pd-PAM/AC 1</b>	One pot	75.50	24.50
<b>Pd-PAM 6h/AC</b>	Two steps	73.04	26.96
<b>Pd-PAM/<math>\alpha</math>-<math>\text{Al}_2\text{O}_3</math> 1</b>	One pot	60.00	40.00
<b>Pd-PAM 6h/<math>\alpha</math>-<math>\text{Al}_2\text{O}_3</math></b>	Two steps	50.12	49.88
<b>Pd-PAM 6h/<math>\text{TiO}_2</math></b>	Two steps	71.73	28.27

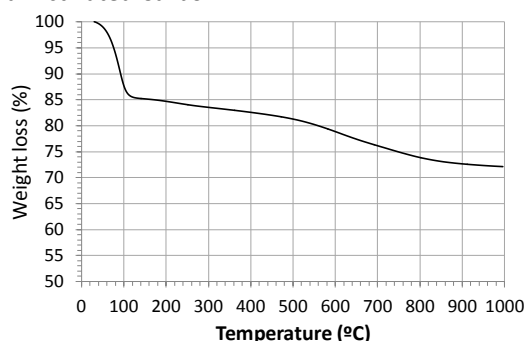
Note that the XPS spectra was only performed on the 2 wt% catalysts since very low intensities of the Pd peaks were obtained resulting in a loss of accuracy of the determined fraction (especially in the case of Pd-PAM 6h/ $\text{TiO}_2$ ). Therefore, with almost four times less Pd in the catalysts (0.6 wt%), the estimation of the content of  $\text{Pd}^0$  and  $\text{Pd}^{2+}$  was expected to be much more complicated.

#### 4.3.5.3. TGA

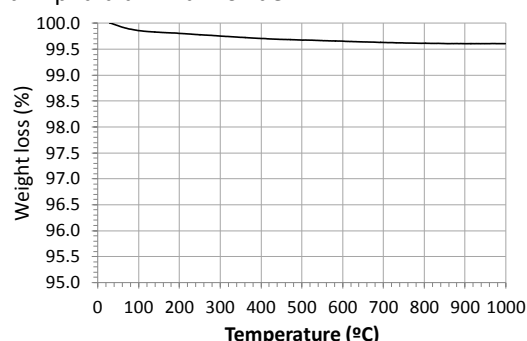
The thermal stability of the supported catalysts was examined by TGA.

The thermograms of the supports and the polyacrylamide stabilizer used to synthesize the Pd-PAM catalysts are displayed in Figure 4.28, their derivatives are given in appendix 4.5.

a. Activated Carbon



b. Alpha-aluminium oxide



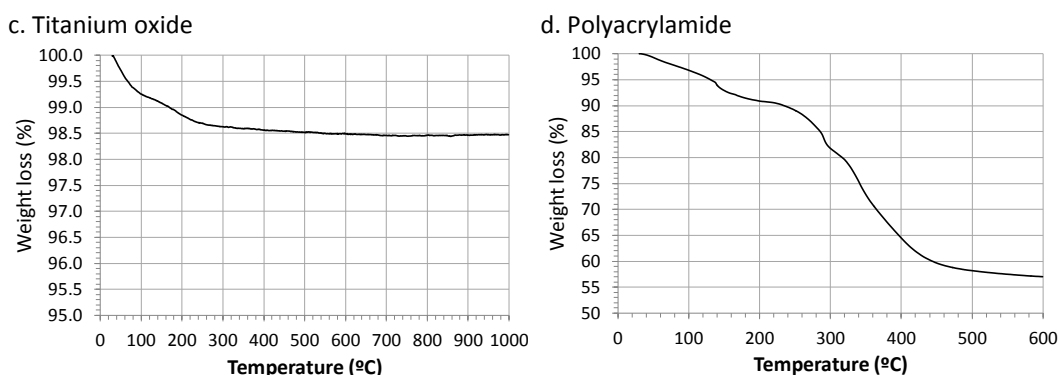


Figure 4.28. TGA thermogram of the supports and the stabilizer used in this chapter

The thermogram corresponding to AC support showed a 14.5% loss between 30°C and 140°C attributed to the loss of absorbed solvent (water for example). Other loss of 1.8% and 11.2% were observed between 150°C and 300°C and 300°C and 985°C, respectively. These losses could be associated to the decomposition of functional groups on the carbon surface.

The thermogram corresponding to  $\alpha$ -Al<sub>2</sub>O<sub>3</sub> support show highly thermal stability of this support and revealed a loss of 0.40% between 30°C and 180°C attributed to the loss of absorbed solvent.

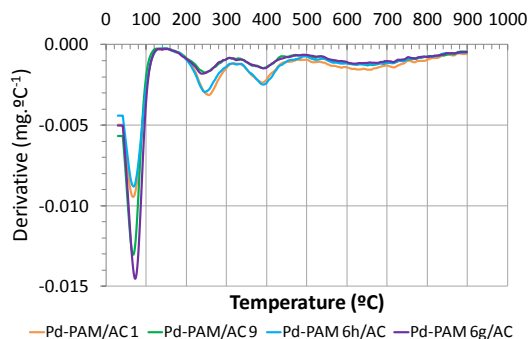
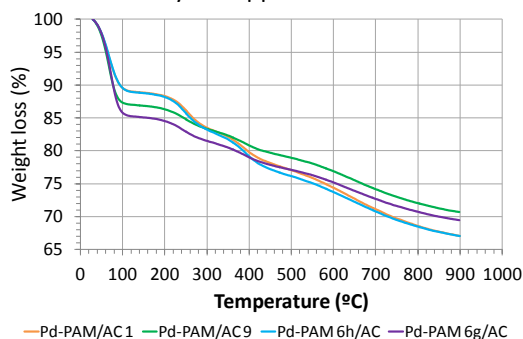
The thermogram corresponding to TiO<sub>2</sub> support showed a loss of 1.4% between 30°C and 400°C.

It could be notice that the AC supports was able to absorb much more quantity of solvent than the  $\alpha$ -Al<sub>2</sub>O<sub>3</sub> and TiO<sub>2</sub> supports.

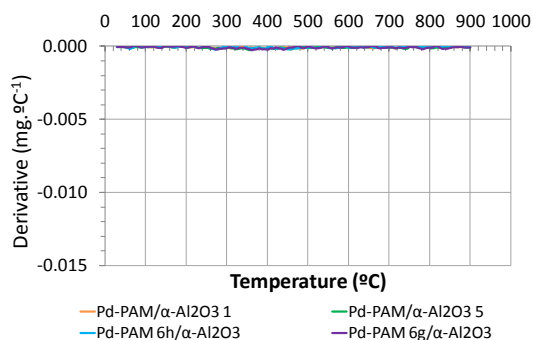
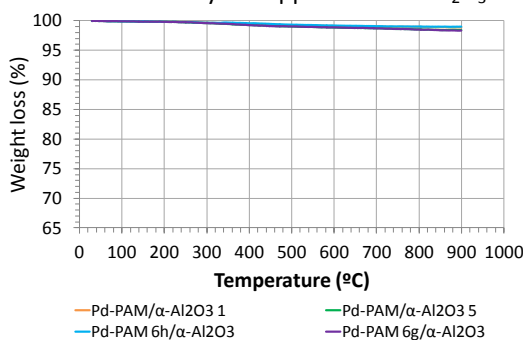
Finally, the thermogram corresponding to polyacrylamide stabilizer showed 9% of loss between 30°C and 200°C attributed to the loss of absorbed solvent. Then, the decomposition of this polymer occurred between 200°C and 500°C. Two slopes were observed. The first one between 200°C and 300°C were 10.1% of weight loss was estimated. The second one between 300°C and 500°C were 23.5% of weight loss was measured.

The thermogram of the Pd-PAM catalysts supported on AC,  $\alpha$ -Al<sub>2</sub>O<sub>3</sub> and TiO<sub>2</sub> supports and their derivatives are given in Figure 4.29

a. Pd-PAM catalysts supported on AC



b. Pd-PAM catalysts supported on  $\alpha$ -Al<sub>2</sub>O<sub>3</sub>



c. Pd-PAM catalysts supported on TiO<sub>2</sub>

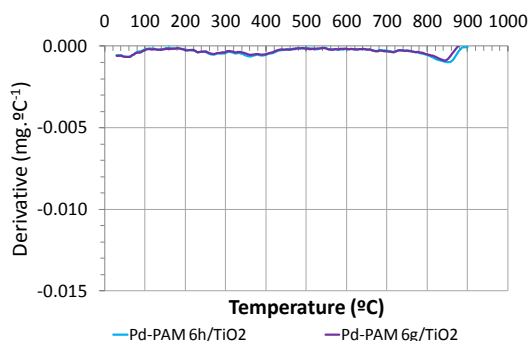
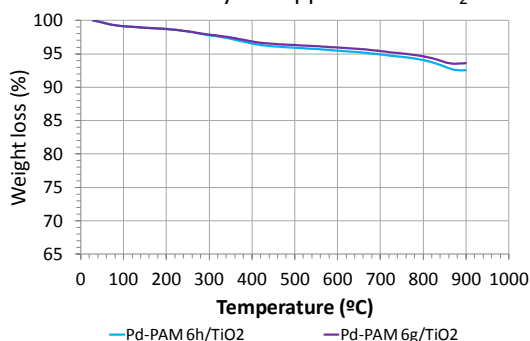


Figure 4.29. TGA thermograms and derivatives of the Pd-PAM catalysts supported on AC,  $\alpha$ -Al<sub>2</sub>O<sub>3</sub> and TiO<sub>2</sub>

Similar trends were observed for each set of catalysts (supported on AC,  $\alpha$ -Al<sub>2</sub>O<sub>3</sub> and TiO<sub>2</sub>). As a general remark the weight loss on  $\alpha$ -Al<sub>2</sub>O<sub>3</sub> and TiO<sub>2</sub> supports were much smaller than on AC. The estimations of these losses are summarized in Table 4.7.

Table 4.7. Estimation of the weight loss as a function of the temperature for the analyzed Pd-PAM catalysts

Catalyst	Synthesis type	Weight loss between 30°C and 200°C (%)	Weight loss between 200°C and 500 °C (%)	Weight loss superior to 500°C (%)
<b>Pd-PAM/AC 1</b>	One pot	10.44	10.95	10.82
<b>Pd-PAM/AC 9</b>	One pot	12.20	7.16	9.13
<b>Pd-PAM 6h/AC</b>	Two steps	10.45	12.67	9.12
<b>Pd-PAM 6g/AC</b>	Two steps	14.25	7.77	7.92
<b>Pd-PAM/<math>\alpha</math>-Al<sub>2</sub>O<sub>3</sub> 1</b>	One pot		1.12	
<b>Pd-PAM/<math>\alpha</math>-Al<sub>2</sub>O<sub>3</sub> 5</b>	One pot		1.57	
<b>Pd-PAM 6h/<math>\alpha</math>-Al<sub>2</sub>O<sub>3</sub></b>	Two steps		1.01	
<b>Pd-PAM 6g/<math>\alpha</math>-Al<sub>2</sub>O<sub>3</sub></b>	Two steps		1.68	
<b>Pd-PAM 6h/TiO<sub>2</sub></b>	Two steps	0.77	3.15	3.49
<b>Pd-PAM 6g/TiO<sub>2</sub></b>	Two steps	0.76	2.78	2.85

The weight loss between 30°C and 200°C were associated to absorbed solvent and the weight loss between 200°C and 500°C were associated to the polymer (polyacrylamide).

In general, it could be observed that much higher quantities of solvent and polymer were absorbed on the surface of the AC catalysts than  $\alpha$ -Al<sub>2</sub>O<sub>3</sub> and TiO<sub>2</sub>.

Concerning the catalyst supported on  $\alpha$ -Al<sub>2</sub>O<sub>3</sub>, the weight loss was so small that it was not possible to distinguish the slope of absorbed solvent and polymer. Thus the percentage given take into account the entire weight loss observed from 30°C to 1000°C.

For the catalyst supported on TiO<sub>2</sub>, *ca.* 3% loss was observed around 850°C, this loss was not observed in the TGA of the naked support. Moreover, it was noticed that this loss was more important for the 2 wt% catalyst than the 0.6 wt% (**Pd-PAM 6h/TiO<sub>2</sub>** and **Pd-PAM 6g/TiO<sub>2</sub>**, respectively). Their preparation method implies that a higher amount of metal was associated to a larger amount of polymer in the reaction media. This observation suggests that this loss could be associated to polyacrylamide. A part of this polymer could have interacted with the TiO<sub>2</sub> support to form a more stable substance decomposing at higher temperatures.

#### 4.3.5.4. ICP

ICP analyses were performed to determine the real Pd content on each catalysts.

The results are summarized in Table 4.8

Table 4.8. XPS analysis of the Pd-PAM supported catalysts - Sum up of the Pd content measured

Catalyst	Synthesis type	ICP measure 1 (%)	ICP measure 2 (%)	Theoretical amount of Pd (%)
<b>Pd-PAM/AC 1</b>	One pot	1.33	1.36	2.00
<b>Pd-PAM/AC 9</b>	One pot	0.46	0.46	0.60
<b>Pd-PAM 6h/AC</b>	Two steps	1.23	1.22	2.00
<b>Pd-PAM 6g/AC</b>	Two steps	0.43	0.42	0.60
<b>Pd-PAM/<math>\alpha</math>-Al<sub>2</sub>O<sub>3</sub> 1</b>	One pot	1.86	1.87	2.00
<b>Pd-PAM/<math>\alpha</math>-Al<sub>2</sub>O<sub>3</sub> 5</b>	One pot	0.61	0.56	0.60
<b>Pd-PAM 6h/<math>\alpha</math>-Al<sub>2</sub>O<sub>3</sub></b>	Two steps	1.72	1.73	2.00
<b>Pd-PAM 6g/<math>\alpha</math>-Al<sub>2</sub>O<sub>3</sub></b>	Two steps	0.48	0.48	0.60
<b>Pd-PAM 6h/TiO<sub>2</sub></b>	Two steps	1.00	1.59	2.00
<b>Pd-PAM 6g/TiO<sub>2</sub></b>	Two steps	0.46	0.46	0.60

The real Pd content were systematically slightly lower than the theoretical Pd content, indicating a loss of Pd metal during synthetic, washing or isolation process.

#### 4.3.5.5. N<sub>2</sub> Physisorption

The N<sub>2</sub> physisorption was performed in order to analyze the porous structure of the Pd-PAM catalyst (surface area, pore volume and pore size distribution). The results are summarized in Table 4.9.

Table 4.9. N<sub>2</sub> physisorption - Sum up of the BET surface area, total pore volume and average pore width of the supported Pd-PAM catalysts

Catalyst	Synthesis type	Theoretical Pd content	BET surface area (m <sup>2</sup> /g)	Total pore volume (cm <sup>3</sup> /g)	BJH average pore width (Å)
<b>Pd-PAM/AC 1</b>	One pot	2.00	625.39	0.67	36.00
<b>Pd-PAM/AC 9</b>	One pot	0.60	1060.36	0.98	30.82
<b>Pd-PAM 6h/AC</b>	Two steps	2.00	641.12	0.67	36.00
<b>Pd-PAM 6g/AC</b>	Two steps	0.60	1024.93	0.95	31.24
<b>Pd-PAM/<math>\alpha</math>-Al<sub>2</sub>O<sub>3</sub> 1</b>	One pot	2.00	7.85	0.03	106.01
<b>Pd-PAM/<math>\alpha</math>-Al<sub>2</sub>O<sub>3</sub> 5</b>	One pot	0.60	7.95	0.03	92.86
<b>Pd-PAM 6h/<math>\alpha</math>-Al<sub>2</sub>O<sub>3</sub></b>	Two steps	2.00	8.19	0.03	101.28
<b>Pd-PAM 6g/<math>\alpha</math>-Al<sub>2</sub>O<sub>3</sub></b>	Two steps	0.60	6.75	0.03	112.48
<b>Pd-PAM 6h/TiO<sub>2</sub></b>	Two steps	2.00	/	/	/
<b>Pd-PAM 6g/TiO<sub>2</sub></b>	Two steps	0.60	51.67	0.39	226.01

It was observed that the BET surface area of the catalysts supported on AC were large and in agreement with the typically BET area reported for carbon supports.<sup>21</sup> It was noticed that the BET area of the supports that contained 2 wt% of Pd was systematically smaller than that of 0.6 wt% (*ca.* 600 and 1000 m<sup>2</sup>/g, respectively). The same observation was made for the total pore volume and the average pore width: the pores were smaller for the 2 wt% catalysts. The pore average width values indicate that these catalysts present micro and meso-porosity contributions.<sup>22</sup>

Concerning the catalysts supported on  $\alpha$ -Al<sub>2</sub>O<sub>3</sub> the BET surface area was very small (*ca.* 7 m<sup>2</sup>/g) and no trends in relation with immobilization process or the Pd content was observed. The total volumes of pores were small (0.03 cm<sup>3</sup>/g) while the width was large (*ca.* 100 Å) that these catalysts were mainly mesoporous.<sup>22</sup>

Finally, only one catalyst on TiO<sub>2</sub> could be analyzed, it revealed small BET surface area but still larger than  $\alpha$ -Al<sub>2</sub>O<sub>3</sub>. The average pore width suggests a mesoporous catalyst.



## 4.4. Conclusions

In this chapter, recipes of well-defined supported Pd-PAM catalysts were delivered. Two immobilization methodologies were studied: the one pot approach and the two-step synthesis.

First, the effect of some synthetic parameters on the formation of supported Pd-PAM NPs on various solid supports via one pot synthesis was investigated. The main conclusions obtained are recalled as follow.

- A decrease of temperature from 50°C to 35°C resulted in smaller NPs sizes on AC and  $\alpha$ -Al<sub>2</sub>O<sub>3</sub> (*ca.* 2 nm and 3.5 nm, respectively). The opposite trend was observed on TiO<sub>2</sub> (*ca.* 2.6 nm and 3.8 nm for 50°C and 35°C, respectively). These results show that the NPs sizes depend on the reaction conditions and the intrinsic properties of the chosen support.
- No effect in terms of NPs size and distribution was observed when the Pd content was decreased from 2 wt% to 0.6 wt% on AC and  $\alpha$ -Al<sub>2</sub>O<sub>3</sub>. In contrast, multiple distributions were obtained on TiO<sub>2</sub> when the Pd content was reduced. This observation was related to the intrinsic properties of the support and the reaction set-up. To obtain well-defined supported NPs on TiO<sub>2</sub> with 0.6 wt% of Pd content, the Pd concentration was decreased from 9.4 mM to 3.1 mM.
- The effect of the PAM-to-Pd ratio on Pd-PAM NPs supported on AC was looked at. A decrease from 40 to 20 equivalents did not affect the formation of the NPs however when 10 equivalents of PAM were used, the NPs distribution was drastically affected. It suggests that a minimum amount of stabilizer is necessary to maintain a narrow distribution.

This study revealed that a precise control of supported NPs size using one pot synthesis is quite complex and depends on a high number of parameters such as reaction conditions, intrinsic properties of the supports and geometry of the set-up.

Afterwards, a simple two-step mixing methodology was proposed to induce the immobilization of colloidal Pd-PAM NPs on various supports. It was confirmed that the NPs size of the colloidal suspension was not affected by this process. Catalysts with 2 wt% and 0.6 wt% on AC,  $\alpha$ -Al<sub>2</sub>O<sub>3</sub> and TiO<sub>2</sub> were synthesized.

Finally, the effects of the type of support, immobilization process, Pd content and scale of the synthesis on the NPs dispersion was studied using ESEM characterization.

The main conclusions are given as follow.

- In all the studied cases, the smallest agglomerates were observed on TiO<sub>2</sub> and the largest on AC indicating that the intrinsic properties of the supports influence the NPs dispersion.
- An effect of the immobilization process on the NPs dispersion was observed with the low Pd content catalysts: smaller agglomerates were obtained using one pot syntheses at 0.6 wt% of Pd content. In contrast, when 2 wt% of Pd content were immobilized on the supports, the trend was not clear. Similar agglomerate sizes were measured on the one pot and two-step catalysts supported on  $\alpha$ -Al<sub>2</sub>O<sub>3</sub> and TiO<sub>2</sub>. However smaller agglomerate sizes were obtained on the two-step synthesis of Pd on AC.

These results suggest that the effects of the immobilization process and Pd content cannot be generalized and may interact between each other.

- A dilution of the slurry of support combined with a reduction of the metal addition velocity in the two-step synthesis led to an improvement in NPs dispersion on  $\alpha$ -Al<sub>2</sub>O<sub>3</sub> and TiO<sub>2</sub>, suggesting that a modification of the mechanical parameters in this recipe favors a better dispersion of the NPs on the mesoporous supports.
- The scale up of the well-defined catalysts obtained via one pot and two-step syntheses were studied. Wide NPs distribution and inefficient immobilization were obtained for the one pot synthesis of Pd-PAM NPs on AC and  $\alpha$ -Al<sub>2</sub>O<sub>3</sub>. In contrast, with two-step immobilization positive effect in terms of NPs dispersion was noticed for all the tested supports with both 0.6 wt% and 2

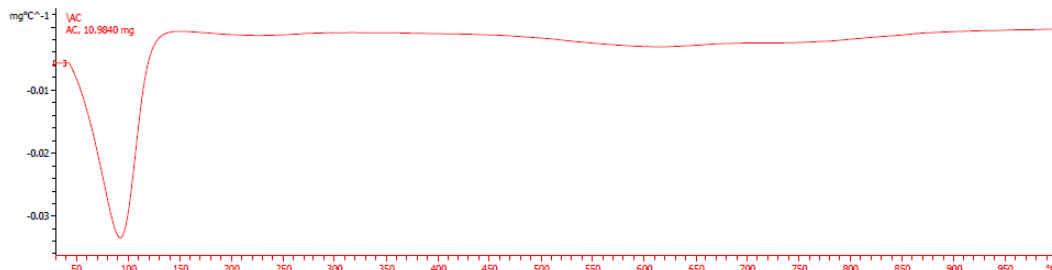
wt% of Pd content. The hydrodynamics induced in these new scale syntheses were favorable to the better dispersion of NPs.

Finally, during this study, a scale up of the reference colloidal Pd-PAM NPs (**Pd-PAM 6** synthesized in chapter 3) was performed and confirmed the robustness of this recipe.

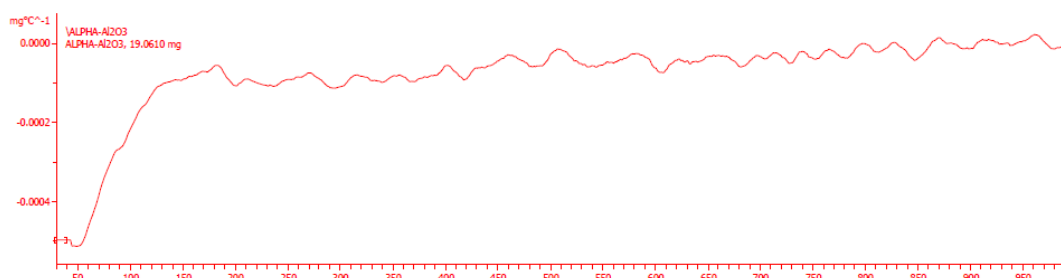
## 4.5. Appendix: TGA characterization

TGA derivatives of support and stabilizer used in this chapter.

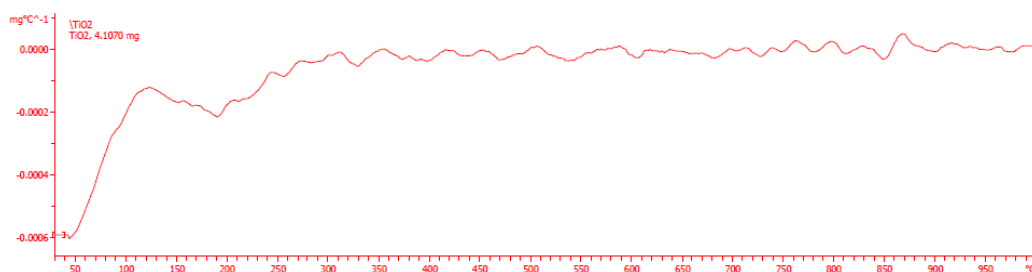
Activated Carbon



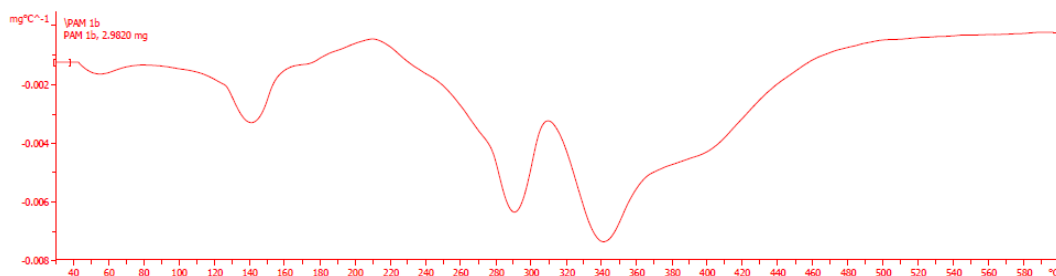
Alpha-aluminium oxide



Titanium oxide



Polyacrylamide



## 4.6. References

- (1) Sant, S. B. *Mater. Manuf. Processes* **2012**, 27, 1462.
- (2) Roucoux, A.; Schulz, J.; Patin, H. *Chem. Rev.* **2002**, 102, 3757.
- (3) Crespo-Quesada, M.; Cárdenas-Lizana, F.; Dessimoz, A.-L.; Kiwi-Minsker, L. *ACS Catal.* **2012**, 2, 1773.
- (4) Llop Castelbou, J.; Szeto, K. C.; Barakat, W.; Merle, N.; Godard, C.; Taoufik, M.; Claver, C. *Chem. Commun.* **2017**, 53, 3261.
- (5) Gong, T.; Qin, L.; Zhang, W.; Wan, H.; Lu, J.; Feng, H. *J. Phys. Chem. C* **2015**, 119, 11544.
- (6) Delgado, J. A.; Claver, C.; Castellón, S.; Curulla-Ferré, D.; Ordonsky, V. V.; Godard, C. *App. Catal. A Gen.* **2016**, 513, 39.
- (7) Hubert, C.; Bilé, E. G.; Denicourt-Nowicki, A.; Roucoux, A. *App. Catal. A Gen.* **2011**, 394, 215.
- (8) Delgado, J. A.; Claver, C.; Castellón, S.; Curulla-Ferré, D.; Ordonsky, V. V.; Godard, C. *J. Mol. Catal. A: Chem.* **2016**, 417, 43.
- (9) Diaz de los Bernardos, M.; Pérez-Rodríguez, S.; Gual, A.; Claver, C.; Godard, C. *Chem. Commun.* **2017**, 53, 7894.
- (10) Montiel, L.; Delgado, J. A.; Novell, M.; Andrade, F. J.; Claver, C.; Blondeau, P.; Godard, C. *ChemCatChem* **2016**, 8, 3041.
- (11) Parrada da Silva, F.; Luiz Fiorio, J.; Marcia Rossi, L. *ACS Omega* **2017**, 2, 6014.
- (12) Hu, J.; Zhou, Z.; Zhang, R.; Li, L.; Cheng, Z. *J. Mol. Catal. A: Chem.* **2014**, 381, 61.
- (13) Brunauer, S.; Emmett, P. H.; Teller, E. *J. Am. Chem. Soc.* **1938**, 60, 309.
- (14) Barrett, E. P.; Joyner, L. G.; Halenda, P. P. *J. Am. Chem. Soc.* **1951**, 73, 373.
- (15) Miyittah, M. K.; Tsaywo, F. W.; Kumah, K. K.; Stanley, C. D.; Rechcigl, J. E. *Commun. soil sci. plan.* **2015**, 47, 101.
- (16) Zetasizer Nano series: Performance, S., Versatility Malvern Instruments Limited, [https://www.malvernpanalytical.com/en/assets/MRK1839\\_tcm50-17228.pdf](https://www.malvernpanalytical.com/en/assets/MRK1839_tcm50-17228.pdf), consulted in 2017.
- (17) Witte, P. T. *Process for the preparation of an aqueous colloidal precious metal suspension*, US Patent 8,822,725 B2 **2014**.
- (18) Crespo-Quesada, M.; Yarulin, A.; Jin, M.; Xia, Y.; Kiwi-Minsker, L. *J. Am. Chem. Soc.* **2011**, 133, 12787.
- (19) Borchert, H.; Shevchenko, E. V.; Robert, A.; Mekis, I.; Kornowski, A.; Grübel, G.; Weller, H. *Langmuir* **2005**, 21, 1931.
- (20) Tressaud, A.; Khairoun, S.; Touhara, H.; Watanabe, N. Z. *Anorg. Allg. Chem.* **1986**, 540, 291.
- (21) Pérez-Rodríguez, S.; Rillo, N.; Lázaro, M. J.; Pastor, E. *Appl. Catal. B* **2015**, 163, 83.
- (22) Sing, K. S. W.; Everett, D. H.; Haul, R. A. W.; Moscou, L.; Pierotti, R. A.; Rouquérol, J.; Siemieniewska, T. *Pure & Appl. Chem.* **1985**, 57, 603.

# Chapter 5

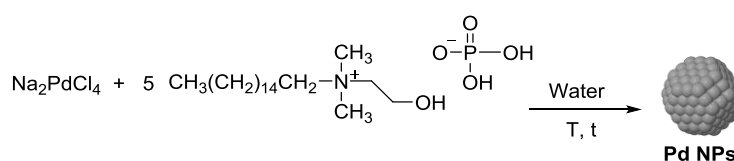
Structure-synthesis relationship study of  
Pd-HHDMA NPs using DOE and impregnation  
onto supports



## 5.1. Introduction

Recent investigations focused on the preparation of heterogeneous catalysts using colloidal chemistry since it appears as a promising tool to obtain well-defined metal NPs with narrow size distribution.<sup>1-3</sup> As detailed in the previous chapters, the control of the metal NPs morphology is of high interest since it can lead to better performing catalysts and to an optimization of the metal content.

P. Witte reported a novel recipe for the formation of well-defined Pd-based catalyst using the colloidal approach.<sup>4</sup> This catalyst was patented by BASF and was commercialized for research purposes under the trademark name Nanoselect. Unlike the conventional reductive precipitation method, this catalyst was prepared via a reduction deposition method. It consisted in the formation of a suspension of Pd NPs by reduction in an aqueous solution in the presence of a stabilizer, followed by the deposition of these NPs onto a solid support. This process involved water rather than organic solvents. Moreover, a commercially available ammonium surfactant hexadecyl(2-hydroxyethyl)dimethylammonium dihydrogenphosphate (HHDMA) was used as both stabilizer and reducing agent (together with the temperature) in a scalable process, as shown in Scheme 5.1.



Scheme 5.1. Colloidal synthesis of Pd NPs stabilized by HHDMA

Activated carbon and titanium silicate powder supports were used to immobilize the NPs.<sup>5</sup> Using the proper reaction conditions, NPs with a diameter smaller than 10 nm were formed with a narrow size distribution.<sup>6</sup>

The performances of these Nanoselect catalysts were evaluated in the semi-hydrogenation of substituted alkynes, a common method to obtain cis-olefins. Traditionally, the Lindlar catalyst was used for these kinds of reactions.<sup>7</sup> This catalyst



contains 5 wt% of Pd supported on porous calcium carbonate and treated with lead and quinoline (Pd/CaCO<sub>3</sub>). Although it has been widely employed for about 60 years, there is a lack of molecular level understanding of this catalyst. It has been accepted that the Pb blocks the more active hydrogenation sites, thus reducing the over-hydrogenation reactions.<sup>6</sup> However, the use of Pb is not environmentally desirable.

The Nanoselect catalysts (called LF 100 and LF 200 for Pd on activated carbon and titanium silicate, respectively) exhibited similar activity and selectivity than the Lindlar catalyst in various hydrogenation reactions.<sup>5</sup> Therefore, these catalysts containing ten times less Pd noble metal than the Lindlar catalyst, are promising lead-free alternatives.

Witte *et al.* investigated on the reasons that caused the high selectivity of these supported colloidal catalysts in alkyne semi-hydrogenation reaction.<sup>6</sup> A focused ion beam scanning electron microscope (FIB-SEM) was used to locate the metal NPs with respect to the surface of the support. The analysis showed the absence of active component inside the support material. The authors related the high selectivity performances with the perfect egg-shell distribution of the nanoselect catalyst.

More recently Perez-Ramirez and co-workers provided explanation for the structural origin of the observed selectivity patterns.<sup>8</sup> They performed the comparison between bare, lead-poisoned and ligand-modified Pd catalysts in the hydrogenation of diverse alkynes using continuous flow three-phase reactor and theoretical calculations. Differences in the catalytic performances were related with the accessibility of the active sites for the substrate. Similarly to the role of lead in the Lindlar catalyst, the electrostatic interactions between the HHDMA and the Pd NPs resulted to isolate the active sites and tailor their accessibility. The authors concluded that this new material drastically improved the metal utilization in liquid phase alkyne hydrogenation and overcome the Pd-only NPs selectivity due to the presence of a HHDMA capping layer.

These findings demonstrate that the determination of the surface structure during the colloidal preparation step can lead to the production of very efficient catalysts.

In this chapter, a structure-synthesis relationship study of the reported recipe of Pd-HHDMA NPs was carried out in order to gain knowledge about this interesting colloidal system. The effects of several experimental factors on the colloidal Pd NPs formation were studied using Design Of Experiments approach (DOE). The objective was to highlight the key parameters and interactions that affect the NPs size and distribution and to postulate empirical models that describes the studied system. This study is one of the first applications of this methodology in the nanocatalysis field.

Moreover, the immobilization of Pd-HHDMA NPs was attempted on activated carbon and titanium silicate using one pot and two-step methodologies.

## 5.2. Experimental Section

### 5.2.1. Set-ups used for the synthesis of colloidal NPs

In this chapter, the Pd NPs were synthesized in aqueous media by chemical reduction method. The HHDMA was used as both stabilizer and reducing agent. The metal precursor used was the sodium tetrachloropalladate (II) ( $\text{Na}_2\text{PdCl}_4$ ).

Throughout this chapter, the Pd-HHDMA NPs were synthesized with two different set-up. In the **Set-up 1**, presented in Figure 5.1 (used in Centre Tecnològic de la Química laboratory, Tarragona), 30 mL of NPs suspension were synthesized in a 200 mL Fischer Porter vessel previously cleaned with aqua regia, soap solution and rinsed with distilled water. The heating set-up consisted in a stirrer-hot plate IKA RCT BASIC™ and a 1000 mL polyethylene glycol bath. The thermocouple measured the temperature of the bath. A manual injection system was used for the addition of the metal precursor. It consisted in a 2 mL syringe with a needle of 0.7 mm of diameter. The volume was injected manually controlling the injection time with a chronometer. The NPs synthesized with this set-up were named **Pd-HHDMA-1 NPs**.

In the **Set-up 2**, presented in Figure 5.1 (used in Total Research & Technology Feluy laboratory), 100 mL of colloidal suspension of NPs were prepared in a 500 mL three

neck flask. A reflux was used to condensate the vapors. The heating set-up was composed by a thermocouple which measured the temperature directly from the reaction solution, an electric heating mantle adapted to the flask size and a temperature regulator EURO THERM™ that controlled the set point. The stirring was performed by an electrical ISOPAD™ stirrer. An automatic injection system was used for the addition of the metal precursor: a peristaltic pump from ISMATEC™. The pump pipe had a diameter of 0.95 mm and the outlet was modified to connect a needle of 0.8 mm of diameter. The calibration of this pump was performed by varying the flow rates from 0.5 mL/min to 5 mL/min at a fixed time (1 minute) and by measuring the resulting pumped volume. The NPs synthesized with this set-up were named **Pd-HHDMA-2 NPs**.

The chemical reagents were purchased from Alfa Aesar for  $\text{Na}_2\text{PdCl}_4$ , Sigma Aldrich for HHDMA solution and Merck for polyethylene glycol. The milli-Q water used for the syntheses came from a Millipore Ultrapure Water Purification system.

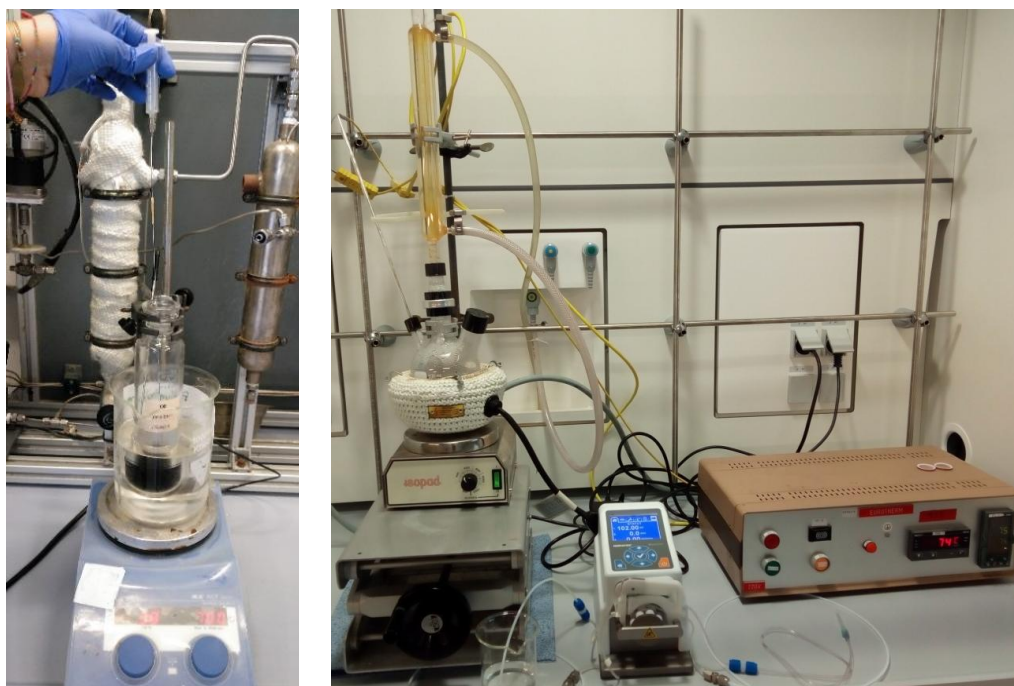


Figure 5.1. Set-up used for the synthesis of colloidal suspensions of Pd-HHDMA NPs: **Set-up 1** on the left side and **Set-up 2** on the right side

### 5.2.2. Set-ups used for the synthesis of supported NPs

The immobilization of the colloidal Pd NPs onto solid supports was performed using two different set-ups.

In the **Set-up 3** (used in Centre Tecnològic de la Química laboratory, Tarragona), 30 mL of solution of supported NPs were prepared in a 50 mL beaker. The stirring set-up consisted in a stirrer-hot plate IKA RCT BASIC<sup>TM</sup>. The controlled addition of the colloidal suspension of NPs to the slurry of solid support was performed manually with a 25 mL burette and a chronometer. This set-up was used for the impregnation of Pd-HHDMA NPs on activated carbon in powder form purchased from Sigma Aldrich.

In the **Set-up 4** (used in Total Research & Technology Feluy laboratory), 90 mL of solution of supported NPs were prepared in a 150 mL beaker. The stirring set-up consisted in a stirrer-hot plate IKA RCT BASIC<sup>TM</sup>. The controlled addition of the colloidal suspension of NPs to the slurry of solid support was performed using a peristaltic pump from ISMATEC<sup>TM</sup>. The pump pipe had a diameter of 3.17 mm. The calibration of this pump was performed by varying the flow rates from 12.5 mL/min to 35 mL/min at a fixed time (1 minute) and by measuring the resulting pumped volume. With this set-up, the Pd-HHDMA NPs were supported on two kinds of activated carbon provided by Cabot and on titanium silicon oxide (TiSiO<sub>4</sub>) provided by VWR.

### 5.2.3. Characterization by Transmission Electron Microscopy

All the synthesized Pd NPs were routinely characterized by conventional TEM in order to obtain the NPs size, distribution, agglomeration and shape. Since the Pd-HHDMA NPs were stable in water, removal of the surfactant excess was tedious; therefore the grids were prepared by adding 20 drops of the fresh aqueous colloidal suspension of Pd NPs on a Cu-formvar grid. The grids were dried under air and then analyzed with the microscope. The TEM measurements were performed with a JEOL 1011 Transmission Electron Microscope operating at 100 kV. For the colloidal and supported NPs synthesized with the **Set-up 1** and **Set-up 3**, the measurements were performed at the “Servei de Recursos Científics i Tècnics” of the Rovira i Virgili University (Tarragona, Spain). For the colloidal and supported NPs synthesized with

the **Set-up 2** and **Setp up 4**, the TEM measurements were performed at the “Département Analyse – Service SFM” of Total Research & Technology Feluy (Seneffe, Belgium).

The TEM images of the colloidal NPs synthesized in this chapter were treated automatically with Fiji Is Just ImageJ software. The precise procedure for this automatic treatment was detailed in the appendix 3.6.1. of the chapter 3. Thanks to this treatment, information about size, area and shape descriptors could be obtained. The data were adjusted to a Gaussian function using a Matlab® routine.

Concerning the supported NPs, they were manually measured with Image J software. A minimum of 400 measurements was systematically carried out. The data were processed with Origin Lab® software. A LogNormal function was adjusted since it fitted better to the set of data than a Gaussian function. The estimation of the average diameter and standard deviation of each sample was given from the arithmetic mean of the fitted curve.

#### **5.2.4. Recipe of the BASF patent for the synthesis of colloidal Pd-HHDMA NPs**

The recipe is described in the BASF Patent US 8,822,725 B2.<sup>4</sup> The reproductions were performed dividing by 30 and 10 the reactant quantities detailed in the original recipe for the preparation of 30 mL (**Set-up 1**) and 100 mL (**Set-up 2**) of Pd NPs colloidal suspension, respectively. The recipe described as follows corresponds to the proportion of the scale 1:10 (used to synthesized 100 mL of NPs with the **Set-up 2**).

5 g (0.036 mol) of HHDMA solution (30 wt% in H<sub>2</sub>O) were diluted in 95 mL of milli-Q water. This solution was homogenized and preheated to 60°C. In parallel, 0,852 g (0.007 mol) of Na<sub>2</sub>PdCl<sub>4</sub>·xH<sub>2</sub>O in 3,5 mL of milli-Q water was prepared and, after homogenization, introduced into the pump pipes (the pump having a dead volume of 2,5 mL). 1 mL of this metal precursor aqueous solution was added to the preheated HHDMA solution with a flow rate of 3,33 mL/min under vigorous stirring (400 rpm). The mixture was then heated to 85°C and stirred at this temperature. After two hours

of reaction, the heating was stopped and the colloidal suspension obtained was stirred for an additional hour during which it was cooled down to 40°C.

### 5.2.5. Recipes of the supported Pd-HHDMA NPs onto different supports

The immobilization of the Pd-HHDMA NPs was first performed on activated carbon (AC) following the “example 2” of the BASF patent.<sup>4</sup> Then, one pot and two-step syntheses were tested to immobilize Pd-HHDMA NPs on different supports. The applied experimental procedures are described in this section. The supports used in this chapter were two types of activated carbon and titanium silicon oxide (TiSiO<sub>4</sub>). The first carbon support, named **AC 1**, was purchased from Sigma Aldrich. No information on the synthesis of this material was available. The second carbon support, named **AC 2**, was purchased from Cabot. It came from coconut source and was sold in extruded form of *ca.* 1.5x3.4 mm. Its main impurities were Na, Si and S and it was activated by streaming process. Finally, the titanium silicon oxide was purchased from VWR in nanopowder form.

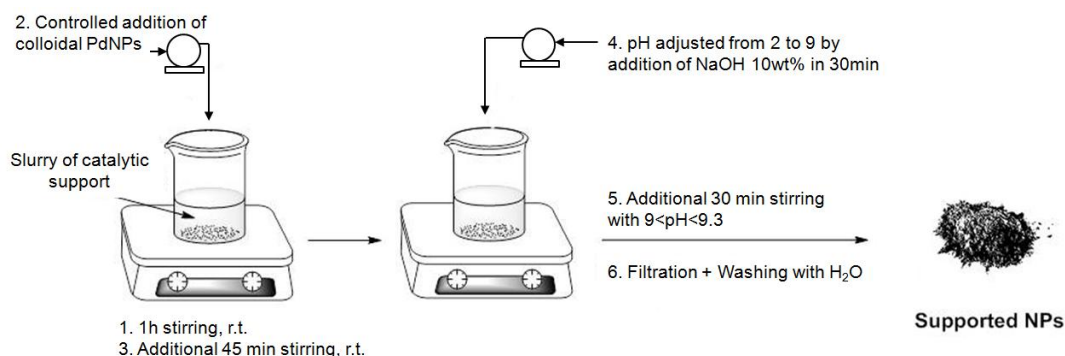
#### 5.2.5.1. Two-step synthesis

Before the immobilization of Pd-HHDMA NPs on different supports, the Point of Zero Charge (PZC) of these support and the  $\zeta$  potential of the colloidal NPs were determined following the procedure previously described in the chapter 4 (section 4.2.3.).

The two-step syntheses performed consisted in the wet impregnation of Pd-HHDMA NPs as described in the BASF patent.<sup>4</sup> In this section, the recipe detailed corresponds to the scale 1:25 used to synthesize 90 mL of a solution of supported NPs with 1 wt% of Pd content using the **Set-up 4**.

A slurry of 2.97 g of support in powder form in 29,7 mL of milli-Q water was vigorously stirred (450 rpm) for 1 hour at room temperature. 40 mL of the colloidal suspension of Pd-HHDMA NPs was added to the slurry of solid support at 25,25 mL/min using the peristaltic pump. The mixture was stirred for an additional 45 minutes. Then, the pH of

the mixture was adjusted from 2.5 to 9.3 by addition of 10 wt% NaOH solution in 30 minutes. Finally, the mixture was stirred for an additional 30 minutes during which the pH was controlled and kept between 9.0 and 9.3 by addition of 10 wt% NaOH if necessary. The solid supported catalyst was filtered off and washed with milli-Q water until the filtrate was chloride-free according to a precipitation test with  $\text{AgNO}_3$ . The obtained supported Pd NPs were then dried in an oven under vacuum. This impregnation recipe is displayed in Scheme 5.2.



Scheme 5.2. Impregnation recipe for the preparation of Pd-HHDMA NPs on AC nanopowder from BASF patent

### 5.2.5.2. One pot synthesis

The one pot synthesis consists in the formation and immobilization of the NPs at once. Thus, the recipe used for the preparation of supported Pd-HHDMA NPs in one pot was the same than that described in section 5.2.4. except that the corresponding amount of support was introduced in the preheating step, at the same time that the HHDMA aqueous solution. The immobilized NPs were filtered off and washed with water until the filtrate was chloride-free according to a precipitation test with  $\text{AgNO}_3$ . The obtained supported Pd NPs were then dried in an oven under vacuum.

## 5.3. Plan of experiments for the structure-synthesis relationship study of colloidal Pd-HHDMA NPs

First, the reproduction of the reference recipe of colloidal NPs described in the BASF patent was planned in two laboratories with two different set-ups and at two different

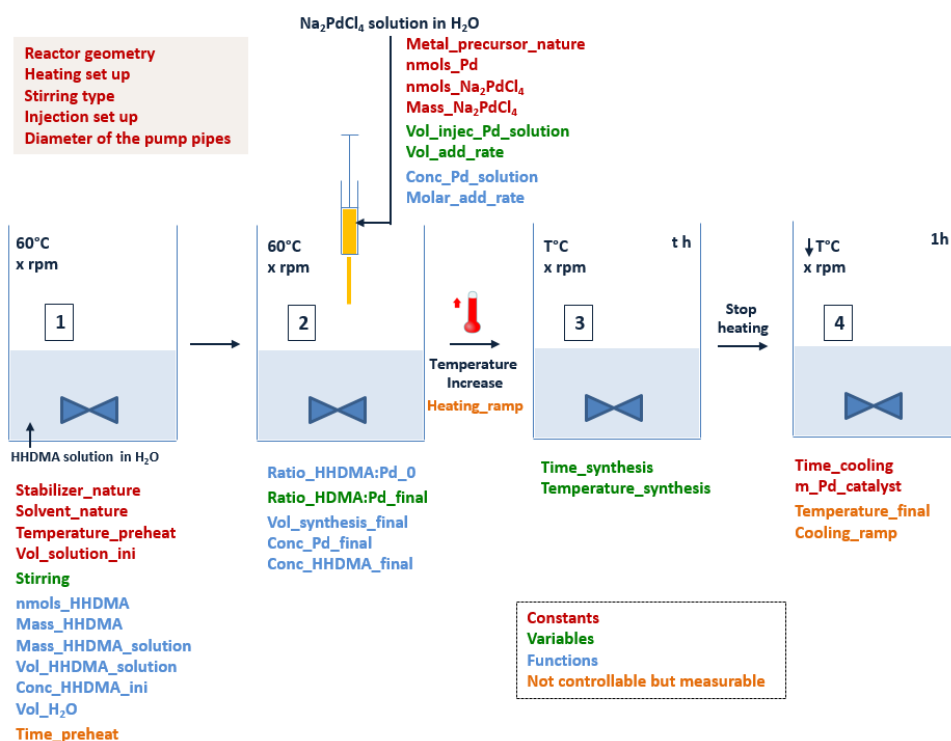
scales. Then, the effects of the synthetic parameters on the NPs size, distribution, agglomeration and shape were studied following the plan of experiments described in this section.

### 5.3.1. Factors included in the DOE

The first step of the study was the identification of the factors that could potentially affect the formation of Pd-HHDMA NPs.

As detailed in the chapter 3, the complete set of experimental factors can be divided into four main subsets: the variables (controlled or constant), the functions, the non-controllable but measurable factors and the non-controllable and non-measurable factors.

The analysis of the reference Pd-HHDMA NPs recipe and the experimental set-up led to the identification of many factors that could influence the NPs formation as shown in Scheme 5.3.



Scheme 5.3. Steps of the Pd-HHDMA NPs synthesis and identification of the experimental factors that can influence the process and responses



The entire set of experimental factors were classified in constants (in red), controlled variables (in green), functions (in blue) and not controllable but measurable variables (in orange). The factors that might have an effect on the Pd NPs size, shape, distribution and agglomeration and that were selected as controllable variables for the study are the following:

- The concentration of Pd in the injection (CONCPD) studied as the volume of the injection of Pd solution (VOLPD)
- The injection volumetric flow rate of Pd solution (VOLRATE)
- The HHDMA-to-Pd molar ratio (RATIO)
- The stirring rate (STIRRING)
- The time of the synthesis (SYNTIME)
- The temperature of synthesis (SYNTEMP)

In this design, it was preferred to vary the volume of Pd solution in the injection (VOLPD) rather than the Pd concentration in the injection (CONCPD) since the first factor was easier and more precise to control experimentally. Both factors are confounded and interchangeable, thus the interpretation of the effect of the Pd concentration in the injection (more relevant from a chemical point of view) was possible.

The DOE study was performed with the **Set-up 2**. The reactor geometry, heating set-up, stirring type and injection set-up remained constant during the study. The target of each synthesis was to prepare 100 mg of Pd in NPs colloidal solution. The initial number of moles of Pd (introduced as  $\text{Na}_2\text{PdCl}_4$ ) was a function of this final catalyst mass. The total volume of HHDMA solution in the preheating step was fixed to 100 mL. Thus, the concentration of HHDMA solution was excluded from the design and confounded with the HHDMA-to-Pd ratio. The preheat temperature of HHDMA solution was fixed to 60°C and the cooling time after the reaction to 1 hour.

Some non-controllable but measurable factors were also identified and their values were recorded for each experiment:

- The pH of the solution after the synthesis at room temperature
- The heating ramp from the preheating step to the synthesis temperature (°C/min)
- The final temperature of the suspension after the cooling time (°C)
- The cooling ramp from the synthesis temperature to the final temperature (°C/min)

The studied experimental factors were varied at two levels. Their values, given in Table 5.1, were selected so that the BASF reference recipe was situated more or less at the center of the design.

Table 5.1. Levels of the studied factors with the DOE

Nº	Factor	Low level -1	High level +1	BASF recipe
1	VOLPD, mL	0.5	2	1
2	VOLRATE, mL/min	2	4	3
3	RATIO, mol/mol	3	7	5
4	STIRRING, rpm	300	500	400
5	SYNTIME, h	1.5	2.5	2
6	SYNTEMP, °C	75	95	85

Possible block effects related to the reagents used for the synthesis were minimized by the use of the same lot of the reagent for all the experiments (metal precursor and stabilizer).

Finally the list of planned experiments was carried out by two operators (operator nº1: Virginie Olivanti and operator nº2: Olivia Benkirane).

### 5.3.2. Design aspects

To respect the scheduling of the project and the limitations of resources, the maximum number of experiments was explicitly limited to sixteen. With the aim to obtain the maximum information with these sixteen experiments, the six identified factors were studied by a fractional factorial design  $2^{6-2}$  of resolution IV. The

reproductions of the BASF patent recipe were used as center points in addition to the sixteen experiments. They were useful to estimate the variability of the studied system. This design implies a screening of the primary effect of the six studied factors being confounded with as minimum third-order interactions. Moreover it allows the study of nine second-order interactions. The third-order effects were considered as negligible and were excluded from the analysis.

The experiments were blocked into two subsets that were carried out independently by the two operators. In this way, the effect of the operator was not confounded with an important primary effect or second-order interaction.

### 5.3.3. Experimental design

#### 5.3.3.1. Matrix of experiments

The design of experiments is displayed on Table 5.2. Four parameters were varied according to the reduced  $2^4$  full factorial design:

- Factor 1 which was defined as the volume of the Pd injection (VOLPD)
- Factor 2 which was defined as the injection volumetric flow rate of the Pd solution (VOLRATE)
- Factor 3 which was defined as the HHDMA-to-Pd molar ratio (RATIO)
- Factor 4 which was defined as the stirring rate (STIRRING)

Two factors were confounded with third-order interactions:

- Factor 5 which was defined as the synthesis time (SYNTIME) and was confounded with the interaction 123 (interaction between VOLPD, VOLRATE and RATIO)
- Factor 6 which was defined as the synthesis temperature (SYNTEMP) and was confounded with the interaction 234 (interaction between VOLRATE, RATIO and STIRRING)

Table 5.2. Two-block Fractional Factorial Design  $2^{6-2}$

RUN	VOLPD mL	VOLRATE mL/min	RATIO mol/mol	STIRRING rpm	SYNTIME h	SYNTEMP °C	OPERATOR 7=124
	1	2	3	4	5=123	6=234	7=124
<b>01</b>	-1	-1	-1	-1	-1	-1	1
<b>02</b>	1	-1	-1	-1	1	-1	-1
<b>03</b>	-1	1	-1	-1	1	1	-1
<b>04</b>	1	1	-1	-1	-1	1	1
<b>05</b>	-1	-1	1	-1	1	1	-1
<b>06</b>	1	-1	1	-1	-1	1	1
<b>07</b>	-1	1	1	-1	-1	-1	1
<b>08</b>	1	1	1	-1	1	-1	-1
<b>09</b>	-1	-1	-1	1	-1	1	-1
<b>10</b>	1	-1	-1	1	1	1	1
<b>11</b>	-1	1	-1	1	1	-1	1
<b>12</b>	1	1	-1	1	-1	-1	-1
<b>13</b>	-1	-1	1	1	1	-1	1
<b>14</b>	1	-1	1	1	-1	-1	-1
<b>15</b>	-1	1	1	1	-1	1	-1
<b>16</b>	1	1	1	1	1	1	1

Table 5.3. Experiments corresponding to the designed matrix  $2^{6-2}$

RUN	VOLPD mL	VOLRATE mL/min	RATIO mol/mol	STIRRING rpm	SYNTIME h	SYNTEMP °C	OPERATOR 7=124
	1	2	3	4	5=123	6=234	7=124
<b>01</b>	0.50	2.00	3.00	300.00	1h30	75.00	1
<b>02</b>	2.00	2.00	3.00	300.00	2h30	75.00	2
<b>03</b>	0.50	4.00	3.00	300.00	2h30	95.00	2
<b>04</b>	2.00	4.00	3.00	300.00	1h30	95.00	1
<b>05</b>	0.50	2.00	7.00	300.00	2h30	95.00	2
<b>06</b>	2.00	2.00	7.00	300.00	1h30	95.00	1
<b>07</b>	0.50	4.00	7.00	300.00	1h30	75.00	1
<b>08</b>	2.00	4.00	7.00	300.00	2h30	75.00	2
<b>09</b>	0.50	2.00	3.00	500.00	1h30	95.00	2
<b>10</b>	2.00	2.00	3.00	500.00	2h30	95.00	1
<b>11</b>	0.50	4.00	3.00	500.00	2h30	75.00	1
<b>12</b>	2.00	4.00	3.00	500.00	1h30	75.00	2
<b>13</b>	0.50	2.00	7.00	500.00	2h30	75.00	1
<b>14</b>	2.00	2.00	7.00	500.00	1h30	75.00	2
<b>15</b>	0.50	4.00	7.00	500.00	1h30	95.00	2
<b>16</b>	2.00	4.00	7.00	500.00	2h30	95.00	1

### 5.3.3.2. Generators

The selected generating relations were 1235 and 2346. It means that the contribution of the factor 5 (SYNTIME) was confused with the interaction between the factors 1, 2 and 3 (VOLPD, VOLRATE and RATIO, respectively). Besides, the contribution of the factor 6 (SYNTEMP) was confused with the interaction between the factors 2, 3 and 4 (VOLRATE, RATIO and STIRRING, respectively). The complete defining relation of this design was an expansion of four words ( $2^2$ ):  $G = 0 + 1235 + 2346 + 1456$ . The term 1456 came from the multiplication of the matrix 1235 and 2346. This defining relation is used to obtain the equations that indicate the confusions introduced in this fractional factorial design. For the studied case, these equations are detailed below.

### 5.3.3.3. Second-order interactions

In this part, our knowledge and chemical intuition about the studied system were used in order to predict the importance of the second-order interactions. They were qualitatively classified in three categories:

- (H) high: interactions that were expected to be significant
- (M) moderate: interactions that were expected to play a moderate role
- (L) low: interactions that were expected not to be significant

From our current understanding, five highly significant interactions were identified as shown in Table 5.4:

- (12): Pd concentration in the injection and injection volumetric flow rate
- (23): Injection volumetric flow rate of Pd solution and HHDMA-to-Pd ratio
- (36): HHDMA-to-Pd ratio and synthesis temperature
- (45): Stirring rate and synthesis time
- (56): Synthesis time and synthesis temperature

Five moderate interactions were also identified:

- (13): Pd concentration in the injection and HHDMA-to-Pd ratio
- (14): Pd concentration in the injection and stirring rate

- (24): Injection volumetric flow rate of Pd solution and stirring rate
- (35): HDDMA-to-Pd ratio and synthesis time
- (16): Pd concentration and synthesis temperature

The remaining second-order interactions were expected to be of low significance.

Table 5.4. Previous qualitative evaluation of the importance of the second-order interactions of the fractional factorial design  $2^{6-2}$

		CONCPD	VOLRATE	RATIO	STIRRING	SYNTIME	SYNTEMP
		1	2	3	4	5=123	6=234
CONCPD	1						
VOLRATE	2	H					
RATIO	3	M	H				
STIRRING	4	M	M	L			
SYNTIME	5=123	L	L	M	H		
SYNTEMP	6=234	M	L	H	L	H	

#### 5.3.3.4. Confounding of effects

The purpose of this design is to screen the significance of the primary effects and some secondary effects on the resulting Pd-HDDMA NPs. The selected design (fractional factorial design with resolution IV) involves confusions between primary effect and third-order interactions as minimum, as well as confusions of various second-order interactions. Some of these confounded interactions might be relevant. Their significances were anticipated and an a priori potential source of error or misinterpretation of the results of this DOE was assessed.

The equations of the confounding of effects, obtained from the relation of definition (previously detailed in section 5.3.3.2.) are given below. They present the confusion of factors and interactions hidden in the estimation of an effect.  $L_i$  represents the estimated effect associated to the factor  $i$  and  $b$  the real contribution of the factor or interaction. For instance,  $L_1$  corresponded to the estimation the main effect of the factor 1. However, since a fractional design was implemented, confusions were introduced and the effect of this factor was confounded with the interaction 235, 456 and 12346. In a first approximation, the interactions of more than three parameters were neglected.

$$\begin{aligned}
 L_0 &= b_0 + b_{1235} + b_{2346} + b_{1456} \\
 L_1 &= b_1 + b_{235} + b_{456} + b_{12346} \\
 L_2 &= b_2 + b_{135} + b_{346} + b_{12456} \\
 L_3 &= b_3 + b_{125} + b_{246} + b_{13456} \\
 L_4 &= b_4 + b_{236} + b_{156} + b_{12345} \\
 L_{12} &= \textcolor{red}{b}_{12} + \textcolor{yellow}{b}_{35} + b_{1346} + b_{2456} \\
 L_{13} &= \textcolor{yellow}{b}_{13} + b_{25} + b_{1246} + b_{3456} \\
 L_{14} &= \textcolor{yellow}{b}_{14} + \textcolor{red}{b}_{56} + b_{2345} + b_{1236} \\
 L_{23} &= \textcolor{red}{b}_{23} + b_{15} + b_{46} + b_{123456} \\
 L_{24} &= b_{24} + \textcolor{red}{b}_{36} + b_{1256} + b_{1345} \\
 L_{34} &= \textcolor{yellow}{b}_{34} + b_{26} + b_{1245} + b_{1356} \\
 L_{123} &= b_{123} + b_5 + b_{146} + b_{23456} \\
 L_{124} &= b_{124} + b_{345} + b_{136} + b_{256} \\
 L_{134} &= b_{134} + b_{245} + b_{126} + b_{356} \\
 L_{234} &= b_{234} + b_6 + b_{145} + b_{12356} \\
 L_{1234} &= b_{1234} + \textcolor{red}{b}_{45} + \textcolor{yellow}{b}_{16} + b_{2356}
 \end{aligned}$$

**Note:** The expected significant second-order interactions (H) are in red; expected moderate second-order interactions (M) are in yellow.

### 5.3.3.5. Blocking

The blocking between the two operators (operator 1 and 2) was performed using the third-order interactions (124).

$$L_{124} = \textcolor{red}{b}_{124} + b_{345} + b_{136} + b_{256}$$

It means that the effect of the operator (if any) was confounded with the third-order interactions (124), as defined, and also the interactions (345), (136) and (256). The meaning of these interactions is given as follow:

- (124) VOLPD, VOLRATE and STIRRING
- (345) RATIO, STIRRING and SYNTIME
- (136) VOLPD, RATIO and SYNTEMP
- (256) VOLRATE, SYNTIME and SYNTEMP

The contribution of the third-order interactions was not expected to be significant, thus a significant effect of this interaction could be associated to an effect of the operator.

## 5.4. Results and Discussion

### 5.4.1. Colloidal NPs stabilized by HHDMA

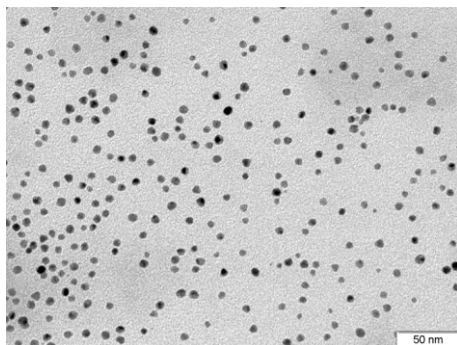
A first objective of these experiments was to perform the reproduction of the patented recipe of Pd-HHDMA NPs in two different laboratories and at different scales. Then, a second objective was to carry out the structure-synthesis relationship study of these NPs to gain knowledge about the way to control their size, distribution and shape.

#### 5.4.1.1. Reproduction of the colloidal BASF Patent recipe at laboratory scale

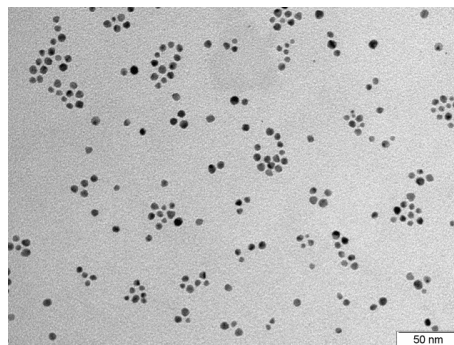
##### Set-up 1: synthesis of a 30 mL suspension of Pd-HHDMA NPs

First, the synthesis of Pd-HHDMA NPs was reproduced twice with the **Set-up 1** in the laboratory of the Centre Tecnològic de la Química (Tarragona). The TEM micrographs and size distribution histograms are displayed Figure 5.2.

a. **Pd-HHDMA-1 1a**,  $6.1 \pm 0.9$  nm (15%)



b. **Pd-HHDMA-1 1b**,  $5.7 \pm 1.1$  nm (20%)





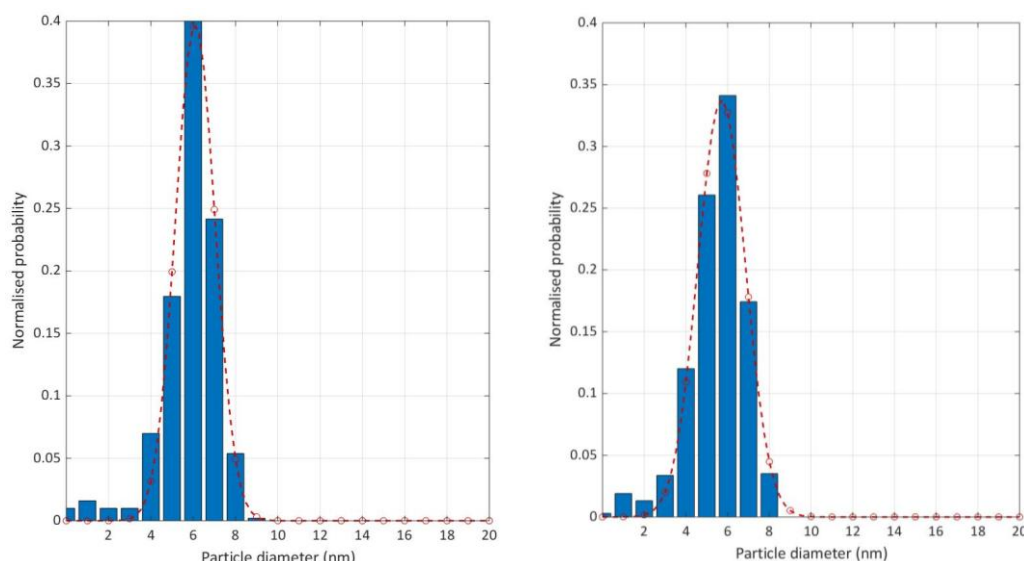
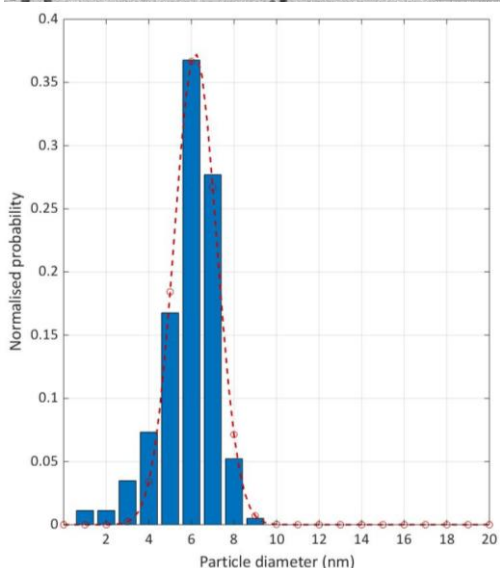
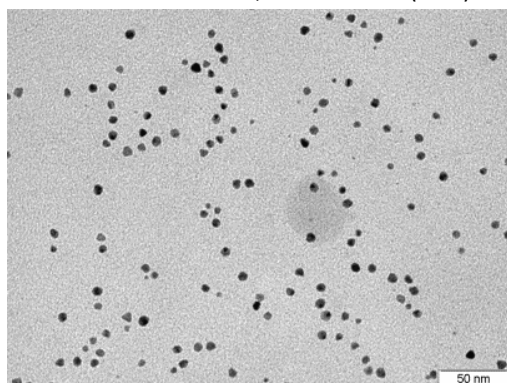


Figure 5.2. TEM micrographs and size distribution histograms of two reproductions of Pd-HHDMA NPs synthesized following the BASF recipe with the **Set-up 1**

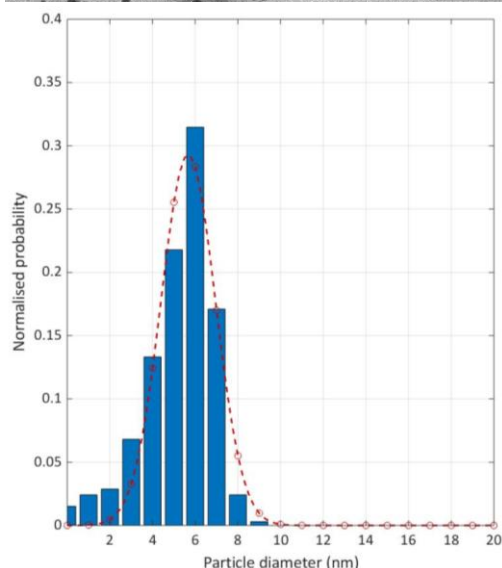
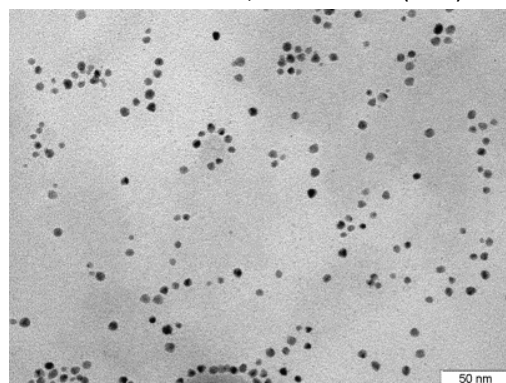
The two batches of Pd-HHDMA NPs showed similar average size and distribution: *ca.*  $5.9 \pm 1.0$  nm. The reported crystallite sizes for these NPs were 7 nm.<sup>5</sup> Witte *et al.* prepared Pd-HHDMA NPs with the same chemical composition but increasing the synthesis pH in order to obtain smaller crystallite sizes.<sup>6</sup> No details about the pH values were provided, however they were also able to obtain NPs crystallite size of 5 nm. Therefore, it was concluded that the recipe of the BASF patent at laboratory scale was successfully reproduced with NPs sizes in the same range than the reported values.

In the reported studies on the Pd-HHDMA NPs, no precise details about the set-up were given.<sup>4,6</sup> Nevertheless, the resulting NPs could probably be formed with different size, distribution or shape depending on the equipment used. As an example, the recipe stipulate a “vigorous agitation” for the homogenization of the suspension, depending on the stirring set-up and the reactor geometry, the number of rotation per minutes (rpm) should be adapted. Moreover, the diameter of the metal injection pipe was also expected to affect the NPs. To confirm this effect, the recipe was reproduced using four different syringe diameters: 0.7, 0.8, 1.0 and 1.2 mm. The TEM micrographs of these syntheses are presented in Figure 5.3.

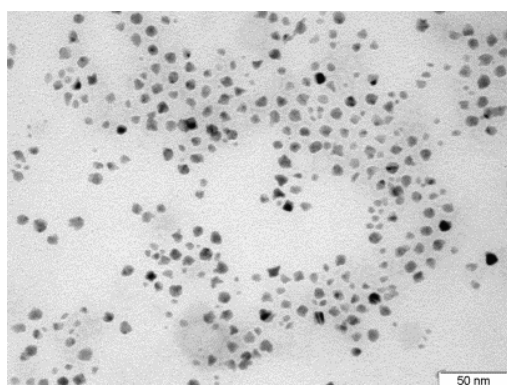
a. **Pd-HHDMA-1 NPs 1c**,  $6.2 \pm 1.0$  nm (16%)



b. **Pd-HHDMA-1 NPs 2**,  $5.7 \pm 1.3$  nm (23%)



c. **Pd-HHDMA-1 NPs 3**, not well-spherical NPs



d. **Pd-HHDMA-1 NPs 4**, star shape NPs of *ca.* 8-12 nm

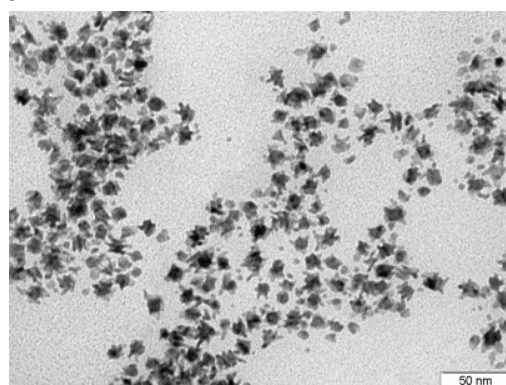


Figure 5.3. Effect of the external diameter of the syringe used to inject the metal precursor in the HHDMA solution – TEM micrographs and size distribution histograms of the reproduction of the BASF patent with syringe diameter of a. 0.7 mm, b. 0.8 mm, c. 1.0 mm and d. 1.2 mm

The suspensions obtained with the use of syringe diameter of 0.7 and 0.8 mm were spherical, monodisperse and well-defined with similar sizes of *ca.* 6 nm. In contrast, when larger diameters were used, the shape of the NPs resulted to be negatively affected (low sphericity for the NPs synthesized with a syringe diameter of 1.0 mm and star-shape NPs for the NPs synthesized with a syringe diameter of 1.2 mm). These results indicate that the pipe diameter used to inject the metal precursor in the HHDMA solution highly affects to the resulting NPs shape. With a diameter of 1.2 mm, the metal solution drops injected were almost twice as big as those injected with a diameter of 0.7 mm. A possible explanation is that the local concentration of HHDMA around these drops during the injection was not high enough to well-stabilize the NPs leading to their shape deformation.

Soulantica and co-workers also reported the importance of the set-up details for the reproduction of nanocrystals.<sup>9</sup> Indeed, they studied the synthesis of Co nanocrystals by chemical reduction and stabilized with a ligand mixture (lauric acid and hexadecylamine). They reported important size and structural differences between nanocrystals prepared using different addition rate of Co precursor into the ligand mixture. They demonstrated that this unexpected comportment was due to side reactions that modified the nucleation step. Consequently, these examples highlight the importance of the precise control over the synthetic protocols and the use, as far as possible, of automated procedure to improve the production of such sensitive reactions.

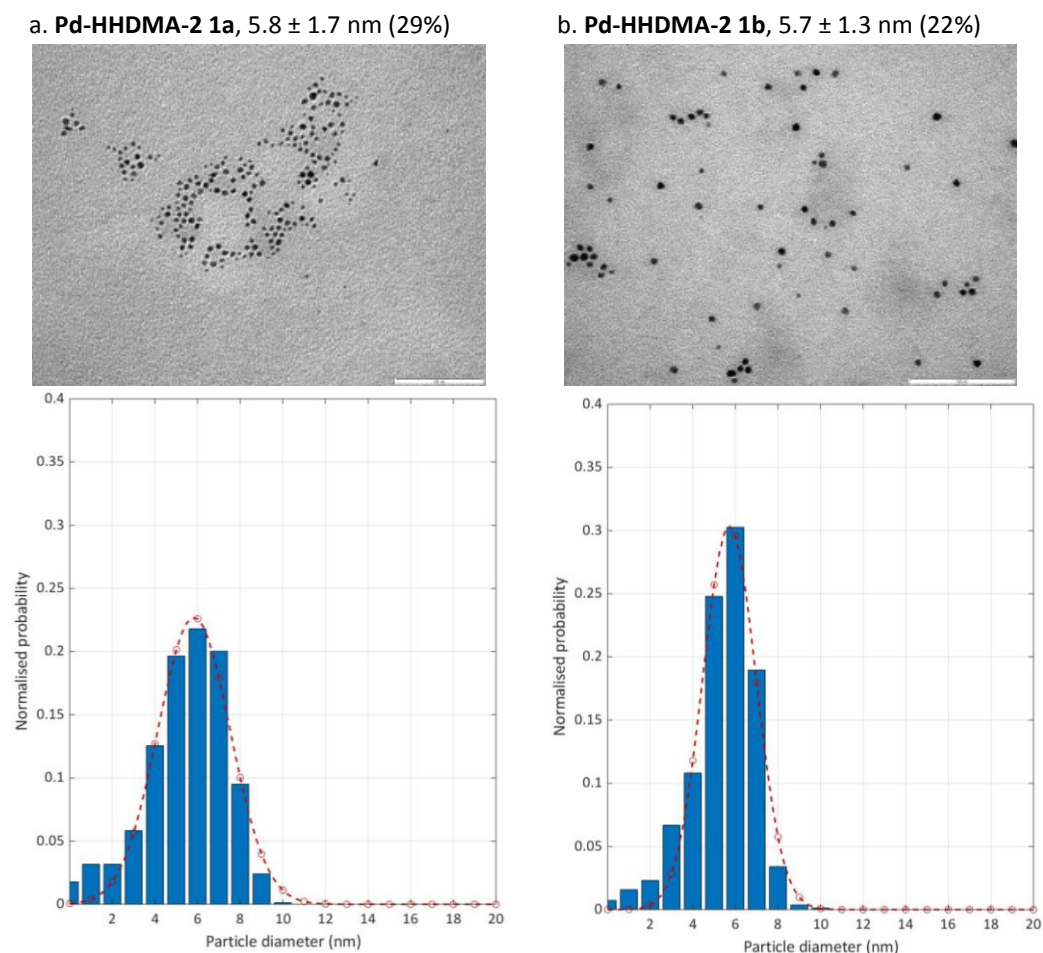
Later, the Pd-HHDMA NPs recipe was reproduced at larger scale in the laboratory of Total Research & Technology Feluy. The results of these syntheses are presented in the next section.

### **Set-up 2: synthesis of a 100 mL suspension of Pd-HHDMA NPs**

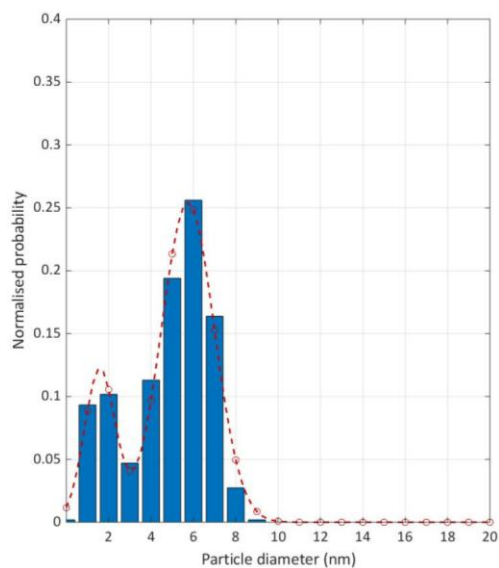
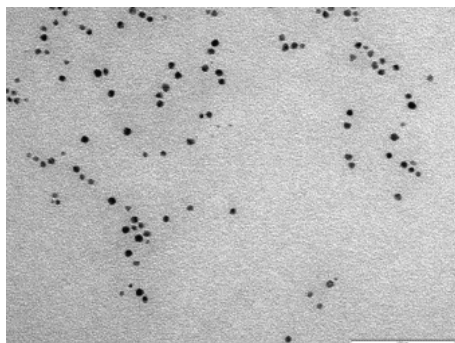
Using the **Set-up 2**, seven reproductions of 100 mL suspension of Pd-HHDMA NPs were performed. These reproductions were used as central point of the matrix of experiments presented in the section 5.4.1.2.

As detailed in the chapter 3, the automatic measurement of the NPs provided valuable information to improve the interpretation of the results. Thanks to this procedure, besides the NPs size and distribution, information about the NPs shape or the synthesis efficiency could be obtained. Therefore, the analyses of these seven central points as well as the experiments of the DOE presented in the next section were carried out applying this methodology.

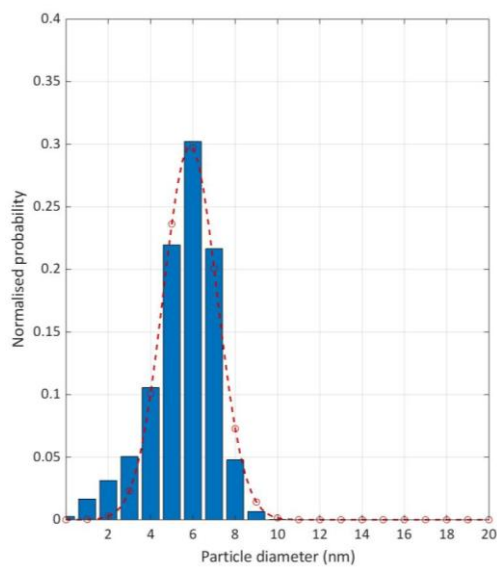
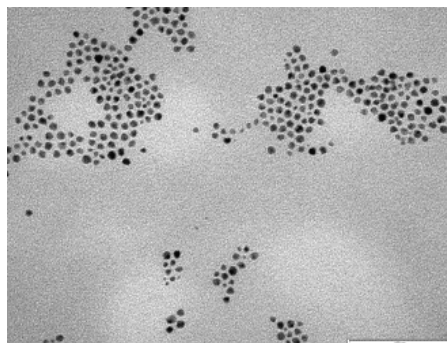
The TEM micrographs and size distribution histograms of the seven reproductions are displayed in Figure 5.4. The cumulative probability plots of these batches are given in appendix 5.6.1. and the numerical results are summarized in Table 5.5.



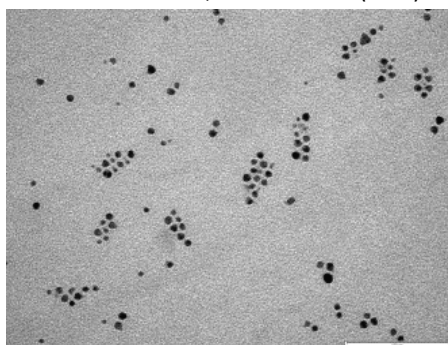
c. **Pd-HHDMA-2 1c**,  $5.7 \pm 1.4$  nm (25%)



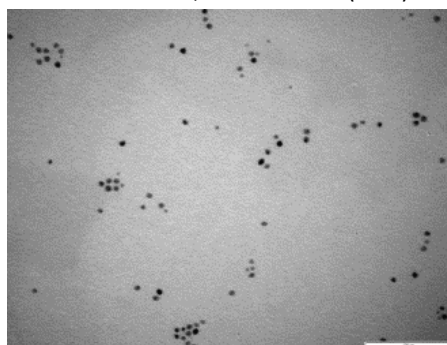
d. **Pd-HHDMA-2 1d**,  $5.9 \pm 1.3$  nm (22%)



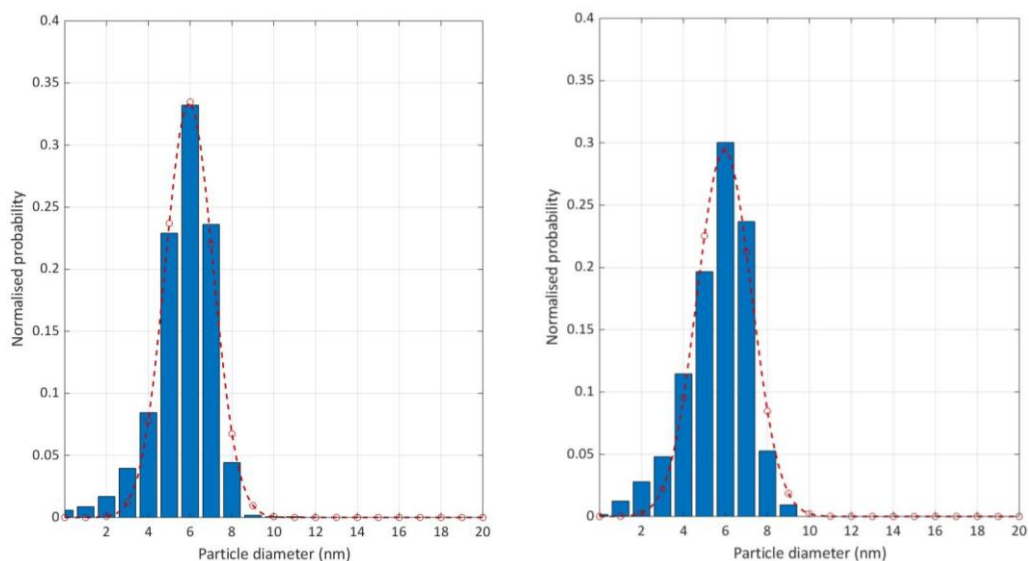
e. **Pd-HHDMA-2 1e**,  $6.0 \pm 1.1$  nm (19%)



f. **Pd-HHDMA-2 1f**,  $6.0 \pm 1.3$  nm (22%)







g. Pd-HHDMA-2 1g,  $5.1 \pm 1.8$  nm (35%)

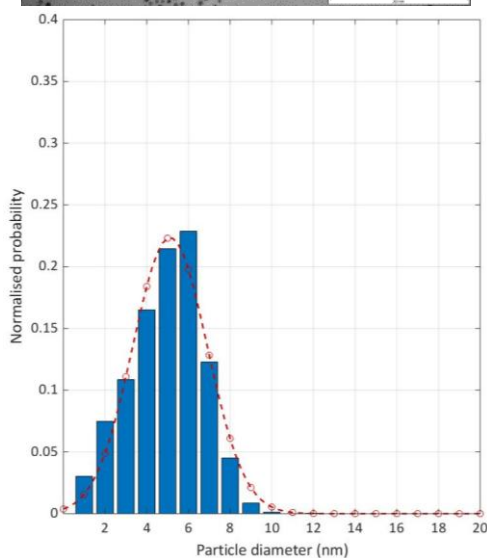
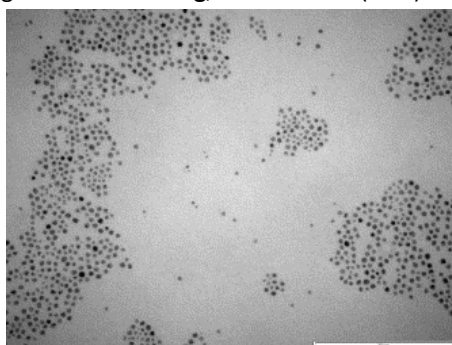


Figure 5.4. TEM micrographs and size distribution histograms of the seven reproductions of Pd-HHDMA NPs synthesized following the BASF recipe with the **Set-up 2**

Table 5.5. Numerical results of the reproduction of seven batches of Pd-HHDMA NPs with the

Set-up 2								
Pd-HHDMA-2 Nº Batch	Mean AR <sup>a</sup>	Median AR <sup>b</sup>	FS (%) <sup>c</sup>	FR (%) <sup>d</sup>	Efficiency (%)	NPs size (nm) <sup>f</sup>	RSD (%)	R <sup>2</sup>
<b>1a</b>	5.5	5.7	3.2	65.9	77.9	5.8	29.1	0.98
<b>1b</b>	5.4	5.6	1.0	74.6	83.4	5.7	21.9	0.98
<b>1c</b>	4.8	5.3	1.9	72.7	48.3 <sup>e</sup>	5.7	21.8	0.83
<b>1d</b>	5.5	5.8	0.7	82.8	88.1	5.9	21.6	0.98
<b>1e</b>	5.7	5.9	0.8	85.4	89.6	6.0	19.2	0.99
<b>1f</b>	5.6	5.8	0.8	89.6	93.8	6.0	21.8	0.97
<b>1g</b>	4.9	5.1	1.4	78.2	87.3	5.1	34.9	0.98

<sup>a</sup>: Mean equivalent diameter of the spherical NPs, <sup>b</sup>: Median equivalent diameter of the spherical NPs, <sup>c</sup>: Fraction of NPs smaller than 1 nm, <sup>d</sup>: Fraction of spherical NPs, <sup>e</sup>: Efficiency estimated by the subtraction of the fraction of agglomerated NPs and the fraction of the small NPs belonging to a Gaussian distribution centered on 1.6 nm, <sup>f</sup>: mean NPs size of the largest area peak obtained by the fitting of one or more Gaussian function(s) to the resulting histogram with bin size of 1 nm.

First, it was noticed that the mean diameter was smaller than the median diameter in all the syntheses. As shown in Figure 5.5, this trend is synonym of a negatively skewed distribution indicating the systematic presence of small NPs in the samples. The fraction of NPs inferior to 1 nm was estimated and confirmed this statement.

However, this fraction of such small NPs was not systematically observed in the TEM micrographs. It was associated to an artifact due to the limitations of the microscope and the analysis. Indeed during the threshold step of the NPs automatic measurements, some point that did not correspond to real NPs could be detected as some when the quality of the picture was not good enough or when the lighting was not homogeneous, as shown in Figure 5.6. Such problem was avoided as much as possible during the treatment. To keep this fraction of non-representative sample population away from the analysis, all data of NPs size lower than 1 nm was removed before the numerical analysis.

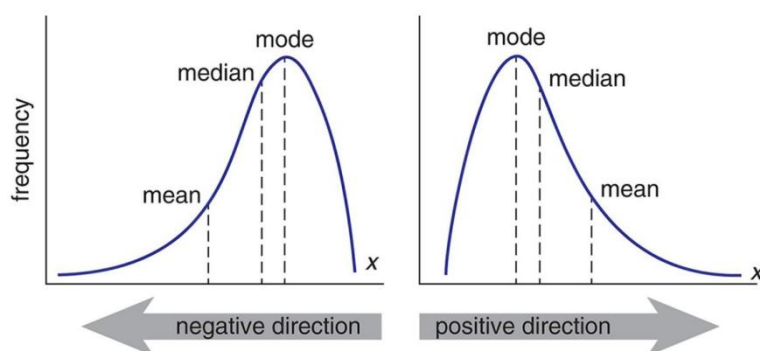


Figure 5.5. To the left: negatively skewed distribution with mean lower than median. To the right: positively skewed distribution with mean higher than median<sup>10</sup>

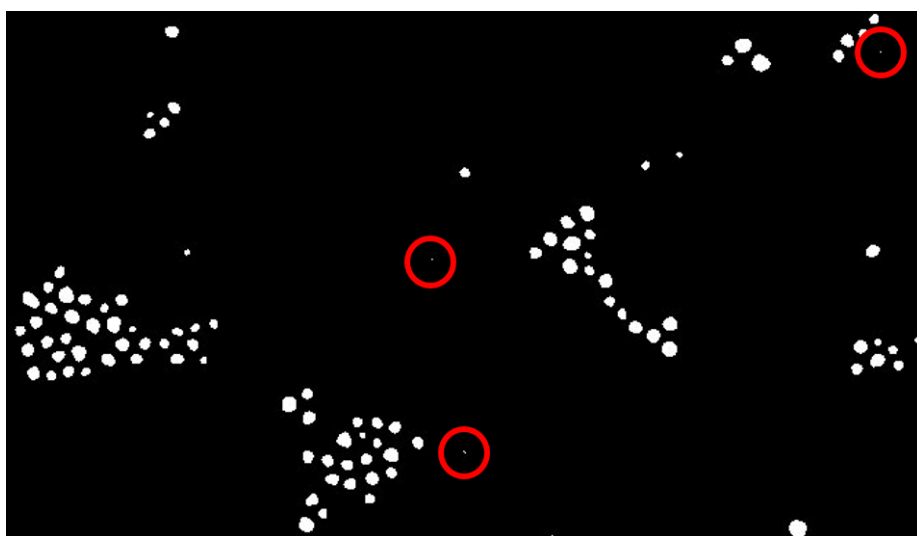


Figure 5.6. Example of TEM micrograph of Pd-HHDMA NPs processed automatically with Fiji is Image J

Large NPs and agglomeration were not detected in TEM micrographs. This trend was confirmed by the high value of synthesis efficiency of the batches **Pd-HHDMA-2 1a**, **1b**, **1d**, **1e**, **1f** and **1g** (between 78% and 94%). Lower percentage was obtained for the batch **Pd-HHDMA-2 1c** that was associated to the presence of a double distribution. A possible explanation of such distribution is that all the batches of NPs were synthesized using a freshly prepared aqueous solution of  $\text{Na}_2\text{PdCl}_4$ . These solutions were always prepared in larger amount than needed in order to fill the dead volume of the pump pipes. Thus, to avoid waste of precious metal, it was tested to reuse the  $\text{Na}_2\text{PdCl}_4$  solution prepared the day before for the batch **Pd-HHDMA-2 1c**. Thus, the



double distribution observed in this batch could be due to the reuse of a 24h-old precursor solution. It was decided to keep working with freshly prepared  $\text{Na}_2\text{PdCl}_4$  solutions and this batch was removed from the list of central points used for the estimation of the variability of the system for the design of experiments presented in the next section.

The percentage of spherical NPs varied quite significantly between the different batches. Its value was included between *ca.* 66% and 90%, giving a mean fraction of spherical NPs of  $78 \pm 8 \%$ .

From this set of experiments, three batches revealed slightly larger relative standard deviation: **Pd-HHDMA-2 1a**, **Pd-HHDMA-2 1c** and **Pd-HHDMA-2 1g** with 29.1%, 24.9% and 34.9%, respectively.

The determination coefficient  $R^2$  was also calculated. It provides a measure of the goodness of fit of a model to a set of observations. It was used to predict how good was the fitting of one or more Gaussian function(s) to the set of NPs. When  $R^2$  is close to a value of 1, it means that the major part of the NPs of the sample follow the fitted Gaussian function(s). For the batch **Pd-HHDMA NPs 1c**, this determination coefficient was equal to 0.83, such a low value suggests that the fitting of a Gaussian was not adapted to the set of data which seems normal since multiple distribution was obtained in this case. For the other six batches,  $R^2$  varied between 0.97 and 0.99, indicating a good fitting of the adjusted single Gaussian function. However, the use of a Gaussian shape to describe the NPs size distribution is questionable. A model of colloidal NPs formation to justify this choice is missing.

Finally, the average mean NPs size of the presented set of experiments is *ca.* 5.7 nm with NPs between 5.1 and 6.0 nm. This average value is close to that obtained with the **Set-up 1** (*ca.* 5.9 nm), suggesting a good interlaboratory reproducibility. To confirm this statement, the statistical Kolmogorov-Smirnov test (K-S test) was used.

As described in chapter 3 (section 3.4.3.), this test enable comparing the similarity of two sets of data. It computes a value that test the null hypothesis that both groups have the same distribution. This value is obtained from the maximum difference between the two cumulative distributions and the sample size. The null hypothesis is rejected when this maximum difference exceeds a certain critical tabulated value (K-S tables), given in appendix 5.6.2.

In the presented case, this test was applied using the values of the 1 nm bins in the range of 0 to 20 nm, thus the degree of freedom was equal to 20. It was decided to apply this test to the two batches of NPs that possess the most different mean diameter of the set of experiments performed with the **Set-up 1**, the **Set-up 2** and finally both set-ups. The cumulative distributions of the three batches performed with the **Set-up 1** and the six batches performed with the **Set-up 2** (remaining the double distributed batch for the reasons detailed above) are depicted in Figure 5.7 and Figure 5.8, respectively. The plots were given separately to better discern the different distributions; the plot with the nine batches prepared with both set-ups is given in appendix 5.6.3.

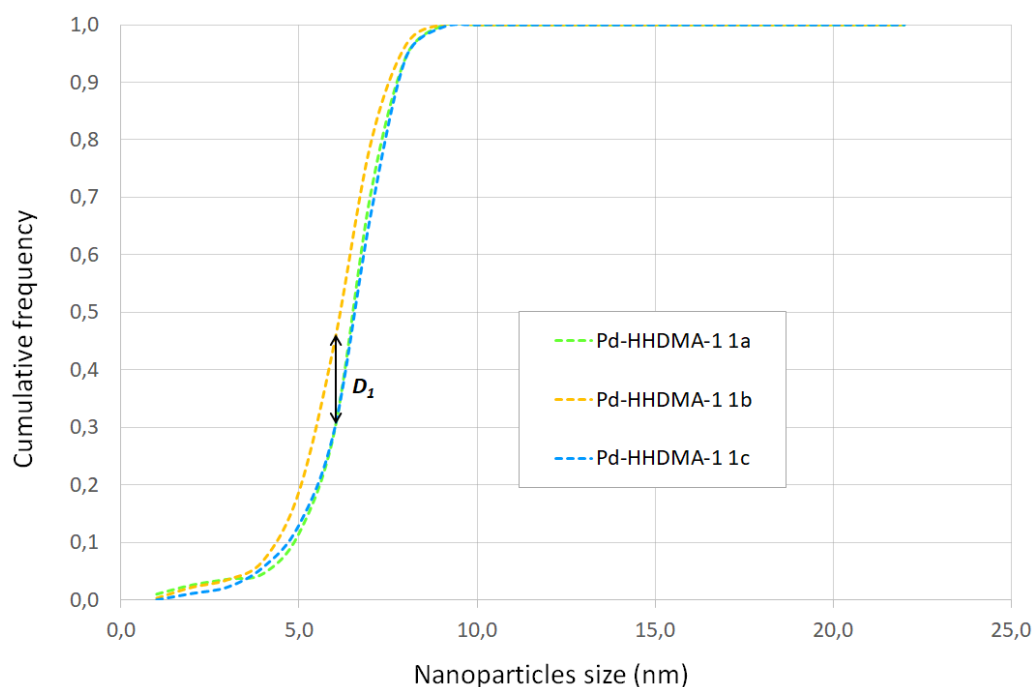


Figure 5.7. Cumulative distribution of the three batches of Pd-HHDMA NPs synthesized with the **Set-up 1**. Kolmogorov-Smirnov test between **Pd-HHDMA-1 1b** and **Pd-HHDMA-1 1c** ( $D_1$ )

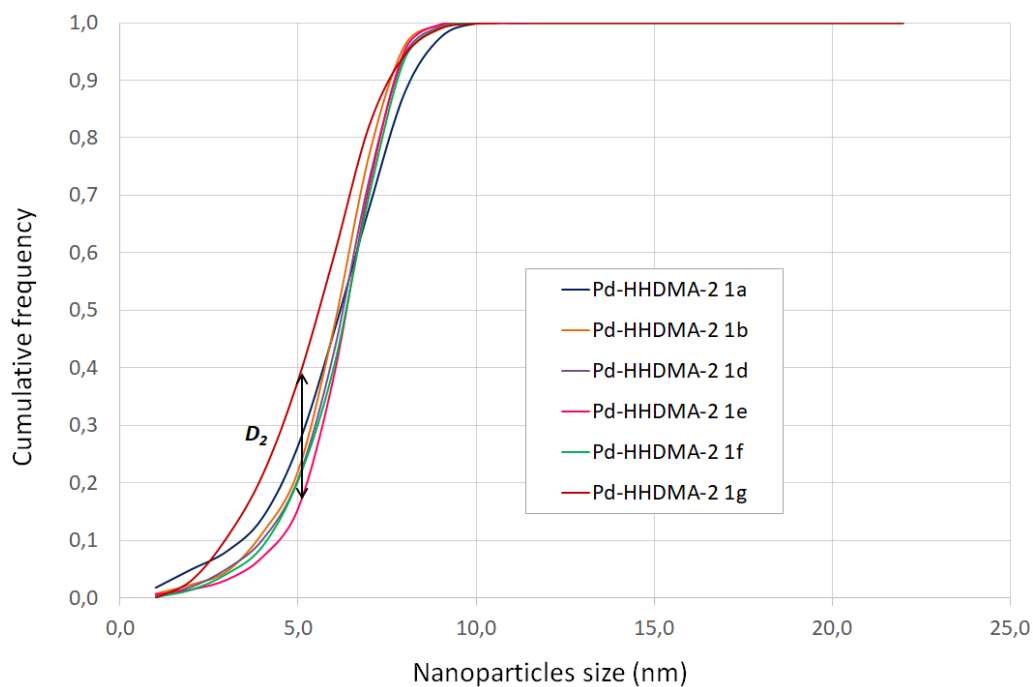


Figure 5.8. Cumulative distribution of the six batches of Pd-HHDMA NPs synthesized with the **Set-up 2**. Kolmogorov-Smirnov test between **Pd-HHDMA-2 1e** and **Pd-HHDMA-2 1g** ( $D_2$ )

The K-S test was performed between:

- **Pd-HHDMA-1 1b** and **Pd-HHDMA-1 1c** for the **Set-up 1**: the maximum difference between the two cumulative distributions was called  $D_1$ , as shown in Figure 5.7.
- **Pd-HHDMA-2 1e** and **Pd-HHDMA-2 1g** for the **Set-up 2**: the maximum difference between the two cumulative distributions was called  $D_2$ , as shown in Figure 5.8.
- **Pd-HHDMA-1 1c** and **Pd-HHDMA-2 1g** for the interlaboratory reproducibility verification (**Set-up 1** and **2**): the maximum difference between the two cumulative distributions was called  $D_3$  as displayed in appendix 5.6.3.
- **Pd-HHDMA-1 1c** and **Pd-HHDMA-2 1b** for the interlaboratory reproducibility verification (**Set-up 1** and **2**): the maximum difference between the two cumulative distributions was called  $D_4$  as displayed in appendix 5.6.3.

In Table 5.6, the  $D$  values calculated for each of these cases are summarized and compared with the corresponding tabulated value (20 degrees of freedom and a level of significance  $\alpha$  of 0.05 which means 95% of confidence on the conclusion of the test).

Table 5.6. Sum up of the Kolmogorov-Smirnov tests performed

Set-up	$D_{\text{estimated}}$	$D_{\text{tabulated}}$	Conclusion of the K-S test
1 ( $D_1$ )	0.1514	0.2941	$D_1 < D_{\text{tabulated}}$ : null hypothesis accepted
2 ( $D_2$ )	0.2230	0.2941	$D_2 < D_{\text{tabulated}}$ : null hypothesis accepted
1&2 ( $D_3$ )	0.2950	0.2941	$D_3 > D_{\text{tabulated}}$ : null hypothesis rejected
1&2 ( $D_4$ )	0.1709	0.2941	$D_4 < D_{\text{tabulated}}$ : null hypothesis accepted

Concerning the reproducibility of the Pd-HHDMA NPs performed with the **Set-up 1**, the K-S test indicated that the null hypothesis was accepted which means that the compared distributions could be considered as similar, confirming thus the reproducibility in this case. The same conclusion was obtained for the Pd-HHDMA NPs synthesized with the **Set-up 2**.

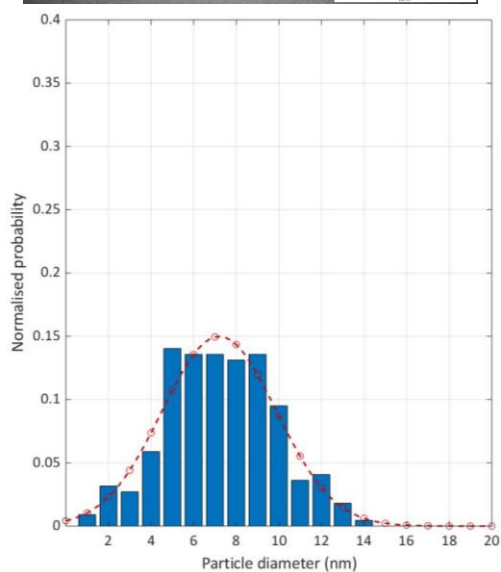
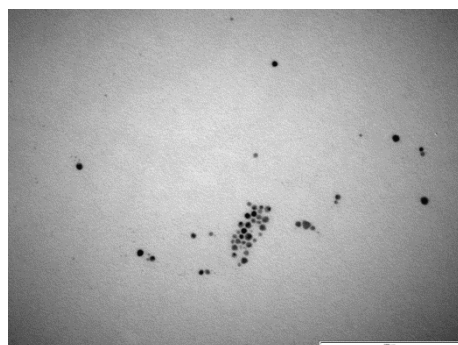
Concerning the verification of the interlaboratory reproducibility, the two batches of NPs that possess the most different mean diameter of both set-ups (which corresponds to **Pd-HHDMA-1 1c** and **Pd-HHDMA-2 1g**) resulted to have a *D* value slightly higher than the tabulated value for a confidence of 95%, indicating that these distributions were likely to be different from a statistical point of view. Indeed, it could be observed on the cumulative distribution plot that the **Pd-HHDMA-1 1g** revealed NPs size slightly smaller than the rest of the syntheses. Consequently, the test was repeated taking into account the two batches of NPs that possess the most different mean diameter of both set-ups but removing the **Pd-HHDMA-2 1g**. The K-S test was performed between **Pd-HHDMA-1 1c** and **Pd-HHDMA-2 1b**. In this case the null hypothesis was accepted, indicating that both distributions were similar.

To conclude, the reproducibility of the synthesis of colloidal Pd-HHDMA NPs through the BASF patent in the CTQ and TRTF laboratories (Centre Tecnològic de la Química, **Set-up 1** and Total Research & Technology Feluy, **Set-up 2**, respectively) was validated statistically. Concerning the interlaboratory reproducibility, eight out of the nine batches were considered reproducible in view of the result of the statistical test. One batch: the **Pd-HHDMA-2 1g** showed slightly smaller NPs size (*ca.* 5.1 nm). To confirm if this batch corresponds to an outlier, more reproductions should be performed.

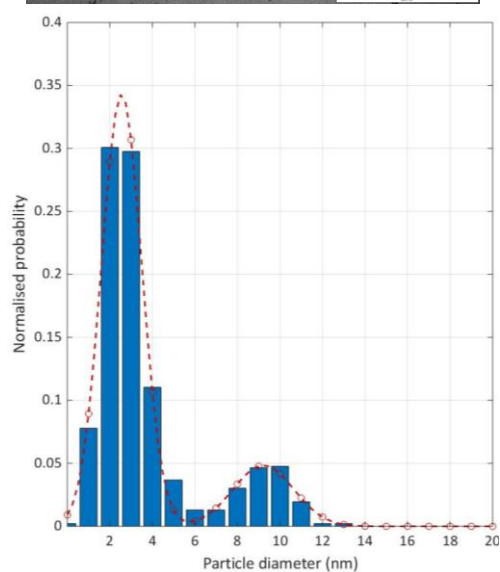
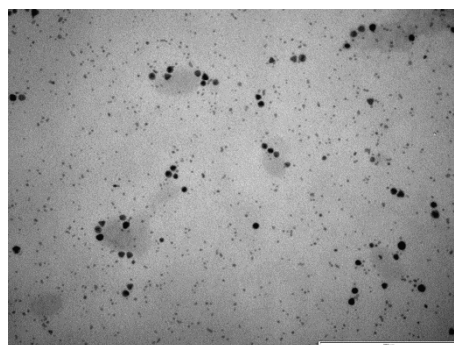
#### 5.4.1.2. Structure-synthesis relationship study using DOE

To study the effect of the selected synthetic parameters on the formation of Pd-HHDMA NP in an efficient way, sixteen experiments were performed following the  $2^{6-2}$  designed matrix presented in section 5.3.3. The TEM micrographs and size distribution histograms of the sixteen experiments are displayed in Figure 5.9. The cumulative probability plots of these batches are given in appendix 5.6.2.

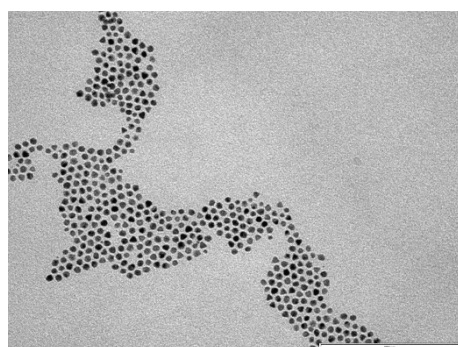
**RUN01**



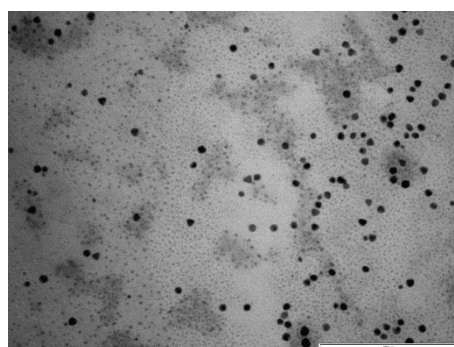
**RUN02**

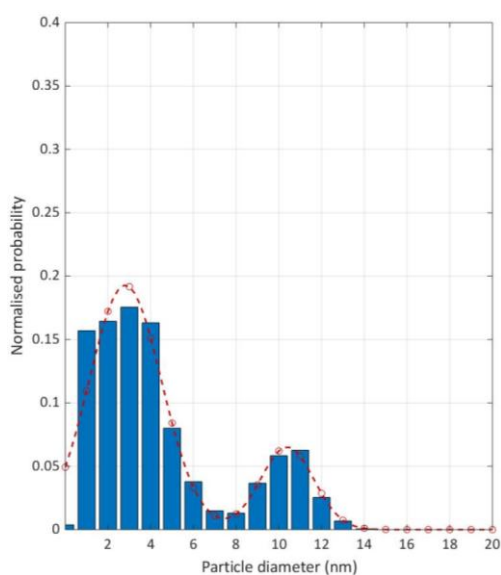
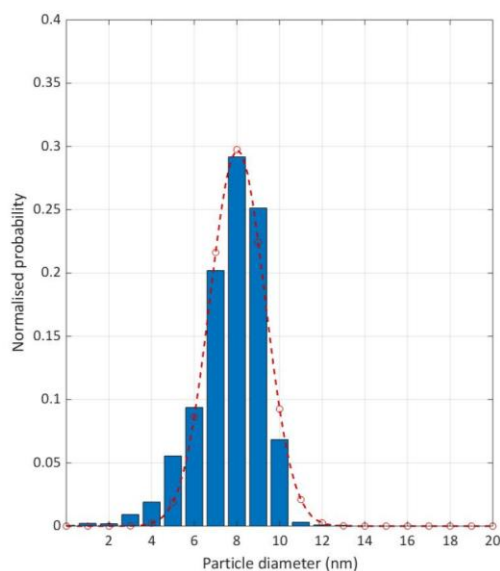


**RUN03**

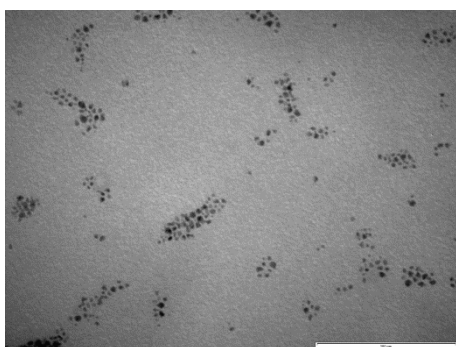


**RUN04**

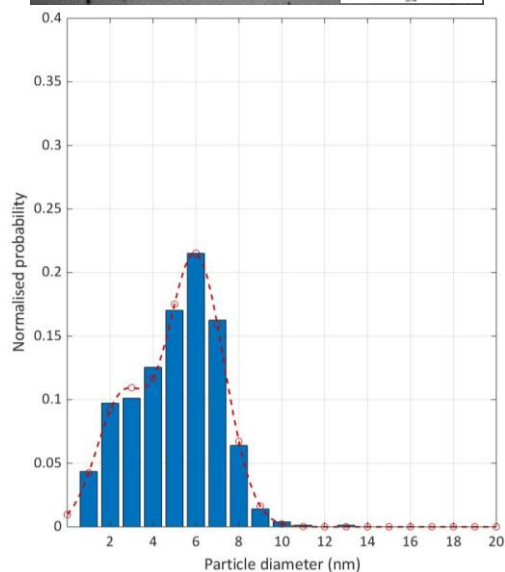
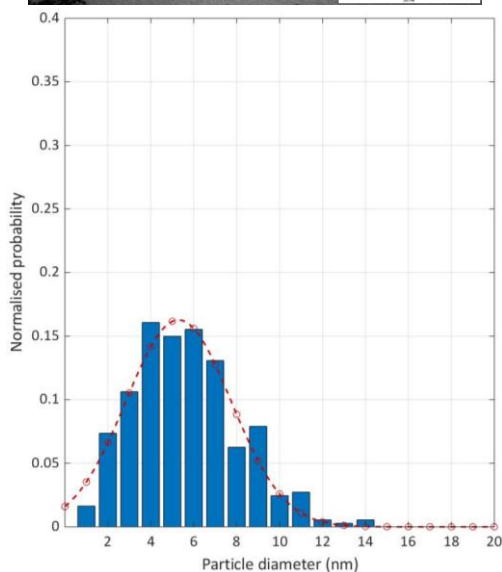
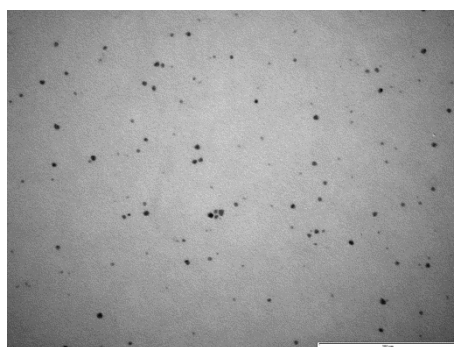




**RUN05**

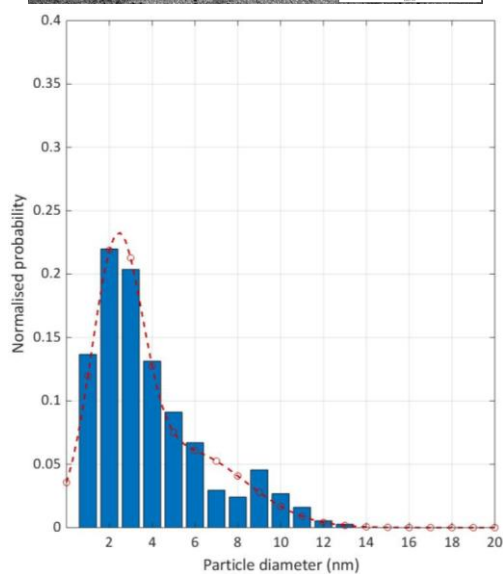
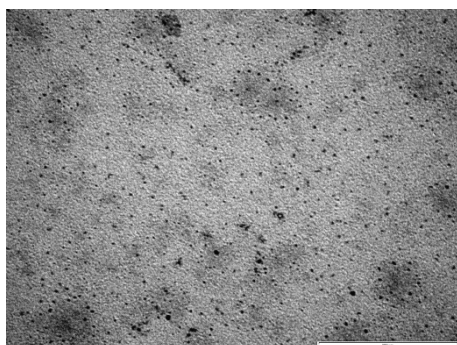


**RUN06**

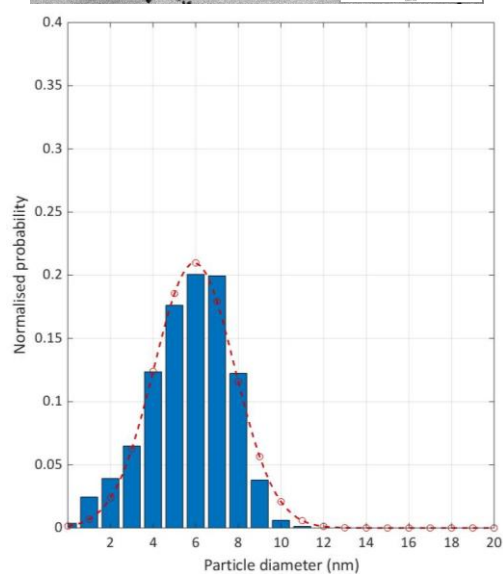
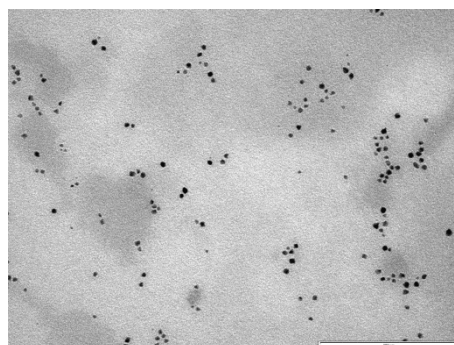




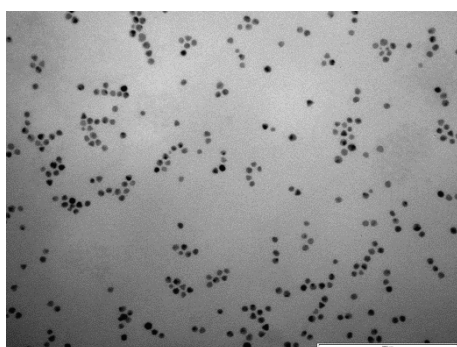
**RUN07**



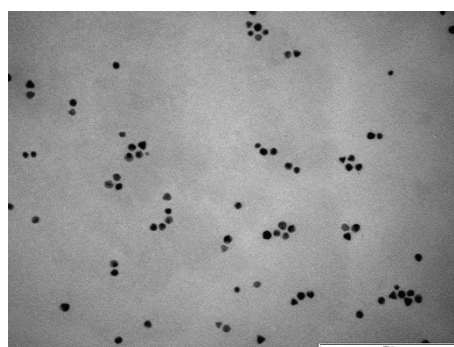
**RUN08**



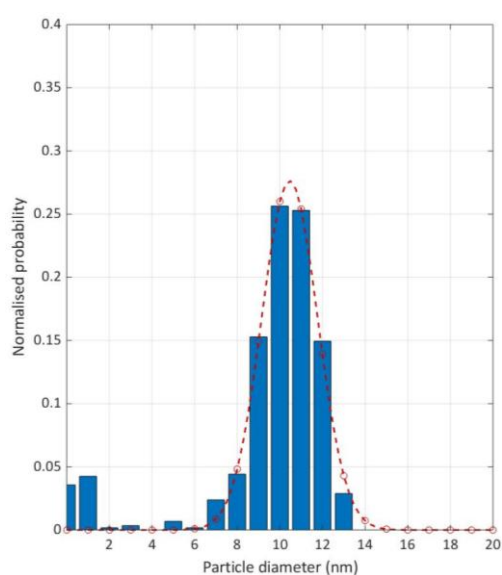
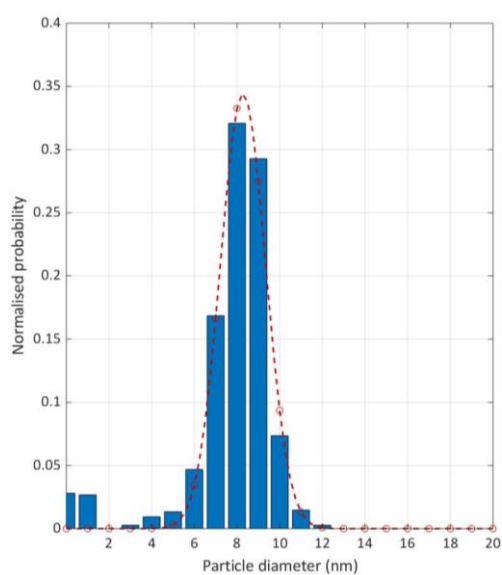
**RUN09**



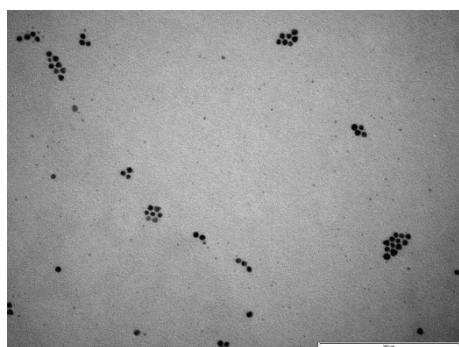
**RUN10**



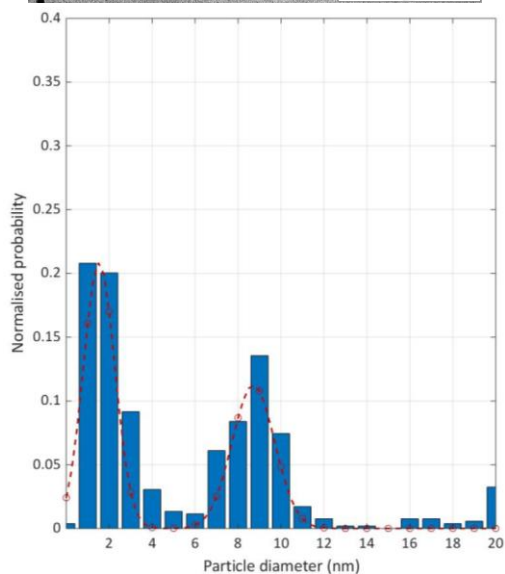
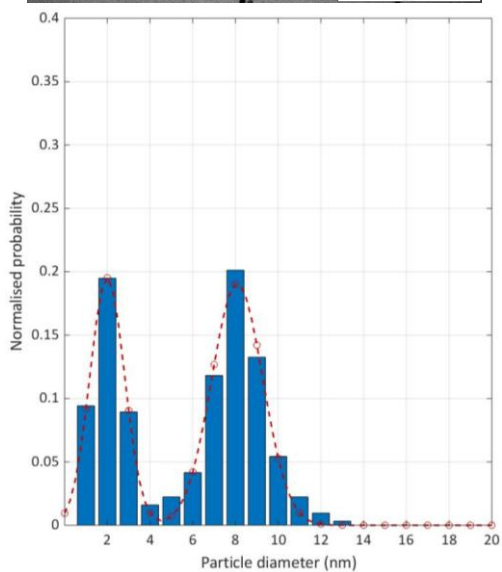
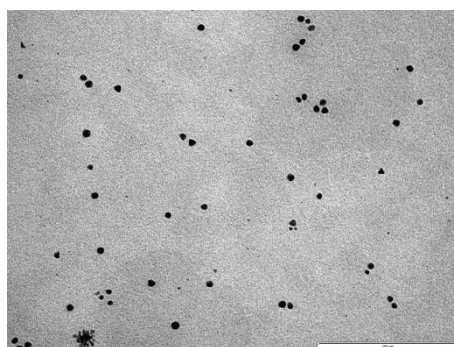




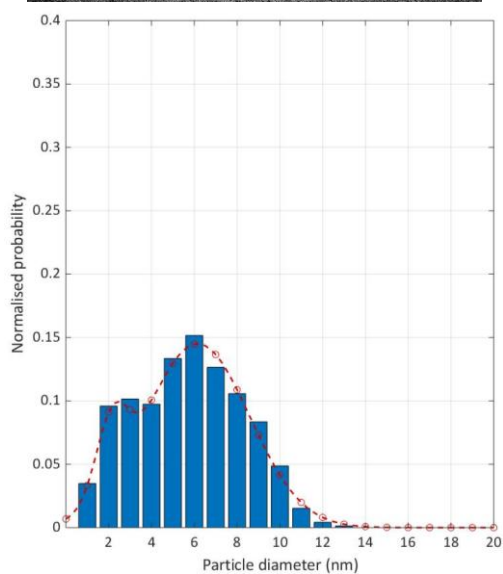
**RUN11**



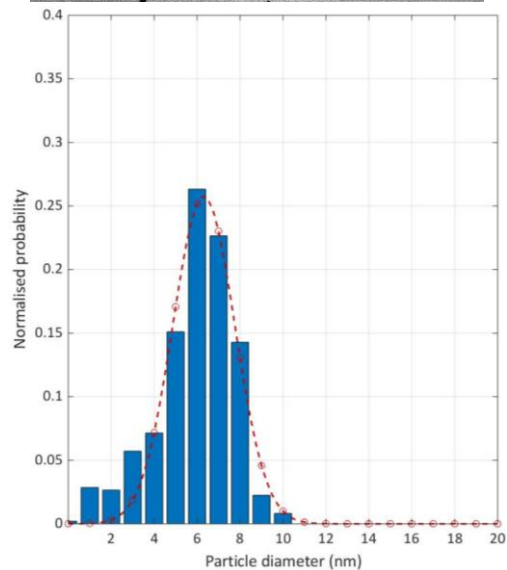
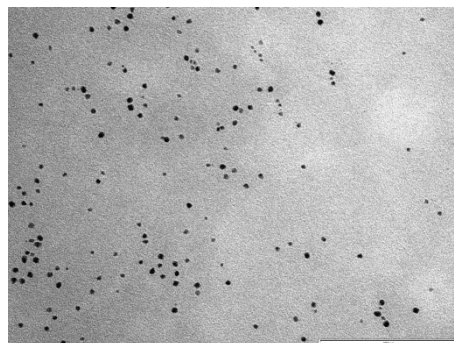
**RUN12**



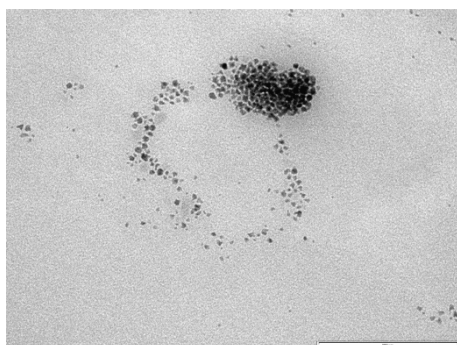
**RUN13**



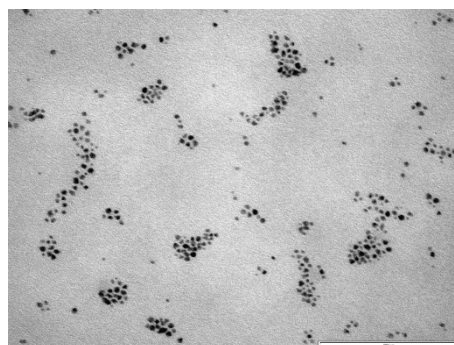
**RUN14**



**RUN15**



**RUN16**



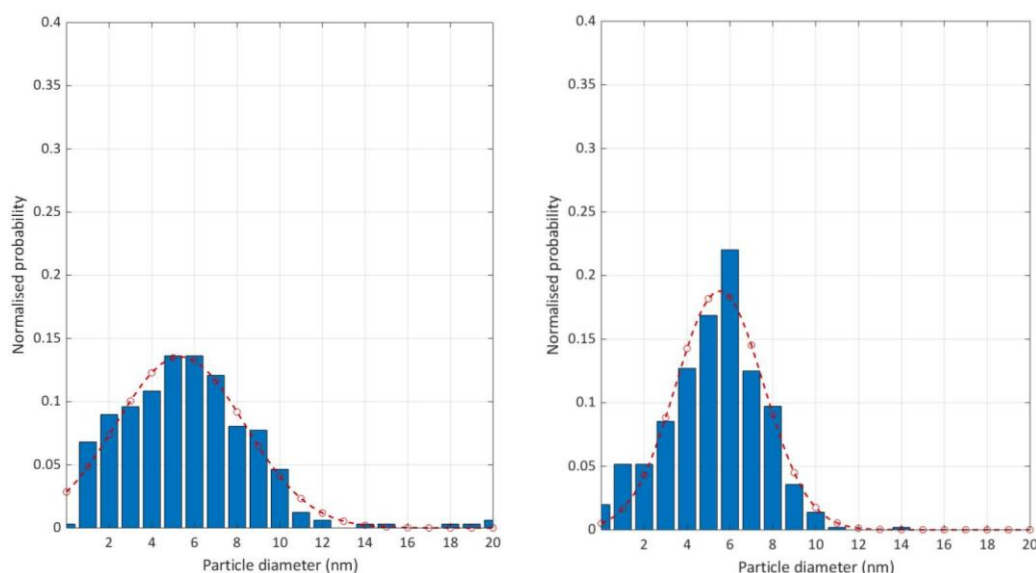


Figure 5.9. TEM micrographs and size distribution histograms of the sixteen experiments of the fractional factorial design  $2^{6-2}$  performed with the **Set-up 2**

A small fraction of small NPs appeared on the TEM histograms of the **RUN09** and **RUN10**. This observation was associated to an artifact of the measurement methodology related to the lack of definition and contrast in some TEM images as shown in Figure 5.10.

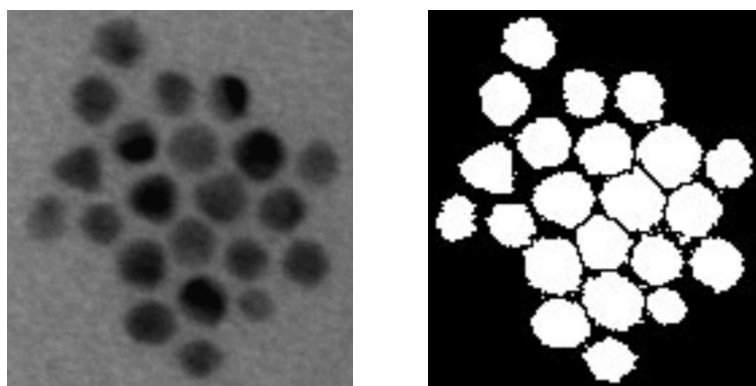


Figure 5.10. On the left a zone of a TEM micrograph of the **RUN09** and on the right the corresponding zone after threshold treatment

Moreover, the proportion of NPs larger than 20 nm observed on the TEM micrograph of the **RUN12** came from the presence of some star shape NPs on the TEM sample. Consequently the sphericity and efficiency of this batch was low.

## Definition of the responses of the design

The aim of this study was the identification of the experimental factors that affect the most the Pd-HHDMA formation. Therefore, to calculate the effects of these factors, it was of high importance to define numerical responses that characterize well what was observed on the TEM images (shape of the NPs, size, distribution and presence of agglomeration). The details of the selected responses of this design are described as follow.

- *Y1: Percentage of spherical NPs in the sample*

The percentage of spherical NPs in the TEM sample was estimated as detailed in chapter 3 (section 3.4.5.) and corresponds to the fraction of NPs having an aspect ratio lower than 1.3.

- *Y2: Nanoparticles size*

The NPs diameter considered in all the study was the equivalent spherical diameter. It corresponds to the diameter of a sphere of equivalent area. In some TEM samples, double distribution were observed, thus the analysis of the effects of factors on the NPs size was carried out using the averaged mean NPs size. This average value was estimated taking into account the contribution percentages of the area of each fitted peak. Although the average size of a double distribution has no physical meaning, this value was used to have insights about which factors affect the most the NPs size.

- *Y3: Type of distribution (single or multiple)*

In at least five batches of Pd-HHDMA NPs, double distribution were clearly observed. To attempt the identification of which of the studied factors causes this phenomenon, an analysis was performed using discrete numbers: 0 which corresponds to a single distribution and 1 which corresponds to a double or multi distribution. A binary logistic regression was used to provide the probability of the multiple distributions to take place. To do so, a Matlab® routine was used. This probability was expressed as  $\pi = \frac{e^z}{1+e^z}$  with  $z$  the linear regression model ( $z = a_0 + a_1x_1 + a_2x_2 + \dots + a_nx_n$ ). To estimate the model, usual least squares model could no longer be used. Instead the

maximum likelihood method was applied. The starting point of this estimation was the Bernoulli distribution:  $P(Y_i) = \pi_i^{Y_i}(1 - \pi_i)^{1-Y_i}$  for  $Y_i = 0,1$ . Iterations were performed to find the best estimates of the coefficients of the model  $(a_0, \dots, a_n)$  that maximize the likelihood. The likelihood of the data was expressed by  $L = \prod_{i=1}^n P(Y_i)$ . Its maximum was obtained by the derivative of the  $\ln(L)$ .

- *Y4: Synthesis efficiency*

The efficiency of the synthesis was estimated as detailed in chapter 3 (section 3.4.5.). It was defined as the fraction of NPs with spherical shape and with a size included in the largest-area peak of the Gaussian distribution.

Table 5.7. Numerical results of the sixteen experiments of the fractional factorial design  $2^{6-2}$  performed with the **Set-up 2**

RUN	FR (%) <sup>a</sup>	Average mean size (nm)	Type of distribution	Efficiency (%)
<b>01</b>	88.00	7.20	0	90.20
<b>02</b>	63.60	4.66	1	36.11 <sup>c</sup>
<b>03</b>	92.40	8.03	0	92.90
<b>04</b>	60.30	5.33	1	53.32 <sup>c</sup>
<b>05</b>	55.00	5.29	0	45.90
<b>06</b>	72.80	4.63	0/1 <sup>b</sup>	30.78 <sup>c</sup>
<b>07</b>	51.30	3.81	1	10.12 <sup>c</sup>
<b>08</b>	72.10	5.94	0	77.40
<b>09</b>	88.90	8.28	0	94.80
<b>10</b>	86.30	10.46	0	96.00
<b>11</b>	78.20	5.32	1	42.46 <sup>c</sup>
<b>12</b>	40.50	4.83	1	7.18 <sup>c</sup>
<b>13</b>	56.40	5.11	0/1 <sup>b</sup>	35.22 <sup>c</sup>
<b>14</b>	72.90	6.31	0	80.00
<b>15</b>	43.10	5.33	0	15.60
<b>16</b>	54.80	5.53	0	56.90

<sup>a</sup>: Fraction of spherical NPs, <sup>b</sup>: The double distribution was not clear, first the analysis was performed considering these batches as monomodal and then a second analysis was performed considering them as double distribution. <sup>c</sup>: Efficiency estimated by the subtraction of the fraction of agglomerated NPs and the fraction of the NPs belonging to the smallest area peak of the two Gaussian functions adjusted to the set of data.

## Analysis of the effects of the studied factors on the percentage of spherical NPs (response $Y1$ )

The normal probability plot and the plot of effects in relation to a t-distribution are displayed in Figure 5.11. The t-distribution was based on the data provided by the six central points. This distribution was drawn with five degrees of freedom and a full width at half maximum (FWHM) of 4.2 which corresponds to twice the standard deviation of the effects,  $std(b)$ , calculated from the experimental standard deviation of the responses,  $std(y)$ , of 8.5.

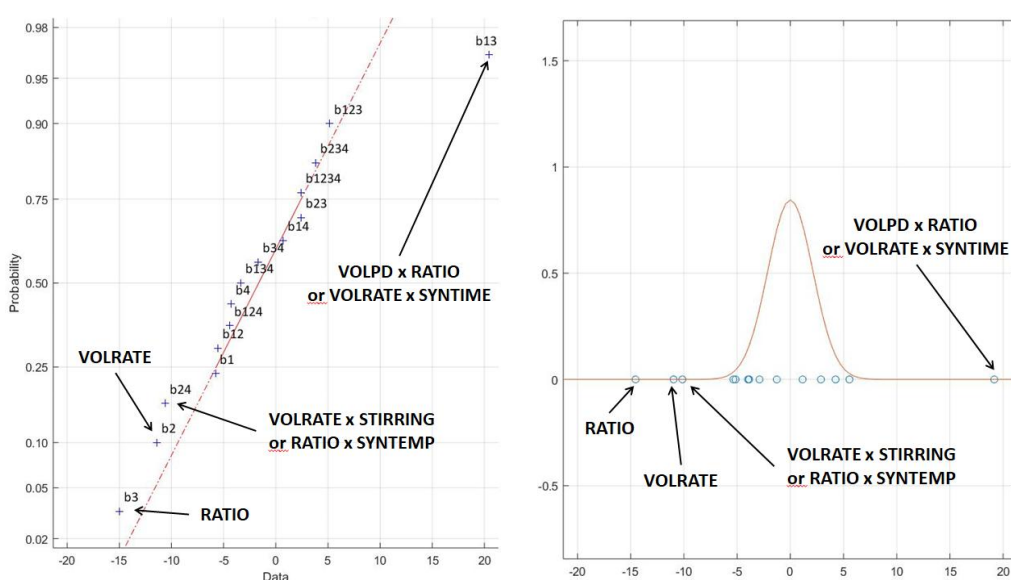


Figure 5.11. On the left: normal probability plot. On the right: t-distribution plot of the effects on the averaged mean NPs size obtained by fitting one or more Gaussian function to the histogram binned with a bin size of 1 nm

To interpret the normal probability plot, the plotted points (that represent the estimated effect of the design) in comparison with the normal line were observed. If these points fitted well to the normal line, it could be concluded that none of the studied factors were significantly affecting the response. In contrast, if some points did not fit with the line, it means that they were not following a normal distribution and thus they probably had a significant effect on the response. In the case of the t-distribution, if the points belonged to the normal distribution, it could be concluded that they were not affecting significantly the studied system. In contrast if outliers



were observed, it means that they were not following the normal distribution estimated from the central points of the design and thus, they probably had significant effect on the response.

In the presented case, four points were highlighted. These results suggest that the formation of spherical NPs was mainly affected by the factors 2 and 3 (VOLRATE and RATIO, respectively) and the second-order interactions 24 and 13. The interaction 24 corresponds to the interaction between VOLRATE and STIRRING and was confounded with the interaction 36: RATIO and SYMTEMP. The interaction 13 corresponds to the interaction between VOLPD and RATIO and was confounded with the interaction 25: VOLRATE and SYNTIME.

The estimated effects of the studied factors and interactions on the fraction of spherical NPs are given in the bar chart and the Pareto plot in Figure 5.12. Both plots give similar information but the Pareto plot makes easier to identify the most important effects since, in this case, they are ordered in descending order.

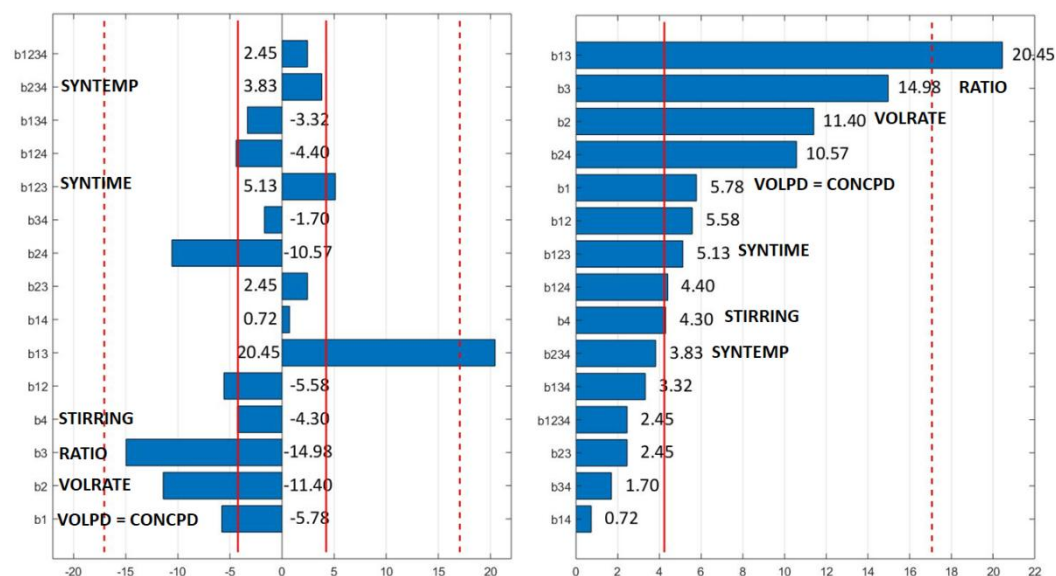


Figure 5.12. Fraction of spherical NPs. On the left, the plot of effects and on the right, the Pareto plot of effects with the standard deviation of the coefficients given by the red line and the interval of confidence with five degrees of freedom represented by the dashed red line

These plots confirmed the fact that the factors 2 and 3 and the second-order interactions 24 and 13 were mostly affecting the fraction of spherical NPs.

An analysis of variance (ANOVA) was performed in order to discriminate the different models that described the studied system. With this analysis, the coefficient of multiple determination  $R^2$ , the effectiveness of the factors, the lack of fit and the purely experimental uncertainty were estimated for the possible models.

A Matlab® routine was used. It computes all the possible models that described the studied set of data as a function of the number of factors and provides the best fit of the model. The steps of this analysis followed a reference guide for the ANOVA for linear models; the main steps of this methodology are given in appendix 5.6.5.<sup>11</sup>

Briefly, the coefficient of multiple determination  $R^2$  indicates how good the factors are explaining the responses. It ranges from 0 to 1. When it is close to 0, it indicates that the factors, as they appear in the model, have no effect upon the response. When it tends to 1, it indicates that the residuals are very small and thus that the factors explain well the data. Moreover, statistical test were performed to verify the effectiveness of factors and the lack of fit. To estimate the effectiveness of factors, the ratio of the variance of the sum of squares of the factors ( $s_{fact}$ ) divided by the variance of the sum of squares of residuals ( $s_{res}$ ) was estimated. The larger this ratio, the more significant the factor effects. Then, to have an idea about how good was the fitting of the considered model to the set of data, a test that compare the variance of the sum of squares of lack of fit ( $s_{lof}$ ) and the sum of squares of purely experimental uncertainty ( $s_{pe}$ ) was computed. If this difference is large, it means that there is still a significant amount of the variation in the measured responses that is not explained by the model, thus lack of fit is detected. This test can be implemented when the number of factor combinations is greater than the number of parameters in the model and when replicates are provided to estimate the variance due to purely experimental uncertainty.



For the studied response (fraction of spherical NPs), the Matlab® routine was used and all the possible models taking into account from 1 to 10 parameters were estimated. The best fittings obtained are given in appendix 5.6.6. For all of these models the effectiveness of the factors and the lack of fit were verified. No lack of fit was detected. The coefficient of multiple determination  $R^2$  and the purely experimental uncertainty were estimated and plotted as a function of the number of parameters considered in the model (cf. Figure 5.13)

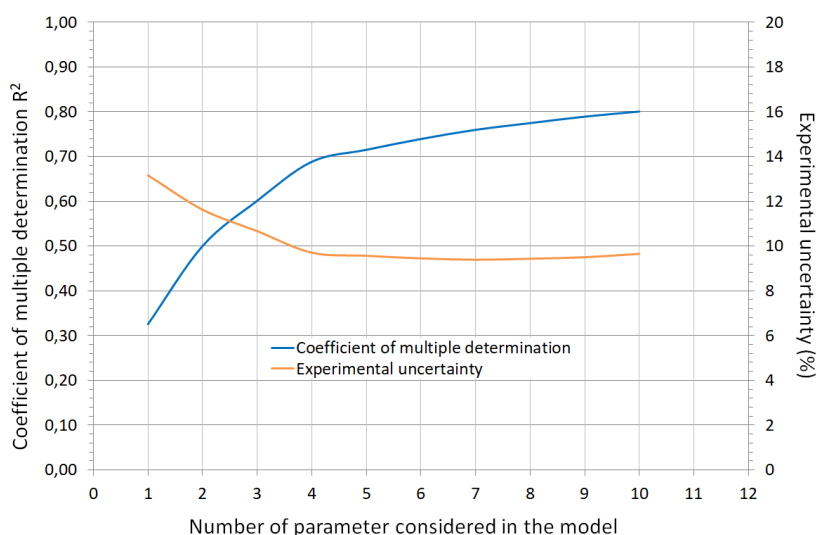


Figure 5.13. Analysis of variance for linear model performed on the response  $Y1$  (fraction of spherical NPs) of the design  $2^{6-2}$ . Evolution of the coefficient of multiple determination and the purely experimental error as a function of the number of parameters considered in the fitted models

This plot indicates a significant increase of  $R^2$  and decrease of the experimental uncertainty estimation when the number of parameters included in the model was increased from 1 to 4. When more than 4 parameters were considered in the model, no decrease of experimental uncertainty was observed suggesting that the lower variability obtained in this system was around 9%.

The 4-parametric model and 10-parametric model explained 70% and 80% of the measured responses, respectively. Only 10% of information was gained with the addition of 6 parameters in the model. The selection of a model to describe a system is subjective; it depends on the context of the study (project deadlines, resources,

required precision, etc). In this study, it was decided that the description of 70% of the measured responses by the control of only 4 parameters and obtaining the lowest estimated experimental uncertainty was quite satisfactory. This selected model was the following one:

$$\hat{y} = 70.60 - 5.70x_2 - 7.49x_3 + 10.23x_1x_3 - 5.29x_2x_4$$

This model indicates that the four factors that mostly affect the measured responses were: factors 2 and 3 (VOLRATE and RATIO, respectively) and the second-order interactions 24 and 13. This conclusion was in agreement with what was observed in the normal probability plot and the plot of the effects presented above which give confidence on this conclusion. The precise effects of each of these parameters are detailed below.

First, the interaction 13 revealed the most significant effect on the responses. This interaction corresponds to the interaction between the factors 1 (VOLPD) and 3 (RATIO) and was confounded with the interaction 25: VOLRATE and SYNTIME:  $L_{13} = b_{13} + b_{25}(+b_{1246} + b_{3456})$ .

Considering that the addition time of the Pd solution was very short in comparison with the total time of synthesis, it was assumed that the interaction 25 was not significant. Thus, the estimated effect  $L_{13}$  was attributed to the interaction between the Pd concentration (varied as Pd volume) and the initial HHDMA-to-Pd molar ratio ( $L_{13} \approx b_{13}$ ).

The plot of effect in Figure 5.12 indicates that higher fraction of spherical NPs was obtained when this interaction was fixed at its high level (the effect  $b_{13}$  had a positive value: +20.45). Therefore it corresponds to a combination of (-1, -1) or (+1, +1) of the factors (1, 3), respectively. To verify if one option was more significant than the other, the diagram of this interaction was drawn and is presented in Figure 5.14.

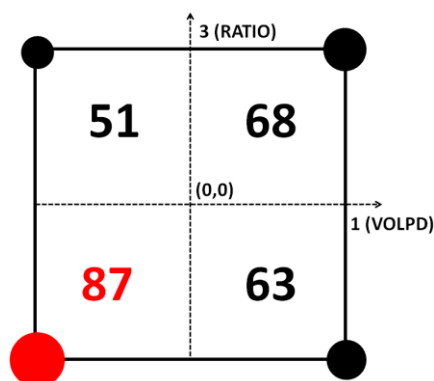


Figure 5.14. Diagram of the interaction 13 (VOLPD vs. RATIO) for the response Y1 (fraction of spherical NPs in %)

This diagram indicates that the combination  $(-1, -1)$  for the factors (1, 3), respectively, gave much higher fraction of spherical NPs than the combination  $(+1, +1)$ . Therefore, it could be concluded that a small volume of Pd injection (or high Pd concentration in the injection) combined with a low initial HHDMA-to-Pd ratio provided larger fraction of spherical NPs.

After that, the plot of effect given in Figure 5.12 indicates that a low level of the parameters 2 and 3 (VOLRATE and RATIO, respectively) provided larger fraction of spherical NPs. It corresponds to a Pd addition rate of 2 mL/min and a HHDMA-to-Pd molar ratio of 3 eq.

Soulantica and co-workers also reported that a slow addition rate of Co precursor to the ligands mixture solution favored the formation of spherical small NPs. They related this trend to the extended nucleation step in which a large part of the cobalt was consumed and the formation of a growth “reservoir” was limited in contrast to the fast addition rate.<sup>9</sup>

Finally, concerning the effect of the interaction 24 (which was confounded with the interaction 36), the plot of effects (Figure 5.12) indicates that higher fraction of spherical NPs were obtained when this interaction was fixed at its low level (the effect  $b_{24}$  has a negative value:  $-10.57$ ). Therefore it corresponds to a combination of  $(-1,$

+1) or (+1, -1) of the factors (2, 4) or (3, 6), respectively. The effects of these interactions were verified using the interaction diagrams presented in Figure 5.15.

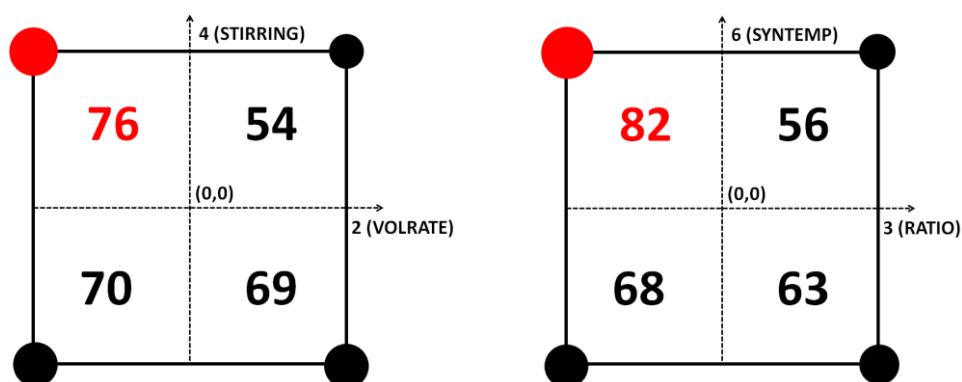


Figure 5.15. Diagram of interactions for the response  $Y1$  (fraction of spherical NPs in %). On the left the interaction between the volumetric addition rate of the Pd solution and the stirring rate. On the right the interaction between the initial HHDMA-to-Pd molar ratio and the temperature of the synthesis

These diagrams show that a combination (-1, +1) for the factors (2, 4) or (3, 6), respectively, provided large amount of spherical NPs. In other words, a slow Pd addition rate (2 mL/min) combined with a high stirring speed (500 rpm) or a low HHDMA-to-Pd molar ratio (3 eq.) combined with a high temperature of synthesis (95°C) provided high percentages of spherical NPs. It was not possible to distinguish both interactions, more experiments should be conducted to be able to separate the effect of each one.

To conclude, the analysis of the effect of the studied factors on the fraction of spherical NPs suggests that the combination of factors (-1, -1, -1, +1, ±1, +1) for (1, 2, 3, 4, 5, 6), respectively, provided highly spherical sample. The **RUN09** of the designed matrix corresponds to one of these combinations (-1, -1, -1, +1, -1, +1) and resulted to give 88.9% of spherical NPs which was one of the highest value obtained from the set of experiments. Nevertheless, four other combinations of factors resulted to give high percentage of spherical NPs: the **RUN01**, **RUN03**, **RUN10** and **RUN11** (88.0%, 92.4%, 86.3% and 78.2%, respectively). A common observation to the **RUN01**, **RUN03**, **RUN09** and **RUN11** was that all these experiments were performed using a high concentration

of Pd solution (low level of factor 1, VOLPD) and a low HHDMA-to-Pd ratio (factor 3) independently of the other parameters. This observation confirms that the interaction 13 is much more significant than all other parameters and interactions. Concerning the **RUN 10**, this interaction (13) was not fixed to its high level, however both factors 2 (VOLRATE) and 3 (RATIO) as well as the interactions 24 (VOLRATE and STIRRING) and 36 (RATIO and SYNTEMP) were fixed to their low levels.

Consequently, to obtain highly spherical NPs by the control of only two factors, the preferred option was to highly concentrate the Pd solution in the injection and to fix a low HHDMA-to-Pd ratio. As far as possible, to ensure the well-formation of spherical NPs, the recipe could be combined with a slow Pd injection, a high stirring rate and high temperature of synthesis. These conclusions, summarized on the radar diagram presented in Figure 5.16, indicate that the injection of the Pd in the HHDMA solution is a key step to control the NPs shape.

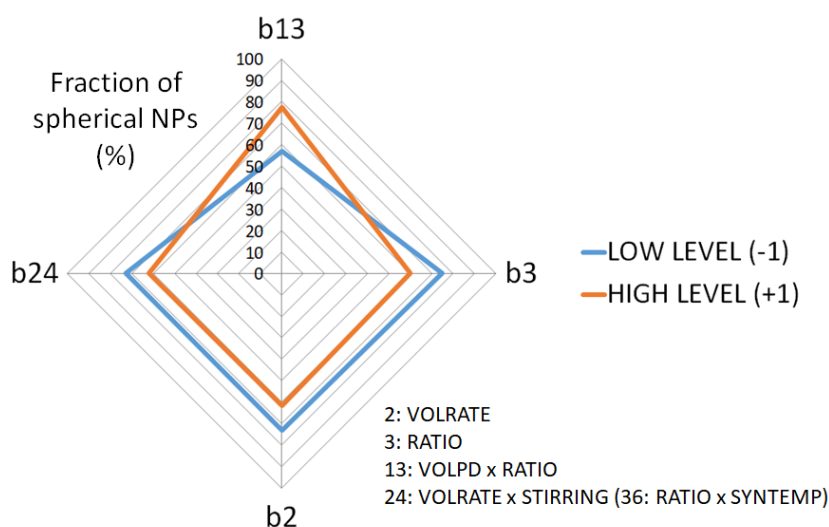


Figure 5.16. Radar diagram of the effects  $b_{13}$  (VOLPD vs. RATIO),  $b_3$  (RATIO),  $b_2$  (VOLRATE) and  $b_{24}$  (VOLRATE vs STIRRING confounded with 36: RATIO vs. SYNTEMP) on the percentage of spherical NPs obtained (response  $Y_1$ )

## Analysis of the effects of the studied factors on the average mean NPs size (response Y2)

The estimated effects of the studied factors and interactions on the average mean NPs size are given in the bar chart and the Pareto plot in Figure 5.17.

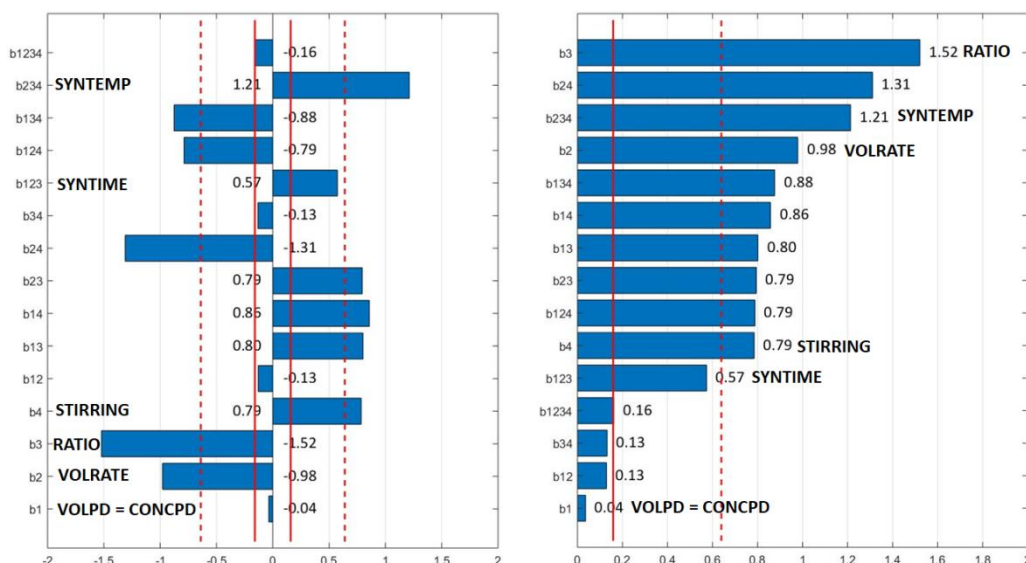


Figure 5.17. Averaged mean NPs size. On the left, the plot of effects and on the right, the Pareto plot of effects with the standard deviation of the coefficients given by the red line and the interval of confidence with five degrees of freedom represented by the dashed red line

These plots revealed that the NPs size was affected by a large number of factors and interactions. The resulting model equation that described the entire studied system was the following 15-parameter equation:

$$\begin{aligned} \hat{y} = & b_0 + b_1x_1 + b_2x_2 + b_3x_3 + b_4x_4 + b_{12}x_1x_2 + b_{13}x_1x_3 + b_{14}x_1x_4 + b_{23}x_2x_3 \\ & + b_{24}x_2x_4 + b_{34}x_3x_4 + b_{123}x_1x_2x_3 + b_{124}x_1x_2x_4 + b_{134}x_1x_3x_4 \\ & + b_{234}x_2x_3x_4 + b_{1234}x_1x_2x_3x_4 \end{aligned}$$

To investigate about the possibility of reducing this model, an analysis of variance (ANOVA) was performed. Models taking into account from 1 to 15 parameters were estimated. From 1 to 8 parameters, lack of fit was detected indicating that the measured data could not be described by a model of less than 9 parameters. It was not surprising since the Pareto plot revealed 10 factors with an effect on the NPs size higher than the margin of error (significant factors). For the best fitting models taking

into account from 9 to 15 parameters, the effectiveness of the factors and the lack of fit were estimated. The coefficient of multiple determination  $R^2$  and the purely experimental uncertainty were estimated and plotted as a function of the number of parameters considered in the model (cf. Figure 5.18).

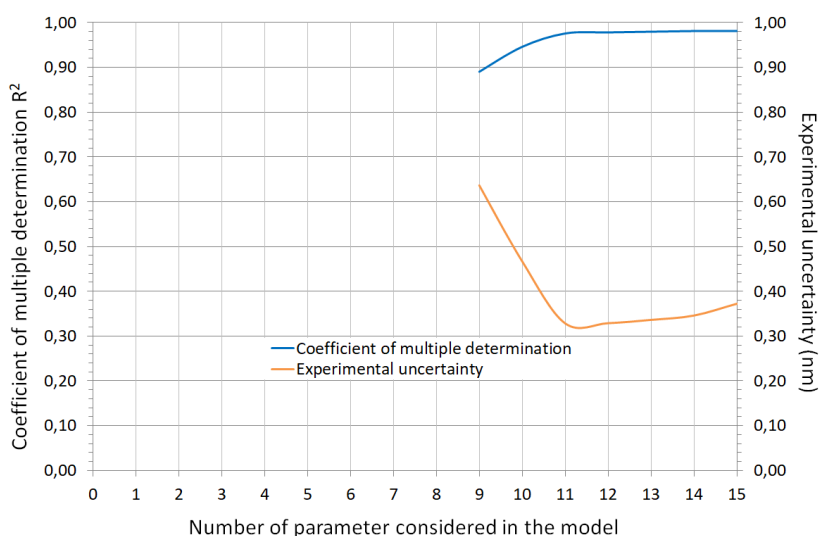


Figure 5.18. Analysis of variance for linear model performed on the response Y2 (average mean NPs size) of the design  $2^{6-2}$ . Evolution of the coefficient of multiple determination and the purely experimental error as a function of the number of parameters considered in the fitted models

This plot indicates a significant increase of  $R^2$  and decrease of the estimation of the experimental uncertainty when the number of parameters included in the model was increased from 9 to 11. When more than 11 parameters were considered, the coefficient of multiple determination  $R^2$  remained constant to a value close to 1 (*ca.* 0.98). Moreover, the estimated experimental uncertainty reached its lowest value with the 11-parametric model. Therefore, with the control of 11 parameters over 15 studied, the data could be described almost perfectly. It was noticed that the reduced model containing 9 parameters also explained well the set of data (*ca.* 90%) however; in this case, the experimental uncertainty was larger. The estimated 11-parametric model was the following:

$$\hat{y} = 5.93 - 0.49x_2 - 0.76x_3 + 0.39x_4 + 0.29x_5 + 0.61x_6 + 0.40x_1x_3 + 0.43x_1x_4 + 0.40x_2x_3 - 0.66x_2x_4 - 0.39x_1x_2x_4 - 0.44x_1x_3x_4$$

The plot of effect presented in Figure 5.17 and the ANOVA revealed that 11 factors and interactions were highly affecting the NPs size. Thus the analysis of this system was not straightforward. First, the main effects are described, then the second-order interactions and finally the third-order interaction.

The factors 2, 3, 4, 5 and 6 (VOLRATE, RATIO, STIRRING, SYNTIME and SYNTEMP, respectively) were affecting the NPs size. Larger NPs were obtained when the addition of the Pd solution was slow, the HDDMA-to-Pd ratio was low, and the stirring rate, synthesis time and temperature were high, as summarized in Figure 5.19.

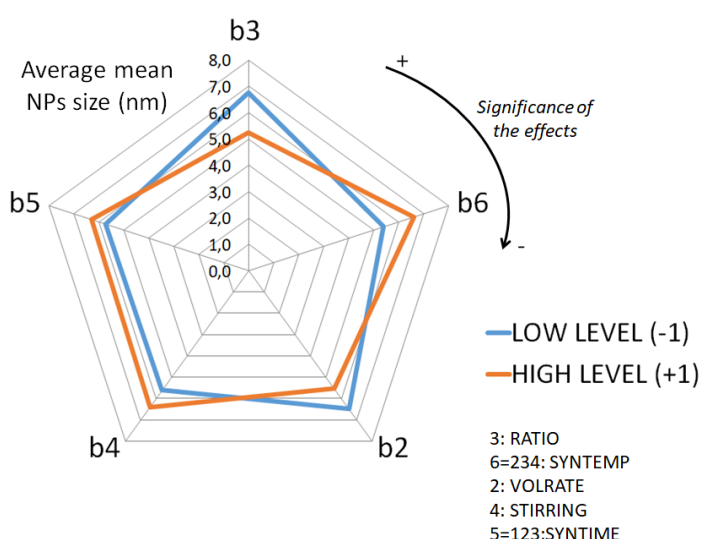


Figure 5.19. Radar diagram of the significant single factor effects on the average mean NPs size (response Y2)

Then, four second-order interactions were identified as important to control the NPs size (24, 14, 13 and 23), they are analyzed below.

- Interaction 24:  $L_{24} = b_{24} + \mathbf{b_{36}}(b_{1256} + b_{1345})$

The interaction 24 corresponds to the interaction between the factors 2 (VOLRATE) and 4 (STIRRING) and was confounded with the second-order interaction 36 (RATIO x SYNTEMP). The discrimination between both interactions was not possible without conducting more experiments. Indeed since temperature is a key factor that controlled the kinetics of the particle seeding and growing, the interaction 36 was expected to play an important role. Likewise, the interaction 24 might be non-



negligible since both factors 2 and 4 appeared to be of similar importance. According to the plot of effects, larger NPs were obtained when these interactions were fixed to their low level. The diagrams of these interactions are presented in Figure 5.20.

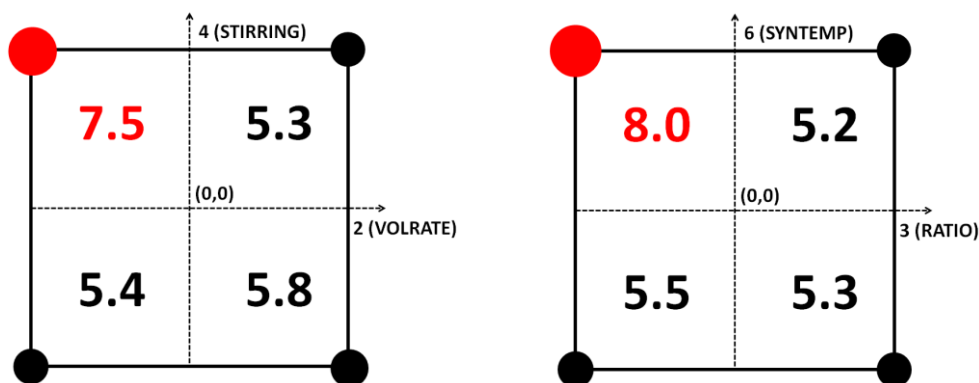


Figure 5.20. Diagram of interactions for the response Y2 (average mean NPs size in nm). On the left the interaction between the volumetric addition rate of the Pd solution and the stirring rate (24). On the right the interaction between the initial HHDMA-to-Pd molar ratio and the temperature of the synthesis (36)

These diagram showed that the combination (-1, +1) for the factors (2, 4) or (3, 6), respectively, provided larger NPs. In other words, larger NPs were obtained with the combination of slow Pd injection with a high stirring rate and the combination of low HHDMA-to-Pd ratio with high temperature.

- Interaction 14:  $L_{14} = b_{14} + b_{56}(+b_{2345} + b_{1236})$

The interaction 14 corresponds to the interaction between the factors 1 (VOLPD) and 4 (STIRRING) and was confounded with the second-order interaction 56 (SYNTEMP x SYNTEMP). As the previous case, the discrimination between both interactions was not straightforward with the available data. Larger NPs were obtained when these interactions was at their high level. The diagrams of these interactions are displayed in Figure 5.21.

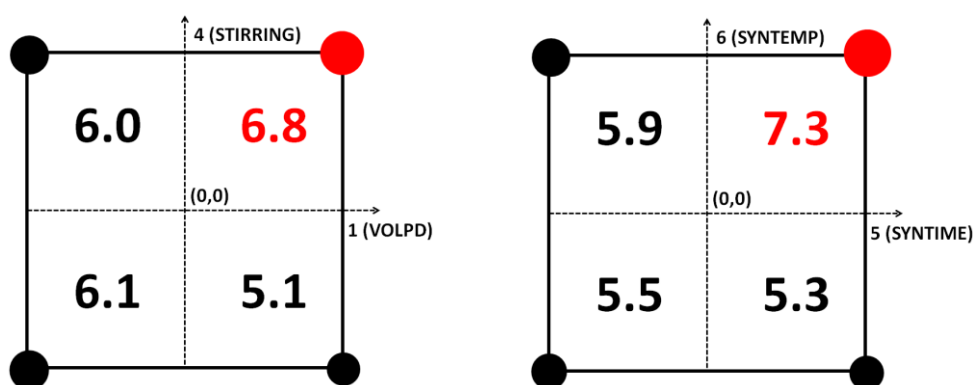


Figure 5.21. Diagram of interactions for the response Y2 (average mean NPs size in nm). On the left the interaction between the Pd volume in the injection and the stirring rate (14). On the right the interaction between the synthesis time and temperature (56)

These diagram showed that the combination (+1, +1) for the factors (1, 4) or (5, 6), respectively, provided larger NPs. In other words, larger NPs were obtained with the combination of high volume in the Pd injection (low concentration) with a high stirring rate and the combination of long time and high temperature.

- Interaction 13:  $L_{13} = b_{13}(+b_{25} + b_{1246} + b_{3456})$

The interaction between the factor 1 (VOLPD) and 3 (RATIO) was confounded with the interaction 25 (VOLRATE x SYNTEMP). It was assumed that the interaction 25 was not significant in comparison with the interaction 13 for the reason explained in the above section. Thus, the estimated effect  $L_{13}$  was attributed to the interaction between the Pd concentration (varied as Pd volume) and the initial HHDMA-to-Pd ( $L_{13} \approx b_{13}$ ). Larger NPs were obtained when it was fixed at its high level. The diagram of this interaction is presented in Figure 5.22.

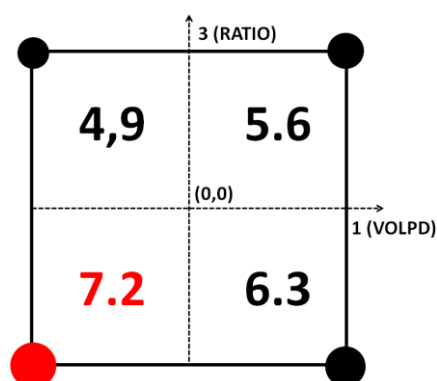


Figure 5.22. Diagram of the interaction 13 (VOLPD x RATIO) for the response Y2 (average mean NPs size)

Larger NPs were obtained when low Pd volume in the injection (high Pd concentration) was combined with low HHDMA-to-Pd ratio.

- Interaction 23:  $L_{23} = \mathbf{b_{23}}(+b_{15} + b_{46} + b_{123456})$

The interaction between the factor 2 (VOLRATE) and 3 (RATIO) was confounded with the interaction 15 (VOLPD x SYNTIME) and 46 (STIRRING x SYNTEMP). They were not expected to be significant. The diagram of the interaction 23 is displayed in Figure 5.23.

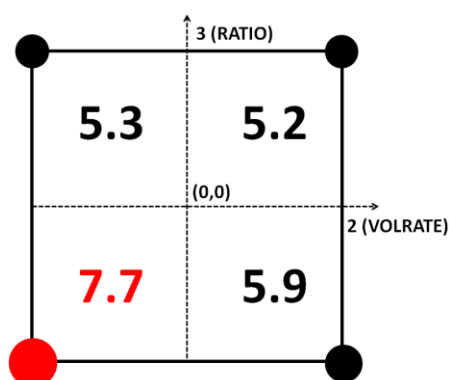


Figure 5.23. Diagram of the interaction 23 (VOLRATE x RATIO) for the response Y2 (average mean NPs size)

Larger NPs were formed by the combination of slow Pd addition and low HHDMA-to-Pd ratio.

To summarize, four second-order interactions resulted to affect in a significant way the NPs size, the concluded combinations of factors are shown in Figure 5.24 and recalled as follow.

Larger NPs were obtained when:

- Slow Pd addition to the HHDMA solution was combined with a high stirring rate
- Low HHDMA-to-Pd ratio was combined with a high temperature of synthesis
- Low Pd concentration in the injection was combined with high stirring rate
- Long synthesis time was combined with high temperature
- High concentration of Pd was combined with low HHDMA-to-Pd ratio
- Slow Pd addition to the HHDMA solution was combined with low HHDMA-to-Pd ratio

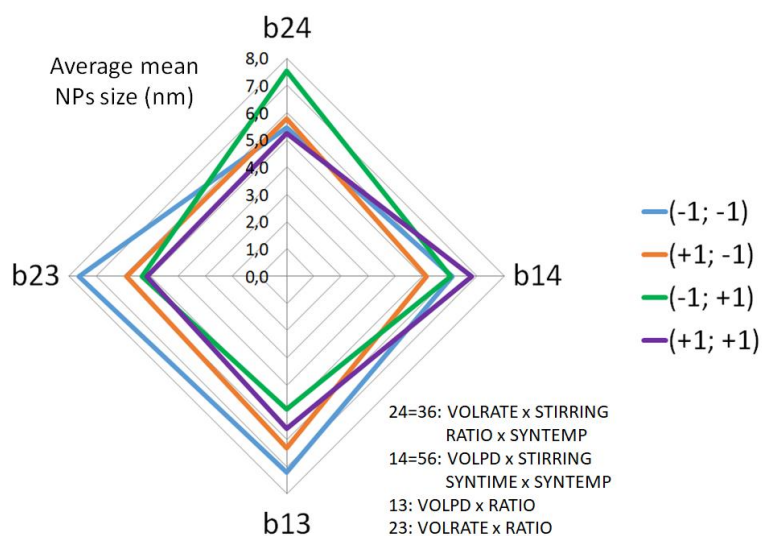


Figure 5.24. Radar diagram of the significant second-order interactions on the average mean NPs size (response Y2)

The second-order interaction 14 and 13 gave different conclusions for the factor 1, leading to two possible combination of factors to obtain large NPs:  $(\pm 1, -1, -1, +1, +1, +1)$  for (1, 2, 3, 4, 5, 6), respectively. It was in agreement with the conclusions of the analysis of the primary effects on the NPs size. The **RUN10** corresponds to the combination  $(+1, -1, -1, +1, +1, +1)$  and provided the largest NPs size of the set of experiments (*ca.* 10.45 nm).

In this analysis, the effect of two third-order interactions also appeared important (134 and 124). These interactions are usually neglected, however this example showed that in complex systems, this assumption is not always correct.

### Analysis of the effects of the studied factors on the type of distribution obtained (response Y3)

As mentioned above, double distributions were observed in some TEM samples. The single factors that could provoke this phenomenon were identified by estimation of the probability of occurrence thanks to a binary regression. As detailed in Table 5.7, from the sixteen experiments performed, five showed explicitly double distributions and for two batches the difference between wide distribution and double distribution was not clear (**RUN06** and **RUN13**). Therefore, the interpretation was performed in two steps: first, the five batches of double distributed population were considered, and then seven batches were taken into account.

The probability plots to obtain double distribution in both cases are given in Figure 5.25 and Figure 5.26.

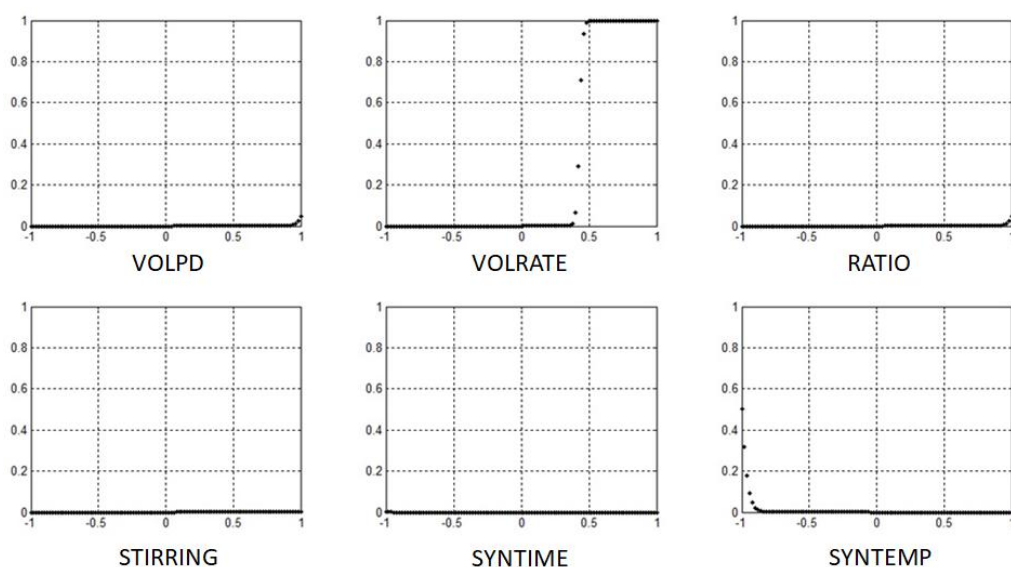


Figure 5.25. Probability to form double distribution as a function of the single factors studied where the abscissa gives the level of each factors (-1 low level and +1 high level) and the ordinate gives the probability – First case considering the **RUN06** and **RUN13** as unimodal

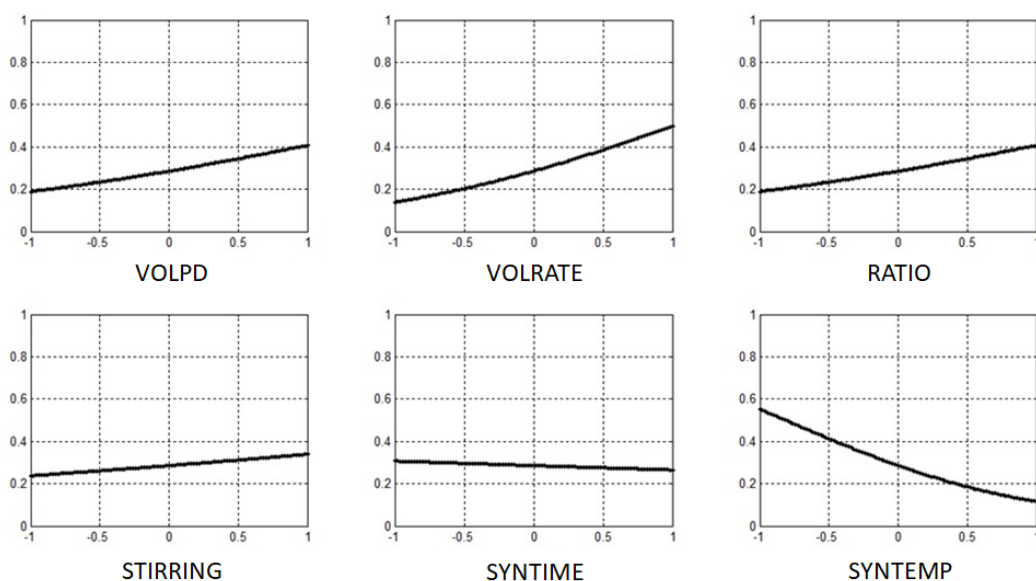


Figure 5.26. Probability to form double distribution as a function of the single factors studied where the abscissa gives the level of each factors (-1 low level and +1 high level) and the ordinate gives the probability – Second case considering the **RUN06** and **RUN13** as double distributed

In the first case (considering only the **RUN02**, **RUN04**, **RUN07**, **RUN11** and **RUN12**), high probability to obtain double distributions were found when the Pd addition rate into the HDDMA solution was fast and the synthesis temperature was low. The other factors did not appear as significant.

In the second case (considering the **RUN02**, **RUN04**, **RUN06**, **RUN07**, **RUN11**, **RUN12** and **RUN13**), the highest probability to obtain double distribution were also observed when the Pd addition rate into the HDDMA solution was fast and the synthesis temperature was low. Moreover, probability to obtain double distribution appeared when the Pd volume in the injection was high (low Pd concentration) and the HDDMA-to-Pd ratio was high. A contribution of the stirring and synthesis time was also observed but not highly significant in the range of studied values.

It is important to note that this analysis was performed using discrete data and applying binary logistic regression. The number of data used was quite low (16 experiments + 1 central point) and thus the confidence in these results could be

questioned. However, it provides an idea about which parameters are responsible for these double distributions. These results suggest that the injection velocity and temperature played an important role, also the Pd concentration in the injection and the HHDMA-to-Pd ratio seemed to affect in a most moderated way under the tested conditions.

### Analysis of the effect of the studied factors on the synthesis efficiency (response Y4)

The effects of the studied factors on the efficiency of the syntheses are displayed in the bar chart and Pareto plot in Figure 5.27.

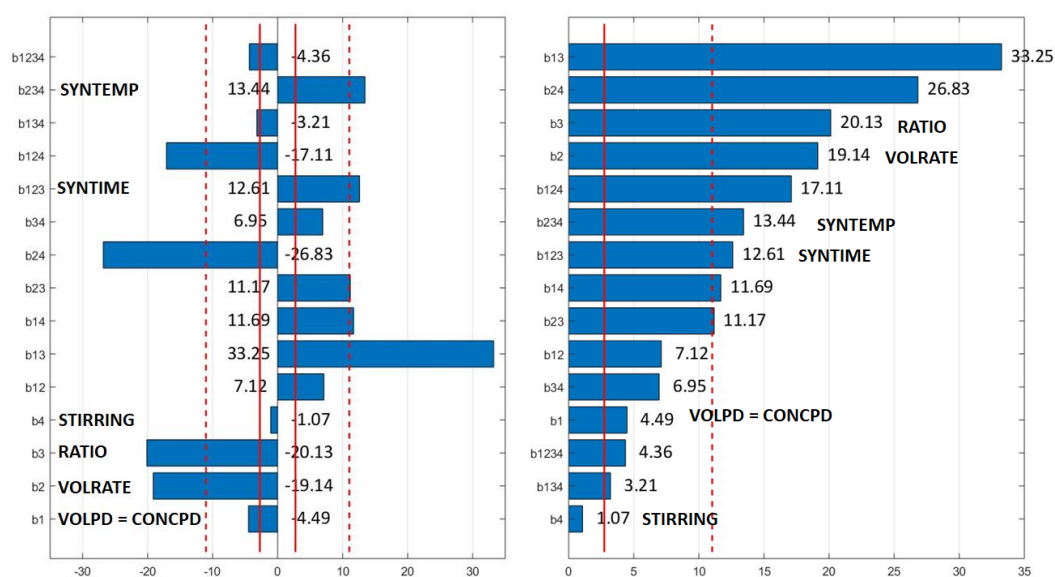


Figure 5.27. Efficiency of the syntheses. On the left, the plot of effects and on the right, the Pareto plot of effects with the standard deviation of the coefficients given by the red line and the interval of confidence with five degrees of freedom represented by the dashed red line

Nine of the fifteen studied factors and interactions showed effects larger than the estimated margin of error:

- Interaction 13: VOLPD and RATIO
- Interaction 24: VOLRATE and STIRRING (confounded with 36: RATIO and SYNTEMP)
- Factor 3: RATIO
- Factor 2: VOLRATE

- Interaction 124: confounded with the effect of the operator
- Interaction 234: confounded with the factor 6 (SYNTEMP)
- Interaction 123: confounded with the factor 5 (SYNTIME)
- Interaction 14: VOLPD and STIRRING (confounded with 56: SYNTIME and SYNTEMP)
- Interaction 23: VOLRATE and RATIO (confounded with 15: VOLPD and SYNTIME)

These results suggest that the control of the synthesis efficiency is not straightforward and depends on a large number of factors and interactions.

With the objective to figure out how many factors could be removed from the equation model without losing an important amount of information, an analysis of variance was performed. All the possible models were computed with Matlab®, however all the fitted models presented lack of fit. It means that the adjusted models were not able to describe an important amount of information given by the data. It could suggest that the effects of the studied factors on the synthesis efficiency did not follow a linear behavior. Therefore, it was not possible to rule out the effect of some factors or interactions by this analysis. It was decided to analyze the most significant effects (in descending order) of the Pareto plot given in Figure 5.27.

First, the interaction 13 revealed to have the most significant effect on the synthesis efficiency. This interaction corresponds to the interaction between VOLPD and RATIO and was confounded with the interaction 25: VOLRATE and SYNTIME. For the reasons given in the previous sections, the interaction 25 was neglected. The plot of effect in Figure 5.27 indicates that higher synthesis efficiencies were obtained when the interaction 13 was fixed to its high level (the effect  $b_{13}$  shows a positive value: +33.25). Therefore it corresponds to a combination of (-1, -1) or (+1, +1) of the factors (1, 3), respectively. To verify if one option was more significant than the other, the diagram of this interaction was drawn and is presented in Figure 5.28.



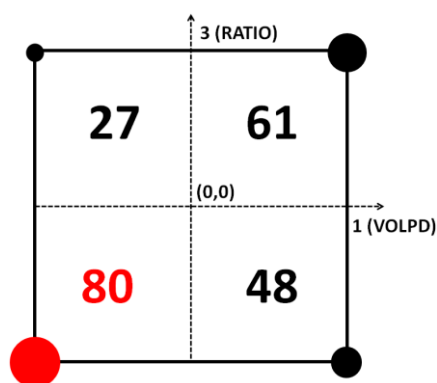


Figure 5.28. Diagram of the interaction 13 (VOLPD vs. RATIO) for the response Y2 (efficiency of the synthesis in %)

This diagram indicates that the combination  $(-1, -1)$  for the factors (1, 3), respectively, gave much higher average synthesis efficiencies than the combination  $(+1, +1)$ . Thus, a combination of small volume of Pd solution (high Pd concentration in the injection) and a low initial HHDMA-to-Pd ratio provided higher synthesis efficiencies (low agglomeration and principally unimodal distributions).

Moreover, the plot of effect given in Figure 5.27 indicates that a low level of the interaction 24 (confounded with the interaction 36) enabled obtaining high efficiencies (the estimated effect  $b_{24}$  shows a negative value:  $-26.83$ ). Therefore it corresponds to a combination of  $(-1, +1)$  or  $(+1, -1)$  of the factors (2, 4) or (3, 6), respectively. The diagrams of these interactions were drawn and are displayed in Figure 5.29.

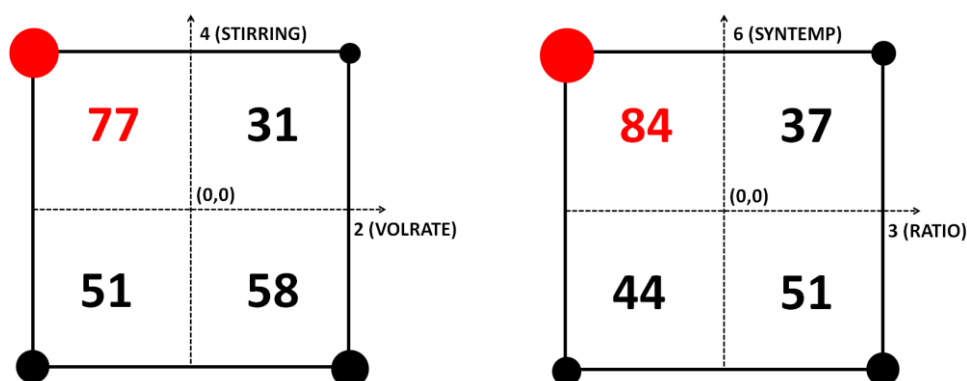


Figure 5.29. Diagram of interactions for the response Y2 (efficiency of the synthesis, %). On the left the interaction between the volumetric addition rate of the Pd solution and the stirring rate. On the right the interaction between the initial HHDMA-to-Pd molar ratio and the temperature of the synthesis

These diagrams show that a combination  $(-1, +1)$  for the factors (2, 4) or (3, 6), respectively, provided higher efficiencies. The combinations correspond to a slow Pd addition rate (2 mL/min) combined with a high stirring speed (500 rpm) and a low HHDMA-to-Pd molar ratio (3 eq.) combined with a high temperature of synthesis (95°C).

The plot of effects presented in Figure 5.27 indicates that low level of the factors 2 and 3 (VOLRATE and RATIO, respectively) and high level of the factors 5 and 6 (SYNTHIME and SYNTEMP, respectively) provided larger fraction of spherical NPs. It corresponds to a Pd addition rate of 2 mL/min, a HHDMA-to-Pd molar ratio of 3 eq., a synthesis time of 2.5 hours and a temperature of 95°C.

Finally, higher efficiencies were obtained when the third-order interaction 124 was at its low level. This interaction was used to perform the blocking between the two operators (the effect of the operator was confounded with this third-order interaction). Moreover 124 was confounded with the third-order interactions 345, 136 and 256. Usually, the third-order interactions are neglected, which could suggest an important effect of the operator on the efficiency of the synthesis. However the

discrimination between all these confusions was not easy and more experiments could help to separate confusions and to give an accurate conclusion for this effect.

The synthesis efficiency depends on a wide variety of factors and interactions. Among them, the most significant were identified and are summarized in Figure 5.30. The detailed analysis of these key factors and interactions revealed that high synthesis efficiency should be obtained with the combination of factors (-1, -1, -1, +1, ±1, +1) for (1, 2, 3, 4, 5, 6), respectively. The **RUN09** corresponds to the combination (-1, -1, -1, +1, -1, +1) and exhibited one of the highest efficiency of the set of experiments: 94.8%.

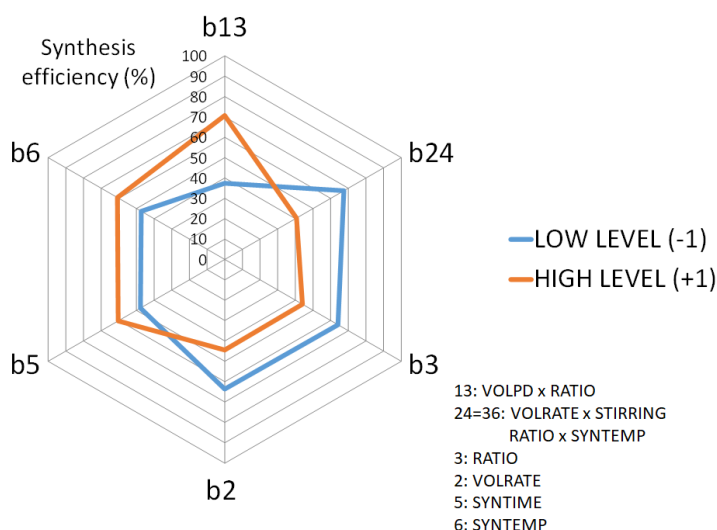


Figure 5.30. Radar diagram of the main single factors and second-order interactions effects on the synthesis efficiency (response Y4)

### Conclusions of the structure-synthesis relationship study on the Pd-HHDMA NPs using DOE

The analysis of the effects of Pd concentration in the injection (varied as Pd solution volume), Pd addition rate, HHDMA-to-Pd ratio, stirring rate, synthesis time and temperature on the formation of Pd-HHDMA NPs was carried out using designed experiments. The studied responses were the fraction of spherical NPs, the NPs size, the type of distribution (monomodal or bimodal) and the synthesis efficiency. Sixteen experiments were performed following a fractional factorial design  $2^{6-2}$  and analyses

of variance were performed to assess the significance of the studied factors and interactions on the studied response. This study showed that the formation of well-defined Pd-HHDMA NPs through a similar recipe than that reported by P. Witte was complex and depends on a wide variety of synthetic parameters.<sup>4</sup>

From these interpretations, different combinations of factors were concluded for each studied response and are summarized in Table 5.8.

Table 5.8. Combinations of factors highlighted for each studied responses

Higher percentage of spherical NPs (Y1)	(-1, -1, -1, +1, $\pm 1$ , +1)
Larger average mean NPs size (Y2)	( $\pm 1$ , -1, -1, +1, +1, +1)
Probability to obtain a single distribution (Y3)	(-1, -1, -1, $\pm 1$ , $\pm 1$ , +1)
Higher synthesis efficiency (Y4)	(-1, -1, -1, +1, $\pm 1$ , +1)

As a general trend, high concentration in the Pd injection, slow Pd addition rate, low HHDMA-to-Pd ratio, high stirring rate, long synthesis time and high temperature provided well-defined spherical NPs with high synthesis efficiency. From the highlighted combinations of factors, two combinations were tested: the **RUN09** (-1, -1, -1, +1, -1, +1) and **RUN10** (+1, -1, -1, +1, +1, +1). These experiments gave fraction of spherical NPs of 89% and 86%, respectively, NPs size of 8.3 nm and 10.5 nm, respectively with single distribution and synthesis efficiency of 95% and 96%, respectively. Moreover the **RUN03** was highlighted for its good results: 92% of spherical NPs, NPs size of 8.0 nm with single distribution and synthesis efficiency of 93%.

At this point, the colloidal Pd-HHDMA NPs were immobilized on activated carbon and titanium silicon oxide following the BASF patent recipe. These tests are described in the next section.

## 5.4.2. Supported Pd-HHDMA NPs onto supports

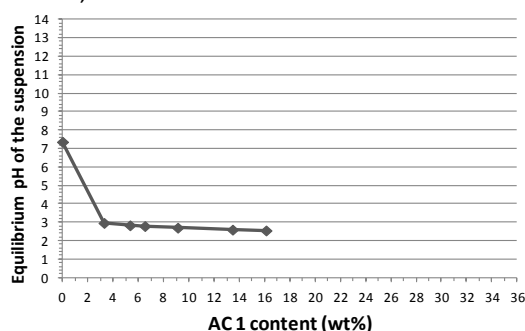
### 5.4.2.1. Reproduction of the BASF two-step immobilization of Pd-HHDMA NPs on different kind of AC supports

The first step of this study was the reproduction of the two-step immobilization detailed in the BASF patent recipe. This recipe consists in the immobilization of a suspension of Pd-HHDMA NPs previously prepared on an activated carbon support by pH variation. However, precise details on the kind of activated carbon support were not provided. Consequently, it was proposed to reproduce this recipe using two activated carbon supports with different intrinsic characteristics. The PZC of these supports as well as the  $\zeta$  potential of the colloidal NPs were first determined.

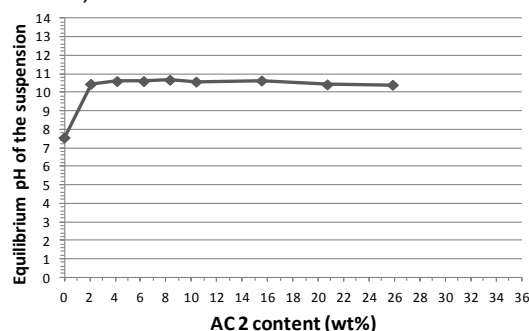
#### Determination of the PZC of the supports and the $\zeta$ potential of the Pd NPs

The PZC of the supports was determined by mass titration as described in chapter 4. The curves of pH vs. percentage mass-to-volume ratio of the supports used in this chapter are displayed in Figure 5.31.

a. AC 1,  $PZC = 2.6$



b. AC 2,  $PZC = 10.4$



c.  $TiSiO_4$ ,  $PZC = 3.3$

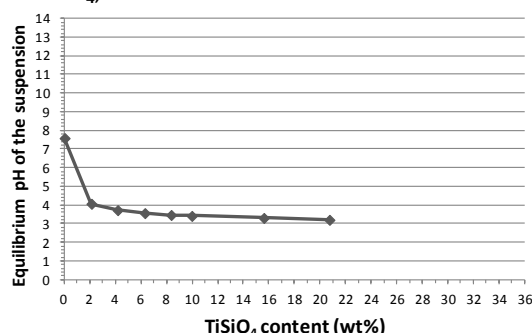


Figure 5.31. Point of Zero Charge of a. AC 1, b. AC 2, c.  $TiSiO_4$ . Determined by mass titration

The PZC of **AC 1**, **AC 2** and **TiSiO<sub>4</sub>** (used in the next section) were equal to 2.6, 10.4 and 3.3, respectively. Note that the **AC 2** was previously crushed to obtain a powder form support.

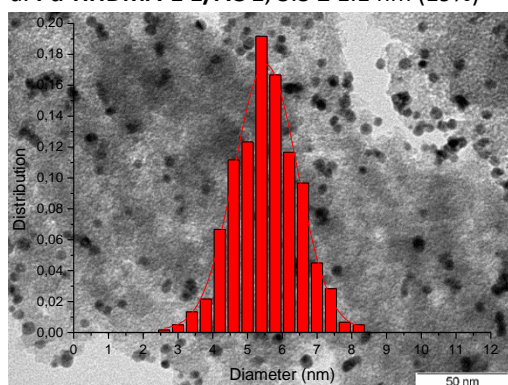
Moreover the  $\zeta$  potential of the Pd-HHDMA NPs was measured and equal to 10. This value was in adequacy with the trend published by Witte *et al.*: these NPs experienced electrostatic repulsion at positively charged surfaces and attraction at negatively charged surfaces.<sup>6</sup>

### Immobilization on AC 1 and AC 2 following the BASF patent recipe

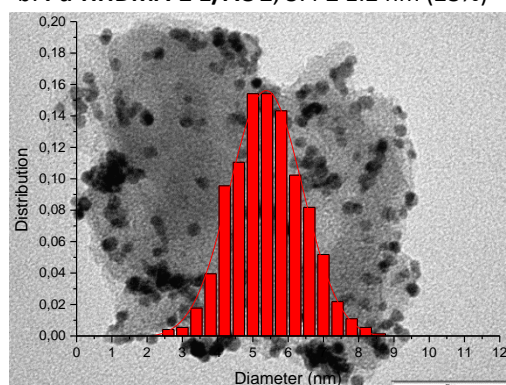
The recipe given by P. Witte in the BASF patent consisted in mixing the Pd-HHDMA NPs with the slurry of AC at pH 2 during 45 minutes and then varied the pH from 2 to 9 with the addition of 10% NaOH to induce the immobilization.<sup>4</sup> This methodology was used for **AC 1** and **AC 2**. The impregnation on the **AC 1** was performed with the **Set-up 3** (Centre Tecnològic de la Química, Tarragona) while the impregnation on **AC 2** was done with the **Set-up 4** (Total Research & Technology Feluy).

The TEM micrographs and size distribution histograms of these catalysts as well as the reference **Pd Nanoselect LF 100** (commercial reference of Pd-HHDMA NPs on activated carbon prepared with the same methodology) are given in Figure 5.32.

a. **Pd-HHDMA-1 1/AC 1**,  $5.5 \pm 1.1$  nm (19%)



b. **Pd-HHDMA-2 1/AC 2**,  $5.4 \pm 1.2$  nm (23%)



c. **Pd Nanoselect LF 100**,  $7.4 \pm 1.7$  nm (23%)

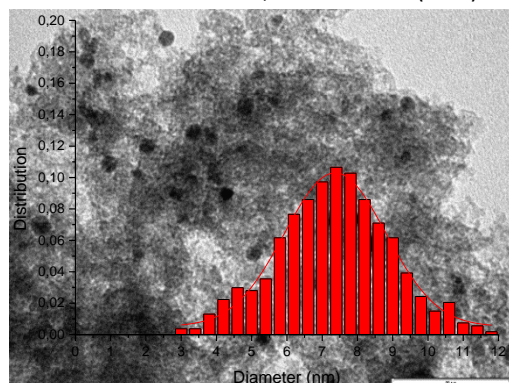
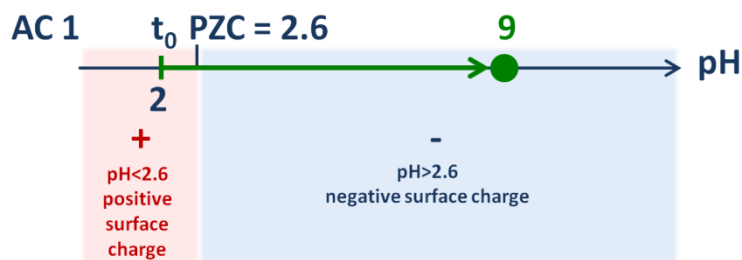


Figure 5.32. a. TEM micrographs and size distribution histograms of the supported a. **Pd-HHDMA-1 1/AC 1**, b. **Pd-HHDMA-2 1/AC 2** and c. the reference **Pd Nanoselect LF 100**

In both cases, the immobilization of the Pd-HHDMA NPs was successful. The Pd NPs on **AC 1** and **AC 2** revealed similar average mean size and distribution of *ca.* 5.5 nm indicating the well-reproducibility of the recipe with two different carbon supports and using two different set-ups. It was noticed that the obtained NPs were slightly smaller than the reference **Nanoselect LF 100** catalyst.

In the case of the carbon **AC 1**, the deposition mechanism followed the trend reported by Witte *et al.*<sup>6</sup> A base was added to the reaction media increasing the pH from 2 to 9, value higher than the PZC of **AC 1**. Thus the surface charge changed from positive to negative leading to the attraction of the Pd-HHDMA NPs. Visual representations of this mechanism are given in Scheme 5.4 and Figure 5.33.



Scheme 5.4. Immobilization of **Pd-HHDMA-1 1** NPs on activated carbon **AC 1** following the BASF patent recipe

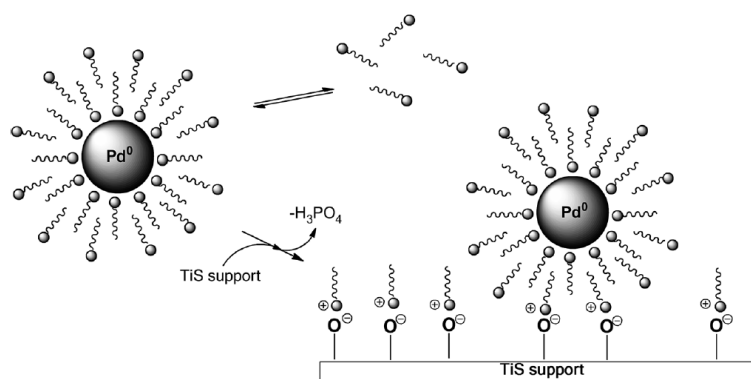


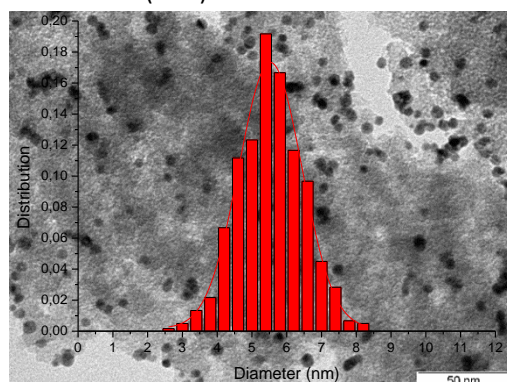
Figure 5.33. Electrostatic nature of the deposition of Pd-HHDMA NPs on TiSi support NPs in the BASF recipe<sup>6</sup>

In the case of the carbon **AC 2**, this mechanism was not well-understood. Indeed, following the same line of reasoning than the previous case, the pH of the solution should have been increased to a value higher than 10.4 (value higher than the PZC of **AC 2**) in order to induce the electrostatic attraction between NPs and support. Nevertheless the NPs immobilization was induced on the positively charged surface. It could be due to the fact that the  $\zeta$  potential can vary depending on the pH of the solution. The  $\zeta$  potential of these Pd-HHDMA NPs was measured at pH 2 (usual pH obtained after their formation) and then NaOH was added to this suspension. The  $\zeta$  potential gave positive value at low pH and negative value after the base addition. Thus the surface properties of these NPs could have been influenced by the pH of the solution.

At this point, the role of the pH modification in this recipe was questioned. An additional experiment was performed: the **Pd-HHDMA-1 1** NPs were immobilized on **AC 1** by a simple mixing methodology, without pH variation (using the **Set-up 3**). Therefore, after the controlled addition of the NPs onto the slurry of support, additional 45 minutes of stirring were applied and the resulting catalyst was isolated by filtration and dried under vacuum. The NPs size and dispersion were characterized in both cases by TEM and ESEM and the results are displayed in Figure 5.34 and Figure 5.35.



a. TEM of BASF patent recipe  
 $5.5 \pm 1.1$  nm (19%)



b. TEM of recipe without pH change  
 $6.4 \pm 1.4$  nm (22%)

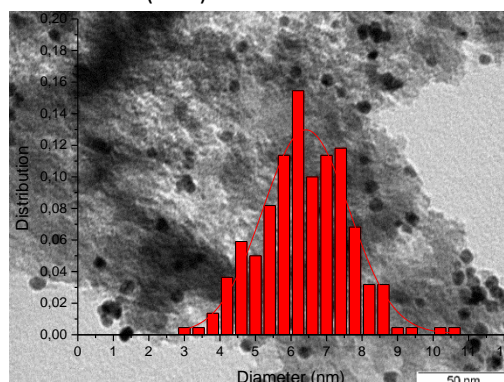


Figure 5.34. TEM micrographs of **Pd-HHDMA-1 1** supported on AC 1 by a. the BASF patent recipe and b. the modified recipe without pH variation

a. ESEM of BASF patent recipe

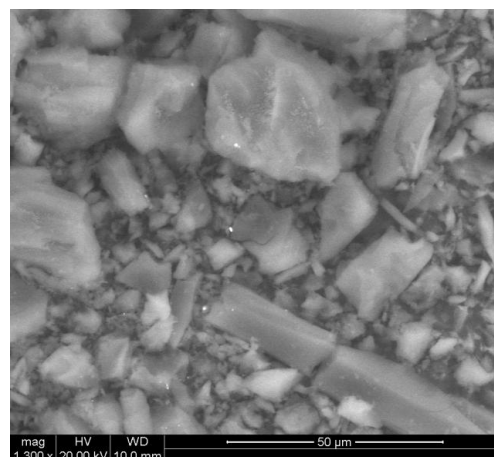
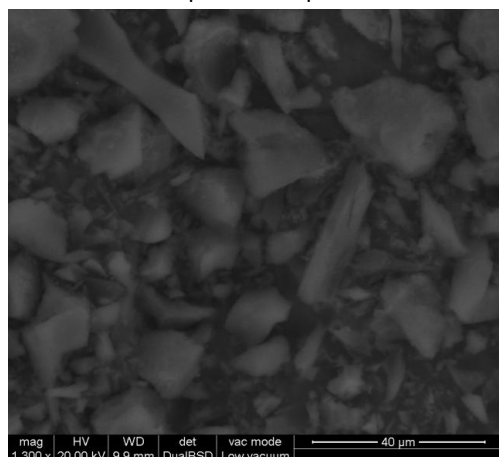


Figure 5.35. ESEM micrographs of **Pd-HHDMA-1 1** supported on AC 1 by a. the BASF patent recipe and b. the modified recipe without pH variation

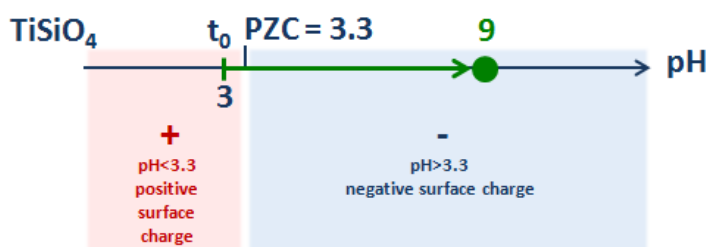
The TEM of the modified recipe revealed slightly larger NPs size (*ca.* 6.4 nm). The difference was probably due to the lower pH of the reaction media. Indeed Witte *et al.* reported that smaller Pd crystallites could be obtained with higher pH.<sup>6</sup>

A small proportion of non-supported NPs were observed on the TEM images suggesting a lower immobilization efficiency without pH variation. These results indicate that the basification of the reaction media improves the immobilization of these NPs on this AC support.

Then, the ESEM micrographs show the presence of very small agglomerates when the immobilization was performed without pH change, while in the BASF patent recipe, no agglomeration was detected. These results show that the addition of NaOH during the immobilization step slightly improved the NPs immobilization and their dispersion on the AC support.

#### 5.4.2.2. Immobilization of Pd-HHDMA NPs on $\text{TiSiO}_4$ support using the BASF recipe

Since the Pd Nanoselect catalyst is commercially available on activated carbon (**LF 100**) and titanium silicate (**LF 200**) supports, the immobilization was also tested on this later support. To do so, the recipe reported in the BASF patent for the activated carbon was repeated using  $\text{TiSiO}_4$  as support. NaOH was added to the reaction medium in order to increase the pH from 3 to 9, value higher than  $\text{TiSiO}_4$  PZC. At this pH, the surface charge should be negative and thus attract the NPs as depicted in Scheme 5.5. However during the filtration step, a yellow supernatant was recovered indicating the non-immobilization of the NPs. This behavior was not well-understood. Attempt of immobilization via one pot were tested and the results are presented in the next section.



Scheme 5.5. Immobilization of Pd-HHDMA-2 1 NPs on titanium silicon oxide following the BASF patent recipe

#### 5.4.2.3. Immobilization of Pd-HHDMA NPs on activated carbon and titanium silicate via one pot synthesis

Finally, the one pot synthesis of Pd-HHDMA NPs was attempted on the **AC 2** and  $\text{TiSiO}_4$  supports in powder form (with the **Set-up 2**).

On the activated carbon support, the NPs were well-immobilized (the Pd content was verified by ICP and revealed 0.72 wt% for a theoretical value of 1 wt%). However, the TEM characterization, presented in Figure 5.36, revealed multiple size distributions (NPs sizes between 5 nm and 20 nm). These results suggest that the one pot synthesis did not influence on the immobilization efficiency on activated carbon but drastically affected the resulting NPs sizes.

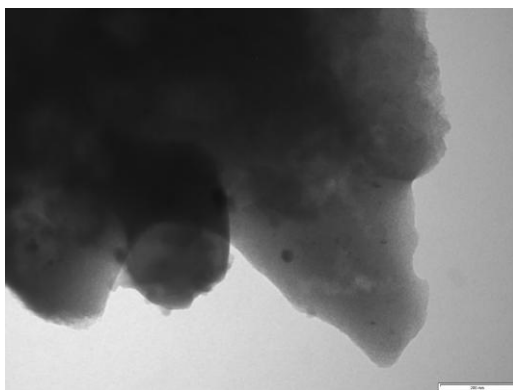


Figure 5.36. TEM micrograph of Pd-HHDMA NPs supported on activated carbon (**AC 2**) using **Set-up 2**

On titanium silicate, TEM characterization revealed presence of NPs on the support as shown in Figure 5.37; however a yellow supernatant was again observed during the filtration of the catalyst indicating the non-efficient immobilization of the NPs.

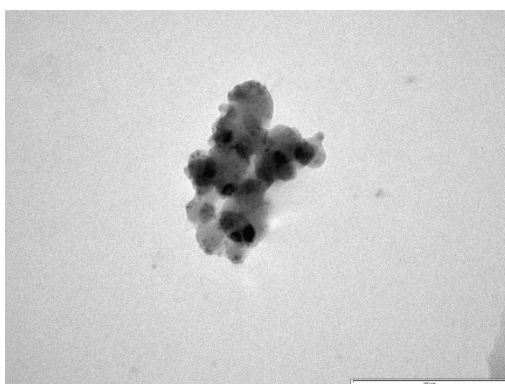


Figure 5.37. TEM micrograph of Pd-HHDMA NPs supported on **TiSiO<sub>4</sub>** using **Set-up 2**

The Pd-HHDMA NPs were immobilized on two kinds of activated carbon using the reported two-step immobilization methodology. The immobilization of these NPs on  $\text{TiSiO}_4$  has not been possible under the tested conditions.

## 5.5. Conclusions

This chapter describes about the study of a reported recipe for the formation of Pd NPs stabilized by HHDMA (colloidal Pd NPs used for the preparation of the Pd Nanoselect catalyst patented by BASF).

In a first part, this recipe was reproduced at different scale and using different set-ups. It consisted in the chemical reduction of  $\text{Na}_2\text{PdCl}_4$  in water using HHDMA as reducing agent (together with the temperature) and as stabilizer. The reproducibility was verified using a Kolmogorov-Smirnov statistical test.

Then, a structure-synthesis relationship study of Pd-HHDMA NPs starting from this reported recipe was performed using design of experiments methodology. The effect of the Pd concentration in the injection, Pd addition rate to the HHDMA solution, HHDMA-to-Pd ratio, stirring rate, synthesis time and temperature on the NPs shape, size, distribution and synthesis efficiency were investigated. Analyses of variance were performed to assess the possibility to rule out the contribution of some non-significant factors in the models that described the studied system. Moreover, linear empirical models that describe the system were provided. The main conclusions of this study were the following:

- The fraction of spherical NPs was mainly affected by the HHDMA-to-Pd ratio, the Pd addition rate and the interactions between the Pd concentration and the HHDMA-to-Pd ratio, the Pd addition rate and the stirring rate and finally the HHDMA-to-Pd ratio and the temperature.

Highly spherical NPs were obtained with high Pd concentration in the injection, slow Pd addition rate, low HHDMA-to-Pd ratio, high stirring rate and high temperature (independently of the synthesis time).

- The NPs size was affected by a wide variety of factors and interactions: Pd addition rate, HHDMA-to-Pd ratio, stirring rate, synthesis time, temperature

and interactions between the Pd addition rate and the stirring rate, the HHDMA-to-Pd ratio and the temperature, the Pd concentration and the stirring rate, the synthesis time and temperature, the Pd concentration and HHDMA-to-Pd ratio and finally the Pd addition rate and HHDMA-to-Pd ratio.

Larger NPs were obtained with slow Pd addition rate, low HHDMA-to-Pd ratio, high stirring rate, long time and high temperature (independently of the Pd concentration in the injection).

- The type of distribution was assessed. The Pd addition rate and temperature seemed to affect significantly the distribution while the HHDMA-to-Pd ratio and the Pd concentration affected it in a more moderate way.

The highest probabilities to obtain single distribution were using high concentrated Pd solution, slow Pd addition rate, low HHDMA-to-Pd ratio and high temperature.

- The synthesis efficiency was also affected by a large variety of factors and interactions. Among them, the most significant were: the Pd addition rate, the HHDMA-to-Pd ratio, the interactions between the Pd concentration and HHDMA-to-Pd ratio, the Pd addition rate and stirring rate and the HHDMA-to-Pd ratio and temperature. Moreover a third-order interaction revealed significant influence and could be associated to the operator.

Larger efficiencies were obtained with high Pd concentration in the injection, slow Pd addition rate, low HHDMA-to-Pd ratio, high stirring rate and high temperature (independently of the synthesis time).

This studied system was complex and depended on a wide variety of parameters. The factors related to the Pd injection steps to the HHDMA solution always showed high influence indicating that this step was a key step to control the well-formation of the NPs.

From this set of experiments, three well-defined Pd-HHDMA NPs were obtained with different sizes: *ca.* 7.2, 8.3 and 10.5 nm (**RUN03**, **RUN09** and **RUN10**, respectively).

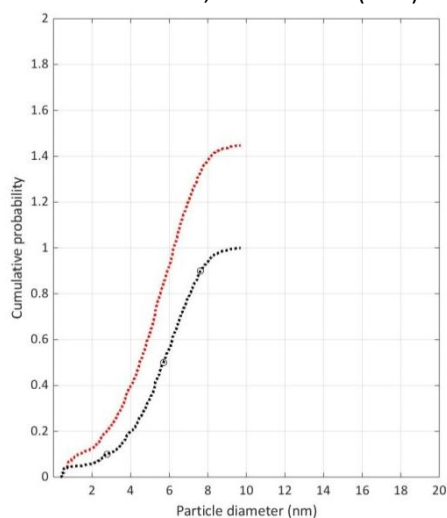
Finally attempts of immobilization of the reported Pd-HHDMA NPs on activated carbon and titanium silicate were performed using two-step and one pot syntheses. The immobilization resulted efficient only with the two-step procedure using two kinds of activated carbon.

## 5.6. Appendix

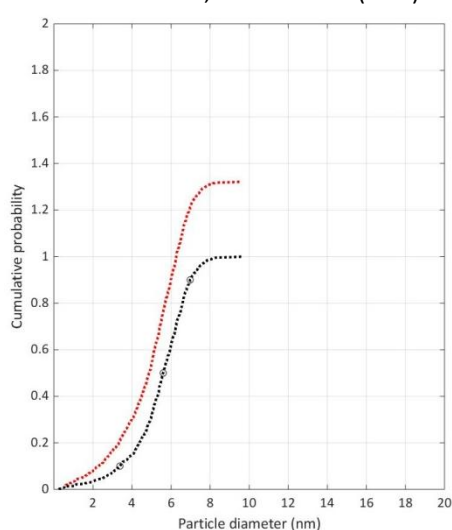
### 5.6.1. Appendix 1: Cumulative probability plots of Pd-HHDMA NPs synthesized by the BASF recipe

This appendix presents the cumulative probability plots of the equivalent diameter of the spherical NPs (black line) and the equivalent diameter of all the NPs (dashed red line) of the seven reproductions of Pd-HHDMA NPs synthesized following the BASF recipe with the **Set-up 2**.

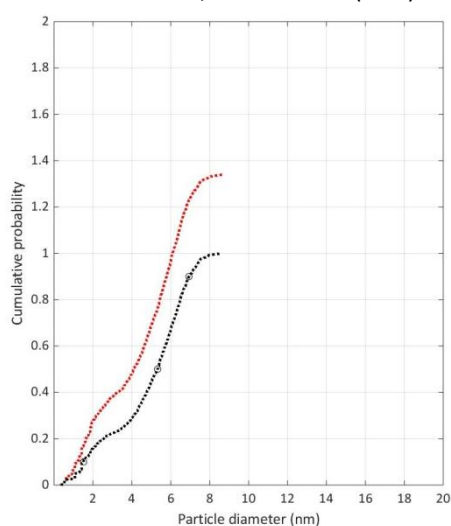
a. **Pd-HHDMA-2 1a**,  $5.8 \pm 1.7$  nm (29%)



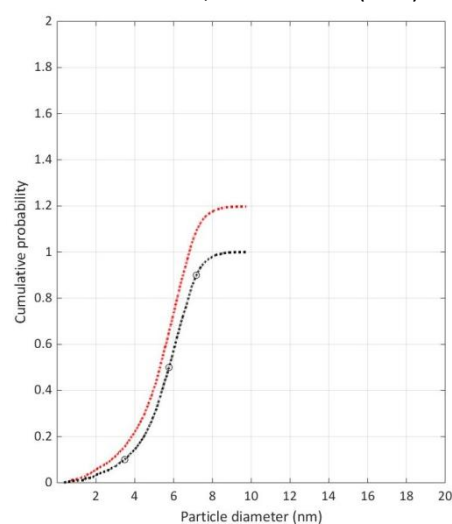
b. **Pd-HHDMA-2 1b**,  $5.7 \pm 1.3$  nm (22%)



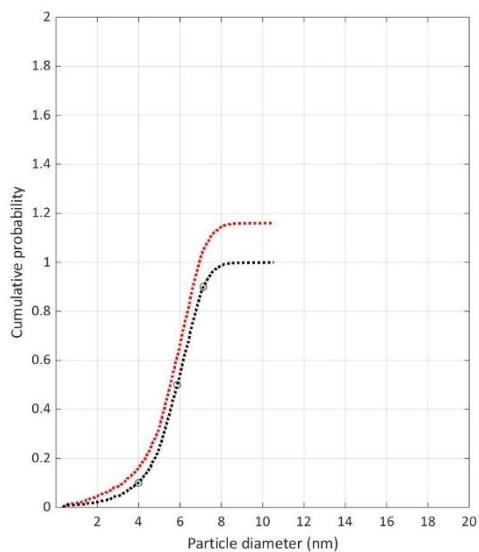
c. **Pd-HHDMA-2 1c**,  $5.7 \pm 1.4$  nm (25%)



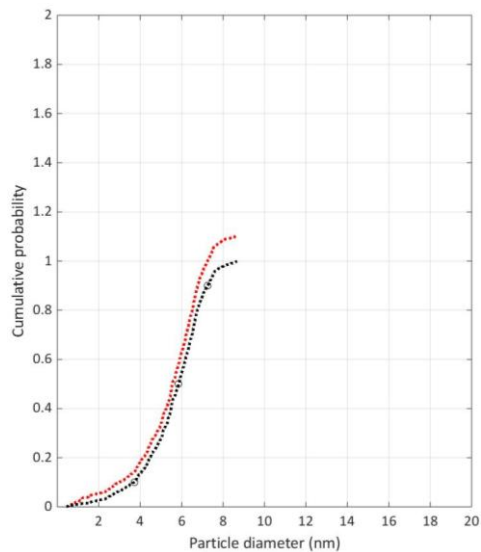
d. **Pd-HHDMA-2 1d**,  $5.9 \pm 1.3$  nm (22%)



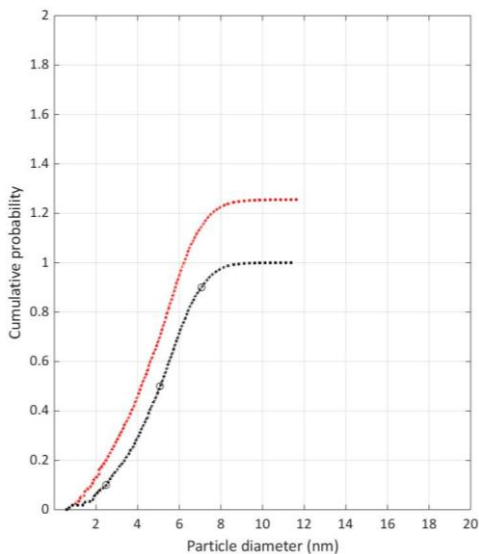
e. **Pd-HHDMA-2 1e**,  $6.0 \pm 1.1$  nm (19%)



f. **Pd-HHDMA-2 1f**,  $6.0 \pm 1.3$  nm (22%)



g. **Pd-HHDMA-2 1g**,  $5.1 \pm 1.8$  nm (35%)





## 5.6.2. Appendix 2: Kolmogorov Smirnov tables

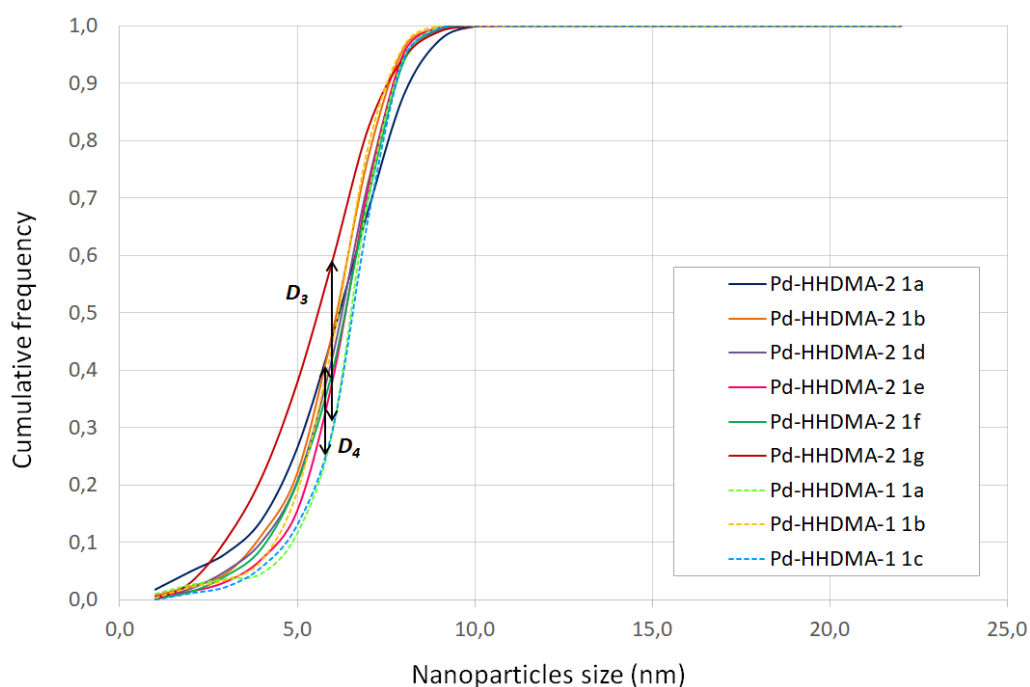
Critical values,  $d_{\alpha;n}(n)^{1/2}$ , of the maximum absolute difference between sample  $F_n(x)$  and population  $F(x)$  cumulative distribution.

Number of trials, $n$	Level of significance, $\alpha$			
	0.10	0.05	0.02	0.01
1	0.95000	0.97500	0.99000	0.99500
2	0.77639	0.84189	0.90000	0.92929
3	0.63604	0.70760	0.78456	0.82900
4	0.56522	0.62394	0.68887	0.73424
5	0.50945	0.56328	0.62718	0.66853
6	0.46799	0.51926	0.57741	0.61661
7	0.43607	0.48342	0.53844	0.57581
8	0.40962	0.45427	0.50654	0.54179
9	0.38746	0.43001	0.47960	0.51332
10	0.36866	0.40925	0.45662	0.48893
11	0.35242	0.39122	0.43670	0.46770
12	0.33815	0.37543	0.41918	0.44905
13	0.32549	0.36143	0.40362	0.43247
14	0.31417	0.34890	0.38970	0.41762
15	0.30397	0.33760	0.37713	0.40420
16	0.29472	0.32733	0.36571	0.39201
17	0.28627	0.31796	0.35528	0.38086
18	0.27851	0.30936	0.34569	0.37062
19	0.27136	0.30143	0.33685	0.36117
20	0.26473	0.29408	0.32866	0.35241
21	0.25858	0.28724	0.32104	0.34427
22	0.25283	0.28087	0.31394	0.33666
23	0.24746	0.27490	0.30728	0.32954
24	0.24242	0.26931	0.30104	0.32286

*Practical Reliability Engineering*, Fifth Edition. Patrick D. T. O'Connor and Andre Kleyner.  
 © 2012 John Wiley & Sons, Ltd. Published 2012 by John Wiley & Sons, Ltd.

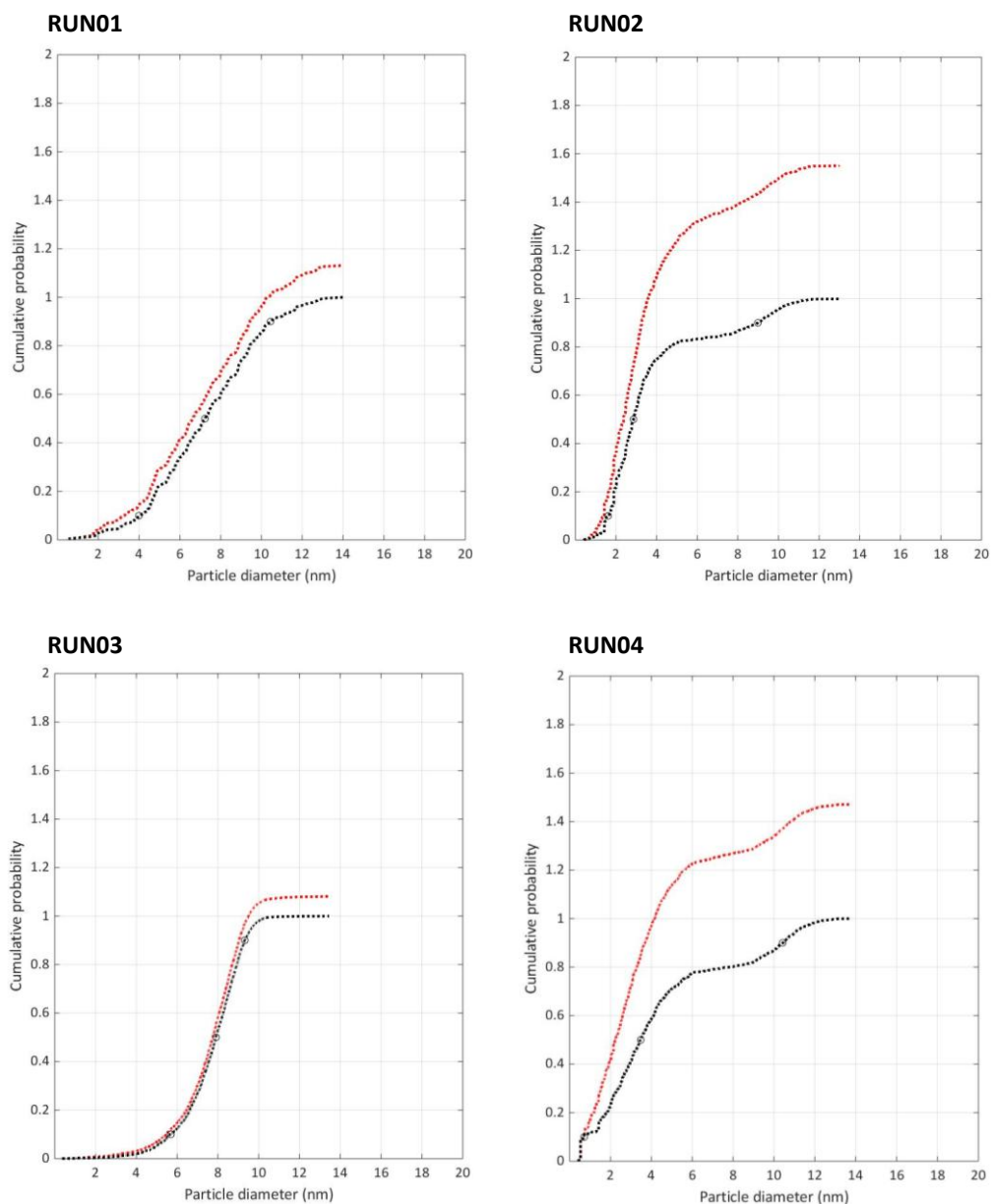
### 5.6.3. Appendix 3: Cumulative distributions of Pd-HHDMA NPs synthesized by the BASF recipe

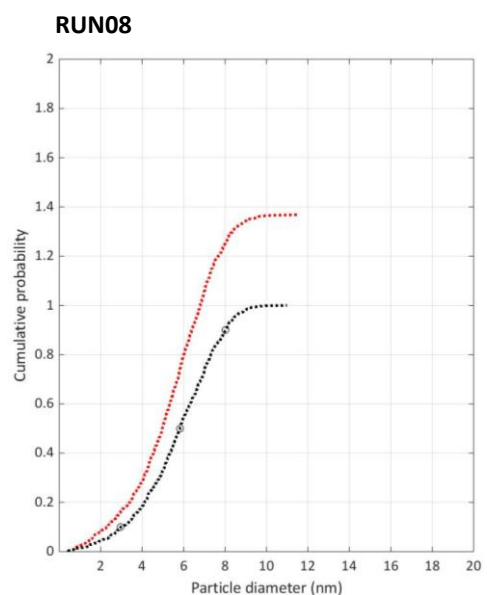
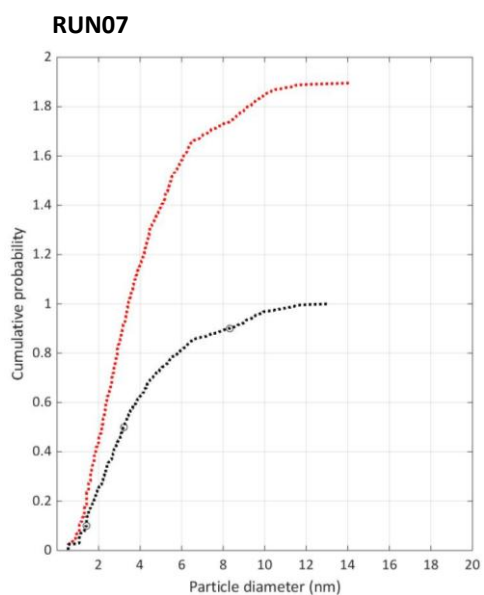
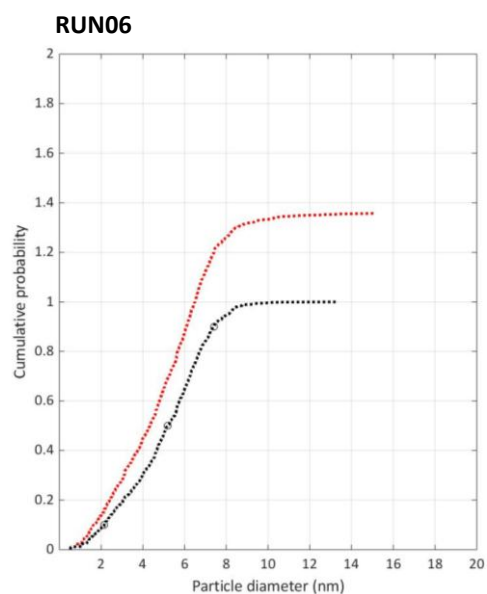
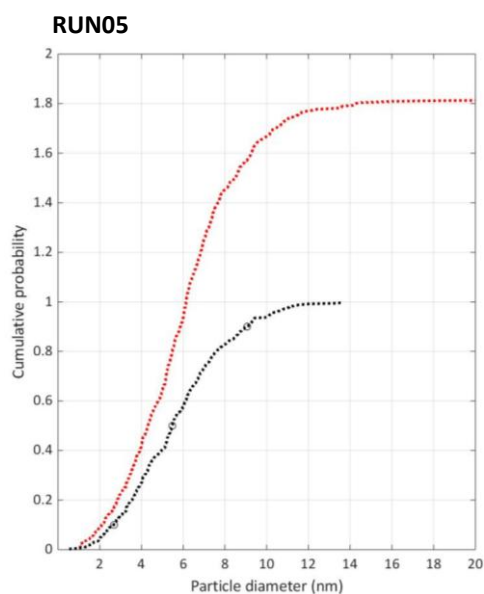
This appendix presents the cumulative distribution of the three batches of Pd-HHDMA NPs synthesized with the **Set-up 1** and the six batches of Pd-HHDMA NPs synthesized with the **Set-up 2**. Kolmogorov-Smirnov test between **Pd-HHDMA-1 1c** and **Pd-HHDMA-2 1g** ( $D_3$ ) and between **Pd-HHDMA-1 1c** and **Pd-HHDMA-2 1b** ( $D_4$ ).

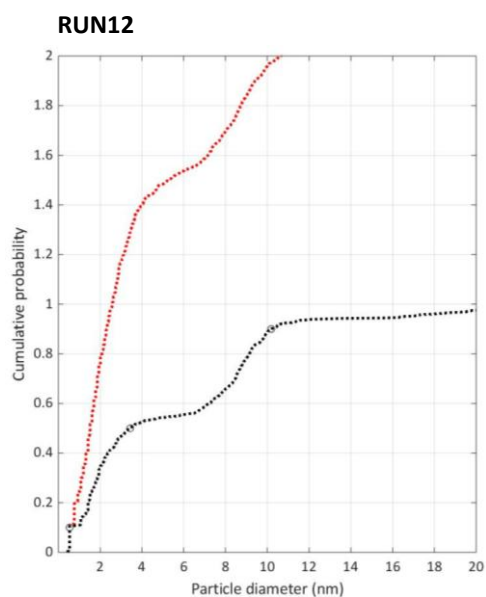
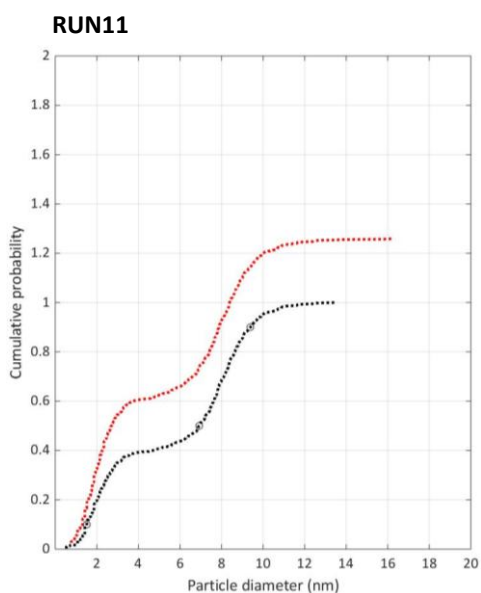
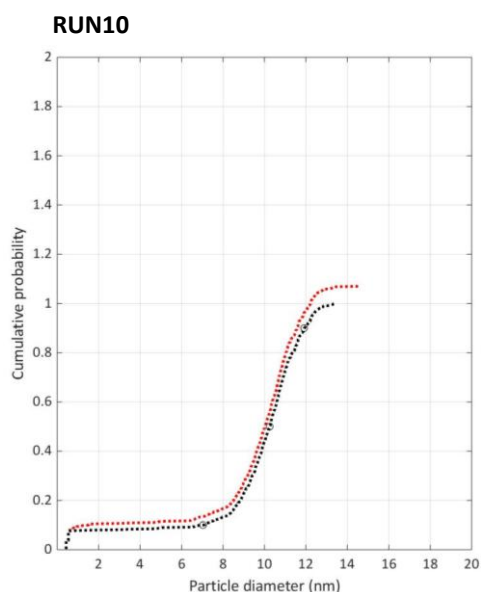
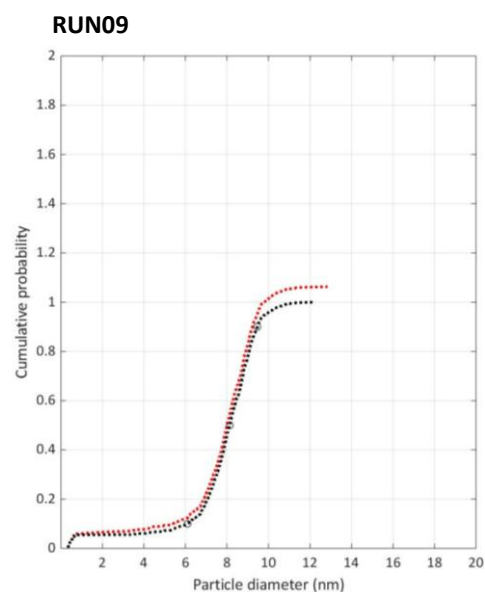


#### 5.6.4. Appendix 4: Cumulative probability plots the Pd-HHDMA NPs of the DOE study

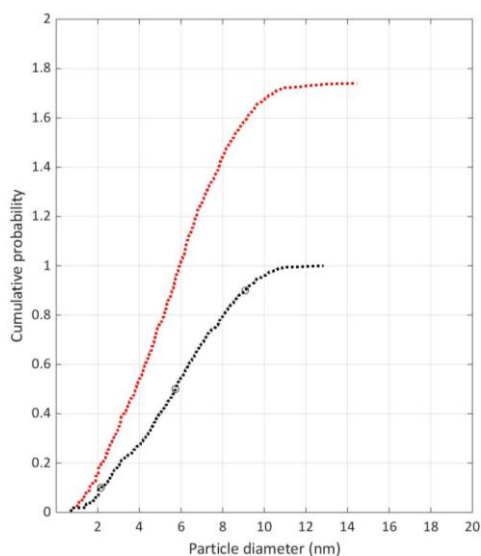
This appendix presents the cumulative probability plot of the equivalent diameter of the spherical NPs (black line) and the equivalent diameter of all the NPs (dashed red line) of the sixteen experiments of the fractional factorial design  $2^{6-2}$  performed with the **Set-up 2**.



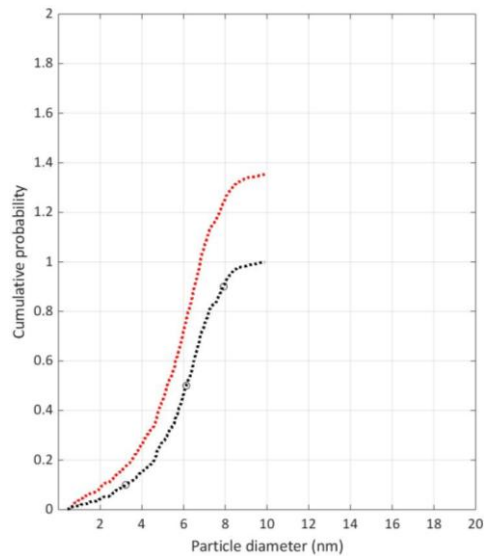




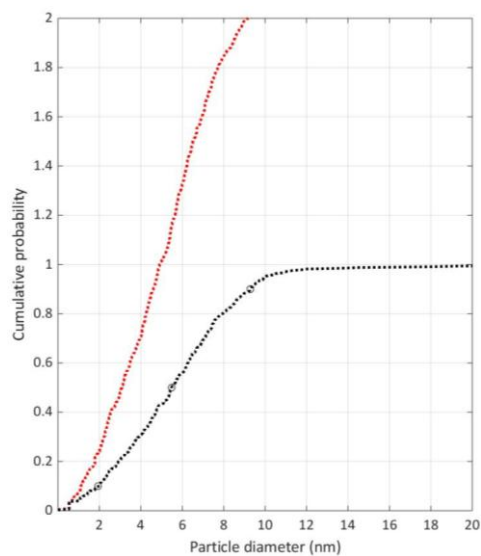
**RUN13**



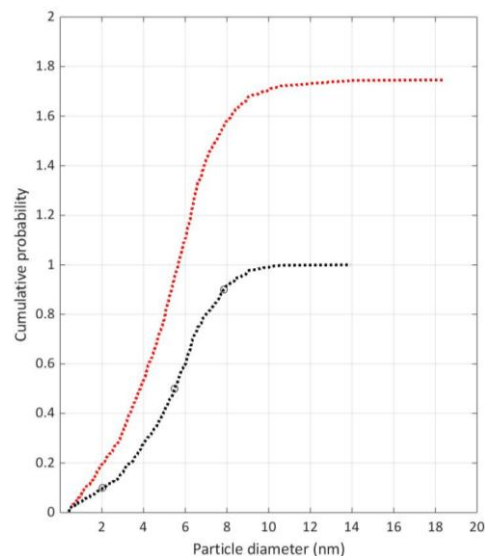
**RUN14**



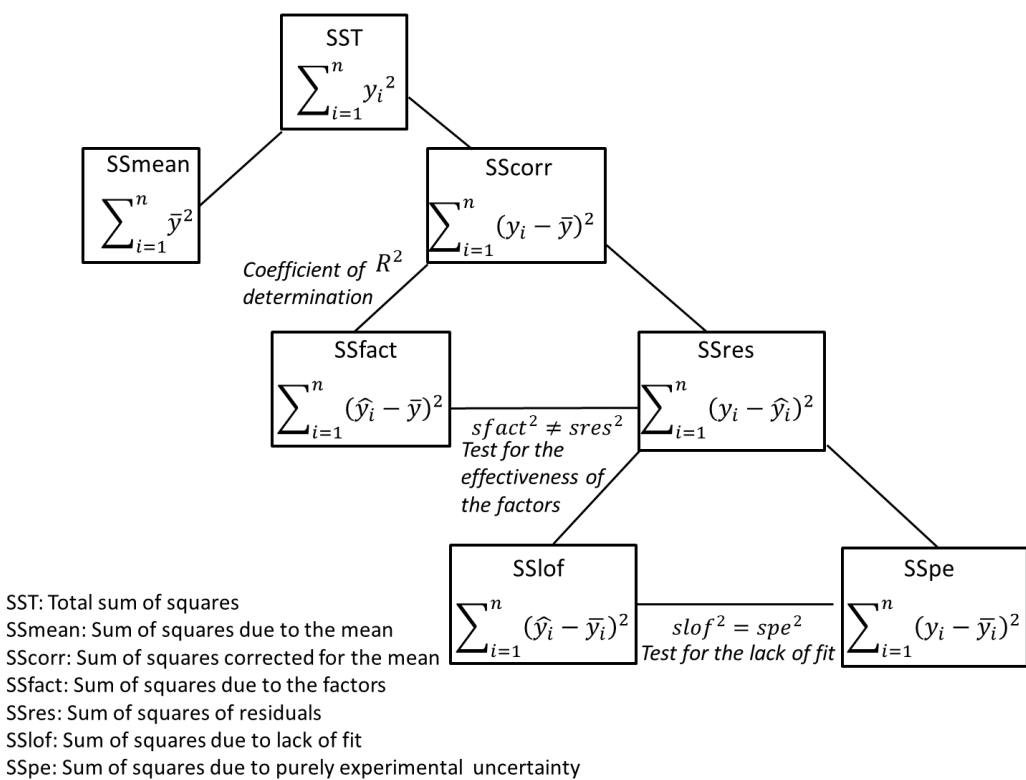
**RUN15**



**RUN16**



5.6.5. Appendix 5: Analysis of Variance for Linear Models



### 5.6.6. Appendix 6: Analysis of variance on response Y1

Best model fitting obtained for the effect on the fraction of spherical NPs considering from 1 to 10 factors

Nb <sup>a</sup>	Best model fitted	R <sup>2</sup>	PE <sup>b</sup> (%)
1	$\hat{y} = 70.60 + 10.23x_1x_3$	0.33	13.16
2	$\hat{y} = 70.60 - 7.49x_3 + 10.23x_1x_3$	0.50	11.63
3	$\hat{y} = 70.60 - 5.70x_2 - 7.49x_3 + 10.23x_1x_3$	0.60	10.67
4	$\hat{y} = 70.60 - 5.70x_2 - 7.49x_3 + 10.23x_1x_3 - 5.29x_2x_4$	0.69	9.71
5	$\hat{y} = 70.33 - 2.89x_1 - 5.70x_2 - 7.49x_3 + 10.23x_1x_3 - 5.29x_2x_4$	0.72	9.57
6	$\hat{y} = 70.33 - 2.89x_1 - 5.70x_2 - 7.49x_3 - 2.79x_1x_2 + 10.23x_1x_3 - 5.29x_2x_4$	0.74	9.45
7	$\hat{y} = 70.33 - 2.89x_1 - 5.70x_2 - 7.49x_3 - 2.79x_1x_2 + 10.23x_1x_3 - 5.29x_2x_4 + 2.56x_1x_2x_3$	0.76	9.39
8	$\hat{y} = 70.33 - 2.89x_1 - 5.70x_2 - 7.49x_3 - 2.79x_1x_2 + 10.23x_1x_3 - 5.29x_2x_4 + 2.56x_1x_2x_3 - 2.20x_1x_2x_4$	0.77	9.44
9	$\hat{y} = 70.33 - 2.89x_1 - 5.70x_2 - 7.49x_3 - 2.15x_4 - 2.79x_1x_2 + 10.23x_1x_3 - 5.29x_2x_4 + 2.56x_1x_2x_3 - 2.20x_1x_2x_4$	0.79	9.50
10	$\hat{y} = 70.33 - 2.89x_1 - 5.70x_2 - 7.49x_3 - 2.15x_4 - 2.79x_1x_2 + 10.23x_1x_3 - 5.29x_2x_4 + 2.56x_1x_2x_3 - 2.20x_1x_2x_4 + 1.91x_2x_3x_4$	0.80	9.65

<sup>a</sup>: Number of parameters considered in the model. <sup>b</sup>: Purely experimental error



## 5.7. References

- (1) Na, K.; Zhang, Q.; Somorjai, G. A. *J. Cluster Sci.* **2014**, *25*, 83.
- (2) Yang, Y.; Liu, X.; Yin, D.; Zhang, Z.; Lei, D.; Yang, J. *J. Ind. Eng. Chem.* **2015**, *26*, 333.
- (3) Baeza, J. A.; Calvo, L.; Rodriguez, J. J.; Gilarranz, M. A. *Chem. Eng. J.* **2016**, *294*, 40.
- (4) Witte, P. T. *Process for the preparation of an aqueous colloidal precious metal suspension*, US Patent 8,822,725 B2 **2014**.
- (5) Strem Chemicals, *Pd and Pt Nanoselect catalysts*, Extracted in August 2018, from [https://www.strem.com/uploads/resources/documents/basf\\_pd\\_and\\_pt\\_nanoselect\\_catalysts.pdf](https://www.strem.com/uploads/resources/documents/basf_pd_and_pt_nanoselect_catalysts.pdf)
- (6) Witte, P. T.; Boland, S.; Kirby, F.; van Maanen, R.; Bleeker, B. F.; de Winter, D. A. M.; Post, J. A.; Geus, J. W.; Berben, P. H. *ChemCatChem* **2013**, *5*, 582.
- (7) García-Mota, M.; Gómez-Díaz, J.; Novell-Leruth, G.; Vargas-Fuentes, C.; Bellarosa, L.; Bridier, B.; Pérez-Ramírez, J.; López, N. *Theor. Chem. Acc.* **2011**, *128*, 663.
- (8) Vilé, G.; Almora-Barrios, N.; Mitchell, S.; López, N.; Pérez-Ramírez, J. *Chem. Eur. J.* **2014**, *20*, 5926.
- (9) Liakakos, N.; Cormary, B.; Li, X.; Lecante, P.; Respaud, M.; Maron, L.; Falqui, A.; Genovese, A.; Vendier, L.; Kořinis, S.; Chaudret, B.; Soulantica, K. *J. Am. Chem. Soc.* **2012**, *134*, 17922.
- (10) [http://schoolbag.info/physics/physics\\_math/71.html](http://schoolbag.info/physics/physics_math/71.html)
- (11) Myers, R. H. *Classical and Modern Regression with Applications*; 2 ed., 1990.

## Chapter 6

Kinetic study of Pd-based catalysts in the  
selective hydrogenation of 1-octyne in stirred  
tank reactor using designed experiments



## 6.1. Introduction

Recently, petrochemicals, fine chemicals and polymer industries increased their interest in the selective hydrogenation of alkynes.<sup>1-3</sup> The alkene products are of high importance in industry since they are used as starting materials in the syntheses of alcohols, plastics, detergents and fuels. Their production by steam reforming results in the presence of alkynes impurities that poisoned subsequent polymerization processes. Therefore, the catalytic semi-hydrogenation of acetylinic compounds appears as an attractive way to purify this stream and to recover valuable olefinic compounds.

The hydrogenation process performances are strongly influenced by the catalyst activity and selectivity, the intrinsic kinetics and mass transfer, as well as the reactor design.<sup>4</sup> A combination of selective catalyst and optimum operational conditions are necessary to avoid the over-hydrogenation of the alkene product.<sup>5</sup>

Among the transition metals reported for this process, Pd has been identified as the most efficient one in terms of activity and selectivity.<sup>6</sup> Its performances have been attributed to the stronger adsorption of the  $C\equiv C$  group (relative to  $C=C$ ) on the Pd surface preventing thus the over-reduction of the alkene product. Pd metal is generally anchored on different supports such as oxides ( $SiO_2$ ,  $Al_2O_3$ ,  $TiO_2$ ),  $CaCO_3$  (Lindlar®) and carbon based materials (activated C, graphite, carbon nanofibers or nanotubes).

As detailed in the previous chapters, colloidal chemistry appears as a great tool for the preparation of well-defined metal nanocatalysts since it allows the precise control of their size, shape, structure and composition.<sup>7</sup> Such control enables a maximization of the available metal surface area and thus improves the catalyst productivity. This chapter aims at studying the catalytic performances of the several Pd-based catalysts previously prepared via colloidal approach in the selective hydrogenation of 1-octyne

in a stirred tank reactor. The selected commercial reference was the Pd Nanoselect catalyst (LF 200) patented by BASF.<sup>8</sup>

The reaction conditions, reactor design and alkynes substrate structure highly influence the semi-hydrogenation of alkynes.<sup>4</sup> Usually, mild pressure and temperature favor high selectivities towards the alkene products.<sup>9</sup> The agitation type and rate are have to be adapted to the reactor geometry and the reaction volume to avoid mass transfer limitations.<sup>10</sup> Finally, the alkyne structure influences the hydrogenation process since the degree of substitution largely affect the binding properties of the substrate and the alkene product.<sup>11</sup> The semi-hydrogenation of terminal alkynes is more challenging to control than that of internal alkynes. Moreover, the presence of hydroxyl groups within the alkynes structures was observed to retard the hydrogenation reaction, thus helping in the selectivity control to the desired alkene.<sup>12</sup>

The design of active and selective metallic nanocatalysts for the production of alkenes via the selective hydrogenation of alkynes is a great challenge. Besides the catalyst intrinsic characteristic, its performances will largely depend on the studied process: the substrate, the set-up, the conditions and operating procedures.<sup>5</sup> Therefore, the acquisition of kinetic data is crucial to gain knowledge about the reaction system.

Before considering kinetic expressions or comparing catalyst performances, it is of high importance to verify that the studied system works in a kinetic regime.<sup>10</sup> Indeed, in a heterogeneous catalytic reaction, the catalyst is usually in a different phase than the reagents. Therefore, the reaction rate is related to mass transfer or diffusion between phases. More specifically when the intrinsic surface reaction is quite fast such as an alkyne hydrogenation over a Pd catalyst, the process is more likely to be limited by mass transfer.<sup>13</sup> In this case, high temperature and pressure conditions led to fast reaction kinetics and thus a stronger negative impact of mass transfer limitations. Consequently, the reaction conditions ensuring the intrinsic kinetic regime are important for maximum process efficiency and for the understanding of the reaction mechanism.

Several kinetic studies on the selective hydrogenation of terminal linear alkynes over Pd based catalysts were previously reported.

For instance, Kiwi-Minsker and co-workers developed a kinetic model for the selective hydrogenation of 1-hexyne over Pd on active carbon fibers (ACF) catalyst.<sup>4</sup> To ensure that the reaction kinetics was not influenced by internal diffusion, they prepared several catalysts with different Pd loading and checked the similarity of the initial activities. Then, they studied the 1-hexyne hydrogenation kinetics over a Pd (0.45 wt%)/ACF catalyst in a stirred tank reactor operating in semi-batch mode. This catalyst provided over 96% of selectivity towards 1-hexene at 1-hexyne conversion up to 90%. A kinetic model assuming a Langmuir-Hinshelwood mechanism with competitive adsorption of the reagents, weak non-dissociative adsorption of hydrogen and bimolecular reaction of the adsorbed species was developed. This model resulted to be consistent with the experimental data and enabled the determination of the enthalpies of adsorption, activation energies and the pre-exponential factors. For the reaction of hydrogenation of 1-hexyne to 1-hexene they reported an activation energy of  $50 \text{ kJ.mol}^{-1}$  and a pre-exponential factor of  $2.10^{12} \text{ kmol.kgPd}^{-1}.\text{s}^{-1}$ . They observed that the adsorption equilibrium constant of 1-hexyne was two orders of magnitude higher than for olefinic product and that the rate constant of the 1-hexene hydrogenation was 2.5 higher than the rate constant of 1-hexyne hydrogenation suggesting that the high selectivity towards alkene products was due to stronger adsorption of the alkyne reagents compared to that of the alkene product.

Barreto and co-workers published a study of the liquid-phase hydrogenation of 1,3-butadiene on commercial Pd/Al<sub>2</sub>O<sub>3</sub> catalyst of eggshell type.<sup>14</sup> They compared the performances of this catalyst under industrial operating conditions using three different experimental set-ups: a slurry reactor, a rotating-basket reactor and a recirculation system with an external fixed bed reactor. The latter was a good alternative to reduce mass transfer limitations and to control more precisely the start of the reaction. Indeed, in this configuration (Figure 6.1), the liquid reagents and the

hydrogen were pre-mixed in a stirred tank vessel under a high stirring rate to maintain the liquid saturated with hydrogen before performing a recirculation of this reagent mixture in the fixed bed reactor where the catalyst was located.

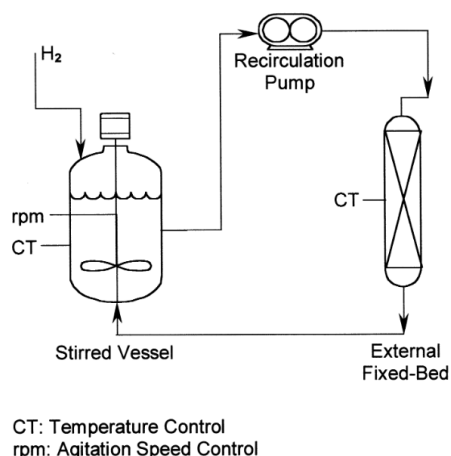


Figure 6.1. Recirculation system with an external fixed-bed reactor used by Barreto and co-workers in their kinetic study of the 1,3-butadiene and 1-butyne hydrogenations<sup>14</sup>

More recently, the same group reported a kinetic study of the hydrogenation of 1-butyne over a commercial Pd/Al<sub>2</sub>O<sub>3</sub> catalysts of eggshell type using this recirculation system.<sup>9</sup> The experiments were designed to reproduce the typical operating conditions of industrial hydrotreating reactors: liquid-phase reaction, temperature between 27 and 62°C, initial concentration of 1-butyne up to 0.6 mol/L and hydrogen partial pressure ranging from 0.8 to 8 bar. Following one-factor-at-a-time (OFAT) experiments, a regression analysis that involved data collected during the hydrogenation of 1-butyne until it becomes the limiting reactant was performed, thus the only reaction taking place was the hydrogenation of 1-butyne to 1-butene. They proposed a kinetic expression to fit these data that showed reaction orders of -1 and 1 for 1-butyne and hydrogen, respectively. The activation energy and kinetic coefficient at 44°C were estimated: 64.9 kJ.mol<sup>-1</sup> and 0.0046 kmol.kg<sub>cata</sub><sup>-1</sup>.s<sup>-1</sup>.

Finally, Maccarrone *et al.* reported the kinetic study of 1-heptyne over Ni/Al<sub>2</sub>O<sub>3</sub> and Pd/Al<sub>2</sub>O<sub>3</sub> catalysts.<sup>15</sup> The study was performed in a stainless steel batch reactor. The temperature was varied between 20 and 50°C, the pressure between 1.4 and 2.4 bar

and the 1-heptyne concentration between 0.10 and 0.20 mol/L. The verification of the kinetic regime was first performed. For the intraparticle mass transfer limitations, different catalysts sizes were tested and the 1-heptyne conversion values were compared. For the external mass transfer limitations, different stirring speeds were tested and for rates higher than 500 rpm, the 1-heptyne conversion values remained constant. The experiments were thus performed at 800 rpm. The authors proposed several models using the Langmuir-Hinshelwood-Hougen-Watson formalisms (LHHW models) and performed model discrimination using the experimental results. For the Pd/Al<sub>2</sub>O<sub>3</sub> catalyst, they concluded that the surface chemical reaction was the limiting step and that the adsorption of hydrogen was dissociative. Reaction orders of -2.6 and -1.5 in hydrogen and 1-heptyne, respectively, and apparent activation energy of 18 kJ.mol<sup>-1</sup> were reported.

All the kinetic studies presented above were carried out using OFAT experiments. However, the planning and analysis of the kinetic experiments could also be performed through design of experiments (DOE) methodology to reduce the number of experiments and obtain more accuracy in the values of the model parameters. Moreover interactions between factors could be systematically estimated. The application of this methodology to obtain kinetic data is not recent but has not been widely used. One of the few reported examples was proposed by Kiwi-Minsker and co-workers.<sup>16</sup> They performed a kinetic study of a solvent-free hydrogenation of 2-methyl-3-butyne-2-ol (MBY) over a Pd-based catalyst. The reaction kinetics were modelled using a Langmuir-Hinshelwood mechanism. They used a 2-factor central composite design (CCD) varying the hydrogen concentration and the reaction temperature to determine the kinetic parameters. To estimate the variability of the system, they performed repetition of the central point. They solved the system with least squares formula and the discrimination of the significant coefficients was performed via analysis of variance (ANOVA). Presence of interaction effects was ruled out and a linear model for the reaction rate was confirmed. With the reduced model obtained, the order of reaction towards hydrogen, the activation energy and the pre-



exponential factor could be determined: 1.0, 25.2 kJ.mol<sup>-1</sup> and 8963.0 m<sup>3</sup>.mol<sub>Pd</sub><sup>-1</sup>.s<sup>-1</sup>, respectively.

This chapter aims at studying the catalytic performances of the Pd-PAM supported nanocatalysts synthesized in chapter 4 in the selective hydrogenation of 1-octyne. The strategy developed for this study was the following:

- The existence of external and/or internal mass transfer limitations in the stirred tank reactor was assessed.
- The effects of 1-octyne concentration, hydrogen pressure and temperature on the performances of a commercial reference catalyst (Pd Nanoselect LF 200) and three Pd-PAM catalysts prepared via two-step synthesis were studied. The experiments followed a Design Of Experiments (full factorial 2<sup>3</sup> design for the reference and fractional designs 2<sup>3-1</sup> for the PAM catalysts).
- The kinetic parameters of these four catalysts were determined and their performances were compared in the selective hydrogenation of 1-octyne.
- Two other Pd-PAM catalysts prepared via one pot synthesis were tested under one set of reaction conditions and compared with the three Pd-PAM catalysts prepared by two steps and the commercial reference.

## 6.2. Experimental Section

### 6.2.1. Set-up for catalytic semi-hydrogenation of 1-octyne

The experimental set-up used for the catalytic semi-hydrogenation of 1-octyne is presented in Figure 6.2 and Figure 6.3.

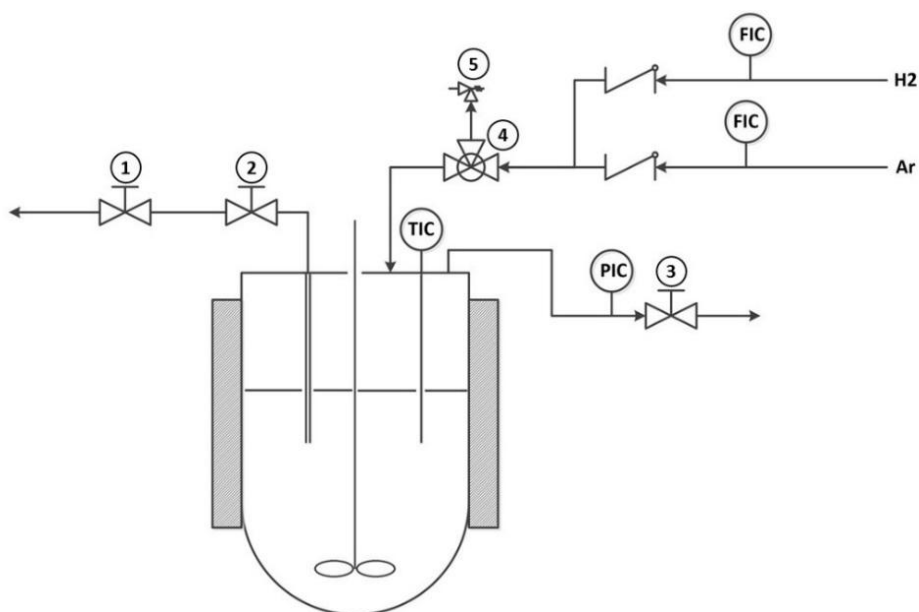


Figure 6.2. Stirred tank reactor used in this study

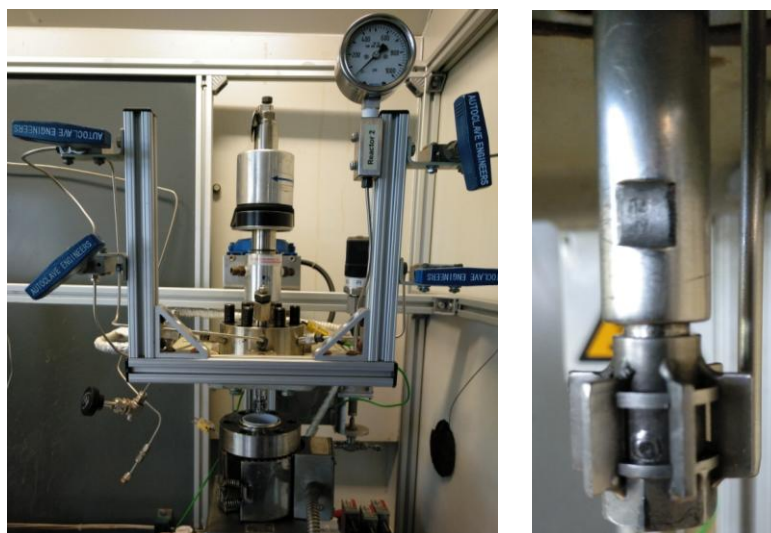


Figure 6.3. On the left: picture of the stirred tank reactor used in this study, on the right: picture of the welded impeller

This set-up consisted in a 100 mL stainless steel stirred tank reactor operating in batch mode. It was equipped with a Teflon liner to avoid contamination issues. The stirring system was composed by a Magnedrive® (MAG075) which allowed the stirring control from 0 to 2000 rpm, a shaft and impeller with six blades (Rushton turbine type) provided with the Dispersimax™ technology. Initially, this turbine was sold with holes

that allow gas recirculation. However in this chapter, the tested catalysts were powders and could remain inside the impeller during the reactions, inducing reproducibility issues. Therefore, these holes were welded with stainless steel by the company Microsold technical as shown in Figure 6.3 (right side).

This autoclave was supplied by hydrogen and argon through mass flow controllers (Bronkhors F-201CV) connected independently to the corresponding bottle. The gas inlet was situated on the top cover of the reactor and a liquid sampler was also available. The temperature was controlled inside the autoclave by communication of the internal thermocouple and the external electric heating mantle. Finally, two evacuation valves enabled manual release of gases: one was located on the inlet line of the reactor (valve nº5 on Figure 6.2) and the other one on the outlet line of the reactor (valve nº3 on Figure 6.2).

All the connections of this set-up were stainless steel tubing of 1/8 OD (Outside Diameter). The control of the mass flow controllers (MFCs), the stirring, pressure and temperature systems were made possible thanks to control units commercialized by PID Eng&Tech. These units were managed by the Process@ software (PID Eng&Tech, Iberfluid). This software allowed automation of the procedures and the continuous acquisition of the different reaction parameters during the experiments.

For the catalytic tests presented in this chapter, n-heptane was used as solvent and bicyclohexyl as internal standard. A maximum of five samples were taken from the reactor using the sampling valve and taking care that the total volume of sample did not exceed 10% of the total volume of the reaction.<sup>17</sup> These samples were analyzed by GC-MS (Gas Chromatograph Mass Spectrometer). Further details about this characterization are given in section 6.2.5. Before starting the series of catalytic tests, leak tests, cleaning of the principal elements and blank tests were performed.

### 6.2.2. Starting procedure

The procedure adopted for the catalytic tests was the following:

- The empty Teflon liner was weighted.
- The amount of the liquid substrate corresponding to the catalytic test was introduced in this liner. This reaction mixture was previously prepared and stored in the fridge.
- A sample of 40  $\mu\text{L}$  of this substrate was extracted from the storage bottle to analyze the feed of the reaction by GC-MS ( $t_0$  of the catalytic test).
- The mass of the tested catalyst was introduced in the liner, taking care that the entire amount weighted went inside the solution and not on the reactor walls.
- The filled Teflon liner was weighted.
- Before sealing the autoclave, a purge of the hydrogen line was performed. To do so, a hydrogen flow rate of 1600 NmL/min was passed through the lines during two minutes (session 1 of the Figure 6.4).
- A purge of the argon line was performed. To do so, an argon flow rate of 200 NmL/min (the maximum allowed) was passed through the lines during 15 minutes (session 2 of Figure 6.4).
- The autoclave was sealed and flushed with argon. To do so, an argon flow rate of 200 NmL/min was set with the inlet valve of the reactor open. Once the pressure of the reactor reached 10 bar, the depressurization valve was open to release the argon (valve n°3 on Figure 6.2). The operation was repeated three times.
- The stirring motor was started to 700 rpm as shown in session 4 of Figure 6.4. The real agitation rate was measured thanks to a laser tachometer since the real values did not correspond to the values introduced in the software. The real rate was systematically controlled and readjusted if necessary during a test.

- The reactor was pressurized with the desired amount of argon. To do so, the argon flow rate was set to 200 NmL/min with the inlet valve of the reactor open until the desired value was reached (valve nº4 on Figure 6.2). After that, the inlet valve of the reactor was manually closed and the gas remaining in the lines was removed through the valve situated on the inlet line of the reactor (valve nº5 on Figure 6.2).
- A leak test was performed during 15 minutes at room temperature.
- The temperature was increased to the desired value. A set point was given to the heating mantle and to the reactor. The set point of the heating mantle needed to be higher than the desired set point inside the reactor to maintain the temperature constant.
- The evolution of the argon pressure was checked while the temperature was increasing. This final pressure value was previously estimated for each catalytic test using the ideal gas law.
- The stirring speed was increased to the desired value.
- The desired pressure of hydrogen was introduced inside the reactor. The inlet valve of the hydrogen MFC was opened and the flow rate was fixed to 1600 NmL/min. Several purges were performed before entering in the reactor by opening the depressurization valve situated in the inlet line of the reactor (valve nº 5 on Figure 6.2). The addition time of hydrogen in the reactor was registered.
- Once the reactor was closed with the initial pressure of hydrogen, the reaction was started ( $t_0$  of the reaction).
- Samples were taken during the reaction using the sampling valve. The total volume of samples never exceeded 10% of the total volume contained in the reactor.

Test Time	Alias	Session 1	Session 2	Session 3	Session 4	Session 5	Session 6	Session 7	Session 8
01:27:20 - Days 01	Description	H2_purge	Ar_purge	Seal_reactor	Ar_flush	Gas_leak	Temperature	Agitation	H2_addition
Session Time	SessionTime (min)	2	15	10	10	15	20	2	12
00:02:14 - Days 01	Conditional Jump?	X	X	X	X	X	X	X	X
Remaining Time	Control Parameter								
00:07:46 - Days 01	Operator								
	Value								
	Next Session #	2	3	4	5	6	7	8	End
<input type="checkbox"/> SHOW ALL	✓ AGITACION 25( SV					700	700	1000	1000
<input type="button" value="RUN"/>	✓ AGITACION 25( R								
<input type="button" value="STOP"/>	✓ AGITACION 25( NF								
<input type="button" value="VIEW"/>	✓ AGITACION 25( HF								
<input type="button" value="1"/>	✓ AGITACION 25( LF								
<input type="button" value="LAUNCH"/>	✓ AGITACION 25( REV								
	✓ ALARMA SV1					50	50	50	
	✓ ARGON SV1	0	200	0	0	0			
	✓ CO SV1								
	✓ H2 SV1	1600	0					0	1600
	✓ PRESSION SV1								
	✓ T LINEA SV1								
	✓ T VAS1JA SV1					40	40	40	

Figure 6.4. Session table used for the control of the argon and hydrogen flow rates, the agitation rate, the temperature and pressure during a typical catalytic test

### 6.2.3. Shut down procedure

Once the reaction time was reached, the reaction was stopped according to the following shutdown procedure:

- When the reaction time was reached, the stirring and heating were immediately stopped using the Process@ software.
- The heating mantle was removed and the reactor was cooled down in an ice bath.
- The reactor was depressurized.
- At atmospheric pressure, the reactor was opened.
- The reactor content was transferred to a 50 mL glass bottle using a pipette to avoid contamination of the metallic part of the reactor.
- The reactor was cleaned following the procedure given in the next section.

### 6.2.4. Washing procedure

The washing procedure was performed immediately after each catalytic test. The procedure was the following:

- The inside part of the reactor vessel, the lid and the agitator shaft (stainless steel) were cleaned with a large amount of acetone.

- The Teflon liner was washed with soap and water, and left in aqua regia (mixture of nitric acid and hydrochloric acid) during 5 minutes. It was washed again with soap and water and let in piranha solution (mixture of sulfuric acid and hydrogen peroxide) during 30 minutes. Finally, it was washed again with soap and water and a bit of acetone to speed up its drying.
- The impeller was washed with soap and water using a pipe cleaner. Then it was introduced in *ca.* 50 mL of ethanol in a small beaker and ultrasound treatments were applied during 30 minutes. After that, the impeller was rinsed with water and introduced into a nitric acid solution of 30% during 30 seconds. Finally it was washed with soap and water and a bit of acetone to speed up its drying.

Blank tests were performed with frequency to check the efficiency of the cleaning. Moreover, additional cleanings were performed twice a week. They consisted in introducing 60 mL of n-heptane in the liner, seal the autoclave and heat until *ca.* 120°C during one hour. At the end of this time, argon was introduced in the reactor and the its content was emptied by the sampling valve.

### 6.2.5. Characterization by GC-MS

For each catalytic test, the liquid samples were analyzed to evaluate the amount of each component in the liquid phase (n-heptane, n-octane, 1-octene, 1-octyne and the internal standard bicyclohexyl). These analyses were performed by GC-MS on an Agilent 7890A with a MS 5975C detector using a Column HP5-MS (30 m, 0.25 mm, 0.25  $\mu$ m) and helium as carrier gas. The chromatographic method consisted in an initial isotherm at 35°C during 10 minutes, followed by a ramp of 40°C/min up to 230°C and a final hold time of 5 minutes. The temperature set point was chosen as a function of the boiling temperature of the bicyclohexyl (227°C, the higher boiling temperature of the compounds contained in the analyzed samples). The identification and quantification of the products was performed by comparison with standards using calibration curves for each compound.

The liquid sample extracted from the reaction was diluted in ethanol prior to the injection in the GC-MS (samples of 40  $\mu\text{L}$  in 1 mL of ethanol were prepared). A typical chromatogram of these liquid samples is given in Figure 6.5.

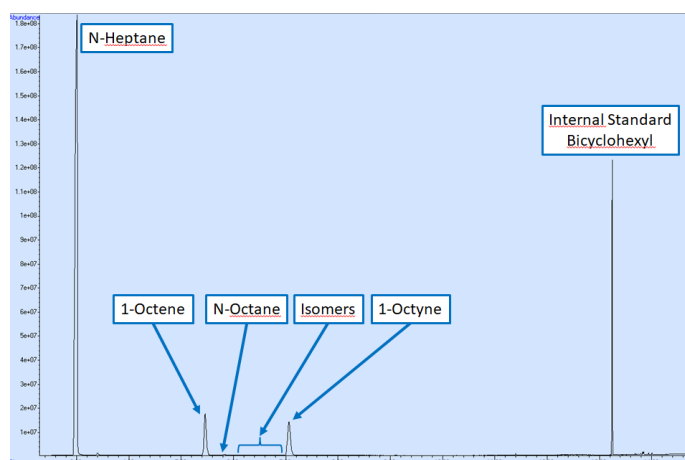


Figure 6.5. Example of chromatogram of liquid sample extracted from the catalytic semi-hydrogenation of 1-octyne

The calibration consisted in the preparation of 11 solutions containing n-heptane, n-octane, 1-octene, 1-octyne and the internal standard bicyclohexyl. The volumetric percentages were varied between 65% and 95% for n-heptane and between 0% and 15% for n-octane, 1-octene and 1-octyne. Concerning the bicyclohexyl, its volumetric percentage was fixed to 5%. These values were selected as a function of the operating conditions. From these 11 solutions, 40  $\mu\text{L}$  were extracted and diluted in 1 mL of ethanol in a GC-MS vial. After analysis by GC-MS, the calibration curves were obtained for each component in the studied range of concentrations. These curves were obtained by plotting the relation of areas  $rA_i$  between the component  $A_i$  and the internal standard (IS)  $A_{IS}$  vs. the real molar concentrations  $C_i$ . A linear curve was fitted to the set of data in order to obtain the equation that relates the measured areas with the real component concentrations:  $rA_i = aC_i + b$ . The curves of n-octane, 1-octene, 1-octyne are given in Figure 6.6. The linear fitting were obtained with  $R^2$  values over 0.99, indicating that the obtained equations were describing well the experimental points.



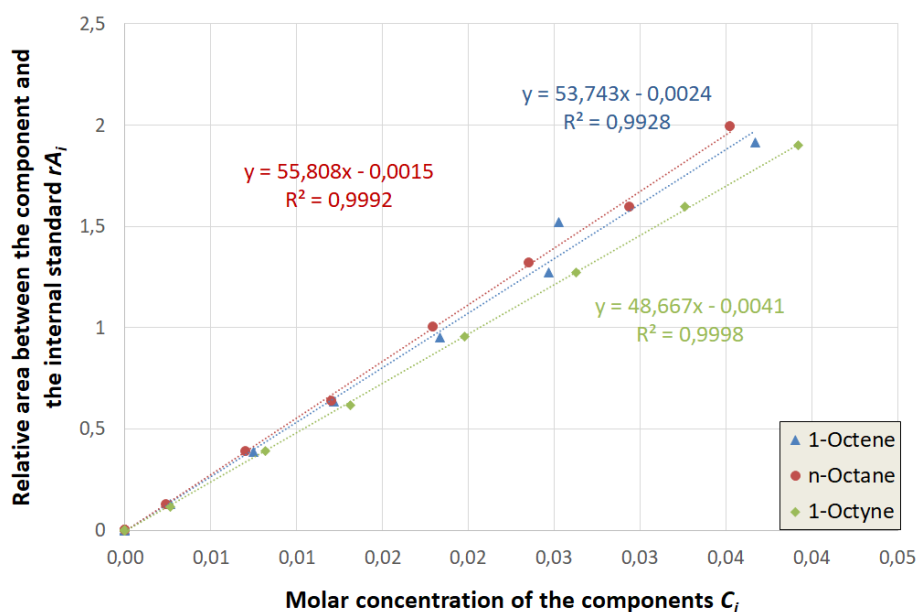


Figure 6.6. Calibration curves of n-octane, 1-octene and 1-octyne

The 1-octyne conversion at a time  $t$  of the reaction was estimated using three different equations ( $Y$  corresponds to 1-octyne and  $E$  to 1-octene):

- Conversion 1:

$$X_{Y1,t} = (1 - x_{Y,t}) \times 100 \quad (6.1)$$

The conversion 1 was calculated from the difference between the 1-octyne molar fraction  $x_{Y,0}$  at initial reaction time ( $t_0$ ) and the 1-octyne molar fraction  $x_{Y,t}$  at time  $t$ .

- Conversion 2:

$$X_{Y2,t} = \frac{[Y]_0 - [Y]_t}{[Y]_0} \times 100 \quad (6.2)$$

The conversion 2 was calculated from the 1-octyne concentrations difference between the initial reaction time and the time  $t$  ( $t_0$  and  $t$ ) divided by the 1-octyne concentration at  $t_0$ .

- Conversion 3:

$$X_{Y3,t} = \frac{[E]_t - [E]_0}{[Y]_0} \times 100 \quad (6.3)$$

The conversion 3 was estimated from the 1-octene production (this assumption is correct as far as the reaction conditions do not provide over-hydrogenation of the 1-octene). It was calculated from the difference between the 1-octene concentrations at  $t$  and  $t_0$  divided by the initial concentration of 1-octyne.

The 1-octyne consumption rate was calculated by two equations:

- Rate 1:

$$r_1 = [Y]_0 \frac{dX_{Y,t}}{dt} \quad (6.4)$$

- Rate 2:

$$r_2 = \frac{-d[Y]_t}{dt} \quad (6.5)$$

Finally, the 1-octene formation rate was also calculated using the following equation:

- Rate 3:

$$r_3 = \frac{d[E]_t}{dt} \quad (6.6)$$

The selectivity towards 1-octene was calculated as follow:

$$S_E = \frac{x_{E,t} - x_{E,0}}{x_{Y,0} - x_{Y,t}} \times 100 \quad (6.7)$$

Where  $x_{E,0}$  and  $x_{Y,0}$  correspond to the molar fraction of 1-octene and 1-octyne at  $t_0$ , respectively and  $x_{E,t}$  and  $x_{Y,t}$  correspond to the molar fraction of 1-octene and 1-octyne at  $t$ , respectively.

## 6.3. Plan of experiments

### 6.3.1. Conditions for the kinetic regime

As detailed in the introduction, the selective hydrogenation process is strongly affected by the interaction between chemical kinetics and mass transfer. Therefore, it is recommended, before starting catalytic tests, to find out the reaction conditions that ensure the kinetic regime.

In this part, the correlations and experiments used to investigate the existence of external and internal transport limitations are presented. The results of the experimental tests are presented in section 6.4.1.

#### **6.3.1.1. Particle suspension**

To provide a good contact between the different phases in a stirred tank reactor, the choice of the agitation type and velocity is of high importance. With the stirred tank reactor used in this chapter, two types of agitation were available: the magnetic stirring or the mechanical stirring. The magnetic stirring consisted in an oval magnet that rotated thanks to a stirrer plate situated below the reactor. The mechanical stirring consisted in the six-blade impeller presented in section 6.2.1. The latter provided better diffusion of hydrogen within the liquid phase, thus it was selected for the presented study.

The minimum agitation rate to ensure a uniform suspension of the catalysts in the reaction media was estimated using the equation 1.3 presented in chapter 1. The calculations were carried out for the Pd Nanoselect LF 200 catalyst (0.5 wt%/TiSi). The minimum stirring speed was calculated for a range of temperature and catalyst loading that represents the boundaries of the studied system (respectively between 20 and 100°C and 0.08 and 0.22 g<sub>cata</sub>/100g<sub>sol</sub>). The numerical data used for the calculation are presented in Table 6.1.

Table 6.1. Parameters used for the calculation of the minimum stirring speed  $N_m$  in the selective hydrogenation of 1-octyne in n-heptane solvent over Pd Nanoselect LF 200 catalyst

Parameter	Value	Units
<i>System geometry</i>		
Reactor inside diameter, $d_T$	4.20	cm
Stirrer diameter, $d_I$	2.20	cm
Dimensionless constant, $\beta^a$	4.73	
<i>Catalyst properties</i>		
Catalyst loading, $\omega$	[0,08 – 0,22]	$g_{cata}/100g_{sol}$
Average diameter of catalyst particles, $d_p$	$4.50 \times 10^{-3}$	cm
Catalyst density, $\rho_p^b$	1.23	$g \cdot cm^{-3}$
<i>Substrate properties between 20 and 100°C</i>		
Liquid viscosity, $\mu_L$	$[4,14 – 1,98] \cdot 10^{-3}$	$g \cdot cm^{-1} \cdot s^{-1}$
Liquid density, $\rho_L$	[0.68 – 0.61]	$g \cdot cm^{-3}$
<i>Others</i>		
Gravitational acceleration, $g$	981	$cm \cdot s^{-2}$

<sup>a</sup> estimated using equation 1.4; <sup>b</sup> estimated following a similar methodology to the ASTM D4781 (Standard test method for mechanically tapped packing density of fine catalyst particles and catalyst carrier particles)<sup>18</sup>

The minimum stirring speed calculated in the most unfavourable case (higher temperature and larger amount of catalyst in the reaction media) resulted to be equal to 509 rpm (8.5 rev/s). Therefore, to ensure a uniform suspension of the catalyst particles in the reaction medium within the limits of the studied system, the agitation rate should be fixed to a value higher than 509 rpm.

### 6.3.1.2. Transport limitations

#### External transport limitations

The external transport corresponds to the reagent diffusion from the bulk phase to the external surface of the catalyst. It happens through four major steps: the diffusion of the bulk gas phase, the mass transfer in the gas-liquid interface, the diffusion in the bulk liquid phase and the mass transfer in the liquid-solid film. Among them, it has been seen that the diffusion in the bulk gas phase and diffusion in the bulk liquid could be neglected (cf. chapter 1 section 1.6.1.1.).

### *Mass transfer in the gas liquid interface*

To check if the mass transport resistance at the gas-liquid interface is negligible in comparison with the reaction rate in the studied system, it is common to perform catalytic tests at different stirring rates.

Previous numerical modelling of a two-phase mixing in the stirred tank reactor used for this study were performed by Vernet and co-workers.<sup>19</sup> The objective of this study was to analyse the two-phase mixing processes that take place in a small-scale stirred tank reactor operated in batch mode. Numerical predictions of mass transfer rates of hydrogen within the liquid phase were presented. Analyses on baffled and unbaffled reactor configurations were performed. They reported that, at the same agitation rate and as long as a bubbly flow was maintained, the unbaffled reactor provided larger mass transfer rates (30% larger). However, once the emulsion was formed, the mass transfer dropped up to 65%. Therefore, above the critical rotation rate where the emulsion was formed (between 1000 and 1500 rpm), the unbaffled reactor was a better option to overcome mass transfer resistances. Up to this critical rotation rate, the baffle reactor resulted to provide larger mass transfer rates. Nevertheless, the authors of this study insisted on the fact that the direct quantitative extrapolation of these conclusions to the real operating conditions of the reactor has to be made carefully. They concluded that the three-flow regime observed experimentally were likely to exist in the real operating conditions of the reactor (no bubble, bubbly flow and emulsion) but probably at different ranges of rotation rates that those determined in the later study.

Concerning the study presented in this chapter, the real operating conditions that were used varied from the operating conditions considered in the modelling study. Indeed the gaseous mix that was used was hydrogen and argon instead of hydrogen and the liquid substrate was mostly n-heptane instead of the aqueous solution considered. Consequently, it was necessary to check experimentally the ranges of rotation rates in which the bubbly flow took place under the studied conditions however the conclusions of this study were helpful to select the conditions to test.

The unbaffled reactor was chosen for the catalytic tests since it was demonstrated that for the same agitation speed, the mass transfer rates were larger in this reactor configuration.<sup>19</sup> In the case of the baffle reactor, it was necessary to increase significantly the rotation speed to reach similar high mass transfer rates implying a negative economic and environmental impact at industrial scale. Moreover, the presence of a baffle could increase the contaminations issues of the reactor.

To determine the range of agitation rates in which the resistance by mass transfer in the gas-liquid interface was negligible, catalytic designed experiments at different stirring rate and liquid volume were performed. The objective of these experiments was to identify the value of for both factors for which the 1-octyne conversion was maximized. In other words, to find out the values for which the limitation by mass transfer in the liquid-gas interface was negligible in comparison with the 1-octyne reaction rate. To do so, an initial full factorial design  $2^2$  was implemented with the addition of three central points. After that, three additional experiments were performed to complete a second full factorial design  $2^2$  in the direction of an increase of the stirring rate, as shown in Figure 6.7 where the red dots corresponds to the experiments.

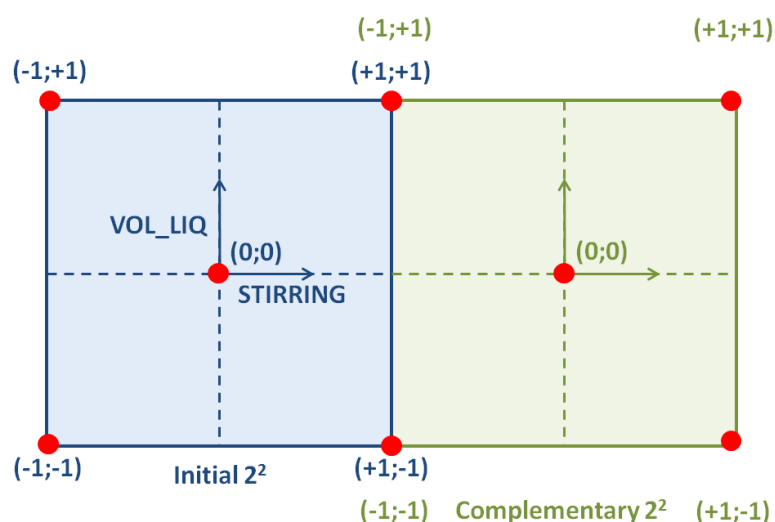


Figure 6.7. Visual representation of the initial designed experiments (full factorial  $2^2$ ) and the complementary experiments for the experimental verification of mass transfer in the liquid-gas interface

- Catalytic test procedure

The procedure adopted for the catalytic tests was the one described in section 6.2.2. During these tests, the sampling valve was not used to avoid disturbances in the system. Two samples were analysed: the  $t_0$  and the  $t_f$  of the reaction. The  $t_0$  corresponds to a sample extracted from the initial reaction substrate and the  $t_f$  to a sample extracted from the reaction at the end of the reaction.

- Factors included in the DOE

The selection of the levels of stirring rate and reaction volume was based on the conclusions of the study reported by Vernet and co-workers detailed above.<sup>19</sup> For the unbaffled configuration, it was demonstrated experimentally that a bubbly flow regime took place at 1000 rpm and with 60 mL of water. In the presented study, it was preferred to use a slightly lower volume for laboratory scale considerations (use of less reagents and catalysts for each test). Therefore, it was supposed that the bubbly flow regime could be obtained at an agitation speed slightly lower than 1000 rpm. That's why the central point of initial  $2^2$  design was fixed to 45 mL and 850 rpm. For this series of catalytic tests, all the other parameters such as reagent concentration, catalyst mass, pressure and temperature remained constant. The levels of the two  $2^2$  designs are given in Table 6.2.

Table 6.2. Levels of the studied factors corresponding to each design (initial and complementary)

Design	Factor	Low level -1	High level +1	Central point (0)
Initial	VOL_LIQ, mL	37.5	52.5	45
	STIRRING, rpm	700	1000	850
Complementary	VOL_LIQ, mL	37.5	52.5	45
	STIRRING, rpm	1000	1300	1150

- Design aspects

The designs considered were full factorial designs  $2^2$  which required four experiments. With this type of design, the maximum information can be obtained since no effects

are confounded. Three central point were added to the initial full factorial design in order to provide an estimation of the standard error of the calculated coefficients.<sup>20</sup>

- Experimental design

The matrix of the DOE is displayed in Table 6.3.

Table 6.3. Effect of the reaction volume and the stirring rate on the mass transfer rate –  
 Experimentation plan

RUN	VOL_LIQ mL	STIRRING rpm
1	37.5	700
2	52.5	700
3	37.5	1000
4	52.5	1000
5	45.0	850
6	45.0	850
7	45.0	850
8	52.5	1300
9	37.5	1300
10	45.0	1150

Reaction conditions: 7.5vol% of 1-octyne, 5vol% of bicyclohexyl, 87.5vol% of n-heptane, 1mol/mol of hydrogen-to-1-octyne, 45°C, 0.025g of Pd Nanoselect LF 200 catalyst, 20min and 45bar of total pressure

During this set of experiments, blank tests were performed every two catalytic tests to check the absence of contamination of the reactor.

- Response of the design

For this part, the studied response was the 1-octyne conversion obtained after 20 minutes of reaction. This conversion was calculated using the equation (6.1) detailed in section 6.2.5.

#### *Mass transfer in the liquid solid film*

As detailed in the introduction of this thesis (chapter 1), the agitation affect principally the gas-liquid transport and the tests of variation of stirring rate might not be sufficient to identify liquid-solid transport limitations. Consequently, additional tests



were performed varying the amount of catalyst in one set of reaction conditions to rule out the presence of liquid-solid limitations. Three tests were performed using 18 mg, 25 mg and 35 mg of a Pd-PAM catalyst supported on  $\alpha\text{-Al}_2\text{O}_3$ . The 1-octyne reaction rates in these three catalytic tests were compared.

### Internal transport limitations

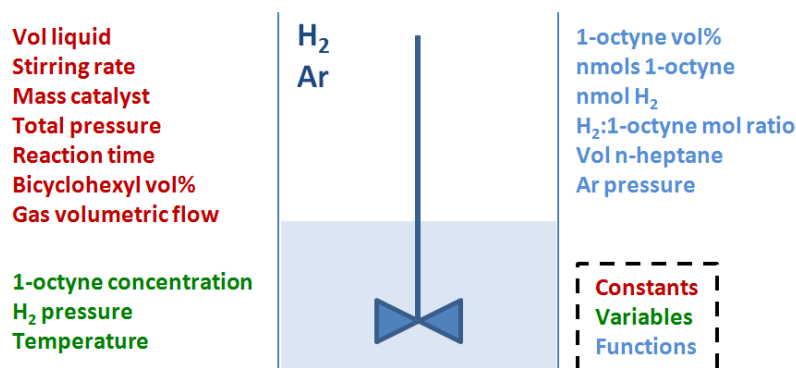
The internal transport limitations were neglected in the presented study since the catalysts used were in nanopowder form.<sup>21</sup>

## 6.3.2. Study of the effect of the reaction conditions on the 1-octyne conversion and reaction rate

### 6.3.2.1. Factors included in the DOE

In a stirred tank reactor, a wide variety of parameters can influence the performances of a catalyst such as the reagent concentrations, the time, the pressure of temperature. In this study, it was decided to focus on the effect of the 1-octyne concentration, hydrogen pressure and temperature. Indeed these parameters are those that affect the rate law thus this design could be used to study the effect of these factors as well as to obtain an estimation of the kinetic data (cf. details about kinetics in the next section).

The analysis of the catalytic set-up and procedure was performed and led to the identification of the factors presented in Scheme 6.1.



Scheme 6.1. Identification of the experimental factors that can influence the catalytic process

The studied factors, as detailed above, were the 1-octyne concentration, hydrogen pressure and temperature. The reaction volume, the stirring rate and the catalyst mass were fixed to the value obtained from the mass transfer verification experiments. The total pressure of the reactor was fixed to 45 bar, the volumetric percentage of the internal standard (bicyclohexyl) was fixed to 5% and the gas volumetric flows were set to the same value for all the experiments (200 NmL/min for argon and 1600 NmL/min for hydrogen). The time of introduction of the hydrogen gas in the reactor vessel was a non-controllable but measurable factor and was registered for each experiment. The studied experimental factors were varied at two levels. Their values are given in Table 6.4

Table 6.4. Levels of the studied factors with DOE

Nº	Factor	Low level -1	High level +1	Central point 0
1	[Y] 1-octyne concentration, mol/L	0.34	0.68	0.51
2	PH <sub>2</sub> Hydrogen pressure, bar	6.00	10.00	14.00
3	T Reaction temperature, °C	30.00	40.00	50.00

#### 6.3.2.2. Design Aspects

The study of the three factors was performed through a full factorial design 2<sup>3</sup> which allows obtaining the maximum information about this system: main effects, second-order interactions and third-order interaction without any confusion.

#### 6.3.2.3. Experimental design

##### Matrix of the experiments

The matrix of the DOE is displayed in Table 6.5. Three factors were varied according to the 2<sup>3</sup> full factorial design and four central points were added. The experiments were blocked into two main subsets that were carried out independently by two operators (operator nº1: Clément Molinet-Chinaglia and operator nº2: Olivia Benkirane). The blocking used the third-order interaction (123) to avoid confounding of blocking with a

main or second-order effect. In Table 6.6 the experimental plan resulting from the full factorial design  $2^3$  is presented. Experiments were run randomly to avoid bias.

Table 6.5. Two-block full factorial design  $2^3$

RUN	[Y]	P <sub>H2</sub>	T	OPERATOR
	<i>mol/L</i>	<i>bar</i>	<i>°C</i>	
	1	2	3	123
1	-1	-1	-1	-1
2	+1	-1	-1	1
3	-1	+1	-1	1
4	+1	+1	-1	-1
5	-1	-1	+1	1
6	+1	-1	+1	-1
7	-1	+1	+1	-1
8	+1	+1	+1	1
9	0	0	0	±1

Table 6.6. Experiments corresponding to the designed matrix  $2^3$

RUN	[Y]	P <sub>H2</sub>	T	OPERATOR
	<i>mol/L</i>	<i>bar</i>	<i>°C</i>	
	1	2	3	123
1	0.34	6.00	30.00	1
2	0.68	6.00	30.00	2
3	0.34	14.00	30.00	2
4	0.68	14.00	30.00	1
5	0.34	6.00	50.00	2
6	0.68	6.00	50.00	1
7	0.34	14.00	50.00	1
8	0.68	14.00	50.00	2
9	0.51	10.00	40.00	1,2

### Responses of the design

The objective of this study was to highlight the effect of 1-octyne concentration, hydrogen pressure and temperature on the 1-octyne conversion and 1-octyne hydrogenation rate. The 1-octyne conversion was estimated using the equations (6.1), (6.2) and (6.3) and the 1-octyne hydrogenation rate was calculated using the equations (6.4), (6.5) and (6.6) detailed in section.6.2.5.

For the kinetic study, a regression analysis was performed involving experimental data collected during the 1-octyne hydrogenation until it becomes the limiting reagent.

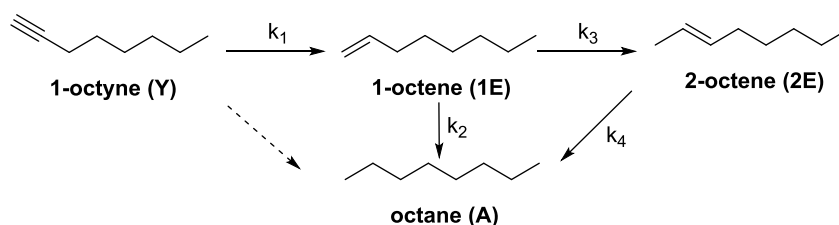
Thus, under these conditions the only reaction taking place was the hydrogenation of 1-octyne to 1-octene.

The sampling valve was used to take two samples from each catalytic test. In order to ensure that these samples were taken before the total conversion of 1-octyne, a preliminar linearity test was performed. To do so the conditions that should provide the higher reaction rate and thus the faster over-hydrogenation of 1-octyne from the matrix of experiments were tested (**RUN 7**). Samples were extracted every five minutes from the reactor in order to know in how many time the 1-octyne could be completely converted. Thus, the sampling times were fixed at values below this time.

### 6.3.3. Intrinsic kinetics studied with DOE

#### 6.3.3.1. Langmuir Hinshelwood mechanism

The kinetic equations were based on a simplified reaction scheme (Scheme 6.2) which has been reported for liquid phase alkyne hydrogenation over Pd catalysts.<sup>4</sup> The substance abbreviations are indicated in brackets and the  $k_i$  are the rate constants. In this approach, the direct hydrogenation of 1-octyne to n-octane is neglected and the transformations of 2-cis- and 2-trans-octenes are assumed to be identical without reverse isomerization to 1-octyne.



Scheme 6.2. Reaction scheme of 1-octyne hydrogenation

The kinetic of 1-octyne hydrogenation was studied over Pd Nanoselect LF 200 catalyst (0.5 wt% of Pd on TiSi).

Based on a similar study in the literature, a Langmuir Hinshelwood assuming competitive adsorption of the reactants with dissociative adsorption of  $H_2$  and a

bimolecular reaction of the adsorbed species was considered.<sup>4</sup> In Table 6.7 the elementary steps of each reaction with their kinetic expression are given. The application of this mechanism leads to the rate expressions displayed in Table 6.8. The mass balance for the surface coverage was performed assuming a low coverage for all intermediate species:  $1 = \theta^* + \theta_Y + \theta_{1E} + \theta_{2E} + \theta_A + \theta_H$ . The coverage of active site become:  $\theta^* = \frac{1}{K_Y[Y] + K_{1E}[1E] + K_{2E}[2E] + K_A[A] + \sqrt{K_H[H_2]}}$ .

Table 6.7. Langmuir Hinshelwood mechanism for 1-octyne hydrogenation

Reaction	Step	Chemical reaction	Kinetic expression
$Y \rightarrow 1E$	1	$Y + * \leftrightarrow Y^*$	$K_Y = \frac{\theta_Y}{[Y]\theta^*}$
	2	$H_2 + 2* \leftrightarrow 2H^*$	$K_H = \frac{\theta_H^2}{[H_2](\theta^*)^2}$
	3	$Y^* + H^* \leftrightarrow (Y-H)^* + *$	$K_{Y-H} = \frac{\theta_{Y-H}\theta^*}{\theta_Y\theta_H}$
	4 <sup>a</sup>	$(Y-H)^* + H^* \rightarrow 1E^* + *$	$r_1 = k_1\theta_{Y-H}\theta_H$
	5	$1E^* \leftrightarrow 1E + *$	$\frac{1}{K_{1E}} = \frac{[1E]\theta^*}{\theta_{1E}}$
$1E \rightarrow A$	1	$1E^* + H^* \leftrightarrow (1E-H)^* + *$	$K_{1E-H} = \frac{\theta_{1E-H}\theta^*}{\theta_{1E}\theta_H}$
	2 <sup>a</sup>	$(1E-H)^* + H^* \rightarrow A^* + *$	$r_2 = k_2\theta_{1E-H}\theta_H$
	3	$A^* \leftrightarrow A + *$	$\frac{1}{K_A} = \frac{[A]\theta^*}{\theta_A}$
$1E \rightarrow 2E$	1 <sup>a</sup>	$1E^* \rightarrow 2E^*$	$r_3 = k_3\theta_{1E}$
	2	$2E^* \leftrightarrow 2E + *$	$\frac{1}{K_{2E}} = \frac{[2E]\theta^*}{\theta_{2E}}$
$2E \rightarrow A$	1	$2E^* + H^* \leftrightarrow (2E-H)^* + *$	$K_{2E-H} = \frac{\theta_{2E-H}\theta^*}{\theta_{2E}\theta_H}$
	2 <sup>a</sup>	$(2E-H)^* + H^* \rightarrow A^* + *$	$r_4 = k_4\theta_{2E-H}\theta_H$
	3	$A^* \leftrightarrow A + *$	$\frac{1}{K_A} = \frac{[A]\theta^*}{\theta_A}$

<sup>a</sup>: Rate determining step

Table 6.8. Reaction rate expressions based on a Langmuir-Hinshelwood mechanism for the modelling of the hydrogenation of 1-octyne

Reaction	Langmuir Hinshelwood expression	
$Y \rightarrow 1E$	$r_1 = k_1 \frac{K_{Y-H}K_Y[Y]K_H[H_2]}{(1 + K_Y[Y] + K_{1E}[1E] + K_{2E}[2E] + K_A[A] + K_H^{1/2}[H_2]^{1/2})^2}$	(6.8)
$1E \rightarrow A$	$r_2 = k_2 \frac{K_{1E-H}K_{1E}[1E]K_H[H_2]}{(1 + K_Y[Y] + K_{1E}[1E] + K_{2E}[2E] + K_A[A] + K_H^{1/2}[H_2]^{1/2})^2}$	(6.9)
$1E \rightarrow 2E$	$r_3 = k_3 \frac{K_{1E}[1E]}{1 + K_Y[Y] + K_{1E}[1E] + K_{2E}[2E] + K_A[A] + K_H^{1/2}[H_2]^{1/2}}$	(6.10)
$2E \rightarrow A$	$r_4 = k_3 \frac{K_{2E-H}K_{2E}[2E]K_H[H_2]}{(1 + K_Y[Y] + K_{1E}[1E] + K_{2E}[2E] + K_A[A] + K_H^{1/2}[H_2]^{1/2})^2}$	(6.11)

The mass balances for 1-octyne and the reaction products are given by the differential equations displayed in Table 6.9.

Table 6.9. Differential equations of the studied kinetics

Compound	Differential equations	
1-Octyne	$\frac{d[Y]}{dt} = -\frac{m_{cat}}{V_L}r_1$	(6.12)
1-Octene	$\frac{d[1E]}{dt} = \frac{m_{cat}}{V_L}(r_1 - r_2 - r_3)$	(6.13)
2-Octene	$\frac{d[2E]}{dt} = \frac{m_{cat}}{V_L}(r_3 - r_4)$	(6.14)
n-Octane	$\frac{d[A]}{dt} = \frac{m_{cat}}{V_L}(r_2 + r_4)$	(6.15)

### 6.3.3.2. Estimation of the kinetic parameter by DOE

To estimate the apparent activation energy and the reaction order towards 1-octyne and hydrogen for the main reaction (hydrogenation of 1-octyne to 1-octene), the equation (6.8) was simplified for initial conditions:

$$r_1^0 = k_1 \frac{K_{Y-H}K_Y[Y]K_H[H_2]}{(1 + K_Y[Y] + K_H^{1/2}[H_2]^{1/2})^2}. \quad (6.16)$$

This expression could also be written as a simple power rate law expression:

$$r_1^0 = k_1'[Y]^n[H_2]^m \quad (6.17)$$

Where  $n, m$  are respectively the reaction order towards 1-octyne and hydrogen and:

$$k'_1 = k_1 \frac{K_{Y-H} K_Y K_H}{\left(1 + K_Y [Y] + K_H^{1/2} [H_2]^{1/2}\right)^2} \quad (6.18)$$

The resulting expression could be linearized if the apparent kinetic constant was expressed in terms of Arrhenius law:  $k'_1 = Ae^{-\frac{Ea}{RT}}$  where  $A$  is the pre-exponential factor,  $Ea$  the activation energy for the reaction,  $R$  the universal gas constant and  $T$  the temperature:

$$\ln r_1^0 = \ln A + n(\ln [Y]) + m(\ln [H_2]) - \frac{Ea}{R} \left(\frac{1}{T}\right) \quad (6.19)$$

As a result, equation (6.19) could be compared to the parametric model:

$$y = a_0 + a_1 x_1 + a_2 x_2 + a_3 x_3 + a_{12} x_1 x_2 + a_{13} x_1 x_3 + a_{23} x_2 x_3 + a_{123} x_1 x_2 x_3 + \varepsilon \quad (6.20)$$

In this model, the variables  $x_1$ ,  $x_2$  and  $x_3$  were respectively  $\ln [Y]$ ,  $\ln [H_2]$  and  $\frac{1}{T}$  and the coefficients estimated  $a_0$ ,  $a_1$ ,  $a_2$  and  $a_3$  could be related to  $\ln A$ ,  $n$ ,  $m$  and  $-\frac{Ea}{R}$ . The coefficients  $a_{12}$ ,  $a_{13}$ ,  $a_{23}$  and  $a_{123}$  were constants that reflect the existence of interactions between variables.

In this chapter, the coefficients of this parametric model were estimated thanks to the design presented in section 6.3.2.3. The same experiments were used but the factors  $[Y]$ ,  $P_{H_2}$  and  $T$  were replaced by  $\ln [Y]$ ,  $\ln P_{H_2}$  and  $\frac{1}{T}$ , respectively. The kinetic parameters  $n$ ,  $m$  and  $Ea$  were then obtained by a transformation of the coordinates using the following equation:

$$\frac{x - x_2}{x_2 - x_1} = \frac{u - u_2}{u_2 - u_1} \quad (6.21)$$

Where  $x$  represents the real variables,  $x_1, x_2$  the coordinate of the real variables,  $u$  represents the coded variables and  $u_1, u_2$  the coordinates of the coded variables. Using this transformation, the reaction order towards 1-octyne and hydrogen, the activation energy and the pre-exponential factor were obtained by the following equations:

$$n = \frac{2a_1}{\ln[Y]_2 - \ln[Y]_1} \quad (6.22)$$

$$m = \frac{2a_2}{\ln P_{H22} - \ln P_{H21}} \quad (6.23)$$

$$Ea = -2a_3R \left( \frac{1}{T_1} - \frac{1}{T_2} \right)^{-1} \quad (6.24)$$

$$\ln A = a_0 + \frac{n}{2} (\ln[Y]_2 - \ln[Y]_1) - n \ln[Y]_2 + \frac{m}{2} (\ln P_{H22} - \ln P_{H21}) - m \ln P_{H22} - \frac{Ea}{2R} \left( \frac{1}{T_2} - \frac{1}{T_1} \right) + \frac{Ea}{RT_2} \quad (6.25)$$

## 6.4. Results and Discussion

### 6.4.1. Verification of mass transfer

#### 6.4.1.1. Experimental verification of mass transfer in the liquid-gas interface via DOE

To study the effect of the reaction volume and the stirring rate on the 1-octyne conversion and to determine the working zone where this value is maximized, ten experiments were performed following the plan detailed in section 6.3.1.2. (Table 6.3). The 1-octyne conversion values obtained after 20 minutes of reaction are displayed in Figure 6.8.

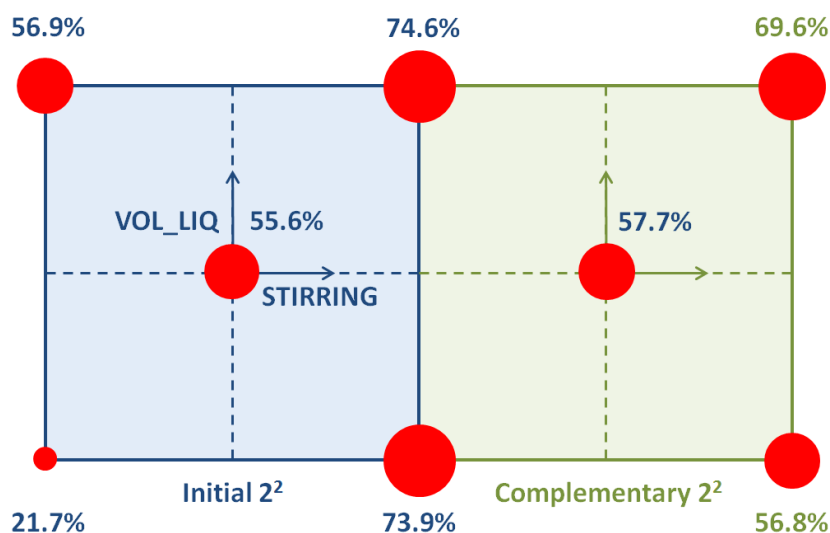


Figure 6.8. Square plots of the results of the initial and complementary full factorial designs for the experimental verification of mass transfer in the liquid-gas interface



The first initial  $2^2$  design (in blue in Figure 6.8), revealed that, independently of the reaction volume, the 1-octyne conversion values increased when increasing the stirring rate to 1000 rpm. To check the behavior of the system after 1000 rpm, three experiments were added to complete a second  $2^2$  design (in green in Figure 6.8). These experiments revealed a decrease of the 1-octyne conversion when the stirring rate reached 1300 rpm. Such negative effect of the high stirring speed was reported by Semagina and co-workers.<sup>10</sup> They performed an experimental study of a fast alkyne semi-hydrogenation in a 300 mL stirred tank reactor and they studied the effects of different stirring rates (500, 900 and 1200 rpm) with measurements of volumetric gas-liquid mass transfer coefficients and flow pattern analysis. They demonstrated that above a certain speed value, the efficiency of gas-liquid mass transfer decreased resulting in a slower reaction rate. They attributed this phenomenon to the high degree of gas recirculation behind the impeller blades. This formation of large gas regions surrounding the blades while increasing the stirring speed was also reported by Vernet and co-workers in the numerical and experimental modelling of the two-phase mixing in the stirred tank reactor used in this chapter.<sup>19</sup>

The coefficients of each design were estimated and two linear models were obtained for the two working zone. For the first model, the standard deviation of the coefficients was estimated from the reproduction of the central points. In the case of the second model, this deviation could not be estimated since reproduction of the central point was not performed. The models were the following:

- From 700 to 1000 rpm:

$$y = 56.2(\pm 0.8) + 9.0(\pm 1.2)x_1 + 17.5(\pm 1.2)x_2 - 8.6(\pm 1.2)x_1x_2 \quad (6.26)$$

- From 1000 to 1300 rpm:

$$y = 66.5 + 3.4x_1 - 5.5x_2 + 3.0x_1x_2 \quad (6.27)$$

Using these equations, a model of the 1-octyne conversion as a function of the reaction volume and the stirring rate was drawn and is given in Figure 6.9.

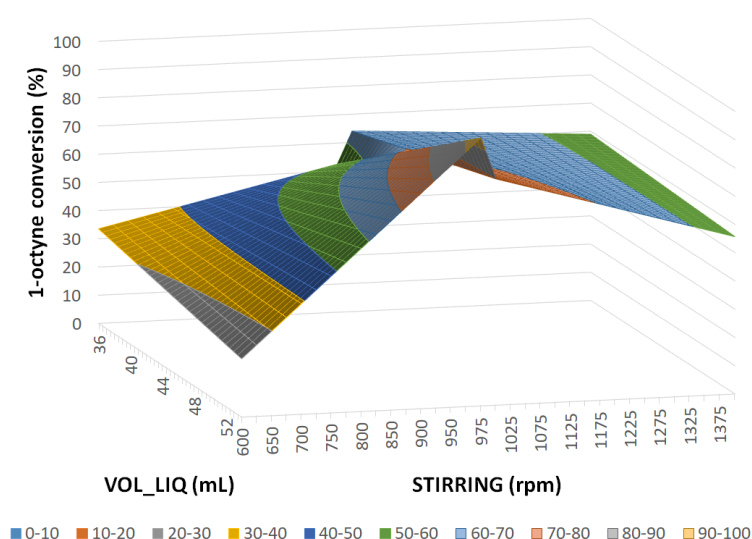


Figure 6.9. Mathematical model of the 1-octyne conversion as a function of the reaction volume (VOL\_LIQ) and the stirring rate (STIRRING) obtained from two separated full factorial designs  $2^2$

These models were based on linear equations; therefore the curvature was not taken into account. The local planarity can be checked by comparison of the average of the four points of the  $2^2$  factorial with the average of the center of the design. If this difference is smaller than the experimental error, thus it can be considered that a linear model is in adequacy with the behavior of the system.

In the case of the initial  $2^2$  factorial, this difference was equal to 1.2, value lower than the error estimated by the repetitions of the central point (*ca.* 2.3%). Thus the adequacy of the planar model was not questioned.

In the case of the complementary  $2^2$  design, the difference between the average of the four point of the design with the unique central point was equal to 11.0. This high value suggested the presence of curvature. However, the error of this second design was not estimated since only one central point was performed. It could be approximated to the error estimated from the first design (*ca.* 2.3%). With this assumption, the planar model was shown to be inadequate. To confirm this observation, additional central points were necessary to estimate the real error of this second design.

Nevertheless, to respect the scheduling of the project, these additional experiments were not performed since the information obtained was sufficient to conclude about the kinetic regime. Indeed, the presented plot displays a peak where the 1-octyne conversion was maximized in the tested range of value: at high reaction volume (52.5 mL) and intermediate stirring rate (1000 rpm). Consequently, these values were used during the rest of the experiments presented in this chapter.

#### 6.4.1.2. Experimental verification of mass transfer in the liquid-solid film

To investigate the presence of liquid-solid film transport limitations, three catalytic tests were performed varying the amount of catalyst while maintaining the other parameters constants. These tests were carried out with 18 mg, 25 mg and 35 mg of a Pd-PAM/ $\alpha$ -Al<sub>2</sub>O<sub>3</sub> catalyst and revealed a 1-octyne reaction rate equal to  $0.007 \pm 0.002$  mmol.s<sup>-1</sup>,  $0.008 \pm 0.001$  mmol.s<sup>-1</sup>, and  $0.011 \pm 0.000$  mmol.s<sup>-1</sup>, respectively. These results showed a linear behavior of the reaction rate versus the Pd amount in the catalytic tests (cf. Figure 6.10) suggesting the absence of mass transfer in the liquid-solid film. For technical limitations and reproducibility issues, it was preferred to work with 25 mg of catalyst for the rest of the experiments.

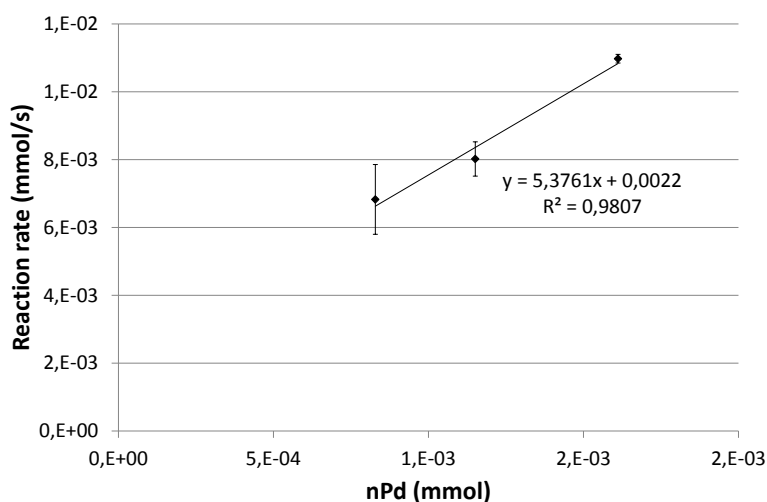


Figure 6.10. Experimental verification of mass transfer in the liquid-solid film. Reaction rate versus the Pd amount in the catalytic tests

### **6.4.1.3. Conclusions of the experimental mass transfer verification**

First, two full factorial designs  $2^2$  were used to study the effect of the reaction volume and the stirring rate on the 1-octyne conversion. The higher conversion values were obtained at 52.5 mL and 1000 rpm suggesting the absence of mass transfer in the liquid-gas interface under these conditions. Then, the liquid-solid film mass transfer verification was performed by varying the amount of catalyst in the reaction media. The reaction rates increased proportionally to the amount of catalyst, indicating the absence of liquid-solid transport limitations. The further catalytic tests were performed using 25 mg of catalyst.

## **6.4.2. Study of the effect of the reaction conditions on the 1-octyne conversion and reaction rate**

### **6.4.2.1. Pd Nanoselect LF 200 catalysts**

First, a preliminary linearity test was performed to determine the time of reaction at which full conversion of 1-octyne was reached. This experiment was performed under 14 bar of hydrogen, at 50°C and with 0.34 mL/L of 1-octyne concentration. These conditions were selected to reach full conversion in the shortest time possible within the range of parameters under study. The concentration profiles and 1-octyne evolution over time are displayed in Figure 6.11.

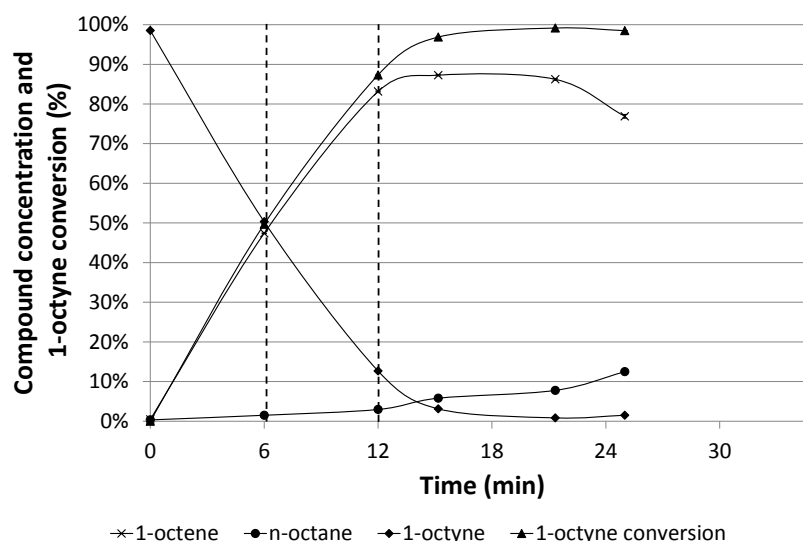


Figure 6.11. Linearity test. Concentration profiles and evolution of 1-octyne conversion over time in 1-octyne hydrogenation. Reaction conditions: **Pd Nanoselect LF 200** catalyst; 0.34 mol/L of 1-octyne concentration; 14 bar of hydrogen pressure and 50°C (**RUN 7** from  $2^3$  matrix).

After *ca.* 15 minutes of reaction, the 1-octyne full conversion was reached. This result indicates that in the experiments of the DOE matrix, the full conversion should not be reached before this time. Therefore, samples were extracted from the reactor at 6 and 12 minutes for the DOE study.

The study of the effect of the 1-octyne concentration, hydrogen pressure and reaction temperature on 1-octyne conversion and reaction rate was performed through the  $2^3$  designed matrix presented in section 6.3.2.3. The 1-octyne conversion at 12 minutes of reaction was estimated using three equations: (6.1), (6.2) and (6.3) detailed in section.6.2.5. In the same way, the 1-octyne hydrogenation rate was estimated using three equations: (6.4), (6.5) and (6.6) detailed in section.6.2.5. For each sample extracted from the reactor, two GC-MS vials were systematically prepared. Therefore, the standard deviation of the sample analysis was estimated. The applied equations are provided in appendix 6.7.1.

It was noticed that the 1-octyne conversion obtained from equation (6.2) (conversion 2) revealed large standard deviations. This equation referred to the evolution of the 1-

octyne concentration, value that was found to oscillate significantly. The conversion obtained from (6.1) and (6.3) revealed smaller standard deviations. The first equation was a ratio of concentrations which minimize the data variability. The second equation referred to 1-octene concentration that did not show such high oscillation. The same observation was made for the reaction rates. The rates obtained through equation (6.5) revealed larger standard deviations than the rates obtained through equations (6.4) and (6.6).

The effects of the studied factors on the 1-octyne conversion and reaction rate were estimated using the data obtained from the three equations ((6.1), (6.2) and (6.3) for 1-octyne conversion and (6.4), (6.5) and (6.6) for reaction rate). Although the system showed a high degree of variability, the estimated effects remained similar independently of the equation used which gave confidence on the conclusions.

Consequently, It was decided to keep working with equation (6.1) for the 1-octyne conversion and equation (6.4) for the reaction rate since it revealed smaller standard deviations and related the evolution of 1-octyne compound (in case of over-hydrogenation of 1-octene, the 1-octyne conversion and reaction rate values will not be affected using these equations). The conversions and reaction rates obtained for each experiment of the design with these equations are displayed in Table 6.10.

Table 6.10. 1-octyne conversions and reaction rates obtained from the experimental matrix  $2^3$  estimated by the equations (6.1) and (6.4), respectively

RUN	Conversion 1 $X_{Y1,t}$ (%)	Rate 1 $r_1$ (mol.mol <sub>Pd</sub> <sup>-1</sup> .s <sup>-1</sup> )
<b>1</b>	23.4 ± 0.2	5.7 ± 0.1
<b>2</b>	9.7 ± 0.3	5.4 ± 0.5
<b>3</b>	41.4 ± 0.3	18.6 ± 1.6
<b>4</b>	28.9 ± 1.4	15.0 ± 3.5
<b>5</b>	41.0 ± 0.6	10.0 ± 1.0
<b>6</b>	18.4 ± 0.1	9.1 ± 0.3
<b>7</b>	87.4 ± 0.2	34.7 ± 1.0
<b>8</b>	50.7 ± 0.5	37.8 ± 1.7
<b>9a</b>	31.7 ± 2.6	15.8 ± 4.3
<b>9b</b>	33.5 ± 0.8	13.4 ± 2.4
<b>9c</b>	29.9 ± 0.3	12.7 ± 0.5
<b>9d</b>	33.5 ± 0.8	19.2 ± 1.3

The **RUN 7** and **8** provided the highest 1-octyne conversion and reaction rate. This observation seems logical since the corresponding reaction conditions involved the high levels of hydrogen pressure and reaction temperature (14 bar and 50°C).

The **RUN 9a** to **9d** correspond to the reproductions of the central point of the design. The average 1-octyne conversion obtained at 12 minutes for these experiments was  $32.2 \pm 1.7\%$  and the average reaction rate was  $15.3 \pm 2.9 \text{ mol.mol}_{\text{Pd}}^{-1}.\text{s}^{-1}$ . Thus the studied system showed a limited reproducibility. It could be explained by the fact that, in batch reactor, the control over the starting reaction time is not precise and thus the study of fast reaction such as terminal alkyne hydrogenation is made difficult.<sup>22</sup> These reproductions of the central point were used to estimate the standard error of the calculated coefficients and the margin of error in the presented study. This estimation was based on the hypothesis that the variability of the central points was similar to that of the designed experiments.

### Effect on the 1-octyne conversion

The effects of the 1-octyne concentration, hydrogen pressure and reaction temperature on the 1-octyne conversion were estimated at 12 minutes of reaction using the equation (6.1). The plot of effects and Pareto plot are displayed in Figure 6.12.

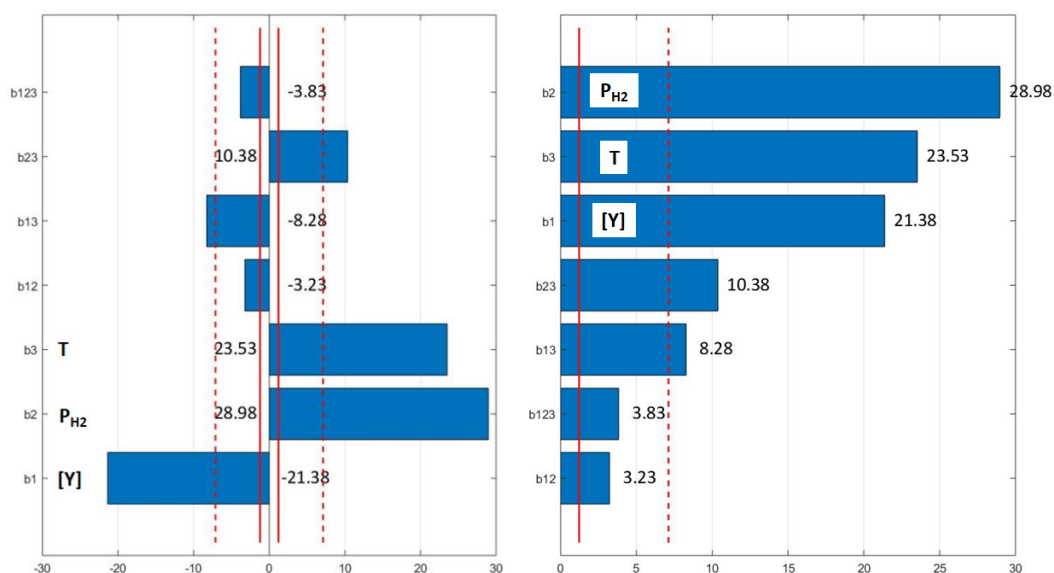


Figure 6.12. Effect of the studied factors and interactions on the 1-octyne conversion at 12 minutes. On the left, the plot of effects and on the right, the Pareto plot. The red line represents the standard deviation of the effects ( $s_b$ ). The dashed red line is the margin of error with 99.5% confidence interval with 3 degrees of freedom

The results suggest that the three studied factors 1,2 and 3 which corresponds to the 1-octyne concentration, hydrogen pressure and temperature, respectively, highly affect of the 1-octyne conversion. The interactions 23 and 13 (hydrogen pressure vs. temperature and 1-octyne concentration vs. temperature, respectively) also resulted to play a moderate role in the catalytic hydrogenation of 1-octyne. In contrast, the interactions 12 (1-octyne concentration vs. hydrogen pressure) and 123 revealed effects inferior to the margin of error (dashed red line in Figure 6.12 , *ca.* 7.1%). It was therefore concluded that they were not affecting the system.

The coefficient of multiple determination  $R^2$ , which ranges from 0 to 1, was estimated. When its value is close to 0, it means that the factors have no effect upon the response. When its value is close to 1, it indicates that the factors “explain” the data “perfectly”.

In the presented case, the complete equation of the model should be a 7-parameter equation since the selected design provided 8 informations: the effects of the 3



studied factors, the 3 second-order interactions, the single third-order interaction and the average value of the coefficients ( $a_0$ ). This equation should have the following form:

$$y = a_0 + a_1x_1 + a_2x_2 + a_3x_3 + a_{12}x_1x_2 + a_{13}x_1x_3 + a_{23}x_2x_3 + a_{123}x_1x_2x_3 \quad (6.28)$$

Since it was seen that the effects of the interactions 12 and 123 were not affecting the 1-octyne conversion, this model could be reduced to a 5-parameter equation:

$$y = 35.8 - 10.7x_1 + 14.5x_2 + 11.8x_3 - 4.1x_1x_3 + 5.2x_2x_3 \quad (6.29)$$

The coefficient of multiple determination  $R^2$  for this reduced model was equal to 0.97, suggesting that it was describing well the experimental data. Interestingly, the even more reduced model of 3 parameters obtained by removing the effects of the interactions 13 and 23 (1-octyne concentration vs. reaction temperature and hydrogen pressure vs. reaction temperature, respectively) was still able to explain 88% of the behavior of the studied system ( $R^2 = 0.88$ ).

The plot of effect (on the left on Figure 6.12) revealed a logical trend: small 1-octyne concentration combined with high hydrogen pressure and reaction temperature favored a higher 1-octyne conversion.

### Effect on the reaction rate

The effects of the 1-octyne concentration, hydrogen pressure and reaction temperature on the reaction rate were estimated. The plot of effects and Pareto plot are displayed in Figure 6.13.

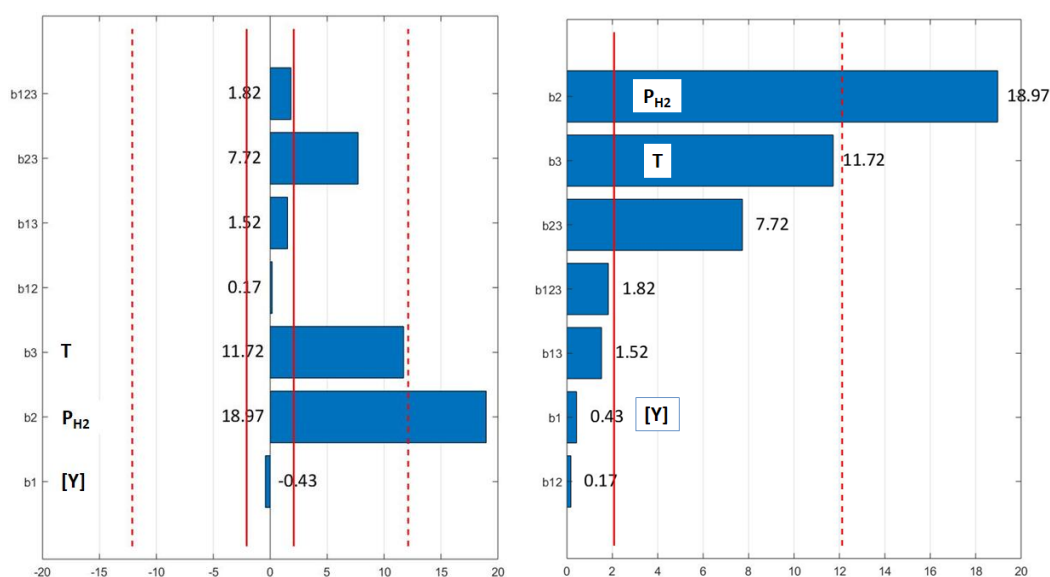


Figure 6.13. Effect of the studied factors and interactions on the reaction rate. On the left, the plot of effects and on the right, the Pareto plot. The red line represents the standard deviation of the effects ( $s_b$ ). The dashed red line is the margin of error with 99.5% confidence interval with 3 degrees of freedom

These results suggest that only the hydrogen pressure (factor 2) was affecting the reaction rate since it corresponds to the only effect higher than the estimated margin of error. The coefficient of multiple determination  $R^2$  of the reduced model that considered only this factor was equal to 0.62 suggesting that other parameters were affecting the reaction rate. Therefore, it was recalculated adding the factor 3 (temperature) and the interaction 23 (hydrogen pressure vs. temperature) in the model and resulted to be equal to 0.96 confirming that the control over these three parameters was necessary to explain 96% of the studied system. This reduced 3-parameter equation was the following one:

$$y = 16.5 + 9.5x_2 + 5.9x_3 + 3.9x_2x_3 \quad (6.30)$$

These results demonstrate that the 1-octyne concentration was not affecting the reaction rate under the tested conditions.

#### 6.4.2.2. Supported Pd-PAM NPs via two steps

At this point, the performances of three Pd-PAM supported catalysts obtained by two-step procedure were evaluated. They correspond to **Pd-PAM 6g/AC**, **Pd-PAM 6g/ $\alpha$ -Al<sub>2</sub>O<sub>3</sub>** and **Pd-PAM 6g/TiO<sub>2</sub>** prepared in chapter 4.

Since, in the case of the **Pd Nanoselect LF 200**, the 1-octyne concentration was not affecting the reaction rate, a reduction of the design presented in section 6.3.2.3. was performed. Instead of performing the eight experiments of the full factorial 2<sup>3</sup> matrix, four experiments were chosen to obtain the fractional factorial design 2<sup>3-1</sup>. This decision was made to respect the experimental schedule and to speed up the acquisition of valuable information.

The choice of a fractional factorial design implied the confusion of single effects and second-order effects. Since it was seen that the 1-octyne concentration and the interactions 12, 13 and 123 were not affecting the reaction rate when the **Pd Nanoselect LF 200** was used, a similar trend was expected for the Pd-PAM catalysts. This option was preferred rather than a full factorial design 2<sup>2</sup> removing the 1-octyne concentration from the study. In this way, the non-influence of this factor could be verified. If, effectively, the 1-octyne concentration is not affecting the reaction rate when Pd-PAM catalysts are used, the full factorial design 2<sup>2</sup> could be recalculated removing this parameter from the analysis using a projection (Figure 6.14). In contrast, if the 1-octyne concentration results to affect the reaction rate, the remaining four experiments of the full factorial design presented in section 6.3.2.3. should be performed. Consequently, in a first approach, the **RUN 1, 4, 6 and 7** of the design presented in Table 6.5 were performed for the three Pd-PAM catalysts prepared by two steps.

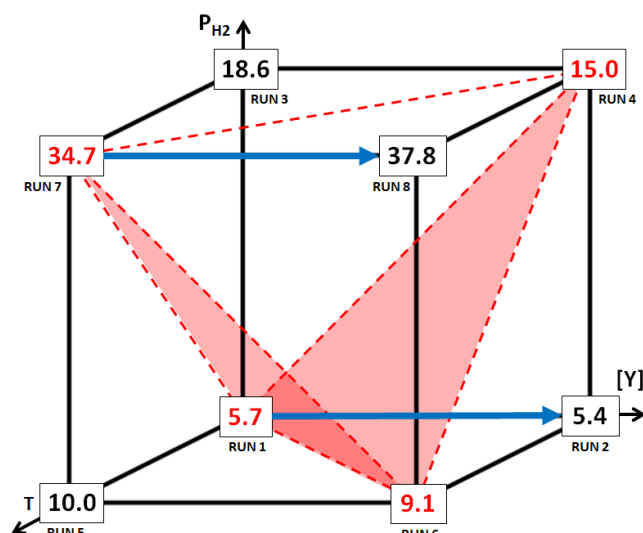


Figure 6.14. Cubic plot of the effect of the 1-octyne concentration, hydrogen pressure and reaction temperature on the reaction rate. Example of reduction of the full factorial design  $2^3$  to a full factorial  $2^2$  by projection of experiments made possible thanks to the non-influence of the 1-octyne concentration

This figure summarizes the reaction rates obtained following the full factorial  $2^3$  using the **Pd Nanoselect LF 200** catalyst. It can be seen in this example that the 1-octyne is not affecting highly to the reaction rate. Therefore the information obtained from this full factorial  $2^3$  is equivalent to the information that would have been possible to obtain through the full factorial  $2^2$  obtained by projection of the **RUN 7** and **1** on the **RUN 8** and **2**, respectively.

### Effect on 1-octyne conversion

The effects of the 1-octyne concentration, hydrogen pressure and reaction temperature on the 1-octyne conversion were estimated at 12 minutes of reaction for the Pd-PAM catalysts obtained by two steps. The plots of effects are displayed in Figure 6.15.

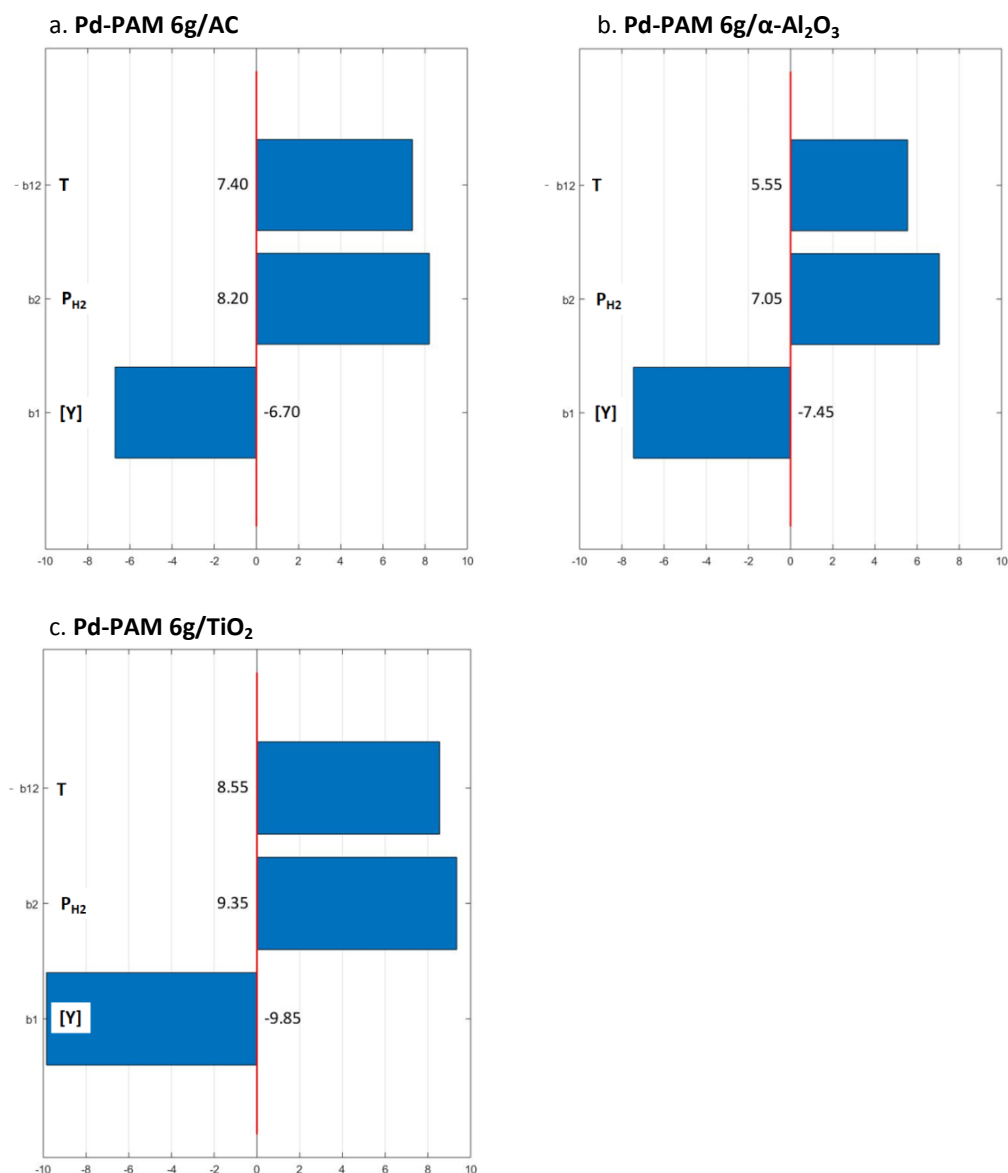


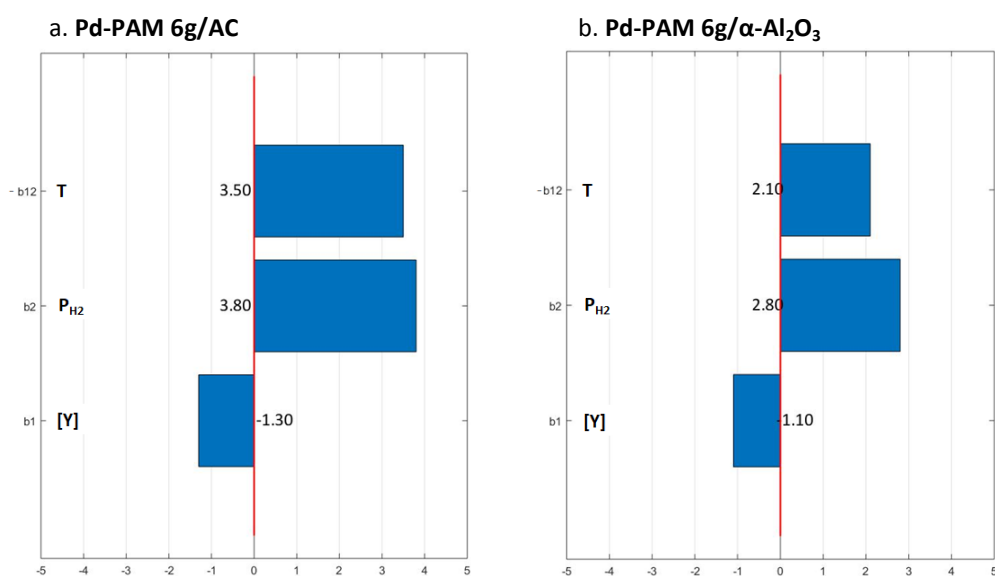
Figure 6.15. Plot of the effects of the 1-octyne concentration (b1), hydrogen pressure (b2) and reaction temperature(-b12) on the 1-octyne conversion at 12 minutes using Pd-PAM supported catalysts synthesized in two steps

These results demonstrate that, as in the case of the **Pd Nanoselect LF 200**, the three studied parameters (1-octyne concentration, hydrogen pressure and reaction temperature) highly affect the 1-octyne conversion for the three catalysts under study.

As in the case of the **Pd Nanoselect LF 200**, the plot of effects revealed a logical trend: small 1-octyne concentration combined with high hydrogen pressure and reaction temperature led to higher 1-octyne conversions.

### Effect on the reaction rate

The effects of the 1-octyne concentration, hydrogen pressure and reaction temperature on the reaction rate were estimated. The plots of effects are displayed in Figure 6.16.



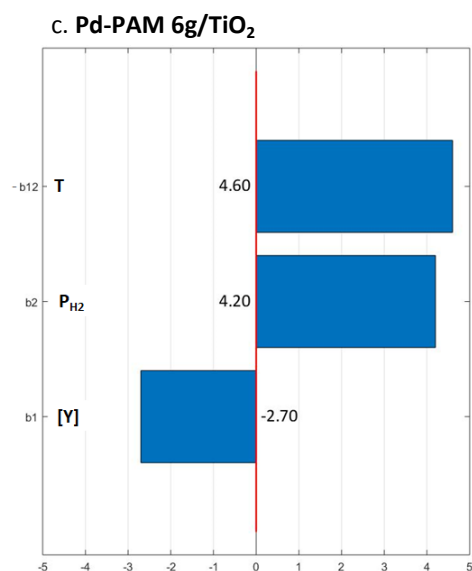


Figure 6.16. Plot of the effects of the 1-octyne concentration ( $b_1$ ), hydrogen pressure ( $b_2$ ) and reaction temperature ( $-b_{12}$ ) on the 1-octyne reaction rate using Pd-PAM supported catalysts synthesized in two steps

These results indicate that, similarly to the case of the **Pd Nanoselect LF 200**, the 1-octyne concentration was not affecting the reaction rates as much as the hydrogen pressure and temperature. The coefficients of multiple determination  $R^2$  considering only the hydrogen pressure and temperature were estimated: 0.93, 0.89 and 0.83 were obtained for **Pd-PAM 6g/AC**, **Pd-PAM 6g/ $\alpha$ -Al<sub>2</sub>O<sub>3</sub>** and **Pd-PAM 6g/TiO<sub>2</sub>**, respectively. These values were close to 1 indicating that, indeed, the 1-octyne concentration was not highly affecting the reaction rate. Thus, for the determination of the kinetic parameters, the model will be recalculated considering a full factorial design  $2^2$  by removing the 1-octyne concentration factor. This part is detailed in 6.4.3.2. after the determination of the kinetic parameters of the **Pd Nanoselect LF 200** catalyst described in section 6.4.3.1.

### 6.4.3. Intrinsic kinetics studied with DOE

#### 6.4.3.1. Pd Nanoselect LF 200

To determine the kinetic parameters for the **Pd Nanoselect LF 200** catalyst in the selective hydrogenation of 1-octyne, the parametric model obtained by the full

factorial  $2^3$  was compared to the linearization of the rate equation as detailed in section 6.3.3.2.

Experimentally the parameters varied were  $[Y]$ ,  $P_{H_2}$  and  $T$ , however for this study, the variables of interests were  $\ln [Y]$ ,  $\ln P_{H_2}$  and  $\frac{1}{T}$ , therefore the coefficients of the model presented in Table 6.5 were recalculated using these mathematical transformations. The coded value of  $\ln [Y]$  and  $\ln P_{H_2}$  remained similar while the coded value of  $\frac{1}{T}$  were inverted (-1 became +1 and vice versa). The response was also recalculated:  $\ln r_1$  (logarithm of the reaction rate calculated by the equation (6.4)). The modified matrix and the corresponding responses are presented in Table 6.11. Note that no additional experiments were performed, the data obtained from the  $2^3$  matrix presented above for the **Pd Nanoselect LF 200** catalyst were just recalculated as explained

Table 6.11. Modified full factorial design  $2^3$  design applied for the estimation of the kinetic parameters of the rate equation of the **Pd Nanoselect LF 200** catalyst and the corresponding responses obtained

RUN	$\ln [Y]$	$\ln P_{H_2}$	$\frac{1}{T}$	$\ln r_1$
	<i>Factor 1</i>	<i>Factor 2</i>	<i>Factor 3</i>	<i>Response</i>
<b>1</b>	-1	-1	+1	1.74
<b>2</b>	+1	-1	+1	1.69
<b>3</b>	-1	+1	+1	2.92
<b>4</b>	+1	+1	+1	2.71
<b>5</b>	-1	-1	-1	2.30
<b>6</b>	+1	-1	-1	2.21
<b>7</b>	-1	+1	-1	3.55
<b>8</b>	+1	+1	-1	3.63
<b>9a</b>	0	0	0	2.76
<b>9b</b>	0	0	0	2.60
<b>9c</b>	0	0	0	2.54
<b>9d</b>	0	0	0	2.95

The normal probability plot and the plot of effects in relation to a t-distribution are displayed in Figure 6.17. The t-distribution was drawn with three ( $n - 1$ ) degrees of freedom since four ( $n$ ) reproductions of the central point were performed. The scale



factor used was 0.07 which corresponds to the standard deviation of the effects obtained from the reproductions of the central points.

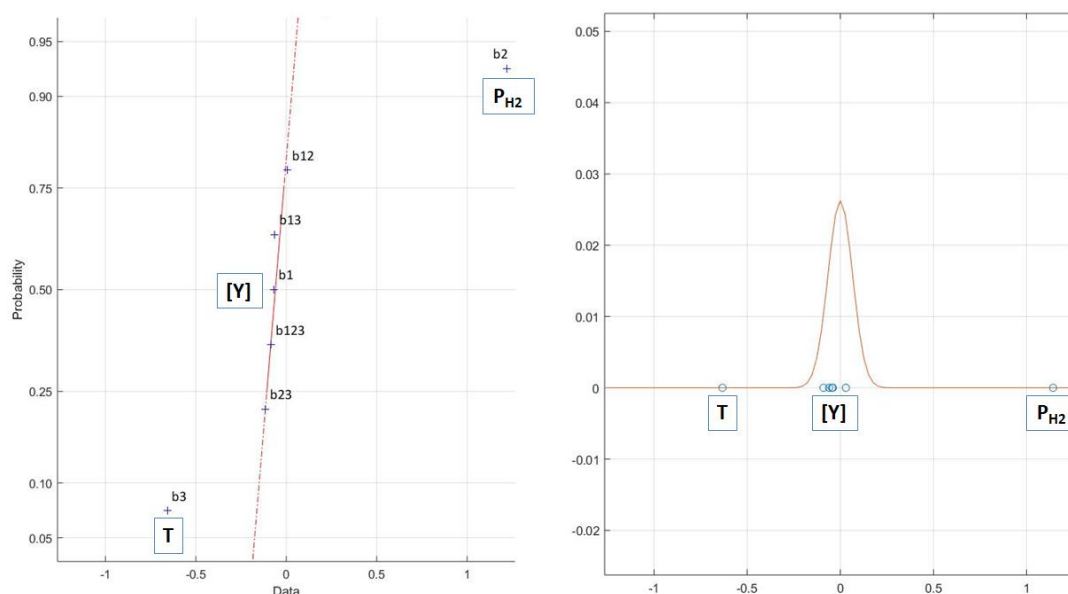


Figure 6.17. On the left the normal probability plot. On the right the t-distribution plot of the effects on  $\ln r_1$

These results demonstrate that the effects of the factor 1 (1-octyne concentration), the second-order interactions 12, 13 and 23 (1-octyne concentration vs. hydrogen pressure, 1-octyne concentration vs. temperature and hydrogen pressure vs. temperature, respectively) and the third-order interaction 123 were not affecting  $\ln r_1$ . To confirm this observation, the coefficient of multiple determination  $R^2$  was estimated for a model that only take into account the effects of the factors 2 and 3 (hydrogen pressure and temperature, respectively). The 2-parameter equation was the following one:

$$y = 2.63 + 0.61x_2 - 0.33x_3 \quad (6.31)$$

$R^2$  was equal to 0.95 confirming the large influence of the hydrogen pressure and temperature over the other studied factors on the reaction rate.

The equation (6.31) was compared to the linearization of the rate equation presented in section 6.3.3.2.

$$\ln r_1^0 = \ln A + n(\ln [Y]) + m(\ln [H_2]) - \frac{Ea}{R} \left( \frac{1}{T} \right) \quad (6.19)$$

Applying the transformation of coordinates detailed in section 6.3.3.2. (equations (6.22), (6.23), (6.24) and (6.25)) the kinetic parameters were obtained and are summarized in Table 6.12.

Table 6.12. Apparent activation energy  $Ea$ , reaction order towards hydrogen  $m$  and pre-exponential factor  $A$  for the 1-octyne semi-hydrogenation to 1-octene using the **Pd Nanoselect LF 200** catalyst

Model parameters			Real parameters			
Parameter	Value	std(a)	Parameter	Value	std	unit
$a_0$	2.63	0.027	$A$	17572	2.43	$m^3.mol_{Pd}^{-1}.s^{-1}$
$a_2$	0.61	0.033	$m$	1.4	0.1	/
$a_3$	-0.33	0.033	$Ea$	26.9	2.7	$kJ.mol^{-1}$

The order towards 1-octyne was equal to 0, the order towards the hydrogen pressure was equal to 1.4, the apparent activation energy was equal to 26.8  $kJ.mol^{-1}$  and the pre-exponential factor was equal to 17572  $mol.molPd^{-1}.s^{-1}$ . The resulting rate equation was thus:

$$r_1^0 = 17572 e^{-\frac{26877}{RT}} P_{H_2}^{1.4} \quad (6.32)$$

The fitting of the experimental results with this equation was checked and are presented in Figure 6.18. It could be seen that the reaction rate expression obtained matched quite well the experimental results. Finally, the evolution of the reaction rate as a function of the hydrogen pressure and temperature was drawn and the obtained surface is presented in Figure 6.19.

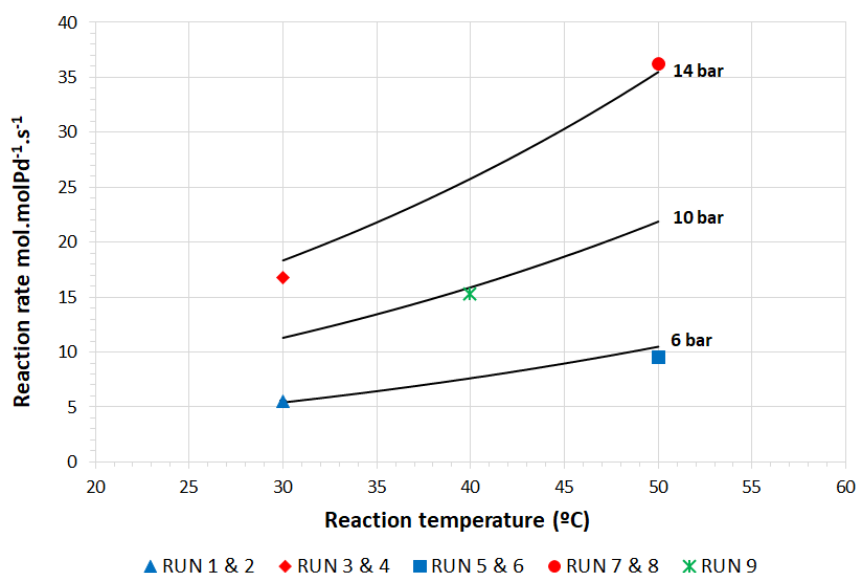


Figure 6.18. Black lines: 1-octyne hydrogenation initial reaction rates as a function of the temperature at three different hydrogen pressures: 6, 10 and 14 bar obtained from the kinetic expression of **Pd Nanoselect LF 200** catalyst. Colored markers: experimental results obtained from the 2<sup>3</sup> factorial design

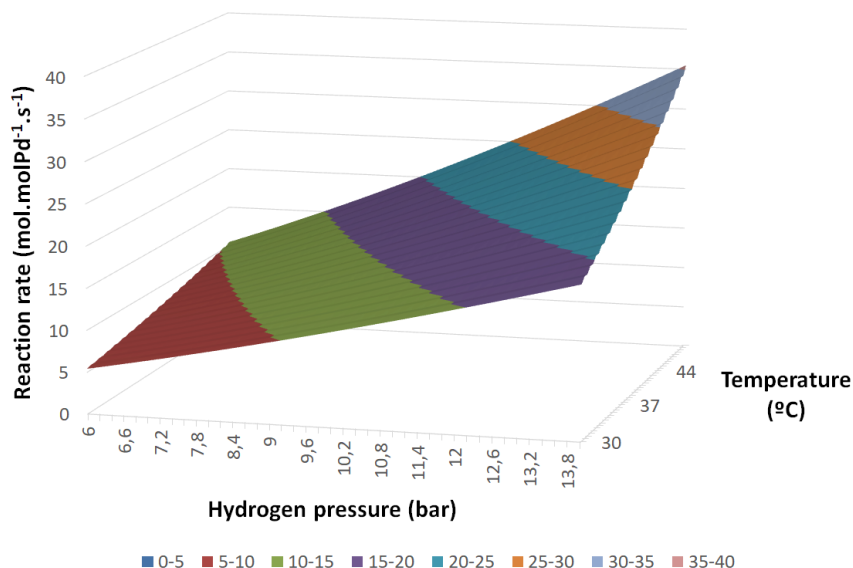


Figure 6.19. 1-octyne hydrogenation initial reaction rate as a function of the hydrogen pressure and temperature obtained from the presented kinetic study of **Pd Nanoselect LF 200** catalyst

To check the local planarity of the rate equation obtained, the average response of the eight points of the 2<sup>3</sup> factorial was compared with the average response of the four central points. This difference resulted to be smaller than the experimental error

indicating the absence of curvature (*ca.*  $0.12 \pm 0.19$ ). This conclusion means that the optimum of the reaction rate was not included in the selected range of values and that increasing even more the hydrogen pressure and temperature could lead to higher reaction rates.

To know precisely which values of pressure and temperature should be used to maximize the rate, the path of the steepest ascent could be determined. It corresponds to a two-dimensional vector that provides the direction in which the studied system should be maximized. The direction of this vector is obtained by the following equation:

$$\frac{\Delta x_1}{\Delta x_2} = \frac{b_1}{b_2} \quad (6.33)$$

Where  $\Delta x_1$  and  $\Delta x_2$  corresponds to the increment of the factor  $x_1$  and  $x_2$ , respectively, and  $b_1$  and  $b_2$  their previously estimated effects.

In the studied case, it was demonstrated that the factor 1 (1-octyne concentration) was not affecting the reaction rate, thus the increment steps of the factors 2 and 3 (hydrogen pressure and temperature, respectively) could be calculated to follow the path of the steepest ascent (in coded values). As an example, for the choice of a step of 0.5 for the factor 2, the corresponding values of the factor 3 are given in Table 6.13.

To transform these values in real values (that could be operated), the following equation was used:

$$\Delta Coded\ value = \frac{\Delta Real\ value}{\frac{1}{2} \times Range} \quad (6.34)$$

Table 6.13. Coded values and real values of the factor  $\ln P_{H_2}$  and  $\frac{1}{T}$  that follow the direction of the steepest ascent. Example of possible additional experiments to find the optimum of the reaction rate

RUN	Coded values		Real values			
	$\ln P_{H_2}$	$\frac{1}{T}$	$\ln P_{H_2}$	$P_{H_2}$ bar	$\frac{1}{T}$	$T$ °C
9	0.0	0.0	2.2	9.2	0.027	37.5
10	0.5	-0.3	2.4	11.3	0.025	40.2
11	1.0	-0.5	2.6	14.0	0.023	43.4
12	1.5	-0.8	2.9	17.3	0.021	47.1
13	2.0	-1.1	3.1	21.4	0.019	51.4
14	2.5	-1.4	3.3	26.4	0.018	56.7
15	3.0	-1.6	3.5	32.7	0.016	63.2

Additional experiments using the same reaction conditions than that used during the catalytic tests presented in this chapter, but increasing the hydrogen pressure and temperature following the path of the steepest ascent should provide higher reaction rates and thus higher 1-octyne conversion after 12 minutes of reaction. Therefore, at higher 1-octyne conversions, valuable information about 1-octene selectivity and over-hydrogenation reactions could be obtained. These experiments were not performed but could be planned as future work.

#### 6.4.3.2. Pd-PAM catalysts

The kinetic parameters of the three Pd-PAM catalysts supported by two steps were determined by the comparison of the full factorial  $2^2$  with the linearization of the rate equation (6.19) given in section 6.3.3.2.

Indeed, since it was demonstrated that the 1-octyne concentration was not affecting the reaction rate, the full factorial design  $2^2$  that only considered the hydrogen pressure and temperature as controlled variables was recalculated using projections of the experiments of the fractional factorial design  $2^{3-1}$ .

As in the case of the **Pd Nanoselect LF 200**, the controlled variables  $P_{H_2}$  and  $T$  were transformed into the variables of interest for the determination of the kinetic law:

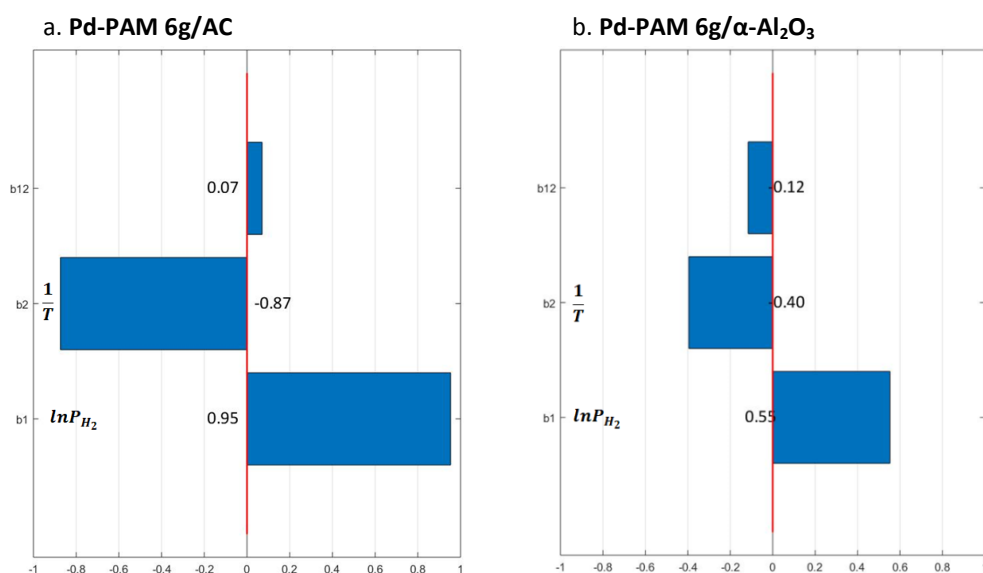
$\ln [P_{H_2}]$  and  $\frac{1}{T}$  and the response was also recalculated to obtain  $\ln r_1$ . The resulting

modified experimental matrix and the corresponding responses for each of the tested catalyst are given in Table 6.14.

Table 6.14. Modified full factorial design  $2^2$  design applied for the estimation of the kinetic parameters of the rate equation of the Pd-PAM supported catalysts synthesized in two steps and the corresponding responses obtained

RUN	$\ln [P_{H_2}]$	$\frac{1}{T}$	Pd-PAM 6g/AC	Pd-PAM 6g/ $\alpha$ -Al <sub>2</sub> O <sub>3</sub>	Pd-PAM 6g/TiO <sub>2</sub>
			$\ln r_1$	$\ln r_1$	$\ln r_1$
	2	3			
1	-1	+1	0.34	1.13	1.06
4	+1	+1	1.36	1.57	1.48
6	-1	-1	1.28	1.41	1.57
7	+1	-1	2.16	2.08	2.46
9	0	0	1.36	1.72	1.63

The plots of effects of the three tested catalysts are presented in Figure 6.20.



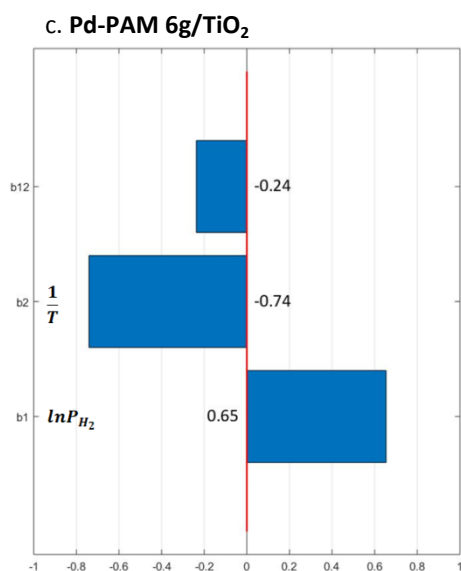


Figure 6.20. Plot of the effects of  $\ln [P_{H_2}]$  ( $b_1$ ),  $\frac{1}{T}$  ( $b_2$ ) and the interaction of both parameters ( $b_{12}$ ) on  $\ln r_1$ . using Pd-PAM supported catalysts synthesized in two steps

These results show the non-significance of the second-order interaction between  $\ln [P_{H_2}]$  and  $\frac{1}{T}$  suggesting that the linearized rate equation did not depend on interaction terms. To confirm this statement, the coefficients of multiple determination  $R^2$  for **Pd-PAM 6g/AC**, **Pd-PAM 6g/ $\alpha$ -Al<sub>2</sub>O<sub>3</sub>** and **Pd-PAM 6g/TiO<sub>2</sub>** were estimated removing this interaction terms and resulted in values close to 1 (0.99, 0.92 and 0.95, respectively). Therefore it confirms that the three studied systems were well-described by a 2-parametric equation model and that the double interaction did not have influence. These 2-parametric equations for the three studied catalysts were the following:

- For **Pd-PAM 6g/AC**:

$$y = 1.30 + 0.48x_2 - 0.44x_3 \quad (6.35)$$

- For **Pd-PAM 6g/ $\alpha$ -Al<sub>2</sub>O<sub>3</sub>**:

$$y = 1.58 + 0.28x_2 - 0.20x_3 \quad (6.36)$$

- For **Pd-PAM 6g/TiO<sub>2</sub>**:

$$y = 1.64 + 0.33x_2 - 0.37x_3 \quad (6.37)$$

Applying the transformation of coordinates detailed in section 6.3.3.2. (equations (6.22), (6.23), (6.24) and (6.25)), the kinetic parameters were obtained. The values of the order towards hydrogen, the activation energy and the pre-exponential factor are summarized in Table 6.15, together with the values of the reference catalyst **Pd Nanoselect LF 200** determined in the previous section.

Table 6.15. Apparent activation energy  $Ea$ , reaction order towards 1-octyne  $n$  and hydrogen  $m$  and pre-exponential factor  $A$  for the 1-octyne semi-hydrogenation to 1-octene using the **Pd Nanoselect LF 200** catalyst and Pd-PAM supported catalysts

Catalyst	Order towards 1-Octyne concentration, $n$	Order towards hydrogen pressure, $m$	Activation energy $Ea, kJ.mol^{-1}$	Pre-exponential factor $A$ , $m^3.molPd^{-1}.s^{-1}$
<b>Pd Nanoselect LF 200</b>	0.0	1.4	26.8	17572
<b>Pd-PAM 6g/AC</b>	0.0	1.1	35.8	287366
<b>Pd-PAM 6g/<math>\alpha</math>-Al<sub>2</sub>O<sub>3</sub></b>	0.0	0.7	16.3	589
<b>Pd-PAM 6g/TiO<sub>2</sub></b>	0.0	0.8	30.1	98801

The resulting 1-octyne initial reaction rates for the tested Pd-PAM catalysts were:

- For **Pd-PAM 6g/AC**:

$$r_1^0 = 287366e^{-\frac{35836}{RT}}P_{H_2}^{1.1} \quad (6.38)$$

- For **Pd-PAM 6g/ $\alpha$ -Al<sub>2</sub>O<sub>3</sub>**:

$$r_1^0 = 589e^{-\frac{16289}{RT}}P_{H_2}^{0.7} \quad (6.39)$$

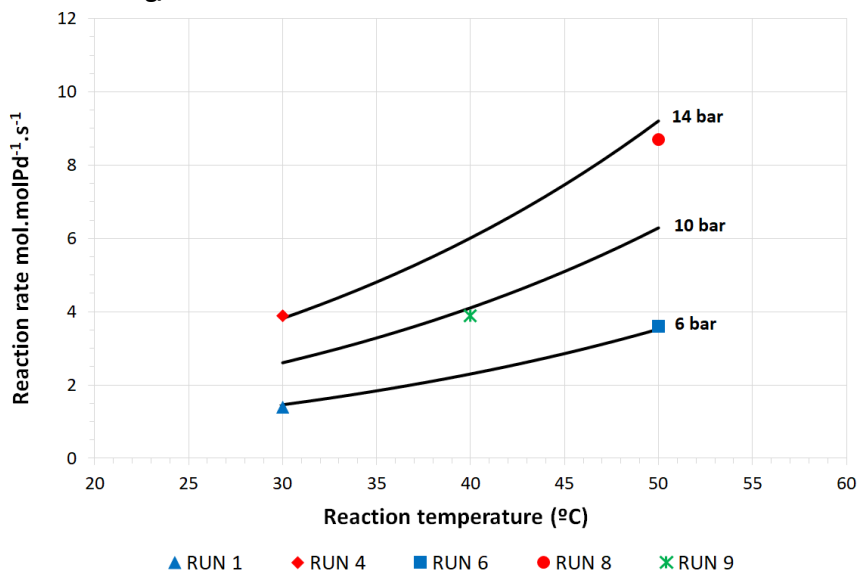
- For **Pd-PAM 6g/TiO<sub>2</sub>**:

$$r_1^0 = 98801e^{-\frac{30135}{RT}}P_{H_2}^{0.8} \quad (6.40)$$

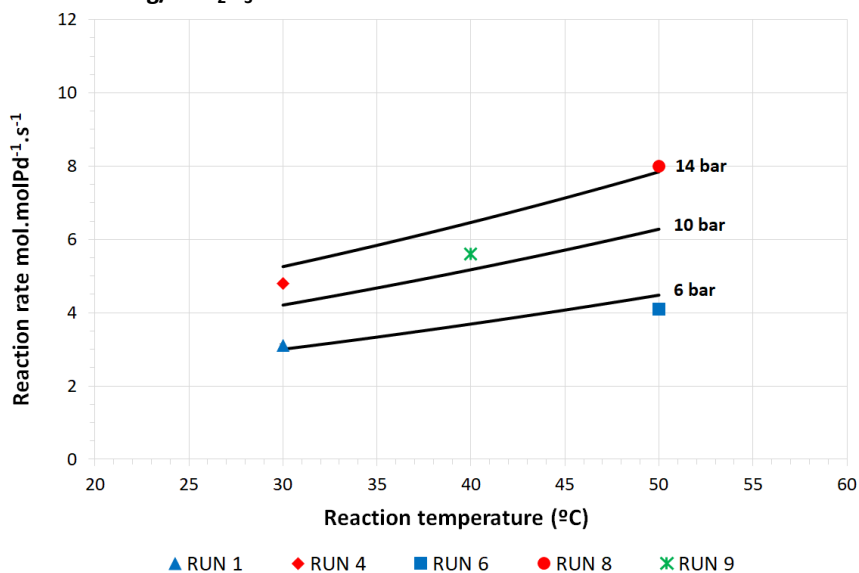
The fitting of the experimental results with these equations was checked and are presented in Figure 6.21.



**a. Pd-PAM 6g/AC**



**b. Pd-PAM 6g/α-Al<sub>2</sub>O<sub>3</sub>**



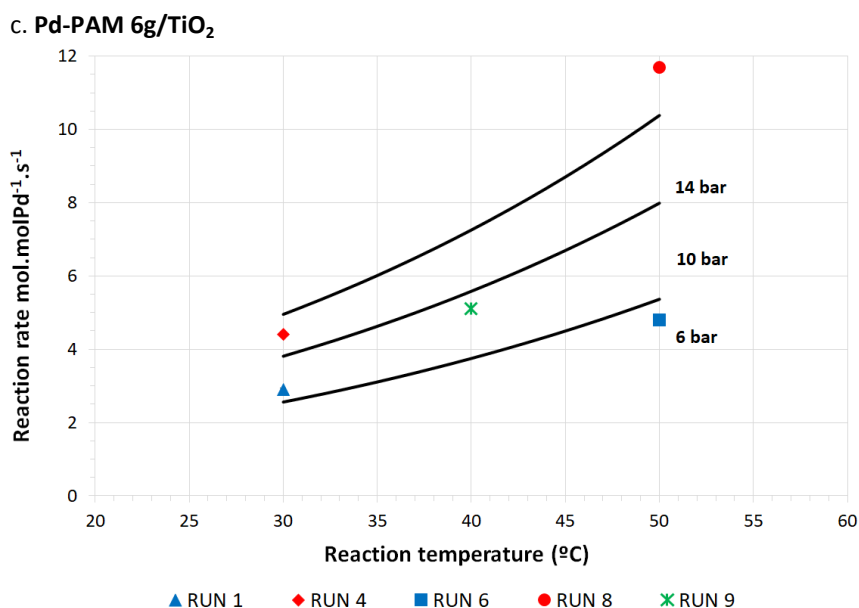
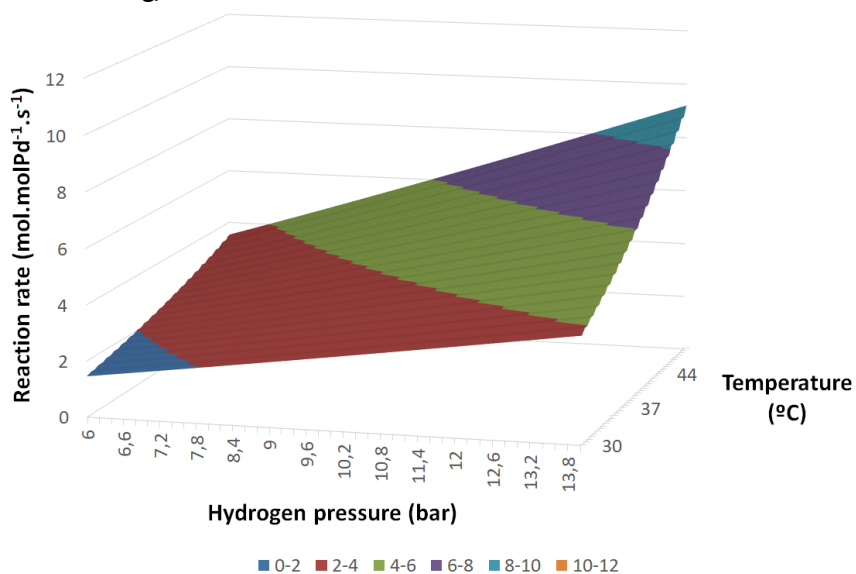


Figure 6.21. Black lines: 1-octyne hydrogenation initial reaction rates as a function of the temperature at three different hydrogen pressures: 6, 10 and 14 bar obtained from the kinetic expressions of a. **Pd-PAM 6g/AC**, b. **Pd-PAM 6g/ $\alpha$ -Al<sub>2</sub>O<sub>3</sub>** and c. **Pd-PAM 6g/TiO<sub>2</sub>** catalysts. Colored markers: experimental results obtained from the  $2^{3-1}$  fractional factorial design

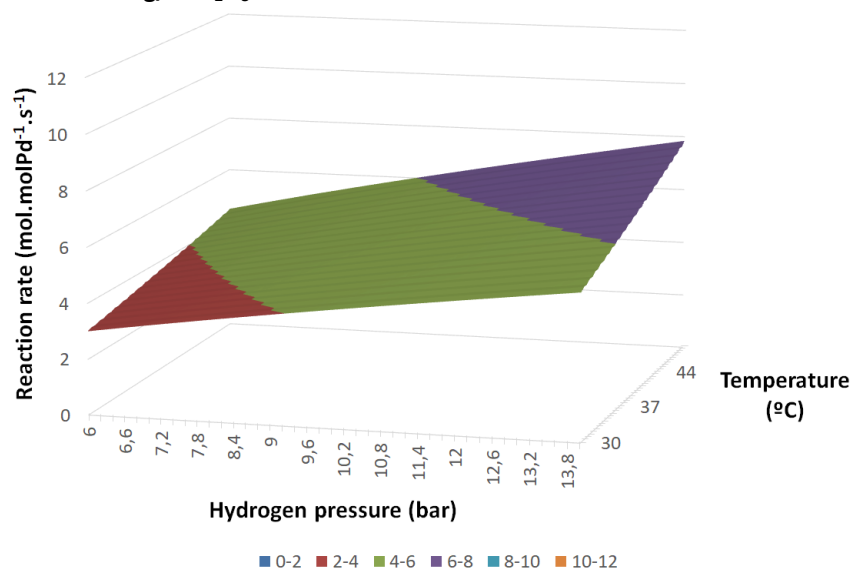
It could be seen that the reaction rate expression obtained matched quite well the experimental results in the case of **Pd-PAM 6g/AC** and **Pd-PAM 6g/ $\alpha$ -Al<sub>2</sub>O<sub>3</sub>**. In the case of **Pd-PAM 6g/TiO<sub>2</sub>**, a slightly larger deviation between the experimental result and the modelled kinetic expression was observed at high pressure (14 bar). These differences could be due to the fact that slightly higher effect of the 1-octyne concentration was obtained in this case and that this parameter was neglected for the determination of the kinetic parameters. Additional four experiments to complete the full factorial design  $2^3$  would be helpful to obtain a more accurate model. Moreover the reproduction of central points could be useful to estimate the variability of these systems.

Finally, the evolution of the reaction rate as a function of the hydrogen pressure and temperature was drawn for each of these catalysts and the obtained surfaces are displayed Figure 6.22.

a. Pd-PAM 6g/AC



b. Pd-PAM 6g/ $\alpha$ -Al<sub>2</sub>O<sub>3</sub>



c. Pd-PAM 6g/TiO<sub>2</sub>

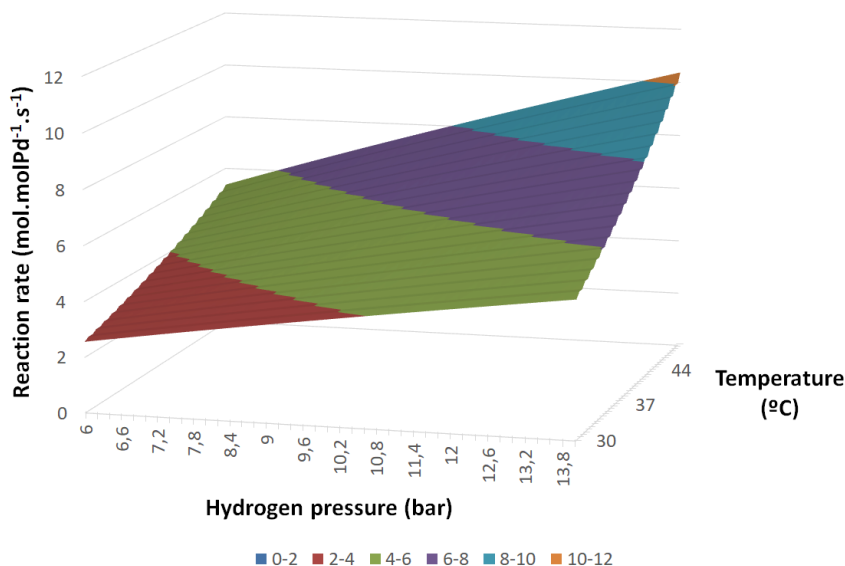


Figure 6.22. 1-octyne hydrogenation initial reaction rate as a function of the hydrogen pressure and temperature obtained from the presented kinetic study of a. **Pd-PAM 6g/AC**, b. **Pd-PAM 6g/ $\alpha$ -Al<sub>2</sub>O<sub>3</sub>** and c. **Pd-PAM 6g/TiO<sub>2</sub>** catalysts

Kinetic studies of similar alkynes substrates (1-butyne, 1-hexyne and 1-heptyne) over Pd-based catalysts were previously reported.

For instance, Barreto and co-workers studied the kinetics of 1-butyne hydrogenation over a commercial Pd/Al<sub>2</sub>O<sub>3</sub> catalysts of eggshell type.<sup>9</sup> The set-up used was different from the one described in this chapter since it consisted in a recirculation system with a fixed-bed reactor. Similar reaction conditions to those used in this chapter were used. They focused on the data related to the hydrogenation of 1-butyne to 1-butene to obtain the kinetic expression. In agreement with the results presented in this chapter, they determined a reaction order towards hydrogen of 1. However they also conclude about an order towards 1-butyne equal to -1 suggesting that the reaction rate was dependent on the reagent concentration in their study. Activation energy of *ca.* 64.9 kJ.mol<sup>-1</sup> was obtained at 44°C. This value is slightly higher than that obtained for the studied reference and Pd-PAM catalysts and indicates that more thermal energy was required for this catalytic system to carry out the reaction. This is in

agreement with the fact that 1-butyne full conversions were obtained after more than 150 minutes of reaction.

Then, Kiwi-Minsker and co-workers published the kinetic study of the 1-hexyne hydrogenation over Pd on active carbon fibers.<sup>4</sup> They used a stirred tank reactor operating in batch mode and under reaction conditions close to those used in this chapter. They obtained an activation energy of  $50 \text{ kJ.mol}^{-1}$  which is also a value slightly higher than that determined in this chapter. Surprisingly, the catalyst tested in the 1-hexyne hydrogenation was able to reach full conversion after only 30 minutes of reaction. However, the reaction orders are not clearly given in the publication.

Finally, Maccarrone *et al.* reported the kinetic study of 1-heptyne hydrogenation over  $\text{Ni/Al}_2\text{O}_3$  and  $\text{Pd/Al}_2\text{O}_3$  catalysts in a batch reactor.<sup>15</sup> The range of temperature used was similar to that presented in this chapter but the range of pressure and 1-heptyne concentration were lower (until 2.4 bar and  $0.2 \text{ mol.l}^{-1}$ ). They reported an order towards hydrogen of -2.6 which is in opposition to those previously reported. As in the study of the 1-butyne, they determined an order towards the 1-heptyne of -1.5. The activation energy was equal to  $18 \text{ kJ.mol}^{-1}$ , a value close to that obtained for the **Pd-PAM 6g/ $\alpha$ - $\text{Al}_2\text{O}_3$**  catalyst and that coincides with the fact that the reaction could proceed at low temperatures.

Moreover, Berenblyum *et al.* studied the kinetics of the selective hydrogenation of phenylacetylene in presence of carbon supported Pd nanocatalyst.<sup>23</sup> A stirred tank glass reactor was used. The kinetic experiments were planned to study the phenylacetylene hydrogenation varying its initial concentration, the hydrogen pressure, the amount of catalyst and the temperature. Also additional experiments of pure styrene hydrogenation and phenylacetylene in styrene rich mixtures were performed. The chosen conditions were similar to those tested in this chapter except for the hydrogen pressure that was varied between 0.3 and 1 bar.

In this study, they reported that the rate of phenylacetylene conversion was independent of its initial concentration in the range of studied parameters. Thus the order towards phenylacetylene was equal to 0. They show that phenylacetylene and styrene hydrogenation rates had a rate order towards hydrogen close to 1. These orders are in agreement with those presented in this chapter. Finally, the activation energies of phenylacetylene hydrogenation to styrene were reported between 30 and 55 kJ.mol<sup>-1</sup>, values that are slightly higher than that obtained in this chapter.

#### 6.4.4. Comparison of the performances of the different tested catalysts

The kinetic studies of the reference **Pd Nanoselect LF 200** and the three Pd-PAM supported catalysts provided the equation of the initial 1-octyne reaction rate for the range of studied pressure and temperature.

The 3D surface plots of these catalysts (cf. Figure 6.19 and Figure 6.22) suggest that the commercial reference catalyst was much more active than the synthesized catalysts.

For a more visual appreciation of this trend, the reaction rate was plotted as a function of the reaction temperature and at a fixed pressure for each of these catalysts (Figure 6.23). It could be observed that at 10 bar of hydrogen pressure, the reaction rate of the **Pd Nanoselect LF 200** catalyst varied between *ca.* 11 and 22 mol.molPd<sup>-1</sup>.s<sup>-1</sup> while the reaction rate of the Pd-PAM catalysts varied between *ca.* 2 and 8 mol.molPd<sup>-1</sup>.s<sup>-1</sup> demonstrating the higher activity of the commercial reference under the studied conditions. Looking at the kinetic parameters obtained for these four catalysts, the higher activity of the **Pd Nanoselect LF 200** catalyst was associated to the order towards hydrogen. Indeed, an order of 1.4 raised to the power of the pressure could easily duplicate or triplicate the reaction rate results compared to the order of *ca.* 1 obtained for the Pd-PAM synthesized catalysts.

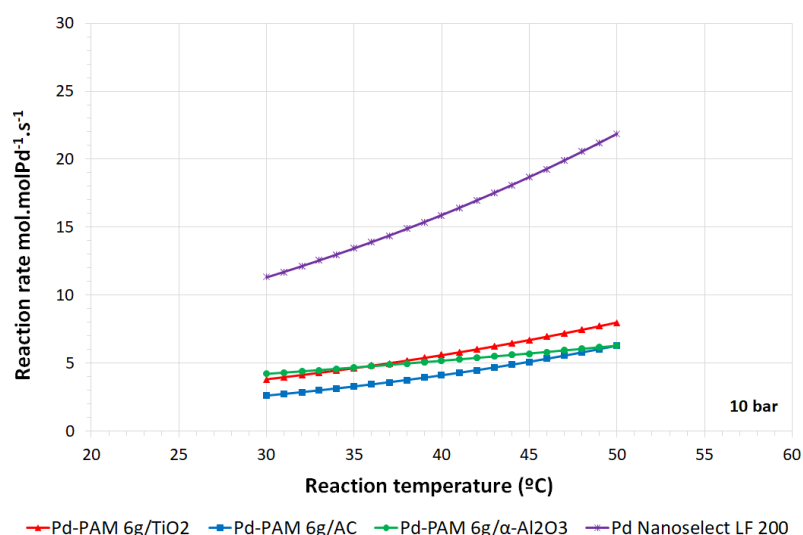


Figure 6.23. 1-octyne initial reaction rate as a function of the reaction temperature at 10 bar of hydrogen pressure for the **Pd Nanoselect LF 200**, **Pd-PAM 6g/AC**, **Pd-PAM 6g/ $\alpha$ -Al<sub>2</sub>O<sub>3</sub>** and **Pd-PAM 6g/TiO<sub>2</sub>** catalysts

Concerning the differences between the three Pd-PAM catalysts, the trends were not so clear. To gain information of their activity as a function of the catalytic conditions, the evolution of the reaction rates as a function of the temperature was plotted again but at two values of hydrogen pressure for each catalyst. This plot is displayed in Figure 6.24.

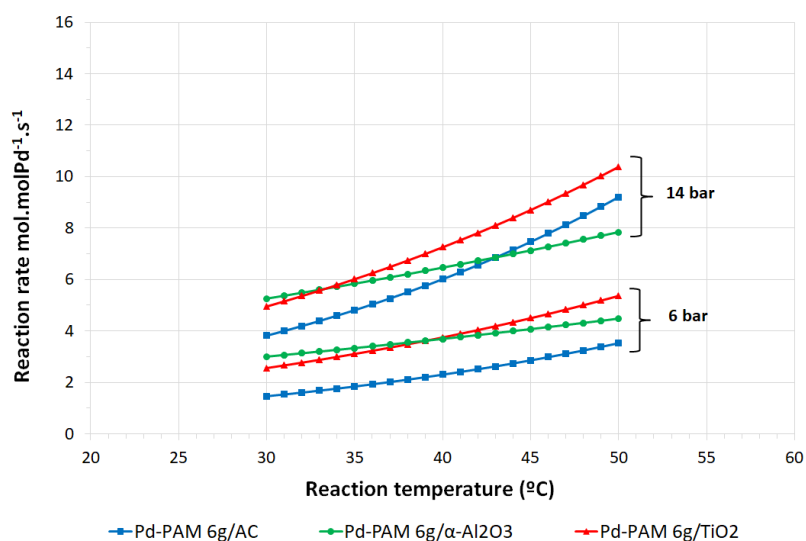


Figure 6.24. 1-octyne initial reaction rate as a function of the reaction temperature at 6 and 14 bar of hydrogen pressure for the **Pd-PAM 6g/AC**, **Pd-PAM 6g/ $\alpha$ -Al<sub>2</sub>O<sub>3</sub>** and **Pd-PAM 6g/TiO<sub>2</sub>** catalysts

The Pd-PAM catalyst supported on activated carbon was less active than the other ones at low temperature (30°C). This observation was in adequacy with the fact that this catalyst provided the higher activation energy of the set of tested catalysts (*ca.* 35.8 kJ.mol<sup>-1</sup>). When this catalyst was used, more thermal energy was required for the reaction to take place. Similarly, the Pd-PAM catalyst supported on alpha-aluminum oxide resulted to be the most active at low temperatures (30°C). The activation energy obtained for this catalyst was quite low: *ca.* 16.3 kJ.mol<sup>-1</sup>. It agrees with the fact that the catalytic tests using this catalyst did not need high temperature to produce the reaction. Then, the evolution of the reaction rate of this catalyst over the studied range of temperature and pressure was really slow. It could be explained by the fact that the pre-exponential factor A found in its kinetic expression was much smaller than for the other catalysts (*ca.* 589 m<sup>3</sup>.molPd<sup>-1</sup>.s<sup>-1</sup>). Moreover, the order towards hydrogen was the smallest obtained (*ca.* 0.7).

At high temperature, the more active catalyst was the Pd-PAM supported on titanium oxide. A combination of the pre-exponential factor and the order towards hydrogen (98 801 m<sup>3</sup>.molPd<sup>-1</sup>.s<sup>-1</sup> and 0.8, respectively) provided this high slope leading to higher reaction rates at high temperatures (50°C).

Interestingly, at 14 bar, the **Pd-PAM 6g/α-Al<sub>2</sub>O<sub>3</sub>** catalyst passed from the fastest catalyst to the slowest one while increasing the temperature. This observation demonstrates that the comparison of catalysts is not a straightforward task and highly depends on the reaction conditions. Taking this example, a comparison of the three tested catalysts at 30°C and 50°C would lead to completely opposite conclusions. For a process at low temperature, the **Pd-PAM 6g/α-Al<sub>2</sub>O<sub>3</sub>** would be preferred. In contrast for a high temperature process, the **Pd-PAM 6g/TiO<sub>2</sub>** would be more adapted. Since these three catalysts were immobilized with the same methodology, using the same batch of colloidal suspension and with the same Pd content, these results suggest that the nature of the support is affecting the catalysts activities. Alpha-aluminum oxide



would be preferred for low temperatures processes and titanium oxide for high temperatures processes.

Finally, two other Pd-PAM supported catalysts synthesized via one pot were tested in the selective hydrogenation of 1-octyne: **Pd-PAM/AC 9** and **Pd-PAM/ $\alpha$ -Al<sub>2</sub>O<sub>3</sub> 5**. However, because of time limitations, these catalysts were tested only under one set of reaction conditions: the conditions of the **RUN 7** of the Table 6.6 presented in section 6.3.2.3. which corresponds to the more drastic conditions of the design matrix (higher pressure and temperature). Since the previously tested Pd-PAM catalysts synthesized by two steps and the reference **Pd Nanoselect LF 200** catalyst were also tested under these conditions (14 bar and 50°C), it has been possible to compare these catalysts. The evolution of the 1-octyne conversion over time for all the tested catalysts is given in Figure 6.25.

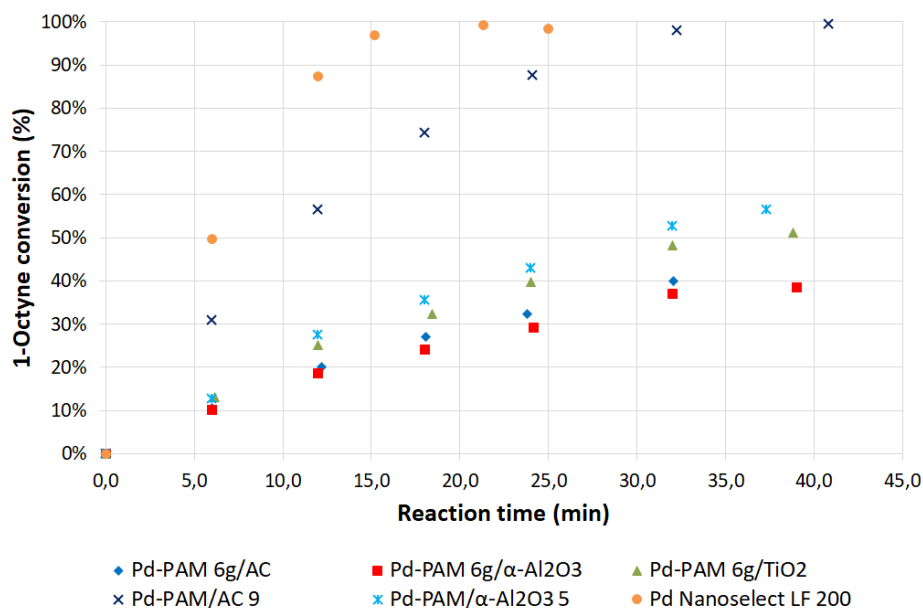


Figure 6.25. Selective hydrogenation of 1-octyne in stirred tank reactor. Evolution of the 1-octyne conversion over time for the Pd-PAM supported catalysts tested and the commercial reference **Pd Nanoselect LF 200**

The two-step **Pd-PAM 6g/ $\alpha$ -Al<sub>2</sub>O<sub>3</sub>** and **Pd-PAM 6g/AC** were the less active catalysts reaching *ca.* 40% of 1-octyne conversion after 32 minutes of reaction. The two-step

**Pd-PAM 6g/TiO<sub>2</sub>** and the one pot **Pd-PAM/  $\alpha$ -Al<sub>2</sub>O<sub>3</sub> 5** were slightly more active reaching *ca.* 50% of 1-octyne conversion after 32 minutes of reaction. The more active catalyst from the synthesized Pd-PAM catalysts was the one pot **Pd-PAM/AC 9**. Under the tested conditions this catalyst reached full conversion after 32 minutes of reaction. All of these synthesized catalysts resulted to be less active than the commercial reference **Pd Nanoselect LF 200** since it reached full conversion in less than 20 minutes under the tested conditions.

The differences between the tested Pd-PAM catalysts were the immobilization process and the nature of the support. A full factorial design 2<sup>2</sup> was calculated considering these two factors using the available data in order to understand the differences observed in terms of activity. The catalyst supported on AC and  $\alpha$ -Al<sub>2</sub>O<sub>3</sub> were considered. In Table 6.16 the levels of the factors are given and in Table 6.17 the design with the corresponding response is presented.

Table 6.16. Levels of the factors

Factor	Low level (-1)	High level (+1)
Immobilization	1 step	2 step
Support	AC	$\alpha$ -Al <sub>2</sub> O <sub>3</sub>

Table 6.17. Full factorial design 2<sup>2</sup> with the corresponding responses

Factors		Responses		
Immobilization	Support	Conversion 6 min (%)	Conversion 18 min (%)	Conversion 32 min (%)
1	2			
-1	-1	30.85	74.36	98.00
+1	-1	10.51	27.09	39.95
-1	+1	12.70	35.50	52.75
+1	+1	10.21	24.03	37.01

Using these data, the effects of the immobilization process and the support on the 1-octyne conversion at three different times of reaction were estimated. The plot of effect and Pareto plot are displayed in Figure 6.26.

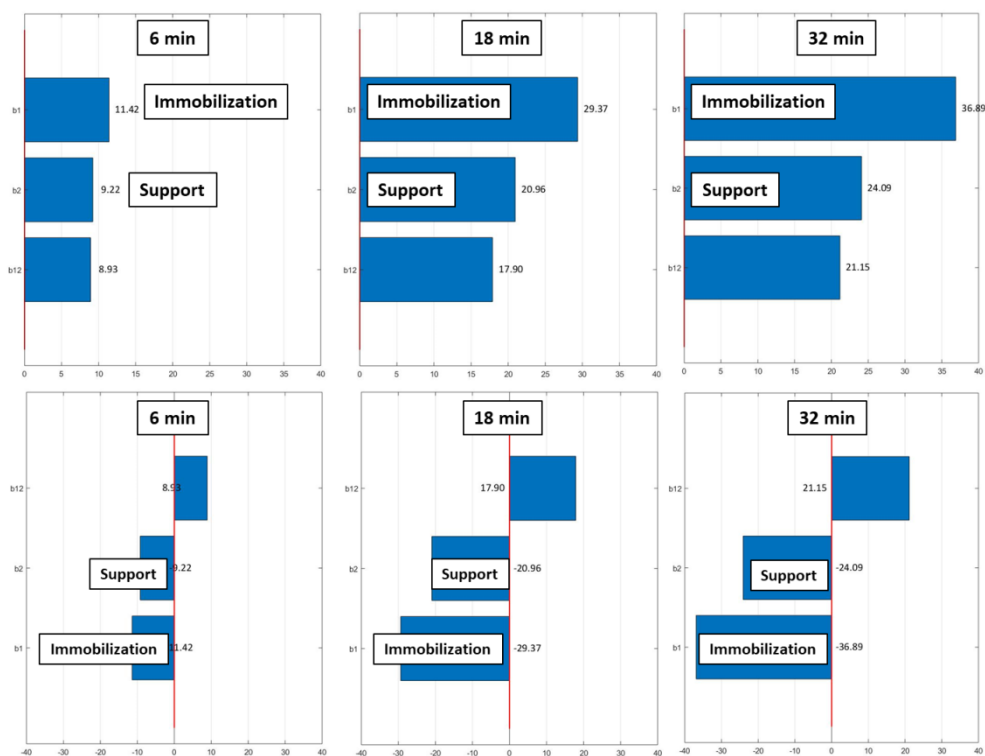


Figure 6.26. Effect of the immobilization process and the supports on the 1-octyne conversion at different reaction times. Up the plot of effects and down the Pareto plots.

The effects of the immobilization process and supports on the 1-octyne conversion were estimated at three different reaction times to verify if the observed trends remained constant over time.

From these plots it could be concluded that both factors were affecting the 1-octyne conversion, however the immobilization process prevailed over the support. These results indicate that the one pot synthesis enabled obtaining higher activities than the two-step procedure. To confirm this trend, an additional test using the corresponding one pot catalyst supported on  $\text{TiO}_2$  would be useful.

The difference in activity between the one pot **Pd-PAM/AC 9** and **Pd-PAM/  $\alpha\text{-Al}_2\text{O}_3$  5** could be related to the difference in NPs sizes: smaller NPs were obtained on AC (*ca.* 3.6 nm vs. 4.8 nm).

Even if full 1-octyne conversion was not always reached, the selectivity towards the 1-octene was estimated using the equation (6.7) presented in section 6.2.5. The

evolution of 1-octene selectivity as a function of 1-octyne conversion for each tested catalyst was plotted and is presented in Figure 6.27.

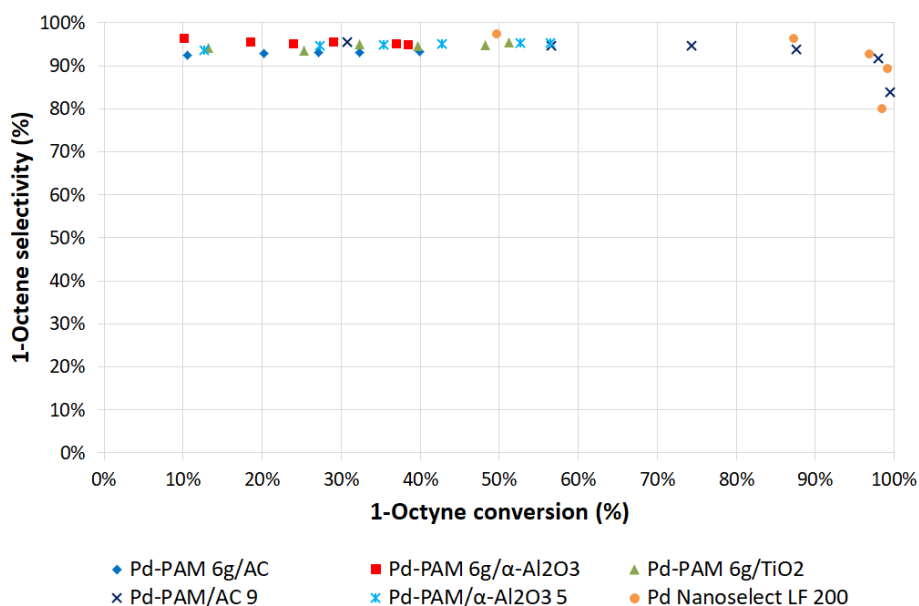


Figure 6.27 Selective hydrogenation of 1-octyne in stirred tank reactor. Evolution of the 1-octene selectivity as a function of the 1-octyne conversion for the tested Pd-PAM supported catalysts and the commercial reference **Pd Nanoselect LF 200**

For all the tested catalysts, the selectivity towards 1-octene remained constant around 95% until 40% of 1-octyne conversion for the two-step **Pd-PAM 6g/α-Al<sub>2</sub>O<sub>3</sub>** and **Pd-PAM 6g/AC** and until 50% of 1-octyne conversion for the two-step **Pd-PAM 6g/TiO<sub>2</sub>** and the one pot **Pd-PAM/ α-Al<sub>2</sub>O<sub>3</sub> 5**.

Interestingly, the **Pd-PAM/AC 9** catalyst showed similar trends than the reference **Pd Nanoselect LF 200**. The selectivity towards 1-octene remained equal to 95% until *ca.* 88% of 1-octyne conversion. After that, a decrease to 90% of 1-octene selectivity was observed at 1-octyne conversion of 98%.

To get more information about the **Pd-PAM/AC 9** catalyst, three additional experiments following the fractional factorial design  $2^{3-1}$  could be performed in order to obtain its kinetic parameters and understand better why its performances are more similar to the **Pd Nanoselect LF 200** than the other Pd-PAM catalysts.

## 6.5. Conclusions

In this chapter, the DOE methodology was applied to study the catalytic performances of novel Pd-PAM nanocatalysts in the selective hydrogenation of 1-octyne. The effects of 1-octyne concentration, hydrogen pressure and temperature were studied on the 1-octyne conversion and reaction rate and the kinetic parameters were determined. Prior to the set of experiments, the kinetic regime was verified.

The main conclusions of this study are detailed as follow.

- For the reference **Pd Nanoselect LF 200**, it was determined that the three main parameters (1-octyne concentration, hydrogen pressure and temperature) were highly affecting the 1-octyne conversion. Interaction effects were not significant. Low concentration combined with high hydrogen pressure and temperature led to high conversion at 12 minutes of reaction. Similar results were obtained for three tested Pd-PAM catalysts (prepared in two steps).
- For the reference **Pd Nanoselect LF 200**, the 1-octyne concentration had no effect on the reaction rate. Only the hydrogen pressure, the temperature and the interaction between both parameters affected the reaction rate. The same trend was confirmed for the **Pd-PAM 6g/AC** and **Pd-PAM 6g/ $\alpha$ -Al<sub>2</sub>O<sub>3</sub>**. In the case of the **Pd-PAM 6g/TiO<sub>2</sub>**, the effect of the 1-octyne concentration was slightly higher, however the system could be well-described just by considering the influence of hydrogen pressure and temperature.
- The kinetic expressions of the reference **Pd Nanoselect LF 200** and the three novel Pd-PAM catalysts synthesized in two steps were determined with only 24 catalytic experiments. Using these expressions, the performances of these catalysts were compared in the selective hydrogenation of 1-octyne.
- The newly synthesized catalysts stabilized by polyacrylamide were all less active than the commercial reference.

- The three two-step Pd-PAM catalysts were compared between each other. Under low temperature conditions (30°C), **Pd-PAM 6g/AC** was the least active catalyst and **Pd-PAM 6g/ $\alpha$ -Al<sub>2</sub>O<sub>3</sub>** the most active. In contrast, at high temperature (50°C) the most active catalyst was the **Pd-PAM 6g/TiO<sub>2</sub>**.
- The reaction rate of **Pd-PAM 6g/ $\alpha$ -Al<sub>2</sub>O<sub>3</sub>** catalyst at high pressure (14 bar) was the fastest one at low temperature and the slower one at high temperature, indicating that the comparison of different catalysts highly depends on the reaction conditions.
- The performances of the three Pd-PAM catalysts supported by two steps were compared with two other Pd-PAM catalysts obtained by one pot under one set of reaction conditions. The **Pd-PAM/AC 9** was highlighted (one pot catalyst that contains 0.6 wt% of Pd), showing high activity and values of 1-octene selectivity similar to those of the reference catalyst.
- The differences in activity were related to the effect of the immobilization methodology and the nature of the support used: one pot procedure and activated carbon support provided higher activities.

## 6.6. Perspectives

The kinetic study presented in this chapter provided information on the catalysts activities. However, one of the major challenges of the catalyst design for the alkyne hydrogenation reactions is to provide highly selective catalysts to avoid over-hydrogenation of the alkenes.

To obtain information about the selectivity of the tested catalyst in the selective hydrogenation of 1-octyne, a proposition of additional experiments is detailed in this section.

According to the mass balance given in section 6.3.3.2. the 1-octene concentration at a time  $t$  depends on its formation rate ( $r_1$ ) and its consumption rate ( $r_2 + r_3$ ).

$$\frac{d[1E]}{dt} = \frac{m_{cat}}{V_L} (r_1 - r_2 - r_3) \quad (6.13)$$

The 1-octene formation rate was determined at initial 1-octyne reaction rates by the kinetic study presented in this chapter.

To obtain information about the 1-octene consumption, pure 1-octene hydrogenation experiments following a full factorial design  $2^3$  similar to the one presented in section 6.3.2.3. could be implemented.

Considering these experiments where the 1-octene would be the only reagent, the equations (6.9) and (6.10) could be simplified for initial conditions:

$$r_2^0 = k_2 \frac{K_{1E-H} K_{1E} [1E] K_H [H_2]}{(1 + K_{1E} [1E] + K_H^{1/2} [H_2]^{1/2})^2}. \quad (6.41)$$

$$r_3^0 = k_3 \frac{K_{1E} [1E]}{1 + K_{1E} [1E] + K_H^{1/2} [H_2]^{1/2}}. \quad (6.42)$$

These expressions can be combined as  $r_{1E}^0 = r_2^0 + r_3^0$  and written as a simple power rate law expression to describe the 1-octene consumption rate:

$$r_{1E}^0 = k'_{1E} [1E]^n [H_2]^m \quad (6.43)$$

Where  $n, m$  are respectively the reaction order towards 1-octene and hydrogen and:

$$k'_{1E} = \frac{k_2 K_{1E-H} K_{1E} K_H + k_3 \frac{1 + K_{1E} [1E] + K_H^{1/2} [H_2]^{1/2}}{[H_2]}}{(1 + K_{1E} [1E] + K_H^{1/2} [H_2]^{1/2})^2} \quad (6.44)$$

The resulting expression could be linearized:

$$\ln r_{1E}^0 = \ln A + n(\ln [1E]) + m(\ln [H_2]) - \frac{Ea}{R} \left( \frac{1}{T} \right) \quad (6.45)$$

Through the variation of the 1-octene concentration, hydrogen pressure and temperature following a full factorial design  $2^3$ , the reaction orders, activation energy and pre-exponential factor could be determined. Therefore the evolution of the 1-octene concentration over time would be determined as:

$$\frac{d[1E]}{dt} = -\frac{m_{cat}}{V_L}(-r_1 + r_{1E}) \quad (6.13)$$

The maximum of this function would give the reaction conditions in which the 1-octene concentration would be higher and thus information about the 1-octene selectivity could be obtain for the studied catalysts.



## 6.7. Appendix

### 6.7.1. Appendix 1: Estimation of the measurement uncertainty with the differential method

The standard deviation of the analytical method was estimated by preparing and analyzing two GC-MS vials from one sample and using the following equation:

$$s_f^2 = \left(\frac{\partial f}{\partial x_1}\right)^2 s_{x_1}^2 + \left(\frac{\partial f}{\partial x_2}\right)^2 s_{x_2}^2 + \dots + \left(\frac{\partial f}{\partial x_n}\right)^2 s_{x_n}^2$$

Where  $f$  is the studied function,  $x_1, x_2, \dots, x_n$  are independent parameters and  $s_{x_1}, s_{x_2}, \dots, s_{x_n}$  their respective uncertainties.

- Estimation of the measurement uncertainty on the **molar fraction**:

$$f = x_{Y,t} = \frac{[Y]_t}{[Y]_t + [E]_t + [A]_t + [I1]_t + [I2]_t}$$

Where  $Y$  is the 1-octyne,  $E$  the 1-octene,  $A$  the n-octane,  $I1$  and  $I2$  the isomer 1 and 2 that can potentially be observed. The uncertainty on the 1-octyne molar fraction was obtained through the following equation:

$$s_{Y,t}^2 = \frac{1}{([Y] + [E] + [A] + [I1] + [I2])^4} [( [E] + [A] + [I1] + [I2] )^2 s_Y^2 + [Y]^2 (s_E^2 + s_A^2 + s_{I1}^2 + s_{I2}^2)]$$

- Estimation of the measurement uncertainty on the **1-octyne conversion** calculating by the equation (6.1):

$$f = X_{Y1,t} = (1 - x_{Y,t}) \times 100$$

Where  $x_{Y,0}$  is the molar fraction of 1-octyne at  $t_0$  and  $x_{Y,t}$  the molar fraction of 1-octyne at  $t$ . The uncertainty on the 1-octyne conversion was obtained by the following equation:

$$s_{X_{Y1,t}}^2 = \left(\frac{\partial X_{Y1,t}}{\partial x_{Y,t}}\right)^2 s_{x_{Y,t}}^2$$

$$s_{X_{Y1,t}}^2 = 100 \times s_{x_{Y,t}}^2$$

- Estimation of the measurement uncertainty on the **1-octyne conversion** calculating by the equation (6.2):

$$f = X_{Y2,t} = \frac{[Y]_0 - [Y]_t}{[Y]_0} \times 100$$

Where  $[Y]_0$  is the 1-octyne concentration at  $t_0$  and  $[Y]_t$  the 1-octyne concentration at  $t$ . The uncertainty on the 1-octyne conversion was obtained by the following equation:

$$s_{X_{Y2,t}}^2 = \left( \frac{\partial X_{Y2,t}}{\partial [Y]_0} \right)^2 s_{[Y]_0}^2 + \left( \frac{\partial X_{Y2,t}}{\partial [Y]_t} \right)^2 s_{[Y]_t}^2$$

$$s_{X_{Y2,t}}^2 = \frac{100}{[Y]_0^2} \left( \frac{[Y]_t^2}{[Y]_0^2} s_{[Y]_0}^2 + s_{[Y]_t}^2 \right)$$

- Estimation of the measurement uncertainty on the **1-octyne conversion** calculated by the equation (6.3):

$$f = X_{Y3,t} = \frac{[E]_t - [E]_0}{[Y]_0} \times 100$$

Where  $[Y]_0$  is the 1-octyne concentration at  $t_0$ ,  $[E]_0$  is the 1-octene concentration at  $t_0$  and  $[E]_t$  the 1-octene concentration at  $t$ . The uncertainty on the 1-octyne conversion was obtained by the following equation:

$$s_{X_{Y3,t}}^2 = \left( \frac{\partial X_{Y3,t}}{\partial [E]_t} \right)^2 s_{[E]_t}^2 + \left( \frac{\partial X_{Y3,t}}{\partial [E]_0} \right)^2 s_{[E]_0}^2 + \left( \frac{\partial X_{Y3,t}}{\partial [Y]_0} \right)^2 s_{[Y]_0}^2$$

$$s_{X_{Y3,t}}^2 = \frac{100}{[Y]_0^2} [s_{[E]_t}^2 + s_{[E]_0}^2 + ([E]_t - [E]_0)^2 s_{[Y]_0}^2]$$

- Estimation of the measurement uncertainty on the **reaction rate** calculated by the equation (6.4)(6.3):

$$f = r_2 = [Y]_0 \frac{dX_{Y,t}}{dt} = [Y]_0 \frac{X_{Y,2} - X_{Y,1}}{t_2 - t_1} \times \frac{V}{60} \times \frac{1}{molPd}$$

Where  $X_{Y,1}$  and  $X_{Y,2}$  are the 1-octyne conversions at  $t_1$  and  $t_2$ , respectively. The uncertainty on the reaction rate was obtained by the following equation:

$$s_{r_2}^2 = \left( \frac{\partial r_2}{\partial [Y]_0} \right)^2 s_{[Y]_0}^2 + \left( \frac{\partial r_2}{\partial X_{Y,2}} \right)^2 s_{X_{Y,2}}^2 + \left( \frac{\partial r_2}{\partial X_{Y,1}} \right)^2 s_{X_{Y,1}}^2$$

$$s_{r_2}^2 = \left[ \frac{V}{60(t_2 - t_1) \text{molPd}} \right]^2 \left[ (X_{Y,2} - X_{Y,1})^2 s_{[Y]_0}^2 + [Y]_0^2 (s_{X_{Y,2}}^2 + s_{X_{Y,1}}^2) \right]$$

- Estimation of the measurement uncertainty on the **reaction rate** calculated by the equation (6.5):

$$f = r_1 = \frac{-d[Y]_t}{dt} = -\frac{[Y]_2 - [Y]_1}{t_2 - t_1} \times \frac{V}{60} \times \frac{1}{\text{molPd}}$$

Where  $[Y]_1$  and  $[Y]_2$  are the 1-octyne concentrations at  $t_1$  and  $t_2$ , respectively. The uncertainty on the reaction rate was obtained by the following equation:

$$s_{r_1}^2 = \left( \frac{\partial r_1}{\partial [Y]_2} \right)^2 s_{[Y]_2}^2 + \left( \frac{\partial r_1}{\partial [Y]_1} \right)^2 s_{[Y]_1}^2$$

$$s_{r_1}^2 = \left[ \frac{V}{60(t_2 - t_1) \text{molPd}} \right]^2 (s_{[Y]_2}^2 + s_{[Y]_1}^2)$$

- Estimation of the measurement uncertainty on the **reaction rate** calculated by the equation (6.6):

$$f = r_3 = \frac{d[E]_t}{dt} = \frac{[E]_2 - [E]_1}{t_2 - t_1} \times \frac{V}{60} \times \frac{1}{\text{molPd}}$$

Where  $[E]_1$  and  $[E]_2$  are the 1-octene concentrations at  $t_1$  and  $t_2$ , respectively. The uncertainty on the reaction rate was obtained by the following equation:

$$s_{r_3}^2 = \left( \frac{\partial r_3}{\partial [E]_2} \right)^2 s_{[E]_2}^2 + \left( \frac{\partial r_3}{\partial [E]_1} \right)^2 s_{[E]_1}^2$$

$$s_{r_3}^2 = \left[ \frac{V}{60(t_2 - t_1) \text{molPd}} \right]^2 (s_{[E]_2}^2 + s_{[E]_1}^2)$$

## 6.7.2. Appendix 2: 1-Octyne conversion and reaction rate results obtained following the fractional factorial design $2^{3-1}$ for the Pd-PAM catalysts

**Experimental plan**

RUN	$[Y]$ $mol.L^{-1}$	$P_{H_2}$ $bar$	$T$ $^{\circ}C$
	1	2	3 = -12
1	0.34 (-1)	6.00 (-1)	30.00 (-1)
4	0.68 (+1)	14.00 (+1)	30.00 (-1)
6	0.68 (+1)	6.00 (-1)	50.00 (+1)
7	0.34 (-1)	14.00 (+1)	50.00 (+1)
9	0.51 (0)	10.00 (0)	40.00 (0)

### Pd-PAM 6g/AC

RUN	Conversion 1 $X_{Y1,t}$ (%)	Rate 1 $r_1$ ( $mol.molPd^{-1}.s^{-1}$ )
1	$4.6 \pm 0.1$	$1.4 \pm 0.1$
4	$6.1 \pm 0.0$	$3.9 \pm 0.2$
6	$5.3 \pm 0.1$	$3.6 \pm 0.3$
7	$20.2 \pm 1.6$	$8.7 \pm 1.6$
9	$7.1 \pm 0.4$	$3.9 \pm 0.6$

### Pd-PAM 6g/ $\alpha$ -Al<sub>2</sub>O<sub>3</sub>

RUN	Conversion 1 $X_{Y1,t}$ (%)	Rate 1 $r_1$ ( $mol.molPd^{-1}.s^{-1}$ )
1	$6.0 \pm 0.2$	$3.1 \pm 0.3$
4	$5.6 \pm 0.1$	$4.8 \pm 0.3$
6	$4.1 \pm 0.1$	$4.1 \pm 0.3$
7	$18.6 \pm 1.0$	$8.0 \pm 1.0$
9	$6.9 \pm 0.1$	$5.6 \pm 0.2$

### Pd-PAM 6g/TiO<sub>2</sub>

RUN	Conversion 1 $X_{Y1,t}$ (%)	Rate 1 $r_1$ ( $mol.molPd^{-1}.s^{-1}$ )
1	$7.4 \pm 0.2$	$2.9 \pm 0.3$
4	$6.9 \pm 0.2$	$4.4 \pm 0.4$
6	$6.1 \pm 0.1$	$4.8 \pm 0.3$
7	$25.3 \pm 0.1$	$11.7 \pm 0.2$
9	$8.3 \pm 0.2$	$5.1 \pm 0.4$

## 6.8. References

- (1) Crespo-Quesada, M.; Cárdenas-Lizana, F.; Dessimoz, A.-L.; Kiwi-Minsker, L. *ACS Catal.* **2012**, *2*, 1773.
- (2) Hugon, A.; Delannoy, L.; Krafft, J.-M.; Louis, C. *J. Phys. Chem. C* **2010**, *114*, 10823.
- (3) Zhang, Y.; Diao, W.; Williams, C. T.; Monnier, J. R. *Appl. Catal., A* **2014**, *469*, 419.
- (4) Semagina, N.; Renken, A.; Kiwi-Minsker, L. *Chem. Eng. Sci.* **2007**, *62*, 5344.
- (5) Maccarrone, M.; Torres, G.; Lederhos, C.; Badano, J.; Vera, C.; Quiroga, M.; Yori, J. J. *Chem. Technol. Biotechnol.* **2012**, *87*, 1521.
- (6) Lopez, N.; Vargas-Fuentes, C. *Chem. Commun.* **2012**, *48*, 1379.
- (7) Odom, T. W.; Pileni, M.-P. *Acc. Chem. Res.* **2008**, *41*, 1565.
- (8) Witte, P. T. *Process for the preparation of an aqueous colloidal precious metal suspension*, US Patent 8,822,725 B2 **2014**.
- (9) Alves, J. A.; Bressa, S. P.; Martínez, O. M.; Barreto, G. F. *Chem. Eng. J.* **2007**, *125*, 131.
- (10) Ayranci, I.; Kresta, S.; Shen, J.; Semagina, N. *Ind. Eng. Chem. Res.* **2014**, *53*, 18091.
- (11) Brown, C. A.; Ahuja, V. K. *J. Org. Chem.* **1973**, *38*, 2226.
- (12) Phua, P.-H.; Lefort, L.; Boogers, J. A. F.; Tristany, M.; de Vries, J. G. *Chem. Commun.* **2009**, 3747.
- (13) Klaewkla, R.; Arend, M.; Hoelderich, W. F. *Intech* **2011**, 667.
- (14) Ardiaca, N. O.; Bressa, S. P.; Alves, J. A.; Martínez, O. M.; Barreto, G. F. *Catal. Today* **2001**, *64*, 205.
- (15) Maccarrone, M. J.; Torre, G. C.; Lederhos, C.; Betti, C.; Badano, J. M.; Quiroga, M.; Yori, J. *Intech* **2012**, Chapter 7, 159.
- (16) Crespo-Quesada, M.; Grasemann, M.; Semagina, N.; Renken, A.; Kiwi-Minsker, L. *Catal. Today* **2009**, *147*, 247.
- (17) Fogler, H. S. *Elements of chemical reaction engineering*; Fourth ed., 1999.
- (18) ASTM D4781-03, Standard Test Method for Mechanically Tapped Packing Density of Fine Catalyst Particles and Catalyst Carrier Particles, 2018, [www.astm.org](http://www.astm.org).
- (19) Varela, S.; Martínez, M.; Delgado, J. A.; Godard, C.; Curulla-Ferré, D.; Pallares, J.; Vernet, A. *J. Ind. and Eng. Chem.* **2018**, *60*, 286.
- (20) Box, G. E. P.; Hunter, W. G.; Hunter, J. S. *Statistics for Experimenters: An Introduction to Design, Data Analysis, and Model Building*, 1978.
- (21) Zhu, J.; Wu, F.; Li, M.; Zhu, J.; van Ommen, J. G.; Lefferts, L. *App. Catal. A Gen.* **2015**, *498*, 222.
- (22) Haber, J.; Block, J. H.; Delmon, B. *Pure & Appl. Chem.* **1995**, *67*, 1257.
- (23) Berenblyum, A. S.; Al-Wadhaf, H. A.; Katsman, E. A. *Pet. Chem.* **2015**, *55*, 118.

# Chapter 7

This chapter is subject to a confidentiality  
agreement (property of Total Research &  
Technology Feluy)



# Chapter 8

## General conclusions





The work of this thesis focused on the design of new Pd-based nanocatalysts for application in alkyne semi-hydrogenation reactions.

The knowledge generated from this thesis led to the conclusions stated below.

- OFAT and DOE approaches allowed the identification of several parameters that affect the formation of novel Pd-polyacrlamide NPs. Short synthesis time, low temperature, low polymer-to-Pd ratio, low Pd concentration and high stirring rate resulted to improve the NPs shape, distribution and synthesis efficiency. The NPs sizes remained between 3 and 5 nm.
- Criteria to estimate the fraction of spherical NPs and agglomerates in the TEM samples using automatic measurements were determined.
- Recipes of well-defined Pd-polyacrylamide NPs were delivered.
- The immobilization of these Pd-polyacrylamide NPs on AC,  $\alpha$ -Al<sub>2</sub>O<sub>3</sub> and TiO<sub>2</sub> supports was achieved by two processes: one pot and two-step synthesis.
- Using the one pot procedure, the temperature and the nature of the support affected the NPs size while the Pd content did not show any significant effect.
- Using the two-step procedure, the NPs size of the colloidal suspension remained constant after the immobilization process.
- The NPs dispersion, observed by ESEM, was affected by the nature of the support and the scale of the synthesis. The agglomerate were the smallest on TiO<sub>2</sub> and the largest on AC. The two-step immobilization performed at large scale provided better NPs dispersion.
- Recipes of well-defined supported Pd-polyacrylamide catalysts prepared by one pot and two steps were delivered.
- The reproduction of the patented recipe of Pd-HHDMA NPs (colloidal NPs used to prepare the commercial Pd Nanoselect catalyst) was achieved and demonstrated by Kolmogorov-Smirnov statistical test.
- The structure-synthesis relationship study on these NPs was performed using DOE methodology. Analyses of variance were used to identify the significant factor contributions and to obtain the possible empirical models that

described the system. Wide amount of factors and interactions affected the NPs formation demonstrating the high complexity of this system.

- These Pd-HHDMA NPs were immobilized on two types of AC support by a two-step synthesis.
- DOE methodology was applied to study the performances of novel Pd-polyacrylamide nanocatalysts in the selective hydrogenation of 1-octyne in stirred tank reactor. The 1-octyne concentration, hydrogen pressure and temperature highly affected the 1-octyne conversion while the reaction rate did not depend on the 1-octyne concentration.
- The kinetic study of 1-octyne hydrogenation over a reference catalyst (Pd Nanoselect LF 200) and three Pd-polyacrylamide catalysts was performed and showed that the newly synthesized catalysts were less active than the reference under the studied reaction conditions. The three newly synthesized Pd-PAM catalysts were compared between each other: under low temperature conditions, the Pd-PAM/AC was the least active and the Pd-PAM/ $\alpha$ -Al<sub>2</sub>O<sub>3</sub> was the most active. However, at high temperature the most active catalyst was the Pd-PAM/TiO<sub>2</sub>.
- Five Pd-PAM catalysts were compared under one set of reaction conditions (three prepared by two steps and two prepared by one pot). The catalysts prepared by one pot were the most active and the catalyst supported on AC revealed similar performances to those of the reference catalyst.
- The conclusions of the chapter 7 are subject to a confidentiality agreement with Total Research & Technology Feluy.

# Appendix



## Short CV

In this section a brief Curriculum Vitae of the doctoral student is presented.

Name: Olivia Benkirane

Born: June 15, 1990 – Lille, France

### Education

- PhD in Nanocatalysis financed by TOTAL Research & Technology Feluy (from March 2015)  
Universitat Rovira I Virgili & Centre Tecnològic de la Química (Tarragona, Spain)
- Intensive course of Life Cycle Assessment including modelling with GaBi (September 2017)  
RWTH Aachen University
- Master Degree in Chemical Engineering – Specialization in Process Engineering (2010 – 2013)  
Ecole Nationale Supérieure des Industries Chimiques (ENSIC) (Nancy, France)
- Classe Préparatoire Intégrée (2008 – 2010)  
Ecole National Supérieure de Chimie de Lille (ENSCL) (Lille, France)

### Work experience

- RESEARCHER in TOTAL Research & Technology Feluy/Universitat Rovira i Virgili (from March 2015)  
Tarragona, Spain and Brussels, Belgium  
Design of nanocatalysts for the selective hydrogenation of alkynes:
  - Structure-synthesis relationship study of colloidal and supported nanoparticles using design of experiments
  - Catalytic tests in stirred tank reactor and fixed bed reactor

- Kinetic study in stirred tank reactor using design of experiments
  - Characterization techniques: (HR)TEM, ESEM, XRD, TGA, ICP, GC-MS
  - People management
  
- PROCESS ENGINEER in AREVA NP  
(April 2013 – April 2014)  
Pierrelatte, France  
Engineering assistance in nuclear safety and process/equipment design
  - Preliminary Hazard Analysis (PHA), HAZard and Operability study (HAZOP) and Explosion Risk Assessment based on ATEX on a nitrate treatment unit
  - Calculation of equipment pressures from P&ID of different units to comply with the Pressure Equipment Directive
  - Jacketed heat exchanger sizing
  - Optimization of a gas treatment process within a nitrate treatment unit (benchmarking, technical analysis and cost estimation)
  
- PROCESS ENGINEER in collaboration with TECHNIP  
(January 2012 – May 2012)  
Industrial project in a team of 5 students in collaboration with TECHNIP engineers. Design of a methanol production process:
  - Reaction kinetics
  - Equipment selection and sizing
  - Process simulation and optimization with Pro II
  - PFD and P&ID drawings

## Publications based on the content of this thesis

- Delgado, J. A.; Benkirane O.; Claver, C.; Curulla-Ferré, D. and Godard, C. Advances in the preparation of highly selective nanocatalysts for the semi-hydrogenation of alkynes using colloidal approaches. *Dalton Trans.*, 2017, 46, 12381-12403.  
<http://doi.org/10.1039/C7DT01607G>
- Benkirane O.; Claver, C.; Ferré, J.; Curulla-Ferré, D. and Godard C. Structure synthesis relationship study of Pd-polyacrylamide NPs using design of experiments. *Manuscript in preparation*
- Benkirane O.; Claver, C.; Ferré, J.; Curulla-Ferré, D. and Godard C. Kinetics of 1-octyne hydrogenation over Pd-based catalysts using design of experiments. *Manuscript in preparation*

## Congress and scientific meetings

- 7<sup>th</sup> Franco-Catalan meeting, 1<sup>st</sup> HC3A meeting: “Hetero elements and coordination chemistry: from concepts to applications”, 26-27<sup>th</sup> January 2016, Toulouse, France.
- XXXIV GEQO congress (Grupo Especializado de Química Organometálica) 7-9<sup>th</sup> September 2016, Gerona, Spain.  
Poster contribution: “Design of novel low cost and reusable heterogeneous Pd nanocatalyst for the selective hydrogenation of alkynes”
- 6<sup>th</sup> EuChemS chemistry congress (European Chemical Society), 11-15<sup>th</sup> September 2016, Sevilla, Spain.  
Poster contribution: “Design of novel low cost and reusable heterogeneous Pd nanocatalyst for selective hydrogenation of alkynes and alkynols”
- XXXVI Bienal de la RSEQ (Real Sociedad Española de Química), 25-29<sup>th</sup> 2017, Sitges, Spain.  
Poster contribution: “Design of novel heterogeneous Pd nanocatalysts for the selective hydrogenation of alkynes”



- TraPCat<sup>2</sup> 2<sup>nd</sup> Trans Pyrenean Meeting in Catalysis, 18-19<sup>th</sup> 2018, Tarragona, Spain.

Poster contribution: “Structure-synthesis relationship study of colloidal Pd-polyacrylamide NPs using design of experiments”

## Stages

Stages at Total Research & Technology Feluy, Seneffe, Belgium from 16<sup>th</sup> October 2017 to 23<sup>th</sup> February 2018.

- Investigation about the synthesis of nanocatalysts via colloidal approach using design of experiments
- Characterization of heterogeneous catalysts
- Catalytic selective hydrogenation of alkynes in stirred tank reactor using design of experiments







